Addressing the data gap in adsorption materials for direct air capture - an investigation of physicochemical, equilibrium sorption, and kinetic sorption properties

by

May-Yin (Ashlyn) Low

submitted to the

Department of Chemical Engineering

Imperial College London

in fulfilment of the requirements for the degree of

Doctor of Philosophy

under the supervision of

Professor Camille Petit

April 2024

Abstract

Using adsorbents for direct air capture (DAC) is a promising and necessary carbon dioxide removal technology for climate change mitigation. However, the deployment of adsorption-based DAC technologies at scale still needs to be greatly accelerated. One area of focus is the development of new adsorbent materials for DAC, which subsequently need to be screened via process modelling and optimisation to assess their process scale performance. Yet, the adsorbent data needed to conduct this evaluation is rarely available.

This thesis aims to address this gap by measuring the physicochemical, equilibrium sorption, and kinetic sorption properties needed to facilitate the process scale evaluation of select adsorbents that represent three distinct classes of materials: polymeric resins, metal organic frameworks (MOFs), and zeolites. Polymeric resins are commercially available, and their amine functionality imparts high CO_2 adsorption. Here, I conducted the first assessment of Purolite A110 for DAC and found that it often surpasses the adsorption performance of a benchmark DAC adsorbent, Lewatit VP OC 1065. Amongst MOFs, ultramicroporous MOFs exhibit high CO_2 affinity and relatively low heat of adsorption. Here, I investigated TIFSIX-3-Ni and showed it could be a promising DAC adsorbent in terms of its CO_2 uptake and manufacturability, but with limited stability under certain process conditions. Finally, zeolites are an industrially established class of adsorbents, though their hydrophilicity and relatively low CO_2 adsorption at low pressure can be an obstacle for DAC. Here, I functionalised a commercially available "hydrophobic" zeolite with amine groups to combine hydrophobicity and CO_2-philicity. Yet, the results showed that functionalisation caused poor CO_2 adsorption kinetics and/or increased H_2O adsorption.

Overall, this thesis increases the synergy between adsorbent and process development for DAC. The new adsorbent data provided can now facilitate process scale evaluation of these adsorbents, which can help advance the deployment of adsorption-based DAC technologies.

Statement of originality

I hereby declare that the work presented in this thesis is my own and all else is appropriately referenced.

Copyright declaration

The copyright of this thesis rests with the author. Unless otherwise indicated, its contents are licensed under a Creative Commons Attribution-Non Commercial 4.0 International Licence (CC BY-NC).

Under this licence, you may copy and redistribute the material in any medium or format. You may also create and distribute modified versions of the work. This is on the condition that: you credit the author and do not use it, or any derivative works, for a commercial purpose.

When reusing or sharing this work, ensure you make the licence terms clear to others by naming the licence and linking to the licence text. Where a work has been adapted, you should indicate that the work has been changed and describe those changes.

Please seek permission from the copyright holder for uses of this work that are not included in this licence or permitted under UK Copyright Law.

Acknowledgements

First and foremost, I would like to thank my PhD supervisor, Professor Camille Petit, for guiding me through this journey. You have been the best mentor and role model I could have asked for, and I am so grateful for your constant support, patience, and wisdom throughout these past few years.

The next big thank you goes to Dr. David Danaci, who has been my friend and mentor since the first day I started my PhD. This journey has been a rollercoaster with many ups and downs, and I could not have gotten through it all without your constant support. Thank you for everything you have done for me, and I am so grateful to have made a life-long friend.

I give thanks to Imperial College London for offering me the President's PhD scholarship which allowed me to travel from overseas to pursue this degree. Thank you as well to the Department of Chemical Engineering for extending this financial support during the last few months of my PhD.

I would like to thank past and present members of the Petit group, who have helped to provide the most enjoyable and supportive work environment. I consider myself so lucky to be able to work with such amazing colleagues and friends every day.

Big thanks as well to my Imperial College Outdoor Club friends who have become a second family to me here in London. Our adventures together have been some of the best highlights of my time here and I am looking forward to many more adventures together in the future.

Finally, I want to give thanks to my family for their unconditional love and support. Thank you to my parents for being OK with me leaving home to pursue this journey halfway around the world, and for instilling in me the belief that I can accomplish whatever I set my mind to. Thank you to my grandparents for always showering me with love and doing whatever they can to help me succeed in my studies. To my Popo, who cooked endless delicious meals for me so that my brain was always properly fuelled (especially during exam time), and to my Nong Nong, who drove me to school every day for four years and often brought me a hot lunch which everyone else was usually jealous of.

This PhD has been an amazing journey, and I thank everyone who played a part in it over the last four and a half years, no matter how small. Now, onwards to the next adventure!

Publications

1. **M.-Y. Low**, L. V. Barton, R. Pini, and C. Petit, "Analytical review of the current state of knowledge of adsorption materials and processes for direct air capture," *Chemical Engineering Research and Design,* vol. 189, pp. 745-767, 2023, doi: 10.1016/j.cherd.2022.11.040.

2. **M.-Y. Low**, D. Danaci, H. Azzan, R. T. Woodward, and C. Petit, "Measurement of Physicochemical Properties and CO_2, N_2, Ar, O_2, and H_2O Unary Adsorption Isotherms of Purolite A110 and Lewatit VP OC 1065 for Application in Direct Air Capture," *Journal of Chemical & Engineering Data,* vol. 68, no. 12, pp. 3499-3511, 2023, doi: 10.1021/acs.jced.3c00401.

3. **M.-Y. Low** *et al.*, "Physicochemical properties, equilibrium adsorption performance, manufacturability, and stability of TIFSIX-3-Ni for direct air capture of CO_2," *Energy Fuels,* vol. 38, no. 13, pp. 11947-11965, 2024, doi: 10.1021/acs.energyfuels.4c01368.

4. **M.-Y. Low**, D. Danaci, C. Sturman, and C. Petit, "Quantification of temperature-dependent CO_2 adsorption kinetics in Lewatit VP OC 1065, Purolite A110, and TIFSIX-3-Ni for direct air capture," *In preparation.*

Conferences

Oral presentations:

- Imperial College Chemical Engineering PhD Symposium, London, UK (2022)
- Imperial College President's PhD Scholars Symposium, London, UK (2022)
- UK Porous Materials Conference, Sheffield, UK (2023)
- Imperial College Chemical Engineering PhD Symposium, London, UK (2023) – 3rd prize
- 3P Instruments Online Symposium on Sorption, online event (2023) – invited speaker

Poster presentations:

- Fundamentals of Adsorption 14th International Conference, Colorado, US (2022)
- International Adsorption Society Twitter Conference, online event (2022) – 1st prize
- Gordon Research Conference on Carbon Capture, Utilization and Storage, Vaud, Switzerland (2023) – 1st prize

Table of contents

Abstract 2
Statement of originality 3
Copyright declaration 3
Acknowledgements 4
Publications 5
Conferences 6
Table of contents 7
List of abbreviations 12
List of figures 16
List of tables 20
Chapter 1: Introduction 21
1.1 Background 21
1.2 Thesis overview 22
Chapter 2: Literature review 23
2.1 Overview of adsorption-based DAC 23
2.1.1 DAC adsorption process 24
2.1.2 Current state of deployment 25
2.1.3 Technical challenges 26
2.1.4 Screening adsorbents for DAC 28
2.2 Characterisation of DAC adsorbents 29
2.2.1 Physicochemical properties 30
2.2.1.1 Skeletal density 32
2.2.1.2 Particle density 32
2.2.1.3 Bed density 33
2.2.1.4 Mechanical stability 34
2.2.1.5 Surface area 34
2.2.1.6 Pore volume 35
2.2.1.7 Specific heat capacity 35
2.2.1.8 Thermal conductivity 36
2.2.1.9 Thermal stability 37
2.2.2 Equilibrium sorption properties 38
2.2.2.1 CO_2 adsorption 39
2.2.2.2 N_2 adsorption 46
2.2.2.3 O_2 adsorption 46
2.2.2.4 H_2O adsorption 48

2.2.2.5 Cyclic adsorption 51
2.2.3 Kinetic sorption properties 52
2.3 Synergy between adsorbent and process development for DAC 53
Chapter 3. Research objectives 56
Chapter 4: Materials and methods 57
4.1 Chemicals 58
4.2. Adsorbent materials 59
4.2.1 Commercial resins (Chapter 5) 59
4.2.2 TIFSIX-3-Ni (Chapter 6) 59
4.2.2.1 Synthesis of $NiTiF_6 \cdot 6H_2O$ 59
4.2.2.2 Synthesis of TIFSIX-3-Ni 59
4.2.2.3 Pelletisation of TIFSIX-3-Ni powder 60
4.2.3 Amine-functionalised zeolite Y (Chapter 7) 60
4.2.3.1 Aminosilane functionalisation of zeolite Y 60
4.2.3.2. Ammonia functionalisation of zeolite Y 61
4.3. Characterisation of chemical features 61
4.3.1 Fourier transform infrared spectroscopy (FTIR) 61
4.3.2 Elemental analysis 62
4.3.3 X-ray diffraction (XRD) 62
4.3.4 X-ray photoelectron spectroscopy (XPS) 63
4.4. Characterisation of textural properties and density 64
4.4.1 N_2 sorption at -196 °C 64
4.4.2 CO_2 sorption at 0 °C 66
4.4.3 Mercury intrusion porosimetry (MIP) 67
4.4.4 Helium pycnometry 68
4.4.5. Bed density 68
4.4.6 Density and porosity calculations 69
4.4.6.1 Lewatit and Purolite 69
4.4.6.2 TIFSIX-3-Ni 69
4.5. Characterisation of thermal properties 70
4.5.1 Thermogravimetric analysis (TGA) 70
4.5.2 Differential scanning calorimetry (DSC) 70
4.6. Characterisation of equilibrium sorption properties 72
4.6.1 Gas and vapour sorption measurements 72
4.6.2 Isotherm model fittings 73
4.6.3 Isosteric heat of adsorption calculations 74
4.6.4 Limiting heat of adsorption calculations 74

4.7 TIFSIX-3-Ni stability studies 74
4.7.1 Exposure to H_2O only 74
4.7.2 Exposure to O_2 and H_2O (closed environment) 75
4.7.3 Exposure to O_2 and H_2O (atmospheric exposure) 75
4.7.4 Adsorption-desorption cycling 75
Chapter 5: Physicochemical and equilibrium sorption properties of Purolite A110 and Lewatit VP OC 1065 for direct air capture 77
5.1 Introduction 77
5.2 Results and discussion 79
5.2.1 Physicochemical properties 79
5.2.1.1 Chemical and textural properties 79
5.2.1.2 Thermal properties 81
5.2.2 Equilibrium sorption properties 83
5.2.2.1 CO_2 sorption 83
5.2.2.2 N_2, Ar, and O_2 sorption 89
5.2.2.3 H_2O sorption 91
5.2.2.4 Isosteric heats of adsorption 93
5.3 Conclusions 97
Chapter 6: Physicochemical properties, equilibrium adsorption performance, manufacturability, and stability of TIFSIX-3-Ni for direct air capture 98
6.1 Introduction 98
6.2 Results and discussion 100
6.2.1 Physicochemical properties 100
6.2.2 Equilibrium adsorption properties 102
6.2.2.1 CO_2 adsorption 102
6.2.2.2 N_2, Ar, and O_2 adsorption 106
6.2.2.3 H_2O adsorption 107
6.2.2.4 Heats of adsorption 109
6.2.3 Manufacturing considerations 111
6.2.3.1 Batch reproducibility 111
6.2.3.2 Pelletisation 114
6.2.4 Adsorbent stability under process conditions 119
6.2.4.1 Humidity studies 119
6.2.4.2 Cyclic studies 126
6.3 Conclusions 130
Chapter 7: Investigation of amine-functionalised “hydrophobic” zeolite Y adsorbents for direct air capture 132
7.1 Introduction 132

7.2 Results and discussion 134
7.2.1 Physicochemical properties 134
7.2.1.1 Chemical features 134
7.2.1.2 Textural properties 138
7.2.2 Equilibrium sorption properties 140
7.2.2.1 CO_2 sorption 140
7.2.2.2 N_2 sorption 143
7.2.2.3 H_2O sorption 145
7.3 Conclusions 146
Chapter 8: Quantification of temperature-dependent CO_2 adsorption kinetics in Lewatit VP OC 1065, Purolite A110, and TIFSIX-3-Ni for direct air capture 148
8.1 Introduction 148
8.2 Experimental section 153
8.2.1 Adsorbent materials 153
8.2.2 Kinetic sorption measurements 154
8.2.3 Data analysis 157
8.3 Results and discussion 158
8.3.1 Optimisation of experimental factors for kinetic sorption measurements 158
8.3.1.1 Effect of crucible 158
8.3.1.2 Effect of flowrate 161
8.3.2 Temperature-dependent kinetic sorption measurements 162
8.4 Conclusions 167
Chapter 9: Conclusions 169
9.1 Summary of findings 169
9.2 Perspectives and future work 170
References 173
Appendices 196
Appendix 1. Literature review 196
A1.1 Tables of physicochemical properties 197
A1.2 Tables of sorption properties 213
A1. References 231
Appendix 2. Materials and methods 247
A2. References 250
Appendix 3. Lewatit and Purolite study 251
A3.1 Physicochemical properties 251
A3.2 Equilibrium sorption properties 253
A3. References 270
Appendix 4. TIFISX-3-Ni study 271

A4.1 Physicochemical properties 271
A4.2 Equilibrium adsorption properties 273
A4.3 Manufacturing considerations 285
A4.3. Adsorbent stability under process conditions 287
A4. References 293
Appendix 5. Functionalised zeolites study 294
A5. References 297
Appendix 6. CO_2 adsorption kinetics study 298
A6. References 306
Appendix 7. Copyrights and permissions 307

List of abbreviations

1°	primary
2-ampd	2-(aminomethyl)piperidine
ads	adsorbent
AE-AE-APS	3-[2-(2 aminoethylamino)ethylamino]propyltrimethoxysilane
AE-APS/APTMS	3-(2-aminoethyl)-3-aminopropyltrimethoxysilane
AE-ESPE	N^1-(2-Aminoethyl)-N^1-(3-(triethoxysilyl)-propyl)ethane-1,2-diamine
AHSA	amine hybrid silsesquioxane aerogel
AHTSA	amine hybrid titania/silsesquioxane aerogel
AP-APS	3-(2-aminopropylamino)propyltrimethoxysilane
APDES	3-aminopropylmethyldiethoxysilane
AP-ESPP	N^1-(3-Aminopropyl)-N^1-(3-(triethoxysilyl)propyl)propane-1,3-diamine
APS/APTMS	3-aminopropyltrimethoxysilane
APTES	3-aminopropyltriethoxysilane
ATR	attenuated total reflectance
B	branched
BA	benzylamine
$bbta^{2-}$	benzo-1,2,4,5-bistriazolate
BC	bamboo cellulose
BCA	bovine carbonic anhydrase
BECCS	bioenergy with carbon capture and storage
BET	Brunauer-Emmett-Teller
BETSI	Brunauer-Emmett-Teller surface identification
$bibta^{2-}$	5,5′-bibenzotriazolate
BJH	Barrett-Joyner-Halenda
$btdd^{2-}$	bis(1,2,3-triazolo)dibenzodioxin
c	coated
CA	cellulose acetate
CaO	calcium oxide
CDR	carbon dioxide removal
CHPTAC	(3-Chloro-2-hydroxypropyl)-trimethylammonium chloride
COF	covalent-organic framework
CP	chemi-physisorption
CSIRO	Commonwealth Scientific and Industrial Research Organisation
CT	computed tomography
CTAB	cetyltrimethylammonium bromide
CTAC	cetyltrimethylammonium chloride
D	dynamic
DA	Dubinin-Astakhov
DAC	direct air capture
DACCS	direct air carbon capture and storage
DB	differential bed
DCB	dynamic column breakthrough

DFT	density functional theory
DMAPS	N,N-dimethyl-3-aminopropyltrimethoxysilane
$dobdc^{4-}$	2,5-dioxido-1,4-benzenedicarboxylate)
$dobpdc^{4-}$	4,4′- dioxidobiphenyl-3,3′-dicarboxylate
DSC	differential scanning calorimetry
DSL	dual-site Langmuir
DT	N^1-(3-trimethoxysilylpropyl)diethylenetriamine
EB	1,2-epoxybutane
ECMWF	European Centre for Medium-Range Weather Forecasts
ED	ethylenediamine
een	N-ethylethylenediamine
EI-den	N^1,N^1,N^3,N^3-tetrakis(2-aminoethyl)propane-1,3-diamine
epn	1-ethylpropane-1,3-diamine
ESA	electric swing adsorption
EtSNT	ethane-bridged organosilica nanotubes
FB	fluidised bed
FR	frequency response
FS	fumed silica
FTIR	Fourier transform infrared spectroscopy
g	grafted
G	gravimetric
GAB	Guggenheim–Anderson–de Boer
HBS	hierarchical bimodal mesoporous silica
HK	Horvath-Kawazoe
HMS	hierarchical meso-/macroporous silica
HPMCP	hypromellose phthalate polymer
i	impregnated
IAST	ideal adsorbed solution theory
ICL	Imperial College London
ie	ion-exchange
IER	ion-exchange resin
IFM	interference microscopy
IPCC	Intergovernmental Panel on Climate Change
ipen	N-isopropylethylenediamine
IRM	infrared microscopy
K_2CO3	potassium carbonate
K_3PO_4	potassium phosphate
L	linear
LDF	linear driving force
LDH	layered double hydroxides
MS	microwave synthesis
MCF	mesocellular foam silica
MF	melamine-formaldehyde
MFS	mesoporous fumed silica

MIP	mercury intrusion porosimetry
mmen	N,N′-dimethylethylenediamine
MMSN	micro-mesoporous silica nanoparticles
MOF	metal-organic framework
mpn	2-methyl-1,3-diaminopropane
MSA	moisture swing adsorption
N	nitrogen
Na_2CO3	sodium carbonate
NFC	nanofibrillated cellulose
NIST	National Institute of Standards and Technology
NLDFT	non-linear density functional theory
nmen	N-methylethylenediamine
NMR	nuclear magnetic resonance
PAN	polyacrylonitrile
PD	propylenediamine
PE	polyetherimide
PEI-XXX	Poly(ethylenimine)-Mw/Mn
PES	Polyethersulfone
PFG	pulsed field gradient
PFO	pseudo-first order
PGA	Poly(glycidyl amine)
PI-den	N^1,N^1,N^3,N^3-tetrakis(3-aminopropyl)propane-1,3-diamine
PMMA	poly(methyl methacrylate)
pn	1,3-diaminopropane
PPG	poly(propyleneguanidine)
PPI-XXX	poly(propylenimine)-Mw/Mn
PSO	pseudo-second order
QA	quartnery ammonium
QCPS	quaternized crosslinked poly(styrene) resin
QDF	quadratic driving force
RH	relative humidity
RT	room temperature
Ru	ruthenium
S	simulation
SBS	polystyrene-block-polybutadiene-block-polystyrene
SiNP	silica nanoparticles
SiO_2 AG	silica aerogel
SIP	solvent impregnanted polymer
spermine	N,N′-bis(3-aminopropyl)-1,4-diaminobutane
ss	steam stable
SSL	single-site Langmuir
ST	solvothermal synthesis
S-TSA	steam-assisted temperature swing adsorption
TAEA	tris (2-amino ethyl) amine

TEPA	tetraethylenepentamine
TETA	triethylenetetramine
TGA	thermogravimetric analyser
TPD	temperature-programmed desorption
TPTA	tripropylenetetramine
TVSA	temperature-vacuum swing adsorption
UNIV6	universal adsorption isotherm model type VI
V	volumetric
VAS	volumetric adsorption system
XPS	X-ray photoelectron spectroscopy
XRD	X-ray diffraction
ZLC	zero length column
ZY	zeolite Y

List of figures

Figure 2.1. Schematic of a typical adsorption-based DAC process. 24

Figure 2.2. Overview of the monthly average temperature and relative humidity distribution of the different DAC project locations listed in Table 2.1, based on data collected between 1999 and 2021 by the European Centre for Medium-Range Weather Forecasts (ECMWF) [34]. Data from the capital cities of each state/country was used as exact locations of projects were not available. Box edges represent the 25th and 75th percentile, whisker edges represent the minimum and maximum data points, the solid line through the box represents the median, and the filled square symbol represents the mean. 28

Figure 2.3. Comparison of a) skeletal density, b) particle density, c) bed density, d) BET surface area (S_{BET}), e) total pore volume, f) micropore volume, g) specific heat capacity, h) thermal conductivity, and i) thermal stability values between different adsorbent categories, both with and without additional functionalisation. Box edges represent the 25th and 75th percentile, whisker edges represent the minimum and maximum data points, the solid line through the box represents the median, and the filled square symbol represents the mean. Total number of data entries are labelled to the left of each box to better understand the spread of data. All data entries can be found in Tables A1.1 to A1.6. 31

Figure 2.4. Comparison of a) CO_2 uptake values (at concentrations lower than 500 ppm and temperatures between 20 to 30 °C, except for unfunctionalised SBA-15 whose uptake of 0.01 mmol g^{-1} was measured at 10,000 ppm [104]) and b) heat of adsorption values for different adsorbent categories, both with and without additional functionalisation. Box edges represent the 25th and 75th percentile, whisker edges represent the minimum and maximum data points, the solid line through the box represents the median, and the filled square symbol represents the mean. Total number of data entries are labelled to the left of each box. All data entries can be found in Tables A1.7 to A1.12. 40

Figure 2.5. Overview of CO_2, N_2, O_2, and H_2O isotherm availability for different classes of adsorbents reported between 2016 and 2021. For CO_2 and N_2 isotherms, the criterion is met if there are isotherms available at three temperatures and at pressures up to 1 bar. Isotherms that were collected at cryogenic temperatures for CO_2 and N_2 were still included in this count, however these are not suitable for DAC applications and are more useful for porosity characterisation rather than isotherm fittings for process modelling. Indication was made in Tables A1.7 to A1.12 if this was the case. For O_2 and H_2O isotherms, our criterion is met provided there is an isotherm available, at any temperature and pressure range below 1 bar. An adsorbent was considered to be studied for DAC if a CO_2 uptake between 0.04%$_{vol}$ to 4%$_{vol}$ was measured. An adsorbent was not double counted if it was studied by multiple publications, and adsorbents with different loadings of the same functionalisation were counted as just one material. Adsorbents of different structural forms (e.g. powder vs. monolith) were counted as two separate materials. All data entries and their corresponding sources are available in Tables A1.7 to A1.12. Isotherms were not always found in DAC related publications. Some adsorbents included in the tables (e.g. silica gel, γ-alumina, activated carbon) were not considered to be studied for DAC and so were not included in these counts even if isotherm data was available. 43

Figure 2.6. CO_2 adsorption isotherms at 25 °C and up to a pressure of 1 bar for materials which have had CO_2 isotherms measured at a minimum of three temperatures (as indicated in Tables A1.7 to A1.12). Unfunctionalised adsorbents are represented by filled markers and solid lines, and functionalised adsorbents are represented by hollow markers and dashed lines. Data points have either been digitised, plotted using a fitted isotherm model, or plotted from tabulated data. 44

Figure 2.7. Comparison of the number of studies using different adsorbent categories in (a) adsorbent studies and (b) process studies. Adsorbent studies refer to studies focusing on materials development. Process studies refer to studies reporting process performance metrics. Several studies investigated more than one adsorbent category. This is reflected in the number of papers associated with each adsorbent type, but did not contribute to the final "adsorbent" and "process" total. 54

Figure 5.1. FTIR spectra for dried and ground Lewatit and Purolite resins. 79

Figure 5.2. Porosity analysis of Lewatit and Purolite resins. a) N_2 sorption isotherms at -196 °C (filled symbols = adsorption; open symbols = desorption). b) Cumulative pore size distribution obtained from N_2 sorption at -196 °C with DFT analysis. 81

Figure 5.3. Thermal analysis of Lewatit and Purolite resins. a) TG curves under N_2 (solid lines) and air (dotted lines) atmospheres up to 900 °C. b) Specific heat capacities of the dried resins measured as a function of temperature from 25 °C to 120 °C, where the darker solid lines represent the fitted results using equation (5.2). Data for polystyrene was obtained from Gaur and Wunderlich [198]. 82

Figure 5.4. Equilibrium adsorption (filled symbols) and desorption (hollow symbols) isotherms for CO_2 measured at 15, 25, 35, 60, 70, 80, and 120 °C up to 1 bar for a) Lewatit and b) Purolite. 84

Figure 5.5. Equilibrium adsorption isotherms for CO_2 measured at 15, 25, 35, 60, 70, 80, and 120 °C up to 1 bar for a) Lewatit and b) Purolite with a log-scale of pressure. Solid lines represent the fitting results from the CP isotherm model while dashed lines represent the fitting results from the td-Toth isotherm model. The fitting parameters of the isotherms are found in Table 5.4. 86

Figure 5.6. Equilibrium adsorption isotherms for N_2 (squares) measured at 15, 25, and 35 °C, and for Ar (diamonds) and O_2 (triangles) at 25 °C up to 1 bar for a) Lewatit and b) Purolite. Solid lines represent the SSL isotherm fitting results (fitting parameters can be found in Table 5.5). 90

Figure 5.7. Equilibrium adsorption (filled symbols) and desorption (hollow symbols) isotherms for H_2O measured at 15 °C up to 0.016 bar, and 25 °C and 35 °C up to 0.023 bar for a) Lewatit and b) Purolite. 91

Figure 5.8. Equilibrium adsorption isotherms for H_2O measured at 15 °C, 25 °C, and 35 °C as a function of relative humidity for a) Lewatit and b) Purolite. Solid lines represent the GAB isotherm fitting results (fitting parameters can be found in Table 5.6). 93

Figure 5.9. Isosteric heats of adsorption of Lewatit and Purolite for a) CO_2, b) N_2, and c) H_2O. 95

Figure 6.1. a) XRD patterns of $NiTiF_6$, TIFSIX-3-Ni precursor, and final TIFSIX-3-Ni. b) N_2 adsorption (filled symbols) and desorption (open symbols) isotherms at -196 °C, c) TG curve under N_2 atmosphere up to 900 °C, and d) specific heat capacity as a function of temperature for TIFSIX-3-Ni. 101

Figure 6.2. a) CO_2 equilibrium adsorption (filled symbols) and desorption (open symbols) isotherms measured at 15, 25, 35, 60, 70, 80, and 120 °C up to 1 bar for TIFSIX-3-Ni powder. b) CO_2 equilibrium adsorption isotherms shown with a log-scale of pressure measured at 15, 25, 35, 60, 70, 80, and 120 °C up to 1 bar for TIFSIX-3-Ni powder. Solid lines represent the fitting results from the DSL isotherm model, whose fitting parameters are found in Table 6.1. 103

Figure 6.3. N_2 equilibrium adsorption isotherms for (squares) measured at 15 °C, 25 °C, and 35 °C, and Ar (diamonds) and O_2 (triangles) equilibrium adsorption isotherms measured at 25 °C up to 1 bar for TIFSIX-3-Ni. Solid lines represent the fitting results from the SSL isotherm model, whose fitting parameters are found in Table 6.1. 106

Figure 6.4. a) H_2O equilibrium adsorption (filled symbols) and desorption (open symbols) isotherms measured at 15 °C, 25 °C, and 35 °C for TIFSIX-3-Ni as a function relative humidity. b) H_2O equilibrium adsorption isotherms measured at 15 °C, 25 °C, and 35 °C as a function of absolute pressure in bar. Solid lines represent the UNIV6 isotherm model fitting results determined from using the 15 °C, 25 °C, and 35 °C experimental data in the fitting process, while dashed lines represent the fitting results using only the 15 °C and 25 °C experimental data. Fitting parameters are found in Table 6.1 and Table A4.5, respectively. 107

Figure 6.5. CO_2, N_2, and H_2O isosteric (lines) and limiting (symbols) heats of adsorption for TIFSIX-3-Ni with the loading plotted on square root scale for clarity. 110

Figure 6.6. XRD patterns of synthesised batches of a) $NiTiF_6$, b) TIFSIX-3-Ni precursor, and c) final TIFSIX-3-Ni. 112

Figure 6.7. a) TG curves under N_2 air atmosphere up to 900 °C, b) N_2 adsorption isotherms at -196 °C, and CO_2 adsorption isotherms at 25 °C with c) linear and d) log-scale of pressure (filled symbols are adsorption; open symbols are desorption) for different batches of TIFSIX-3-Ni. 113

Figure 6.8. a) XRD patterns and b) N_2 adsorption (filled symbols) and desorption (open symbols) isotherms at -196 °C of batch 5 TIFSIX-3-Ni powder, ground powder, and pellet. c) Cumulative pore volume as a function of pore diameter of TIFSIX-3-Ni pellet, obtained from N_2 adsorption at -196 °C (circles) and mercury intrusion porosimetry (triangles). d) CO_2 adsorption (filled symbols) and desorption (open symbols) isotherms at 25 °C for batch 5 TIFSIX-3-Ni powder, ground powder, and pellet, with log-scale of pressure shown in the inset. 116

Figure 6.9. Equilibrium adsorption (filled symbols) and desorption (open symbols) isotherms for H_2O measured at 25 °C for batch 5 TIFSIX-3-Ni powder up to 15% RH, 48% RH, and 77% RH. 120

Figure 6.10. a) XRD patterns, b) N_2 adsorption isotherms at -196 °C, and CO_2 adsorption isotherms at 25 °C with c) linear and d) log-scale of pressure (filled symbols are adsorption; open symbols are desorption) for batch 5 TIFSIX-3-Ni powder before (purple) and after exposure to 15% RH (light navy), 48% RH (medium navy), and 77% RH of H_2O (dark navy). 121

Figure 6.11. a) XRD patterns, b) N_2 adsorption isotherms at -196 °C, and CO_2 adsorption isotherms at 25 °C with c) linear and d) log-scale of pressure (filled symbols are adsorption; open symbols are desorption) for batch 3 TIFSIX-3-Ni powder before (blue) and after exposure to 40 °C and 75% RH air for 14 days (yellow), 40 °C and 90% RH air for 14 days (orange), and ambient air for 6 months (red). 124

Figure 6.12. a) Mass change of TIFSIX-3-Ni pellet (batch 5) per gram of activated sample (i.e. sample mass just before the first cycle) over 50 adsorption-desorption cycles under a flow of ambient air with varying relative humidity. b) Working capacity of the activated sample (i.e. sample mass just before the first cycle) and average relative humidity of the ambient air over 50 cycles. 127

Figure 6.13. a) XRD patterns, b) N_2 adsorption isotherms at -196 °C, and c) CO_2 adsorption isotherms at 25 °C with log-scale of pressure (filled symbols are adsorption; open symbols are desorption) for batch 5 TIFSIX-3-Ni pellet before (pink) and after post-cyclic testing (bronze). Images of the sample before and after cycling are shown as insets in c). 129

Figure 7.1. Ideal reaction of *m* aminosilanes with the zeolite Y surface in the presence of water. ... 134

Figure 7.2. FTIR spectra for a) ZY samples functionalised with aminosilanes and b) ZY samples functionalised with NH_3. (No bands were observed for ZY-NH_3 samples beyond 2400 cm^{-1}; the full spectrum up to 4000 cm^{-1} is shown in Figure A5.1). 135

Figure 7.3. XPS analyses of original and functionalised ZY samples. For ZY samples functionalised with aminosilanes: a) elemental composition by weight and b) deconvolution of N 1*s* core level. For ZY samples functionalised with NH_3: c) elemental composition by weight and d) deconvolution of N 1*s* core level. 136

Figure 7.4. Porosity analyses of original and functionalized ZY samples. a), c) N_2 sorption isotherms at -196 °C (filled symbols = adsorption; open symbols = desorption). b), d) BET areas, micropore volumes ($V_{micropores}$), and total pore volumes ($V_{total\ pores}$) extracted from the measured N_2 sorption isotherms. 140

Figure 7.5. Equilibrium adsorption (filled symbols) and desorption (hollow symbols) isotherms for CO_2 measured at 25 °C up to 1 bar with linear and log-scales of pressure for a) and b) aminosilane-functionalised samples and c) and d) ZY-NH_3 samples, respectively. 142

Figure 7.6. Equilibrium adsorption (filled symbols) and desorption (hollow symbols) isotherms for N_2 measured at 25 °C up to 1 bar for a) aminosilane-functionalised samples and b) ZY-NH_3 samples.. 144

Figure 7.7. Equilibrium adsorption (filled symbols) and desorption (hollow symbols) isotherms for H_2O measured at 25 °C as a function of relative humidity for a) aminosilane-functionalised samples and b) and ZY-NH_3 samples. 145

Figure 8.1. Schematic of the different adsorbent scales and their associated mass transfer mechanisms, measurement techniques, and sample masses. 150

Figure 8.2. a) Simplified schematic of the set-up used for the kinetic sorption measurements, which includes (1) gas cylinders, (2) pressure reducing regulators, and a thermogravimetric analyser containing the following components: (3) mass flow controllers, (4) microbalance, (5) sample chamber, (6) crucible and (7) sample holder, (8) heating elements, and (9) gas outlet. b) Example of mass and temperature profiles over the course of a kinetic sorption measurement for a Purolite sample. Step 1: temperature increased from 30 to 120 °C and held for 4 h under a 100 mL min^{-1} He flow. Step 2: temperature decreased back to 30 °C and held for 20 min under the same He flow. Step 3: a 100 mL min^{-1} flow of the 800 ppm CO_2/He cylinder is then turned on for 10 h, at 30 °C. 155

Figure 8.3. a) Photographs of the standard alumina crucible, perforated aluminium crucible, and perforated aluminium crucible in the makeshift basket. b) Comparison of the experimental (filled circles) and fitted (solid lines) fractional uptakes and corresponding k_{LDF} constants of Purolite samples measured using the standard alumina crucible, perforated aluminium crucible, and perforated aluminium crucible in the makeshift basket. Time is plotted on a square root scale for clarity. 160

Figure 8.4. Comparison of the average k_{LDF} constants with error bars for a 95% confidence interval for Purolite and TIFSIX-3-Ni calculated at 100 mL min^{-1}, 200 mL min^{-1}, and 300 mL min^{-1} total flowrates of 400 ppm CO_2 in He 162

Figure 8.5. Comparison of temperature-dependent k_{LDF} constants with uncertainty bounds (dashed lines) for a 95% confidence interval between 20 °C and 70 °C for Lewatit, Purolite, and TIFSIX-3-Ni. Individual data points indicate the temperatures at which k_{LDF} constants were experimentally measured. 164

Figure 8.6. Comparison of the averaged equilibrium CO_2 loadings for Lewatit, Purolite, and TIFSIX-3-Ni at 30 °C, 45 °C, and 60 °C and 400 ppm CO_2 concentration determined from TGA experiments and CO_2 sorption isotherm models with error bars for a 95% confidence interval 167

List of tables

Table 2.1. Overview of commissioned adsorption-based DAC projects using data compiled by the IEA [23], Sovacool et al. [24], Ozkan et al. [25], and Low et al. [10]. 26

Table 2.2. Summary of adsorbate and adsorbent properties required in the modelling of an adsorption-based DAC process. 29

Table 4.1. Details of the chemicals used throughout this thesis. 58

Table 5.1. Summary of CHN elemental analysis for Lewatit and Purolite resins, with uncertainty bounds for a 95% confidence interval 80

Table 5.2. Summary of density (skeletal, pellet, bed) and textural property (total pore volume, pellet voidage, BET area) values for dried Lewatit and Purolite resins. Uncertainty bounds for a 95% confidence interval are provided when available. 81

Table 5.3. Fitting parameters for the specific heat capacity of Lewatit and Purolite. 83

Table 5.4. Fitting parameters with uncertainty bounds for a 95% confidence interval for the td-Toth and CP isotherm models for CO_2 adsorption for Lewatit and Purolite. 87

Table 5.5. Fitting parameters with uncertainty bounds for a 95% confidence interval for the SSL isotherm model for N_2 adsorption for Lewatit and Purolite. 91

Table 5.6. Fitting parameters with uncertainty bounds for a 95 % confidence interval for the GAB isotherm model for H_2O adsorption for Lewatit and Purolite. 93

Table 5.7. Limiting heats of adsorption of CO_2, N_2, and H_2O for Lewatit and Purolite with uncertainty bounds for a 95% confidence interval 94

Table 6.1. Fitting parameters with uncertainty bounds for a 95% confidence interval for the DSL, SSL, and UNIV6 isotherm model for CO_2, N_2, and H_2O adsorption on TIFSIX-3-Ni, respectively. 105

Table 6.2. Summary of the synthesis procedure for different batches of TIFSIX-3-Ni. 111

Table 6.3. Summary of the textural properties derived from N_2 adsorption at -196 °C, and CO_2 adsorption at 0.4 mbar and 25 °C for different batches of TIFSIX-3-Ni. 114

Table 6.4. Summary of textural properties and densities of TIFSIX-3-Ni powder, ground powder, and pellet (batch 5), as derived from N_2 adsorption at -196 °C and MIP measurements. 117

Table 6.5. Summary of the textural properties derived from N_2 adsorption at -196 °C and CO_2 adsorption at 0.4 mbar and 25 °C for TIFSIX-3-Ni samples exposed to various stability studies. 122

Table 7.1. Nitrogen loading in mmol g^{-1} of original and functionalised ZY samples derived from XPS and TGA analyses. 137

Table 8.1. Fitting parameters for equation (8.7) with uncertainty bounds for a 95% confidence interval for Lewatit, Purolite, and TIFSIX-3-Ni. k_0 is the pre-exponential factor (or k_{LDF} at infinite temperature) of the Arrhenius equation and E_a is the activation energy for mass transfer. 163

Chapter 1: Introduction

Parts of this discussion were previously published by the thesis author in the Journal of Chemical & Engineering Data [1] or on ChemRxiv [2].

1.1 Background

The 2015 Paris Agreement saw 196 countries commit to limiting global temperature rise to below 2 °C, and preferably below 1.5 °C. According to recent reports by the Intergovernmental Panel on Climate Change (IPCC), this scenario can only be achieved with carbon dioxide removal (CDR) technologies [3]. The use of adsorbents to remove CO_2 directly from the atmosphere, *i.e.* adsorption-based direct air capture (DAC), is a CDR technology actively being investigated. It is a challenging process due to the ultra-dilute concentration of CO_2 in the air (~ 0.04%$_{vol}$ or 0.4 mbar) and varying ambient conditions (i.e. temperature and relative humidity), but it allows the amount of CO_2 captured to be quantitatively measured and facilitates a pathway for long-term carbon storage.

The current CO_2 capture capacity of commissioned adsorption-based DAC plants worldwide is on the order of ~ 10 kt year^{-1} [4]. However, this only equates to 0.0002% of the CO_2 removal goal of 4.8 Gt year^{-1} by 2050 stipulated in the "below 2 °C" scenario (of which 2.7 Gt year^{-1} is thought to be removed by engineered CDR technologies such as DAC) [5]. Hence, much work is still needed for the scale-up of these DAC processes.

One aspect actively being researched is the development of new adsorbent materials. Since 2016, hundreds of adsorbents have been proposed for DAC in the literature, including silicas, metal oxides, metal-organic frameworks (MOFs), zeolites, carbons, and polymers. Some of the most reported metrics are the adsorbents' CO_2 uptake at 0.4 mbar, or a CO_2 isotherm at a single temperature (usually 25 °C). However, it has been established that simple metrics such as these are not sufficient for adsorbent screening. Instead, key performance indicators determined from process modelling and optimisation, such as purity, recovery, productivity, and energy consumption, should be used [6-9]. In the case of DAC, these are especially important to determine the net CO_2 removal achieved by the process.

To facilitate this process scale evaluation, various adsorbent properties are required such as: equilibrium isotherms of all relevant species, heat and mass transfer coefficients, porosity, density (skeletal, pellet, bed), heat capacity, and heat of adsorption. Furthermore, while not direct inputs for process modelling, other factors such as an adsorbent's manufacturability (i.e. reproducibility and shaping) and stability to process conditions (i.e. humidity, temperature, and cycling) will influence the practicality of its use in a DAC process and even the process design. Currently, it is extremely rare to find adsorbents in the literature with all the necessary properties reported, even when considering numerous sources. My thesis aims to minimise this data gap by investigating the physicochemical, equilibrium sorption, and kinetic sorption properties of select promising DAC adsorbents. The adsorbents are either commercially available, emerging adsorbents, or new adsorbents developed as part of this thesis. By doing so, I hope to facilitate process scale evaluation of these adsorbents for DAC and help the advancement and scale-up of this technology.

1.2 Thesis overview

This thesis consists of nine chapters. Chapter 1 (this chapter) provides a brief introduction to the current state of adsorption-based DAC. Chapter 2 provides a thorough literature review of the current data availability for DAC adsorbent materials before covering in Chapter 3 my research objectives based on the data gaps highlighted throughout the literature review. Chapter 4 describes the materials, synthesis procedures, and experimental methods used throughout my PhD. Chapters 5 to 7 present the results of my studies on the physiochemical and equilibrium sorption properties of commercial polymeric resins (Lewatit VP OC 1065 and Purolite A110, Chapter 5), an ultramicroporous MOF (TIFSIX-3-Ni, Chapter 6), and synthesised amine-functionalised zeolite adsorbents (Chapter 7). Chapter 8 then covers the kinetic sorption studies conducted for the resins and MOF. Finally, Chapter 9 summarises the key findings of each study and highlights future work still to be done. Supplementary results that complement each chapter are provided in associated Appendices.

Chapter 2: Literature review

Some of the discussion and figures/tables used in this chapter were previously published by the thesis author in Chemical Engineering Research and Design [10] and the Journal of Chemical & Engineering Data [1]. Production of Figures 2.1 and 2.6, and calculation of the volumes of different gas streams processed for capturing 1 kg of CO_2, were done by Lucy Barton at Imperial College London. All other work was completed by the thesis author.

2.1 Overview of adsorption-based DAC

The Intergovernmental Panel on Climate Change (IPCC) has established that carbon dioxide removal (CDR) technologies are essential to meeting the "below 2 °C" targets set out by the 2015 Paris Agreement [3]. These technologies remove CO_2 from the atmosphere and store it durably in soils, geological formations, biomass, or in the ocean. Examples of CDR technologies include afforestation/reforestation, enhanced weathering, biochar, soil carbon sequestration, ocean alkalinisation, bioenergy with carbon capture and storage (BECCS), and direct air carbon capture and storage (DACCS) [5]. Amongst these technologies, DACCS offers long-term carbon storage and allows the amount of CO_2 captured to be accurately measured.

Direct air capture (DAC) is accomplished using either absorption- or adsorption-based processes. Absorption-based processes capture CO_2 within the bulk of the sorbent material which can include aqueous hydroxides, solid alkali metal oxides, and aqueous amine solutions [11]. These processes require high regeneration energies, where reacted hydroxides and oxides forming carbonates undergo calcination temperatures upwards of 700 °C [12], and aqueous amine solutions must contend with the high specific heat capacity of water [13]. In comparison, adsorption processes capture CO_2 on the surface of a solid porous material and typically require milder regeneration conditions closer to 100 °C [11]. From here, this thesis focuses on adsorption-based DAC.

2.1.1 DAC adsorption process

In a typical DAC adsorption process (Figure 2.1), air is delivered as a feed gas to a contactor containing the adsorbent which selectively captures CO_2 under the local atmospheric conditions (i.e. temperature and relative humidity (RH)). Here, CO_2 adsorption happens via either physisorption due to intermolecular forces such as electrostatic and van der Waals' forces, or chemisorption due to a chemical reaction between CO_2 and the adsorbent surface where covalent or coordination bonds are formed. The separation of CO_2 from other compounds in air such as N_2, O_2, and H_2O occurs through equilibrium, kinetic, or molecular sieving separation. Equilibrium separations are due to differences in affinity between different adsorbates with the adsorbent. Kinetic separations depend on differences in adsorbate diffusion rates through the pores, where molecules with slower diffusion do not have sufficient time to reach the adsorption site and adhere to the surface, and thus can be separated from the mixture. Lastly, molecular sieving separates adsorbates based on their size, where molecules that are larger than the pore size of the adsorbent are unable to be adsorbed.

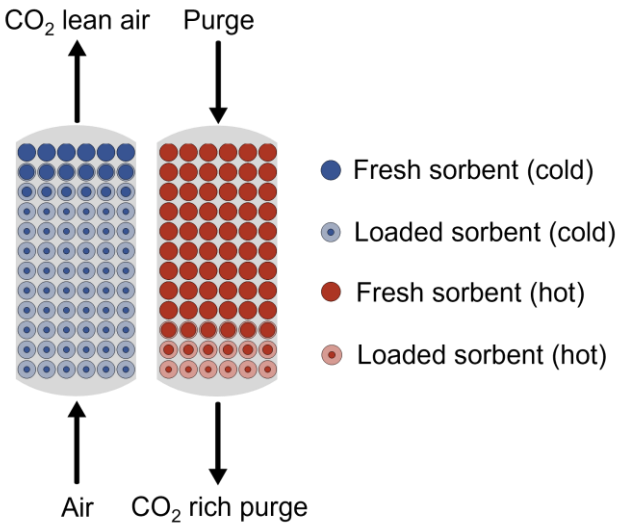


Figure 2.1. Schematic of a typical adsorption-based DAC process.

After adsorption, the CO_2 is purged from the adsorbent material using a chosen desorption method such as steam-assisted temperature swing adsorption (S-TSA), temperature-vacuum swing adsorption (TVSA), or moisture swing adsorption (MSA). A review of different desorption processes (as well as different contactor designs) can be found in the review article by Low et al. [10], while a recent review

by An et al. [14] covers more novel desorption methods such as microwave regeneration [15-17] and electric swing adsorption (ESA) [18]. The recovered CO_2 is then either permanently stored in geological sites [19], utilised, or converted for additional applications [13, 20].

2.1.2 Current state of deployment

Over 20 adsorption-based DAC projects have been commissioned around the world at the demonstrator, pilot, and commercial scale (Table 2.1). Without accounting for projects which have explicitly been stated to be non-operational, and assuming all other projects are currently operational, the current CO_2 capture capacity of adsorption-based DAC is ~ 7 kt $year^{-1}$. This is in line with the International Energy Agency's assessment that 27 DAC plants (both absorption- and adsorption-based) have been commissioned worldwide as of July 2023, with a total CO_2 capture capacity of almost 10 kt $year^{-1}$ [4]. To put this value into perspective, 10 kt $year^{-1}$ is only equivalent to 0.0002% of the CO_2 removal goal by 2050 stipulated in the "below 2 °C" scenario (a total of 4.8 Gt $year^{-1}$, of which 2.7 Gt $year^{-1}$ is thought to be removed by engineered CDR technologies such as DAC) [5]. The most recent summaries of the industrial deployment of DAC, including yet to be commissioned projects, can be found in reports by Bisotti et al. [21] and Wang et al. [22].

Table 2.1. Overview of commissioned adsorption-based DAC projects using data compiled by the IEA [23], Sovacool et al. [24], Ozkan et al. [25], and Low et al. [10].

Company	Location	CO_2 capture capacity (t_{metric} $year^{-1}$)	CO_2 fate	Start date
Climeworks	Germany	1	Utilisation	2015
	Switzerland	50	Utilisation	2016
	Switzerland	900	Utilisation	2017
	Iceland	50	Storage	2017
	Switzerland	600	Utilisation	2018
	Switzerland	3	Utilisation	2018
	Italy*	150	Utilisation	2018
	Germany	3	Utilisation	2019
	Netherlands	3	Utilisation	2019
	Germany	3	Utilisation	2019
	Germany	50	Utilisation	2019
	Germany	50	Utilisation	2020
	Germany	3	Utilisation	2020
	Germany	3	Utilisation	2020
	Iceland	4000	Storage	2021
Global Thermostat	California, USA*	500	Unknown	2010
	California, USA*	1000	Unknown	2013
	Alabama, USA*	1000	Unknown	2018
	Colorado, USA [26]	1000	Unknown	2022
Infinitree	New York, USA	100	Utilisation	2014
CSIRO	Australia	2	Unknown	2020
Soletair Power	Finland [27]	20	Unknown	2023

*: project explicitly stated to be non-operational

2.1.3 Technical challenges

DAC presents unique challenges when compared to more mature carbon capture technologies such as post-combustion capture. The first is the ultra-dilute concentration of ~ 0.04%$_{vol}$ (or 400 ppm) CO_2 in air. At the conditions of 1 atm, 25 °C, and 50% RH, ~ 1400 m^3 of air would need to be processed to capture 1 kg of CO_2 assuming 100% capture rate. In comparison, the volume of gas that would need to be processed from a natural gas or cement flue gas stream is only ~ 14 m^3 or ~ 2.5 m^3, respectively,

i.e. roughly a 100- or 500-fold decrease. As a result, adsorbents used for DAC not only need to be extremely selective for CO_2, but they must also have fast adsorption kinetics to maintain adequate productivity (i.e. tonnes of CO_2 produced per day, per tonne of adsorbent).

Another challenge DAC faces is the wide variation in global atmospheric conditions. While a benefit of DAC is its siting flexibility, subsequently, adsorbents and machinery used for DAC will have to be tolerant to temperatures ranging from below -30 °C (e.g. Alberta, Canada) to above 40 °C (e.g. Dubai, UAE). Figure 2.2 showcases the range of temperatures and relative humidity in different locations where DAC projects have been commissioned. Not only is there wide variation between different geographical locations, the average monthly temperature and relative humidity in a year can vary by more than 25 °C and 35% RH, respectively, within the same site. Therefore, adsorbents used for DAC should be viable across the range of temperatures and relative humidity relevant to the geographical location of interest. The impact of varying atmospheric conditions such as cold temperatures and humidity on an adsorbent's performance for DAC has been highlighted in several recent works [28-33].

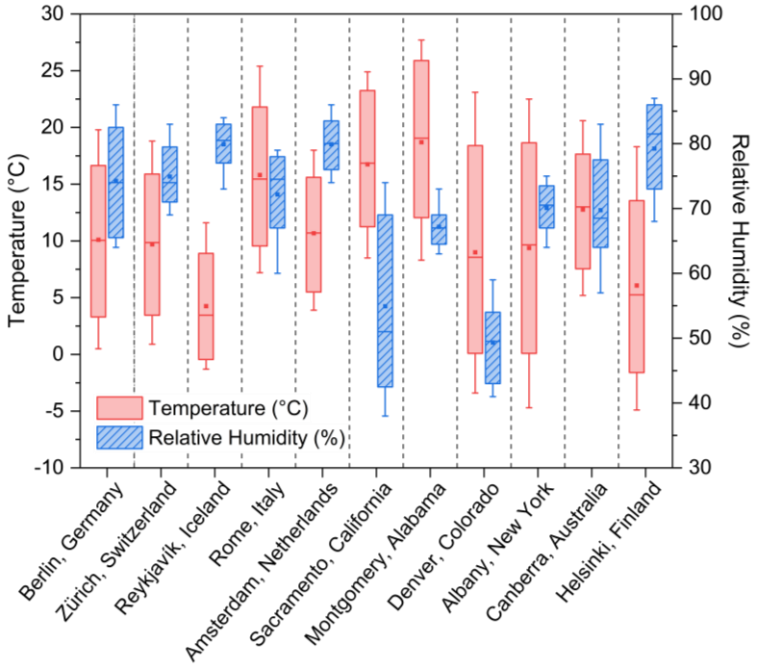


Figure 2.2. Overview of the monthly average temperature and relative humidity distribution of the different DAC project locations listed in Table 2.1, based on data collected between 1999 and 2021 by the European Centre for Medium-Range Weather Forecasts (ECMWF) [34]. Data from the capital cities of each state/country was used as exact locations of projects were not available. Box edges represent the 25th and 75th percentile, whisker edges represent the minimum and maximum data points, the solid line through the box represents the median, and the filled square symbol represents the mean.

2.1.4 Screening adsorbents for DAC

Hundreds of CO_2 adsorbents currently exist in the literature. To determine their suitability for DAC applications, adsorbent screening needs to be conducted. Recent studies have shown that the design of the adsorption process closely influences the performance of the adsorbent material [6-9]. Therefore, key performance indicators determined from process modelling and optimisation such as purity, recovery, productivity, and energy consumption should be used for adsorbent screening [35]. In the case of DAC, these are especially important to determine the net CO_2 removal achieved by the process. To conduct process scale evaluation, various adsorbent properties are needed as outlined in Table 2.2. In addition, while not direct value inputs into process modelling, other properties such as the

ability to shape an adsorbent and its mechanical, thermal, hydrolytic, oxidative, and cyclic stability will also influence its use in, and design of, an adsorption process.

Table 2.2. Summary of adsorbate and adsorbent properties required in the modelling of an adsorption-based DAC process.

Adsorbent property required	**Process modelling output**
Equilibrium isotherms considering co-adsorption for ALL adsorbing components in ambient air at multiple temperatures	Total amount adsorbed and desorbed
Overall mass transfer coefficient	Rate of mass transfer and adsorption
Density (skeletal, particle, bed)	Mass of solid and volume of process contactor required
Porosity (particle, bed) derived from pore volume estimation	Total volume of gas in vessel space and mass of adsorbent
Heat capacity (adsorbent and adsorbed phase)	Heat required to perform desorption
Heat of adsorption (of all adsorbing components)	Required energy input for desorption and process temperature changes
Overall heat transfer coefficient (related to thermal conductivity of adsorbent)	Rate of heat transfer in material

2.2 Characterisation of DAC adsorbents

In this section, I review the data availability of the different adsorbent properties highlighted in Table 2.2 which are needed to facilitate process modelling. These can be sub-divided into physicochemical, equilibrium sorption, and kinetic sorption properties. I also review data regarding the shaping and mechanical, thermal, hydrolytic, oxidative, and cyclic stability of adsorbents as these still influence the design of an adsorption process.

I conduct a thorough review of DAC adsorbents developed between 2016 and 2021 as an update to the adsorption component of the 2016 review by Sanz-Pérez et al. [12]. A detailed tabulation of the adsorbent properties for these materials are provided in Appendix A1 (Tables A1.1 to A1.12). Key studies from 2022 onwards are also highlighted throughout this chapter. While there have been numerous reviews on adsorbent materials for DAC in recent years [36-42], my focus on the connections and current data gaps between adsorbent development and process studies for DAC is a relatively

unique approach. Only very recently have other works such as those by Young et al. [43] and Wu et al. [44] also begun to highlight the connection between DAC adsorbent development/characterisation and process performance.

To put the following discussions into perspective, it is important to note that there is currently no "official" benchmark adsorbent for DAC, which leads to an absence of reference DAC adsorbent properties. A convenient benchmark would be an adsorbent used in current DAC commercial processes, yet today, many of their properties remain proprietary. Recently, Young et al. proposed semi-quantitative guidelines for the optimisation of different adsorbent parameters for an "ideal" DAC adsorbent for a TVSA and steam-assisted TVSA process [43]. However, calculations of theoretical optimal values for each adsorbent property are still unavailable. While a priori possible, building such theoretical framework remains complex, owing to the interdependent nature of the various adsorbent properties.

2.2.1 Physicochemical properties

Physicochemical properties encompass an adsorbent's density (skeletal, particle, bed), textural properties (surface area, total pore volume, micropore volume), and thermal properties (specific heat capacity, thermal conductivity, thermal stability). These data for adsorbents studied between 2016 and 2021 are summarised in Figure 2.3, where I have classed the adsorbents being investigated for DAC into six categories: silicas, metal oxides, metal organic frameworks (MOFs), carbons, zeolites, and polymers. These adsorbents can either be functionalised or unfunctionalised, where functionalisation typically "converts" a physisorbent into a chemisorbent. Amines are the most common chemicals used for functionalisation, e.g. polyamines and aminosilanes. Primary and secondary amines perform better for DAC adsorption compared to tertiary amines, which require the presence of moisture to react with CO_2 [12]. Amines can either be physically impregnated (class 1), or covalently grafted to the adsorbent's surface either by silane linkages (class 2) or via in-situ polymerisation (class 3) [12]. Carbonate functionalisation can also be used for CO_2 capture, although in this case, adsorption occurs only in the presence of moisture [45]. For each physicochemical property, I first explain how it can be

measured and then discuss the data collected in terms of both their availability and the implications of the values reported.

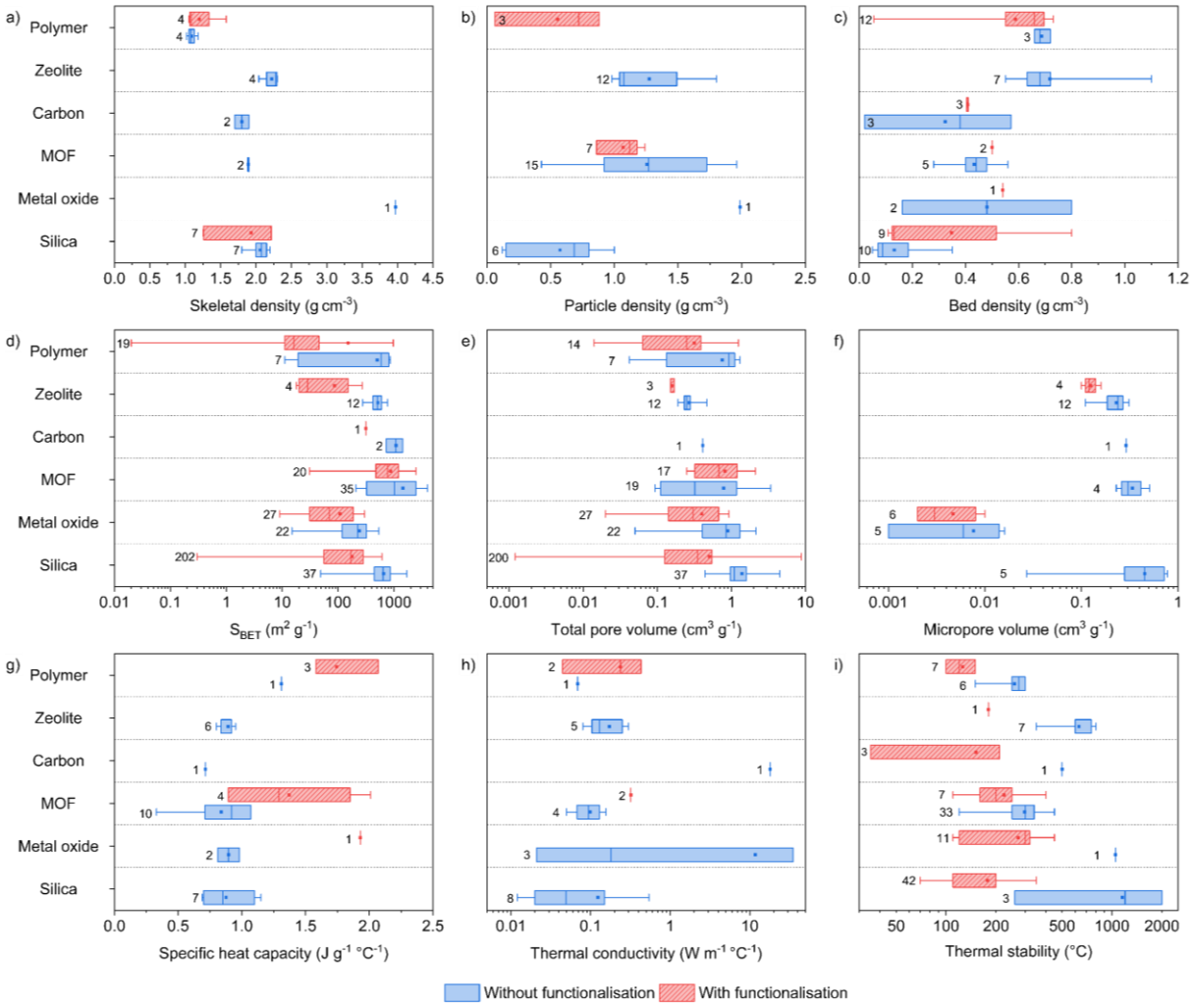


Figure 2.3. Comparison of a) skeletal density, b) particle density, c) bed density, d) BET surface area (S_{BET}), e) total pore volume, f) micropore volume, g) specific heat capacity, h) thermal conductivity, and i) thermal stability values between different adsorbent categories, both with and without additional functionalisation. Box edges represent the 25th and 75th percentile, whisker edges represent the minimum and maximum data points, the solid line through the box represents the median, and the filled square symbol represents the mean. Total number of data entries are labelled to the left of each box to better understand the spread of data. All data entries can be found in Tables A1.1 to A1.6.

2.2.1.1 Skeletal density

Skeletal density ($\rho_{skeletal}$) is defined as the mass of a single particle of adsorbent divided by the volume of the particle without including any open pores. The term particle can refer either to a single powder particle of the adsorbent, or to a single bead/pellet macrostructure. The skeletal density can be measured experimentally using a variety of methods such as helium pycnometry [46], helium gravimetry [47], or a combination of N_2 adsorption at -196 °C and mercury intrusion porosimetry [48]. Skeletal density is not always a direct input in process models but is needed to calculate other necessary parameters such as the total adsorbent porosity. While commonly measured for high pressure adsorption experiments, only three DAC specific publications reported skeletal densities and most of the values reported in Figure 2.3a were collected from 'non-DAC' publications. Overall, the availability of skeletal density is still sparse for adsorbents considered for DAC.

2.2.1.2 Particle density

Particle density ($\rho_{particle}$) is defined as the mass of a single particle of adsorbent divided by the envelope volume of the particle, which includes both the open and closed pores. It can be measured experimentally using mercury intrusion porosimetry [47] or gas pycnometry [49]. For unfunctionalised crystalline materials (e.g. MOFs and zeolites), the particle density can be calculated based on the crystalline structure of the materials. For process modelling, the pellet or bead density is needed rather than the density of the powder particle. Indeed it has been identified as one of the key adsorbent parameters affecting the productivity of a DAC process as it directly impacts the adsorbent bed density [43]. A higher particle density typically yields a higher bed density, lower porosity, and greater mechanical stability. The particle densities presented in Figure 2.3b are mostly for powders except for the polymer materials, which are for a single bead, and some zeolites, which have both powder and pellet densities reported (specified in Tables A1.1 to A1.6). Figure 2.3b highlights the sparsity of particle density data for most materials except MOFs and zeolites.

2.2.1.3 Bed density

The bed density (ρ_{bed}) is defined as the mass of the adsorbent divided by the volume of the vessel it occupies. It can be measured by simply filling a container of known volume with adsorbent and accurately weighing the contents [50]. However, due to the quantity of material needed, typically on the gram scale, this technique is not suited to non-commercial adsorbents. As such, much less data is available compared to other parameters which require less sample mass for measurement, such as the surface area and pore volume. The lower the bed density, the less adsorbent can be placed within the vessel volume, and the lower the volumetric CO_2 adsorption capacity of the bed. However, a higher bed density implies lower adsorbent porosity, which in turn could lead to restricted kinetics. Functionalisation fills the adsorbent pores which thus decreases the adsorbent porosity and increases the bed and particle density. Figure 2.3c shows a rather large span of mean density values, from ~ 0.10 to 0.70 g cm^{-3}. For context, commercial zeolite 13X beads from BASF have a reported bed density of 0.65 to 0.70 g cm^{-3} [51].

Approximately half of the bed densities reported in Figure 2.3c are for adsorbents in powder form, while more than 75% of the adsorbents tabulated in Tables A1.1 to A1.6 are synthesised as powders. However, adsorbents in this form are often impractical to use in an actual process as they would be difficult to handle, and their dense packing would result in high pressure drop and poor heat and mass transfer. Rather, shaping powder adsorbents and reporting the shaped adsorbent's bed density would be more useful for adsorption processes. In a positive trend, there appears to be an increase in studies reporting on shaped adsorbents for DAC, with roughly the same number of studies (~ 20 to 30) published between 2022 to 2024 and 2016 to 2021. Examples of shaped forms investigated in the last two years include monoliths [18, 52-55], fibres [56-63], pellets [53, 64, 65], and laminates [66]. The choice of the best adsorbent structure depends on the balance of various parameters such as volumetric working capacity, mass transfer, thermal behaviour, and pressure drop. The adsorbent structure selected will also determine the packing porosity in the bed. Studies such as those by Rezaei and Webley provide further information on the pros and cons of different structured adsorbents [67] and methodologies to compare their performance [68], while a recent review by Wu et al. provides a summary of the various shaping techniques used for adsorbents employed in gas separation applications [69].

2.2.1.4 Mechanical stability

Adsorbents with higher mechanical stability can have a longer lifetime, as they are more resistant to vibrational or frictional forces within the bed. The mechanical stability of the adsorbent can be assessed through a variety of mechanical properties, such as the tensile strength, compression strength, or Youngs modulus, but can only be done for shaped adsorbents. Although these mechanical properties are not needed for process modelling, they help evaluate the robustness of the material. Assessments of mechanical stability remain rare in the DAC literature as most adsorbents being investigated are in powder form. Amongst the studies which evaluate shaped adsorbents for DAC, only a handful report on their mechanical properties. The materials studied were MOF monoliths [52, 70], zeolite monoliths [71], silica pellets [64], alumina pellets [53], silica-based fibres [72], and polymer fibres [73].

2.2.1.5 Surface area

The surface area of an adsorbent is traditionally obtained by collecting N_2 isotherms at -196 °C and extracting the information using the Brunauer-Emmett-Teller (BET) method [74]. While this is the most common approach seen in the reviewed DAC literature, this adsorbate does not always provide accurate measurements due to the quadrupole moment of N_2 and possible diffusional limitations in microporous materials at -196 °C [75]. Some publications have also reported the Langmuir surface area (as noted in Tables A1.1to A1.6), but these were not included in Figure 2.3d, where only the BET surface areas (S_{BET}) are reported. Surface area is a parameter which largely influences the adsorption capacity of a material. Although not a direct input parameter for process modelling, it remains one of the most reported parameters in materials papers. The larger the surface area, the higher the total gas uptake. This inevitably leads to a reduction in CO_2 selectivity as the uptake of N_2, O_2, H_2O, and all other gases present in the atmosphere increases. Supports with larger surface areas can accommodate higher functionalisation loadings via grafting, which can increase the adsorbent's CO_2 capacity. As seen from Figure 2.3d, surface areas span a large range depending on the material and functionalisation typically decreases an adsorbent's surface area, sometimes by over two orders of magnitude.

2.2.1.6 Pore volume

The total pore volume ($V_{total\ pores}$) influences many other properties of the adsorbent. The pore volume of adsorbents is often measured using N_2 adsorption at - 196 °C, though as stated in the previous section, this may not always be the most appropriate adsorbate to use. The methods employed to extract the pore size information, such as Dubinin-Astakhov (DA) [76, 77], Horvath-Kawazoe (HK) [78], density functional theory (DFT) [79, 80], or Barrett-Joyner-Halenda (BJH) [81], are only reliable in the micropore (pore diameter < 2 nm) and/or mesopore (pore diameter 2 – 50 nm) range. For macroporous materials (pore diameter > 50 nm) such as polymeric resins, the use of N_2 - 196 °C adsorption alone would lead to an underestimation of the total pore volume. In these cases, other methods capable of accurate measurements in the macropore region, such as mercury intrusion porosimetry, should be used in conjunction with N_2 - 196 °C adsorption to obtain a complete pore size distribution [48].

The total pore volume of the adsorbent is needed in process modelling to calculate the total adsorbent porosity. A higher pore volume implies a higher porosity, which in turn leads to lower bed and particle density, and potentially lower thermal conductivity [82, 83] and higher heat capacity [82, 84], the impacts of which are discussed in their respective sections. The higher the total pore volume, the greater the potential for functionalisation loading. For chemisorbents, this will increase the CO_2 saturation capacity of the adsorbent. However, as seen in Figure 2.3e, functionalisation can severely reduce the pore volume of an adsorbent. Comparing the data entries in Figure 2.3e vs Figure 2.3f, it is evident that functionalisation often eliminates the presence of micropore volume ($V_{micropores}$) due to pore filling. This could severely limit gas diffusion within the adsorbent and result in poor kinetics for the adsorption process.

2.2.1.7 Specific heat capacity

The specific heat capacity (c_p) is the amount of heat needed to produce a unit change of temperature in a unit mass of the adsorbent. This can vary with temperature and gas uptake, and can be measured using differential scanning calorimetry [85, 86]. For a temperature swing adsorption process, an adsorbent with a lower c_p will require less energy to be heated to a high temperature for desorption, leading to lower operational costs. Similarly, for the same energy input, an adsorbent with a lower c_p

can be heated to a higher desorption temperature, thus increasing the working capacity. However, adsorbents with low c_p may also undergo a larger temperature swing during adsorption due to the exothermic nature of adsorption, which would reduce the amount adsorbed and thus the overall working capacity. Materials with higher porosity tend to have higher heat capacity [82, 84].

Although this parameter is needed for process modelling, it is rarely reported in DAC adsorbent papers and the same c_p value is often assumed for a range of different materials for process modelling. Few studies experimentally measure the c_p themselves [55, 66, 87-90], with most c_p values either found from DAC process papers or other non-DAC articles. Recently, Moosavi et al. developed a machine learning approach to predict the specific heat capacity of zeolites, MOFs, and covalent-organic frameworks (COFs) based on DFT simulations [91].

Figure 2.3g shows that functionalisation tends to increase the c_p of an adsorbent. Narayanan et al. experimentally determined the c_p values of alumina powder and poly(ethylenimine) (PEI) scaffolds to be ~ 0.8 J g^{-1} $°C^{-1}$ and ~ 1.7 J g^{-1} $°C^{-1}$ respectively at 40 °C, with samples synthesised from different ratios of alumina and PEI having c_p values within this range [55]. To provide perspective on the reported values, the heat capacity of commercial zeolite 13X powder is ~ 0.8 J g^{-1} $°C^{-1}$ [92], while that of a 20 wt% MEA-based aqueous solvent is ~ 3.9 J g^{-1} $°C^{-1}$ [93].

I note that all values reported in Figure 2.3g and Tables A1.1 to A1.6 are for pristine adsorbents, i.e. not loaded with CO_2 and/or other species. The temperature ranges of the reported heat capacities are also indicated in the tables when available.

2.2.1.8 Thermal conductivity

Thermal conductivity (κ) is a measure of an adsorbent's ability to conduct heat. It can vary with temperature and is often determined theoretically rather than measured experimentally [82]. A higher thermal conductivity is desirable for adsorption if the system is being operated isothermally, where heat needs to dissipate through the adsorbent and out of the bed. However, for adiabatic operation, lower thermal conductivity would be preferable to minimise the increase in the adsorbent temperature during adsorption, which would decrease the working capacity. For desorption, a higher thermal conductivity is desirable as heat can diffuse faster through the adsorbent when the bed is heated, thus increasing

productivity. The design of the contactor and/or desorption process can compensate to some extent the low thermal conductivity of an adsorbent [17]. Adsorbents with lower porosity tend to have higher thermal conductivity [83].

This parameter has been identified as a key adsorbent property which affects process performance [43], but there is still extremely limited data available for investigated DAC adsorbents. Similar to the specific heat capacity, the same value is often assumed for a range of different materials. The data entries in Figure 2.3h were found in DAC process papers or other non-DAC articles, with temperature ranges of the reported thermal conductivities indicated in Tables A1.1 to A1.6 when available. As seen in Figure 2.3h, unmodified metal oxides such as alumina and semimetals such as activated carbon (in monolith form), respectively, conduct heat well and have high thermal conductivities (35 W m^{-1} $°C^{-1}$ [94] and 18 W m^{-1} $°C^{-1}$ [45], respectively), while materials such as silica and MOFs have relatively poor thermal conductivities (< 0.5 W m^{-1} $°C^{-1}$).

2.2.1.9 Thermal stability

The thermal stability of an adsorbent is the maximum temperature the material can withstand before it starts to degrade, for example due to decomposition of the chemical structure or leaching of some functionalisation compounds. While not a direct input in process models, this temperature determines the maximum temperature which can be used during the desorption process, and is typically measured using a thermogravimetric analyser (TGA) either in a N_2 or air environment. To be viable for most commercialised DAC processes, adsorbents will need to be thermally stable up to at least 80 °C [95] to withstand the regeneration procedure.

Amongst unfunctionalised materials, metal oxides, silicas, zeolites, and carbons have high thermal stability above 500 °C, while polymers and MOFs exhibit moderate thermal stability between 100 °C and 500 °C. Once adsorbents are functionalised however, the thermal stability depends on the functionalisation compound, and thus functionalisation typically lowers the thermal stability of an adsorbent owing to the organic nature of the compounds that are commonly used for functionalisation. Functionalisation carried out via impregnation leads to less stable materials than grafting due to a lack of chemical bonds. As well, functionalised amines of lower molecular weights tend to be more prone

to evaporation or leaching. This may be mitigated by using additives to increase the amine's molecular weight and impart stronger interactions with the support, though often at the sacrifice of some CO_2 adsorption capacity [96, 97].

As seen from Figure 2.3i, most functionalised materials being considered for DAC exhibit thermal stabilities above 100 °C. One exception is a study done by Pang et al. [98], who investigated SBA-15 adsorbents impregnated with small molecule linear or dendritic PEI or poly(propylenimine) (PPI) which had maximum regeneration temperatures of 70 °C. Cuesta and Song [99] also developed carbon black adsorbents immobilized with bovine carbonic anhydrase enzymes for regeneration at 35 °C. These adsorbents need to be refrigerated or frozen for short or long-term storage, respectively, and exposure to temperatures higher than 35 °C could start to induce enzyme denaturation. Overall, thermal stability data is available for most of the investigated DAC adsorbents reviewed here, either from the original study or from other sources.

2.2.2 Equilibrium sorption properties

An adsorbent for DAC needs to have a high affinity for CO_2. This can be challenging as other species such as N_2, O_2, and H_2O are in much higher concentrations in air. The equilibrium sorption properties for these species should therefore be investigated and are reviewed in the following sub-sections following the same adsorbent classification adopted in the previous section. This analysis focuses almost exclusively on single-component uptake measurements, as multi-component adsorption isotherms are experimentally challenging and time-consuming to measure and thus are rare in the DAC literature. The co-adsorption of multiple gas species can be predicted from the single-component isotherms using approaches such as ideal adsorbed solution theory (IAST) [100] or empirically extended binary isotherm equations [101].

2.2.2.1 CO_2 adsorption

CO_2 uptake at 400 ppm

The CO_2 working capacity, *i.e.* the difference between the CO_2 uptakes at adsorption and desorption conditions, is an important feature of a DAC adsorbent which can vary depending on the desorption process chosen. However, most studies in the DAC adsorbent literature only report the CO_2 adsorption uptake at 400 ppm. The CO_2 uptake can be measured using volumetric (e.g. commercial manometric adsorption analyser), gravimetric (e.g. TGA), or dynamic set-ups (e.g. packed bed column). The CO_2 uptake values measured up to 500 ppm CO_2 concentrations and between 20 and 30 °C for adsorbents developed between 2016 to 2021 are presented in Figure 2.4a, with the values and measurement methods tabulated in Tables A1.7 to A1.12. It is worth noting that there has also been increasing interest in the last two years in investigating the CO_2 uptake at sub-ambient temperatures such as 0 °C and -20 °C [31, 58, 102, 103]. Tables A1.7 to A1.12 also cover publications which report the CO_2 uptake at concentrations up to $4\%_{vol}$, i.e. the threshold for natural gas-fired post-combustion capture applications. While data at these higher concentrations may provide useful insights into the material performance, effort should be made to conduct experiments at the relevant conditions for DAC as the trends observed may not hold true at 400 ppm CO_2 concentration.

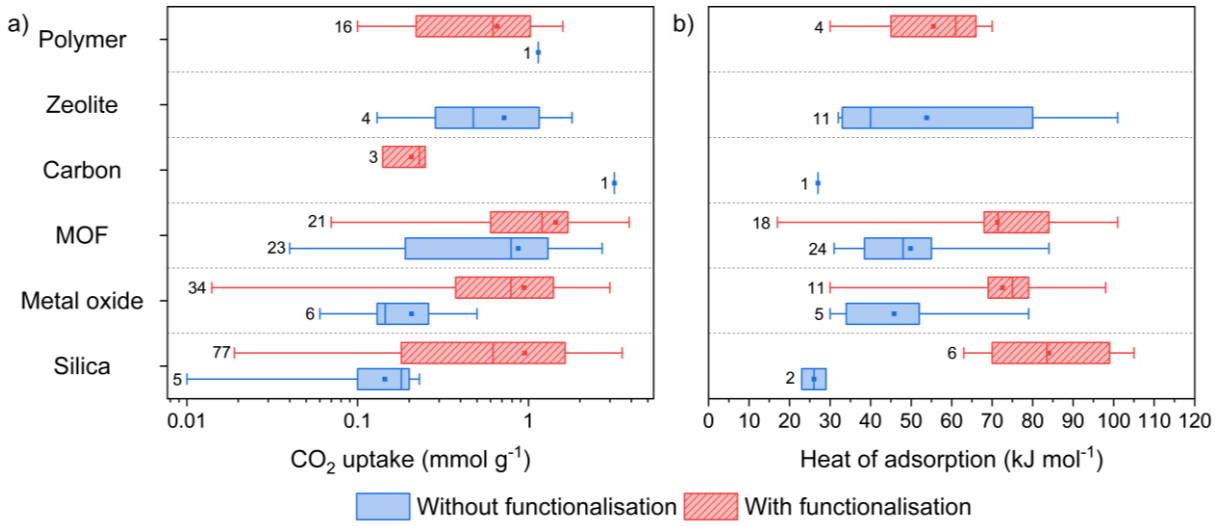


Figure 2.4. Comparison of a) CO_2 uptake values (at concentrations lower than 500 ppm and temperatures between 20 to 30 °C, except for unfunctionalised SBA-15 whose uptake of 0.01 mmol g^{-1} was measured at 10,000 ppm [104]) and b) heat of adsorption values for different adsorbent categories, both with and without additional functionalisation. Box edges represent the 25th and 75th percentile, whisker edges represent the minimum and maximum data points, the solid line through the box represents the median, and the filled square symbol represents the mean. Total number of data entries are labelled to the left of each box. All data entries can be found in Tables A1.7 to A1.12.

As seen in Figure 2.4a, the CO_2 uptake by different adsorbents ranges from as low as 0.01 mmol g^{-1} to over 3.0 mmol g^{-1}. In general, functionalisation of the adsorbent increases its CO_2 uptake compared to its non-functionalised form, and the higher the functionalisation loading, the higher the CO_2 uptake. However, past a certain threshold, pore blockage can occur causing increased diffusion resistance and therefore decreased CO_2 uptake. An example is TEPA-functionalised ZSM-5 and SAPO-34, for which amine functionalisation resulted in blockage of the zeolites' micropores and prevented access to both amine and zeolite binding sites for CO_2 [105].

When comparing different adsorbents however, it is difficult to distinguish a clear trend in CO_2 uptakes between physisorbents and chemisorbents. For example, some unfunctionalised MOFs have comparable CO_2 uptake to functionalised MOFs. Most of the former are classed as ultramicroporous MOFs, which have pore sizes smaller than 0.7 nm [106]. The small pore size and presence of fluorinated

ions in MOFs such as TIFSIX-3-Ni [107], SIFSIX-3-Cu [108], and NbOFFIVE-1-Ni [109] yield relatively high CO_2 adsorption uptake (~ 1.0 to 1.5 mmol g^{-1}) with the added advantage of lower heats of adsorption compared to the functionalised MOFs. In the class of zeolites, a Ca^{2+} ion-exchanged A-type zeolite physisorbent developed by Oda et al. [110] demonstrated a high CO_2 uptake of 1.8 mmol g^{-1} at 400 ppm, attributed to each CO_2 molecule bridging between two Ca^{2+} ions. A recent study by Tao et al. reported a CO_2 uptake of 1.1 mmol g^{-1} on another Ca^{2+} ion-exchanged A-type zeolite [111]. They systematically determined that Ca^{2+} has the optimal charge-to-size ratio amongst various cations, as it has sufficiently high interaction energy with CO_2 without excessive H_2O adsorption. The addition of Zn^{2+} ions in chabazite-type zeolites was also shown to improve the CO_2 uptake from 0.03 mmol g^{-1} in the parent sample to 0.67 mmol g^{-1} in the new ion-exchanged zeolite [112]. A mordenite-type zeolite with a CO_2 uptake of 1.2 mmol g^{-1} was also recently studied [113]. These uptakes are higher than those reported for some amine-functionalised zeolites (~ 0.3 to 0.6 mmol g^{-1}) [114], with some uptakes measured at much higher CO_2 concentrations of 5000 ppm [105].

Conversely, some functionalised adsorbents have very low CO_2 uptakes (< 0.1 mmol g^{-1}) as seen in Figure 2.4a. This is often due to insufficient loadings or unsuitable functionalisation. For example, tertiary amines have been shown to have poor CO_2 uptakes in dry conditions, and their uptakes in the presence of humidity may still be lower when compared to primary or secondary amines in dry conditions [115]. Many of the highest adsorbing materials though are amine-functionalised materials, such as tetraethylenepentamine (TEPA)-impregnated hierarchial silica (5.2 mmol g^{-1}) [64], TEPA-impregnated SBA-15 (3.4 mmol g^{-1}) [116], *N*,*N*′-dimethylethylenediamine (mmen)-grafted Mg_2(dopbdc) (3.1 mmol g^{-1}) [117], and hydrazine-grafted Mg-MOF-74 (3.9 mmol g^{-1}) [89]. One exception is the unfunctionalised biochar adsorbent synthesised from sawdust by Kua et al. [118] which is reported to have a gravimetric CO_2 uptake of 3.2 mmol g^{-1} at 500 ppm. However, no CO_2 isotherm data was provided nor any material characterisation data.

CO_2 isotherms

A key process model input is the numerical expression of the CO_2 adsorption isotherm, which is obtained by fitting experimental adsorption data collected at constant temperature, typically between

0 to 1 bar. As with the CO_2 uptake, adsorption isotherms can be measured using volumetric, gravimetric, or dynamic techniques. One of the main sources of uncertainty in a process model stems from the parameters of the adsorption isotherm model, but this variability can be reduced by collecting data at several temperatures and over a wide range of temperatures [119].

In Figure 2.5, we consider as criterion that at least three temperatures be measured for CO_2 isotherms. This is also the minimum number of isotherm temperatures that need to be measured to extract the heat of adsorption, which is discussed in the following section. Isotherm data meeting this requirement remains largely unavailable/unreported for most proposed DAC adsorbents. This data gap is one which requires significant attention. Figure 2.6 displays CO_2 isotherms at 25 °C for different adsorbents which have isotherms measured at three or more temperatures and up to 1 bar. Here, materials with the highest CO_2 uptake at 1 bar do not necessarily have the highest uptake at 400 ppm (e.g. zeolites compared to silicas). Rather, materials with steep isotherms in the low-pressure range (i.e. the Henry regime) tend to have high CO_2 uptake at the relevant concentrations for DAC. Some studies also do not collect sufficient isotherm points in the low-pressure range. While gathering this data may be time consuming, it is essential to ensure the isotherm model fitting is accurate in this range in order to accurately capture the CO_2 affinity [43]. Additionally, even if some publications do collect isotherms at multiple temperatures, they do not always do so up to 1 bar. Although adsorption for DAC occurs at 400 ppm, the adsorption information up to 1 bar becomes relevant for the desorption process, where a CO_2-enriched stream is produced.

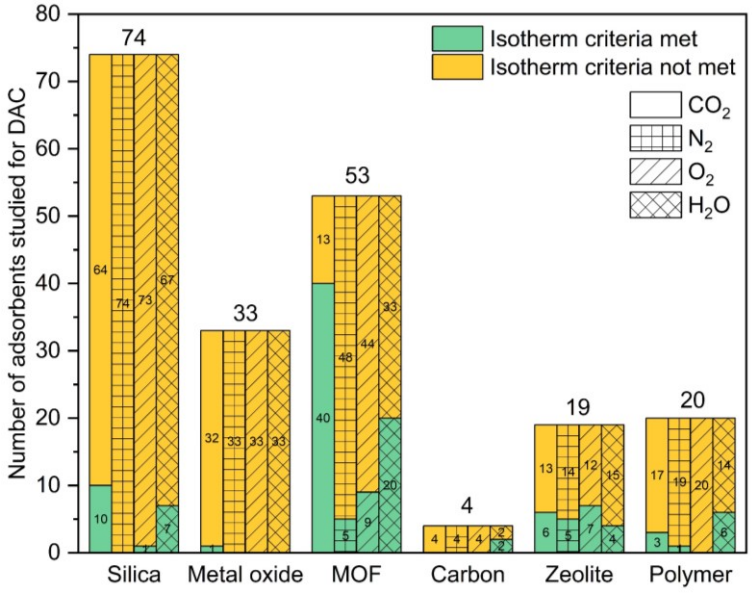


Figure 2.5. Overview of CO_2, N_2, O_2, and H_2O isotherm availability for different classes of adsorbents reported between 2016 and 2021. For CO_2 and N_2 isotherms, the criterion is met if there are isotherms available at three temperatures and at pressures up to 1 bar. Isotherms that were collected at cryogenic temperatures for CO_2 and N_2 were still included in this count, however these are not suitable for DAC applications and are more useful for porosity characterisation rather than isotherm fittings for process modelling. Indication was made in Tables A1.7 to A1.12 if this was the case. For O_2 and H_2O isotherms, our criterion is met provided there is an isotherm available, at any temperature and pressure range below 1 bar. An adsorbent was considered to be studied for DAC if a CO_2 uptake between $0.04\%_{vol}$ to $4\%_{vol}$ was measured. An adsorbent was not double counted if it was studied by multiple publications, and adsorbents with different loadings of the same functionalisation were counted as just one material. Adsorbents of different structural forms (e.g. powder vs. monolith) were counted as two separate materials. All data entries and their corresponding sources are available in Tables A1.7 to A1.12. Isotherms were not always found in DAC related publications. Some adsorbents included in the tables (e.g. silica gel, γ-alumina, activated carbon) were not considered to be studied for DAC and so were not included in these counts even if isotherm data was available.

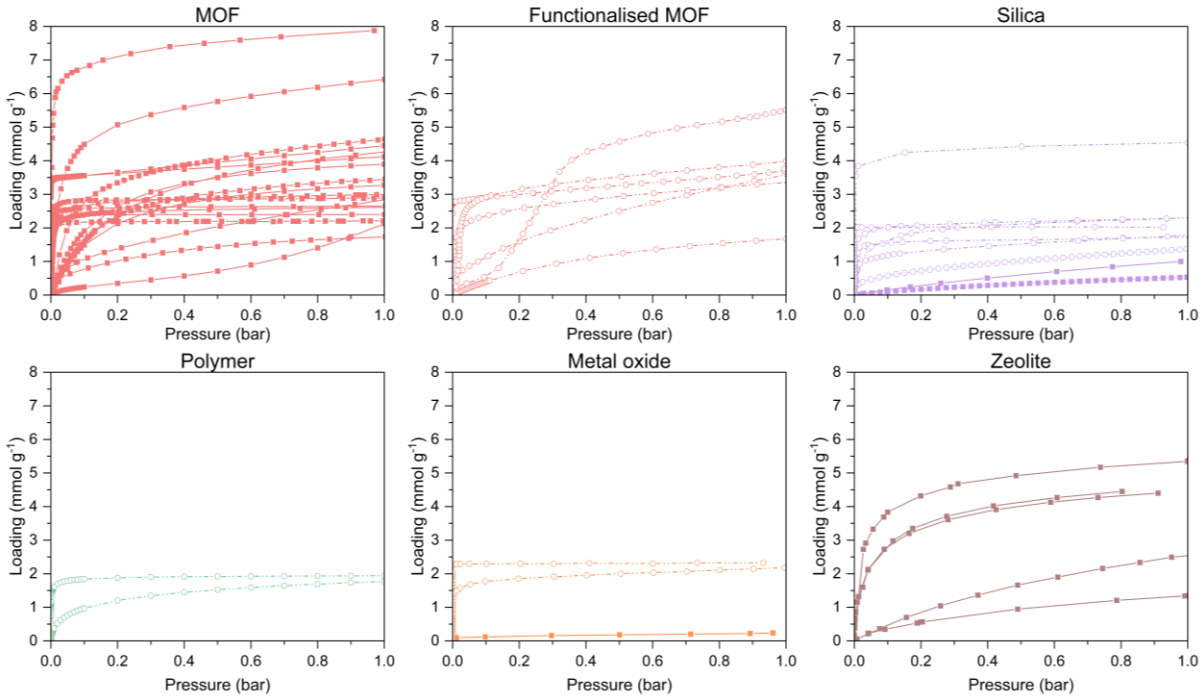


Figure 2.6. CO_2 adsorption isotherms at 25 °C and up to a pressure of 1 bar for materials which have had CO_2 isotherms measured at a minimum of three temperatures (as indicated in Tables A1.7 to A1.12). Unfunctionalised adsorbents are represented by filled markers and solid lines, and functionalised adsorbents are represented by hollow markers and dashed lines. Data points have either been digitised, plotted using a fitted isotherm model, or plotted from tabulated data.

Heat of adsorption

The CO_2 heat of adsorption gives an indication of the strength of adsorption between the material and CO_2, and is a necessary input in process models. The higher the value, the more likely the adsorbent will be able to selectively adsorb CO_2 even at dilute concentrations. Yet, a high heat of adsorption also implies higher energy to regenerate the adsorbent and thus higher operating costs. The heat of adsorption is traditionally obtained by measuring three or more isotherms spaced 10 °C apart, and by either applying the van 't Hoff equation or virial analysis [120, 121]. For the former, the heat of adsorption at a specific CO_2 loading can be determined from the slope of a plot of $\ln(P)$ vs $1/T$ at a given amount adsorbed, where P is the pressure and T is the temperature. For the latter, the adsorption isotherm data is fitted directly with a virial expansion, generating virial coefficients from which the heat of adsorption can be determined. The isosteric heat of adsorption is the heat of adsorption expressed as

a function of the CO_2 loading. At zero loading, one refers to it as the limiting heat of adsorption (ΔH_0). Tables A1.7 to A1.12 list the limiting heats of adsorption of candidate DAC adsorbents, along with the heats of adsorption at loadings corresponding to the adsorbent's CO_2 uptake at DAC concentrations if the values greatly differ. All data entries are included in Figure 2.4b to show the entire possible range of heat of adsorption values. The general guideline is that materials with heat of adsorption values less than 50 kJ mol^{-1} are classed as physisorbents and those with higher values are classed as chemisorbents [122]. As mentioned earlier, unfunctionalised adsorbents are typically physisorbents, and functionalised adsorbents are typically chemisorbents. As seen in Figure 2.4b, this classification holds true for most adsorbents. Most amine-functionalised adsorbents exhibit heats of adsorption greater than 70 kJ mol^{-1}, while most unfunctionalised adsorbents exhibit heats of adsorption lower than 50 kJ mol^{-1}.

There remain exceptions to the classification mentioned above. In some cases, unfunctionalised materials are chemisorbents and display high heats of adsorption. Examples include the bare γ-alumina supports, on which CO_2 binds and forms bicarbonate and carbonate species on the basic alumina surface [123], and the benzotriazolate MOFs with metal hydroxyl sites which allow for CO_2 chemisorption [124-126]. Some physisorbents, such as the ultramicroporous MOF families of TIFSIX [107], SIFSIX [108, 127, 128], and NbOFFIVE [109], also exhibit heat of adsorption values bordering either side of 50 kJ mol^{-1}. The alkaline-earth-metal ion-exchanged MFI-type zeolites display even higher heats of adsorption values between 80 to 100 kJ mol^{-1} due to the strong electrostatic interactions between acidic CO_2 and the M^{2+}-O-M^{2+} sites of the adsorbent, where M^{2+} is the alkaline-earth-metal ion [129].

General trends are also observed with the heat of adsorption versus CO_2 loading. In most cases, the heat of adsorption is highest at zero loading, and decreases as the loading increases. This pattern implies the presence of heterogenous CO_2 binding sites, where the stronger sites are filled first. However, some adsorbents maintain a constant heat of adsorption over a wide loading range. This is the case with some members of the SIFSIX family, which according to the authors, suggests the presence of homogenous energetic sites throughout the adsorbent [127]. For other materials, the heat of adsorption increases with loading. An example of this is the diamine-appended Mg_2(dobpdc) MOF developed by McDonald et al., where the increase in heat of adsorption is attributed to cooperative CO_2 adsorption [130, 131].

Despite the importance of the heat of adsorption, there is still a big data gap in this area, as can be seen when comparing Figures 2.4a and 2.4b and in Tables A1.7 to A1.12. Except for MOFs and zeolites, most adsorbents in all material classes do not have reported heats of adsorption, which corresponds with the data gaps in the CO_2 isotherms. More recently however, a few more studies on amine-functionalised silica adsorbents have reported the CO_2 heat of adsorption [64, 66, 132-134].

2.2.2.2 N_2 adsorption

N_2 isotherm information should be included in process models for DAC as N_2 accounts for over 78%$_{vol}$ of the feed gas composition (i.e. atmospheric air). For physisorbents, N_2 is a competitive adsorbate against CO_2 and its uptake will reduce the CO_2 capacity of the adsorbent. For chemisorbents, this is often less of an issue, however some N_2 adsorption can still occur on unfunctionalised surfaces. Even if only a slight amount is adsorbed during the process, performance indicators such as CO_2 working capacity and purity may be impacted. Therefore, like for CO_2, one should collect N_2 sorption isotherms at a minimum of three temperatures to parameterise a suitable adsorption isotherm model and to calculate the N_2 heat of adsorption. Isotherms up to 1 bar should be collected to cover the possible concentration range of N_2 throughout the process. As seen in Figure 2.5, it is quite rare to find N_2 isotherms at three temperatures up to 1 bar for DAC adsorbents, even when considering non-DAC related papers. Most commonly, only one isotherm is measured and the impact of N_2 on the process is assumed to be negligible.

2.2.2.3 O_2 adsorption

O_2 isotherms

O_2 accounts for over 20%$_{vol}$ of the gas composition in the atmosphere, and like N_2, can be a competitive adsorbate particularly for physisorbents. Hence, one should study its adsorption behaviour. If the adsorption is non-negligible, one should collect isotherms at three temperatures up to 1 bar to allow for isotherm fitting and heat of adsorption calculation. In addition, O_2 can react with and damage certain adsorbents as discussed in the following section. Assessing the extent of O_2 adsorption is therefore useful to understand how much O_2 can potentially interact with the material. As shown in

Figure 2.5, there is an obvious lack of data in the O_2 isotherms available for candidate DAC adsorbents, even when considering non-DAC related publications.

Oxidative stability

Oxidative stability is a necessary feature of adsorbents for DAC as O_2 is present throughout the entire process. Amongst the discussed adsorbent categories, amine-functionalised adsorbents are the most susceptible to oxidative degradation, particularly at the high temperatures experienced during desorption (i.e. > 75 °C). Exposure after just one day has been observed to result in the loss of CO_2 adsorption sites [135]. This can also occur at lower temperatures experienced during adsorption over longer periods of time, and under ambient storage conditions [136, 137]. Products of amine oxidative degradation include imines, amides, ammonia, aminoacetaldehyde, and hydroxylamines. Works by Carneiro et al. [137], Guta et al. [138], Li et al. [139], and Yan and Sayari [140] offer detailed studies into the various mechanisms of amine oxidative degradation.

Primary and tertiary amines have been observed to be more resistant to oxidation compared to secondary amines, as the latter can readily form imines or amides [141]. For aminopolymers, the presence of additional carbons between amine groups (e.g. propylene vs. ethylene linkers) imparts higher oxidation stability, and higher molecular weights are hypothesised to better prevent O_2 penetration within the polymer bulk to initiate degradation [98, 142, 143]. The latter would however also hinder CO_2 diffusion within the adsorbent. Epoxide modification of amines has also been investigated for improved oxidative stability, where the newly formed hydroxyethyl groups interact with amine sites via hydrogen bonding and impart steric hindrance, thus shielding them from oxidation reactions [61, 144, 145]. This improved stability often comes at the sacrifice of CO_2 adsorption capacity however, as the number of amine sites available for CO_2 reaction is reduced. Miao et al. also reported the reduced impact of oxidative degradation when operating DAC at sub-ambient temperatures [146].

While the studies discussed above have focused specifically on developing DAC adsorbents with improved oxidative stability, others are limited to either measuring one O_2 adsorption isotherm and claiming minimal adsorption, or running their experiments using an ambient air stream. In these cases, further investigation is still needed to look at the impact of O_2 at higher temperatures as well as

long-term exposure, as this will be important for the desorption process and shelf-life, respectively. The impacts of O_2 on adsorbents are summarised in Tables A1.7 to A1.12 where data is available, although there is clearly a data gap on this topic in the current literature. If the impact of O_2 on the CO_2 uptake was provided, I identify if more than ("> 50% CO_2") or less than 50% ("< 50% CO_2") of the CO_2 uptake was maintained, and if these studies were conducted at CO_2 concentrations higher than $4\%_{vol}$. For papers which looked at the structural integrity of the adsorbent, "N" indicates that either the adsorbent support or functionalisation material degrades in the presence of oxygen, while "Y" indicates that the adsorbent appears to be structurally stable or regenerable. I also indicate if papers reported a low O_2 uptake from their measured isotherms. Where possible, I include the % RH and temperature conditions used for these oxidation studies.

2.2.2.4 H_2O adsorption

H_2O isotherms

Water is always present in the atmosphere to some degree (see Figure 2.2) and can compete with CO_2, occupying the same binding sites, and reducing the CO_2 adsorption capacity. In some cases, H_2O increases the CO_2 capacity of the adsorbent. Regardless of the situation – competitive or synergistic adsorption – a material adsorbing a high amount of H_2O will require higher energy consumption for full desorption/regeneration. Young et al. previously identified H_2O adsorption as one of the critical adsorbent parameters affecting DAC process performance [43]. Therefore, it is recommended for at least one H_2O adsorption isotherm to be measured in DAC adsorbent studies. As with O_2, if the H_2O uptake is non-negligible, isotherms at three temperatures should be measured to obtain the necessary information for process modelling. As seen in Figure 2.5, collecting at least one H_2O isotherm is more frequent than for N_2 or O_2. Yet, there is still a significant lack of data in this area for candidate DAC adsorbents, even when searching in non-DAC related publications. If a steam-assisted desorption process is of interest, measuring H_2O isotherms at higher temperatures is critical. Steam adsorption equilibrium data at 110 °C was recently reported for the first time for a candidate DAC adsorbent (Lewatit VP OC 1065) by Wilkins et al. [147].

Due to the complex interactions that can occur between CO_2 and H_2O as well as the adsorbent, measuring CO_2-H_2O co-adsorption equilibrium isotherms is also critical. Such measurement represents more accurately the impact of H_2O on DAC processes compared to predictions from single-component adsorption data. However, binary adsorption isotherms are experimentally challenging to measure and remain largely unavailable in the DAC literature, save for a few studies such as those by Gebald et al. [148], Elfving and Sainio [149], and Young et al. [150]. CO_2-H_2O co-adsorption isotherm data is also available for zeolite 13X, though these were measured in the context of post-combustion capture [151]. Reviews by Rajendran et al. [152] and Shade et al. [153] provide further insight into experimental techniques for measuring co-adsorption isotherms.

Hydrolytic stability

As mentioned above, water adsorption can either enhance, or compete with, CO_2 adsorption in DAC adsorbents. In general, the CO_2 uptake for amine-functionalised adsorbents increases in the presence of humidity due to a change in the adsorption mechanism. Under dry conditions, two N atoms are needed to react with CO_2 via carbamate formation (equation (2.1)). In the presence of water, only one N atom is theoretically needed to adsorb CO_2 via bicarbonate formation (equation (2.2)) [12].

$$2RNH_2 + CO_2 \leftrightarrow RNH_3^+ \, RNHCO_2^- \quad (2.1)$$

$$RNH_2 + H_2O + CO_2 \leftrightarrow RNH_3^+ \, HCO_3^- \quad (2.2)$$

Moisture can also help to maintain the long-term stability of amine-functionalised adsorbents by preventing the formation of urea, which would otherwise eliminate CO_2 adsorption sites [154, 155]. However, Carneiro et al. also recently showed that the presence of water vapour can accelerate oxidative degradation in solid amines [137]. Some adsorbents even require the presence of moisture for CO_2 adsorption to occur. Tertiary amines cannot react to form carbamates, and only adsorb CO_2 in the presence of water via bicarbonate formation (equation (2.3)) [12]. Sodium or potassium carbonate-functionalised adsorbents also only react with CO_2 in the presence of moisture to form sodium or potassium bicarbonate (equation (2.4), M = Na or K) [156, 157].

$$R_1R_2R_3N + H_2O + CO_2 \leftrightarrow R_1R_2R_3NH^+HCO_3^- \quad (2.3)$$

$$M_2CO_3 + H_2O + CO_2 \leftrightarrow 2MHCO_3 \quad (2.4)$$

The latter are typically moisture-swing adsorbents, which adsorb and desorb CO_2 upon exposure to low and high humidity, respectively. Here, the presence of excessive H_2O molecules at high humidity conditions destabilises the bicarbonate ions and causes CO_2 to desorb [158].

For most physisorbents such as unfunctionalised MOFs, zeolites, and carbons, the presence of humidity typically reduces their CO_2 uptake due to the competitive adsorption of water on CO_2 adsorption sites [159]. The use of hydrophobic coatings/modifications has been investigated in some studies to combat this effect [160-162], as well as to reduce the energy consumption associated with water desorption in amine-functionalised adsorbents [60, 163, 164].

Some adsorbents are also simply not structurally stable in the presence of water vapour, such as SIFSIX-3-Cu [165], TIFSIX-3-Co [166], and Mg-MOF-74 [106]. Depending on the extent of the impact of moisture on these adsorbents, the removal of water may need to be incorporated into the process, though this could increase capital and operating costs. Works by Fu and Davis [167], Holmes et al. [168], Song et al. [52], and Wilson and Tezel [30] investigate the impacts of this strategy, particularly with the use of zeolite adsorbents, on costs and/or energy consumption for DAC in detail. Further in-depth explanations of the effect of water on CO_2 adsorption for both physisorbents and chemisorbents can be found in the review by Kolle et al. [159].

The impact of humidity on DAC adsorbents are summarised in Tables A1.7 to A1.12 where data is available. “N” indicates the worst-case scenario where the structure of the adsorbent itself has deteriorated due to the collapse of the crystal and/or pore structure and is unregenerable. “Y” indicates that the adsorbent structure, including its functionalisation, is unaffected or is regenerable after humidity exposure. Where possible, these are then further classified into “+” or “-” categories, which indicate whether the CO_2 uptake increases or decreases in the presence of humidity, respectively, along with the % RH and temperatures used for these studies. Indication is also made if the material was determined to be stable under steam regeneration (“ss”). This method of categorisation follows that proposed by Kong et al. in their recent perspective article on DAC [28]. For the purposes of simplicity, I did not consider the effect of humidity on the CO_2 adsorption kinetics in this categorisation. I also note that the effect of humidity on the adsorbents reviewed in these tables were not always investigated at low CO_2 concentrations relevant to DAC. While an adsorbent may maintain high CO_2 capacity in the presence

of moisture at high concentrations, the effect of humidity may be more severe when the CO_2 concentration is reduced to 400 ppm. Therefore, one should conduct experiments at the relevant conditions whenever possible.

2.2.2.5 Cyclic adsorption

As discussed previously, one of the key properties for a DAC adsorbent is its CO_2 working capacity. For practical use at scale, DAC adsorbents should exhibit sufficient structural and chemical longevity with minimal loss in working capacity upon repeated cyclic exposure to adsorption and desorption conditions. The longer an adsorbent's working capacity is maintained, the less frequently it will need to be replaced, leading to lower operation costs and smaller carbon footprints. Recently, Holmes et al. highlighted that a replacement rate was an oversimplification of an adsorbent's stability, and rather an analysis of its capacity loss over time would provide a more accurate assessment of the economics associated with a DAC process [169]. Therefore, long term cyclic studies need to be conducted to properly evaluate the potential of a DAC adsorbent at scale.

The presence ("Y") or absence ("N") of cyclic studies in DAC adsorbent studies from 2016 to 2021 are summarised in Tables A1.7 to A1.12. Overall, over 85% of the studies report some form of cyclic testing, although the majority measure 10 cycles or less and not all studies are carried out at DAC conditions. These experiments were usually conducted using either packed bed columns or TGA, and commonly employ a simple temperature swing adsorption (TSA) process, where CO_2 adsorption occurs at ambient temperature, followed by desorption at elevated temperatures (~70 to 120 °C) using either an inert gas or air stream.

However, some studies have investigated the CO_2 working capacity of adsorbents over 50 or more cycles under DAC conditions [143, 170-174]. In particular, Guo et al. [160], Ge et al. [175], and Ahsan et al. [176] studied a polymer-coated MOF, an amine-grafted metal oxide, and an amine-grafted silica over 2000, 200, and 100 adsorption-desorption cycles, respectively. Parvazinia et al. [177] also studied the stability of Lewatit VP OC 1065 over 200 cycles, however this was done with $10\%_{vol}$ CO_2. These adsorbents demonstrated only minor losses (< 10%) in their working capacity over the course of their respective cycles. Hunt et al. also investigated the cyclic stability of Lewatit VP OC 1065, but

observed a 31% decrease in working capacity after 180 cycles [178]. Here, ambient air was used for adsorption and 80 °C and 100 mbar of vacuum was used for desorption. In comparison, Parvazinia et al. had utilised 10%$_{vol}$ CO_2 balanced with N_2 for adsorption, and 105 °C and N_2 for desorption. Therefore, the choice of adsorption and desorption conditions greatly affects the cyclic stability of the adsorbent studied.

2.2.3 Kinetic sorption properties

CO_2 mass transfer/adsorption kinetics has been identified as another critical factor impacting the key performance indicators of a DAC process [43, 44]. Rapid kinetics enable shorter cycle times, which in turn results in higher productivity and reduced capital costs. Slower kinetics hamper CO_2 recovery as a greater portion of feed gas will break through the adsorption bed, resulting in a loss of CO_2 back into the atmosphere. Higher energy consumption and operating costs then result to process a larger volume of feed gas to capture a given amount of CO_2. Therefore, quantification of the gas diffusion and adsorption kinetics is critical to the deployment of adsorption-based DAC technologies.

Studies reporting DAC adsorbents often only focus on the CO_2 adsorption kinetics, as the diffusion of feed gas through the contactor is a process-scale consideration. The former can be measured experimentally using a variety of techniques such as direct uptake rate measurements (for example with a TGA) and dynamic column breakthrough. Over 90% of the papers reviewed in Tables A1.7 to A1.12 include some form of kinetic experiment using either of the aforementioned techniques. However, most of these studies report parameters such as rates of adsorption, or breakthrough, retention, or saturation times, which are not usable inputs in process models. Instead, a mathematical model is needed to extract the information regarding mass transfer coefficients. In the last two years, an increasing number of DAC studies are employing the latter approach compared to between 2016 to 2021, and are more often conducting their experiments at CO_2 concentrations relevant to DAC. The most commonly used models are the linear driving force model [30, 35, 53, 179, 180], Avrami model, and pseudo-first and -second order rate models [44, 62, 116, 134, 173, 181-185]. Despite this encouraging trend, most kinetic experiments are still not systematically conducted. As a result, the parameters reported are dependent

on many experimental factors such as adsorbent particle size, gas flow rates, column dimensions, system temperature and pressure, and feed gas concentration. This makes it very difficult to compare the kinetic results of different publications. There are however a few recent studies which do investigate the impacts of one or more of these factors on the adsorption kinetics [59, 149, 179, 186-188].

2.3 Synergy between adsorbent and process development for DAC

Since an adsorbent must ultimately be integrated into an adsorption process, adsorbent and process development should occur harmoniously [189]. Applying a promising adsorbent in a process model provides understanding of how the adsorbent properties can influence the process performance indicators. To apply an adsorbent in a process model, key adsorbent properties such as those described throughout this review need to be available.

Figure 2.7 shows the comparison between an estimation of the total number of adsorbent and process studies published since 2016, and the distribution of adsorbent types. The number of DAC publications per year has been rising exponentially since 2016, with more studies published between 2022 to 2024 than between 2016 to 2021. Adsorbent studies are those focused on materials development, and process studies are defined as those which report process performance metrics. As shown in Figure 2.7, there have been almost three times the number of adsorbent studies published compared to process studies. Most adsorbent studies focus on silica and MOF adsorbents, while almost half of the published process studies utilise polymer adsorbents in their modelling. This discrepancy is largely due to the lack of data in the adsorbent properties, as the full extent of adsorbent characterisation that is required for application in a process model is rarely completed. As a result, many promising adsorbents are not screened/assessed for a given adsorption process, leaving a gap in understanding their suitability for DAC processes.

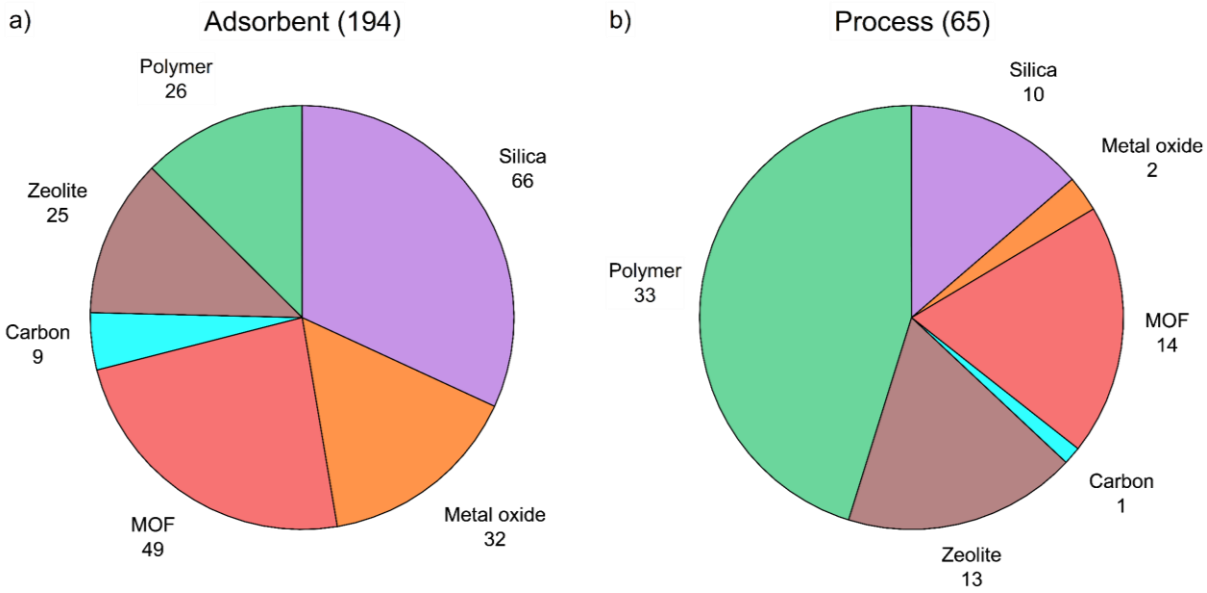


Figure 2.7. Comparison of the number of studies using different adsorbent categories in (a) adsorbent studies and (b) process studies. Adsorbent studies refer to studies focusing on materials development. Process studies refer to studies reporting process performance metrics. Several studies investigated more than one adsorbent category. This is reflected in the number of papers associated with each adsorbent type, but did not contribute to the final "adsorbent" and "process" total.

Based on the data tabulated in Tables A1.1 to A1.12, amongst the hundreds of adsorbents studied for DAC, only two adsorbents, zeolite 13X and Lewatit VP OC 1065 (an amine-functionalised polymeric resin), appear to have the sufficient data required for DAC process modelling. These include: CO_2, N_2, and H_2O isotherms measured at three or more temperatures from which isotherm model fitting parameters and heats of adsorption can be determined, bed density, particle density, skeletal density and/or total pore volume, heat capacity, thermal conductivity, and mass transfer coefficients at low CO_2 composition. For zeolite 13X in particular, much of the data is scattered across numerous sources.

Only a handful of other adsorbents previously investigated for DAC are close to having the full set of adsorbent characterisations completed. Zeolites such as 5A, H-ZSM-5, and SAPO-34 have the necessary physicochemical and equilibrium sorption properties available, but are lacking in adsorption kinetics parameters calculated at low CO_2 composition. The same is true for MOFs such as Ni-MOF-74 and MIL-101(Cr), though these are known not to perform well when exposed to humidity. Another

adsorbent, aminopropylmethyldiethoxysilane (APDES)-grafted nanofibrillated cellulose (NFC), was previously utilised by the DAC company Climeworks and has nearly all the listed properties available, except for measured N_2 isotherms, and the particle density found was for NFC grafted with a slightly different amine (*N*-(2-aminoethyl)-3-aminopropylmethyldimethoxysilane). The adsorbent data and corresponding references for all adsorbents can be found in Tables A1.1 to A1.12.

Based on the findings here and throughout this chapter, there is clearly a need to improve the synergy between adsorbent and process development for DAC. To do so, all the adsorbent properties necessary for process modelling should be measured and reported when investigating new materials for DAC. This will expand the choice of adsorbents which can be screened for and then potentially implemented in DAC processes, and will thus help to accelerate the deployment of adsorption-based DAC technologies.

Chapter 3. Research objectives

My literature review has highlighted the large data gaps in the reporting of adsorbent properties, resulting in many promising adsorbents not able to be screened for DAC adsorption processes. At this point, the full extent of adsorbent characterisation in the context of DAC appears to only be complete for two materials, zeolite 13X and Lewatit VP OC 1065. The overall research goal of my thesis is to minimise this data gap in adsorption materials for DAC by conducting a thorough assessment of select adsorbents that purposely represent three distinct classes of materials. This will be done through the following research objectives:

1. Investigate the physicochemical properties. These include an adsorbent's chemical features, textural properties, density, thermal properties, and shaping.
2. Investigate the equilibrium sorption properties. These include an adsorbent's CO_2, N_2, H_2O, Ar, and O_2 adsorption isotherms, heats of adsorption, and stability under process conditions such as humidity and adsorption-desorption cycling.
3. Investigate the kinetic sorption properties. These include the CO_2 adsorption kinetics under the influence of flowrate and temperature.

The adsorbents investigated in this thesis include: two polymeric resins (i.e. Lewatit VP OC 1065, Purolite A110), an ultramicroporous MOF (i.e. TIFSIX-3-Ni), and in-house developed amine-functionalised zeolite Y adsorbents. Lewatit VP OC 1065 is analysed as a benchmark adsorbent for comparison throughout this thesis, while Purolite A110 is assessed here for the first time for DAC. Interestingly, preliminary investigations showed a higher nitrogen content in Purolite A110 than Lewatit VP OC 1065, suggesting it may outperform Lewatit VP OC 1065 in terms of its CO_2 adsorption capacity. TIFSIX-3-Ni is a previously developed ultramicroporous MOF which has shown promise for DAC based on its CO_2 adsorption and reported humidity stability, but many adsorbent properties such as its density, heat capacity, and adsorption kinetics have yet to be reported. Lastly, amine functionalisation is conducted on a commercially available "hydrophobic" zeolite Y. It is hypothesised that this procedure will yield adsorbents with high affinity for CO_2 while maintaining minimal H_2O adsorption, thus making them suitable for DAC applications.

Chapter 4: Materials and methods

This chapter discusses the synthesis of the adsorbent materials investigated in this thesis, as well as the experimental methods used to analyse their physicochemical and equilibrium sorption properties. Parts of this discussion were previously published by the thesis author in the Journal of Chemical & Engineering Data [1] and on ChemRxiv [2]. The experimental methods used to study the adsorbents' kinetic sorption properties are discussed in Chapter 8.

All work described in this chapter was conducted by thesis author except for the following:

- The synthesis of one batch of TIFSIX-3-Ni was conducted by Dr. David Danaci at Imperial College London (ICL) to investigate the reproducibility of the procedure.
- Elemental analysis was conducted by Dr. Robert Woodward at the University of Vienna.
- Powder X-ray diffraction (XRD) measurements were conducted by Ioanna Itskou, Dr. Tian Tian, or Dr. Giulia Schukraft in the Department of Materials at ICL when the XRD instrument in the Department of Chemical Engineering was out of service.
- In-situ XRD measurements were conducted by Ioanna Itskou at ICL.
- CO_2 0 °C isotherm measurements on the Quantachrome Autosorb iQ3 porosity analyser were conducted by Hassan Azzan at ICL.
- The 3D-printed cylinder used for bed density measurements was manufactured by the Department of Chemical Engineering's Mechanical Workshop team at ICL.
- The software package used for all isotherm model fittings was originally developed and then further adapted for my studies by Hassan Azzan at ICL.
- Investigation of the cyclic stability of TIFSIX-3-Ni was carried out by undergraduate students Amanda Lim Jiayi and Gordon Wu Shun Yong at ICL as part of their 4th year research project.
- The aluminium crucible used for cyclic and kinetic studies was drilled by the Department of Chemical Engineering's Mechanical Workshop team at ICL, while the stainless-steel basket was designed and produced by Dr. David Danaci.
- Kinetic measurements for TIFSIX-3-Ni (Chapter 8) were conducted by undergraduate student Callum Sturman at ICL as part of his summer research placement.

4.1 Chemicals

Details of the chemicals used throughout this thesis are presented in Table 4.1.

Table 4.1. Details of the chemicals used throughout this thesis.

Chapter	Product name	Source	Source location	Product code	Lot number
4	Zeolite 13X	Micromeritics	Tewkesbury, UK	004-16843-00	9266-33
	Silica-alumina	Micromeritics	Tewkesbury, UK	004-16821-00	A-501-53
	Aluminium oxide (γ-phase, 99.97 %)	Alfa Aesar	Heysham, UK	1344-28-1	X30G032
5	Lewatit VP OC 1065	Sigma-Aldrich	Gillingham, UK	94136-100G-F	BCCC7234
	Purolite A110	Purolite	Llantrisant, UK	SR60210479	T014Z/21/6
6	Nickel (II) carbonate (anhydrous, 98%)	Alfa Aesar	Heysham, UK	22897	M02G009
	Dihydrogen hexafluorotitanate	Alfa Aesar	Heysham, UK	39736	X30F034
	Pyrazine	Fluorochem	Hadfield, UK	00275	FCB111997
	Sodium chloride	VWR	Lutterworth, UK	27788	-
	Potassium nitrate	Sigma-Aldrich	Gillingham, UK	221295-100G	MKCN5388
7	Zeolite H-Y (Si:Al = 40)	Zeolyst	Conshohocken, USA	CBV 901	2493.84
	Toluene (ACS grade, ≥ 99.5 %)	VWR	Lutterworth, UK	28676.297	21D124026
	Toluene (99 %)	Alfa Aesar	Heysham, UK	L.10967.0F	10233794
	3-aminopropyl-trimethoxysilane	Fluorochem	Hadfield, UK	S00825	FCB037369
	3-(2-aminoethyl)-3-aminopropyl-trimethoysilane	Fluorochem	Hadfield, UK	ISI0200	9042298183
	N-pentane	Fluorochem	Hadfield, UK	995196	FCB113169

The purity of the gases used throughout this thesis were as follows. For elemental analysis: He (Messer (Frankfurt, Germany), N5.0 grade). For in-situ XRD measurements: CO_2 (BOC (Guildford,

UK), N4.5 grade), N_2 (BOC, N4.8 grade). For pycnometry measurements: He (BOC, N5.0 grade). For thermogravimetric degradation measurements: N_2 (BOC, N4.8 grade), compressed air (BOC, industrial grade). For differential scanning calorimetry (DSC) measurements: N_2 (BOC, N5.2 grade). For synthesis in the tubular furnace: Ar (BOC, N4.8 grade), NH_3 (BOC, micrographic grade). For equilibrium gas sorption measurements: CO_2 (BOC, N5.0 grade), N_2 (BOC, N6.0 grade), Ar (BOC, N5.0 grade), O_2 (BOC, N5.0 grade). For kinetic sorption measurements: He (BOC, N5.0 grade), 800 ppm CO_2 in He (BOC, research grade).

4.2. Adsorbent materials

4.2.1 Commercial resins (Chapter 5)

Lewatit VP OC 1065 (referred to from here as Lewatit) and Purolite A110 (referred to from here as Purolite) were used as supplied.

4.2.2 TIFSIX-3-Ni (Chapter 6)

4.2.2.1 Synthesis of $NiTiF_6{\cdot}6H_2O$

Nickel hexafluorotitanate hexahydrate crystals were synthesised following the procedure published by Wu at one fourth scale [190]. Specifically, 3.823 g of anhydrous nickel (II) carbonate was dispersed in a plastic beaker containing 10.678 g of deionised water while stirring. Then, 6.125 mL of dihydrogen hexafluorotitanate was added dropwise while the solution was stirring continuously. The solution was then filtered through a polyethersulfone (PES) 0.45 µm syringe filter into a PTFE evaporating dish and left in the fume cupboard at room temperature to crystallise. Green hexagonal crystal pillars formed over five days which were then ground with a pestle and mortar and left to dry in the fume cupboard at room temperature for a further two days.

4.2.2.2 Synthesis of TIFSIX-3-Ni

TIFSIX-3-Ni powder was synthesised following the procedure published by Kumar et al. [107]. First, 2.50 g of pyrazine was dissolved in 1.00 mL of deionized water in a 30 mL glass vial (solution

was stirred at 1000 rpm for 30 min and then sonicated to fully dissolve pyrazine). Then, 500 mg of ground $NiTiF_6$ crystals were added to the solution, which was left to stir at room temperature for 48 h with a closed lid. This yielded a blue powder precursor, which was air dried for 2 h and then heated in an oven at 160 °C for 24 h, to yield approximately 500 mg of the final TIFSIX-3-Ni powder. The same synthesis was also successfully done at four times scale to yield approximately 2 g of final product per synthesis.

4.2.2.3 Pelletisation of TIFSIX-3-Ni powder

Powdered TIFSIX-3-Ni (400 mg) was ground using a marble mortar and pestle and placed into a pellet die (13 mm evacuable stainless steel, Specac). This was positioned into a manual hydraulic press (Atlas™ Manual 15T, Specac) fitted with a low tonnage gauge conversion kit (0–1 t, Specac). A load of 0.5 t was applied and maintained for 45 s to form a pellet of 13 mm diameter and approximately 5 mm in height. The pellet was then ejected with a small load applied to an extractor ring placed onto the base of the pellet die. Using a scalpel, the 13 mm pellet was then cut into 9 pieces following a grid pattern, yielding new pellets of ~ 4 mm in width and 5 mm in height. These smaller pellets were then directly used for mercury intrusion porosimetry measurements and N_2 sorption at -196 °C. For adsorption-desorption cycling and kinetic experiments, one of these 4 mm by 5 mm pellet pieces was roughly cut using a scalpel into granules of ~ 1 to 2 mm in diameter.

4.2.3 Amine-functionalised zeolite Y (Chapter 7)

4.2.3.1 Aminosilane functionalisation of zeolite Y

Functionalisation of zeolite Y (ZY) with aminosilane, either 3-aminopropyltrimethoxysilane (APTMS) or 3-(2-aminoethyl)-3-aminopropyltrimethoysilane (AE-APTMS), was done following a procedure adapted from Harlick and Sayari [191]. First, 1.0 g of zeolite Y powder was dried overnight in an oven at 150 °C. This dried powder was then added to a 250 mL multi-neck round bottom flask set up with a reflux condenser and containing 150 mL of toluene (ACS grade). This set up was then lowered into an oil bath, and the mixture was stirred at 1000 rpm for 30 min at room temperature. 0.3 mL of

deionised water was then added to the mixture and stirred at 1000 rpm for another 3 h. After that time, the temperature of the oil bath was increased to 85 °C. Once the temperature was reached (~ 20 min), 3.0 mL of aminosilane, either APTMS or AE-APTMS was added into the mixture, which was left to stir at 1000 rpm for 16 h under reflux. The mixture was then filtered in a Büchner funnel and washed five times with toluene and a final wash with pentane. The filtered product was then dried in an oven for 4 h at 120 °C to yield the final aminosilane functionalised zeolite Y powder, either ZY-APTMS or ZY-AE-APTMS.

4.2.3.2. Ammonia functionalisation of zeolite Y

Functionalisation of zeolite Y with ammonia (NH_3) was done following a procedure adapted from Srasra et al. [192]. 0.5 g of zeolite Y powder was loaded into an alumina boat and placed into a horizontal tubular furnace (Carbolite Gero STF 16/180). The furnace was first purged with a 250 mL min^{-1} flow of Ar at room temperature for 15 min. The gas was then switched to a 100 mL min^{-1} flow of NH_3, and the temperature increased to 700 °C, 800 °C, or 900 °C at a rate of 10 °C min^{-1} and maintained for 8 h. After this time, the temperature was turned off and the gas flow switched to 20 mL min^{-1} of Ar, and the furnace was left to cool overnight at these conditions. For experiments conducted at 700 °C or 900 °C, the sample was removed from the furnace the following morning to yield the final products, ZY-NH_3-700-8 or ZY-NH_3-900-8, respectively. For experiments conducted at 800 °C, the sample was either removed from the furnace the following morning, or the same procedure was repeated for either one or two more consecutive days without removing the sample to accomplish 16 h and 24 h of NH_3 functionalisation, respectively. The final products obtained were then ZY-NH_3-800-8, ZY-NH_3-800-16, or ZY-NH_3-800-24.

4.3. Characterisation of chemical features

4.3.1 Fourier transform infrared spectroscopy (FTIR)

Fourier transform infrared spectroscopy (FTIR) was used to analyse the chemical features of Lewatit, Purolite, and amine-functionalised ZY samples, where the absorbance of specific radiation

wavelengths corresponds to the vibrational energy of specific chemical bonds. FTIR spectra were collected using an Agilent Cary 630 FTIR spectrometer equipped with an attenuated total reflectance (ATR) accessory. Lewatit and Purolite samples were first degassed ex-situ at 120 °C and 0.02 mbar for at least 12 h using a Micromeritics VacPrep^{TM} 061 and then ground using a pestle and mortar before analysis. Amine-functionalised ZY samples were analysed without prior treatment. Sixteen spectra were measured per sample and an averaged spectrum was obtained over the wavenumber range of 400–4000 cm^{-1} with a resolution of 2 cm^{-1}.

4.3.2 Elemental analysis

Elemental analysis was used to quantify the presence of C, N, and H in Lewatit and Purolite, where the samples underwent high-temperature combustion yielding gaseous oxides for subsequent analysis with a thermal conductivity detector. Elemental analysis was performed using a Eurovector EA 3000 CHNS-O Elemental Analyser on Lewatit and Purolite samples weighing between 0.75 and 3.0 mg, which were weighed into tin vials (4×6 mm) prior to measurement. Samples were degassed ex-situ at 120 °C and 0.02 mbar for at least 12 h prior to measurement, and each sample was run in triplicate. Accurate sample weighing was achieved using a microbalance (Sartorius, ME 5 OCE). The operating temperatures for the combustion and reduction were 1000 °C and 750 °C, respectively. He was used as the carrier gas in all cases.

4.3.3 X-ray diffraction (XRD)

Powder X-ray diffraction (XRD) was used to analyse the crystal structure of TIFSIX-3-Ni samples. Here, an X-ray beam is directed at the sample and rotated over a range of angles. As the beam rotates, it diffracts off the different lattice planes in the crystal, yielding an X-ray diffraction pattern associated with the sample's specific crystal structure. XRD was carried out using three different instruments depending on their availability. The first option was a PANalytical X'Pert Pro X-ray diffractometer with an anode voltage of 40 kV and an emission current of 20 mA using monochromatic Cu Kα radiation (λ = 1.54178 Å). The detector used was an X'Celerator silicon strip detector. Points

were recorded over a 2θ angle range of 5 ° to 45 ° with a step size of 0.0167 °. The second option was a PANalytical X'Pert Pro X-ray diffractometer with an anode voltage of 40 kV and an emission current of 40 mA using monochromatic Cu Kα radiation (λ = 1.54178 Å). The detector used was an X'Celerator silicon strip detector. Points were recorded over a 2θ angle range of 5 ° to 45 ° or 50 ° with a step size of 0.0167 °. The third option was a Bruker 2D PHASE X-ray diffractometer with an anode voltage of 30 kV and an emission current of 10 mA using monochromatic Cu Kα radiation (λ = 1.54178 Å). The detector used was a LYNXEYE SSD160. Points were recorded over a 2θ angle range of 6 ° to 45 ° with a step size of 0.0161 °.

In-situ XRD was used to detect changes in the crystal structure of TIFSIX-3-Ni samples as they were exposed to different gas environments. This was performed using a PANalytical Empyrean X-ray diffractometer with an anode voltage of 40 kV and an emission current of 40 mA using monochromatic Cu Kα radiation (λ = 1.54178 Å). The detector used was a PIXcel^{1D} detector. Points were recorded over a 2θ angle range of 5 to 50 ° with a step size of 0.0131 °. Samples were subjected to the following procedure, where an XRD pattern was measured at the end of steps 1, 2, 3, and 5: 1) Sample exposed to ambient air. 2) Flow N_2 at 2 mL min^{-1} for 10 min at room temperature. 3) Increase the temperature to 160 °C at a rate of 10 °C min^{-1} and hold for 10 min at 160 °C under the same N_2 flow. 4) Cool down to room temperature under the same N_2 flow. 5) Flow CO_2 at 2 mL min^{-1} for 40 min at room temperature.

4.3.4 X-ray photoelectron spectroscopy (XPS)

X-ray photoelectron spectroscopy (XPS) was used to analyse the composition and chemical environment of the elements present in TIFSIX-3-Ni and amine-functionalised ZY samples. In this process, X-ray photons are directed at the sample which ejects electrons at specific kinetic energies from the different atoms. The difference between the incident photon energy and the measured ejected electron kinetic energy yields the electrons' binding energies, which correspond to specific atoms and chemical environments. XPS analyses were performed using a Thermo Scientific K-Alpha X-ray photoelectron spectrometer equipped with an MXR3 Al Kα monochromatic X-ray source (hν = 1486.6 eV) set to 72 W (6 mA and 12 kV). Powder samples were mounted onto carbon tape for

measurement. For TIFSIX-3-Ni samples, the data was analysed with Thermo Scientific Avantage™ software for C 1*s*, N 1*s*, O 1*s*, Ni 2*p*, Ti 2*p* and F 1*s* spectra. For amine-functionalised ZY samples, the data was analysed with Thermo Scientific Avantage™ software for Si 2*p*, Al 2*p*, O 1*s*, C 1*s*, and N 1*s* spectra. The adventitious carbon (C–C) peak set at 284.8 eV was used for binding energy calibration.

4.4. Characterisation of textural properties and density

4.4.1 N_2 sorption at -196 °C

N_2 sorption isotherms at -196 °C were measured using a Micromeritics 3Flex porosity analyser to determine the specific surface areas and pore volumes of all samples. This instrument employs a volumetric technique, where the change in pressure of a calibrated volume as gas is exposed to a sample tube is associated with the amount adsorbed. The amount of gas adsorbed can then be linked to the surface area and pore volume of the sample by knowing the adsorbate cross section.

Prior to measurement, all samples were degassed ex-situ using a Micromeritics VacPrep™ 061 before being moved to the porosity analyser for in-situ degassing. For Lewatit, Purolite and aminosilane-functionalised ZY, samples were degassed ex-situ at 120 °C and 0.02 mbar for at least 12 h, cooled to room temperature, then degassed in-situ at 120 °C and 0.00002 mbar for 24 h, with the temperature increased at a rate of 5 °C min^{-1}. For TIFSIX-3-Ni, both powder and pellet samples were degassed ex-situ at 0.02 mbar and 160 °C for 24 h, with the temperature increased from room temperature at a rate of 10 °C min^{-1}, cooled to room temperature, then degassed in-situ at 120 °C and 0.00002 mbar for 24 h, with the temperature increased at a rate of 5 °C min^{-1}. For unfunctionalised ZY and ZY-NH_3, samples were degassed ex-situ at 350 °C and 0.02 mbar for at least 12 h, cooled to room temperature, then degassed in-situ at 350 °C and 0.00002 mbar for 8 h, where the temperature was first increased to 120 °C at a rate of 5 °C min^{-1}, and then increased to 350 °C at a rate of 10 °C min^{-1}. A higher degassing temperature was used for these samples to ensure any adsorbed impurities would be removed from the zeolite micropores. This temperature could not be used for the resins and aminosilane-functionalised ZY samples due to the risk of reversing the functionalisation.

Approximately 100 mg of dried samples were used for all measurements. For pelletised TIFSIX-3-Ni, this corresponded to 2 to 3 pellet pieces of ~ 4 mm in width and 5 mm in height.

Validation of the porosity analyser for -196 °C N_2 measurements was done by measuring N_2 sorption isotherms at -196 °C for a silica-alumina reference material purchased from Micromeritics. Independent aliquots were also measured on all three ports to confirm data reproducibility. This data was then compared to reference data provided by Micromeritics (Figure A2.1).

The specific surface area for all samples was determined using the "BET surface identification" method (BETSI) [193]. The original BET method [74] involves fitting the BET isotherm model describing multilayer adsorption to a measured isotherm within the linear relative pressure range of ~ 0.05 to 0.3 [75] to determine the volume of the adsorbed monolayer, which can then subsequently be used to calculate the specific surface area, or BET area. As the BET method was not originally devised for microporous adsorbents where monolayer and multilayer adsorption are often indistinguishable [194], identification of the linear relative pressure range in these isotherms can be very difficult. A set of conditions known as the Rouquerol criteria [75] are therefore used to help select the appropriate range of relative pressure points that should be included in the BET calculations. Firstly, in a plot of $n \cdot (1-P/P°)$ against $P/P°$ (i.e. the BET plot), where n is the loading and $P/P°$ is the relative pressure, the y-intercept should be positive. Secondly, the values of $n \cdot (1-P/P°)$ should always be increasing within the chosen relative pressure range. Lastly, the monolayer adsorption capacity should correspond to a relative pressure point within the selected range. The BETSI software eliminates the need for manual selection and uses an iterative algorithm to return an optimal BET area, thus reducing user error and bias.

The total pore volumes for all TIFSIX-3-Ni and ZY samples were estimated from the N_2 loading (in mmol g^{-1}) at a relative pressure (P/P_0) of 0.97, using a molar volume of 28.775 mmol cm^{-3} for N_2 at 1.00 atm and -196 °C. For Lewatit and Purolite samples, the total pore volume was estimated at a relative pressure of 0.99, and the cumulative pore size distribution was determined using the density functional theory (DFT) model available in the 3Flex software, "N2 – DFT Model", with a slit-shaped pore geometry kernel and 0.10000 regularisation.

For TIFSIX-3-Ni samples, the micropore volume was estimated using the Dubinin-Astakhov (DA) method [76, 77] available in the 3Flex software. Here, the isotherm data is converted to a plot of $[\log(P°/P)]^n$ against $\log(Q)$, where $P°$ and P are the saturation and equilibrium adsorption pressure respectively, Q is the adsorbate loading, and n is the Astakhov exponent. Fitting of the isotherm data to the DA equation (equation (4.1)) yields Q_{micro} as the intercept, i.e. the adsorbate loading due to micropore filling, which can then be converted to a micropore volume:

$$\log(Q) = \log(Q_{micro}) - \left(\frac{RT}{\beta E_0}\right)^n \cdot \left[\log\left(\frac{P°}{P}\right)\right]^n \qquad (4.1)$$

where R is the universal gas constant, β is the adsorbate affinity parameter, and E_0 is the characteristic energy.

For pelletised TIFSIX-3-Ni specifically, a pore size distribution in the pore width range 0.45 to 45 nm was determined using the density functional theory (DFT) model available in the 3Flex software, "N2 – Tarazona NLDFT, Esf = 30.0K", with a cylinder pore geometry kernel and 0.20000 regularisation. This model is likely not well suited for TIFSIX-3-Ni as it was originally derived for a system of hard spheres, however this was chosen in preference to other models in the software which were for oxide surfaces, pillared clay, and carbon nanotubes [195].

For amine-functionalised ZY samples, the micropore volume was extracted from the pore size distribution, which was determined using the density functional theory (DFT) model available in the 3Flex software, "N2 – Cylindrical Pores – Oxide Surface", with a cylinder pore geometry kernel and varying regularisation for different samples as follows: ZY, ZY-NH_3-800-8, ZY-NH_3-800-16, ZY-NH_3-800-24, and ZY-NH_3-900-8: 0.03160; ZY-NH_3-700-8: 0.10000; ZY-3-APTMS: 0.31600; ZY-3-2-AE-3-APTMS: 0.20000.

4.4.2 CO_2 sorption at 0 °C

CO_2 sorption isotherms at 0 °C were measured volumetrically using a Micromeritics 3Flex porosity analyser to further assess specific surface areas and pore volumes for TIFSIX-3-Ni samples as N_2 at -196 °C may be kinetically restricted when trying to enter the ultramicropores present in these samples. Temperature control at 0 °C was achieved by filling the provided liquid nitrogen dewar with

an ice bath. Samples were first degassed ex-situ using a Micromeritics VacPrep^{TM} 061 at 0.02 mbar and 160 °C for 24 h, with the temperature increased from room temperature at a rate of 10 °C min^{-1}. The sample was then cooled to room temperature, moved to the porosity analyser, and degassed in-situ at 120 °C and 0.00002 mbar for 24 h, with the temperature increased at a rate of 5 °C min^{-1}. Approximately 100 mg of dried samples were used for the measurements.

Validation of the porosity analyser for CO_2 measurements was done by measuring CO_2 sorption isotherms at 0 °C for a zeolite 13X reference material purchased from Micromeritics. Independent aliquots were also measured on all three ports to confirm data reproducibility. This data was then compared to reference data provided by Micromeritics, along with data measured for the same sample on a Quantachrome Autosorb iQ3 (QC) porosity analyser (Figure A2.2).

The specific surface area was determined using the BET method [74] with the Rouquerol criteria (described in Section 4.4.1) applied [75]. The micropore volume was estimated using the Dubinin-Astakhov method [76, 77].

4.4.3 Mercury intrusion porosimetry (MIP)

Mercury intrusion porosimetry (MIP) was used to determine a pore size distribution beyond 45 nm for pelletised TIFSIX-3-Ni, where the amount of pressure needed to cause the non-wetting mercury to enter a pore is inversely related to the pore diameter, and the volume of mercury intruded corresponds to the volume of the pores. The volume of the pellets can also be determined from the difference in mercury needed to fill an empty penetrometer compared to the amount needed to fill a penetrometer containing sample (without applying external pressure to intrude into intraparticle pores). MIP was performed using a Micromeritics AutoPore IV Series Mercury Porosimeter. A 400 mg pellet of 13 mm diameter and ~ 5 mm height was cut into 9 pieces following a grid pattern as described in Section 4.2.2.3. All 9 pellet pieces were then degassed ex-situ at 0.02 mbar and 160 °C for at least 12 h, using a Micromeritics VacPrep^{TM} 061, with the temperature increased from room temperature at a rate of 10 °C min^{-1}. These were then added to a mercury penetrometer with a capillary intrusion stem volume of 1.1 cm^3 and subjected to measurements in the pressure range of 3.7×10^{-2} bar to 2.23×10^3 bar. The

AutoPore IV software (version 9500) was used to obtain the pore size distribution in the pore width range 5 nm to 345 μm.

For pelletised TIFSIX-3-Ni samples, the total pore volume was estimated by combining the pore size distribution results from N_2 adsorption at -196 °C and MIP measurements, based on the procedure described by Azzan et al. [48]. Here, the pore size distribution from both techniques were converted to a cumulative pore volume as a function of the pore diameter. The two data sets were then combined, where the cumulative pore volume below a pore diameter of 45 nm was taken from the N_2 adsorption results, and the cumulative pore volume above 45 nm was taken from the MIP results. 45 nm was chosen as the transition point as the N_2 adsorption results would be more accurate than the MIP results in the micro to mesoporous range.

4.4.4 Helium pycnometry

Helium pycnometry was used to determine the skeletal densities of Lewatit and Purolite by measuring the pressure of He used to fill a chamber of known volume containing the sample. The difference in pressure compared to filling an empty chamber corresponds to the volume (and subsequently density) of the solid sample, not including any interparticle or intraparticle pore volumes. Helium pycnometry was performed using a Micromeritics AccuPyc II 1340 pycnometer. Samples were first degassed ex-situ at 120 °C and 0.02 mbar for at least 12 h using a Micromeritics VacPrep™ 061, and approximately 1.7 g of dried sample was used to fill a 3.5 cm^3 sample holder. Samples were then exposed to 20 purge cycles of He dosing (~1.34 bar) followed by 10 measurement cycles at the same conditions (equilibrium rate of 0.005 psig min^{-1}).

4.4.5. Bed density

Bed densities (ρ_{bed}) for Lewatit and Purolite were measured by filling a 3D-printed cylindrical container (2.0 cm x 2.0 cm cube with a 1.6 cm diameter by 1.2 cm height cylindrical cavity, see Figure A2.3 for an image) with dried sample (degassed at 120 °C and 0.02 mbar for at least 12 h using a Micromeritics VacPrep™ 061). The container was overfilled with the dried sample, tapped 20 times,

and the excess swept off using a straight-edged spatula. The total weight of the container and sample was then measured on an analytical balance (OHAUS Adventurer Pro), from which the weight of the empty container was subtracted to obtain the mass of sample. This was then divided by the known volume of the cylinder, determined by weighing the mass of water required to fill its cavity (~ 2.4 cm^3), to determine the final bed density. This procedure was repeated three times for each sample.

4.4.6 Density and porosity calculations

4.4.6.1 Lewatit and Purolite

Using the skeletal densities determined from helium pycnometry (Section 4.4.4), the bed densities determined from the procedure described in Section 4.4.5, and assuming a spherical bed voidage (ε_{bed}) of 0.36 [196], the pellet (i.e. bead) density (ρ_{pellet}), total pore volume ($V_{total\ pores}$), and pellet (i.e. bead) porosity (ε_{pellet}) of Lewatit and Purolite were calculated from the following equations (4.2) to (4.4):

$$\rho_{pellet} = \frac{\rho_{bed}}{1-\varepsilon_{bed}} \quad (4.2)$$

$$V_{total\ pores} = \frac{1}{\rho_{pellet}} - \frac{1}{\rho_{skeletal}} \quad (4.3)$$

$$\varepsilon_{pellet} = \frac{V_{total\ pores}}{1/\rho_{pellet}} \quad (4.4)$$

4.4.6.2 TIFSIX-3-Ni

The pellet density (ρ_{pellet}) of pelletised TIFSIX-3-Ni was extracted from the MIP results, and the total pore volume ($V_{total\ pores}$) was determined as described in Section 4.4.3. Assuming that cylindrical pellets with a height to diameter aspect ratio of 0.9 can be manufactured, a maximum random packing density of 0.72 can be achieved [196], or a bed voidage (ε_{bed}) of 0.28. From these parameters, the bed density (ρ_{bed}), skeletal density ($\rho_{skeletal}$), and porosity (ε_{pellet}) of TIFSIX-3-Ni pellets were calculated by rearranging equations (4.2) and (4.3), and using equation (4.4), respectively.

4.5. Characterisation of thermal properties

4.5.1 Thermogravimetric analysis (TGA)

Thermogravimetric analysis (TGA) was used to determine the thermal stability of Lewatit, Purolite, and TIFSIX-3-Ni, and to quantify the aminosilane loading on functionalised ZY samples by measuring the change in sample mass due to sample decomposition with increasing temperature. TGA was carried out with a Netzsch TG 209 F1 Libra thermal analyser using ~ 20 mg of untreated sample placed in an alumina crucible. Lewatit and Purolite samples were subjected to a heat treatment from 30 °C to 900 °C at a ramp rate of 10 °C min^{-1}. This was done under either protective N_2 flow (100 mL min^{-1}), or a mixture of air (100 mL min^{-1}) and protective N_2 flow (20 mL min^{-1}). TIFSIX-3-Ni samples were subjected to a heat treatment from 30 °C to 900 °C at a ramp rate of 10 °C min^{-1} under protective N_2 flow (100 mL min^{-1}). Aminosilane-functionalised ZY samples were subjected to the following heat treatment adapted from Harlick and Sayari [191]: increase temperature from 30 °C to 200 °C at a rate of 10 °C min^{-1}, hold at 200 °C for 1 h, and heat to 900 °C at a rate of 10 °C min^{-1}, all under a protective N_2 flow of 100 mL min^{-1}. The isothermal step at 200 °C was used to remove any dangling methoxy ligands due to incomplete reaction, while above this temperature, mass loss was associated to degradation of the functionalised aminosilane chains [191]. The heat treatment was completed with a subsequent temperature increase to 1000 °C at a rate of 10 °C min^{-1} under a mixture of air (100 mL min^{-1}) and protective N_2 flow (20 mL min^{-1}) to remove any residual organic material. A correction run with an empty alumina crucible and identical analysis conditions was performed prior to measurements to account for buoyancy effects.

4.5.2 Differential scanning calorimetry (DSC)

Differential scanning calorimetry (DSC) was used to determine the specific heat capacities of Lewatit, Purolite, and TIFSIX-3-Ni. For this technique, the heat flow into a sample chamber containing an empty pan, reference material, and then sample is measured against a reference chamber always containing an empty pan, over a specified temperature range. These heat flows are then used to calculate the specific heat capacity of the sample.

DSC was performed using a PerkinElmer DSC 8000 differential scanning calorimeter following a methodology adapted from Moosavi et al. [91]. For Lewatit and Purolite, samples were first degassed ex-situ at 120 °C and 0.02 mbar for at least 12 h using a Micromeritics VacPrep^{TM} 061, and then ground into powder using a pestle and mortar before analysis. For TIFSIX-3-Ni, the sample was analysed without prior treatment. For all measurements, ~ 5 to 6 mg of powder was placed into an aluminium DSC pan and crimped with a corresponding aluminium lid with a manually pierced pinhole. The sample pan was placed into the sample chamber, while an identical empty aluminium pan and lid (uncrimped) was placed into the reference chamber. The external chiller was set to -20 °C, and the chambers were then subjected to the following temperature profiles. For Lewatit and Purolite: isothermal at 20 °C for 5 min, heating ramp to 120 °C at a rate of 10 °C min^{-1}, isothermal at 120 °C for 15 min, all under a N_2 flow of 40 mL min^{-1}. For TIFSIX-3-Ni: isothermal at 20 °C for 5 min, heating ramp to 160 °C at a rate of 10 °C min^{-1}, isothermal at 160 °C for 15 min, all under a N_2 flow of 40 mL min^{-1}. Measurements were repeated without opening the sample and reference chambers until three overlapping heat flow curves were obtained. Prior to each series of measurements, an empty aluminium DSC pan and lid, and an α-alumina (i.e. sapphire) standard, were used to obtain baseline and reference curves, respectively. The same procedure as outlined above was used for these measurements, though the aluminium pans were not crimped. The specific heat capacity curves for the samples were then derived with the PerkinElmer DSC 8000 software using the last of the three overlapping heat flow curves for each component (baseline, reference, sample).

This methodology was verified by measuring the heat capacities of γ-alumina powder and the α-alumina disc provided by the DSC instrument manufacturer, which were comparable (< 5% deviation) to the literature values provided by the National Institute of Standards and Technology (NIST) [197] (Figure A2.4). The measured specific heat capacity data for Lewatit, Purolite, and TIFSIX-3-Ni were fitted to a commonly used specific heat capacity equation [198] using the non-linear curve fit function in OriginPro with the orthogonal distance regression iteration algorithm.

4.6. Characterisation of equilibrium sorption properties

4.6.1 Gas and vapour sorption measurements

Gas and vapour sorption isotherms were measured volumetrically using a Micromeritics 3Flex porosity analyser for CO_2 at 15, 25, 35, 60, 70, 80, and 120 °C, for N_2 and H_2O at 15, 25, and 35 °C, and for Ar and O_2 at 25 °C. Additional temperatures were not measured for Ar and O_2 as it was assumed that their sorption behaviour, and subsequently their fitted isotherm parameters, would be similar to that of N_2. All samples were degassed ex-situ using a Micromeritics VacPrep^{TM} 061 before being moved to the porosity analyser for in-situ degassing and subsequent measurements. Degassing protocols (both ex-situ and in-situ) were tailored for each adsorbent.

Lewatit and Purolite samples were degassed ex-situ at 120 °C and 0.02 mbar for at least 12 h, cooled to room temperature, then degassed in-situ at 120 °C and 0.00002 mbar for 24 h, with the temperature increased at a rate of 5 °C min^{-1}. For CO_2 measurements, ~ 100 to 200 mg of dried sample was used, and a fresh aliquot of sample was used for each temperature measurement. For H_2O measurements, ~ 100 to 200 mg of dried sample was used, and the same aliquot of sample was used to measure all temperatures. For N_2, Ar, and O_2 measurements, ~ 1.0 to 1.5 g of dried sample was used, and the same aliquot of sample was used for all measurements, which were done in the gas order listed. Measurements were done in this order (i.e. inert gases followed by O_2) to avoid any measurement on possibly oxidised/degraded samples. A glass stirring rod was also placed in each sample tube for N_2, Ar, and O_2 measurements to reduce the free space volume.

TIFSIX-3-Ni samples were degassed ex-situ at 0.02 mbar and 160 °C for 24 h, with the temperature increased from room temperature at a rate of 10 °C min^{-1}. The sample was then cooled to room temperature and degassed in-situ at 120 °C and 0.00002 mbar for 24 h, with the temperature increased at a rate of 5 °C min^{-1}. A given aliquot of sample was used to measure all isotherms for CO_2, and a new aliquot used for all H_2O isotherms. A final new aliquot of sample was used for the N_2, Ar, and O_2 measurements, which were done in the gas order listed to again avoid any potential oxidative degradation to the sample. Approximately 100 mg of dried sample was used for all measurements. A

glass stirring rod was also placed in each sample tube for all measurements to reduce the free space volume.

Aminosilane-functionalised ZY samples were degassed ex-situ at 120 °C and 0.02 mbar for at least 12 h, cooled to room temperature, then degassed in-situ at 120 °C and 0.00002 mbar for 24 h, with the temperature increased at a rate of 5 °C min^{-1}. Approximately 100 mg of dried sample was used for CO_2 and H_2O measurements at 25 °C, while ~ 350 mg was used for N_2 measurements at 25 °C. Parent ZY and functionalised ZY-NH_3 samples were degassed ex-situ at 350 °C and 0.02 mbar for at least 12 h. The samples were then cooled to room temperature and degassed in-situ at 350 °C and 0.00002 mbar for 8 h, where the temperature was first increased to 120 °C at a rate of 5 °C min^{-1}, and then increased to 350 °C at a rate of 10 °C min^{-1}. A higher degassing temperature was used for these samples to ensure any adsorbed impurities would be removed from the zeolite micropores. This temperature could not be used for the aminosilane-functionalised ZY samples due to the risk of reversing the functionalisation. Approximately 400 mg, 100 mg, and 250 mg of dried sample was used for CO_2, H_2O, and N_2 measurements at 25 °C, respectively. For all measurements, a glass stirring rod was placed in each sample tube to reduce the free space volume.

For measurements at and below 35 °C, temperature control was achieved by submerging the sample tubes in a dewar containing a water-glycol based bath fluid. The bath temperature was measured with a glass thermometer and maintained using a Julabo F250 recirculating cooler. For measurements at and above 60 °C, temperature control was achieved by using the heating mantle provided with the 3Flex instrument.

4.6.2 Isotherm model fittings

Isotherm model fits for CO_2, N_2, and H_2O adsorption data were carried out with MATLAB R2020a (The Mathworks Inc.) using the in-house software package isothermFittingTool which employs a maximum likelihood estimator [199]. Further details regarding the fitting procedures and uncertainty calculations used in this software are detailed in the works of Hwang et al. [200] and Azzan et al. [48, 201].

4.6.3 Isosteric heat of adsorption calculations

The isosteric heats of adsorption for CO_2, N_2, and H_2O were calculated using the van 't Hoff equation for specified loading (n) and corresponding pressure (P) values. Isotherm data (P vs. n) at each temperature (T) were first interpolated using smoothing spline interpolation in MATLAB. A set of points with 0.01 mmol g^{-1} intervals were generated over the loading range common to all temperatures, and the corresponding P values were determined using the smoothing spline interpolation. A linear regression was then applied to the ln(P) vs 1/T data for each value of n using the LINEST function in Microsoft Excel. The heat of adsorption for each value of n (ΔH_n) was then calculated using equation (4.5), where the derivative corresponds to the slope of the linear regression and R is the universal gas constant.

$$\Delta H_n = -R\left[\frac{\partial lnP}{\partial(1/T)}\right]_n \quad (4.5)$$

4.6.4 Limiting heat of adsorption calculations

The limiting heats of adsorption (ΔH_0) for CO_2, N_2, and H_2O were calculated using the Henry constants determined for each isotherm temperature [202]. Virial plots (n vs. ln(P/n)) were created and the low loading data at each temperature was fit to a linear equation. The negative exponent of the intercept gives the Henry constant (K). A linear regression can then be applied to ln$K$ vs 1/T, from which the slope can be used to calculate ΔH_0 as shown in equation (4.6).

$$\Delta H_0 = -R\left[\frac{\partial lnK}{\partial(1/T)}\right]_0 \quad (4.6)$$

4.7 TIFSIX-3-Ni stability studies

4.7.1 Exposure to H_2O only

H_2O adsorption isotherms were measured volumetrically using a Micromeritics 3Flex porosity analyser at 25 °C up to 15% relative humidity (RH), 48% RH, and 77% RH, respectively, following the procedure in Section 4.6.1. These samples were then removed from the 3Flex, where ~ 5 mg were used for XRD measurements following the procedure in Section 4.3.3. N_2 isotherms at -196 °C and CO_2

isotherms at 25 °C were measured on the remaining ~ 95 mg samples following the procedures in Sections 4.4.1 and 4.6.1, respectively.

4.7.2 Exposure to O_2 and H_2O (closed environment)

Samples were subjected to a closed environment of 75% RH and 90% RH at 40 °C for 14 days following a procedure adapted from Kumar et al. [107]. Two 250 mL beakers were filled with separate saturated salt solutions of sodium chloride and potassium nitrate to produce RH levels of 75% and 90%, respectively [203]. Each beaker was placed in its own 1 L Kilner clip top mason jar with a rubber seal, along with ~ 100 mg of sample placed in an open 10 mL glass vial and a digital hygrometer-thermometer (Figure A2.5). Both mason jars were then placed in an oven set to 40 °C for 14 days. After this time, the samples were removed and XRD patterns were immediately measured using ~ 5 mg of these wet samples following the procedure in Section 4.3.3. N_2 isotherms at -196 °C and CO_2 isotherms at 25 °C were then measured on the remaining ~ 95 mg samples following the procedures in Sections 4.4.1 and 4.6.1, respectively.

4.7.3 Exposure to O_2 and H_2O (atmospheric exposure)

Approximately 100 mg of sample was placed in an open 30 mL glass vial and left on a shelf in the laboratory for 6 months. The average temperature and RH level in the lab is approximately 22 °C and 45% RH, respectively. After this time, XRD was performed on ~ 5 mg of sample following the procedure in Section 4.3.3, and N_2 isotherms at -196 °C and CO_2 isotherms at 25 °C were measured on the remaining ~ 95 mg samples following the procedures in Sections 4.4.1 and 4.6.1, respectively.

4.7.4 Adsorption-desorption cycling

TIFSIX-3-Ni granules of 1 to 2 mm in diameter were prepared as described in Section 4.2.2.3. Approximately 20 mg of these granules were subjected to multiple adsorption-desorption cycles in ambient air using a Netzsch TG 209 F1 Libra thermal analyser. The sample was first subjected to a "long cycle" to achieve gas adsorption saturation as follows: sample heated to 160 °C from 30 °C at a

rate of 5 °C min^{-1}, held at 160 °C for 6 h, cooled to 30 °C, held at 30 °C for 14 h, heated to 160 °C at a rate of 5 °C min^{-1}, and held at 160 °C for 6 h, under a mixture of ambient air (190 mL min^{-1}) and protective He flow (10 mL min^{-1}). Protective He flow was required for this experiment to preserve the TGA balance, where 10 mL min^{-1} was the lowest possible flowrate able to be used. The same sample was then subjected to 50 "short cycles" under the same gas conditions as follows: sample initially heated to 160 °C from 30 °C at a rate of 5 °C min^{-1}, held at 160 °C for 6 h, cooled to 30 °C, held at 30 °C for 1 h, heated to 160 °C at a rate of 5 °C min^{-1}, held at 160 °C for 15 minutes, and the final cooling and heating steps repeated another 49 times. After the series of "short cycles", the same sample was subjected to another "long cycle" exactly as described previously. The relative humidity of the ambient air was recorded over the course of each measurement using a Lascar EL-SIE-2 temperature and humidity data logger.

Before each cycling measurement, the sample was degassed ex-situ at 0.02 mbar and 160 °C for at least 12 h using a Micromeritics VacPrep™ 061, with the temperature increased from room temperature at a rate of 10 °C min^{-1}. A correction run with an empty crucible and identical analysis conditions was also performed before each measurement to account for buoyancy effects. An aluminium crucible with 0.2 mm holes drilled at 0.5 mm pitch and placed in a perforated stainless-steel holder was used for these measurements to ensure optimal gas flow through the sample (Figure A2.6). The post-cyclic sample was characterised using XRD, N_2 adsorption at -196 °C, and CO_2 adsorption at 25 °C as described in Sections 4.3.3, 4.4.1, and 4.6.1, respectively. For XRD measurements, the post-cyclic TIFSIX-3-Ni sample was crushed into powder as the granules did not have a sufficient surface width for the beam. For isotherm measurements, glass beads of 2 mm diameter were used in addition to a glass rod to fill the remaining volume of the 3Flex tubes to minimise measurement error as only ~ 20 mg of the post-cyclic sample was available. The same procedure and amount of sample were also used to characterise and compare as-synthesised TIFSIX-3-Ni pellets.

Chapter 5: Physicochemical and equilibrium sorption properties of Purolite A110 and Lewatit VP OC 1065 for direct air capture

The work and discussions in this chapter were previously published by the thesis author in the Journal of Chemical & Engineering Data [1]. The new Chemi-Physisorption isotherm model was conceived by Dr. David Danaci.

5.1 Introduction

Amongst the various adsorbent classes, polymers are currently the most often investigated for DAC process studies (Figure 2.7) [10]. This is largely because Lewatit VP OC 1065 (i.e. Lewatit), a commercially available polymeric resin functionalised with primary amines, seems to be the only material other than zeolite 13X for which sufficient adsorbent data is available to conduct process modelling for DAC. While 13X is a well-known commercial benchmark for post-combustion carbon capture, it has a relatively low CO_2 adsorption capacity of 0.2 – 0.3 mmol g^{-1} at 0.4 mbar CO_2 and 25 °C [31, 204]. In comparison, Lewatit has a relatively high CO_2 adsorption capacity of 1.0 mmol g^{-1} at 0.4 mbar CO_2 and 25 °C under dry conditions [205]. This is due to its chemisorbent nature, where two amine groups react with and capture CO_2 to form ammonium carbamate [12] (equation (5.1)).

$$CO_2 + 2RNH_2 \leftrightarrow RNH_3^+ + RNHCOO^- \qquad (5.1)$$

Lewatit is therefore often regarded as a benchmark DAC adsorbent. The current literature consists of investigating the performance of Lewatit using different cycle processes [43, 150, 178, 205-208] and contactor designs [17, 209-213], the impact of climate variations [32, 214], a few pilot-scale investigations [215, 216], and some kinetic studies at low CO_2 compositions [44, 150, 217, 218].

Expanding this group of easily-accessible commercial materials for DAC with the necessary data available to facilitate their process scale evaluation will help accelerate the deployment of adsorption-based DAC technologies. In the field of polymeric resins, Shu et al. investigated a commercial resin (AmberLite HPR4800 OH) using pH swing regeneration in an electrochemical cell [219], which had a CO_2 adsorption capacity of 1.76 mmol g^{-1} under humid conditions at 0.4 mbar CO_2 and 25 °C. The pellet (i.e. bead) and bed density of the adsorbent are available from the manufacturer

[220], but other properties needed for process modelling were not reported in this study. Elfving et al. studied an undisclosed resin supplied by Oy Hydrocell Ltd. under various process cycles [221], regeneration conditions [222], and dry vs. humid conditions [149, 223]. The adsorbent consists of a polystyrene matrix functionalised with primary amines, like Lewatit, with a dry CO_2 adsorption capacity of 0.8 mmol g^{-1} at 0.4 mbar CO_2 and 25 °C. Single component CO_2 and H_2O isotherms at multiple temperatures, as well as CO_2-H_2O co-adsorption isotherms have been measured. Corresponding isotherm equations and heats of adsorption were also reported, along with the bed density, pellet density, and specific heat capacity. Parvazinia et al. studied another amine-functionalised polymeric resin, Purolite A109, for CO_2 capture at 20 mbar and 25 °C [177], which had a CO_2 adsorption capacity of 0.2 mmol g^{-1} at those conditions. More recently, Purolite A110, the successor of Purolite A109, appeared in the literature for the first time for DAC applications [224]. However, the authors had modified the material with a $CuCl_2$ solution to form their Polyam-N-Cu^{2+} adsorbent, which would capture CO_2 only under humid conditions via a carbonate reaction. This material was reported to have a CO_2 adsorption capacity of 5.1 mmol g^{-1} at 0.4 mbar CO_2, 25 °C, and 50% RH. Under the same conditions, unmodified Purolite A110 captured 1.8 mmol g^{-1} of CO_2, which is comparable to Lewatit at similar conditions (~ 0.35 mbar, 25 °C, 55% RH) [150]. However, the necessary data needed for process scale evaluation, such as equilibrium isotherms and heats of adsorption, have not been measured.

In this study, I propose unmodified Purolite A110 (i.e. Purolite) as a new candidate benchmark adsorbent for DAC and compare its properties to the current benchmark, Lewatit. The objective is to measure all the physicochemical and equilibrium sorption properties needed to perform process modelling and compare the results to that of Lewatit. For both Purolite and Lewatit, I report their chemical features, chemical composition, skeletal, pellet (i.e. bead), and bed density, total pore volume, pellet porosity, BET area, thermal stability, and specific heat capacity. To analyse their sorption properties, I measure CO_2, N_2, and H_2O isotherms at multiple temperatures, and Ar and O_2 isotherms at a single temperature. For CO_2, N_2, and H_2O, I also fit corresponding isotherm models and heats of adsorption.

5.2 Results and discussion

5.2.1 Physicochemical properties

5.2.1.1 Chemical and textural properties

Lewatit and Purolite present as spherical beads with 50 – 60 % water content and particle sizes between 0.3 – 1.2 mm [225, 226]. Images of the beads before and after drying are shown in Figure A3.1. Lewatit and Purolite are reported by their manufacturers to both consist of styrene-divinylbenzene polymer backbones functionalised with primary amines, which should drive CO_2 adsorption. I confirmed the presence of these functionalities for both resins using FTIR (Figure 5.1). The spectra exhibit bands between 1625 cm^{-1} and 1500 cm^{-1} corresponding to aromatic C=C bonds, bands between 3400 cm^{-1} and 3300 cm^{-1} and 895 cm^{-1} and 650 cm^{-1} characteristic of NH_2 vibrations, and bands around 1200 cm^{-1} characteristic of C-N bonds [227]. I then used elemental analysis to quantify the nitrogen (N) content in each resin, which is representative of the level of amine functionalisation. As seen in Table 5.1, Purolite has a higher amine content (10.2 wt% of N) than Lewatit (8.3 wt% of N). The N content measured for Lewatit is not far off from the value of 9.5 wt% reported by Yu et al. [228]. Assuming CO_2 adsorption only occurs under dry conditions where two N atoms are needed to capture one CO_2 molecule (see equation (5.1)), the theoretical CO_2 capacity for Purolite would be higher than that of Lewatit (3.6 mmol g^{-1} vs. 3.0 mmol g^{-1}, respectively).

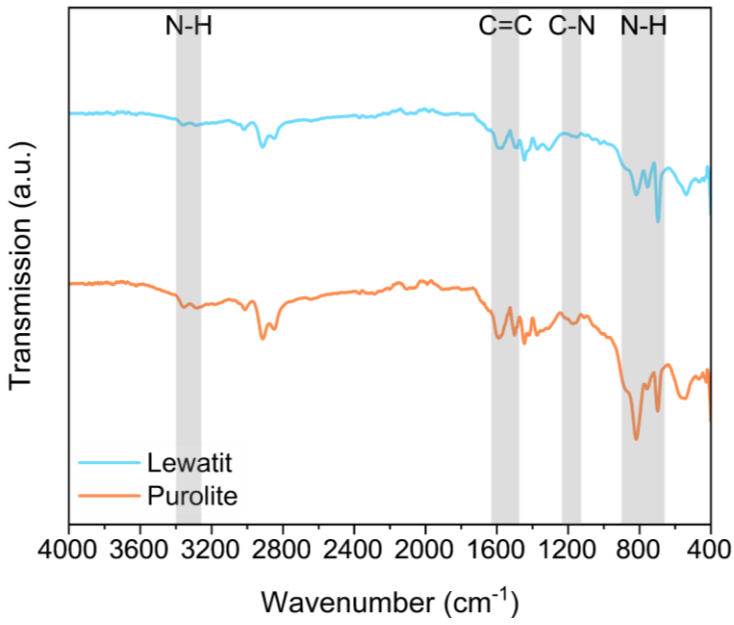


Figure 5.1. FTIR spectra for dried and ground Lewatit and Purolite resins.

Table 5.1. Summary of CHN elemental analysis for Lewatit and Purolite resins, with uncertainty bounds for a 95% confidence interval.

Sample	C (wt%)	H (wt%)	N (wt%)
Lewatit	82.5 ± 0.1	8.1 ± 0.1	8.3 ± 0.1
Purolite	79.6 ± 0.4	8.2 ± 0.1	10.2 ± 0.3

I used N_2 sorption at -196 °C to determine the BET area and pore size distribution for Lewatit and Purolite, which are reported as macroporous resins by the manufacturers. Images of the porous surface of both resins are shown in Figure A3.2. Both resins have similarly low BET areas of 32 and 29 $m^2\ g^{-1}$, respectively, indicative of macroporous materials. I can also observe from the N_2 sorption isotherms and pore size distribution the absence of micropores in the materials (Figure 5.2). The total pore volumes of Lewatit and Purolite, obtained by direct reading of the N_2 isotherms at 0.99 P/P°, are 0.34 $cm^3\ g^{-1}$ and 0.23 $cm^3\ g^{-1}$, respectively. This, however, is an underestimation of the actual total pore volume for these materials, as N_2 sorption at -196 °C is ill-suited for macropore analysis. Indeed, when I calculated the total pore volumes of Lewatit and Purolite using their measured bed and skeletal densities, the total pore volumes were 0.43 $cm^3\ g^{-1}$ and 0.64 $cm^3\ g^{-1}$, respectively. Therefore, while Lewatit has a larger volume of pores below 200 nm diameter, Purolite seems to have significantly more macropores beyond this pore size, which were not detectable by N_2 sorption.

Using He pycnometry, we found that Purolite and Lewatit exhibit similar skeletal densities (1.15 g cm^{-3} vs 1.12 g cm^{-3}, respectively), but Purolite has a lower bed density than Lewatit (0.42 g cm^{-3} vs 0.48 g cm^{-3}, respectively). This result implies that a lower mass of Purolite can fill a specified bed volume compared to Lewatit. Purolite also has a higher total pore volume, higher porosity, and lower pellet density than Lewatit. The values of bed density, pellet density, and porosity are typically needed as inputs for process modelling and are reported in Table 5.2, along with the total pore volumes and BET areas. Literature values for these properties are provided in Table A3.1 where available for comparison.

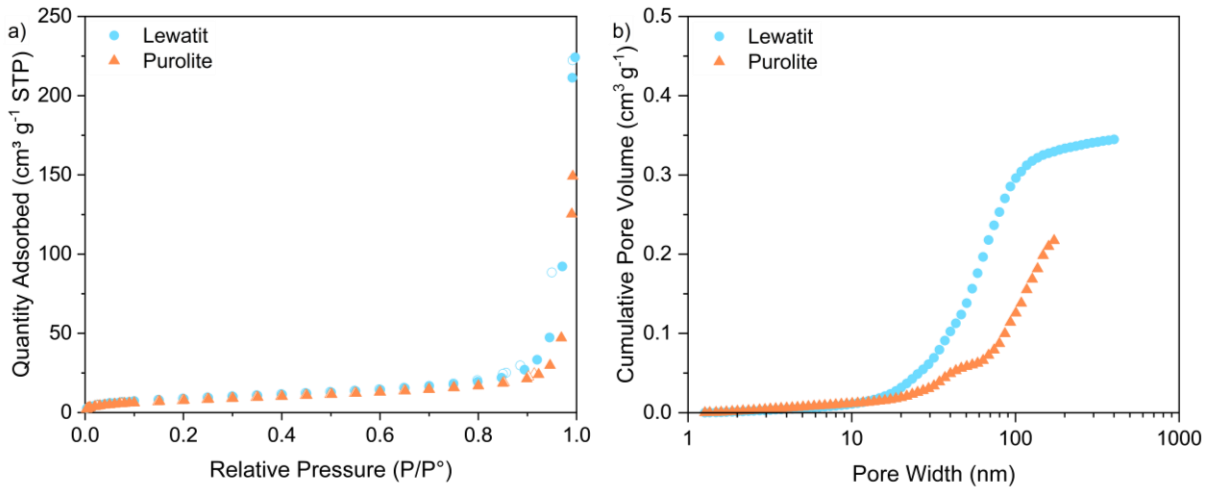


Figure 5.2. Porosity analysis of Lewatit and Purolite resins. a) N_2 sorption isotherms at -196 °C (filled symbols = adsorption; open symbols = desorption). b) Cumulative pore size distribution obtained from N_2 sorption at -196 °C with DFT analysis.

Table 5.2. Summary of density (skeletal, pellet, bed) and textural property (total pore volume, pellet voidage, BET area) values for dried Lewatit and Purolite resins. Uncertainty bounds for a 95% confidence interval are provided when available.

	Lewatit	**Purolite**
$\rho_{skeletal}$ **(g cm^{-3})**	1.1231 ± 0.0002	1.1471 ± 0.0002
ρ_{pellet} **(g cm^{-3})**	0.744 ± 0.001	0.663 ± 0.002
ρ_{bed} **(g cm^{-3})**	0.476 ± 0.001	0.424 ± 0.002
$V_{total\ pores}$ **(cm^3 g^{-1})**	0.454 ± 0.001	0.637 ± 0.001
ε_{pellet}	0.338 ± 0.001	0.422 ± 0.001
S_{BET} **(m^2 g^{-1})**	32	29

5.2.1.2 Thermal properties

I used thermogravimetric analysis (TGA) to determine the thermal stability of the resins, which dictates the maximum temperature that can be used for desorption in a DAC process without degrading the material. The manufacturer of Lewatit recommends a maximum operating temperature of 100 °C [226], while none is recommended for Purolite. As seen in Figure 5.3a, both resins contain adsorbed water (weight loss < 100 °C) with Purolite having approximately 20% higher water content than

Lewatit. Small reductions in mass are observed for both Lewatit and Purolite starting at 125 °C under both N_2 and air atmospheres (see Figure A3.3), likely associated with amine degradation [229]. The larger decreases in mass between 300 °C to 400 °C for both materials under both conditions corresponds to degradation of the polymer backbone.

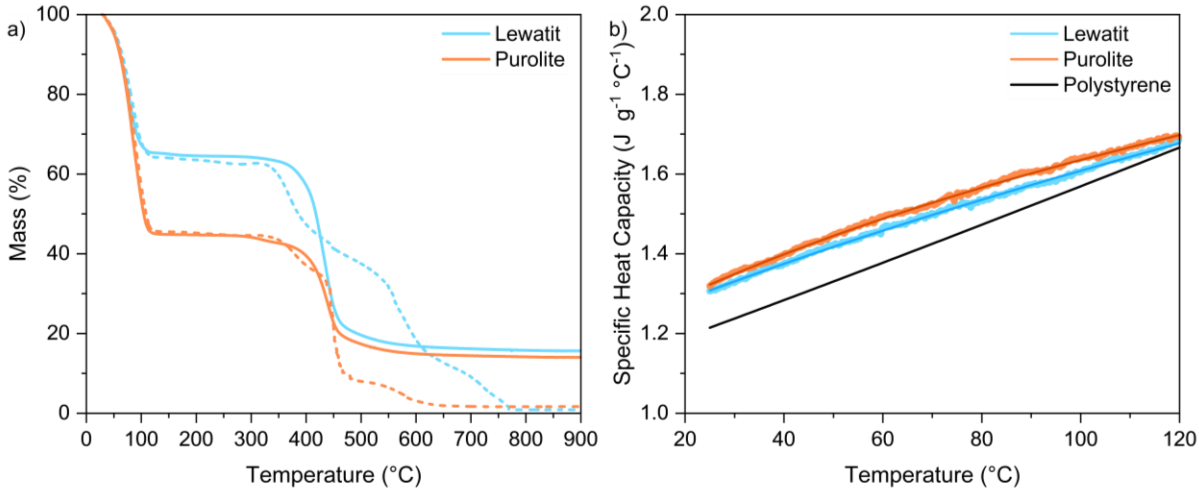


Figure 5.3. Thermal analysis of Lewatit and Purolite resins. a) TG curves under N_2 (solid lines) and air (dotted lines) atmospheres up to 900 °C. b) Specific heat capacities of the dried resins measured as a function of temperature from 25 °C to 120 °C, where the darker solid lines represent the fitted results using equation (5.2). Data for polystyrene was obtained from Gaur and Wunderlich [198].

I used differential scanning calorimetry (DSC) to determine the specific heat capacities of the resins in the temperature range 25 °C to 120 °C, which is a possible range of temperatures that the materials might experience in a DAC process. The heat capacity is a necessary input in process modelling as it relates to the energy input needed to heat an adsorbent during the desorption process, where an adsorbent with a higher heat capacity would require more energy to be heated to a set temperature. As seen in Figure 5.3b, both Lewatit and Purolite have similar heat capacities (derived from the heat flow curves shown in Figure A3.4), as expected due to their similar chemical structures. Both values are similar to the heat capacity of polystyrene in the same temperature range (1.2 – 1.7 J g^{-1} °C^{-1}) [198], which forms the backbone of both resins, and agrees well with previously measured

specific heat capacity values for Lewatit of 1.6 J g^{-1} °C^{-1} [230]. The experimental data can be modelled using equation (5.2) shown below [198]:

$$c_p = a \cdot (T + 273.15)^{-2} + b \cdot (T + 273.15) - c \qquad (5.2)$$

Where c_p is the specific heat capacity, T is the temperature (in °C), and a, b, and c are fitted parameters presented in Table 5.3 for Lewatit and Purolite.

Table 5.3. Fitting parameters for the specific heat capacity of Lewatit and Purolite.

Parameter	Unit	Lewatit	Purolite
a	($\times 10^4$) J °C g^{-1}	-2.97 ± 0.06	-5.63 ± 0.06
b	($\times 10^{-3}$) J g^{-1} °C^{-2}	2.40 ± 0.03	1.11 ± 0.03
c	J g^{-1} °C^{-1}	-0.93 ± 0.02	-1.62 ± 0.02

5.2.2 Equilibrium sorption properties

5.2.2.1 CO_2 sorption

I measured the equilibrium CO_2 adsorption and desorption isotherms up to 1 bar for Lewatit and Purolite at 15, 25, 35, 60, 70, 80, and 120 °C (Figure 5.4). I ensured equilibrium was reached by repeating the adsorption and desorption measurements at 35 °C with the equilibrium interval increased from 60 s to 90 s and observed no change in the results (Figure A3.5). The results demonstrate that Purolite adsorbs more CO_2 than Lewatit at 0.4 mbar CO_2 pressure, which is representative of the CO_2 feed stream for a DAC process. At an adsorption temperature of 25 °C and in the presence of 0.4 mbar CO_2, the gravimetric CO_2 adsorption capacity for Purolite vs. Lewatit is approximately 1.3 mmol g^{-1} vs. 0.95 mmol g^{-1}. Considering the adsorbents' bed densities (see Table 5.2), Purolite also has a higher volumetric CO_2 adsorption capacity of 0.55 mmol cm^{-3}_{bed} compared to that of Lewatit (0.45 mmol cm^{-3}_{bed}). This trend correlates to the higher N content observed for Purolite compared to Lewatit. CO_2 isotherms for Purolite have not yet been reported in the literature, while CO_2 isotherms for Lewatit have been measured before [150, 217, 231, 232]. I compared my adsorption data obtained at 25 °C with that obtained by Young et al. [150] in Figure A3.6a. The data aligns very well at low CO_2 pressures, but the CO_2 loading reported by Young et al. at pressures closer to 1 bar are higher than my experimental data.

This deviation could be due to the different sorption measurement techniques used, i.e. gravimetrically (Young et al.) vs volumetrically (this study).

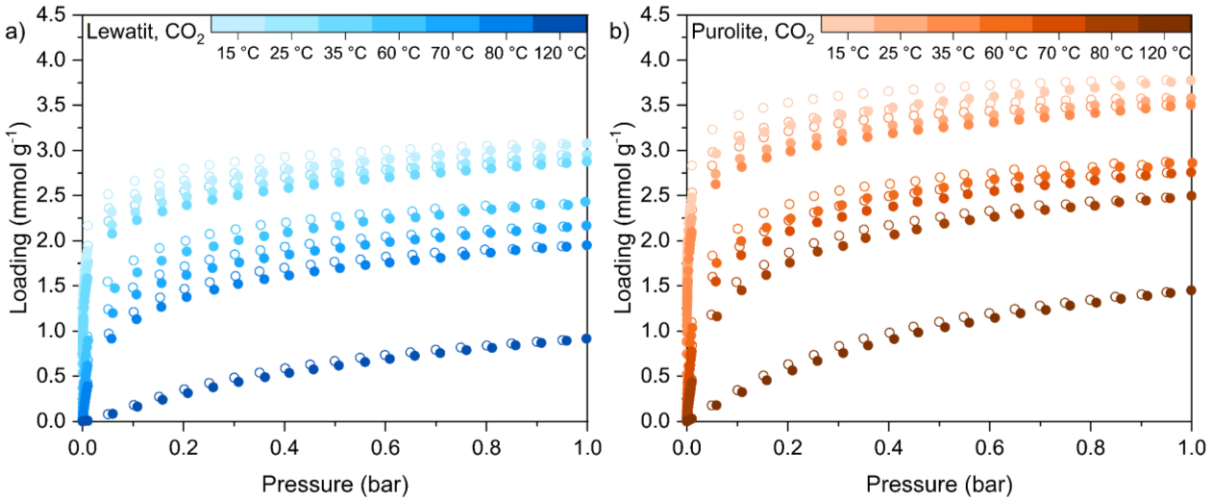


Figure 5.4. Equilibrium adsorption (filled symbols) and desorption (hollow symbols) isotherms for CO_2 measured at 15, 25, 35, 60, 70, 80, and 120 °C up to 1 bar for a) Lewatit and b) Purolite.

Hysteresis is observed for both Lewatit and Purolite in Figure 5.4. In both cases, the extent of hysteresis decreases as the temperature increases, which is indicative of the chemisorbent nature of the materials. At lower temperatures, there is insufficient energy available to remove the chemisorbed CO_2 at a given pressure, while at higher temperatures (e.g. 120 °C), the process is reversible. We attribute this behaviour to a true equilibrium effect rather than a kinetic effect. As mentioned previously, I repeated measurements with a longer equilibration interval (Figure A3.5) and did not observe any change in the degree of hysteresis in the isotherms.

I also measured adsorption and desorption isotherms at 35 °C for both materials approximately a year after the original measurements on the same batch of resins to test if there was any degradation of the adsorbents. As seen from Figure A3.7, there is no discernible difference between the two measurements for Lewatit, however, there is a slight decrease in loading in the later Purolite measurement compared to the original, which could be attributed to minor degradation of the material during storage. A pilot scale study by van Paasen et al. [136] using Lewatit for post-combustion CO_2 capture observed that approximately 10% of the adsorbent degradation after 33 days was due to shelf-life instability, while the major contributor was oxidative degradation at high operating temperatures

during regeneration. These and other sources of oxidative degradation during a DAC process cycle were recently described by Carneiro et al. [137].

Isotherm model equations that represent the experimental data well are needed to implement the data in process modelling. All previous studies with Lewatit have used the temperature-dependent Toth (td-Toth) isotherm model to describe the loading n of CO_2, given by equations (5.3) to (5.6):

$$n = \frac{q_\infty(T) \cdot b(T) \cdot P}{\left[1+(b(T)\cdot P)^{\tau(T)}\right]^{\frac{1}{\tau(T)}}} \quad (5.3)$$

$$q_\infty(T) = q_{\infty,0} \cdot \exp\left[\chi\left(1 - \frac{T}{T_0}\right)\right] \quad (5.4)$$

$$b(T) = b_0 \cdot \exp\left(\frac{-\Delta U}{RT}\right) \quad (5.5)$$

$$\tau(T) = \tau_0 + \alpha\left(1 - \frac{T_0}{T}\right) \quad (5.6)$$

where P is the pressure, T is the temperature, $q_\infty(T)$ is the maximum CO_2 capacity, $q_{\infty,0}$ is the maximum CO_2 capacity at the reference temperature T_0, $b(T)$ is the CO_2 adsorption coefficient defined by a constant b_0 and the internal energy change during adsorption ΔU, R is the universal gas constant, $\tau(T)$ is the surface heterogeneity parameter, τ_0 is the surface heterogeneity parameter at T_0, and χ and α are factors determining the temperature dependencies of $q_\infty(T)$ and $\tau(T)$. As seen below in Figure 5.5, this model does not fit our measured data very well for either Lewatit or Purolite at the lower temperatures of 15, 25, and 35 °C. The fitted parameters are found in Table 5.4, while the upper and lower bounds imposed on each parameter during the fitting are summarized in Table A3.2. The fitting parameters determined by Young et al. [150] (Table A3.3) are also unable to represent my data well, as shown in Figure A3.6. This may be due to varying factors, such as a different temperature range and a greater number of data points, particularly in the low-pressure region below 0.01 bar.

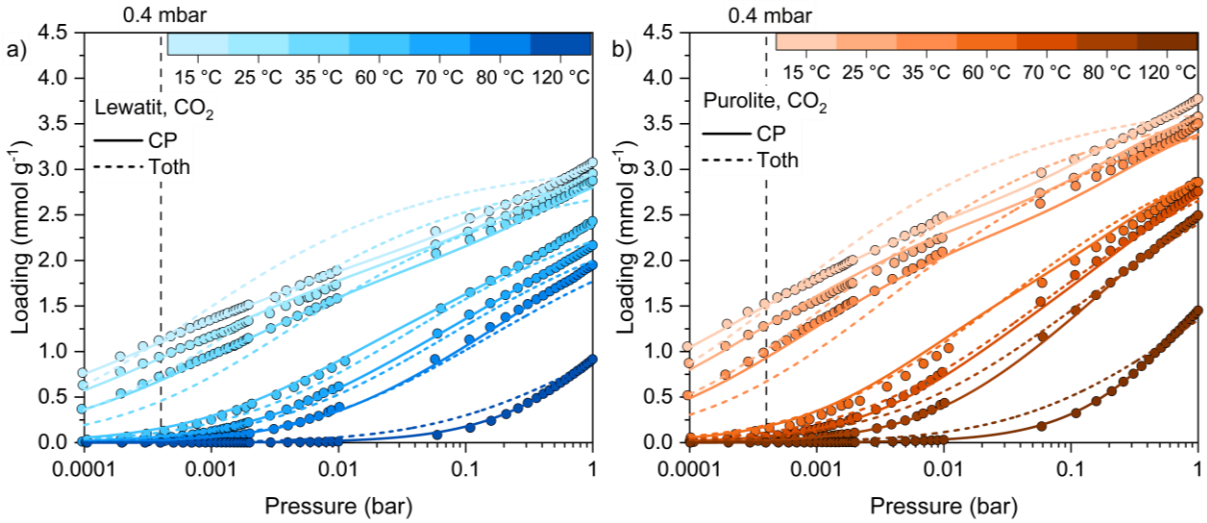


Figure 5.5. Equilibrium adsorption isotherms for CO_2 measured at 15, 25, 35, 60, 70, 80, and 120 °C up to 1 bar for a) Lewatit and b) Purolite with a log-scale of pressure. Solid lines represent the fitting results from the CP isotherm model while dashed lines represent the fitting results from the td-Toth isotherm model. The fitting parameters of the isotherms are found in Table 5.4.

Table 5.4. Fitting parameters with uncertainty bounds for a 95% confidence interval for the td-Toth and CP isotherm models for CO_2 adsorption for Lewatit and Purolite.

Equation	Parameter	Unit	Lewatit	Purolite
td-Toth	$q_{\infty,0}$	mmol g^{-1}	3.0023 ± 0.0500	3.7476 ± 0.0492
	b_0	($\times 10^{-9}$) bar^{-1}	1.9940 ± 0.2112	3.3802 ± 0.2905
	$-\Delta U$	kJ mol^{-1}	70.149 ± 0.278	70.100 ± 0.228
	T_0	K	298.15	298.15
	τ_0	-	0.43120 ± 0.00872	0.40085 ± 0.00595
	α	-	$1.4611 \times 10^{-10} \pm 1.0593 \times 10^{-2}$	$1.4329 \times 10^{-4} \pm 5.7833 \times 10^{-2}$
	X	-	0.68591 ± 0.19907	0.25122 ± 0.1451
CP	$q_{\infty,0}$	mmol g^{-1}	2.5649 ± 0.0112	2.9094 ± 0.0189
	$b_{0,p}$	($\times 10^{-14}$) bar^{-1}	1.0481 ± 0.0340	0.95981 ± 0.04947
	$-\Delta U_p$	kJ mol^{-1}	105.51 ± 0.09	105.23 ± 0.14
	T_0	K	298.15	298.15
	τ_0	-	0.34307 ± 0.00177	0.40143 ± 0.00360
	α	-	1.3867 ± 0.0384	1.9943 ± 0.0951
	χ	-	1.6364 ± 0.0535	2.5219 ± 0.0864
	$q_{\infty c}$	mmol g^{-1}	1.0509 ± 0.0259	3.5580 ± 0.0910
	$b_{0,c}$	($\times 10^{-2}$) bar^{-1}	1.0335 ± 0.0524	21.190 ± 1.370
	$-\Delta U_c$	kJ mol^{-1}	13.496 ± 0.137	6.9953 ± 0.1802
	E_a	kJ mol^{-1}	0.60049 ± 0.06427	3.1302 ± 0.0696

Given that td-Toth does not represent our data well, I considered other approaches. While the dominant mechanism in amine-functionalised adsorbents is known to be chemisorption via the reaction shown in equation (5.1), previous works have also observed a non-negligible contribution from physisorption on the adsorbent surface, which would be more prevalent at lower temperatures [233, 234]. This seems to also apply to Lewatit and Purolite as their sorption isotherms do not plateau in our measured pressure range. As such, an isotherm model which accounts for both physisorption and chemisorption was previously proposed by Serna-Guerrero et al. to describe CO_2 adsorption on triamine-grafted pore-expanded MCM-41 from 0.001 to 20 bar [233], and used by Elfving et al. for CO_2 adsorption on a proprietary amine-functionalised resin from 0.1 to 5 mbar for DAC applications [223]. This model is given by the following equation:

$$n = n_{phys} + n_{chem} = \left[\frac{q_\infty(T)\cdot b(T)\cdot P}{\left[1+(b(T)\cdot P)^{\tau(T)}\right]^{\frac{1}{\tau(T)}}}\right]_{phys} + \left[\frac{q_\infty(T)\cdot b(T)\cdot P}{\left[1+(b(T)\cdot P)^{\tau(T)}\right]^{\frac{1}{\tau(T)}}}\right]_{chem} \quad (5.7)$$

where $q_\infty(T)$, $b(T)$, and $\tau(T)$ are given by equations (5.4) to (5.6). However, to implement this model, the contributions from n_{phys} and n_{chem} must be separately determined experimentally. Serna-Guerrero et al. did so by measuring adsorption isotherms for un-grafted MCM-41 and assumed this was the contribution for n_{phys}, while Elfving et al. used a N_2 purge with and without heat to separately desorb CO_2 captured by chemisorption vs. physisorption, respectively. Other studies such as those by Pai et al. [235], Hefti et al. [236], and Hughes et al. [237] have also proposed solutions for modelling isotherms with both chemisorption and physisorption contributions, either by using a weighted isotherm model or modelling the chemisorption and physisorption separately, though the application here was for S-shaped isotherms from diamine-appended MOFs.

For this study, I propose a modification of equation (5.7) as follows, which I refer to from here as the Chemi-Physisorption (CP) isotherm model.

$$n = n_{phys} + n_{chem}\cdot\eta = \left[\frac{q_\infty(T)\cdot b_p(T)\cdot P}{\left[1+\left(b_p(T)\cdot P\right)^{\tau(T)}\right]^{\frac{1}{\tau(T)}}}\right]_{phys} + \left[\frac{q_{\infty,c}\cdot b_c(T)\cdot P}{1+b_c(T)\cdot P}\right]_{chem}\cdot\exp\left(\frac{-E_a}{RT}\right) \quad (5.8)$$

where $q_{\infty,c}$ is the maximum CO_2 capacity associated with chemisorption, E_a is the activation energy, and again $q_\infty(T)$, $b_p(T)/b_c(T)$, and $\tau(T)$ are given by equations (5.4) to (5.6). Here, the contribution from physisorption is given by the td-Toth isotherm model, while the contribution from chemisorption is given by the single-site Langmuir (SSL) model. I assume that the transition between physisorption and chemisorption follows an Arrhenius behavior given by η (i.e. at a given temperature, some fraction of molecules will have sufficient activation energy to participate in chemisorption). Thus, the model favours physisorption at lower temperatures, and increases the contribution of chemisorption as the temperature increases, while still allowing for the exothermic nature of adsorption at even higher temperatures. As shown in Figure 5.5, the model provides an improved fit of the experimental data. I performed an F-test between the CP and td-Toth isotherm model fitting results and confirmed that the improved results were indeed significant and not due to additional fitting parameters (see Appendix 3).

The fitted parameters can be found in Table 5.4, while the upper and lower bounds imposed on each parameter during the fitting are summarised in Table A3.2.

As the above CP isotherm model has not yet been thoroughly validated, I also fitted the experimental data to the well-known virial equation as an alternative (Figure A3.8), given by:

$$\ln(P/n) = \frac{1}{T} \cdot \sum_{j=0}^{m_1} a_j \cdot n^j + \sum_{j=0}^{m_2} b_j \cdot n^j \qquad (5.9)$$

where a and b are the characteristic virial coefficients, n is the loading, P is the pressure, T is the temperature, $m_1 = 3$, and $m_2 = 1$. The fitted parameters can be found in Table A3.4, and the upper and lower bounds imposed on each parameter during the fitting are summarised in Table A3.2. The virial equation provides a reasonable fit of the data, however, it is unable to account for competitive adsorption when used in process modelling, and is often difficult to implement due to the need for the equation to be solved numerically as it returns pressure as a function of loading, rather than the conventional loading as a function of pressure. As a result, the CP isotherm model I propose is likely the most appropriate method to use thus far to represent my measured data.

5.2.2.2 N_2, Ar, and O_2 sorption

I measured N_2 sorption isotherms up to 1 bar for Lewatit and Purolite at 15 °C, 25 °C, and 35 °C (Figure 5.6, desorption shown in Figures A3.9a and A3.9b), as well as Ar and O_2 isotherms up to 1 bar at 25 °C (Figure 5.6, desorption shown in Figures A3.9c and A3.9d). These are all gases present in air at higher concentrations than CO_2. They may be competitive for CO_2 adsorption sites or adsorb on the backbone and impact the achievable product purity. The desorption data shown in Figure A3.9 exhibits an irregular pattern which I attribute to the low loading levels, which are on the same order of magnitude as the error of the porosity analyser.

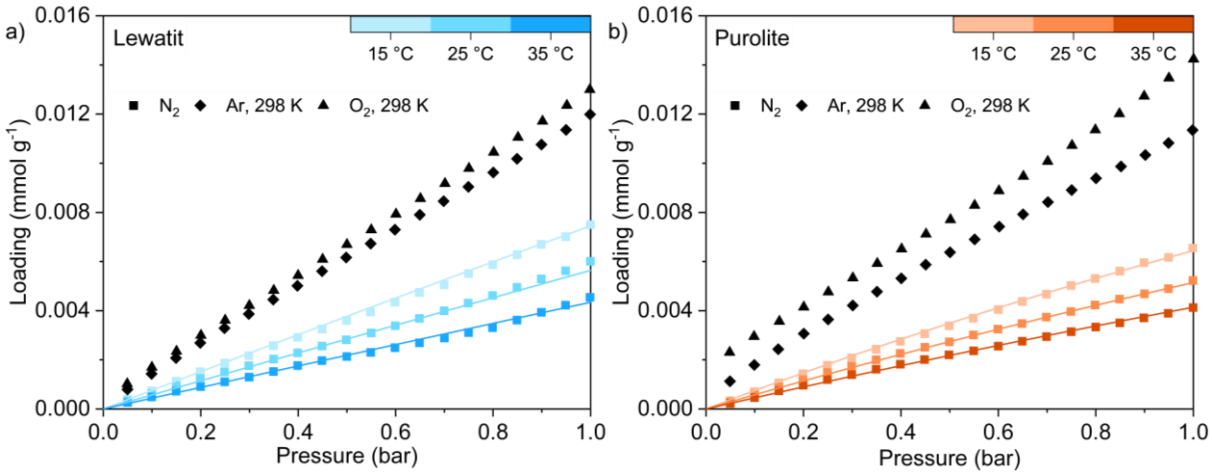


Figure 5.6. Equilibrium adsorption isotherms for N_2 (squares) measured at 15, 25, and 35 °C, and for Ar (diamonds) and O_2 (triangles) at 25 °C up to 1 bar for a) Lewatit and b) Purolite. Solid lines represent the SSL isotherm fitting results (fitting parameters can be found in Table 5.5).

Compared to CO_2 adsorption, the N_2, Ar, and O_2 adsorption levels are almost negligible. The SSL isotherm model shown below in equation (5.10) can be used to represent the N_2 isotherm experimental data and the fitting parameters are reported in Table 5.5,

$$n = \frac{q_{\infty} \cdot b(T) \cdot P}{1 + b(T) \cdot P} \quad (5.10)$$

where q_{∞} is the maximum CO_2 capacity, $b(T)$ is given by equation (5.5), n is the loading, P is the pressure, and T is the temperature. Upper and lower bounds imposed on each parameter during the fitting are summarised in Table A3.2. Interestingly, both Lewatit and Purolite are O_2 selective compared to N_2, where many traditional adsorbents such as zeolites have the opposite performance. Although their O_2 adsorption capacities are low, these materials may have potential applications in air separation where it would be more energy and cost effective to adsorb O_2 ($21\%_{vol}$ in air) vs. N_2 ($78\%_{vol}$ in air). To the best of my knowledge, O_2 isotherms have not been previously measured for Lewatit and so this characteristic was not observed. In addition, the O_2 isotherm on Purolite at 25 °C does not appear to intersect the origin. This may be an indication for degradation of, or reaction with, the amine functionalisation of the sorbent. It also aligns with the impact of oxidative degradation of the amines on CO_2 capacity, discussed in Section 5.2.2.1.

Table 5.5. Fitting parameters with uncertainty bounds for a 95% confidence interval for the SSL isotherm model for N_2 adsorption for Lewatit and Purolite.

Equation	Parameter	Unit	Lewatit	Purolite
SSL	q_∞	mmol g^{-1}	0.31479 ± 0.00379	0.041908 ± 0.000247
	b_0	($\times 10^{-6}$) bar^{-1}	5.0560 ± 0.0618	75.574 ± 0.049
	$-\Delta U$	kJ mol^{-1}	20.304 ± 0.030	18.650 ± 0.016

5.2.2.3 H_2O sorption

I measured the H_2O adsorption and desorption isotherms for Lewatit and Purolite at 15 °C up to 0.016 bar, and at 25 °C and 35 °C up to 0.023 bar (Figure 5.7). Water adsorption behaviour is particularly important to understand for amine-functionalised adsorbents as the presence of H_2O from relative humidity in the air is known to increase the CO_2 uptake of these materials as well as minimise amine degradation [12, 159, 238]. While directly measuring CO_2-H_2O co-adsorption isotherms is ideal, it remains experimentally challenging; for this study I chose to only measure unary water sorption isotherms.

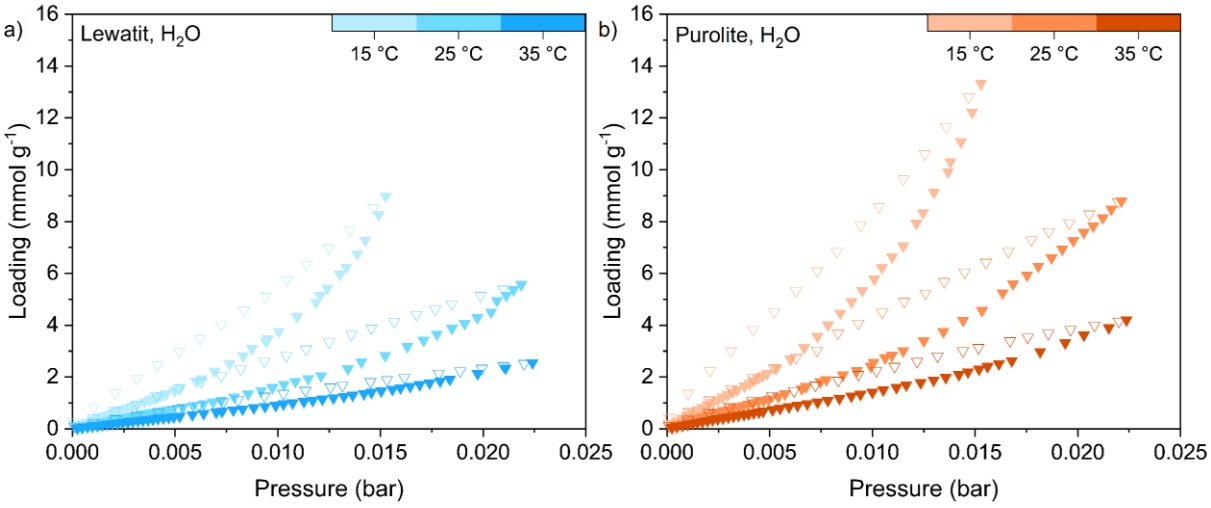


Figure 5.7. Equilibrium adsorption (filled symbols) and desorption (hollow symbols) isotherms for H_2O measured at 15 °C up to 0.016 bar, and 25 °C and 35 °C up to 0.023 bar for a) Lewatit and b) Purolite.

The water adsorption behaviour of both resins follows a Type III isotherm behaviour according to IUPAC classification [75], which represents unrestricted multilayer adsorption on macroporous materials. When the loading data is plotted against the adsorption potential, ϵ, given by:

$$\epsilon = -R \cdot T \cdot \ln(x) \quad (5.11)$$

where R is the universal gas constant, T is the temperature, and x is the relative pressure, the results collapse on to a characteristic curve typical of non-microporous adsorbents (Figure A3.10) [239].

I used the Guggenheim–Anderson–de Boer (GAB) model to fit the experimental data as a function of relative pressure for both materials, as used by Young et al. for Lewatit [150]. The model is as follows:

$$n = \frac{q_m \cdot k \cdot c \cdot x}{(1-k \cdot x)(1+(c-1) \cdot k \cdot x)} \quad (5.12)$$

$$c = \exp\left(\frac{E_1 - E_{10+}}{RT}\right) \quad (5.13)$$

$$k = \exp\left(\frac{E_{2-9} - E_{10+}}{RT}\right) \quad (5.14)$$

$$E_1 = C - \exp(D \cdot T) \quad (5.15)$$

$$E_{2-9} = F + G \cdot T \quad (5.16)$$

$$E_{10+} = -44.38 \cdot T + 57220 \quad (5.17)$$

where n is the water loading on the resins, x is the relative pressure, q_m is the water loading of the monolayer, and k and c are affinity parameters governed by the heats of adsorption of the first (E_1), second to ninth (E_{2-9}), and tenth and higher (E_{10+}) layers of adsorbed water. E_{10+} is also equivalent to the heat of condensation of water, and C, D, F, and G are constants to be fitted.

The fitting results are shown in Figure 5.8 and the fitting parameters are reported in Table 5.6, while the upper and lower bounds imposed on each parameter during the fitting are summarised in Table A3.2. A comparison of my adsorption data obtained at 25 °C with that obtained by Young et al. [150] is shown in Figure A3.11a and we observe good agreement between the two data sets. An overlay of their fitted isotherm parameters (Table A3.5) with my experimental data is also shown in Figure A3.11b. Their parameters reasonably fit my measured 35 °C data, but deviate from my data at 15 and 25 °C. This could be because Young et al. fitted their parameters to experimental data collected at a wider and higher temperature range, from 25 °C to 100 °C.

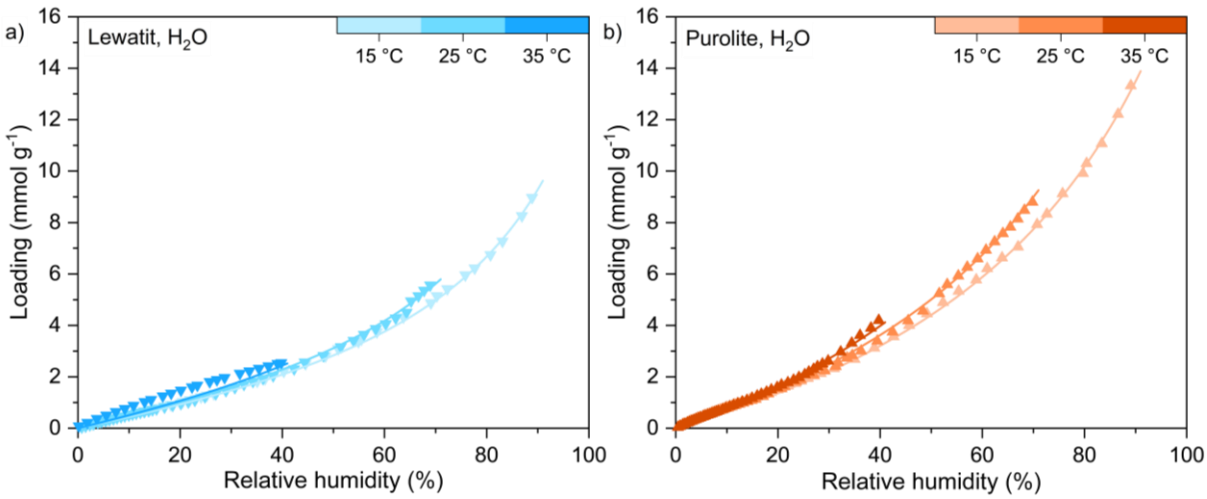


Figure 5.8. Equilibrium adsorption isotherms for H_2O measured at 15 °C, 25 °C, and 35 °C as a function of relative humidity for a) Lewatit and b) Purolite. Solid lines represent the GAB isotherm fitting results (fitting parameters can be found in Table 5.6).

Table 5.6. Fitting parameters with uncertainty bounds for a 95 % confidence interval for the GAB isotherm model for H_2O adsorption for Lewatit and Purolite.

Equation	Parameter	Unit	Lewatit	Purolite
GAB	q_m	mmol g^{-1}	3.2245 ± 0.0268	7.7526 ± 0.0679
	C	kJ mol^{-1}	46.832 ± 0.042	45.794 ± 0.0367
	D	K^{-1}	0.024457 ± 0.000082	0.024412 ± 0.000076
	F	kJ mol^{-1}	53.306 ± 0.011	52.522 ± 0.012
	G	kJ mol^{-1} K^{-1}	-0.032677 ± 0.000039	-0.031085 ± 0.000042

5.2.2.4 Isosteric heats of adsorption

I calculated the limiting heat of adsorption (Table 5.7), as well as the heat of adsorption as a function of loading (i.e. isosteric heat of adsorption), of CO_2, N_2, and H_2O for both Lewatit and Purolite (Figure 5.9). The intermediate results obtained during calculation of the limiting heats of adsorption are presented in Figures A3.12 to A3.17. Confidence intervals associated with the heat of adsorption as a function of loading calculations are presented in Figures A3.18 and A3.19, along with additional data calculated using alternative isotherm temperatures for CO_2. The smoothing parameter values applied for each adsorbent-adsorbate combination are presented in Table A3.6. The heats of adsorption serve

as inputs in process models and link to the energy requirements for desorption in a DAC process, where a higher heat of adsorption implies higher energy needed to regenerate the adsorbent. Both materials have high CO_2 heats of adsorption characteristic of chemisorbents. At the loading levels corresponding to 0.4 mbar CO_2, Lewatit and Purolite have heats of adsorption of ~ 81 kJ mol^{-1} and 69 kJ mol^{-1}, respectively. The data presented in Figure 5.9a was obtained using the 60, 70, 80, and 120 °C CO_2 isotherms. The isosteric heats of adsorption calculated using the lower temperatures of 15, 25, and 35 °C are shown in Figure A3.18 and show an eventual transition to the physisorption range, commonly said to be below 50 kJ mol^{-1}.

Table 5.7. Limiting heats of adsorption of CO_2, N_2, and H_2O for Lewatit and Purolite with uncertainty bounds for a 95% confidence interval.

	Lewatit	**Purolite**
$-\Delta H_0$, CO_2 (kJ mol^{-1})	107 ± 8	104 ± 9
$-\Delta H_0$, N_2 (kJ mol^{-1})	16 ± 8	13 ± 13
$-\Delta H_0$, H_2O (kJ mol^{-1})	49 ± 29	50 ± 42

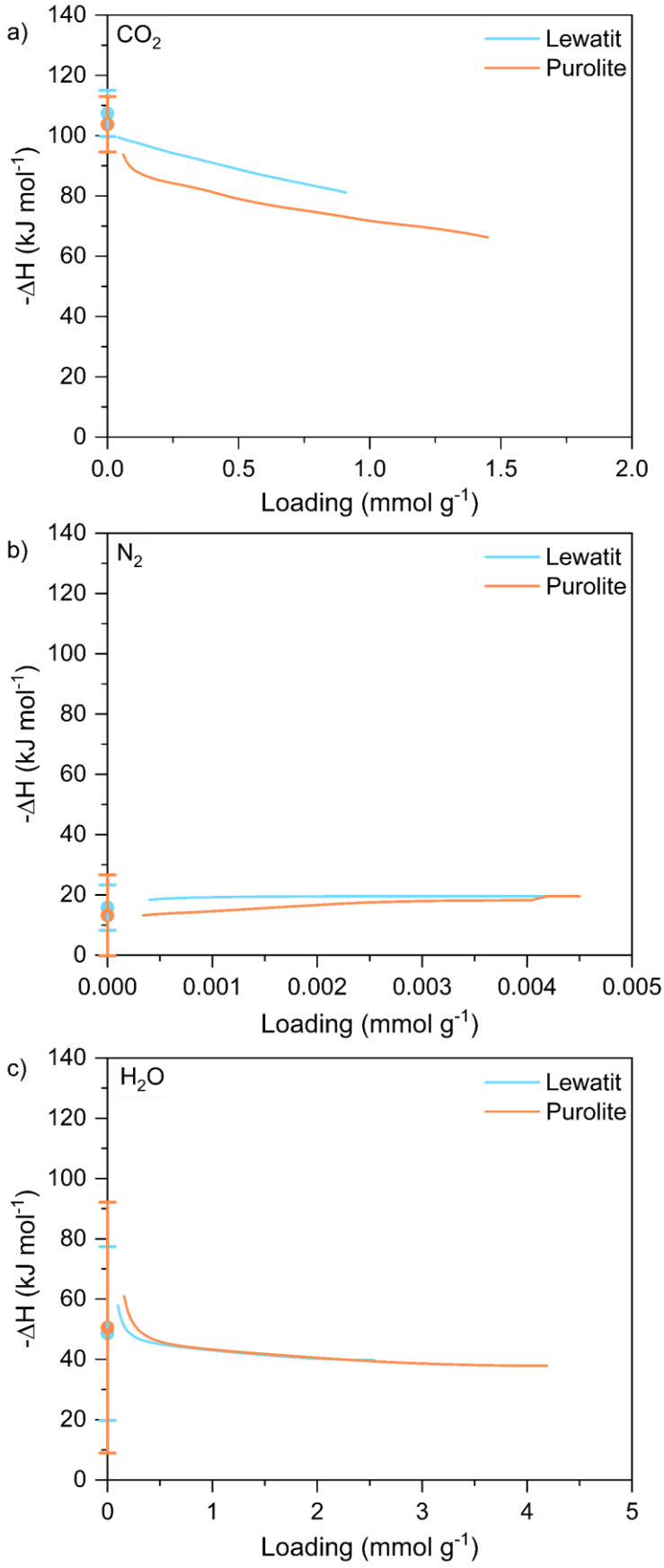


Figure 5.9. Isosteric heats of adsorption of Lewatit and Purolite for a) CO_2, b) N_2, and c) H_2O.

Also characteristic of many chemisorbents, both materials exhibit low N_2 heats of adsorption of ~ 20 kJ mol^{-1}. The N_2 heat of adsorption stays relatively constant as a function of loading, indicating homogenous coverage of the adsorbent surface. For H_2O, the heat of adsorption steeply decreases from 60 kJ mol^{-1} between 0 to 0.5 mmol g^{-1} loading, before plateauing at approximately 40 kJ mol^{-1}, which is close to the heat of condensation of water of 44.0 kJ mol^{-1} at 25 °C given by equation (5.17) and corroborated by NIST [240]. This trend possibly reflects two different sorption mechanisms consisting of a monolayer of resin – H_2O interactions, followed by multilayers of H_2O – H_2O interaction.

To test this hypothesis, the heats of adsorption associated with monolayer formation can be calculated using equation (5.15) and the fitted parameters provided in Table 5.6, and are ~ 45.4 kJ mol^{-1} and 44.3 kJ mol^{-1} for Lewatit and Purolite, respectively. From Figure 5.9c, the H_2O loadings associated with these heats of adsorption, i.e. the supposed monolayer loadings, are ~ 0.44 mmol g^{-1} and 0.73 mmol g^{-1} for Lewatit and Purolite, respectively. These values can then be used to estimate a corresponding surface area (S) for Lewatit and Purolite using equation (5.18) [75]:

$$S = q \cdot N_A \cdot \sigma_A \quad (5.18)$$

where q (in mmol g^{-1}) is the H_2O loading corresponding to the selected heat of adsorption (in kJ mol^{-1}), N_A is Avogadro's constant, and σ_A is 11.130 Å^2, i.e. the cross-sectional area of a water molecule. From this calculation, the surface areas for Lewatit and Purolite are 28 m^2 g^{-1} and 46 m^2 g^{-1}, respectively. For Lewatit, this value corresponds well with the BET area of 32 m^2 g^{-1} calculated using N_2 sorption at -196 °C, while for Purolite there is a larger discrepancy with the previously measured value of 29 m^2 g^{-1}. Overall, the proposal of a monolayer of resin – H_2O interactions followed by multilayers of H_2O – H_2O interaction does not seem unreasonable based on these calculations, though different types of surface features on the resins could be another possible explanation for the shape of the heat of adsorption curve."

5.3 Conclusions

In this study, I have endeavoured to experimentally determine as many of the physicochemical and equilibrium sorption properties needed for process scale evaluation of DAC adsorbents as possible for Purolite A110, a commercially available amine-functionalised polymeric resin, and compared its properties to that of Lewatit VP OC 1065, a current benchmark adsorbent for DAC. Lewatit and Purolite have similar chemical features, specific heat capacities, thermal stability, and skeletal density. Purolite has lower bed and pellet density than Lewatit, and higher total pore volume and porosity. In terms of its gas sorption performance, Purolite has a higher gravimetric and volumetric CO_2 adsorption capacity than Lewatit, attributed to its higher N content, as well as higher H_2O adsorption, while both materials have low and comparable adsorption of N_2, Ar, and O_2. Purolite has a lower CO_2 heat of adsorption compared to Lewatit and similar H_2O heat of adsorption. This trend suggests potentially lower energy requirements for desorption and thus lower process operating costs but this will ultimately depend on actual loadings. I also proposed an empirical CO_2 sorption isotherm model combining chemisorption and physisorption terms. The model fitted the data well and could be used for numerical expression of the sorption isotherms. Based on the data I have collected, I propose that Purolite A110 is indeed a suitable adsorbent for DAC. With this work, I hope I have provided the adsorption community with the necessary information to conduct initial process scale modelling and optimisation to assess the process performance of Purolite for adsorption-based DAC and continue to advance the development and scale-up of this technology.

Chapter 6: Physicochemical properties, equilibrium adsorption performance, manufacturability, and stability of TIFSIX-3-Ni for direct air capture

The work and discussions in this chapter were previously published by the thesis author in Energy and Fuels [2].

6.1 Introduction

While polymers are often investigated in DAC process studies, another class of adsorbent which has received a lot of attention for DAC are metal organic frameworks (MOFs). In fact, 25% of recent DAC adsorbent studies are focused on these materials [10]. Amongst these, ultramicroporous MOFs, i.e. MOFs with pores smaller than 0.7 nm [107], are often highlighted. Their small pore sizes and chemical nature allow for high CO_2 adsorption capacity at the relevant low pressures (> 1.0 mmol g^{-1} at 0.4 mbar CO_2 and 25 °C) and limited N_2 adsorption, as well as lower CO_2 heat of adsorption than many amine-functionalised chemisorbents. Notable ultramicroporous MOFs reported for DAC include NbOFFIVE-1-Ni, SIFSIX-3-Cu, SIFSIX-18-Ni-β, TIFSIX-3-Ni, TIFSIX-3-Co, GeFSIX-3-Ni, WO_2F_4-1-Ni, and FJI-H38 [107-109, 128, 241-244]. Recent reviews by Zhang et al. [245] and Bose et al. [246] provide a comprehensive overview of these, and other MOF adsorbents for DAC.

Amongst ultramicroporous MOFs, TIFSIX-3-Ni is a particularly promising candidate adsorbent for DAC. It is formed of a grid-like framework of Ni nodes joined together by pyrazine organic linkers and TiF_6^- anion pillars, with a pore size of 0.325 nm [247], defined as the diagonal F-F distance across a channel [246]. TIFSIX-3-Ni was first studied for DAC in 2017 by Kumar et al. [107]. They reported a high CO_2 adsorption capacity of 1.1 mmol g^{-1} at 0.4 mbar and 25 °C, a moderate CO_2 heat of adsorption of 50 kJ mol^{-1}, and minimal loss in BET area and CO_2 adsorption performance after exposure to 75% relative humidity (RH) at 40 °C for 14 days. Volumetric CO_2 adsorption isotherms measured at 0, 10 and 25 °C, and a N_2 adsorption isotherm measured at 25 °C were also reported, though no isotherm model fitting was conducted. Mukherjee et al. [128] also reported a gravimetric H_2O adsorption isotherm measurement at 25 °C. In addition, they conducted dynamic column breakthrough (DCB) measurements for TIFSIX-3-Ni using both dry and humid CO_2 at 1 mbar and 3 mbar balanced

with N_2, where they observed a significant decrease in CO_2 adsorption capacity in the presence of humidity. However, Ullah et al. [247] reported slow H_2O kinetics in comparison to CO_2 from their DCB experiments and that shortened adsorption cycles would allow for ~ 90% retention of the dry CO_2 adsorption capacity. They further elucidated the CO_2-H_2O co-adsorption mechanisms using in-situ spectroscopy and molecular simulations, proposing that CO_2 and H_2O can occupy the same ultramicropore at low water loadings, up to a maximum of one CO_2 molecule and three H_2O molecules. At higher water loadings however, an energetically favoured water network will form with four H_2O molecules in one ultramicropore and displace CO_2.

TIFSIX-3-Ni also seems to be promising in terms of its manufacturability and scalability. Its synthesis is relatively straightforward and does not require the use of hydrofluoric acid as a precursor, unlike other ultramicroporous MOFs such as NbOFFIVE-1-Ni [109]. However, the presence of Ni in the material still poses serious toxicity risks for chemical manufacturers, plant operators, and the environment. A disclosure by the Commonwealth Scientific and Industrial Research Organisation (CSIRO) has documented the synthesis of up to 65 g of powdered TIFSIX-3-Ni to be used in a MOF-polymer nanocomposite coating for application in a DAC adsorption unit [248]. CSIRO termed this nanocomposite technology “Airthena” and conducted a pilot-scale demonstration of their DAC unit where they captured 8 kg of CO_2 from ambient air over 2680 cycles [248, 249]. The company MOF Technologies (now known as Nuada) previously sold TIFSIX-3-Ni in both powder and shaped form, though no further details are currently available. [250, 251]. Kearns et al. [18] produced 3D printed monoliths of TIFSIX-3-Ni mixed with graphite and bentonite, and also proposed an improved synthesis of TIFSIX-3-Ni powder using a lower-cost nickel hydroxide precursor instead of anhydrous nickel carbonate. Warfsmann et al. [252] had also previously reported a thin-film synthesis of TIFSIX-3-Ni.

Despite many promising studies on TIFSIX-3-Ni, this MOF has not yet been widely considered in DAC process modelling and optimisation studies. This is due to the unavailability of key properties for TIFSIX-3-Ni such as its density, porosity, specific heat capacity, and isotherm model fitting parameters for CO_2, N_2, and H_2O. Isotherms for other gases present in air which may compete with CO_2, such as O_2 and Ar, have also not been measured. Besides, the previous studies highlighted above present some discrepancies regarding the effect of moisture on TIFSIX-3-Ni stability and performance.

Therefore, in this study, I aim to report as many of the physicochemical and equilibrium adsorption properties for TIFSIX-3-Ni as possible, to facilitate process-scale evaluation of the adsorbent for DAC. These include: physical properties such as the skeletal, pellet, and bed density; thermal properties such as the specific heat capacity and thermal stability; textural properties such as micropore and total pore volume, BET area, and pellet porosity; and adsorption properties including Ar and O_2 isotherms at a single temperature, and CO_2, N_2, and H_2O isotherms at multiple temperatures. Where isotherms at multiple temperatures are measured, I determined isotherm model fitting parameters and heats of adsorption. I also assessed the practicality of using this adsorbent in a DAC process by studying its manufacturability in terms of reproducibility and binderless shaping, as well as investigating its stability to different process conditions such as humidity and cyclic adsorption.

6.2 Results and discussion

6.2.1 Physicochemical properties

The X-ray diffraction (XRD) patterns of ground $NiTiF_6$ crystals, TIFSIX-3-Ni precursor powder, and the final TIFSIX-3-Ni powder (Figure 6.1a) match those reported in the literature [107, 253] (Figure A4.1) and suggest the successful synthesis of the final TIFSIX-3-Ni sample. Images of these compounds are shown in Figure A4.2. I then used N_2 adsorption at -196 °C to assess its porosity (Figure 6.1b), revealing a total pore volume of 0.50 $cm^3\ g^{-1}$, a micropore volume of 0.11 $cm^3\ g^{-1}$, and a BET area of 264 $m^2\ g^{-1}$.

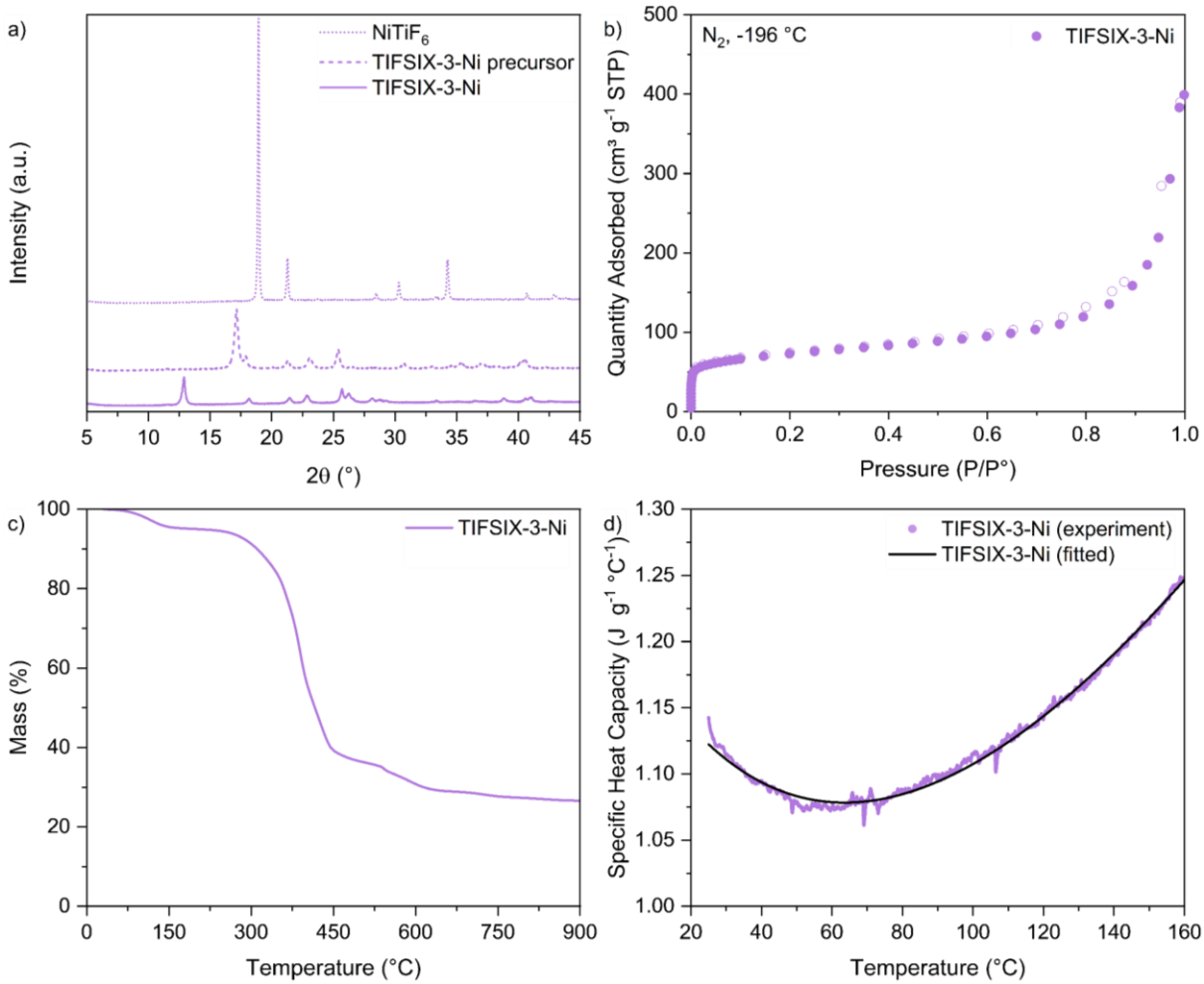


Figure 6.1. a) XRD patterns of $NiTiF_6$, TIFSIX-3-Ni precursor, and final TIFSIX-3-Ni. b) N_2 adsorption (filled symbols) and desorption (open symbols) isotherms at -196 °C, c) TG curve under N_2 atmosphere up to 900 °C, and d) specific heat capacity as a function of temperature for TIFSIX-3-Ni.

To determine the thermal stability of TIFSIX-3-Ni, which influences the maximum temperature that can be used for regeneration of this material in a DAC process, I conducted thermogravimetric analysis (TGA) with a N_2 flow up to 900 °C. From Figure 6.1c, we see that water desorbs from the sample up to 150 °C, after which there is no further mass loss until 230 °C, when the crystal structure begins to degrade. The results correspond with those reported by Kumar et al., who reported a thermal stability up to 280 °C in a N_2 atmosphere [107].

I also used differential scanning calorimetry (DSC) to determine the specific heat capacity of TIFSIX-3-Ni between 25 °C to 160 °C (Figure 6.1d), i.e. a range of temperatures relevant to a DAC

process. The specific heat capacity relates to the energy input required for sensible heating of the adsorbent during regeneration, where a higher specific heat capacity indicates that the adsorbent requires more energy to be heated to a given temperature. This property is a necessary input in process modelling and was not previously reported for TIFSIX-3-Ni. The specific heat capacity of TIFSIX-3-Ni ranged from 1.06 to 1.25 J g^{-1} °C^{-1} (derived from the heat flow curves shown in Figure A4.3). This is comparable to the specific heat capacity reported for SIFSIX-3-Ni (1.07 J g^{-1} °C^{-1}) [254], which has the same crystal structure as TIFSIX-3-Ni with Si atoms in place of Ti.

The experimental data can be modelled using equation (6.1) [198]:

$$c_p = a \cdot (T + 273.15)^{-2} + b \cdot (T + 273.15) - c \qquad (6.1)$$

where c_p is the specific heat capacity, T is the temperature (in °C), and a, b, and c are fitted parameters with values and uncertainty bounds of 1.077 ± 0.004 ×10^5 J °C g^{-1}, 5.65 ± 0.02 ×10^{-3} J g^{-1} °C^{-2}, and 1.773 ± 0.008 J g^{-1} °C^{-1}, respectively. The increase in c_p as the temperature decreases below approximately 60 °C is opposite to the expected trend. This "anomaly" has been observed in ZIF-8 and was associated to flexibility in its crystal structure due to linker rotation [255]. The possibility of flexibility in the crystal structure of TIFSIX-3-Ni is further discussed in Section 6.2.3.2.

6.2.2 Equilibrium adsorption properties

6.2.2.1 CO_2 adsorption

I measured equilibrium CO_2 adsorption and desorption isotherms up to 1 bar for TIFSIX-3-Ni powder at 15, 25, 35, 60, 70, 80, and 120 °C (Figure 6.2a). I confirmed equilibrium was reached for these analyses by measuring the isotherms at 35 °C using 60 s and 90 s as the equilibrium interval and observing no change in the results (Figure A4.4). According to Ullah et al. [247], the CO_2 capture mechanism in TIFSIX-3-Ni is that one CO_2 molecule fits within the cavity of a single unit cell cage, giving a theoretical maximum gravimetric CO_2 loading for TIFSIX-3-Ni of 2.6 mmol g^{-1} (see Appendix 4 for details). At 0.4 mbar, which is representative of the CO_2 feed stream for a DAC process, and at an adsorption temperature of 25 °C, TIFSIX-3-Ni has a gravimetric CO_2 adsorption capacity of 1.11 mmol g^{-1}. This is very similar to the value reported by Kumar et al. (1.05 mmol g^{-1}) [107] and is higher than

the gravimetric CO_2 adsorption capacity measured at the same conditions for Lewatit VP OC 1065 (0.95 mmol g^{-1}) [1], a current benchmark adsorbent for DAC.

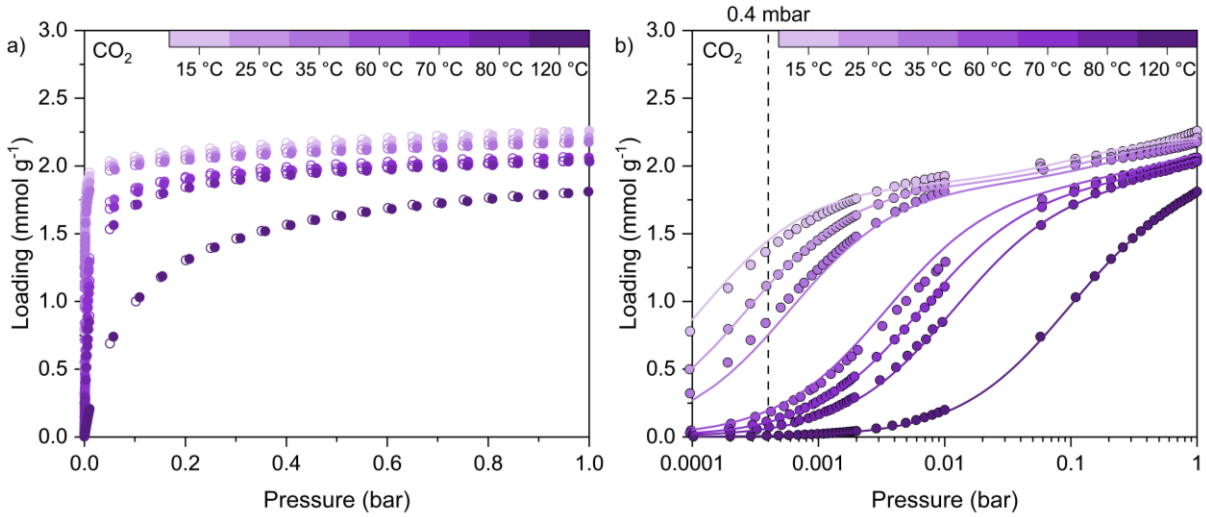


Figure 6.2. a) CO_2 equilibrium adsorption (filled symbols) and desorption (open symbols) isotherms measured at 15, 25, 35, 60, 70, 80, and 120 °C up to 1 bar for TIFSIX-3-Ni powder. b) CO_2 equilibrium adsorption isotherms shown with a log-scale of pressure measured at 15, 25, 35, 60, 70, 80, and 120 °C up to 1 bar for TIFSIX-3-Ni powder. Solid lines represent the fitting results from the DSL isotherm model, whose fitting parameters are found in Table 6.1.

The isotherms of 15 °C, 25 °C, and 35 °C seem to converge at the same saturation capacity at 1 bar, and the same can be observed for the 60, 70 and 80 °C isotherms. This convergence of CO_2 isotherms can also be observed in the isotherms reported by Kumar et al. in their supplementary information [107]. Interestingly, the CO_2 loadings at 1 bar for the 15 °C, 25 °C, and 35 °C isotherms are all ~ 2.2 $mmol^{-1}$ g^{-1}, and those of the 60 °C, 70 °C, and 80 °C isotherms are ~ 2.0 mmol g^{-1}. Both of these values are below the maximum theoretical loading of 2.6 mmol g^{-1}. I hypothesised that this could be due to defects in the crystal structure and/or impurities in the sample which would decrease the number of adsorption sites for CO_2. I performed X-ray photoelectron spectroscopy (XPS) analysis on as-synthesised TIFSIX-3-Ni to investigate this and identified a non-negligible presence of oxygen in my sample (Table A4.1, approx. 5 at%). Deconvolution of the O 1*s*, N 1*s*, Ti 2*p*, and Ni 2*p* core levels (Figure A4.5) suggested the presence of $NiO/Ni(OH)_2$ and $TiO_2/TiOF_2$ species and interaction of

oxygen with the pyrazine linker [256, 257], perhaps due to surface oxidation of the TIFSIX-3-Ni sample during synthesis, storage, and/or handling. Indeed, Barsoum et al. recently reported the presence of nickel oxide nanolayers on SIFSIX-3-Ni (the silicon analogue of TIFSIX-3-Ni) after exposure to humidity, though these were at different conditions (70 °C and 80% RH) than those that would be experienced by my sample during synthesis and/or storage [258]. No anomalies were observed in the C 1*s* and F 1*s* spectra.

To enable the use of the adsorption data in process models, I fitted the experimental CO_2 isotherms using isotherm model equations using the dual-site Langmuir (DSL) isotherm model shown below in equations (6.2) to (6.4):

$$n = \frac{q_{s1} \cdot b_1(T) \cdot P}{1 + b_1(T) \cdot P} + \frac{q_{s2} \cdot b_2(T) \cdot P}{1 + b_2(T) \cdot P} \qquad (6.2)$$

$$b_1(T) = b_{0,1} \cdot \exp\left(\frac{-\Delta U_1}{RT}\right) \qquad (6.3)$$

$$b_2(T) = b_{0,2} \cdot \exp\left(\frac{-\Delta U_2}{RT}\right) \qquad (6.4)$$

where T is the temperature, P is the pressure, q_{s1} and q_{s2} are the maximum CO_2 capacities, $b_1(T)$ and $b_2(T)$ are the CO_2 adsorption coefficients defined by constants $b_{0,1}$ and $b_{0,2}$ and the internal energy change during adsorption ΔU_1 and ΔU_2, respectively, and R is the universal gas constant. The fitting results are shown in Figure 6.2b, with the fitted parameters and corresponding uncertainty bounds found in Table 6.1. The lower and upper bounds applied on each parameter during the fitting process are summarised in Table A4.2.

Table 6.1. Fitting parameters with uncertainty bounds for a 95% confidence interval for the DSL, SSL, and UNIV6 isotherm model for CO_2, N_2, and H_2O adsorption on TIFSIX-3-Ni, respectively.

Adsorbate	Equation	Parameter	Unit	TIFSIX-3-Ni
CO_2	DSL	q_{s1}	mmol g^{-1}	0.38737 ± 0.02037
		$b_{0,1}$	($\times 10^{-5}$) bar^{-1}	3.4932 ± 0.4670
		$-\Delta U_1$	kJ mol^{-1}	29.256 ± 0.360
		q_{s2}	mmol g^{-1}	1.8730 ± 0.0085
		$b_{0,2}$	($\times 10^{-7}$) bar^{-1}	1.2200 ± 0.0355
		$-\Delta U_2$	kJ mol^{-1}	59.798 ± 0.079
N_2	SSL	q_s	mmol g^{-1}	1.7934 ± 0.0059
		b_0	($\times 10^{-5}$) bar^{-1}	1.9277 ± 0.0069
		$-\Delta U$	kJ mol^{-1}	21.175 ± 0.009
H_2O	UNIV6	q_s	mmol g^{-1}	79.519 ± 1.780
		α_1	-	0.069935 ± 0.003326
		α_2	-	0.62604 ± 0.02311
		α_3	-	0.022151 ± 0.004976
		ε_1	kJ mol^{-1}	45.444 ± 1.089
		ε_2	kJ mol^{-1}	33.169 ± 0.092
		ε_3	kJ mol^{-1}	37.485 ± 0.201
		ε_4	kJ mol^{-1}	31.471 ± 0.243
		m_1	kJ mol^{-1}	2.6902 ± 0.6773
		m_2	kJ mol^{-1}	0.59117 ± 0.04319
		m_3	kJ mol^{-1}	0.056502 ± 0.141182
		m_4	kJ mol^{-1}	2.8646 ± 0.1485
		K	($\times 10^{-5}$) bar^{-1}	3.6905 ± 0.1113

Interestingly, the single-site Langmuir (SSL) isotherm model did not accurately represent the experimental data (Figure A4.6 and Table A4.3), particularly at the higher pressures and lower temperatures. This suggests additional binding sites for CO_2 other than within the cavity of a unit cell cage as previously reported [247], which would support my previous hypotheses of the presence of defects, the presence of oxides of Ni and/or Ti, and/or the flexibility of the crystal structure.

6.2.2.2 N_2, Ar, and O_2 adsorption

I measured N_2 adsorption and desorption isotherms up to 1 bar for TIFSIX-3-Ni powder at 15 °C, 25 °C, and 35 °C, as well as Ar and O_2 adsorption and desorption isotherms up to 1 bar at 25 °C (Figure 6.3, desorption data in Figure A4.7). N_2, Ar, and O_2 are more abundant than CO_2 in air and could compete for CO_2 adsorption sites. For TIFSIX-3-Ni, the adsorption levels of all three gases are very low compared to CO_2, with N_2 showing slightly higher adsorption compared to Ar and O_2 at the same temperature. However, these adsorption levels are a magnitude higher than those observed for Lewatit VP OC 1065 [1]. As a result, the CO_2 selectivity of TIFSIX-3-Ni is likely lower than that of the resin, which is not unexpected when comparing a physisorbent to a chemisorbent. I used the SSL isotherm model shown below in equation (6.5) to represent the measured N_2 isotherm data:

$$n = \frac{q_s \cdot b(T) \cdot P}{1 + b(T) \cdot P} \quad (6.5)$$

where n is the loading, P is the pressure, T is the temperature, q_s is the maximum CO_2 capacity, and $b(T)$ is given by equation (6.3). The fitting parameters and corresponding uncertainty bounds are reported in Table 6.1, while the lower and upper bounds applied on each parameter during the fitting process are summarised in Table A4.2.

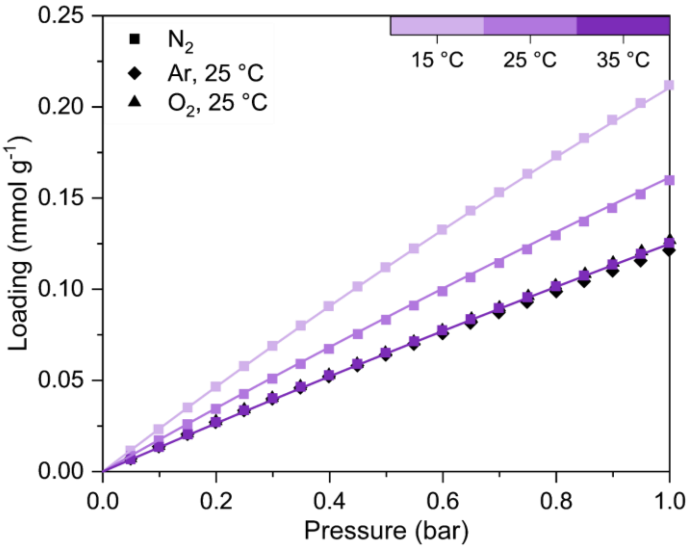


Figure 6.3. N_2 equilibrium adsorption isotherms for (squares) measured at 15 °C, 25 °C, and 35 °C, and Ar (diamonds) and O_2 (triangles) equilibrium adsorption isotherms measured at 25 °C up to 1 bar for TIFSIX-3-Ni. Solid lines represent the fitting results from the SSL isotherm model, whose fitting parameters are found in Table 6.1.

6.2.2.3 H_2O adsorption

I measured H_2O adsorption and desorption isotherms for TIFSIX-3-Ni powder at 15 °C up to 0.016 bar (94% RH), and at 25 °C and 35 °C up to 0.023 bar (73% RH and 41% RH, respectively) (Figure 6.4). I note that I measured these H_2O isotherms on a different batch of TIFSIX-3-Ni, denoted by the grey colour scheme instead of purple, as compared to all previous measurements up to this point. Differences in batches of TIFSIX-3-Ni are discussed later in Section 6.2.3.1.

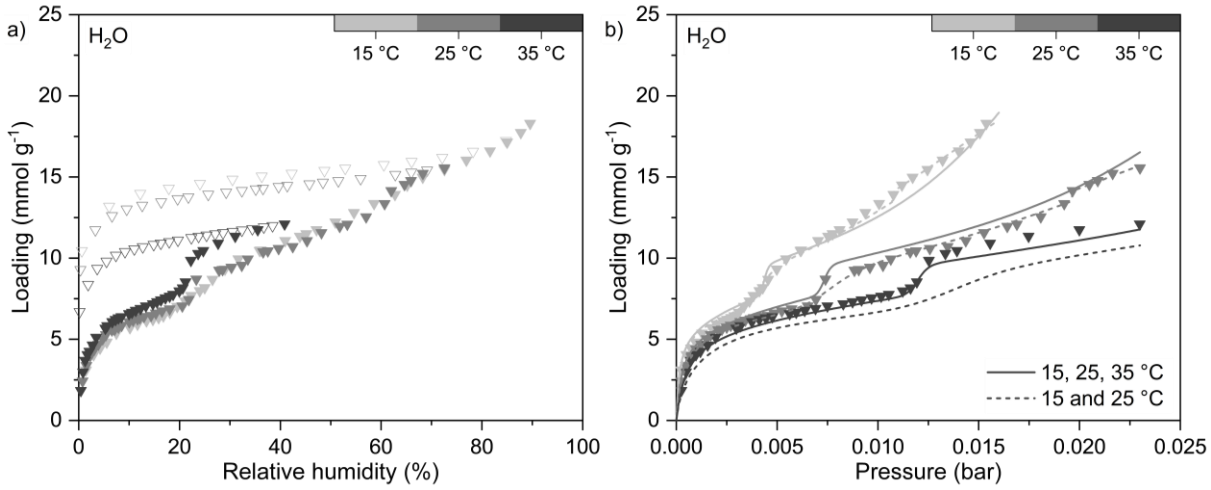


Figure 6.4. a) H_2O equilibrium adsorption (filled symbols) and desorption (open symbols) isotherms measured at 15 °C, 25 °C, and 35 °C for TIFSIX-3-Ni as a function relative humidity. b) H_2O equilibrium adsorption isotherms measured at 15 °C, 25 °C, and 35 °C as a function of absolute pressure in bar. Solid lines represent the UNIV6 isotherm model fitting results determined from using the 15 °C, 25 °C, and 35 °C experimental data in the fitting process, while dashed lines represent the fitting results using only the 15 °C and 25 °C experimental data. Fitting parameters are found in Table 6.1 and Table A4.5, respectively.

TIFSIX-3-Ni has almost three times higher H_2O loading compared to Lewatit at 25 °C and 70% RH [1], and displays an unusual step-wise adsorption behaviour at all temperatures along with severe hysteresis demonstrating irreversible adsorption. This step-wise adsorption was observed previously by Mukherjee et al. [128], but desorption data was not measured. They reported slightly lower loading at 25 °C (~ 13 mmol g^{-1} at 0.025 bar, i.e. 79% RH) and only observed a single step at ~ 0.008 bar (i.e. 25%

RH). They also reported a step decrease in the H_2O loading after 0.025 bar, a humidity level I was not able to measure up to with the Micromeritics 3Flex porosity analyser.

According to Ullah et al. [247], four H_2O molecules can fit within the cavity of a single TIFSIX-3-Ni unit cell cage, leading to a theoretical maximum H_2O loading of 10.5 mmol g^{-1}. However, from Figure 6.4, the adsorption isotherms measured at all temperatures exceed this value. Furthermore, the data measured at 35 °C does not overlay with those measured at 15 °C and 25 °C when the loading data is plotted as a function of the relative humidity (Figure 6.4a), as well as the adsorption potential ϵ [239] (Figure A4.8), given by equation (6.6):

$$\epsilon = -R \cdot T \cdot \ln(x) \qquad (6.6)$$

where R is the universal gas constant, T is the temperature, and x is the relative pressure. These observations (i.e. unusual step-wise adsorption, hysteresis, exceeding the theoretical H_2O loading, and apparent disagreement of the 35 °C isotherm) again suggest that the TIFSIX-3-Ni sample may have flexibility/defects in its crystal structure, and/or be degrading upon exposure to H_2O, both of which have recently been observed for SIFSIX-3-Ni [258]. A more thorough investigation of the H_2O interaction with, and H_2O stability of, TIFSIX-3-Ni is discussed in Section 6.2.4.1.

According to the IUPAC classification [75], the step-wise H_2O adsorption behaviour follows that of a Type VI isotherm. This can be modelled using the universal adsorption isotherm model for a Type VI isotherm reported by Ng et al. [259]:

$$n = q_s \cdot \sum_{i=1}^{4} \alpha_i \cdot \left(\left[1 + \exp\left(\frac{-RTln(KP) - \varepsilon}{m} \right) \right]^{-1} \right)_i \qquad (6.7)$$

$$\alpha_4 = 1 - \alpha_1 - \alpha_2 - \alpha_3 \qquad (6.8)$$

where n is the loading, T is the temperature, P is the pressure, q_s is the saturation capacity, K is the adsorption equilibrium constant, α_i are probability factors, ε_i is the adsorption energy site with maximum frequency, m_i is the surface heterogeneity, and R is the universal gas constant. From here on, I refer to this model as the UNIV6 isotherm model.

Figure 6.4b shows the fitted results from using the isotherm data measured at all three temperatures for the fitting process, as well as using only the 15 °C and 25 °C isotherm data to obtain the fitting parameters. The first method provides a relatively good fit for the experimental data at all

three temperatures, although the presence of the third adsorption step for 15 °C and 25 °C is not captured. The latter procedure provides an excellent fit of the experimental data at 15 and 25 °C, but underestimates the loading at 35 °C. This is not unexpected given that the 35 °C loading data did not overlap with the 15 °C and 25 °C data when plotted against the relative humidity and adsorption potential as discussed previously. Overall, the fitting parameters obtained using all three temperatures would be more representative of the experimental data for process modelling, and these are reported in Table 6.1 along with their corresponding uncertainty bounds. The lower and upper bounds applied on each parameter during the fitting process are summarized in Table A4.4. The fitting parameters and corresponding uncertainty bounds obtained using only the 15 °C and 25 °C isotherm data are presented in Table A4.5, along with the lower and upper bounds applied on each parameter during the fitting process.

6.2.2.4 Heats of adsorption

I calculated the CO_2, N_2, and H_2O heats of adsorption as a function of loading (i.e. isosteric heat of adsorption), as well as the limiting heats of adsorption (Figure 6.5), for TIFSIX-3-Ni. These parameters are necessary inputs in process models and relate to the energy required for adsorbate desorption in a DAC process, where a higher heat of adsorption means higher desorption energy needed. Confidence intervals linked to the isosteric heats of adsorption calculations are presented in Figure A4.9, along with results determined using an alternative set of isotherm temperatures for CO_2. The smoothing parameter values used for each gas are presented in Table A4.6. The intermediate calculation steps for the limiting heats of adsorption are presented in Figures A4.10 to A4.12.

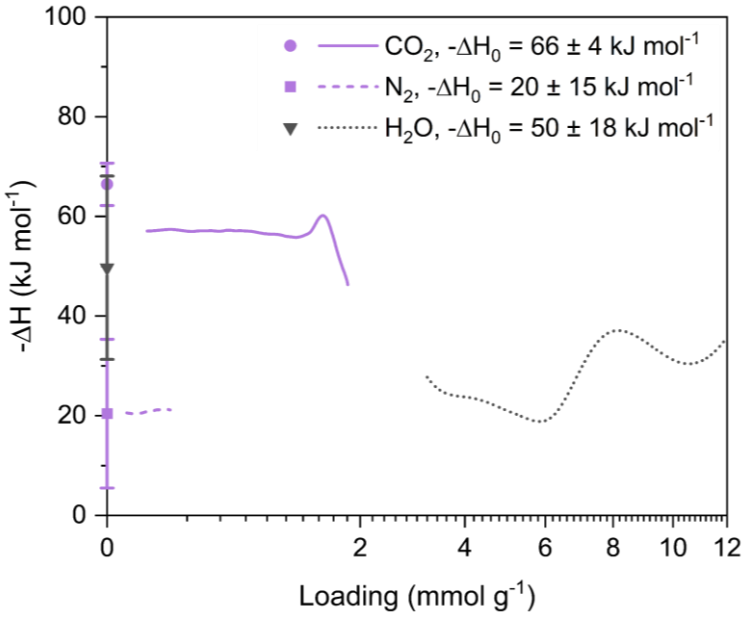


Figure 6.5. CO_2, N_2, and H_2O isosteric (lines) and limiting (symbols) heats of adsorption for TIFSIX-3-Ni with the loading plotted on square root scale for clarity.

The CO_2 isosteric heat of adsorption presented in Figure 6.5 is based on the 60 °C, 70 °C, 80 °C, and 120 °C CO_2 isotherm data, as calculations done with the 15 °C, 25 °C, and 35 °C isotherms resulted in large uncertainty bounds at loading levels above ~ 1.7 mmol g^{-1}, corresponding with the convergence of the isotherms. At the loading level corresponding to 0.4 mbar CO_2, TIFISX-3-Ni has a heat of adsorption of ~ 56 kJ mol^{-1}, which agrees well with the values previously reported in the literature [107, 128]. This is also significantly lower than the CO_2 heat of adsorption at the same loading of Lewatit VP OC 1065 (81 kJ mol^{-1}) [1]. The heat of adsorption stays relatively constant up to a loading of approximately 1.5 mmol g^{-1}, indicating the presence of homogenous CO_2 binding sites, i.e. the cavity of each cage. Beyond this loading, the heat of adsorption begins to decrease, which corresponds with the convergence of the isotherms at higher loadings observed in Figure 6.2. This suggests the presence of additional CO_2 binding sites of lower energy and correlates with the need to use the DSL model to fit the CO_2 experimental isotherm data instead of the SSL model. As discussed previously, these additional binding sites could be due to defects, the presence of oxides of Ni and/or Ti, and/or flexibility of the crystal structure.

For N_2, TIFSIX-3-Ni exhibits a low and constant heat of adsorption of ~ 20 kJ mol^{-1}, where the latter indicates homogenous interaction with the adsorbent. This was also observed for Lewatit VP OC 1065 [1]. For H_2O, I determined the limiting heat of adsorption to be 50 kJ mol^{-1}, but was unable to calculate the subsequent isosteric heat of adsorption between 0 mmol g^{-1} and 3 mmol g^{-1} due to the lack of experimental data in this range. Between 3 mmol g^{-1} and 6 mmol g^{-1} the heat of adsorption averages between 20 kJ mol^{-1} to 25 kJ mol^{-1}, after which it increases to between 30 kJ mol^{-1} to 40 kJ mol^{-1}. This increase in heat of adsorption corresponds with the loading level at which we observe the first step in the experimental H_2O isotherm data at all temperatures. I note however that there is a large uncertainty range in the calculated isosteric heat of adsorption for H_2O (Figure A4.9), likely associated with the previously discussed discrepancy between the 35 °C isotherm and the 15 °C and 25 °C isotherms.

6.2.3 Manufacturing considerations

The ability to manufacture consistent batches of TIFSIX-3-Ni, both as powder and in shaped form should be investigated to understand the deployment potential of this MOF.

6.2.3.1 Batch reproducibility

Lack of batch-to-batch conformity in TIFSIX-3-Ni will impact its materials and adsorption properties and thereby process performance metrics. To investigate this, we synthesised various batches of $NiTiF_6$, TIFSIX-3-Ni precursor, and final TIFSIX-3-Ni powder at various times, scales, and using separate researchers. These details are summarised below in Table 6.2.

Table 6.2. Summary of the synthesis procedure for different batches of TIFSIX-3-Ni.

$NiTiF_6$ batch	**TIFSIX-3-Ni precursor batch**	**TIFSIX-3-Ni batch**	**TIFISX-3-Ni synthesis scale**	**Synthesising researcher (all)**	**Synthesis date ($NiTiF_6$ / TIFSIX-3-Ni)**
A	1	1	1 ×	MYL	01/09/21 / 13/09/21
B	2	2	1 ×	DD	02/12/21 / 10/12/21
C	3	3	1 ×	MYL	02/12/21 / 10/12/21
A	4	4	4 ×	MYL	01/09/21 / 10/12/21
C	5	5	4 ×	MYL	02/12/21 / 04/05/22

The XRD patterns of $NiTiF_6$, TIFSIX-3-Ni precursor, and final TIFSIX-3-Ni samples are shown in Figure 6.6. The same peaks are present and are not shifted between the different batches of each material, indicating good reproducibility of the crystal structure. I do note however the presence of an extra peak at 17° in batches 2 and 3 of TIFSIX-3-Ni, which might be associated to incomplete conversion of the precursor to the final TIFSIX-3-Ni product.

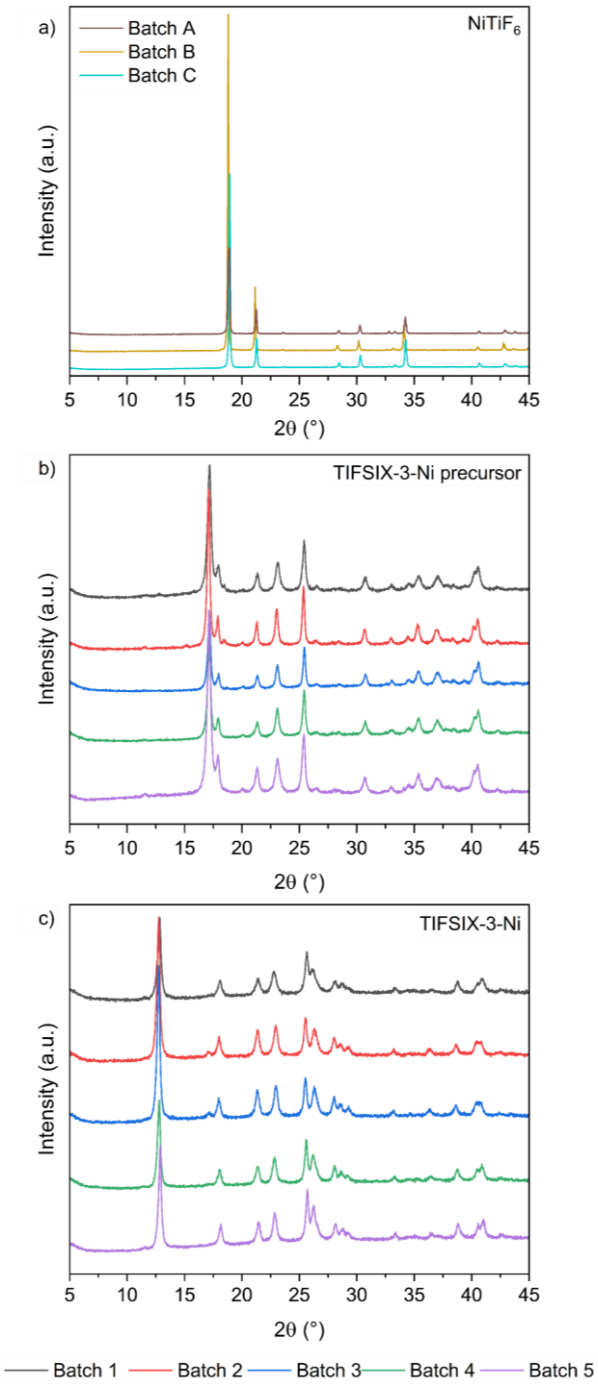


Figure 6.6. XRD patterns of synthesised batches of a) $NiTiF_6$, b) TIFSIX-3-Ni precursor, and c) final TIFSIX-3-Ni.

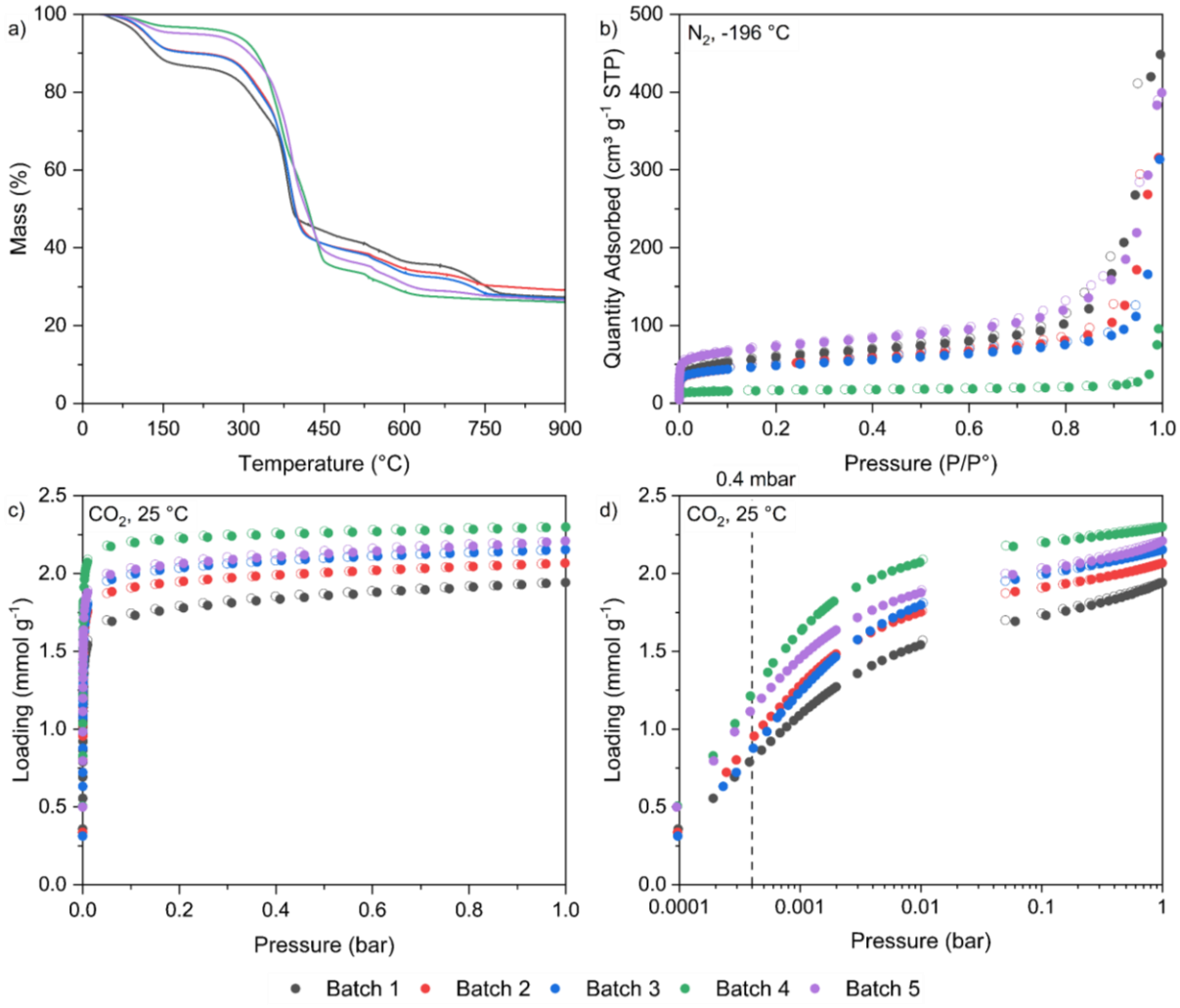


Figure 6.7. a) TG curves under N_2 air atmosphere up to 900 °C, b) N_2 adsorption isotherms at -196 °C, and CO_2 adsorption isotherms at 25 °C with c) linear and d) log-scale of pressure (filled symbols are adsorption; open symbols are desorption) for different batches of TIFSIX-3-Ni.

The N_2 adsorption data at -196 °C are shown in Figure 6.7b, with log-log scales of pressure and loading shown in Figure A4.13a, from which I determined the BET areas, micropore volumes, and total pore volumes. I observed significant variation in these parameters (> 70%) as shown below in Table 6.3. The CO_2 adsorption at 25 °C results are shown in Figure 6.7c and 6.7d and summarised in Table 6.3. Here, there is a 35% variation between the highest and lowest values of CO_2 adsorption at 0.4 mbar. There does not seem to be a correlation between the textural properties of the samples and the CO_2 adsorption, as the batch with the lowest BET area, micropore volume, and total pore volume has the highest CO_2 adsorption (batch 4), and the batch with the highest BET area, micropore volume, and total

pore volume has the second highest CO_2 adsorption (batch 5). This suggests that N_2 and CO_2 have different mechanisms to access the pore structure.

Table 6.3. Summary of the textural properties derived from N_2 adsorption at -196 °C, and CO_2 adsorption at 0.4 mbar and 25 °C for different batches of TIFSIX-3-Ni.

TIFSIX-3-Ni batch	S_{BET} ($m^2\ g^{-1}$)	$V_{micropores}$ ($cm^3\ g^{-1}$)	$V_{total\ pores}$ ($cm^3\ g^{-1}$)	CO_2 uptake @ 0.4 mbar, 25 °C (mmol g^{-1})
1	213	0.11	0.65	0.79
2	175	0.08	0.42	0.96
3	175	0.08	0.26	0.88
4	62	0.03	0.06	1.21
5	264	0.11	0.50	1.11

Overall, it appears that the crystal structure and thermal stability are reproducible between different batches of TIFSIX-3-Ni despite different researchers, times of synthesis, and scale, however there is wide variation in the textural properties and CO_2 adsorption, which may be linked to the presence of impurities/defects as highlighted earlier. All the physicochemical and equilibrium adsorption properties discussed in previous sections were measured using batch 5 TIFSIX-3-Ni with the results shown in purple, except for the H_2O adsorption isotherms which were measured with batch 1 TIFSIX-3-Ni and these results are shown in grey.

6.2.3.2 Pelletisation

TIFSIX-3-Ni is synthesised as a powder, however, adsorbents in this form would not be practical in an actual process as they would be difficult to handle, and their dense packing would result in high pressure drop and poor heat and mass transfer. The ability to shape TIFSIX-3-Ni powder into a structured form such as pellets without significantly affecting its performance for DAC is therefore another important factor to investigate.

I pelletised TIFSIX-3-Ni powder (batch 5) without any binders by applying a pressure equivalent to ~ 37 MPa. This pressure is well below the compression pressure of 340 MPa previously reported to induce irreversible amorphisation on ZIF-8 [260]. A study by Ribeiro et al. also demonstrated that compression

pressures of 62 and 125 MPa still allowed the crystallinity of ZIF-8 and MIL-53(Al) to be maintained, though reductions in the textural properties of ~ 10% and ~ 30% to 40%, respectively, were observed [261].

The XRD patterns of the as-synthesised TIFSIX-3-Ni powder, intermediate ground powder, and final pellet are shown in Figure 6.8a. Overall, the crystallinity of TIFSIX-3-Ni appears to be maintained in pellet form. Yet, most peaks are very slightly left-shifted in the ground powder and pellet sample compared to the original powder. There is also an additional peak that appears in the ground powder sample at 32 °, which is then left-shifted in the pellet sample. This could be due to cross-contamination of the sample during grinding if the marble pestle and mortar used was not properly cleaned

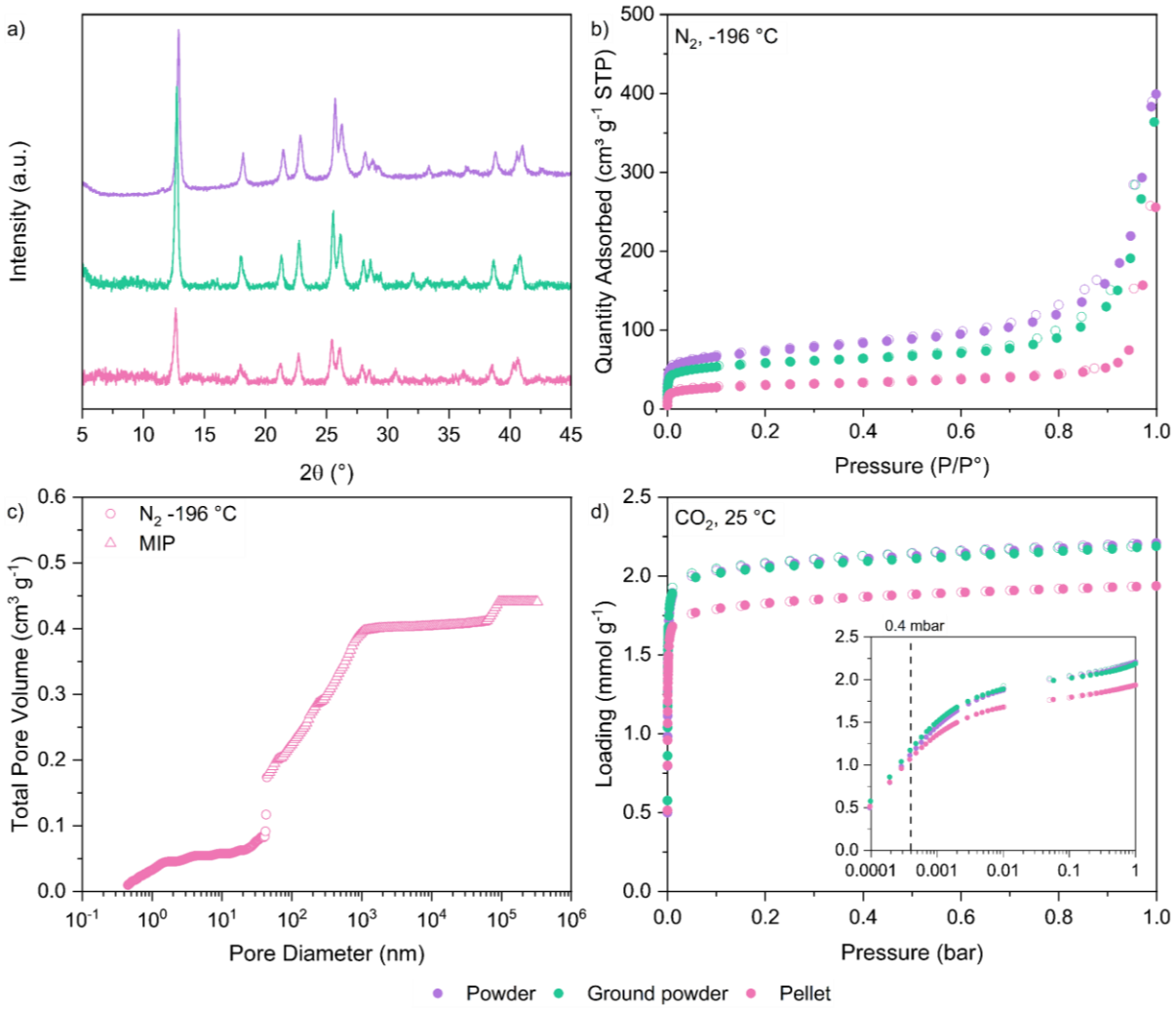


Figure 6.8. a) XRD patterns and b) N_2 adsorption (filled symbols) and desorption (open symbols) isotherms at -196 °C of batch 5 TIFSIX-3-Ni powder, ground powder, and pellet. c) Cumulative pore volume as a function of pore diameter of TIFSIX-3-Ni pellet, obtained from N_2 adsorption at -196 °C (circles) and mercury intrusion porosimetry (triangles). d) CO_2 adsorption (filled symbols) and desorption (open symbols) isotherms at 25 °C for batch 5 TIFSIX-3-Ni powder, ground powder, and pellet, with log-scale of pressure shown in the inset.

The N_2 adsorption data at -196 °C are reported in Figure 6.8b, with log-log scales of pressure and loading shown in Figure A4.13b, from which I determined the textural parameters. Grinding of TIFSIX-3-Ni powder resulted in a 20% decrease in the BET area, micropore volume, and total pore volume of the sample, while pelletisation resulted in a further 30% to 40% decrease for all three parameters, with final values of 106 $m^2\ g^{-1}$, 0.06 $cm^3\ g^{-1}$, and 0.24 $cm^3\ g^{-1}$, respectively. For pelletised

samples, macropores contribute significantly to the total pore volume. To account for this, I estimated the total pore volume of the pelletised sample through a combination of N_2 adsorption and MIP measurements as previously done in our group [48] (Figure 6.8c), yielding a total pore volume of 0.44 $cm^3\ g^{-1}$. The MIP measurement also provided me with the pellet density, determined to be 0.81 g cm^{-3}. This value is similar to the pellet density of 0.85 g cm^{-3} reported for a binder-free zeolite 13X pellet [48]. Using these values, I then calculated the bed density, skeletal density, and porosity of the pellet sample, all necessary inputs in process models. These values, along with the textural properties of the as-synthesised powder and ground powder samples, are summarised below in Table 6.4.

Table 6.4. Summary of textural properties and densities of TIFSIX-3-Ni powder, ground powder, and pellet (batch 5), as derived from N_2 adsorption at -196 °C and MIP measurements.

TIFSIX-3-Ni (batch 5)	**S_{BET} ($m^2\ g^{-1}$)**	**$V_{micropores}$ ($cm^3\ g^{-1}$)**	**$V_{total\ pores}$ ($cm^3\ g^{-1}$)**	**$\rho_{skeletal}$ (g cm^{-3})**	**ρ_{pellet} (g cm^{-3})**	**ρ_{bed} (g cm^{-3})**	**ε_{pellet}**
Powder	264	0.11	0.50	-	-	-	-
Ground powder	213	0.09	0.41	-	-	-	-
Pellet	106	0.06	0.44	1.26	0.81	0.58	0.36

For further analysis, I measured CO_2 adsorption at 0 °C for all three samples to see if this could facilitate access to the ultramicropores of TIFSIX-3-Ni, as N_2 at -196 °C may be kinetically restricted when trying to enter these pores [262]. The measured isotherms are shown in Figure A4.14, and the calculated textural properties are summarised and compared with that of N_2 adsorption at -196 °C in Table A4.7. From the results, CO_2 can access the same amount of micropores in all three samples at 0 °C, while N_2 at -196 °C appears to be more restricted in accessing some of the pores in the pellet sample. Pelletisation may have compressed the sample's crystal structure and reduced the pore size to an extent which further hindered N_2 access, but left CO_2 unaffected. As a result, the BET area determined from N_2 adsorption decreases from powder to ground powder to pellet, while the BET area determined from CO_2 adsorption stays relatively constant for all three samples. However, due to the inability of CO_2 at 0 °C to probe the larger pores, and the lack of suitable DFT models to calculate the pore size distribution

and thus total pore volume, I continue to use N_2 adsorption at -196 °C to assess the textural properties of TIFSIX-3-Ni throughout this study.

I observed an unusual hysteresis (as well as the beginning of an inflection point) in the CO_2 0 °C isotherm in Figure A4.14 for the pellet sample, which might indicate flexibility in the crystal structure. Other observations discussed previously such as the unusual trend of the specific heat capacity and the behaviours of the CO_2 and H_2O isotherms also suggested possible flexibility in the crystal structure. The pyrazine linkers in TIFSIX-3-Ni are only coordinated at one point on each pole, which would allow a rotational degree of freedom. This was indeed recently reported for SIFSIX-3-Ni [258], and also previously observed for ZIFs-7, -8, -11, -65, -71, and -90 [255, 263-266].

I tested this hypothesis by performing in-situ XRD measurements of both powder and pellet samples of TIFSIX-3-Ni under ambient air, then under a flow of N_2 at room temperature and 160 °C, and then under a flow of CO_2 at room temperature to observe how the samples might change at different stages of a DAC process. Figures A4.15a and A4.15b reveal peak shifts and new peaks under the different conditions, as well as differences between the powder and pellet sample that were not present in Figure 6.8a, that could further suggest flexibility or change in the TIFSIX-3-Ni crystal structure. However, a dedicated investigation involving further measurements at higher pressures or lower temperatures, as well as structure refinement is needed to draw any quantitative conclusions.

Finally, to assess the impact of pelletisation on the CO_2 adsorption performance of TIFSIX-3-Ni, I measured CO_2 adsorption isotherms at 25 °C up to 1 bar, shown in Figure 6.8d. The results show that grinding has minimal impact on the CO_2 adsorption of the sample across the whole pressure range. Pelletisation causes a ~ 10% decrease in the CO_2 adsorption capacity at 1 bar compared to the powder, but there is minimal difference at 0.4 mbar (Figure 6.8d inset). Therefore, while pelletisation seems to have restricted N_2 access (at least at -196 °C) within the crystal structure, it has not negatively impacted CO_2 access at the relevant DAC conditions. Pelletised TIFSIX-3-Ni may therefore have higher CO_2/N_2 selectivity when compared to its powder form. With a bed density of 0.58 g cm^{-3} and gravimetric CO_2 adsorption capacity of 1.07 mmol g^{-1} at 0.4 mbar and 25 °C, the volumetric CO_2 adsorption capacity of pelletised TIFSIX-3-Ni is 0.62 mmol cm^{-3}_{bed} at these conditions. This is higher than the volumetric CO_2 adsorption capacity of 0.45 mmol cm^{-3}_{bed} previously reported for Lewatit VP OC 1065 [1].

6.2.4 Adsorbent stability under process conditions

Although not a direct input for process modelling, the lifetime of an adsorbent based on its rate of degradation when subjected to various process conditions, will greatly influence the cost and carbon footprint associated with adsorbent production and disposal [169]. Factors that could potentially impact the adsorbent include exposure to humidity, at both ambient and elevated temperatures, and exposure to multiple adsorption-desorption cycles.

6.2.4.1 Humidity studies

Exposure to H_2O only

To understand the stability of TIFSIX-3-Ni to humidity alone without the presence of oxygen, samples of batch 5 TIFSIX-3-Ni powder were used to measure H_2O isotherms at 25 °C, up to 15% RH, 48% RH, and 77% RH, where the latter is the highest relative humidity the Micromeritics 3Flex porosity analyser can achieve at this temperature (Figure 6.9). These humidity levels correspond to the different steps observed in the H_2O isotherms from Figure 6.4 (obtained with batch 1 TIFSIX-3-Ni), where 15% RH would be before the first isotherm step, 48% RH would be between the first and second isotherm step, and 77% RH would be the complete isotherm (after the second step). However, when I measured the H_2O isotherms described above with batch 5 TIFSIX-3-Ni, I only observed one distinct step in the isotherm and achieved slightly lower loading compared to batch 1, both similar to that reported by Mukherjee et al. [128]. This observation indicates that the H_2O adsorption can vary between different synthesised batches of TIFSIX-3-Ni, as was also observed with the N_2 and CO_2 adsorption in Section 6.2.3.1. I note again the presence of an irreversible hysteresis in these isotherms. The hysteresis is much more severe when the RH level is beyond that where we observe the first isotherm step, suggesting that above a certain RH level, the MOF may irreversibly react with water.

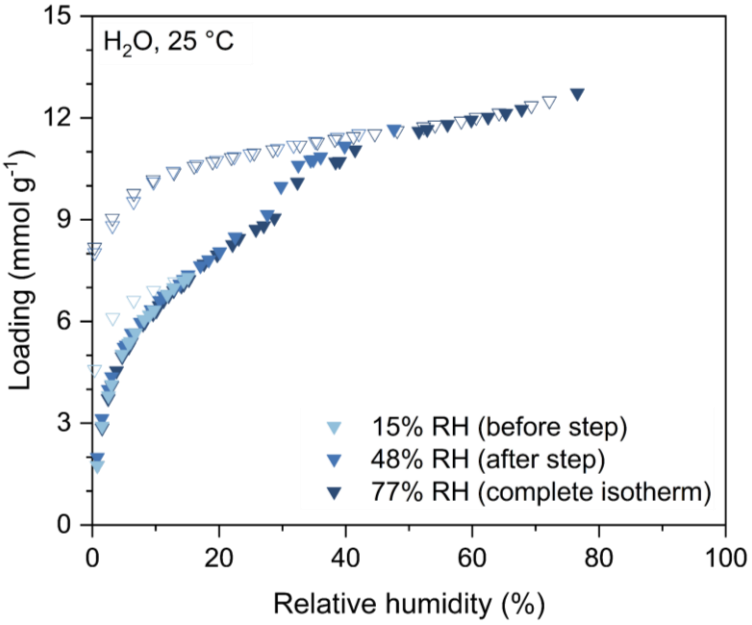


Figure 6.9. Equilibrium adsorption (filled symbols) and desorption (open symbols) isotherms for H_2O measured at 25 °C for batch 5 TIFSIX-3-Ni powder up to 15% RH, 48% RH, and 77% RH.

I then characterised the samples' crystallinity, textural properties, and CO_2 adsorption and compared them to that of the as-synthesised sample, as shown in Figure 6.10. I measured XRD patterns of the samples immediately after the H_2O isotherm measurements, i.e. when there should still be adsorbed water in the sample, and after the same samples were degassed. I then measured N_2 adsorption isotherms at -196 °C and CO_2 adsorption isotherms at 25 °C on these degassed samples. Figure 6.10a reports the changes in the XRD pattern of all three samples before degassing compared to the as-synthesised sample. These include a left shift in most peaks such as those originally at 12 ° and 26 °, the presence of additional peaks in the 15 ° to 20 ° range, and the disappearance of peaks in the 37 ° to 40 ° range. These changes are more prominent in the 48% RH and 77% RH samples, i.e. after the step in the H_2O isotherm has occurred. After degassing of the samples, their XRD patterns are very similar to that of the as-synthesised sample, with all the original peaks still present, though some are now slightly left-shifted. I also observed a slight colour change in the 48% RH and 77% RH samples as shown in Table A4.8, while the colour of the 15% RH sample is very similar to that of the as-synthesised sample. Overall, there appears to be minimal change in the crystal structure of TIFSIX-3-Ni after exposure to H_2O under these conditions and subsequent degassing.

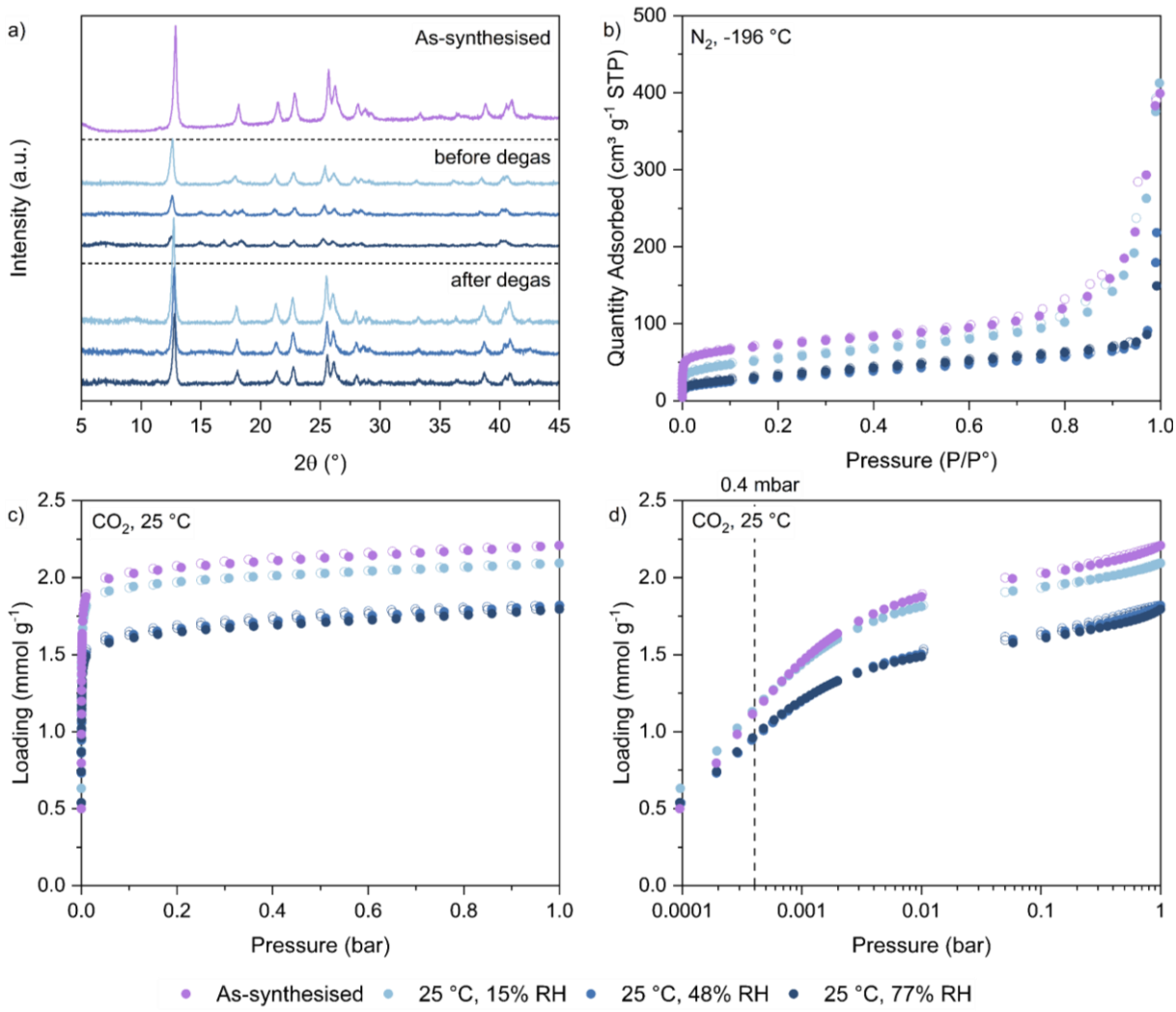


Figure 6.10. a) XRD patterns, b) N_2 adsorption isotherms at -196 °C, and CO_2 adsorption isotherms at 25 °C with c) linear and d) log-scale of pressure (filled symbols are adsorption; open symbols are desorption) for batch 5 TIFSIX-3-Ni powder before (purple) and after exposure to 15% RH (light navy), 48% RH (medium navy), and 77% RH of H_2O (dark navy).

I also performed XPS analysis on the degassed 77% RH sample. Compared to the as-synthesised sample, there appears to be a slight increase in the oxygen content in the sample (Table A4.9), and deconvolution of the O 1*s* and Ti 2*p* core level suggests an increased presence of oxides of Ti (e.g. TiO_2/$TiOF_2$) [257] (Figure A4.16). No distinct changes were observed for the C 1*s,* N 1*s*, F 1*s*, and Ni 2*p* spectra.

The N_2 adsorption data at -196 °C are shown in Figure 6.10b and Figure A4.17a, from which I determined the textural parameters summarised in Table 6.5. After exposure to 15% RH, i.e. before the

first step in the H_2O isotherm, TIFSIX-3-Ni experiences a 20% to 30% reduction in its textural properties. After exposure to 48% RH and 77% RH, i.e. after the step in the H_2O isotherm, there is a more significant reduction in the BET area and micropore volume of the samples of ~ 60%, and a 75% loss in total pore volume. Hence, despite the XRD patterns suggesting a "recovery" of the initial crystallinity, it seems that while part of the crystalline structure is maintained/recovered after exposure to water beyond the H_2O isotherm step, another part is lost and leads to a reduced porosity.

Table 6.5. Summary of the textural properties derived from N_2 adsorption at -196 °C and CO_2 adsorption at 0.4 mbar and 25 °C for TIFSIX-3-Ni samples exposed to various stability studies.

Study	Sample	Condition	S_{BET} ($m^2\ g^{-1}$)	$V_{micropores}$ ($cm^3\ g^{-1}$)	$V_{total\ pores}$ ($cm^3\ g^{-1}$)	CO_2 uptake @ 0.4 mbar, 25 °C (mmol g^{-1})
H_2O exposure	TIFSIX-3-Ni batch 5, powder	As-synthesised	264	0.11	0.50	1.11
		15% RH	196	0.08	0.41	1.13
		48% RH	109	0.05	0.14	0.94
		77% RH	120	0.05	0.13	0.96
H_2O and O_2 exposure	TIFSIX-3-Ni batch 3, powder	As-synthesised	175	0.08	0.26	0.88
		40 °C, 75% RH air, 14 days	36	0.02	0.05	0.51
		40 °C, 90% RH air, 14 days	49	0.02	0.05	0.47
		Ambient air, 6 months	40	0.02	0.05	0.39
Adsorption cycling	TIFSIX-3-Ni batch 5, pellet	As-synthesised	147	0.07	0.34	0.94
		Post-cyclic	82	0.04	0.11	0.44

Lastly, from the CO_2 isotherms shown in Figures 6.10c and 6.10d, I observe reductions in the CO_2 adsorption capacity at 1 bar for all three samples, which follows the reduction in porosity. After exposure to 15% RH, the CO_2 adsorption capacity decreased by ~ 5% at 1 bar. After exposure to 48% RH and 77% RH, the CO_2 adsorption capacity decreased by ~ 20% at 1 bar. The CO_2 loading at 0.4 mbar is summarised below in Table 6.5, where, despite the changes in the textural properties, I observe

no significant decrease in the CO_2 adsorption performance after exposure to 15% RH, and a 15% decrease after exposure to 48% RH and 77% RH. Mukherjee et al. reported a much more severe reduction in CO_2 saturation capacity of ~ 60% from their dynamic column breakthrough tests at 25 °C under a flow of 3000 ppm CO_2 and 74% RH [128]. Ullah et al. reported a similar decrease in CO_2 adsorption of ~ 70% after temperature-programmed desorption (TPD) experiments conducted at 25 °C with pure CO_2 and 75% RH [247]. For both these cases, the comparison was between the CO_2 uptake when co-adsorbed with H_2O, vs. the CO_2 uptake under a dry stream. In our experiments, we compared the single-component CO_2 adsorption of a sample before and after exposure to pure H_2O. Therefore, while our experiments suggest that the CO_2 adsorption performance of TIFSIX-3-Ni is recoverable after exposure to humidity at ambient temperatures, results in the literature suggest that the CO_2 adsorption will be more severely limited when co-adsorbed with H_2O at similar conditions. In addition, since there is already a ~ 15% decrease in CO_2 adsorption capacity at 0.4 mbar for the samples exposed to 48% RH and 77% RH at 25 °C, it is unlikely that TIFSIX-3-Ni would be able to withstand a steam desorption process.

Exposure to H_2O and O_2

To assess the stability of the adsorbent under humid air, TIFSIX-3-Ni powder (batch 3) was exposed to air environments of 40 °C and either 75% RH or 90% RH for 14 days, or to an ambient air environment for 6 months. I then characterised the samples' crystallinity, textural properties, and CO_2 adsorption and compared them to that of the as-synthesised sample, as shown in Figure 6.11. I measured XRD patterns of the samples immediately after their humidity treatment, i.e. when there should still be adsorbed water in the sample, and after the same samples were degassed. I then measured N_2 adsorption isotherms at -196 °C and CO_2 adsorption isotherms at 25 °C on these degassed samples.

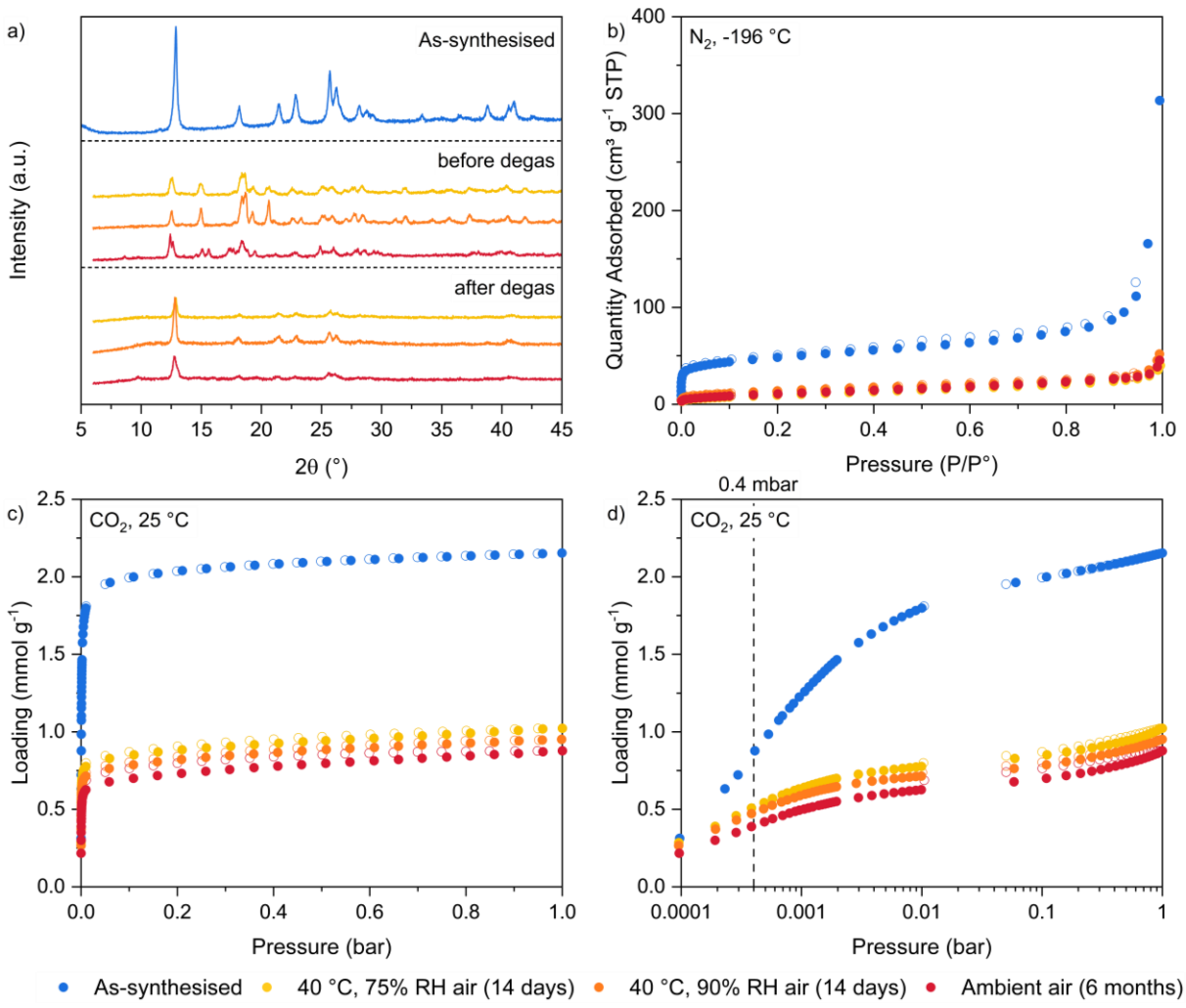


Figure 6.11. a) XRD patterns, b) N_2 adsorption isotherms at -196 °C, and CO_2 adsorption isotherms at 25 °C with c) linear and d) log-scale of pressure (filled symbols are adsorption; open symbols are desorption) for batch 3 TIFSIX-3-Ni powder before (blue) and after exposure to 40 °C and 75% RH air for 14 days (yellow), 40 °C and 90% RH air for 14 days (orange), and ambient air for 6 months (red).

From Figure 6.11a, I see distinct changes in the XRD pattern of all three samples, both before and after degassing, compared to the as-synthesised sample. These changes are different than those I previously observed for the transition of the TIFSIX-3-Ni precursor to final TIFSIX-3-Ni powder (Figure 6.6). For the "before degas" samples, there are very noticeable changes including a left shift in many of the prominent peaks, such as those originally at 12 ° and 26 °, the presence of additional peaks in the 15 ° to 20 ° range, and the disappearance of peaks in the 37 ° to 40 ° range. These changes in the XRD pattern suggest that water and/or oxygen is interacting with and perhaps inserting itself within the

crystal structure of TIFSIX-3-Ni. Indeed, Barsoum et al. studied the structural changes in SIFSIX-3-Ni after exposure to 70 °C and 80% RH for 4 days, and reported that H_2O was hydrogen bonding to SiF_6^{2-} and forming coordination bonds with the Ni sites [258]. After these samples are degassed, the XRD patterns are more comparable to the as-synthesised sample, however some crystallinity has been lost. Key changes include the broadening of remaining peaks, and the disappearance of peaks after ~ 30 °. The observed changes in the XRD pattern for the "after degas" sample exposed to 40 °C and 75% RH correspond well with those by Kumar et al. [107], who had subjected TIFSIX-3-Ni sample to 40 °C and 75% RH for 1, 7, and 14 days.

Along with these structural changes, I observed colour changes in the samples after degassing under vacuum at 160 °C as shown in Table A4.10, where the new colour is somewhat reminiscent to that of $NiTiF_6$ (Figure A4.2), further suggesting a change in the crystal structure/coordination. To understand this observation better, I performed XPS analysis on the sample exposed to ambient air for 6 months after it had been degassed. Compared to the as-synthesised sample, the oxygen content has almost doubled (Table A4.9), and there are noticeable shifts in the O 1*s* and Ti 2*p* core levels that may correspond to an increased presence of oxides of Ti (e.g. TiO_2/$TiOF_2$) (Figure A4.16). No distinct changes were observed for the C 1*s*, N 1*s*, F 1*s*, and Ni 2*p* spectra.

The N_2 adsorption isotherms shown in Figure 6.11b and Figure A4.17b, indicate a severe decrease in porosity of all three samples compared to the as-synthesised sample, with a 70% to 80% decrease in BET areas, micropore volumes, and total pore volumes for all three samples (Table 6.5). Lastly, the CO_2 isotherms shown in Figures 6.11c and 6.11d highlight significant reductions in the CO_2 adsorption capacity at both 0.4 mbar and 1 bar for all three samples. At 0.4 mbar, I observe a 40% to 55% reduction in the CO_2 uptake after exposure to all three conditions, with exposure to ambient air for 6 months having the most significant impact (Table 6.5). My observations are not in alignment with the findings from Kumar et al. [107], who observed "negligible loss in terms of CO_2 adsorption performance" after 14 days at 40 °C and 75% RH. However, Barsoum et al. also observed a drastic reduction in the CO_2 uptake of SIFSIX-3-Ni after exposure to 70 °C and 80% RH, and suggested that SiF_6^{2-} units were being displaced into the pores of SIFSIX-3-Ni which blocked the CO_2 binding sites [258].

Overall, my findings indicate that TIFSIX-3-Ni would not be suitable for DAC processes implemented in tropical climates with warm temperatures and high humidity. Furthermore, TIFSIX-3-Ni would likely need to be replaced in a process at a minimum of once every 6 months, as exposure to ambient air for this period already results in more than a 50% decrease in CO_2 adsorption capacity of the sample. In comparison, the lifetime of adsorbents currently used for other industrial separation processes, e.g. zeolites, silicas, and activated carbons, is 5 to 10 years [267]. However, given the differences in findings between my work and Kumar et al. [107], it is evident that further work is required to investigate the performance of TIFSIX-3-Ni in humid air, particularly around the interaction of water with the crystal structure of TIFSIX-3-Ni and its subsequent impacts.

6.2.4.2 Cyclic studies

During a DAC process, an adsorbent will likely be subjected to multiple cycles of adsorption at ambient temperatures and desorption at elevated temperatures. The longer an adsorbent can maintain its CO_2 adsorption performance under these conditions, the less frequently it will need to be replaced, leading to lower operation costs. Various desorption methods are currently considered for DAC, such as temperature swing, steam-assisted temperature swing, and temperature vacuum swing. Here, I investigated the stability of TIFSIX-3-Ni pellets (batch 5) under multiple cycles of a temperature swing adsorption process using ambient air. After an initial in-situ activation of the sample at 160 °C under a flow of ambient air to remove any pre-adsorbed gases, TIFSIX-3-Ni was subjected to 50 cycles of adsorption at 30 °C for 1 h and desorption at 160 °C for 15 min under a flow of ambient air with varying humidity (Figure 6.12a) using a thermogravimetric analyser. Including the time needed to increase or decrease the temperature between 30 and 160 °C, the total time per cycle was 127 min. I chose 30 °C for the adsorption temperature as this was the minimum temperature which could be accurately maintained by the instrument. I chose 160 °C for the desorption temperature as this was the temperature used by Kumar et al. [107] to degas the adsorbent, and which I have subsequently applied for all my measurements thus far. I chose 1 h and 15 min for our adsorption and desorption times respectively, not including the time needed to reach the set temperatures, as the majority of adsorption (~ 72%) and

desorption (~ 89%) could be achieved within this time based on the "long cycle" measurement shown in Figure A4.18 where saturation of the sample was achieved.

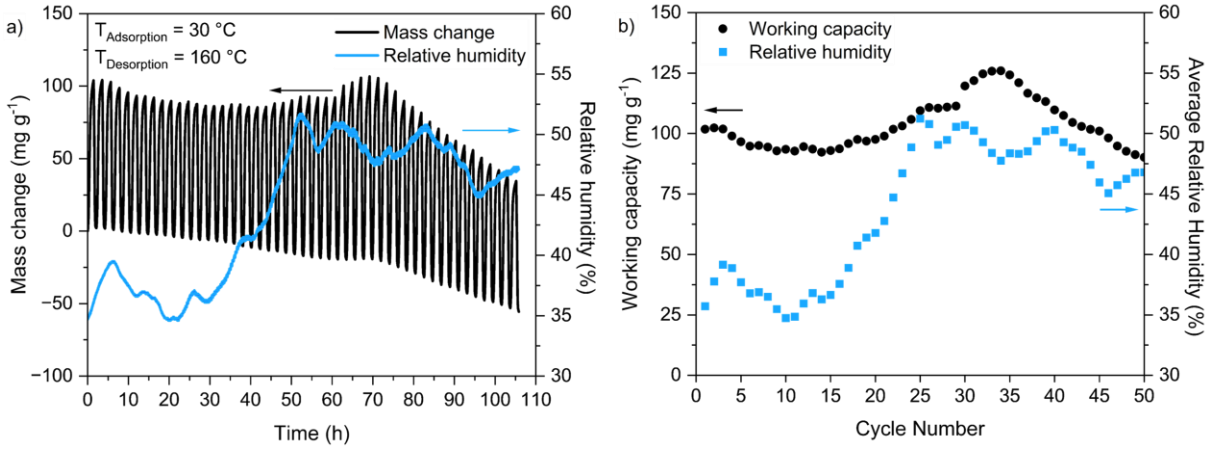


Figure 6.12. a) Mass change of TIFSIX-3-Ni pellet (batch 5) per gram of activated sample (i.e. sample mass just before the first cycle) over 50 adsorption-desorption cycles under a flow of ambient air with varying relative humidity. b) Working capacity of the activated sample (i.e. sample mass just before the first cycle) and average relative humidity of the ambient air over 50 cycles.

The resulting working capacity of each cycle was calculated as shown in Figure 6.12b, along with the average relative humidity during each cycle. Since there was not a gas analyser connected to the TGA to isolate the amount of CO_2 adsorbed, I can only report the working capacity as an adsorbed mass per gram of activated sample. Over the first 15 cycles, there is a ~ 10% decrease in the adsorbent's working capacity. Then, over the next 20 cycles, there is a ~ 40% increase in the working capacity. This increase correlates with the increasing relative humidity over these cycles, which would result in higher H_2O adsorption and overall mass uptake by the sample. For the remaining 15 cycles, the relative humidity stays constant, but there is a ~ 30% decrease in the working capacity. I link this change in the working capacity to the degradation of the sample. Indeed, when another "long cycle" was repeated on the same sample after cyclic testing, I observed a 36% decrease in its adsorption capacity under ambient air (Figure A4.19). In addition, the actual mass of the sample seems to be steadily decreasing overtime as seen in Figure 6.12a. This could be due to the continued removal of strongly adsorbed moisture, or more likely is another sign of degradation of the sample.

My observations contrast with those reported by CSIRO, who observed no CO_2 capacity loss in their Airthena DAC pilot-scale demonstrator based on a TIFSIX-3-Ni composite over 2680 cycles [249]. CSIRO used similar adsorption and desorption times of 1 h and 30 min respectively, however their desorption was conducted under vacuum at 80 °C, and their air feed stream was pre-dried to ~ 3% RH at 25 °C. These differences, along with the presence of binder in the Airthena composite, could account for the enhanced stability observed by CSIRO.

I further characterised the post-cyclic sample by comparing its crystallinity, textural properties, and CO_2 adsorption to that of as-synthesised sample. From Figure 6.13a, peaks between 15 ° to 20 ° as well as after 26 ° have disappeared in the XRD pattern of post-cyclic TIFSIX-3-Ni compared to as-synthesised TIFSIX-3-Ni, indicating some loss in crystallinity. The N_2 adsorption data at -196 °C are shown in Figure 6.13b and Figure A4.17c with the textural parameters in Table 6.5. Here, I observe a ~ 40% decrease in BET area and micropore volume, and ~ 70% decrease in total pore volume. Lastly, as seen in Figure 6.13c, I observe a significant reduction in the CO_2 adsorption capacity both at 1 bar and 0.4 mbar between the two samples. After 50 adsorption-desorption cycles, TIFSIX-3-Ni has suffered a ~ 50% decrease in its CO_2 adsorption capacity at 0.4 mbar. There is also a noticeable colour change in the sample after cycling as shown in the insets in Figure 6.13c, which suggests a change in the crystal structure/coordination. Here, the sample has changed from a blue colour to a colour reminiscent of $NiTiF_6$ (Figure A4.2).

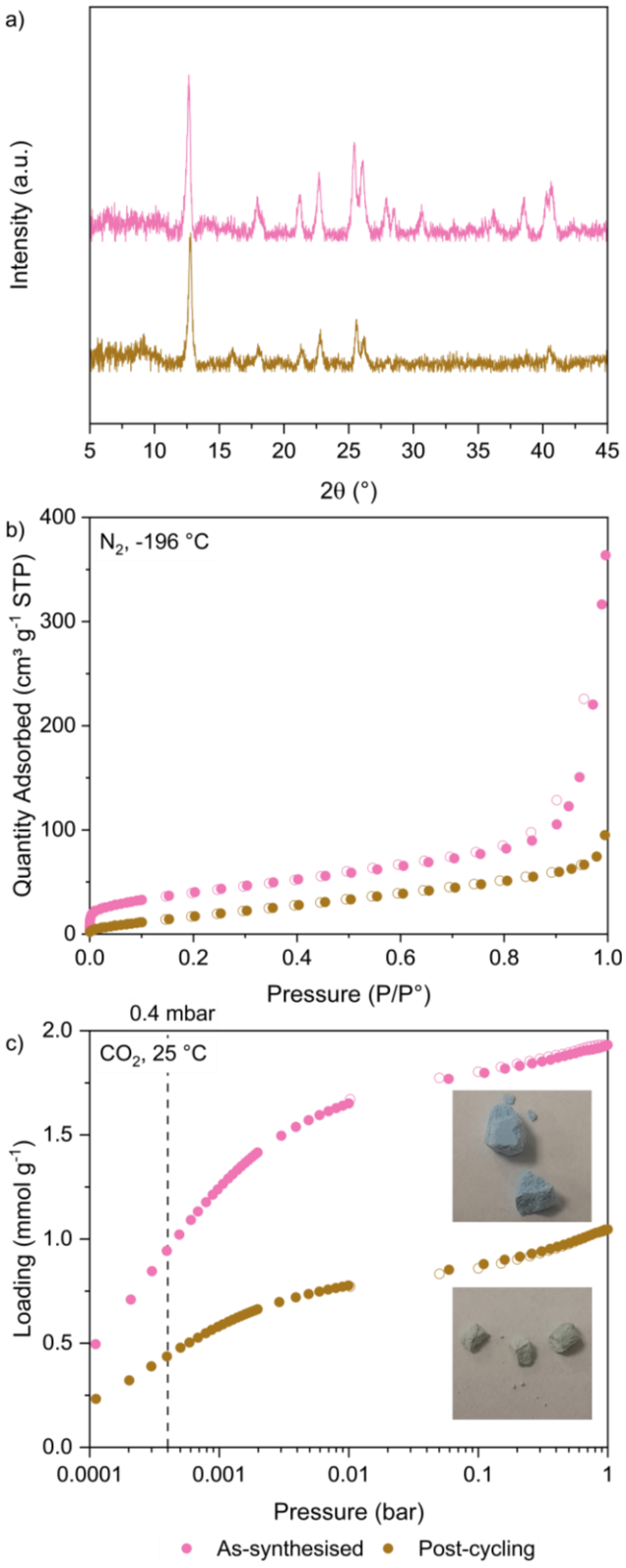


Figure 6.13. a) XRD patterns, b) N_2 adsorption isotherms at -196 °C, and c) CO_2 adsorption isotherms at 25 °C with log-scale of pressure (filled symbols are adsorption; open symbols are desorption) for batch 5 TIFSIX-3-Ni pellet before (pink) and after post-cyclic testing (bronze). Images of the sample before and after cycling are shown as insets in c).

I note that the BET area and CO_2 adsorption at 0.4 mbar of the as-synthesised pellet samples reported in Table 6.5 (147 m^2 g^{-1} and 0.94 mmol g^{-1}) are different than those previously reported in Section 6.2.3.2 (106 m^2 g^{-1} and 1.07 mmol g^{-1}). This is likely due to the difference in sample mass used for the isotherm measurements, though we attempted to reduce this error by compensating with glass beads. Remeasuring the as-synthesised sample with the same methodology also allows a relative comparison between the samples.

Overall, TIFSIX-3-Ni would need to be replaced in a process after fewer than 50 cycles under these conditions. The lifetime of TIFSIX-3-Ni could likely be extended by using a lower desorption temperature such as 100 °C, but its working capacity would be reduced. An inert gas or vacuum could also be used for desorption such as with the CSIRO process, however this would likely add extra cost to the process. The lifetime of TIFSIX-3-Ni also still would not exceed more than 6 months based on our findings in Section 6.2.4.1.

6.3 Conclusions

In this work, I aimed to thoroughly assess the potential of using TIFSIX-3-Ni as a DAC adsorbent by measuring as many of the physicochemical and equilibrium adsorption properties needed to perform process scale modelling and optimisation as possible, and investigating its shaping and stability under realistic process conditions.

I confirmed the successful synthesis of TIFSIX-3-Ni powder and reported its textural properties, thermal stability, and specific heat capacity. I also measured equilibrium adsorption isotherms of CO_2, N_2, Ar, O_2, and H_2O, and reported isotherm model fitting parameters and heats of adsorption for CO_2, N_2, and H_2O. Compared to a benchmark DAC adsorbent, Lewatit VP OC 1065, TIFSIX-3-Ni may have higher gravimetric and volumetric CO_2 adsorption capacity, but also higher N_2, Ar, O_2, and H_2O adsorption capacity. Therefore, the CO_2 selectivity of TIFSIX-3-Ni is likely lower than that of Lewatit. TIFSIX-3-Ni also has lower CO_2 heat of adsorption compared to Lewatit and comparable N_2 and H_2O heats of adsorption, suggesting lower desorption energy requirements.

I easily scaled up the synthesis procedure of TIFSIX-3-Ni powder 4-fold but observed large variations in the textural properties and CO_2 adsorption capacity between different batches. I also successfully pelletised TIFSIX-3-Ni powder with minimal loss in CO_2 adsorption at 0.4 mbar, and I reported the skeletal, pellet, and bed density, total pore volume, and pellet porosity.

When subjected to humidity, TIFSIX-3-Ni is relatively stable at mild temperatures such as 25 °C, but it suffers a reduction in crystallinity, porosity, and CO_2 adsorption at higher temperatures such as 40 °C, and there is a noticeable colour change in the material. TIFSIX-3-Ni also has a relatively short lifetime, with again noticeable colour changes and reduction in crystallinity, porosity, and CO_2 adsorption after 50 sorption cycles in ambient air, or even storage in ambient air for 6 months. Future work still needs to be done however, to gain a better fundamental understanding on the interaction of water with the crystal structure of TIFSIX-3-Ni and to further probe the possible structure flexibility under different conditions.

Overall, with this study, I hope I have provided the required data to facilitate initial process scale evaluation of TIFSIX-3-Ni for adsorption-based DAC, which can help continue the advancement and scale-up of this technology.

Chapter 7: Investigation of amine-functionalised "hydrophobic" zeolite Y adsorbents for direct air capture

7.1 Introduction

Previous chapters thus far have focused on commercially available or preliminarily tested adsorbents for DAC. In this chapter, I attempt to develop my own set of DAC adsorbents. While many novel adsorbents are currently being developed for DAC such as MOFs or mixed metal oxides, further expanding the option of easily accessible commercial adsorbents could help to scale up this technology quickly.

Zeolites are a class of adsorbents widely used in industry for applications such as catalysis, ion exchange, and gas separations. Various zeolites have now also been investigated for DAC, including X-type zeolites (Na-X i.e. 13X, 13X modified with Fe, Ca-X, Li-X) [30, 31, 71, 103, 167, 204, 268], A-type zeolites (Na-A i.e. 4A, NaCa-A i.e. 5A, and other ion-exchanged zeolites A such as K, Mg, and Ca.) [31, 71, 110, 111], Y-type zeolites (amine-functionalised NH_4-Y, Na-Y, and H-Y) [105, 114, 187, 238, 269], CHA-type zeolites (amine-functionalised SAPO-34, zinc-containing CHA, K-CHA) [105, 112, 270], MFI-type zeolites (amine-functionalised H-ZSM-5, Ba-MFI, Ca-MFI, Sr-MFI) [105, 129], mordernite-type zeolites [167], GIS-type zeolites [270], and RHO-type zeolites [271]. In fact, zeolites such as 13X and 5A have been used since the 1980s to separate CO_2 from air as a pre-treatment for air separation processes [272, 273].

However, only ~ 10% of the recent DAC adsorbent literature appears to be focused on the use of zeolites [10]. This is likely due to the hydrophilicity of most zeolites, which results in high levels of competitive H_2O adsorption and consequently significant loss in CO_2 adsorption capacity in humid gas streams. For example, the H_2O loading of zeolite 13X is 14.2 mmol g^{-1} at 58% RH and 25 °C [274], while its CO_2 loading is only 0.23 mmol g^{-1} at 0.4 mbar and 25 °C [31]. Zeolite 5A has a H_2O loading of 13.8 mmol g^{-1} at 50% RH and 25 °C [274], and a CO_2 loading of 0.16 mmol g^{-1} at 0.4 mbar at 25 °C [31]. When exposed to a low humidity level of 4% RH at 22 °C, zeolite 13X already shows a reduction in CO_2 loading of 86 % [151]. For zeolite 5A, an even lower humidity level of 0.02% RH at 25 °C already reduces the CO_2 loading by more than 50 % [275].

Many studies thus report the need to implement a drying step for the incoming air stream before arrival at the adsorbent bed [30, 71, 110, 167, 268, 272, 273], however this could increase both the capital and operating costs of the DAC process. Very recently, a new start-up utilising zeolite adsorbents for DAC combined with desiccant for atmospheric water harvesting was announced [276]. It has also been suggested to use zeolite adsorbents in colder climates (< 0 °C) where the absolute humidity would be lower compared to more temperate climates, however the process was still found to be very energy-intensive [31]. Restricting to cold climates would also limit the location options for plant deployment, and cold temperatures would result in additional challenges regarding plant construction and daily operation. The introduction of amine groups in zeolites could enhance the CO_2 loading in the presence of humidity by creating new reaction sites for CO_2 [114, 238]. Indeed, H_2O in turn is known to enhance the CO_2 loading in amine-functionalised adsorbents [12]. However, high levels of H_2O adsorption on the zeolite structure would still result in substantial energy requirements for adsorbent regeneration and thus elevated operating costs. A reduction in hydrophilicity of these zeolites would therefore be ideal to mitigate this issue.

Subsequently, I propose to functionalise a reportedly hydrophobic Y-type zeolite, CBV 901 [277], with amine groups to potentially yield adsorbents for DAC with high CO_2 affinity while limiting H_2O adsorption. CBV 901 is a microporous H-Y zeolite commercially produced and sold by the company Zeolyst, with a Si:Al ratio of 40 [278]. The hydrophobic nature of CBV 901 (water uptake of 0.1 mmol g^{-1} at 21 °C and 45% RH) [277] is reportedly due to siliceous nanolayers free of Al and defects on the surface of its crystallites, which prevents the penetration of H_2O into the bulk of the adsorbent [279]. CBV 901 has previously been studied as an adsorbent for the removal of fatty acids, hydrocarbons, and steroids from wastewater [280, 281], but has yet to be considered for DAC.

In this study, I introduced amine groups to CBV 901 (referred to from here as ZY) via either aminosilane functionalisation or ammonia (NH_3) functionalisation, and preliminarily assessed the suitability of these adsorbents for DAC by measuring CO_2, N_2, and H_2O isotherms at 25 °C. Aminosilane functionalisation is a well-known technique that has previously been used to synthesise amine-functionalised adsorbents for CO_2 capture/DAC, where support structures included SBA-15 [282], silica gel [283], MCM-41 [191], and alumina [123]. Here, the new amine groups should provide

new CO_2 reaction sites while the hydrophobic ZY support should help to reduce the H_2O loading compared to previous zeolites studied for DAC. In comparison, NH_3 is traditionally used in its aqueous form for post-combustion CO_2 capture [284-286], while a previous report on the nitridation of zeolite Ys using NH_3 was for catalytic applications [192]. Functionalisation of ZY adsorbents using NH_3 should achieve the same properties as aminosilane functionalisation, however the direct attachment of NH_2 / NH to the zeolite Y surface rather than via an alkyl chain could also improve the CO_2 adsorption kinetics by minimising mass transfer limitations.

7.2 Results and discussion

7.2.1 Physicochemical properties

7.2.1.1 Chemical features

Functionalisation of ZY with aminosilane occurs via reaction of the methoxy groups of the aminosilanes with silanol groups on the pore surface of the zeolite Y. In an idealised scenario, in the presence of H_2O, the methoxy groups of adjacent aminosilanes can crosslink and require only one silanol group rather than three to react with an aminosilane (Figure 7.1).

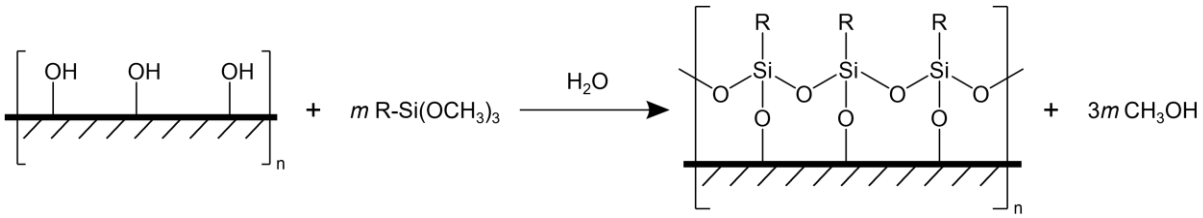


Figure 7.1. Ideal reaction of *m* aminosilanes with the zeolite Y surface in the presence of water.

Functionalisation of ZY with NH_3 can occur via the two reaction mechanisms shown in equations (7.1) and (7.2) [287]:

$$\equiv Si - OH + NH_3 \rightarrow \equiv Si - NH_2 + H_2O \qquad (7.1)$$

$$\equiv Si - O - Si \equiv + NH_3 \rightarrow \equiv Si - NH_2 + Si - OH \qquad (7.2)$$

At higher temperatures, the reaction shown below in equation (7.3) is also possible [287]:

$$\equiv Si - NH_2 + Si - OH \rightarrow \equiv Si - NH - Si \equiv + H_2O \qquad (7.3)$$

I first used FTIR to qualitatively confirm the presence of new functionalities for both synthesis routes (Figure 7.2). For the aminosilane-functionalised samples, the spectra shown in Figure 7.2a exhibit new bands between 1650 cm^{-1} to 1550 cm^{-1} corresponding to N-H vibrations, while bands around 2900 cm^{-1} and 1450 cm^{-1} are characteristic of CH_2 vibrations (hardly visible for ZY-APTMS) [227]. The sharp bands between 1210 cm^{-1} and 1170 cm^{-1} in the parent ZY sample appear to have been replaced by a broader band potentially corresponding to C-N vibrations [227]. Furthermore, the sharpness of the band at 830 cm^{-1} is greatly reduced in the aminosilane-functionalised samples compared to the parent ZY sample, along with the disappearance of the left shoulder of the band around 1050 cm^{-1}, both likely associated to a decrease in Si-OH groups [227]. The latter changes are also observed for the ZY-NH_3 samples in Figure 7.2b, along with the appearance of additional bands at 990 cm^{-1}, which can be associated with Si-N bonds [227]. These changes are more prominent in the samples as the synthesis time and temperature increases.

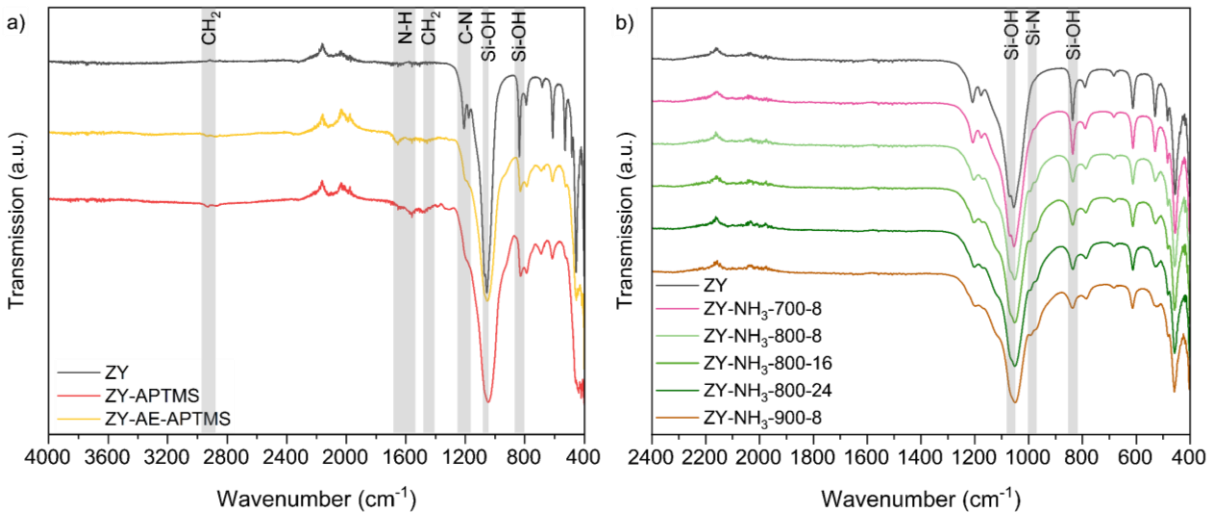


Figure 7.2. FTIR spectra for a) ZY samples functionalised with aminosilanes and b) ZY samples functionalised with NH_3. (No bands were observed for ZY-NH_3 samples beyond 2400 cm^{-1}; the full spectrum up to 4000 cm^{-1} is shown in Figure A5.1).

I next used XPS to quantitatively assess the extent of amine functionalisation on ZY samples (Figure 7.3). Survey scans of the samples provided their atomic compositions, from which I derived their percentage weight composition (wt%). The N wt% obtained can then also be converted to a N loading in mmol g^{-1} (Table 7.1).

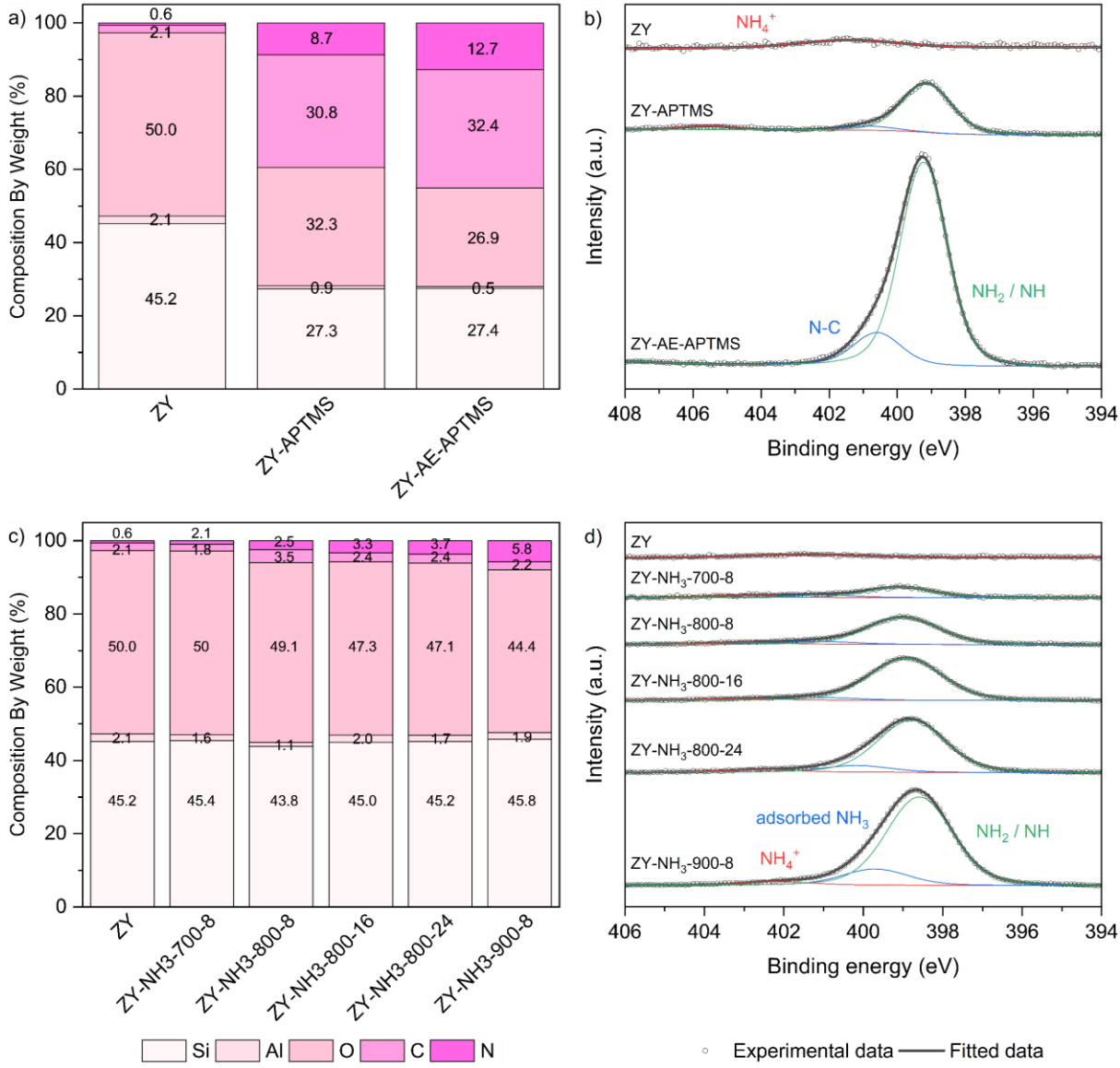


Figure 7.3. XPS analyses of original and functionalised ZY samples. For ZY samples functionalised with aminosilanes: a) elemental composition by weight and b) deconvolution of N 1*s* core level. For ZY samples functionalised with NH_3: c) elemental composition by weight and d) deconvolution of N 1*s* core level.

Table 7.1. Nitrogen loading in mmol g^{-1} of original and functionalised ZY samples derived from XPS and TGA analyses.

Sample	N loading (mmol g^{-1}), XPS	N loading (mmol g^{-1}), TGA
ZY	0.44	nil
ZY-APTMS	6.2	3.9
ZY-AE-APTMS	9.1	5.4
ZY-NH_3-700-8	0.74	n.d.
ZY-NH_3-800-8	1.8	n.d.
ZY-NH_3-800-16	2.4	n.d.
ZY-NH_3-800-24	2.6	n.d.
ZY-NH_3-900-8	4.1	n.d.

As seen from Figure 7.3a, the aminosilane-functionalised samples have a significant increase in the N and C content compared to the parent ZY, with ZY-AE-APTMS having higher wt% of these elements than ZY-APTMS due to the longer alkane chain and two N per silane group instead of one. However, since the N loading of ZY-AE-APTMS is less than double that of ZY-APTMS, this implies that more aminosilane chains were grafted in ZY-APTMS compared to ZY-AE-APTMS. Deconvolution of the N 1*s* core level shown in Figure 7.3b confirms the presence of NH_2 / NH groups and C-N bonds in these samples, while only a small peak associated with NH_4^+ is detected in the original ZY sample [288]. I also carried out thermal decomposition of the samples using TGA to confirm actual grafting of the aminosilane groups to the ZY pore surface, rather than impregnation of the pores (Figure A5.2). Boiling points of APTMS and AE-APTMS are 91 °C [289] and 146 °C [290], while most of decomposition in the ZY-APTMS and ZY-AE-APTMS samples starts at a much higher temperature of ~ 300 °C. Therefore, it is very likely that grafting did occur, as a higher temperature is needed to remove the chemically bonded aminosilane chains. Any mass loss below 200 °C is associated to the removal of adsorbed water, impregnated aminosilanes, and / or dangling methoxy ligands [191]. The N loading in mmol g^{-1} can be calculated from the mass loss above 200 °C (22.6 % for ZY-APTMS and 27.4 % for ZY-AE-APTMS), where we assume that only the alkyl chain beyond the Si group is lost. The N loadings derived from TGA are lower than those determined from XPS. As XPS is a surface-sensitive technique,

the higher N loadings obtained could suggest a higher concentration of aminosilanes at the external surface compared to the internal pore structure.

The ZY-NH_3 samples also have increased N content compared to the parent ZY, with higher synthesis temperature and time resulting in higher N content (Figure 7.3c). The synthesis temperature seems to have a bigger impact on the extent of N functionalisation compared to the synthesis time, as ZY exposed to NH_3 for 8 h at 900 °C has higher N content compared to ZY exposed to NH_3 for 24 h at 800 °C. Deconvolution of the N 1*s* core level for the ZY-NH_3 samples confirms a majority functionalisation of NH_3 as the desired NH_2 / NH groups, though some adsorbed NH_3 does appear to be present, along with NH_4^+ originally present in the parent ZY sample (Figure 7.3d) [192].

7.2.1.2 Textural properties

I used N_2 sorption at -196 °C to determine the BET area, micropore volume ($V_{micropores}$), and total pore volume ($V_{total\ pores}$) of the original and functionalised ZY samples. Pore size distributions of all samples are also provided in Figure A5.3. Figures 7.4a and 7.4c show the experimental N_2 isotherms measured at -196 °C, where a drastic decrease in porosity is observed for both aminosilane-functionalised samples, while the isotherms for the ZY-NH_3 samples are very similar compared to that of the parent ZY. These isotherms are shown in log-scale of pressure in Figure A5.4 for clearer differentiation.

Figures 7.4b and 7.4d tabulate the BET area, micropore volume, and total pore volumes extracted from the measured N_2 sorption isotherms of the aminosilane-functionalised samples and ZY-NH_3 samples, respectively. For the former, the BET area of both samples has been reduced to 6 $m^2\ g^{-1}$, compared to the BET area of the parent ZY sample of 724 $m^2\ g^{-1}$. The micropore and total pore volumes of ZY-APTMS and ZY-AE-APTMS are now negligible compared to the micropore and total pore volume of 0.24 $cm^3\ g^{-1}$ and 0.48 $cm^3\ g^{-1}$ of the parent ZY sample. These results indicate that the pores of the parent ZY have been filled / blocked by aminosilane functionalisation, which is restricting N_2 access at this temperature and could have negative impacts on the CO_2 adsorption kinetics. Pore blockage with the aminosilanes could also account for a higher concentration of N at the zeolite Y

surface and explain the discrepancy between the N loadings derived from XPS and TG analysis, as blockage of the pores would prevent further functionalisation of the internal structure.

For the ZY-NH_3 samples, the BET area and micropore volumes are only slightly reduced to between 685 to 700 $m^2\ g^{-1}$ and approximately 0.20 $cm^3\ g^{-1}$, respectively, while the total pore volume is relatively unchanged (0.48 to 0.50 $cm^3\ g^{-1}$) from the parent ZY sample. NH_3 is a comparably small molecule to the aminosilanes and should not greatly reduce the porosity of the zeolite Y, which is beneficial for minimising mass transfer resistances and allowing fast CO_2 adsorption kinetics. However, the NH_3 treatment at the high temperatures used could have partially collapsed some of the zeolite Y cages, which could explain the reduction in micropore volume [291]. Despite this, this particular ZY still seems to be more robust compared to other ZYs with lower Si:Al ratios. Srasra et al. [192] reported up to 50% decreases in the BET area, micropore volume, and total pore volume of ZY samples (Si:Al ratios of 2.6, 13, and 37) associated with a reduction in crystallinity when treated with NH_3 at 800 °C, though for a longer time of 48 h.

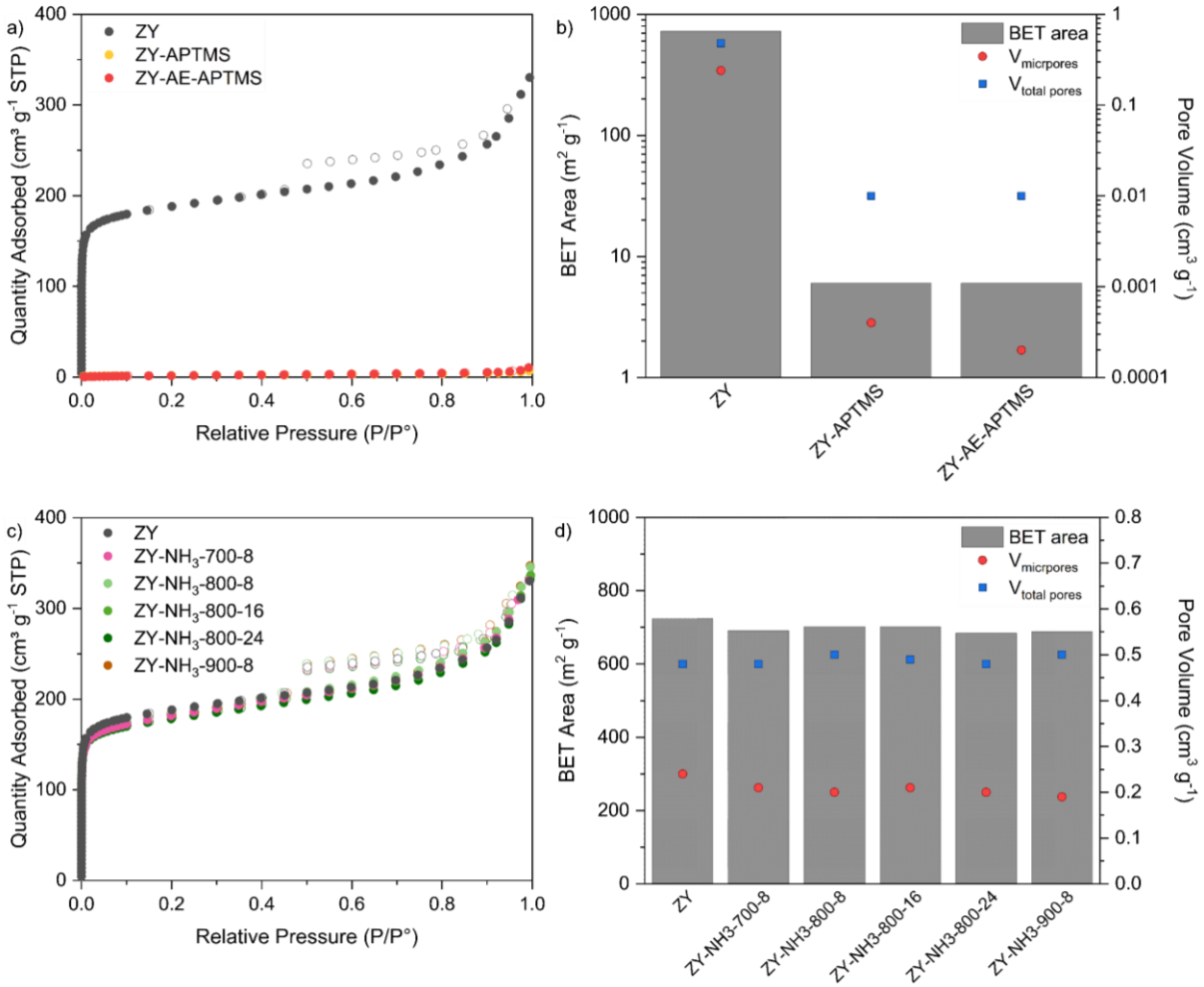


Figure 7.4. Porosity analyses of original and functionalized ZY samples. a), c) N_2 sorption isotherms at -196 °C (filled symbols = adsorption; open symbols = desorption). b), d) BET areas, micropore volumes ($V_{micropores}$), and total pore volumes ($V_{total\ pores}$) extracted from the measured N_2 sorption isotherms.

7.2.2 Equilibrium sorption properties

7.2.2.1 CO_2 sorption

To preliminarily investigate the CO_2 sorption performance of the functionalised ZY samples, I measured equilibrium CO_2 sorption isotherms at 25 °C. Figures 7.5a and 7.5b show the CO_2 isotherms for the aminosilane-functionalised samples with a linear and log-scale of pressure, respectively. The parent ZY sample has minimal CO_2 adsorption at 0.4 mbar of ~ 0.003 mmol g^{-1}. For the aminosilane-functionalised samples, I was not able to measure complete adsorption isotherms due to the extremely

slow speed of the measurements. Isotherms for ZY-APTMS and ZY-AE-APTMS were measured simultaneously, and both measurements were terminated after the loading of 0.59 mmol g^{-1} at 0.4 mbar was obtained for ZY-APTMS, which took 20 days. For ZY-AE-APTMS, it took 11 days to obtain a loading of 0.46 mmol g^{-1} at 0.4 mbar. In comparison, it took 7 days to measure the complete adsorption and desorption isotherm up to 1 bar for Lewatit VP OC 1065 (i.e. Lewatit), which had a higher loading of 0.95 mmol g^{-1} at 0.4 mbar [1]. These results imply that these samples have extremely slow CO_2 adsorption kinetics, which is likely due to overfilling / blockage of the pores with aminosilane molecules as discussed in Section 7.2.1.2. The amount of aminosilane I used in the synthesis procedure was based on a study by Harlick and Sayari [191], where they had optimised the aminosilane loading for a synthesis using pore-expanded MCM-41 with an average pore diameter of ~ 10 nm. In comparison, most pores in the parent ZY sample have diameters below 2 nm (Figure A5.3). Therefore, the amount of aminosilane needs to be optimised for this specific ZY in future syntheses to reduce mass transfer resistances but still maintain high CO_2 loading.

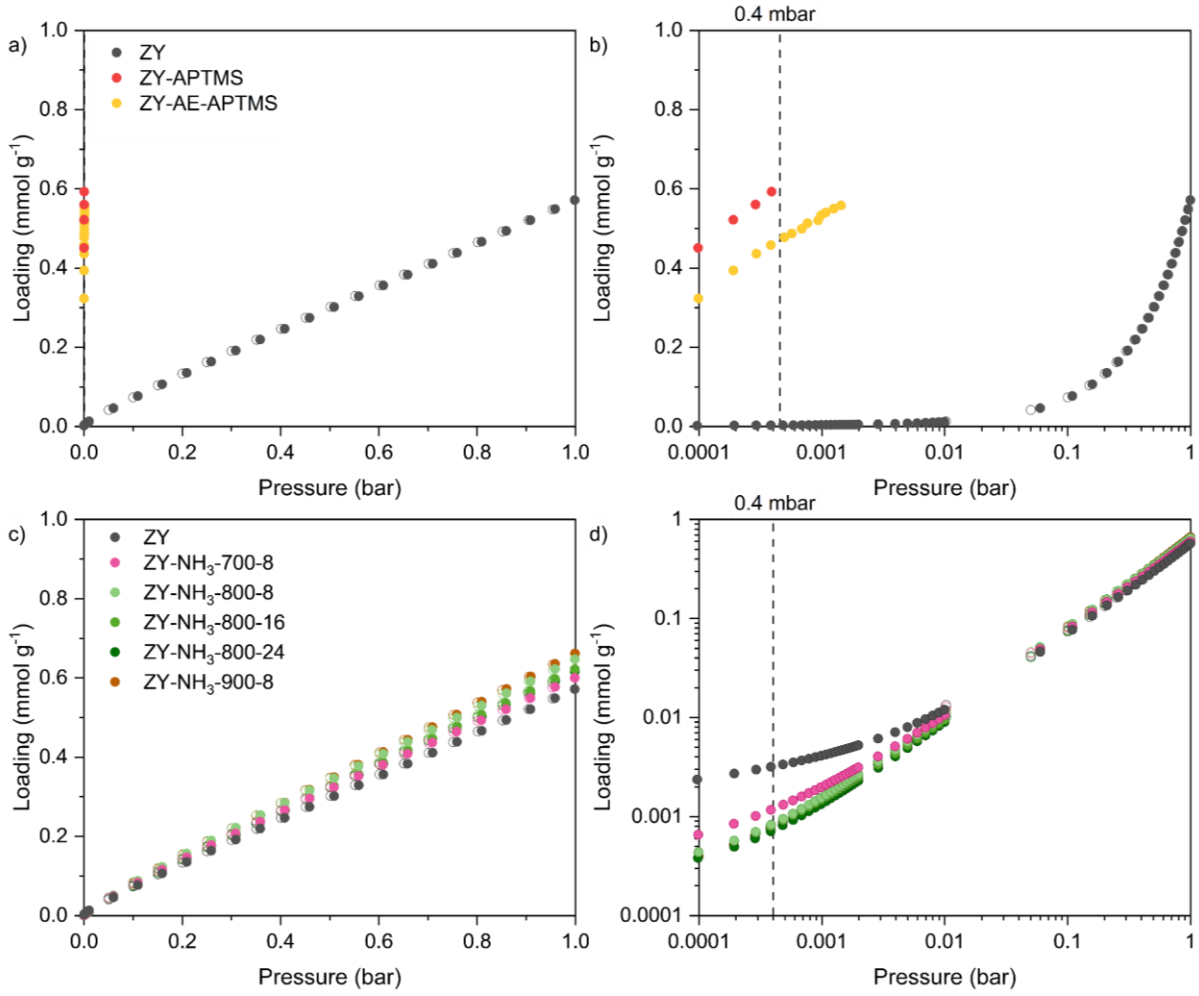


Figure 7.5. Equilibrium adsorption (filled symbols) and desorption (hollow symbols) isotherms for CO_2 measured at 25 °C up to 1 bar with linear and log-scales of pressure for a) and b) aminosilane-functionalised samples and c) and d) ZY-NH_3 samples, respectively.

Interestingly, ZY-AE-APTMS with higher N loading had lower CO_2 adsorption compared to ZY-APTMS. This may suggest that only the primary amine groups in the aminosilane chains react with CO_2, as more chains were grafted in ZY-APTMS than ZY-AE-APTMS as explained in Section 7.2.1.1. As these CO_2 isotherms are measured in dry conditions, two adjacent amine groups are needed to react with and capture CO_2 via ammonium carbamate formation [12] as shown in equation (7.4):

$$CO_2 + 2RNH_2 \leftrightarrow RNH_3^+ + RNHCOO^- \quad (7.4)$$

For ZY-APTMS and ZY-AE-APTMS, the primary amines at the end of the chains may have more flexibility to come into sufficient proximity to react with CO_2, whereas the spacing of the secondary amine groups between chains may not be sufficient for this purpose.

The CO_2 isotherms measured for ZY-NH_3 samples are shown in Figures 7.5c and 7.5d with linear and log-scales of pressure, respectively. Surprisingly, functionalisation in these samples did not result in significantly improved CO_2 adsorption. In fact, at 0.4 mbar, lower CO_2 adsorption is observed for all functionalised samples compared to the already minimal CO_2 loading on the parent ZY sample, though these loading levels are likely on the same order of magnitude as the error of the porosity analyser. At 1 bar, there is a 5% to 15% increase in CO_2 adsorption for the ZY-NH_3 samples compared to the parent ZY sample, where the loading increases with synthesis temperature. I also normalised the CO_2 loadings as mmol per gram of zeolite Y rather than per gram of adsorbent (i.e. not accounting for the mass of N), but no changes were observed when comparing the CO_2 loading at 0.4 mbar between the parent ZY and ZY-NH_3 (Figure A5.5). The negligible impact of NH_3 functionalisation on the CO_2 loading at 0.4 mbar of ZY samples could be due to insufficient amine density and/or lack of amine flexibility to allow for the reaction of CO_2 with two amine groups. In the case of NH_3 functionalisation, there is no additional alkyl chain and NH_2/NH is directly attached to the pore walls of ZY. Therefore, these amine groups will need to be in very close proximity to capture CO_2. If this is the case, improved CO_2 adsorption should be observed in the presence of humidity, where only one amine group is needed to react with CO_2 to form ammonium bicarbonate [12], as shown in equation (7.5):

$$CO_2 + RNH_2 + H_2O \leftrightarrow RNH_3^+HCO_3^- \quad (7.5)$$

7.2.2.2 N_2 sorption

I measured equilibrium N_2 adsorption and desorption isotherms up to 1 bar at 25 °C for the original and functionalised ZY samples. Figures 7.6a shows the N_2 isotherms for the aminosilane-functionalised samples. The N_2 uptake for these samples is noticeably less than that of the parent ZY sample, likely due to the reduced BET area after functionalisation, which also resulted in a conversion of these samples from physisorbent to chemisorbent. The N_2 uptake of these aminosilane-functionalised

samples is also approximately three times higher than that of Lewatit at 25 °C [1], and thus they will have lower CO_2 selectivity.

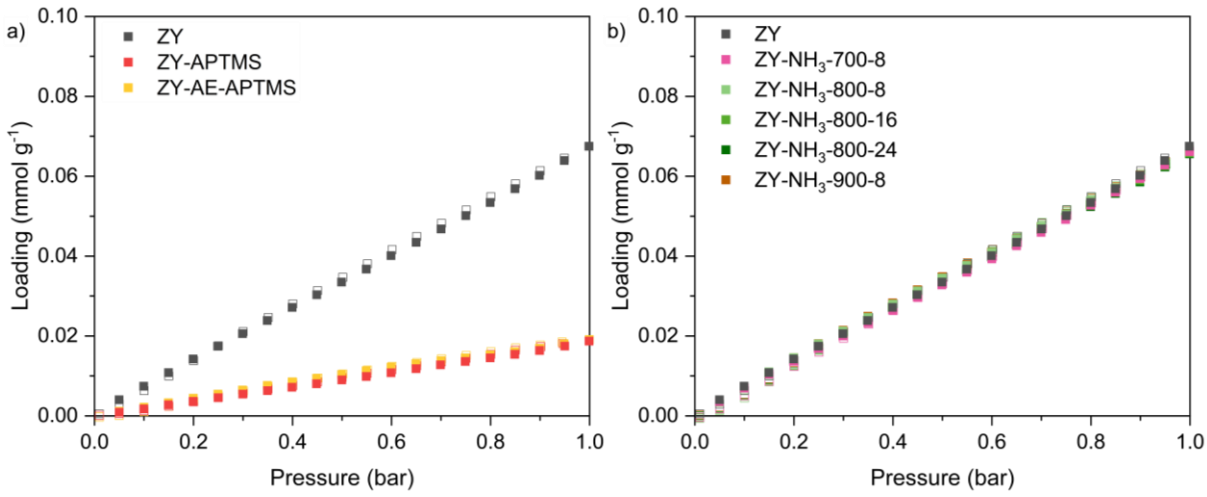


Figure 7.6. Equilibrium adsorption (filled symbols) and desorption (hollow symbols) isotherms for N_2 measured at 25 °C up to 1 bar for a) aminosilane-functionalised samples and b) ZY-NH_3 samples..

Figures 7.6b shows the N_2 isotherms for ZY-NH_3 samples. Here, the N_2 uptake is unchanged between the parent and functionalised ZY samples, as the BET area was comparable before and after functionalisation. Due to the low CO_2 uptake of ZY-NH_3 samples at 0.4 mbar, it is not immediately clear if these samples are still selective for CO_2 under DAC conditions when compared to N_2. The pure component CO_2:N_2 selectivity can be calculated using equation (7.6):

$$S = \frac{q_{CO_2}}{q_{N_2}} \cdot \frac{P_{N_2}}{P_{CO_2}} \qquad (7.6)$$

where S is the selectivity, q_{CO2} and q_{N2} are the CO_2 and N_2 loadings at P_{CO2} and P_{N2}, i.e. the partial pressures of CO_2 and N_2, respectively. For DAC conditions, P_{CO2} = ~ 0.0004 and P_{N2} = ~ 0.8. For the ZY-NH_3 samples, the CO_2:N_2 selectivity ranges from 28 to 44 depending on the synthesis conditions. Therefore, these samples are still selective for CO_2 under DAC conditions. However, in comparison, ZY-APTMS and Lewatit have CO_2:N_2 selectivities of ~ 81,000 and ~ 410,000, respectively.

7.2.2.3 H_2O sorption

I measured equilibrium H_2O adsorption and desorption isotherms up to ~ 70% relative humidity at 25 °C for aminosilane-functionalised samples (Figure 7.7a) and ZY-NH_3 samples (Figure 7.7b), respectively, and compared them to that of the parent ZY sample. While low H_2O loading would be desirable to minimise the energy required for adsorbent regeneration, the presence of H_2O is also known to improve the CO_2 uptake and adsorption kinetics in amine-functionalised adsorbents [159]. Process modelling would thus need to be conducted to determine what is an acceptable H_2O loading for these materials.

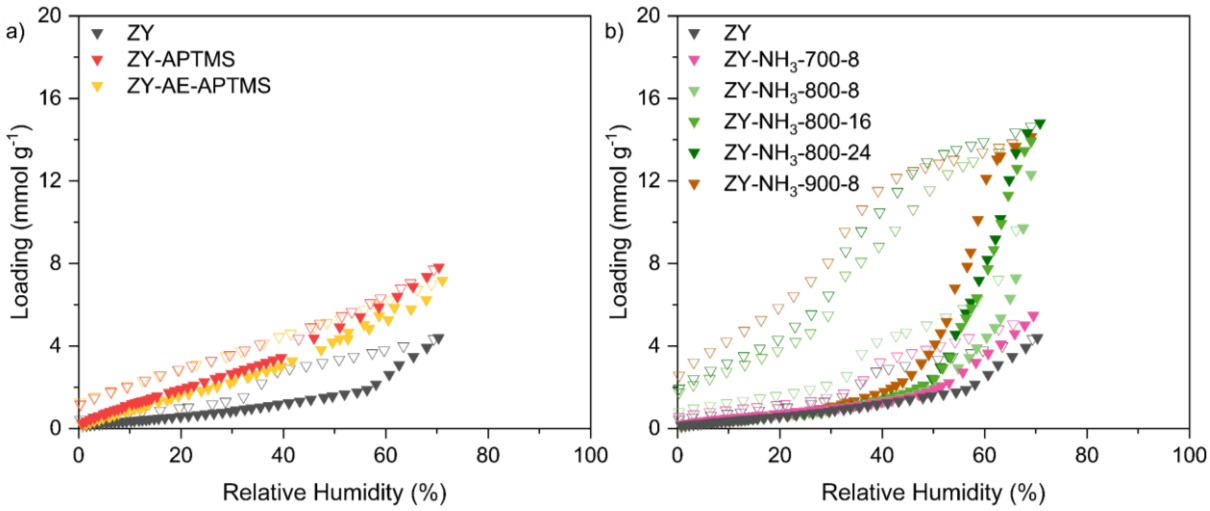


Figure 7.7. Equilibrium adsorption (filled symbols) and desorption (hollow symbols) isotherms for H_2O measured at 25 °C as a function of relative humidity for a) aminosilane-functionalised samples and b) and ZY-NH_3 samples.

As seen from Figure 7.7, the parent ZY sample is indeed hydrophobic in comparison to other zeolites such as 13X and 5A (~ 14 mmol g^{-1} at ~ 50 % RH) [274]. However, the loading measured here (1.4 mmol g^{-1} at 45 % RH) is much higher than the H_2O loading of 0.1 mmol g^{-1} at 45 % RH and 21 °C previously reported by Halasz et al. [277]. That study was published more than 20 years ago and so Zeolyst could have perhaps modified its formulation for the parent ZY sample over the years.

ZY-APTMS and ZY-AE-APTMS show increased and more linear H_2O adsorption compared to the parent ZY sample, and their isotherms are very comparable to that of Lewatit [1] (Figure A5.6). ZY-NH_3 samples demonstrate a wide range of H_2O loadings dependent on the synthesis conditions. ZY-

NH_3-700-8 has very similar H_2O adsorption to the parent ZY sample, while ZY-NH_3-800-8 has almost three times higher H_2O loading at 70% RH. For the samples exposed to harsher NH_3 treatment conditions (ZY-NH_3-800-16, ZY-NH_3-800-24, and ZY-NH_3-900-8), the H_2O loading is further increased and a substantial hysteresis indicates irreversible adsorption. NH_3 treatment at these conditions may thus have caused defects in the zeolite Y framework and created unwanted H_2O reaction sites. For example, OH groups may have been stripped off without being replaced by amine groups, thus leaving open reaction sites. If H_2O reacts irreversibly at these sites, for example creating new OH groups, this hysteresis may not be observed when the same sample is used for additional cycles. However, despite the increased H_2O adsorption for most ZY-NH_3 samples, all samples still maintain a relatively low H_2O loading (< 5 mmol g^{-1}) up to at least 50% RH, after which point a steep step-like rise in H_2O adsorption is observed. The relative humidity at which this step occurs decreases with harsher NH_3 treatment.

7.3 Conclusions

In this study, I explored amine-functionalised H-Y zeolites as adsorbents for DAC with potentially high CO_2 affinity but minimal H_2O adsorption. I imparted amine functionality onto a commercially available hydrophobic H-Y zeolite with a high Si:Al ratio of 40 via either aminosilane or NH_3 functionalisation. I confirmed the presence of new amine functionality for all samples using either FTIR, XPS, and/or TGA, and reported their BET area, micropore volume, and total pore volume determined from N_2 sorption at -196 °C. I then measured equilibrium isotherms of CO_2, N_2, and H_2O at 25 °C for all samples to preliminarily assess their suitability for DAC. While additional isotherm temperatures are needed to facilitate the fitting of isotherm parameters and the calculation of heats of adsorption, these were not measured due to the sub-optimal results obtained for these samples, which are summarised below.

ZY-APTMS and ZY-AE-APTMS had CO_2 loadings of 0.59 and 0.46 mmol g^{-1}, respectively at 0.4 mbar and 25 °C, which was significantly higher than the parent zeolite Y sample under similar conditions. However, it took 20 and 11 days respectively to collect this data. The extremely slow CO_2

adsorption kinetics of these samples, due to blockage of the pores with aminosilane molecules as evidenced by the loss of BET area and micropore volume, made it impractical to measure the complete adsorption and desorption isotherms. Future work will need to be conducted to optimise the aminosilane amounts used in the synthesis to decrease mass transfer resistances to a point where these samples could be practical to use in a DAC process, while still maintaining a satisfactory CO_2 loading. As they are now, these aminosilane-functionalised samples have lower CO_2:N_2 selectivity compared to Lewatit, but similar H_2O adsorption levels.

Functionalisation of ZY with NH_3 did not increase its pure-component CO_2 loading. This could be due to insufficient amine density/flexibility, and thus humidity would be required to facilitate CO_2 adsorption. This should be investigated in the future by performing binary CO_2-H_2O co-adsorption experiments. If CO_2 adsorption is improved in the presence of humidity, the relatively unchanged textural properties of these ZY-NH_3 adsorbents compared to the parent ZY suggests that they could also have relatively fast CO_2 adsorption kinetics. Furthermore, despite the current minimal pure-component CO_2 loading, these samples are still selective for CO_2 over N_2. In terms of their H_2O adsorption, samples that were subjected to harsher NH_3 treatment conditions have significantly increased H_2O loadings at relative humidity levels above 50% and substantial hysteresis compared to the parent ZY. This suggests that defects in the zeolite Y framework may have formed and created unwanted H_2O reaction sites, though these may be "filled" after one reaction cycle with H_2O. All samples still maintain low H_2O loadings of less than 5 mmol g^{-1} below 50% RH, suggesting they could be suitable for use in temperate climates.

Overall, my hypothesis for this chapter did not hold true. Only the adsorbents synthesised via aminosilane functionalisation incurred improved CO_2 adsorption (though with extremely limited adsorption kinetics), and H_2O adsorption was increased in both adsorbent types, particularly for NH_3-functionalised adsorbents at moderate to high relative humidity. I note that the parent zeolite Y was more hydrophilic than previously reported which may have impacted the results as well. Further optimisation of the synthesis routes and/or adsorption process will be needed to make these adsorbents suitable for DAC.

Chapter 8: Quantification of temperature-dependent CO_2 adsorption kinetics in Lewatit VP OC 1065, Purolite A110, and TIFSIX-3-Ni for direct air capture

The work and discussions in this chapter are being prepared by the thesis author for publication. Uncertainty bounds on the CO_2 loading values determined from isotherm fitting models were calculated by Dr. David Danaci.

8.1 Introduction

One of the critical factors that influences the performance of a DAC process are the CO_2 adsorption kinetics. For this work, the CO_2 adsorption kinetics refers to both the intraparticle CO_2 diffusion from the exterior pellet surface to the active site, and the CO_2 rate of adsorption/reaction at the active site. The CO_2 adsorption kinetics impact the productivity, energy consumption, and therefore capital and operating costs of a process [43, 44]. If the adsorption kinetics are not considered, the performance of a slow adsorbent could be greatly overestimated, and the costs underestimated. Rapid kinetics enable shorter cycle times, which in turn, results in higher productivity (tonnes of product per day, per tonne of adsorbent). Enhanced productivity means that a given amount of CO_2 can be captured with fewer contactor units, leading to reduced capital costs. Slow adsorption kinetics cause not only a decline in the aforementioned productivity, but may also hamper CO_2 recovery. For a given contactor size and feed gas velocity, slow kinetics result in a greater portion of that feed gas breaking through the bed, resulting in a loss of CO_2 back to the atmosphere. This can be compensated for by reducing the feed gas velocity, however, that further hampers the process productivity. With reduced CO_2 recovery, more feed gas needs to be processed to capture a given amount of CO_2, which results in greater energy consumption and operating costs. For these reasons, investigating and quantifying adsorption kinetics become critical to the deployment of adsorption-based DAC technologies.

The CO_2 adsorption kinetics can be experimentally measured at various scales; the crystal, the shaped adsorbent (e.g. pellet), or packed adsorption column, using a variety of techniques to extract different diffusion coefficients (Figure 8.1) [292-294]. All experiments described here will also

encompass any intrinsic CO_2 reaction kinetics present in the adsorbent, though more comprehensive mathematical models and additional experiments would be needed to decouple the reaction kinetics from diffusion resistances. For example, determination of an effectiveness factor, which relates the overall adsorption kinetics to the adsorption kinetics if the active sites were exposed to the particle's external surface conditions, could help to compare the influence of intraparticle diffusion vs. the rate of adsorption/reaction on the overall adsorption kinetics [295].

At the crystal scale, nuclear magnetic resonance (NMR) techniques such as pulsed field gradient (PFG) can track the diffusion of individual adsorbate molecules within the crystal, where attenuations in the NMR signal relate to molecular displacement [296]. Here, resistances due to micropore/surface diffusion (arising from the transport of physically adsorbed molecules) are captured, and typically less than 10 mg of sample is needed. Shifts in the NMR peaks corresponding to new reacted species and growth of the peaks over time can also allow for extraction of the reaction kinetics [297, 298].

At the pellet scale, techniques such as direct uptake/desorption rate measurements, zero length column measurements, and imaging utilise ~ 10 to 100 mg of sample and can account for both micropore and macropore resistances, where the latter comprises molecular diffusion, Knudsen diffusion, surface diffusion, and Poiseuille flow. Uptake/desorption rate measurements can often be done using commercial instruments either volumetrically, where the pressure change in the system is tracked over time, or gravimetrically, by measuring the mass change of the adsorbent over time after a stepwise introduction of the adsorbate [299]. The latter can be conducted using either constant pressure or constant volume experiments, though constant volume experiments require a correction to account for the changing driving force during the period of gas uptake. In the zero length column (ZLC) method, the desorption curve is tracked as a previously saturated adsorbent is exposed to a flow of inert gas. Here, the setup can be considered a perfectly mixed continuous flow cell and axial concentration gradients and heat transfer resistances are considered negligible [300]. It is also possible to directly track the diffusion of the adsorbate through the adsorbent pellet using imaging techniques such as interference microscopy (IFM), infra-red microscopy (IRM), and X-ray computed tomography (CT),

which allow one to measure the internal transient concentration profile of the adsorbate in the adsorbent [301, 302].

Finally, one can also extract kinetic information from the breakthrough response of a column packed with an adsorbent (usually > 1 g) as the adsorbate is continuously flowed through the system [303]. At this scale, contributions from convection, axial dispersion, and external diffusion can be accounted for along with the aforementioned macropore and micropore diffusion resistances.

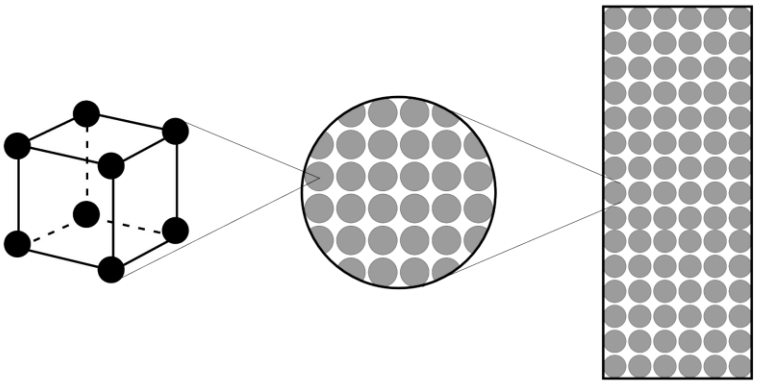
Adsorbent scale	**Crystal** (< 10 mg)	**Pellet** (10 - 100 mg)	**Adsorption column** (> 1 g)
			
Measurement technique	NMR	Direct uptake/desorption ZLC Imaging	Breakthrough
Reaction kinetics	✓	✓	✓
Mass transfer mechanisms	Micropore diffusion	Micropore diffusion Macropore diffusion	Micropore diffusion Macropore diffusion External diffusion Convection Axial dispersion

Figure 8.1. Schematic of the different adsorbent scales and their associated mass transfer mechanisms, measurement techniques, and sample masses.

In this study, I utilise a thermogravimetric analyser to conduct CO_2 uptake rate measurements at constant pressure for different adsorbents. This technique was chosen due to the ease of accessibility and the small sample mass required. The experimental data must then be fitted to appropriate mathematical models to extract and quantify the adsorption kinetics. One of the simplest and most common ways to describe the CO_2 adsorption kinetics is with the linear driving force (LDF) model [304, 305]:

$$\frac{dq}{dt} = k_{LDF}(q_e - q) \qquad (8.1)$$

where q is the amount of CO_2 adsorbed at time t, q_e is the CO_2 equilibrium adsorption capacity, and the linear driving force constant, k_{LDF}, is a lumped mass transfer coefficient accounting for both diffusion resistances (macropore and micropore) and the intrinsic reaction kinetics in cases where chemisorption occurs. This model has been used in the literature to describe the adsorption kinetics of both chemisorbents (i.e. amine-functionalised adsorbents) and physisorbents for DAC [30, 35, 53, 179, 180].

Other models used to describe the kinetics of DAC adsorbents include various rate order models (e.g. pseudo-first order (PFO), pseudo-second order (PSO), fractional order) [62, 116, 134, 173, 181-185, 187, 188, 306-309], the Avrami model [62, 97, 116, 134, 181, 182, 184, 187, 188, 308], combined PFO and Avrami [117], and reaction-mechanism based models [149, 186]. Modified forms of the shrinking core model have also been investigated, where the adsorbed phase is modelled as a product layer forming around a core of unreacted sorption sites, which shrinks as the reaction proceeds [310-312].

In contrast to the LDF model, one of the most rigorous methods to describe the kinetics within an adsorbent pellet is with the Fickian diffusion model [294, 305] given by equations (8.2) and (8.3):

$$J = -D\frac{\partial C}{\partial r} \qquad (8.2)$$

$$D = B\left[\frac{d\ lnP}{d\ lnC}\right]_T \qquad (8.3)$$

where J is the flux of the adsorbate, C is the adsorbate concentration, r is the radius of the adsorbent particle, P is the pressure, T is the temperature, D is the Fickian diffusivity, and B is the mobility of the adsorbate. In the case of chemisorbents, the intrinsic CO_2 reaction kinetics would need to be determined in addition to and independently from diffusion resistances, which can be experimentally challenging. For example, one could theoretically isolate the diffusion resistance by conducting additional experiments with a non-reacting sample gas, however this gas may not adsorb in sufficient quantities to provide suitable uptake curves which are usable for subsequent fitting. It is also mathematically/computationally intensive to incorporate this model into adsorption-based process simulations as the equations need to be repeatedly integrated at the pellet and column levels until cyclic steady state is achieved. Furthermore, since most processes will realistically operate under non-

isothermal and non-isobaric conditions, these calculations would also have to be coupled with mass, heat, and energy balance equations across all scales.

As a simpler option, Sircar and Hufton have shown that the LDF model can indeed be sufficient for process modelling, as the information from a detailed kinetic model describing local rates of adsorption (i.e. spatial variation) within a pellet is often lost during the numerous integration/averaging steps [305]. For example, the LDF model was used to simulate the mass transfer resistances in: pressure swing adsorption cycles using activated carbon for pre-combustion CO_2 capture by Subraveti et al. [313]; steam-assisted temperature-vacuum swing adsorption cycle using amine-functionalised nanofibrillated cellulose for direct air capture by Stampi-Bombelli et al. [180]; vacuum swing adsorption cycles using diamine-appended MOFs for post-combustion capture by Pai et al. [235]; and to describe the mass transfer resistances from breakthrough experiments using zeolite 13X by Wilkins et al. [151]. There are some limitations to the LDF model when used for the modelling of rapid cycles [314-316], however, DAC cycles are not expected to operate in that way. For this work, I thus utilise the LDF model for quantification of the experimental adsorption kinetics and obtain lumped mass transfer coefficients encompassing both intraparticle diffusion and rate of reaction/adsorption information.

Here, I analyse Lewatit VP OC 1065 (i.e. Lewatit), Purolite A110 (i.e. Purolite), and TIFSIX-3-Ni, as I previously highlighted these materials as promising adsorbents for DAC and reported many of their physicochemical and equilibrium sorption properties [1, 2]. In terms of their CO_2 adsorption kinetics, no data is currently available for Purolite and TIFSIX-3-Ni. For Lewatit, Young et al. fitted the LDF model to dynamic column breakthrough data, with experiments conducted at 25 °C, 50 °C, and 70 °C and $1\%_{vol}$ CO_2 balanced with N_2, and reported a constant k_{LDF} of 3×10^{-3} s^{-1} within this temperature range [150]. Bos et al. measured the intrinsic reaction kinetics of Lewatit in absence of external or intraparticle transport limitations using a flat bed reactor at 5 °C to 40 °C and pure CO_2 pressures of 50 mbar, 100 mbar, and 200 mbar. They compared the use of the LDF model, quadratic driving force (QDF) model, and a Toth rate reaction model, and found that the Toth rate reaction model was best able to fit the CO_2 uptake data across the varying temperatures and pressures [217]. In that study, the reported k values for the LDF fitting of data measured at 50 mbar (i.e. $5\%_{vol}$) CO_2 ranged from 8×10^{-2} s^{-1} to 27.3×10^{-2} s^{-1} between 5 °C and 40 °C. Recently, Wu et al. measured the CO_2 uptake

rate of Lewatit at 25 °C and 400 ppm (i.e. 0.04%$_{vol}$) CO_2 balanced with N_2 using a thermogravimetric analyser. The data was fitted to the Avrami model and a mass transfer coefficient (k_A) of 2.5×10^{-4} s^{-1} was reported [44]. The temperature dependence of the mass transfer coefficient remains unknown. For perspective, the k_{LDF} value for zeolite 13X beads of 1 mm in diameter at 10 °C at 1 mbar (i.e. 0.1%$_{vol}$) CO_2 is 1.6×10^{-2} s^{-1}. Assuming the k_{LDF} value of 3×10^{-3} s^{-1} reported by Young et al. for Lewatit was also for bead sizes of 1 mm in diameter (Lewatit bead sizes range from 0.3 to 1.2 mm [226]), the adsorption kinetics of zeolite 13X is already a magnitude faster than that of Lewatit at 10 times lower CO_2 concentration and 15 °C lower temperature.

This study aims to fill the gaps in adsorption kinetics for Lewatit, Purolite and TIFSIX-3-Ni by estimating their temperature-dependent mass transfer coefficient at relevant DAC conditions. While such coefficients cannot decouple intraparticle diffusion and intrinsic reaction kinetics, it remains useful as inputs for process modelling. This work relies on using a thermogravimetric analyser to measure the mass of CO_2 adsorbed as a function of time at multiple temperatures for each adsorbent under a flow of 400 ppm CO_2, representative of dry ambient air. The experiments were run using a constant pressure approach (i.e. the concentration of CO_2 in the bulk gas phase is equal to the concentration of CO_2 at the bead/pellet surface), where external mass transfer limitations were minimised as much as possible by modifying the thermogravimetric analyser sample holder and optimising the gas flowrates. The resulting experimental data was then fitted simultaneously to a temperature-dependent LDF equation to obtain temperature-dependent *kLDF* constants, which can be used to describe the lumped CO_2 adsorption kinetics of these materials in subsequent process models.

8.2 Experimental section

8.2.1 Adsorbent materials

Lewatit and Purolite resins are formed as spherical beads with particle sizes between 0.3 to 1.2 mm (average particle size is ~ 0.5 mm in diameter) and containing up to 60% water content [225, 226]. Further details of the adsorbent properties of these resins can be found in Chapter 5 [1].

TIFSIX-3-Ni in powder and then pellet form was synthesised as described in Chapter 4, and further details of its adsorbent properties can be found in Chapter 6 [2]. For the experiments discussed here, ~ 400 mg of the powder sample referred to as "batch 5" in that work was used to form a 13 mm diameter pellet with ~ 5 mm thickness. This pellet was then cut into 9 pieces using a scalpel following a grid pattern, yielding new pellets of ~ 4 mm in width and 5 mm in height. One of these pieces was then further cut into granules of ~ 1 to 2 mm in dimension to achieve more similar particle sizes compared to the resin beads to allow for a better comparison of the adsorption kinetics between the two classes of adsorbents. Pellets were also used in this study instead of powder as adsorbents in structured form would need to be used in an actual DAC process.

8.2.2 Kinetic sorption measurements

A NETZSCH TG 209 *F1* Libra thermogravimetric analyser (TGA) was used to conduct all kinetic sorption measurements. A simplified schematic of the instrument is shown in Figure 8.2a. For each experiment, gas from a pure He cylinder (BOC, N5.0 grade) was used as the protective gas, which interacted with the balance system before entering the sample chamber. He gas was chosen instead of N_2 to minimise additional adsorption on the samples, especially for the physisorbent TIFSIX-3-Ni. Gas from a cylinder containing ~ 800 ppm CO_2 balanced with He (BOC, research grade) was used as the sample gas, which entered above the balance and directly into the sample chamber. Here, the two gas streams mixed and interacted with the adsorbent sample in the crucible as they flowed up through the chamber and out of the top of the instrument. Three mixed gas cylinders were used to complete all measurements, whose CO_2 concentrations were 806 ppm, 832 ppm, and 834 ppm due to manufacturing variability. To create as close to a 400 ppm CO_2 in He environment within the sample chamber as possible to mimic dry ambient air, flowrate ratios between the mixed gas cylinder and pure He cylinder were varied between 0.9:1 to 1:1.

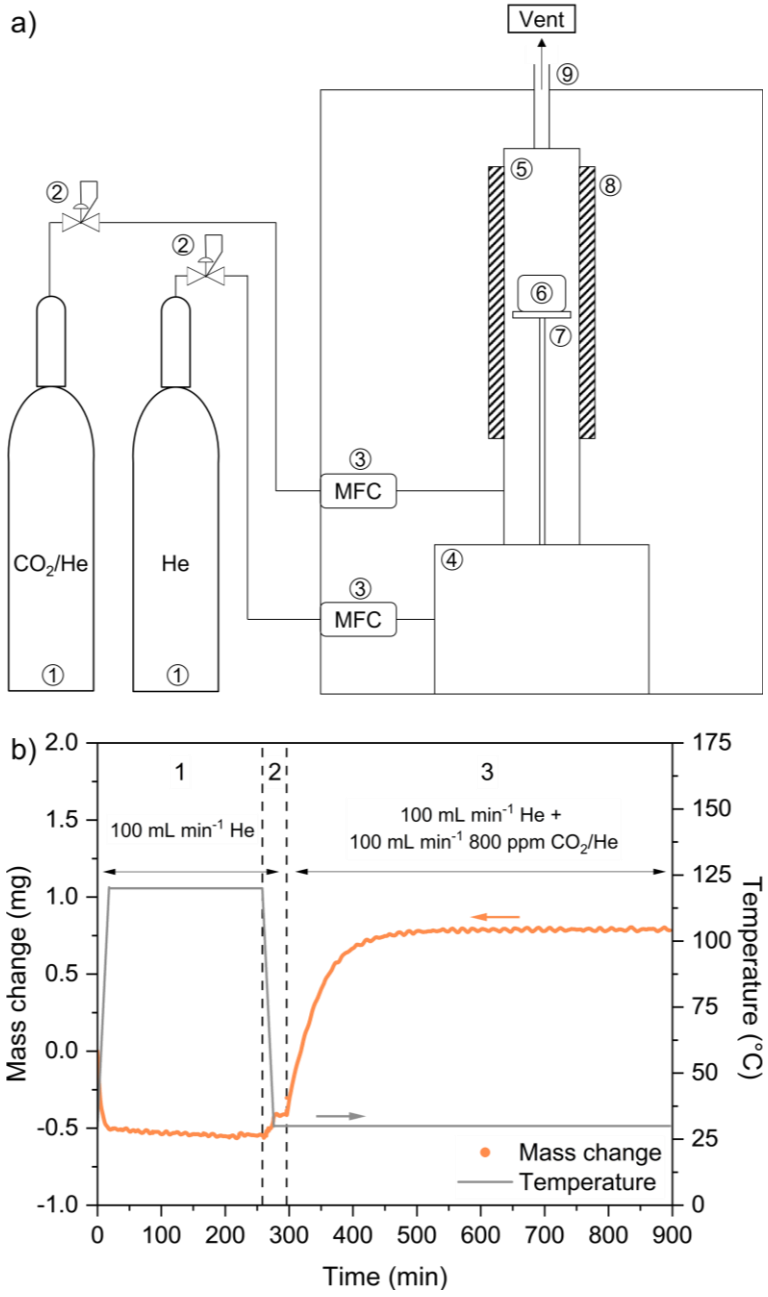


Figure 8.2. a) Simplified schematic of the set-up used for the kinetic sorption measurements, which includes (1) gas cylinders, (2) pressure reducing regulators, and a thermogravimetric analyser containing the following components: (3) mass flow controllers, (4) microbalance, (5) sample chamber, (6) crucible and (7) sample holder, (8) heating elements, and (9) gas outlet. b) Example of mass and temperature profiles over the course of a kinetic sorption measurement for a Purolite sample. Step 1: temperature increased from 30 to 120 °C and held for 4 h under a 100 mL min^{-1} He flow. Step 2: temperature decreased back to 30 °C and held for 20 min under the same He flow. Step 3: a 100 mL min^{-1} flow of the 800 ppm CO_2/He cylinder is then turned on for 10 h, at 30 °C.

A typical kinetic experiment consisted of three steps as shown in Figure 8.2b, during which the mass change of the sample was recorded as a function of time. First (step 1), sample was loaded into the TGA crucible and degassed under a flow of inert He gas until the mass remained stable. For experiments using Lewatit and Purolite, ~ 25 mg to 30 mg of sample was heated from 30 °C to 120 °C at a rate of 5 °C min^{-1} and held at this temperature for 4 h. For TIFSIX-3-Ni, ~ 15 mg to 20 mg of sample was heated from 30 °C to 160 °C at a rate of 5 °C min^{-1} and held at this temperature for 2 h. 30 °C was chosen as the starting temperature for all experiments as it was difficult to consistently maintain a lower temperature. After this time, the temperature was decreased to the desired temperature for CO_2 adsorption and allowed to equilibrate for 20 min (step 2). In this work, experiments were conducted at adsorption temperatures of 30 °C, 45 °C, and 60 °C. Finally (step 3), the flow of CO_2 was turned on to achieve an overall gas stream of 400 ppm CO_2 balanced with He, and the mass change of the sample due to CO_2 adsorption was recorded as a function of time. A total flowrate of 200 mL min^{-1} was used for measurements at 30 °C and 45 °C, while flowrates of 100 mL min^{-1}, 200 mL min^{-1}, and 300 mL min^{-1} were investigated for measurements at 60 °C. For Lewatit and Purolite, samples were exposed to 400 ppm CO_2 flow for 10 h, 6 h, and 4 h at 30 °C, 45 °C, and 60 °C, respectively, and a fresh sample was used for each measurement. For TIFSIX-3-Ni, the same sample was exposed to 400 ppm CO_2 flow for 3 h, 2.5 h, and 2 h at 30 °C, 45 °C, and 60 °C, respectively. These times were chosen to ensure that saturation of the sample would be achieved within this period, i.e. when the mass reaches a plateau. Three experiments were repeated at each temperature and flowrate.

Prior to the measurements, samples were degassed ex-situ overnight using a Micromeritics VacPrep™ 061 at 0.02 mbar and either 120 °C (Lewatit and Purolite) or 160 °C (TIFSIX-3-Ni), with the temperature increased from room temperature at a rate of 10 °C min^{-1} for the latter. A correction run with an empty crucible and identical analysis conditions was also performed before each measurement to account for buoyancy effects. I note that oscillations in the TGA mass signal, as can be seen in Figure 8.2b, sometimes occurred during experiments for both correction and sample measurements for indeterminate reasons (see Figures A6.1 to A6.5), but this did not significantly impact subsequent fitting and analysis procedures.

8.2.3 Data analysis

To calculate the k_{LDF} constant for each experiment, the data collected in step 3 of the procedure discussed above was first adjusted to the mass of CO_2 adsorbed as a function of time, with both mass and time starting at 0. This was then converted to a fractional uptake using equation (8.4):

$$f(t) = \frac{m(t) - m_{initial}}{m_{final} - m_{initial}} \qquad (8.4)$$

where $f(t)$ is the fractional mass uptake between 0 and 1 as a function of time t, $m(t)$ is the mass of CO_2 adsorbed at a given t, $m_{initial}$ is the mass of CO_2 adsorbed at $t = 0$, i.e. $m_{initial} = 0$, and m_{final} is the average mass of CO_2 adsorbed in the last 30 min of the experiment. This data was then fitted to an exponential form of the LDF model [305] using the non-linear curve fit function in OriginPro with the orthogonal distance regression iteration algorithm to give the k_{LDF} constant:

$$f(t) = 1 - e^{-k_{LDF} \cdot t} \qquad (8.5)$$

To compare the effect of different flowrates, the three sets of fractional uptake curves measured at each flowrate were averaged at each time data point, and the resulting mean $f(t)$ data set was fitted to equation (8.5) to obtain the k_{LDF} values using the non-linear curve fit function in OriginPro, with the standard deviation at each time point used to weight the fitting.

To compare the effect of different temperatures, a temperature dependence of the k_{LDF} constant was described using the Arrhenius equation shown in equation (8.6):

$$k_{LDF}(T) = k_0 \exp\left(\frac{-E_a}{RT}\right) \qquad (8.6)$$

where k_0 is the pre-exponential factor (or k_{LDF} at infinite temperature), E_a is the commonly called activation energy for mass transfer (though we note that not all mechanisms are necessarily activated), R is the universal gas constant, and T is the temperature.

To determine this temperature dependence for each adsorbent, fractional uptake curves repeated at each temperature were averaged at each time data point, and the resulting mean $f(t)$ data set at each temperature were fitted simultaneously to equation (8.5) and an alternative form of the Arrhenius equation shown as equation (8.7):

$$k_{LDF}(T) = \exp\left(ln(k_0) - \frac{E_a}{RT}\right) \qquad (8.7)$$

with the standard deviation at each time point used to weight the fitting. $\ln(k_0)$ and E_a were obtained as fitted parameters with associated uncertainty bounds for a 95% confidence interval which could then be used to calculate $k_{LDF}(T)$. The fitting procedure was again done using the non-linear curve fit function in OriginPro with the orthogonal distance regression iteration algorithm.

8.3 Results and discussion

8.3.1 Optimisation of experimental factors for kinetic sorption measurements

As mentioned previously, the k_{LDF} constant is an overall mass transfer coefficient describing the CO_2 adsorption kinetics, which accounts for both the CO_2 intraparticle diffusion and CO_2 rate of adsorption/reaction. In other words, any differences in the k_{LDF} constants should only be due to the adsorbent itself and not affected by external mass transfer limitations. The constant pressure approach used in this work requires the bulk gas phase composition to remain constant, therefore, one must ensure that mass transfer limitations from moving through the bed of beads/pellets are avoided and gas around the sample is adequately refreshed and not depleted of CO_2. This can be affected by the gas flow path in the instrument (not within user control), the dimensions of the crucible containing the sample, the amount of sample used, and the gas flow rate. The first part of this work therefore requires optimisation of the sample holder and gas flow rates to minimise external mass transfer limitations for the sample masses used (~ 15 to 30 mg). I assumed that these masses were sufficiently low to avoid any heat transfer effects, and calculations were subsequently conducted to confirm operation in near isothermal conditions (see Appendix 6 for details).

8.3.1.1 Effect of crucible

The standard alumina crucibles are only open to fluid flow at the top and therefore not ideal for the envisioned measurements. As explained in Section 8.2.2, gas flows from the bottom and up through this TGA's sample chamber, which prevents a good mixing with the sample when using a standard crucible. In this scenario, the gas only flows around the crucible and directly interacts with the top layer

of sample particles, before diffusing through the crucible to reach the particles below. As a result, the calculated k_{LDF} would be an underestimation.

To optimise the gas flow through the sample, I used an aluminium crucible modified by drilling 0.2 mm holes at the base with a 0.5 mm square pitch. This was meant to allow gas flow through the sample, rather than around the crucible. A significant proportion of these drilled holes on the base however would have been blocked by the TGA sample holder platform. Hence, to further optimise the set-up, a makeshift basket made of perforated stainless steel was formed in which the aluminium crucible could be placed. The rim of the crucible rests on the edge of the basket and elevates the base of the crucible from the sample holder platform. Photographs of all three crucible iterations are shown in Figure 8.3a.

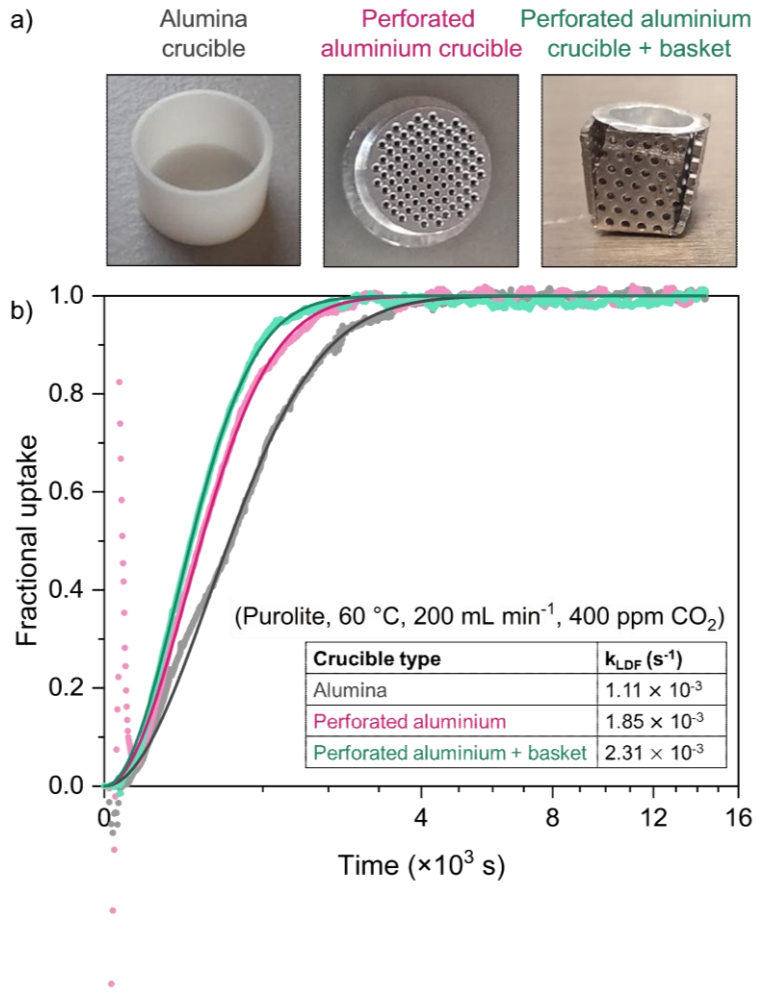


Figure 8.3. a) Photographs of the standard alumina crucible, perforated aluminium crucible, and perforated aluminium crucible in the makeshift basket. b) Comparison of the experimental (filled circles) and fitted (solid lines) fractional uptakes and corresponding k_{LDF} constants of Purolite samples measured using the standard alumina crucible, perforated aluminium crucible, and perforated aluminium crucible in the makeshift basket. Time is plotted on a square root scale for clarity.

To test each set-up (i.e. standard alumina crucible, perforated aluminium crucible, and perforated aluminium crucible with a makeshift basket), I conducted TGA measurements on samples of Purolite at 60 °C under a total flowrate of 200 mL min^{-1} of 400 ppm CO_2 balanced with He (Figure 8.3b). I chose to use 60 °C since the adsorption kinetics would be fastest at this temperature amongst the selected range, thus any impacts of external mass transfer resistance would be amplified. As seen from Figure 8.3b, using the perforated aluminium crucible with the makeshift basket allowed for the

fastest CO_2 adsorption kinetics. This set-up was therefore used for all further experiments. I note the presence of some sharp spikes/dips in the experimental fractional uptake, particularly for the perforated aluminium crucible during the first few seconds of step 3. This is likely an artefact of the sudden introduction of CO_2, and was also sometimes observed in subsequent experiments (Figures A6.1 to A6.5). However, these experimental discrepancies did not significantly affect the fitting of the k_{LDF} constant. Overall, these modifications improved the mixing of gas with the sample and reduced any mass transfer limitations due to the crucible as much as possible.

8.3.1.2 Effect of flowrate

Having minimised mass transfer limitations from the crucible, I then investigated the optimal gas flowrate for the experiments. The flowrate should be high enough such that gas supply to the adsorbent does not affect the CO_2 adsorption kinetics, but not unnecessarily high, leading to excessive gas consumption. To identify an appropriate flowrate, TGA experiments and subsequent k_{LDF} calculations were conducted as described in Section 8.2.2 and 8.2.3 for Purolite and TIFSIX-3-Ni samples at 60 °C with total flowrates of 100 mL min^{-1}, 200 mL min^{-1}, and 300 mL min^{-1}. I assumed that the optimal flowrate determined for Purolite would be applicable for Lewatit, as these adsorbents exhibit similar particle size, morphology, and CO_2 adsorption mechanisms [1]. I again chose to use 60 °C to ensure that any external mass transfer limitations are overcome at the most stringent conditions.

Purolite and TIFSIX-3-Ni samples were exposed to a 400 ppm CO_2 flow for 4 h and 2 h, respectively, to ensure saturation was achieved. Experiments were conducted in triplicates for each flowrate and for each adsorbent. The experimental and fitted *f(t)* data for these measurements are shown in Figures A6.1 and A6.2. For experiments using the 806 ppm CO_2 mixed gas cylinder, the flowrates used were either 50 mL min^{-1}, 100 mL min^{-1}, or 150 mL min^{-1} for both CO_2/He and He to achieve total flowrates of 100 mL min^{-1}, 200 mL min^{-1}, and 300 mL min^{-1}, respectively. For experiments using the 832 or 834 ppm CO_2 mixed gas cylinder, the flowrates used for CO_2/He and He were 50 and 50 mL min^{-1}, 95 and 105 mL min^{-1}, and 145 and 155 mL min^{-1}, to achieve total flowrates of 100 mL min^{-1}, 200 mL min^{-1}, and 300 mL min^{-1}, respectively.

The results of these experiments are summarised in Figure 8.4. For Purolite and TIFSIX-3-Ni adsorbents, increasing the total flowrate from 100 mL min^{-1} to 200 mL min^{-1} resulted in a 48% and 97% increase in the average k_{LDF}, respectively. Further increasing the flowrate from 200 mL min^{-1} to 300 mL min^{-1} resulted in limited increases of 4% and 9%, respectively. Therefore, 200 mL min^{-1} was selected as the optimal flowrate to minimise external mass transfer limitations while also conserving gas supply, and this flowrate was used for all further experiments.

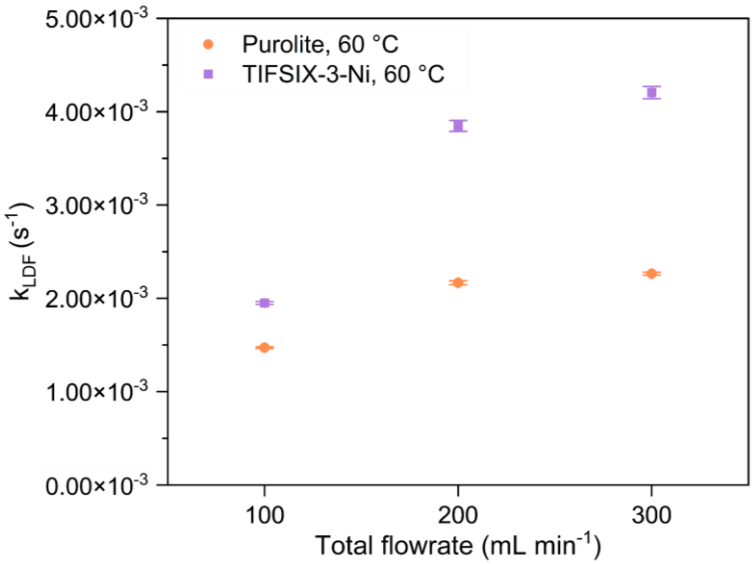


Figure 8.4. Comparison of the average k_{LDF} constants with error bars for a 95% confidence interval for Purolite and TIFSIX-3-Ni calculated at 100 mL min^{-1}, 200 mL min^{-1}, and 300 mL min^{-1} total flowrates of 400 ppm CO_2 in He.

8.3.2 Temperature-dependent kinetic sorption measurements

For process modelling, a temperature-dependent k_{LDF} constant should be determined for adsorbents of interest, as it allows accurate modelling of the kinetics throughout the entire cycle (i.e. adsorption, desorption, and transition steps). Similarly, the dependence of the k_{LDF} values on the CO_2 concentration should also be investigated since the CO_2 concentration may vary along the length of the column as gas is adsorbed. However, in this work I focused my experiments on the initial feed gas concentration in a DAC process of 400 ppm CO_2. To obtain a temperature-dependent k_{LDF} for Lewatit, Purolite, and TIFSIX-3-Ni, experiments were carried out as described in Section 8.2.2 for each

adsorbent at 30 °C, 45 °C, and 60 °C, with a total flowrate of 200 mL min^{-1} of 400 ppm CO_2 balanced with He using the perforated aluminium crucible with a stainless-steel basket. For each adsorbent, three experiments were repeated at each of the three temperatures, and subsequent data analysis was conducted following the procedure outlined in Section 8.2.3. The experimental and fitted *f(t)* data for these measurements are shown in Figures A6.3 to A6.5. The fitted parameter values for $\ln(k_0)$ and E_a are shown below in Table 8.1, along with associated uncertainty bounds for a 95% confidence interval. These parameters are then used to calculate k_{LDF} as a function of temperature, and their uncertainty bounds can be propagated to determine uncertainty bounds on $k_{LDF}(T)$ (see Appendix 6 for details). These fitted results are shown in Figure 8.5, with an extrapolation of 10 °C above and below the measured temperature range.

Table 8.1. Fitting parameters for equation (8.7) with uncertainty bounds for a 95% confidence interval for Lewatit, Purolite, and TIFSIX-3-Ni. k_0 is the pre-exponential factor (or k_{LDF} at infinite temperature) of the Arrhenius equation and E_a is the activation energy for mass transfer.

	$\ln(k_0)$ (s^{-1})	E_a (kJ mol^{-1})
Lewatit	4.987 ± 0.055	32.90 ± 0.14
Purolite	11.00 ± 0.09	47.89 ± 0.25
TIFSIX-3-Ni	6.778 ± 0.174	33.79 ± 0.44

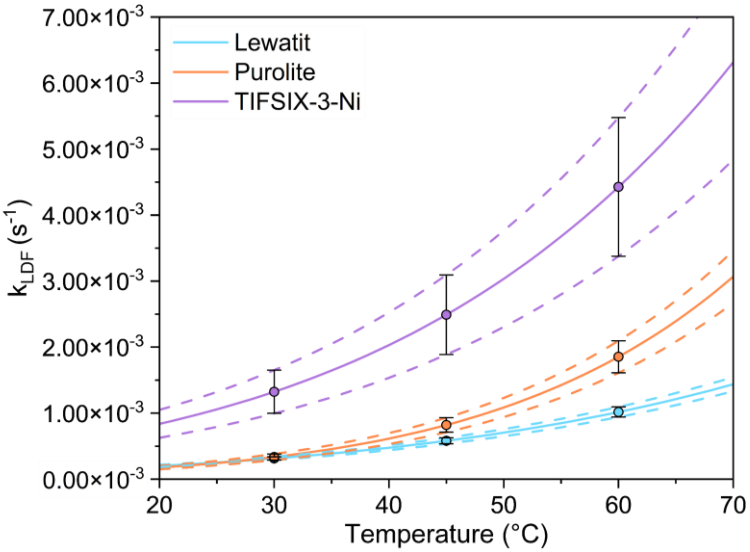


Figure 8.5. Comparison of temperature-dependent k_{LDF} constants with uncertainty bounds (dashed lines) for a 95% confidence interval between 20 °C and 70 °C for Lewatit, Purolite, and TIFSIX-3-Ni. Individual data points indicate the temperatures at which k_{LDF} constants were experimentally measured.

The two resins, Lewatit and Purolite, exhibit similar k_{LDF} constants up to 40 °C, with values of 4.76×10^{-4} s^{-1} and 6.14×10^{-4} s^{-1}, respectively at this temperature. As the temperature increases beyond 40 °C, Purolite begins to have significantly faster adsorption kinetics compared to Lewatit. The kinetic resistances dependent on temperature are molecular diffusion ($T^{1.7}$ dependence), Knudsen diffusion ($T^{1/2}$ dependence), surface diffusion, and the rate of chemical reaction (both $e^{-Ea/RT}$ dependence) [294]. Therefore, one or more of these resistances may be more dominant in Purolite compared to Lewatit, though the dominant resistance may change throughout our measured temperature range. Since the k_{LDF} of Purolite increases faster with temperature compared to Lewatit, this may suggest a lower activation energy for surface diffusion and/or reaction in Purolite.

At 25 °C, we calculated the k_{LDF} for Lewatit to be 2.52×10^{-4} s^{-1}. This agrees well with the k_A value of 2.5×10^{-4} s^{-1} reported by Wu et al. [44] for Lewatit, who fitted their TGA uptake data measured at 25 °C and 400 ppm CO_2 to the Avrami model given by equation (8.8):

$$q = q_e\left(1 - e^{-(k_A t)^n}\right) \quad (8.8)$$

where q is the amount of CO_2 adsorbed at time t, q_e is the CO_2 equilibrium adsorption capacity, k_A is the Avrami mass transfer coefficient, and n is the Avrami constant. Since the authors reported an n value of 0.9710 (i.e. close to 1), k_A can be roughly compared to k_{LDF}.

In another comparison, Young et al. reported a constant k_{LDF} of 0.003 s^{-1} for Lewatit at 1%$_{vol}$ (or 10,000 ppm) CO_2 concentration between 25 °C and 70 °C [150], which represents an order of magnitude difference between our results at 25 °C. We note that Young et al. performed dynamic column breakthrough experiments with ~ 200 mg of sample and assumed isothermal operation of their column, where any changes in the temperature of the adsorbent would not be accounted for and could result in an inflated k_{LDF}. This discrepancy is also likely due to the difference in CO_2 concentration, as Lewatit is a macroporous resin and thus it is likely there is a mass transfer resistance arising from macropore diffusion, which is impacted by the gas phase concentration. Indeed, Bos et al. previously reported a concentration dependence of the CO_2 adsorption kinetics for Lewatit, where the CO_2 uptake of Lewatit was faster with pure CO_2 compared to 50% and 25% CO_2 diluted with N_2 [217]. Therefore, it is important for future studies to conduct their kinetic sorption experiments at the relevant CO_2 concentrations for DAC to achieve accurate kinetic estimations. Confirmation of the presence of macropore diffusion in the resins could also be achieved by varying the bead size through sieving and observing a change in the k_{LDF} values, where smaller particles would demonstrate faster kinetics.

TIFSIX-3-Ni displays significantly faster adsorption kinetics compared to Lewatit and Purolite over the 20 °C to 70 °C temperature range, ranging from 8.38×10^{-4} to 6.32×10^{-3} s^{-1}. I hypothesise that this is due to the absence of reaction kinetics in TIFSIX-3-Ni as it is a physisorbent, resulting in an overall faster CO_2 adsorption rate. In terms of the intraparticle diffusion, there is likely a contribution of both micropore and macropore diffusion due to the intrinsic ultramicropores in TIFSIX-3-Ni and pelletisation of the sample, respectively. Varying the pellet size of TIFSIX-3-Ni used in these experiments and observing changes in the k_{LDF} would confirm the presence of macropore diffusion, however it still would not be possible to quantify the contribution of each resistance without further experiments.

I also calculated the average equilibrium CO_2 loading for the TGA experiments conducted at each temperature (see Appendix 6 for details). I compared these to the CO_2 loadings calculated from

the CO_2 isotherm fitting model parameters determined from volumetric sorption experiments as discussed in Chapters 5 and 6 [1, 2]. This analysis helps to verify that the equilibrium results from the TGA are indeed reasonable, and that subsequently the kinetic results which rely on the final equilibrium loading should be reliable as well. The CO_2 isotherm models and their fitted parameters for Lewatit, Purolite, and TIFSIX-3-Ni were previously presented in Chapters 5 and 6, and here again in Appendix 6. As seen from Figure 8.6, the average loadings determined from the two methods are in relatively good agreement at 45 °C and 60 °C (~ 5% to 20% difference, except for ~ 30% difference for TIFSIX-3-Ni at 60 °C), while there is a larger discrepancy between the averaged results at 30 °C (~ 20% to 35% difference). The temperature calibration for the TGA used in this study was performed using elements with relatively high melting points (~ 150 °C to 1110 °C), and so the temperature control may not be as accurate at 30 °C compared to higher temperatures. Fluctuations in the TGA balance reading as observed in Figures A6.3 to A6.5 were likely another source of error. In comparison, the porosity analyser used for the volumetric sorption experiments could achieve better resolution, better sample activation (degassed in-situ at 120 °C and 0.00002 mbar for 24 h), and experimental checks were done in our previous works to ensure that equilibrium was indeed reached during measurements (Figures A3.5 and A4.4). Overall, however, the results from the two methods are relatively comparable with almost all error bars overlapping, and are in better agreement with increasing temperature.

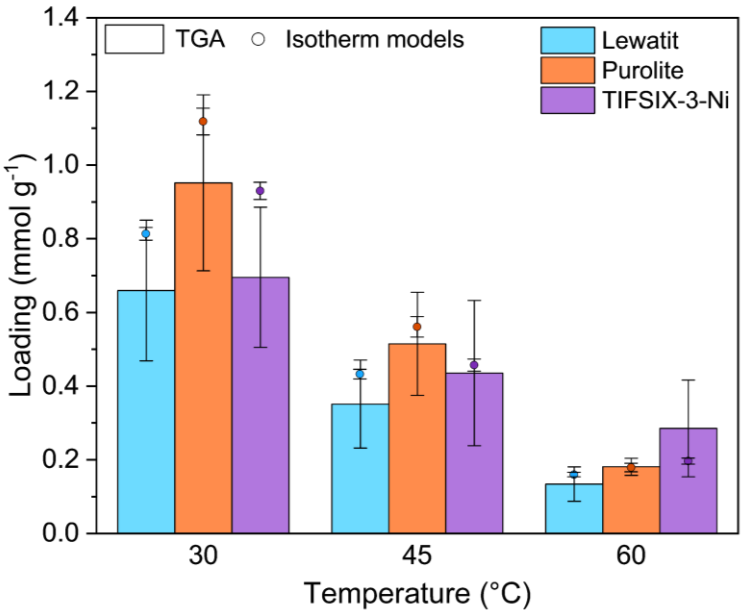


Figure 8.6. Comparison of the averaged equilibrium CO_2 loadings for Lewatit, Purolite, and TIFSIX-3-Ni at 30 °C, 45 °C, and 60 °C and 400 ppm CO_2 concentration determined from TGA experiments and CO_2 sorption isotherm models with error bars for a 95% confidence interval.

8.4 Conclusions

This work provides a quantitative evaluation of the CO_2 adsorption kinetics for three promising DAC adsorbents, Lewatit VP OC 1065, Purolite A110, and TIFSIX-3-Ni, by extracting temperature-dependent linear driving force constants, $k_{LDF}(T)$ under DAC conditions (i.e. 400 ppm CO_2). I measured the mass of CO_2 adsorbed over time using a thermogravimetric analyser from a flow of 400 ppm CO_2 balanced with He at 30 °C, 45 °C, and 60 °C, and fitted the experimental data using the linear driving force model. To ensure the accuracy of the method, I minimised external mass transfer limitations by adapting the experimental set-up and operating conditions, i.e. sample holder and gas flow rates.

The results show that TIFSIX-3-Ni displays faster adsorption kinetics than the resins between 20 °C to 70 °C. At 25 °C, the k_{LDF} constant for TIFSIX-3-Ni is 1.13×10^{-3} s^{-1}, compared to 2.36×10^{-4} $s^{-1}$and 2.77×10^{-4} s^{-1} for Lewatit and Purolite, respectively. I attribute this to the lack of chemical reaction with CO_2 as TIFSIX-3-Ni is a physisorbent, resulting in a faster CO_2 rate of adsorption compared to the resins which have additional resistance from their reaction kinetics. Purolite and Lewatit have

comparable kinetics up to 40 °C, after which Purolite exhibits faster kinetics than Lewatit, potentially due to a smaller activation energy for surface diffusion and/or reaction rate.

In terms of future work, additional experiments should be done if k_{LDF} constants at temperatures below 20 °C or above 70 °C are desired, rather than relying on further extrapolation. The k_{LDF} values calculated here are also only valid for the particle sizes measured. Future experiments should be conducted with a range of adsorbent particle sizes to determine its influence on the adsorption kinetics. In addition, repeating some experiments with a lower sample mass would help to confirm the absence of external mass transfer limitations due to adsorbent packing, especially if higher temperatures are used where the intraparticle adsorption kinetics may no longer be the limiting step. The k_{LDF} values calculated here are also only valid at a CO_2 concentration of 400 ppm, however the CO_2 concentration may vary along the length of the column as gas is adsorbed. Therefore, additional kinetic measurements should be conducted which account for variations in concentration, either by repeating the procedure used in this work at multiple CO_2 concentrations, or using a different experimental methodology from which the micropore and macropore diffusion resistances can be extracted, such as the zero length column method [48, 300]. Overall, the $k_{LDF(T)}$ values determined in this work can now be used for initial process scale modelling to assess the process performance of Lewatit, Purolite, and TIFSIX-3-Ni for DAC.

Chapter 9: Conclusions

9.1 Summary of findings

The objectives of this thesis were to investigate the physicochemical, equilibrium sorption, and kinetic sorption properties of select promising DAC adsorbents representing three classes of materials, i.e. polymeric resins, ultramicroporous MOFs and functionalized zeolite Ys. The specific adsorbents studied included: Lewatit VP OC 1065, Purolite A110, TIFSIX-3-Ni, and in-house developed amine-functionalised zeolite Ys.

In Chapter 5, I conducted the first assessment of Purolite A110 for DAC applications by measuring its physicochemical and equilibrium sorption properties and comparing them to those of Lewatit VP OC 1065, one of only two materials with all the necessary adsorbent properties needed for DAC process modelling reported. Purolite showed great promise as an adsorbent for DAC, exhibiting higher gravimetric and volumetric CO_2 adsorption capacity and lower CO_2 heat of adsorption compared to Lewatit, while maintaining similar N_2 and H_2O heats of adsorption. A new empirical CO_2 isotherm model combining chemisorption and physisorption terms was also proposed which provided a better fit of the experimental data compared to existing models.

In Chapter 6, I successfully synthesised TIFSIX-3-Ni and measured its physicochemical and equilibrium adsorption properties. I demonstrated that the adsorbent can be shaped into pellets without the use of binder and with minimal loss in CO_2 adsorption performance. Adsorbent properties such as densities, specific heat capacity, CO_2, N_2 and H_2O isotherm model parameters, and N_2 and H_2O heats of adsorption were reported for TIFSIX-3-Ni for the first time. Based on these properties, TIFSIX-3-Ni showed great promise as a DAC adsorbent. However, I also determined that TIFSIX-3-has limited stability under high temperature and humidity conditions (e.g. 40 °C and 75% RH), though its stability may be improved when used in more temperate climates. TIFSIX-3-Ni also has a maximum lifetime of no more than 6 months, as exposure to ambient air for this period already resulted in more than 50% reduction in its CO_2 adsorption capacity.

In Chapter 7, I hypothesised that amine-functionalisation of a hydrophobic zeolite Y would yield an adsorbent with high affinity for CO_2 while maintaining minimal H_2O adsorption. I synthesised

these adsorbents via either aminosilane or NH_3 functionalisation, and preliminarily assessed their suitability for DAC applications by measuring CO_2, N_2, and H_2O isotherms at 25 °C. Only the adsorbents synthesised via aminosilane functionalisation yielded improved CO_2 adsorption, though the extremely slow isotherm measurement time suggested the presence of pore blockage. H_2O adsorption was also increased in both adsorbent types, particularly for NH_3-functionalised adsorbents at moderate to high relative humidity (i.e. greater than 50% RH). Without further optimisation, these adsorbents are currently not suitable for use in a DAC process.

Lastly, in Chapter 8, I determined the temperature-dependent CO_2 adsorption kinetics of Lewatit, Purolite, and TIFSIX-3-Ni at 400 ppm CO_2 concentration using a gravimetric sorption set-up. The gravimetric CO_2 uptake was measured over time at multiple temperatures, and the experimental data fitted to the linear driving force model. External mass transfer limitations were also minimised by adjusting the experimental set-up and operating conditions, i.e. sample holder and gas flow rates. Amongst the three adsorbents, TIFSIX-3-Ni had the fastest adsorption kinetics across all temperatures most likely due to its lack of chemical reaction with CO_2. Purolite and Lewatit had comparable kinetics up to 40 °C, after which Purolite exhibited faster kinetics than Lewatit, potentially due to a smaller activation energy for surface diffusion and/or reaction rate.

Overall, my PhD has helped address the data gap in adsorption materials for DAC and improve the synergy between adsorbent and process development. The adsorbent data collected can now be used to facilitate process scale evaluation of these adsorbents, which will help continue the advancement and scale-up of adsorption-based DAC.

9.2 Perspectives and future work

While my thesis has advanced the knowledge of the DAC adsorbents selected for this work, further studies could still be conducted to provide deeper insights.

Due to a lack of nearby experimental resources, I was not able to measure the thermal conductivity of the adsorbents studied. This parameter would be important to measure directly as it influences the overall heat transfer in a DAC process. For now, the thermal conductivity of Purolite

could be assumed to be the same as that of Lewatit, whose data is currently available in the literature [217]. Similarly, the thermal conductivities of Ni-MOF-74 or MIL-101(Cr) powder [317] could be used to approximate that of TIFSIX-3-Ni. I note that the pore sizes of these MOFs are larger than those of the ultramicroporous TIFSIX-3-Ni, however these were the only MOFs reviewed with experimentally measured thermal conductivities reported.

For TIFSIX-3-Ni specifically, further studies are needed to gain a better fundamental understanding on the interaction of water with the crystal structure of TIFSIX-3-Ni, which could eventually help improve the stability of TIFSIX-3-Ni at high humidity. Possible experiments could include single crystal XRD or in-situ total X-ray scattering measurements [258]. Additional studies to probe the possible structure flexibility of TIFSIX-3-Ni would also be useful to better understand its gas and vapour adsorption performance. These could include additional XRD measurements at higher pressures / lower temperatures coupled with structure refinement procedures.

For the amine-functionalised zeolite Ys, an optimisation study should be done on the aminosilane amounts to determine an ideal loading which minimises mass transfer resistances and H_2O adsorption while still allowing for satisfactory CO_2 uptake. In addition, NH_3 functionalisation may have yielded sufficient amine loading but without the proximity/flexibility needed for CO_2 adsorption in dry conditions, where two amine groups are needed to react with CO_2. Binary CO_2-H_2O co-adsorption experiments using zero length column (ZLC) or temperature-programmed desorption techniques should therefore be conducted to investigate if the CO_2 adsorption is improved in the presence of humidity, where only one amine group would be needed to react with CO_2.

Lastly, for the CO_2 adsorption kinetics, additional uptake experiments encompassing a wider temperature range and different CO_2 concentrations should be conducted to cover the full range of possible DAC process conditions. Alternatively, a different experimental set-up such as the ZLC technique could be used [48, 300], which can account for temperature and concentration dependence through the extraction of micropore and macropore diffusion contributions.

In a broader context, I hope my work will encourage others in the field to improve the synergy between adsorbent and process development for DAC by adopting a similar systematic approach when characterising and reporting new promising adsorbents. I do acknowledge however that it is extremely

time consuming to conduct all the experiments needed for thorough adsorbent characterisation, and it would not be practical to do so for every adsorbent studied. However, conducting the full suite of characterisation might still remain useful for reference adsorbents. In addition, researchers involved in DAC process development should therefore help to identify the adsorbent parameters which have the largest impact on process performance. These can then be measured by researchers developing new adsorbents to allow for initial adsorbent screening in a particular process. A thorough set of adsorbent characterisations can then be done for the most promising adsorbents. Works such as those by Young et al. [43] and Wu et al. [44] have already begun to address this need.

References

[1] M.-Y. Low, D. Danaci, H. Azzan, R. T. Woodward, and C. Petit, "Measurement of Physicochemical Properties and CO_2, N_2, Ar, O_2, and H_2O Unary Adsorption Isotherms of Purolite A110 and Lewatit VP OC 1065 for Application in Direct Air Capture," *Journal of Chemical & Engineering Data,* vol. 68, no. 12, pp. 3499-3511, Dec 14 2023, doi: 10.1021/acs.jced.3c00401.

[2] M. A. Low, D. Danaci, H. Azzan, A. L. Jiayi, G. W. S. Yong, I. Itskou, and C. Petit, "Physicochemical Properties, Equilibrium Adsorption Performance, Manufacturability, and Stability of TIFSIX-3-Ni for Direct Air Capture of CO_2," *Energy Fuels,* vol. 38, no. 13, pp. 11947-11965, Jul 4 2024, doi: 10.1021/acs.energyfuels.4c01368.

[3] P. A. Arias, B. N, E. Coppola, R. G. Jones, G. Krinner, J. Marotzke, M. D. P. V. Naik, G. K. Plattner, J. Rogelj, M. Rojas, J. Sillmann, T. Storelvmo, P. W. Thorne, B. Trewin, K. A. Rao, B. Adhikary, R. P. Allan, K. Armour, G. Bala, R. Barimalala, S. Berger, J. G. Canadell, C. Cassou, A. Cherchi, W. Collins, W. D. Collins, S. L. Connors, S. Corti, F. Cruz, F. J. Dentener, C. Dereczynski, A. D. Luca, A. D. Niang, F. J. Doblas-Reyes, A. Dosio, H. Douville, F. Engelbrecht, V. Eyring, E. Fischer, P. Forster, B. Fox-Kemper, J. S. Fuglestvedt, J. C. Fyfe, N. P. Gillett, L. Goldfarb, I. Gorodetskaya, J. M. Gutierrez, R. Hamdi, E. Hawkins, H. T. Hewitt, P. Hope, A. S. Islam, C. Jones, D. S. Kaufman, R. E. Kopp, Y. Kosaka, J. Kossin, S. Krakovska, J.-Y. Lee, T. M. J. Li, T. K. Maycock, M. Meinshausen, S.-K. Min, P. M. S. Monteiro, T. Ngo-Duc, F. Otto, I. Pinto, A. Pirani, K. Raghavan, R. Ranasinghe, A. C. Ruane, L. Ruiz, J.-B. Sallée, B. H. Samset, S. Sathyendranath, S. I. Seneviratne, A. A. Sörensson, S. Szopa, I. Takayabu, A.-M. Tréguier, B. v. d. Hurk, R. Vautard, K. v. Schuckmann, S. Zaehle, X. Zhang, and K. Zickfeld, "Climate Change 2021: The Physical Science Basis. Contribution of Working Group I to the Sixth Assessment Report of the Intergovernmental Panel on Climate Change," IPCC, 2021.

[4] S. Budinis. "Direct Air Capture." International Energy Agency. https://www.iea.org/energy-system/carbon-capture-utilisation-and-storage/direct-air-capture (accessed 2024).

[5] S. M. Smith, O. Geden, G. F. Nemet, M. J. Gidden, W. F. Lamb, C. Powis, R. Bellamy, M. W. Callaghan, A. Cowie, E. Cox, S. Fuss, T. Gasser, G. Grassi, J. Greene, S. Lück, A. Mohan, F. Müller-Hansen, G. P. Peters, Y. Pratama, T. Repke, K. Riahi, F. Schenuit, J. Steinhauser, J. Strefler, J. M. Valenzuela, and J. C. Minx, "The State of Carbon Dioxide Removal - 1st Edition," The State of Carbon Dioxide Removal, 2023. [Online]. Available: http://dx.doi.org/10.17605/OSF.IO/W3B4Z

[6] A. Rajendran, S. G. Subraveti, K. N. Pai, V. Prasad, and Z. Li, "How Can (or Why Should) Process Engineering Aid the Screening and Discovery of Solid Sorbents for CO_2 Capture?," *Accounts of Chemical Research,* vol. 56, no. 17, pp. 2354-2365, Sep 5 2023, doi: 10.1021/acs.accounts.3c00335.

[7] M. Khurana and S. Farooq, "Adsorbent Screening for Postcombustion CO_2 Capture: A Method Relating Equilibrium Isotherm Characteristics to an Optimum Vacuum Swing Adsorption Process Performance," *Industrial & Engineering Chemistry Research* vol. 55, no. 8, pp. 2447-2460, Mar 2 2016, doi: 10.1021/acs.iecr.5b04531.

[8] A. K. Rajagopalan, A. M. Avila, and A. Rajendran, "Do adsorbent screening metrics predict process performance? A process optimisation based study for post-combustion capture of CO_2," *International Journal of Greenhouse Gas Control,* vol. 46, pp. 76-85, 2016, doi: 10.1016/j.ijggc.2015.12.033.

[9] A. H. Farmahini, S. Krishnamurthy, D. Friedrich, S. Brandani, and L. Sarkisov, "Performance-Based Screening of Porous Materials for Carbon Capture," *Chemical Reviews,* vol. 121, no. 17, pp. 10666-10741, Sep 8 2021, doi: 10.1021/acs.chemrev.0c01266.

[10] M.-Y. Low, L. V. Barton, R. Pini, and C. Petit, "Analytical review of the current state of knowledge of adsorption materials and processes for direct air capture," *Chemical Engineering Research and Design,* vol. 189, pp. 745-767, 2023, doi: 10.1016/j.cherd.2022.11.040.

[11] M. Erans, E. S. Sanz-Pérez, D. P. Hanak, Z. Clulow, D. M. Reiner, and G. A. Mutch, "Direct air capture: process technology, techno-economic and socio-political challenges," *Energy and Environmental Science,* vol. 15, pp. 1360-1405, 2022, doi: 10.1039/d1ee03523a.

[12] E. S. Sanz-Perez, C. R. Murdock, S. A. Didas, and C. W. Jones, "Direct Capture of CO_2 from Ambient Air," *Chemical Reviews,* vol. 116, no. 19, pp. 11840-11876, 2016, doi: 10.1021/acs.chemrev.6b00173.

[13] L. Jiang, W. Liu, R. Q. Wang, A. Gonzalez-Diaz, M. F. Rojas-Michaga, S. Michailos, M. Pourkashanian, X. J. Zhang, and C. Font-Palma, "Sorption direct air capture with CO_2 utilization," *Progress in Energy and Combustion Science,* vol. 95, 2023, doi: 10.1016/j.pecs.2022.101069.

[14] K. An, K. Li, C.-M. Yang, J. Brechtl, and K. Nawaz, "A comprehensive review on regeneration strategies for direct air capture," *Journal of CO_2 Utilization,* vol. 76, 2023, doi: 10.1016/j.jcou.2023.102587.

[15] T. H. Lim, J. E. Foster, B. R. Ellis, and S. J. Skerlos, "Microwave-based CO_2 desorption for enhanced direct air capture: experimental validation and techno-economic perspectives," *Environmental Research Letters,* vol. 19, no. 3, 2024, doi: 10.1088/1748-9326/ad239f.

[16] T. Ji, H. Zhai, C. Wang, C. M. Marin, W. C. Wilfong, Q. Wang, Y. Duan, R. Xia, F. Jiao, Y. Soong, F. Shi, and M. Gray, "Energy-efficient and water-saving sorbent regeneration at near room temperature for direct air capture," *Materials Today Sustainability,* vol. 21, 2023, doi: 10.1016/j.mtsust.2023.100321.

[17] T. N. van Schagen, P. J. van der Wal, and D. W. F. Brilman, "Development of a novel, through-flow microwave-based regenerator for sorbent-based direct air capture," *Chemical Engineering Journal Advances,* vol. 9, 2022, doi: 10.1016/j.ceja.2021.100187.

[18] E. R. Kearns, Q. Xia, R. Gillespie, N. Proschogo, P. W. Doheny, M. B. Solomon, and D. M. D'Alessandro, "3D Printing of Monoliths Using TIFSIX-Ni-Based Formulations for the Electric Swing Adsorption of CO_2," *ACS Applied Materials & Interfaces,* vol. 15, no. 27, pp. 32935-32944, Jul 12 2023, doi: 10.1021/acsami.3c05495.

[19] "Carbfix." https://www.carbfix.com/ (accessed 2024).

[20] J. V. Veselovskaya, P. D. Parunin, O. V. Netskina, and A. G. Okunev, "A Novel Process for Renewable Methane Production: Combining Direct Air Capture by K_2CO_3/Alumina Sorbent with CO_2 Methanation over Ru/Alumina Catalyst," *Topics in Catalysis,* vol. 61, no. 15-17, pp. 1528-1536, 2018, doi: 10.1007/s11244-018-0997-z.

[21] F. Bisotti, K. A. Hoff, A. Mathisen, and J. Hovland, "Direct air capture (DAC) deployment: A review of the industrial deployment," *Chemical Engineering Science,* vol. 283, 2024, doi: 10.1016/j.ces.2023.119416.

[22] E. Wang, R. Navik, Y. Miao, Q. Gao, D. Izikowitz, L. Chen, and J. Li, "Reviewing direct air capture startups and emerging technologies," *Cell Reports Physical Science,* vol. 5, no. 2, 2024, doi: 10.1016/j.xcrp.2024.101791.

[23] S. Budinis, "Direct Air Capture," International Energy Agency, 2022. [Online]. Available: https://iea.blob.core.windows.net/assets/78633715-15c0-44e1-81df-41123c556d57/DirectAirCapture_Akeytechnologyfornetzero.pdf

[24] B. K. Sovacool, C. M. Baum, S. Low, C. Roberts, and J. Steinhauser, "Climate policy for a net-zero future: ten recommendations for Direct Air Capture," *Environmental Research Letters,* vol. 17, no. 7, 2022, doi: 10.1088/1748-9326/ac77a4.

[25] M. Ozkan, S. P. Nayak, A. D. Ruiz, and W. Jiang, "Current status and pillars of direct air capture technologies," *iScience,* vol. 25, no. 4, p. 103990, Apr 15 2022, doi: 10.1016/j.isci.2022.103990.

[26] "Global Thermostat unveils one of the world's largest units for removing carbon dioxide directly from the air." Global Thermostat. https://www.globalthermostat.com/news-and-updates/global-thermostat-colorado-headquarters (accessed 2024).

[27] "About Soletair Power." Soletair Power. https://www.soletairpower.fi/about-us/ (accessed 2024).

[28] F. Kong, G. Rim, M. G. Song, C. Rosu, P. Priyadarshini, R. P. Lively, M. J. Realff, and C. W. Jones, "Research needs targeting direct air capture of carbon dioxide: Material & process performance characteristics under realistic environmental conditions," *Korean Journal of Chemical Engineering,* vol. 39, pp. 1-19, 2022, doi: 10.1007/s11814-021-0976-0.

[29] J. F. Wiegner, A. Grimm, L. Weimann, and M. Gazzani, "Optimal Design and Operation of Solid Sorbent Direct Air Capture Processes at Varying Ambient Conditions," *Industrial & Engineering Chemistry Research* vol. 61, no. 34, pp. 12649-12667, 2022, doi: 10.1021/acs.iecr.2c00681.

[30] S. M. W. Wilson and F. H. Tezel, "Direct Dry Air Capture of CO_2 Using VTSA with Faujasite Zeolites," *Industrial & Engineering Chemistry Research* vol. 59, no. 18, pp. 8783-8794, 2020/05/06 2020, doi: 10.1021/acs.iecr.9b04803.

[31] M. Song, G. Rim, F. Kong, P. Priyadarshini, C. Rosu, R. P. Lively, and C. W. Jones, "Cold-Temperature Capture of Carbon Dioxide with Water Coproduction from Air Using Commercial Zeolites," *Industrial & Engineering Chemistry Research* vol. 61, no. 36, pp. 13624-13634, 2022, doi: 10.1021/acs.iecr.2c02041.

[32] M. Sendi, M. Bui, N. Mac Dowell, and P. Fennell, "Geospatial analysis of regional climate impacts to accelerate cost-efficient direct air capture deployment," *One Earth,* vol. 5, no. 10, pp. 1153-1164, 2022, doi: 10.1016/j.oneear.2022.09.003.

[33] S. K. S. Boetcher, J. B. Perskin, Y. Maidenberg, M. J. Traum, and T. von Hippel, "Direct atmospheric cryogenic carbon capture in cold climates," *Carbon Capture Science & Technology,* vol. 8, 2023, doi: 10.1016/j.ccst.2023.100127.

[34] "Climate Data." https://en.climate-data.org/ (accessed 2024).

[35] B. M. Balasubramaniam, P.-T. Thierry, S. Lethier, V. Pugnet, P. Llewellyn, and A. Rajendran, "Process-performance of solid sorbents for Direct Air Capture (DAC) of CO_2 in optimized temperature-vacuum swing adsorption (TVSA) cycles," *Chemical Engineering Journal,* vol. 485, 2024, doi: 10.1016/j.cej.2024.149568.

[36] Y. Zhang, L. Ding, Z. Xie, X. Zhang, X. Sui, and J.-R. Li, "Porous sorbents for direct capture of carbon dioxide from ambient air," *Chinese Chemical Letters,* 2024, doi: 10.1016/j.cclet.2024.109676.

[37] X. Shi, Y. Lin, and X. Chen, "Development of sorbent materials for direct air capture of CO_2," *MRS Bulletin,* vol. 47, no. 4, pp. 405-415, 2022, doi: 10.1557/s43577-022-00320-7.

[38] X. Shi, H. Xiao, H. Azarabadi, J. Song, X. Wu, X. Chen, and K. S. Lackner, "Sorbents for the Direct Capture of CO_2 from Ambient Air," *Angewandte Chemie International Edition,* vol. 59, no. 18, pp. 6984-7006, Apr 27 2020, doi: 10.1002/anie.201906756.

[39] Y. Shi, R. Ni, and Y. Zhao, "Review on Multidimensional Adsorbents for CO_2 Capture from Ambient Air: Recent Advances and Future Perspectives," *Energy & Fuels,* vol. 37, no. 9, pp. 6365-6381, 2023, doi: 10.1021/acs.energyfuels.3c00381.

[40] J. Sun, M. Zhao, L. Huang, T. Zhang, and Q. Wang, "Recent progress on direct air capture of carbon dioxide," *Current Opinion in Green and Sustainable Chemistry,* vol. 40, 2023, doi: 10.1016/j.cogsc.2023.100752.

[41] J. Wang, R. Fu, S. Wen, P. Ning, M. H. Helal, M. A. Salem, B. B. Xu, Z. M. El-Bahy, M. Huang, Z. Guo, L. Huang, and Q. Wang, "Progress and current challenges for CO_2 capture materials from ambient air," *Advanced Composites and Hybrid Materials,* vol. 5, no. 4, pp. 2721-2759, 2022, doi: 10.1007/s42114-022-00567-3.

[42] X. Zhu, W. Xie, J. Wu, Y. Miao, C. Xiang, C. Chen, B. Ge, Z. Gan, F. Yang, M. Zhang, D. O'Hare, J. Li, T. Ge, and R. Wang, "Recent advances in direct air capture by adsorption," *Chemical Society Reviews,* vol. 51, no. 15, pp. 6574-6651, Aug 1 2022, doi: 10.1039/D1CS00970B

[43] J. Young, F. McIlwaine, B. Smit, S. Garcia, and M. van der Spek, "Process-informed adsorbent design guidelines for direct air capture," *Chemical Engineering Journal,* vol. 456, 2023, doi: 10.1016/j.cej.2022.141035.

[44] J. Wu, X. Zhu, Y. Chen, R. Wang, and T. Ge, "The analysis and evaluation of direct air capture adsorbents on the material characterization level," *Chemical Engineering Journal,* vol. 450, 2022, doi: 10.1016/j.cej.2022.137958.

[45] R. Rodriguez-Mosqueda, E. A. Bramer, T. Roestenberg, and G. Brem, "Parametrical Study on CO_2 Capture from Ambient Air Using Hydrated K_2CO_3 Supported on an Activated Carbon Honeycomb," *Industrial & Engineering Chemistry Research* vol. 57, no. 10, pp. 3628-3638, Mar 14 2018, doi: 10.1021/acs.iecr.8b00566.

[46] H. G. T. Nguyen, J. C. Horn, M. Bleakney, D. W. Siderius, and L. Espinal, "Understanding Material Characteristics through Signature Traits from Helium Pycnometry," *Langmuir,* vol. 35, no. 6, pp. 2115-2122, Feb 12 2019, doi: 10.1021/acs.langmuir.8b03731.

[47] R. Pini, "Interpretation of net and excess adsorption isotherms in microporous adsorbents," *Micropor Mesopor Mat,* vol. 187, pp. 40-52, Mar 15 2014, doi: 10.1016/j.micromeso.2013.12.005.

[48] H. Azzan, A. K. Rajagopalan, A. L'Hermitte, R. Pini, and C. Petit, "Simultaneous Estimation of Gas Adsorption Equilibria and Kinetics of Individual Shaped Adsorbents," *Chemistry of Materials,* vol. 34, no. 15, pp. 6671-6686, Aug 9 2022, doi: 10.1021/acs.chemmater.2c01567.

[49] Micromeritics. *Density Analysis*, 2001. [Online]. Available: https://www.micromeritics.com/Repository/Files/Density_Brochure.pdf.

[50] *Standard Test Methods for Apparent Density, Bulk Factor, and Pourability of Plastic Materials*, ASTM, 2017.

[51] BASF. "BASF 13X Molecular Sieve Product Data Sheet." https://catalysts.basf.com/files/literature-library/BASF_13X-Molecular-Sieve_Datasheet_Rev.08-2020.pdf (accessed 2022).

[52] Y. Wang, G. Rim, M. Song, H. E. Holmes, C. W. Jones, and R. P. Lively, "Cold Temperature Direct Air CO_2 Capture with Amine-Loaded Metal-Organic Framework Monoliths," *ACS Applied Materials & Interfaces,* vol. 16, no. 1, pp. 1404-1415, Jan 10 2024, doi: 10.1021/acsami.3c13528.

[53] Q. Grossmann, V. Stampi-Bombelli, A. Yakimov, S. Docherty, C. Coperet, and M. Mazzotti, "Developing Versatile Contactors for Direct Air Capture of CO_2 through Amine Grafting onto Alumina Pellets and Alumina Wash-Coated Monoliths," *Industrial & Engineering Chemistry Research* vol. 62, no. 34, pp. 13594-13611, Aug 30 2023, doi: 10.1021/acs.iecr.3c01265.

[54] E. Tegeler, Y. Cui, M. Masoudi, A. M. Bahmanpour, T. Colbert, J. Hensel, and V. Balakotaiah, "A novel contactor for reducing the cost of direct air capture of CO_2," *Chemical Engineering Science,* vol. 281, 2023, doi: 10.1016/j.ces.2023.119107.

[55] P. Narayanan, P. Guntupalli, R. P. Lively, and C. W. Jones, "Alumina Incorporation in Self-Supported Poly(ethylenimine) Sorbents for Direct Air Capture," *Chem & Bio Engineering,* 2024, doi: 10.1021/cbe.3c00079.

[56] A. K. Sekizkardes, V. A. Kusuma, J. T. Culp, P. Muldoon, J. Hoffman, J. A. Steckel, and D. Hopkinson, "Single polymer sorbent fibers for high performance and rapid direct air capture," *Journal of Materials Chemistry A,* vol. 11, no. 22, pp. 11670-11674, 2023, doi: 10.1039/d2ta09270k.

[57] F. Kong, G. Rim, P. Priyadarshini, M. Song, M. J. Realff, R. P. Lively, and C. W. Jones, "Dynamic study of direct CO_2 capture from indoor air using poly(ethylenimine)-impregnated fiber sorbents," *Sustainable Energy & Fuels,* vol. 7, no. 18, pp. 4461-4473, 2023, doi: 10.1039/d3se00618b.

[58] M. Song, G. Rim, Y. Wang, I. Borne, C. W. Jones, and R. P. Lively, "Amine-functionalized MIL-101(Cr) fibers for direct air capture at cold temperatures using rapid temperature vacuum swing adsorption," *Chemical Engineering Journal,* vol. 477, 2023, doi: 10.1016/j.cej.2023.147135.

[59] J. Zhang, S. Guo, S. Wang, and X. Tan, "Separation and capture of CO_2 from ambient air using TEPA-functionalized PAN hollow fibers," *Separation and Purification Technology,* vol. 324, 2023, doi: 10.1016/j.seppur.2023.124635.

[60] K. D. Kersey, G. A. Lee, J. H. Xu, M. K. Kidder, A. H. A. Park, and Y. L. Joo, "Encapsulation of Nanoparticle Organic Hybrid Materials within Electrospun Hydrophobic Polymer/Ceramic Fibers for Enhanced CO_2 Capture," *Advanced Functional Materials,* vol. 33, no. 32, 2023, doi: 10.1002/adfm.202301649.

[61] L. Tao, Q. Zhang, T. Li, and S. Deng, "Mild-temperature regenerable modified activated carbon fiber felt loaded with epoxide-modified aminating agents for efficient CO_2 capture from simulated indoor air," *Journal of Environmental Chemical Engineering,* vol. 10, no. 6, 2022, doi: 10.1016/j.jece.2022.108620.

[62] M. Modayil Korah, S. Ly, T. Stangherlin Barbosa, R. Nile, K. Jin, K. S. Lackner, and M. D. Green, "Electrospun Poly(vinyl alcohol)–l-Arginine Nanofiber Composites for Direct Air Capture of CO_2," *ACS ES&T Engineering,* vol. 3, no. 3, pp. 373-386, 2022, doi: 10.1021/acsestengg.2c00307.

[63] J. Zhang, Q. Zhao, S. Wang, and X. Tan, "Direct capture of low concentration CO_2 using tetraethylenepentamine-grafted polyacrylonitrile hollow fibers," *Separation and Purification Technology,* vol. 287, 2022, doi: 10.1016/j.seppur.2022.120562.

[64] V. Kulkarni, D. Panda, and S. K. Singh, "Direct Air Capture of CO_2 over Amine-Modified Hierarchical Silica," (in English), *Industrial & Engineering Chemistry Research* vol. 62, no. 8, pp. 3800-3811, Mar 1 2023, doi: 10.1021/acs.iecr.2c02268.

[65] V. Kulkarni and S. K. Singh, "Direct CO_2 capture from simulated and ambient air over silica-rich MIL-101(Cr)," *Reaction Chemistry & Engineering,* vol. 8, no. 12, pp. 3185-3195, 2023, doi: 10.1039/d3re00329a.

[66] Y. J. Min, A. Ganesan, M. J. Realff, and C. W. Jones, "Direct Air Capture of CO_2 Using Poly(ethyleneimine)-Functionalized Expanded Poly(tetrafluoroethylene)/Silica Composite Structured Sorbents," *ACS Applied Materials & Interfaces,* vol. 14, no. 36, pp. 40992-41002, Sep 14 2022, doi: 10.1021/acsami.2c11143.

[67] F. Rezaei and P. Webley, "Optimum structured adsorbents for gas separation processes," *Chemical Engineering Science,* vol. 64, pp. 5182-5191, 2009, doi: 10.1016/j.ces.2009.08.029.

[68] F. Rezaei and P. Webley, "Structured adsorbents in gas separation processes," *Separation and Purification Technology,* vol. 70, pp. 243-256, 2010, doi: 10.1016/j.seppur.2009.10.004.

[69] J. Wu, X. Zhu, F. Yang, R. Wang, and T. Ge, "Shaping techniques of adsorbents and their applications in gas separation: a review," *Journal of Materials Chemistry A,* vol. 10, no. 43, pp. 22853-22895, 2022, doi: 10.1039/d2ta04352a.

[70] H. Thakkar, S. Eastman, Q. Al-Naddaf, A. A. Rownaghi, and F. Rezaei, "3D-Printed Metal-Organic Framework Monoliths for Gas Adsorption Processes," *ACS Applied Materials & Interfaces,* vol. 9, no. 41, pp. 35908-35916, Oct 18 2017, doi: 10.1021/acsami.7b11626.

[71] H. Thakkar, S. Eastman, A. Hajari, A. A. Rownaghi, J. C. Knox, and F. Rezaei, "3D-Printed Zeolite Monoliths for CO_2 Removal from Enclosed Environments," *ACS Applied Materials & Interfaces,* vol. 8, no. 41, pp. 27753-27761, 2016/10/19 2016, doi: 10.1021/acsami.6b09647.

[72] A. R. Sujan, S. H. Pang, G. Zhu, C. W. Jones, and R. P. Lively, "Direct CO_2 Capture from Air using Poly(ethylenimine)-Loaded Polymer/Silica Fiber Sorbents," *ACS Sustainable Chemistry & Engineering,* vol. 7, no. 5, pp. 5264-5273, 2019, doi: 10.1021/acssuschemeng.8b06203.

[73] W. C. Wilfong, Q. Wang, T. Ji, J. S. Baker, F. Shi, S. Yi, and M. L. Gray, "Directly Spun Epoxy-Crosslinked Polyethylenimine Fiber Sorbents for Direct Air Capture and Postcombustion Capture of CO_2," *Energy Technology,* vol. 10, no. 9, 2022, doi: 10.1002/ente.202200356.

[74] S. Brunauer, P. H. Emmett, and E. Teller, "Adsorption of Gases in Multimolecular Layers," *Journal of the American Chemical Society,* vol. 60, no. 2, pp. 309-319, 1938, doi: 10.1021/ja01269a023.

[75] M. Thommes, K. Kaneko, A. V. Neimark, J. P. Olivier, F. Rodriguez-Reinoso, J. Rouquerol, and K. S. W. Sing, "Physisorption of gases, with special reference to the evaluation of surface area and pore size distribution (IUPAC Technical Report)," *Pure and Applied Chemistry,* vol. 87, no. 9-10, pp. 1051-1069, 2015, doi: 10.1515/pac-2014-1117.

[76] M. M. Dubinin, "Porous structure of adsorbents and catalysts," *Advances in Colloid and Interface Science,* vol. 2, no. 2, pp. 217-235, 1968, doi: 10.1016/0001-8686(68)85004-3.

[77] M. M. Dubinin and V. A. Astakhov, "Development of the concepts of volume filling of micropores in the adsorption of gases and vapors by microporous adsorbents," *Bulletin of the Academy of Sciences of the USSR Division of Chemical Science,* vol. 20, no. 1, pp. 8-12, 1971, doi: 10.1007/bf00849308.

[78] G. Horvath and K. Kawazoe, "Method for the calculation of effective pore size distribution in molecular sieve carbon," *Journal of Chemical Engineering of Japan,* vol. 16, no. 6, pp. 470-475, 1983, doi: 10.1252/jcej.16.470.

[79] J. P. R. B. Walton and N. Quirke, "Capillary Condensation: A Molecular Simulation Study," *Molecular Simulation,* vol. 2, no. 4-6, pp. 361-391, 1989, doi: 10.1080/08927028908034611.

[80] C. Lastoskie, K. E. Gubbins, and N. Quirke, "Pore size distribution analysis of microporous carbons: a density functional theory approach," *The Journal of Physical Chemistry,* vol. 97, no. 18, pp. 4786-4796, 2002, doi: 10.1021/j100120a035.

[81] E. P. Barrett, L. G. Joyner, and P. P. Halenda, "The Determination of Pore Volume and Area Distributions in Porous Substances. I. Computations from Nitrogen Isotherms," *Journal of the American Chemical Society,* vol. 73, no. 1, pp. 373-380, 1951, doi: 10.1021/ja01145a126.

[82] M. Taddei and C. Petit, "Engineering metal–organic frameworks for adsorption-based gas separations: from process to atomic scale," *Molecular Systems Design & Engineering,* 10.1039/D1ME00085C vol. 6, no. 11, pp. 841-875, 2021, doi: 10.1039/D1ME00085C.

[83] H. Babaei, A. J. H. McGaughey, and C. E. Wilmer, "Effect of pore size and shape on the thermal conductivity of metal-organic frameworks," *Chemical Science,* 10.1039/C6SC03704F vol. 8, no. 1, pp. 583-589, 2017, doi: 10.1039/C6SC03704F.

[84] J. Wieme, S. Vandenbrande, A. Lamaire, V. Kapil, L. Vanduyfhuys, and V. Van Speybroeck, "Thermal Engineering of Metal–Organic Frameworks for Adsorption Applications: A Molecular Simulation Perspective," *ACS Applied Materials & Interfaces,* vol. 11, no. 42, pp. 38697-38707, 2019/10/23 2019, doi: 10.1021/acsami.9b12533.

[85] B. Mu and K. S. Walton, "Thermal Analysis and Heat Capacity Study of Metal–Organic Frameworks," *The Journal of Physical Chemistry C,* vol. 115, no. 46, pp. 22748-22754, 2011/11/24 2011, doi: 10.1021/jp205538a.

[86] *Standard Test Method for Determining Specific Heat Capacity by Differential Scanning Calorimetry*, ASTM, 2018.

[87] J. A. Wurzbacher, C. Gebald, S. Brunner, and A. Steinfeld, "Heat and mass transfer of temperature-vacuum swing desorption for CO_2 capture from air," *Chemical Engineering Journal,* vol. 283, pp. 1329-1338, 2016, doi: 10.1016/j.cej.2015.08.035.

[88] R. L. Siegelman, P. J. Milner, A. C. Forse, J. H. Lee, K. A. Colwell, J. B. Neaton, J. A. Reimer, S. C. Weston, and J. R. Long, "Water Enables Efficient CO_2 Capture from Natural Gas Flue Emissions in an Oxidation-Resistant Diamine-Appended Metal-Organic Framework," *Journal of the American Chemical Society,* vol. 141, no. 33, pp. 13171-13186, Aug 21 2019, doi: 10.1021/jacs.9b05567.

[89] P. Q. Liao, X. W. Chen, S. Y. Liu, X. Y. Li, Y. T. Xu, M. Tang, Z. Rui, H. Ji, J. P. Zhang, and X. M. Chen, "Putting an ultrahigh concentration of amine groups into a metal-organic framework for CO_2 capture at low pressures," *Chemical Science,* vol. 7, no. 10, pp. 6528-6533, Oct 19 2016, doi: 10.1039/c6sc00836d.

[90] B. Ge, M. Zhang, B. Hu, D. Wu, X. Zhu, U. Eicker, and R. Wang, "Innovative process integrating high temperature heat pump and direct air capture," *Applied Energy,* vol. 355, 2024, doi: 10.1016/j.apenergy.2023.122229.

[91] S. M. Moosavi, B. A. Novotny, D. Ongari, E. Moubarak, M. Asgari, O. Kadioglu, C. Charalambous, A. Ortega-Guerrero, A. H. Farmahini, L. Sarkisov, S. Garcia, F. Noe, and B. Smit, "A data-science approach to predict the heat capacity of nanoporous materials," *Nature Materials,* vol. 21, no. 12, pp. 1419-1425, Dec 2022, doi: 10.1038/s41563-022-01374-3.

[92] K. C. Chan, C. Y. H. Chao, and C. L. Wu, "Measurement of properties and performance prediction of the new MWCNT-embedded zeolite 13X/CaCl composite adsorbents," *Int J Heat Mass Tran,* vol. 89, pp. 308-319, Oct 2015, doi: 10.1016/j.ijheatmasstransfer.2015.05.063.

[93] R. H. Weiland, J. C. Dingman, and D. B. Cronin, "Heat Capacity of Aqueous Monoethanolamine, Diethanolamine, N-Methyldiethanolamine, and N-Methyldiethanolamine-Based Blends with Carbon Dioxide," *Journal of Chemical & Engineering Data,* vol. 42, no. 5, pp. 1004-1006, 1997, doi: 10.1021/je960314v.

[94] M. Vasheghani, E. Marzbanrad, C. Zamani, M. Aminy, B. Raissi, T. Ebadzadeh, and H. Barzegar-Bafrooei, "Effect of Al_2O_3 phases on the enhancement of thermal conductivity and viscosity of nanofluids in engine oil," *Heat and Mass Transfer,* vol. 47, no. 11, pp. 1401-1405, 2011/11/01 2011, doi: 10.1007/s00231-011-0806-8.

[95] M. Fasihi, O. Efimova, and C. Breyer, "Techno-economic assessment of CO_2 direct air capture plants," *J Clean Prod,* vol. 224, pp. 957-980, Jul 1 2019, doi: 10.1016/j.jclepro.2019.03.086.

[96] S. Park, K. Choi, H. J. Yu, Y.-J. Won, C. Kim, M. Choi, S.-H. Cho, J.-H. Lee, S. Y. Lee, and J. S. Lee, "Thermal Stability Enhanced Tetraethylenepentamine/Silica Adsorbents for High Performance CO_2 Capture," *Industrial & Engineering Chemistry Research* vol. 57, no. 13, pp. 4632-4639, 2018, doi: 10.1021/acs.iecr.7b04912.

[97] Y. Wang, Y. Miao, B. Ge, Z. He, X. Zhu, S. Liu, J. Li, and L. Yu, "Additives enhancing supported amines performance in CO_2 capture from air," *SusMat,* vol. 3, no. 3, pp. 416-430, 2023, doi: 10.1002/sus2.141.

[98] S. H. Pang, L. C. Lee, M. A. Sakwa-Novak, R. P. Lively, and C. W. Jones, "Design of Aminopolymer Structure to Enhance Performance and Stability of CO_2 Sorbents:

Poly(propylenimine) vs Poly(ethylenimine)," *Journal of the American Chemical Society,* vol. 139, no. 10, pp. 3627-3630, Mar 15 2017, doi: 10.1021/jacs.7b00235.

[99] A. R. Cuesta and C. Song, "pH swing adsorption process for ambient carbon dioxide capture using activated carbon black adsorbents and immobilized carbonic anhydrase biocatalysts," *Applied Energy,* vol. 280, 2020, doi: 10.1016/j.apenergy.2020.116003.

[100] K. S. Walton and D. S. Sholl, "Predicting multicomponent adsorption: 50 years of the ideal adsorbed solution theory," *AIChE Journal,* vol. 61, no. 9, pp. 2757-2762, 2015, doi: 10.1002/aic.14878.

[101] J. Schell, N. Casas, R. Pini, and M. Mazzotti, "Pure and binary adsorption of CO_2, H_2, and N_2 on activated carbon," *Adsorption,* vol. 18, no. 1, pp. 49-65, 2011, doi: 10.1007/s10450-011-9382-y.

[102] G. Rim, F. Kong, M. Song, C. Rosu, P. Priyadarshini, R. P. Lively, and C. W. Jones, "Sub-Ambient Temperature Direct Air Capture of CO_2 using Amine-Impregnated MIL-101(Cr) Enables Ambient Temperature CO_2 Recovery," *JACS Au,* vol. 2, no. 2, pp. 380-393, Feb 28 2022, doi: 10.1021/jacsau.1c00414.

[103] S. M. W. Wilson, "The potential of direct air capture using adsorbents in cold climates," *iScience,* vol. 25, no. 12, p. 105564, Dec 22 2022, doi: 10.1016/j.isci.2022.105564.

[104] X. C. Zhu, T. S. Ge, F. Yang, M. Lyu, C. P. Chen, D. O'Hare, and R. Z. Wang, "Efficient CO_2 capture from ambient air with amine-functionalized Mg-Al mixed metal oxides," *Journal of Materials Chemistry A,* vol. 8, no. 32, pp. 16421-16428, Aug 28 2020, doi: 10.1039/d0ta05079b.

[105] H. Thakkar, A. Issa, A. A. Rownaghi, and F. Rezaei, "CO_2 Capture from Air Using Amine-Functionalized Kaolin-Based Zeolites," *Chemical Engineering & Technology,* vol. 40, no. 11, pp. 1999-2007, 2017, doi: 10.1002/ceat.201700188.

[106] A. Kumar, D. G. Madden, M. Lusi, K. J. Chen, E. A. Daniels, T. Curtin, J. J. t. Perry, and M. J. Zaworotko, "Direct Air Capture of CO_2 by Physisorbent Materials," *Angewandte Chemie International Edition,* vol. 54, no. 48, pp. 14372-7, Nov 23 2015, doi: 10.1002/anie.201506952.

[107] A. Kumar, C. Hua, D. G. Madden, D. O'Nolan, K. J. Chen, L. J. Keane, J. J. Perry, and M. J. Zaworotko, "Hybrid ultramicroporous materials (HUMs) with enhanced stability and trace carbon capture performance," *Chemical Communications,* vol. 53, no. 44, pp. 5946-5949, May 30 2017, doi: 10.1039/c7cc02289a.

[108] O. Shekhah, Y. Belmabkhout, Z. Chen, V. Guillerm, A. Cairns, K. Adil, and M. Eddaoudi, "Made-to-order metal-organic frameworks for trace carbon dioxide removal and air capture," *Nature Communications,* vol. 5, no. 1, p. 4228, 2014/06/25 2014, doi: 10.1038/ncomms5228.

[109] P. M. Bhatt, Y. Belmabkhout, A. Cadiau, K. Adil, O. Shekhah, A. Shkurenko, L. J. Barbour, and M. Eddaoudi, "A Fine-Tuned Fluorinated MOF Addresses the Needs for Trace CO_2 Removal and Air Capture Using Physisorption," *Journal of the American Chemical Society,* vol. 138, no. 29, pp. 9301-7, Jul 27 2016, doi: 10.1021/jacs.6b05345.

[110] A. Oda, S. Hiraki, E. Harada, I. Kobayashi, T. Ohkubo, Y. Ikemoto, T. Moriwaki, and Y. Kuroda, "Unprecedented CO_2 adsorption behaviour by 5A-type zeolite discovered in lower pressure region and at 300 K," *Journal of Materials Chemistry A,* vol. 9, no. 12, pp. 7531-7545, 2021, doi: 10.1039/d0ta09944a.

[111] Z. Tao, Y. Tian, S. Y. Ou, Q. Gu, and J. Shang, "Direct air capture of CO_2 by metal cation-exchanged LTA zeolites: Effect of the charge-to-size ratio of cations," *AIChE Journal,* vol. 69, no. 8, 2023, doi: 10.1002/aic.18139.

[112] D. Fu, Y. Park, and M. E. Davis, "Zinc Containing Small-Pore Zeolites for Capture of Low Concentration Carbon Dioxide," *Angewandte Chemie International Edition,* vol. 61, no. 5, p. e202112916, Jan 26 2022, doi: 10.1002/anie.202112916.

[113] D. Fu, Y. Park, and M. E. Davis, "Confinement effects facilitate low-concentration carbon dioxide capture with zeolites," *Proceedings of the National Academy of Sciences,* vol. 119, no. 39, p. e2211544119, Sep 27 2022, doi: 10.1073/pnas.2211544119.

[114] R. Kumar, S. Ohtani, and N. Tsunoji, "Direct air capture on amine-impregnated FAU zeolites: Exploring for high adsorption capacity and low-temperature regeneration," *Micropor Mesopor Mat,* vol. 360, 2023, doi: 10.1016/j.micromeso.2023.112714.

[115] J. J. Lee, C.-H. Chen, D. Shimon, S. E. Hayes, C. Sievers, and C. W. Jones, "Effect of Humidity on the CO_2 Adsorption of Tertiary Amine Grafted SBA-15," *The Journal of Physical Chemistry C,* vol. 121, no. 42, pp. 23480-23487, 2017, doi: 10.1021/acs.jpcc.7b07930.

[116] Y. Miao, Z. He, X. Zhu, D. Izikowitz, and J. Li, "Operating temperatures affect direct air capture of CO_2 in polyamine-loaded mesoporous silica," *Chemical Engineering Journal,* vol. 426, 2021, doi: 10.1016/j.cej.2021.131875.

[117] L. A. Darunte, T. Sen, C. Bhawanani, K. S. Walton, D. S. Sholl, M. J. Realff, and C. W. Jones, "Moving Beyond Adsorption Capacity in Design of Adsorbents for CO_2 Capture from Ultradilute Feeds: Kinetics of CO_2 Adsorption in Materials with Stepped Isotherms," *Industrial & Engineering Chemistry Research* vol. 58, no. 1, pp. 366-377, 2018, doi: 10.1021/acs.iecr.8b05042.

[118] H. W. Kua, C. Pedapati, R. V. Lee, and S. Kawi, "Effect of indoor contamination on carbon dioxide adsorption of wood-based biochar – Lessons for direct air capture," *J Clean Prod,* vol. 210, pp. 860-871, 2019, doi: 10.1016/j.jclepro.2018.10.206.

[119] A. Ward and R. Pini, "Integrated uncertainty quantification and sensitivity analysis of single-component dynamic column breakthrough experiments," *Adsorption,* vol. 28, no. 3, pp. 161-183, 2022/05/01 2022, doi: 10.1007/s10450-022-00361-z.

[120] F. Rouquerol, J. Rouquerol, and K. Sing, "Thermodynamics of Adsorption at the Gas–Solid Interface," in *Adsorption by Powders and Porous Solids*, 1999, pp. 27-50.

[121] A. Nuhnen and C. Janiak, "A practical guide to calculate the isosteric heat/enthalpy of adsorption via adsorption isotherms in metal–organic frameworks, MOFs," *Dalton Transactions,* 10.1039/D0DT01784A vol. 49, no. 30, pp. 10295-10307, 2020, doi: 10.1039/D0DT01784A.

[122] A. Samanta, A. Zhao, G. K. H. Shimizu, P. Sarkar, and R. Gupta, "Post-Combustion CO_2 Capture Using Solid Sorbents: A Review," *Industrial & Engineering Chemistry Research* vol. 51, no. 4, pp. 1438-1463, 2011, doi: 10.1021/ie200686q.

[123] M. E. Potter, K. M. Cho, J. J. Lee, and C. W. Jones, "Role of Alumina Basicity in CO_2 Uptake in 3-Aminopropylsilyl-Grafted Alumina Adsorbents," *ChemSusChem,* vol. 10, no. 10, pp. 2192-2201, May 22 2017, doi: 10.1002/cssc.201700115.

[124] C. E. Bien, K. K. Chen, S. C. Chien, B. R. Reiner, L. C. Lin, C. R. Wade, and W. S. W. Ho, "Bioinspired Metal-Organic Framework for Trace CO_2 Capture," *Journal of the American Chemical Society,* vol. 140, no. 40, pp. 12662-12666, Oct 10 2018, doi: 10.1021/jacs.8b06109.

[125] C. E. Bien, Q. Liu, and C. R. Wade, "Assessing the Role of Metal Identity on CO_2 Adsorption in MOFs Containing M–OH Functional Groups," *Chemistry of Materials,* vol. 32, no. 1, pp. 489-497, 2019, doi: 10.1021/acs.chemmater.9b04228.

[126] Z. Cai, C. E. Bien, Q. Liu, and C. R. Wade, "Insights into CO_2 Adsorption in M–OH Functionalized MOFs," *Chemistry of Materials,* vol. 32, no. 10, pp. 4257-4264, 2020, doi: 10.1021/acs.chemmater.0c00746.

[127] O. Shekhah, Y. Belmabkhout, K. Adil, P. M. Bhatt, A. J. Cairns, and M. Eddaoudi, "A facile solvent-free synthesis route for the assembly of a highly CO_2 selective and H_2S tolerant NiSIFSIX metal–organic framework," *Chemical Communications,* 10.1039/C5CC04487A vol. 51, no. 71, pp. 13595-13598, 2015, doi: 10.1039/C5CC04487A.

[128] S. Mukherjee, N. Sikdar, D. O'Nolan, D. M. Franz, V. Gascon, A. Kumar, N. Kumar, H. S. Scott, D. G. Madden, P. E. Kruger, B. Space, and M. J. Zaworotko, "Trace CO_2 capture by an ultramicroporous physisorbent with low water affinity," *Science Advances,* vol. 5, no. 11, p. eaax9171, Nov 2019, doi: 10.1126/sciadv.aax9171.

[129] A. Itadani, A. Oda, H. Torigoe, T. Ohkubo, M. Sato, H. Kobayashi, and Y. Kuroda, "Material Exhibiting Efficient CO_2 Adsorption at Room Temperature for Concentrations Lower Than 1000 ppm: Elucidation of the State of Barium Ion Exchanged in an MFI-Type Zeolite," *ACS Applied Materials & Interfaces,* vol. 8, no. 13, pp. 8821-33, Apr 6 2016, doi: 10.1021/acsami.6b00909.

[130] T. M. McDonald, W. R. Lee, J. A. Mason, B. M. Wiers, C. S. Hong, and J. R. Long, "Capture of Carbon Dioxide from Air and Flue Gas in the Alkylamine-Appended Metal–Organic Framework mmen-Mg_2(dobpdc)," *Journal of the American Chemical Society,* vol. 134, no. 16, pp. 7056-7065, 2012/04/25 2012, doi: 10.1021/ja300034j.

[131] T. M. McDonald, J. A. Mason, X. Kong, E. D. Bloch, D. Gygi, A. Dani, V. Crocellà, F. Giordanino, S. O. Odoh, W. S. Drisdell, B. Vlaisavljevich, A. L. Dzubak, R. Poloni, S. K. Schnell, N. Planas, K. Lee, T. Pascal, L. F. Wan, D. Prendergast, J. B. Neaton, B. Smit, J. B. Kortright, L. Gagliardi, S. Bordiga, J. A. Reimer, and J. R. Long, "Cooperative insertion of CO_2 in diamine-appended metal-organic frameworks," *Nature,* vol. 519, no. 7543, pp. 303-308, 2015/03/01 2015, doi: 10.1038/nature14327.

[132] K. S. K. Reddy, A. M. Varghese, A. E. Ogungbenro, and G. N. Karanikolos, "Aminosilane-Modified Ordered Hierarchical Nanostructured Silica for Highly-Selective Carbon Dioxide Capture at Low Pressure," *ACS Applied Engineering Materials,* vol. 1, no. 2, pp. 720-733, 2023, doi: 10.1021/acsaenm.2c00136.

[133] S. Qadir, H. Su, D. Li, Y. Gu, S. Zhao, S. Wang, and S. Wang, "Low-cost preferential different amine grafted silica spheres adsorbents for DAC CO_2 removal," *Journal of Energy Chemistry,* vol. 75, pp. 494-503, 2022, doi: 10.1016/j.jechem.2022.09.005.

[134] A. A. Al-Absi, M. Mohamedali, A. Domin, A. M. Benneker, and N. Mahinpey, "Development of in situ polymerized amines into mesoporous silica for direct air CO_2 capture," *Chemical Engineering Journal,* vol. 447, 2022, doi: 10.1016/j.cej.2022.137465.

[135] A. Heydari-Gorji and A. Sayari, "Thermal, Oxidative, and CO_2-Induced Degradation of Supported Polyethylenimine Adsorbents," *Industrial & Engineering Chemistry Research* vol. 51, no. 19, pp. 6887-6894, 2012/05/16 2012, doi: 10.1021/ie3003446.

[136] S. van Paasen, M. Infantino, J. Yao, S. H. A. M. Leenders, J. M. van de Graaf, A. Klingler, F. Zerobin, T. Pröll, G. Schöny, J. Fuchs, and H. Hofbauer, "Development of the solid sorbent technology for post combustion CO_2 capture towards commercial prototype," *International Journal of Greenhouse Gas Control,* vol. 109, p. 103368, 2021/07/01/ 2021, doi: 10.1016/j.ijggc.2021.103368.

[137] J. S. A. Carneiro, G. Innocenti, H. J. Moon, Y. Guta, L. Proaño, C. Sievers, M. A. Sakwa-Novak, E. W. Ping, and C. W. Jones, "Insights into the Oxidative Degradation Mechanism of Solid Amine Sorbents for CO_2 Capture from Air: Roles of Atmospheric Water," *Angewandte Chemie International Edition,* vol. 135, no. 24, 2023, doi: 10.1002/ange.202302887.

[138] Y. A. Guta, J. Carneiro, S. Li, G. Innocenti, S. H. Pang, M. A. Sakwa-Novak, C. Sievers, and C. W. Jones, "Contributions of CO_2, O_2, and H_2O to the Oxidative Stability of Solid Amine Direct Air Capture Sorbents at Intermediate Temperature," *ACS Applied Materials & Interfaces,* vol. 15, no. 40, pp. 46790-46802, Oct 11 2023, doi: 10.1021/acsami.3c08140.

[139] S. Li, M. R. Ceron, H. V. Eshelman, A. J. Varni, A. Maiti, S. Akhade, and S. H. Pang, "Probing the Kinetic Origin of Varying Oxidative Stability of Ethyl- vs. Propyl-spaced Amines for Direct Air Capture," *ChemSusChem,* vol. 16, no. 5, p. e202201908, Mar 8 2023, doi: 10.1002/cssc.202201908.

[140] C. Yan and A. Sayari, "Spectroscopic investigation into the oxidation of polyethylenimine for CO_2 capture: Mitigation strategies and mechanism," *Chemical Engineering Journal,* vol. 479, 2024, doi: 10.1016/j.cej.2023.147498.

[141] P. Bollini, S. Choi, J. H. Drese, and C. W. Jones, "Oxidative Degradation of Aminosilica Adsorbents Relevant to Postcombustion CO_2 Capture," *Energy & Fuels,* vol. 25, no. 5, pp. 2416-2425, 2011/05/19 2011, doi: 10.1021/ef200140z.

[142] C.-J. Yoo, S. J. Park, and C. W. Jones, "CO_2 Adsorption and Oxidative Degradation of Silica-Supported Branched and Linear Aminosilanes," *Industrial & Engineering Chemistry Research* vol. 59, no. 15, pp. 7061-7071, 2019, doi: 10.1021/acs.iecr.9b04205.

[143] S. H. Pang, R. P. Lively, and C. W. Jones, "Oxidatively-Stable Linear Poly(propylenimine)-Containing Adsorbents for CO_2 Capture from Ultradilute Streams," *ChemSusChem,* vol. 11, no. 15, pp. 2628-2637, Aug 9 2018, doi: 10.1002/cssc.201800438.

[144] A. Goeppert, H. Zhang, R. Sen, H. Dang, and G. K. S. Prakash, "Oxidation-Resistant, Cost-Effective Epoxide-Modified Polyamine Adsorbents for CO_2 Capture from Various Sources Including Air," *ChemSusChem,* vol. 12, no. 8, pp. 1712-1723, Apr 23 2019, doi: 10.1002/cssc.201802978.

[145] W. Choi, K. Min, C. Kim, Y. S. Ko, J. W. Jeon, H. Seo, Y. K. Park, and M. Choi, "Epoxide-functionalization of polyethyleneimine for synthesis of stable carbon dioxide adsorbent in temperature swing adsorption," *Nature Communications,* vol. 7, p. 12640, Aug 30 2016, doi: 10.1038/ncomms12640.

[146] Y. Miao, Y. Wang, X. Zhu, W. Chen, Z. He, L. Yu, and J. Li, "Minimizing the effect of oxygen on supported polyamine for direct air capture," *Separation and Purification Technology,* vol. 298, 2022, doi: 10.1016/j.seppur.2022.121583.

[147] N. S. Wilkins, J. A. Sawada, and A. Rajendran, "Steam Adsorption Equilibrium Data at 110 °C on Activated Carbon, Lewatit VP OC 1065, and CALF-20 Using a Microscale Dynamic Column Breakthrough Apparatus," *Journal of Chemical & Engineering Data,* 2024, doi: 10.1021/acs.jced.3c00697.

[148] C. Gebald, J. A. Wurzbacher, A. Borgschulte, T. Zimmermann, and A. Steinfeld, "Single-Component and Binary CO_2 and H_2O Adsorption of Amine-Functionalized Cellulose," *Environmental Science & Technology,* vol. 48, no. 4, pp. 2497-2504, 2014/02/18 2014, doi: 10.1021/es404430g.

[149] J. Elfving and T. Sainio, "Kinetic approach to modelling CO_2 adsorption from humid air using amine-functionalized resin: Equilibrium isotherms and column dynamics," *Chemical Engineering Science,* vol. 246, 2021, doi: 10.1016/j.ces.2021.116885.

[150] J. Young, E. García-Díez, S. Garcia, and M. van der Spek, "The impact of binary water–CO_2 isotherm models on the optimal performance of sorbent-based direct air capture processes," *Energy & Environmental Science,* vol. 14, no. 10, pp. 5377-5394, 2021, doi: 10.1039/d1ee01272j.

[151] N. S. Wilkins, J. A. Sawada, and A. Rajendran, "Measurement of competitive CO_2 and H_2O adsorption on zeolite 13X for post-combustion CO_2 capture," *Adsorption,* vol. 26, no. 5, pp. 765-779, 2020, doi: 10.1007/s10450-020-00199-3.

[152] A. Rajendran, G. K. H. Shimizu, and T. K. Woo, "The Challenge of Water Competition in Physical Adsorption of CO_2 by Porous Solids for Carbon Capture Applications - A Short Perspective," *Advanced Materials,* p. e2301730, Jul 26 2023, doi: 10.1002/adma.202301730.

[153] D. Shade, B. W. S. Bout, D. S. Sholl, and K. S. Walton, "Opening the Toolbox: 18 Experimental Techniques for Measurement of Mixed Gas Adsorption," *Industrial & Engineering Chemistry Research* vol. 61, no. 6, pp. 2367-2391, 2022, doi: 10.1021/acs.iecr.1c03756.

[154] A. Sayari and Y. Belmabkhout, "Stabilization of amine-containing CO_2 adsorbents: dramatic effect of water vapor," *Journal of the American Chemical Society,* vol. 132, no. 18, pp. 6312-4, May 12 2010, doi: 10.1021/ja1013773.

[155] A. Sayari, A. Heydari-Gorji, and Y. Yang, "CO_2-induced degradation of amine-containing adsorbents: reaction products and pathways," *Journal of the American Chemical Society,* vol. 134, no. 33, pp. 13834-42, Aug 22 2012, doi: 10.1021/ja304888a.

[156] R. Rodríguez-Mosqueda, J. Rutgers, E. A. Bramer, and G. Brem, "Low temperature water vapor pressure swing for the regeneration of adsorbents for CO_2 enrichment in greenhouses via direct air capture," *Journal of CO_2 Utilization,* vol. 29, pp. 65-73, 2019, doi: 10.1016/j.jcou.2018.11.010.

[157] N. Masoud, G. Bordanaba-Florit, T. van Haasterecht, and J. H. Bitter, "Effect of Support Surface Properties on CO_2 Capture from Air by Carbon-Supported Potassium Carbonate," *Industrial & Engineering Chemistry Research* vol. 60, no. 38, pp. 13749-13755, 2021, doi: 10.1021/acs.iecr.1c01229.

[158] W. K. Shi, Y. Ji, X. J. Zhang, M. X. Fang, T. Wang, and L. Jiang, "Understandings on design and application for direct air capture: From advanced sorbents to thermal cycles," *Carbon Capture Science & Technology,* vol. 7, 2023, doi: 10.1016/j.ccst.2023.100114.

[159] J. M. Kolle, M. Fayaz, and A. Sayari, "Understanding the Effect of Water on CO_2 Adsorption," *Chemical Reviews,* vol. 121, no. 13, pp. 7280-7345, 2021/07/14 2021, doi: 10.1021/acs.chemrev.0c00762.

[160] M. Guo, H. Wu, L. Lv, H. Meng, J. Yun, J. Jin, and J. Mi, "A Highly Efficient and Stable Composite of Polyacrylate and Metal-Organic Framework Prepared by Interface Engineering for Direct Air Capture," *ACS Applied Materials & Interfaces,* vol. 13, no. 18, pp. 21775-21785, May 12 2021, doi: 10.1021/acsami.1c03661.

[161] M. Kim, J. W. Lee, S. Kim, and Y. T. Kang, "CO_2 adsorption on zeolite 13X modified with hydrophobic octadecyltrimethoxysilane for indoor application," *J Clean Prod,* vol. 337, 2022, doi: 10.1016/j.jclepro.2022.130597.

[162] X. Shi, G. A. Lee, S. Liu, D. Kim, A. Alahmed, A. Jamal, L. Wang, and A.-H. A. Park, "Water-stable MOFs and hydrophobically encapsulated MOFs for CO_2 capture from ambient air and wet flue gas," *Materials Today,* vol. 65, pp. 207-226, 2023, doi: 10.1016/j.mattod.2023.03.004.

[163] M. Yang, S. Wang, and L. Xu, "Hydrophobic functionalized amine-impregnated resin for CO_2 capture in humid air," *Separation and Purification Technology,* vol. 315, 2023, doi: 10.1016/j.seppur.2023.123606.

[164] J. Wu, Y. Chen, Y. Xu, S. Chen, H. Lv, Z. Gan, X. Zhu, R. Wang, C.-H. Wang, and T. Ge, "Facile synthesis of structured adsorbent with enhanced hydrophobicity and low energy consumption for CO_2 capture from the air," *Matter,* vol. 7, no. 1, pp. 123-139, 2024, doi: 10.1016/j.matt.2023.10.019.

[165] D. G. Madden, H. S. Scott, A. Kumar, K.-J. Chen, R. Sanii, A. Bajpai, M. Lusi, T. Curtin, J. J. Perry, and M. J. Zaworotko, "Flue-gas and direct-air capture of CO_2 by porous metal-organic materials," *Philosophical Transactions of the Royal Society A: Mathematical,*

Physical and Engineering Sciences, vol. 375, no. 2084, p. 20160025, 2017, doi: doi:10.1098/rsta.2016.0025.

[166] A. Kumar, "Crystal engineering of hybrid ultramicroporous materials for study of direct air capture of carbon dioxide," PhD, Faculty of Science & Engineering, University of Limerick, 2018.

[167] D. Fu and M. E. Davis, "Toward the feasible direct air capture of carbon dioxide with molecular sieves by water management," *Cell Reports Physical Science,* vol. 4, no. 5, 2023, doi: 10.1016/j.xcrp.2023.101389.

[168] H. E. Holmes, M. J. Realff, and R. P. Lively, "Water management and heat integration in direct air capture systems," *Nature Chemical Engineering,* vol. 1, no. 3, pp. 208-215, 2024, doi: 10.1038/s44286-024-00032-6.

[169] H. E. Holmes, S. Banerjee, A. Vallace, R. P. Lively, C. W. Jones, and M. J. Realff, "Tuning sorbent properties to reduce the cost of direct air capture," *ChemRxiv,* 2024, doi: 10.26434/chemrxiv-2024-8sc71.

[170] X. Zhu, M. Lyu, T. Ge, J. Wu, C. Chen, F. Yang, D. O'Hare, and R. Wang, "Modified layered double hydroxides for efficient and reversible carbon dioxide capture from air," *Cell Reports Physical Science,* vol. 2, no. 7, 2021, doi: 10.1016/j.xcrp.2021.100484.

[171] A. Ahmadian Hosseini and M. Jahandar Lashaki, "A comprehensive evaluation of amine-impregnated silica materials for direct air capture of carbon dioxide," *Separation and Purification Technology,* vol. 325, 2023, doi: 10.1016/j.seppur.2023.124580.

[172] Y. Miao, Y. Wang, B. Ge, Z. He, X. Zhu, J. Li, S. Liu, and L. Yu, "Mixed Diethanolamine and Polyethyleneimine with Enhanced CO_2 Capture Capacity from Air," *Advanced Science,* vol. 10, no. 16, p. e2207253, Jun 2023, doi: 10.1002/advs.202207253.

[173] C. Zhang, S. Sun, S. He, and C. Wu, "Direct air capture of CO_2 by KOH-activated bamboo biochar," *Journal of the Energy Institute,* vol. 105, pp. 399-405, 2022, doi: 10.1016/j.joei.2022.10.017.

[174] M. Zhao, J. Xiao, W. Gao, and Q. Wang, "Defect-rich Mg-Al MMOs supported TEPA with enhanced charge transfer for highly efficient and stable direct air capture," *Journal of Energy Chemistry,* vol. 68, pp. 401-410, 2022, doi: 10.1016/j.jechem.2021.12.031.

[175] B. Ge, C. Chen, Z. Gan, X. Zhu, Y. Miao, Y. Wang, T. Ge, D. O'Hare, and R. Wang, "Scalable Synthesis of Amine-Grafted Ultrafine Layered Double Hydroxide Nanosheets with Improved Carbon Dioxide Capture Capacity from Air," *ACS Sustainable Chemistry & Engineering,* vol. 11, no. 25, pp. 9282-9287, 2023, doi: 10.1021/acssuschemeng.3c01183.

[176] S. Ahsan, A. Ayub, D. Meeroff, and M. Jahandar Lashaki, "A comprehensive comparison of zeolite-5A molecular sieves and amine-grafted SBA-15 silica for cyclic adsorption-desorption of carbon dioxide in enclosed environments," *Chemical Engineering Journal,* vol. 437, 2022, doi: 10.1016/j.cej.2022.135139.

[177] M. Parvazinia, S. Garcia, and M. Maroto-Valer, "CO_2 capture by ion exchange resins as amine functionalised adsorbents," *Chemical Engineering Journal,* vol. 331, pp. 335-342, 2018, doi: 10.1016/j.cej.2017.08.087.

[178] R. Hunt, J. Gillbanks, J. Czapla, Z. Wan, C. Karmelich, C. White, and C. Wood, "Representative longevity testing of direct air capture materials," *Chemical Engineering Journal,* vol. 481, 2024, doi: 10.1016/j.cej.2024.148901.

[179] H. Liu, H. Lin, S. Dai, and D.-e. Jiang, "Minimal Kinetic Model of Direct Air Capture of CO_2 by Supported Amine Sorbents in Dry and Humid Conditions," *Industrial & Engineering Chemistry Research* 2024, doi: 10.1021/acs.iecr.3c04535.

[180] V. Stampi-Bombelli, M. van der Spek, and M. Mazzotti, "Analysis of direct capture of CO_2 from ambient air via steam-assisted temperature–vacuum swing adsorption," *Adsorption,* vol. 26, pp. 1183-1197, 2020, doi: 10.1007/s10450-020-00249-w.

[181] S. Wang, Y. Liu, C. Zhang, S. Guo, and Y. Li, "High Gravity-Enhanced Direct Air Capture: A Leap Forward in CO_2 Adsorption Technology," *Atmosphere,* vol. 15, no. 2, 2024, doi: 10.3390/atmos15020238.

[182] S. Wang, Y. Liu, C. Zhang, S. Guo, Y. Li, and S. Cheng, "The amine-functionalized alumina captures CO_2 directly from the ambient air in the rotating adsorption bed," *Chemical Engineering and Processing - Process Intensification,* vol. 199, 2024, doi: 10.1016/j.cep.2024.109735.

[183] F. Liu, T. Wang, H. Dong, and W. Liu, "Modified metal–organic framework by a novel coordinatively unsaturated amine grafting mechanism for direct air capture of CO_2," *Chemical Engineering Journal,* vol. 454, 2023, doi: 10.1016/j.cej.2022.140431.

[184] L. Samaddoost, M. Soltani, E. Fatehifar, and E. Abbasi Asl, "Design of amine-functionalized resin via a facial method with efficient CO_2 capture from air," *Process Safety and Environmental Protection,* vol. 171, pp. 18-27, 2023, doi: 10.1016/j.psep.2023.01.008.

[185] C. Hou, Y. Wu, T. Wang, X. Wang, and X. Gao, "Preparation of Quaternized Bamboo Cellulose and Its Implication in Direct Air Capture of CO_2," *Energy & Fuels,* vol. 33, no. 3, pp. 1745-1752, 2018, doi: 10.1021/acs.energyfuels.8b02821.

[186] W. Jung, J. Park, and K. S. Lee, "Kinetic modeling of CO_2 adsorption on an amine-functionalized solid sorbent," *Chemical Engineering Science,* vol. 177, pp. 122-131, 2018, doi: 10.1016/j.ces.2017.11.003.

[187] N. T. D. Hanh, J.-Y. Shih, K.-H. Chen, P. Srinophakun, C.-Y. Chiu, B.-L. Liu, S.-L. Tsai, Y.-H. Cheng, and Y.-K. Chang, "Dynamic kinetic studies of CO_2 capture using polyethyleneimine-modified cylindrical NaY zeolite in packed beds under ambient conditions," *Journal of the Taiwan Institute of Chemical Engineers,* vol. 156, 2024, doi: 10.1016/j.jtice.2024.105366.

[188] J. R. Hoffman, A. E. Baumann, and C. M. Stafford, "Thickness Dependent CO_2 Adsorption of Poly(ethyleneimine) Thin Films for Direct Air Capture," *Chemical Engineering Journal,* vol. 481, Feb 2024, doi: 10.1016/j.cej.2023.148381.

[189] S. Sircar, "Applications of Gas Separation by Adsorption for the Future," *Adsorption Science & Technology,* vol. 19, no. 5, pp. 347-366, 2016, doi: 10.1260/0263617011494222.

[190] H. M. Wu, "An NMR study of nickel fluorotitanate," Master of Science, Physics, Texas Tech University, 1984.

[191] P. J. E. Harlick and A. Sayari, "Applications of Pore-Expanded Mesoporous Silica. 5. Triamine Grafted Material with Exceptional CO_2 Dynamic and Equilibrium Adsorption Performance," *Industrial & Engineering Chemistry Research* vol. 46, no. 2, pp. 446-458, 2006, doi: 10.1021/ie060774+.

[192] M. Srasra, S. Delsarte, and E. M. Gaigneaux, "Effects of the Nitridation of Y and USY Zeolites on their Catalytic Activity for the Base Catalyzed Knoevenagel Condensation," *Topics in Catalysis,* vol. 52, no. 11, pp. 1541-1548, 2009, doi: 10.1007/s11244-009-9290-5.

[193] J. W. M. Osterrieth, J. Rampersad, D. Madden, N. Rampal, L. Skoric, B. Connolly, M. D. Allendorf, V. Stavila, J. L. Snider, R. Ameloot, J. Marreiros, C. Ania, D. Azevedo, E. Vilarrasa-Garcia, B. F. Santos, X. H. Bu, Z. Chang, H. Bunzen, N. R. Champness, S. L. Griffin, B. Chen, R. B. Lin, B. Coasne, S. Cohen, J. C. Moreton, Y. J. Colon, L. Chen, R. Clowes, F. X. Coudert, Y. Cui, B. Hou, D. M. D'Alessandro, P. W. Doheny, M. Dinca, C. Sun, C. Doonan, M. T. Huxley, J. D. Evans, P. Falcaro, R. Ricco, O. Farha, K. B. Idrees, T. Islamoglu, P. Feng, H. Yang, R. S. Forgan, D. Bara, S. Furukawa, E. Sanchez, J. Gascon, S. Telalovic, S. K. Ghosh, S. Mukherjee, M. R. Hill, M. M. Sadiq, P. Horcajada, P. Salcedo-

Abraira, K. Kaneko, R. Kukobat, J. Kenvin, S. Keskin, S. Kitagawa, K. I. Otake, R. P. Lively, S. J. A. DeWitt, P. Llewellyn, B. V. Lotsch, S. T. Emmerling, A. M. Putz, C. Marti-Gastaldo, N. M. Padial, J. Garcia-Martinez, N. Linares, D. Maspoch, J. A. Suarez Del Pino, P. Moghadam, R. Oktavian, R. E. Morris, P. S. Wheatley, J. Navarro, C. Petit, D. Danaci, M. J. Rosseinsky, A. P. Katsoulidis, M. Schroder, X. Han, S. Yang, C. Serre, G. Mouchaham, D. S. Sholl, R. Thyagarajan, D. Siderius, R. Q. Snurr, R. B. Goncalves, S. Telfer, S. J. Lee, V. P. Ting, J. L. Rowlandson, T. Uemura, T. Iiyuka, M. A. van der Veen, D. Rega, V. Van Speybroeck, S. M. J. Rogge, A. Lamaire, K. S. Walton, L. W. Bingel, S. Wuttke, J. Andreo, O. Yaghi, B. Zhang, C. T. Yavuz, T. S. Nguyen, F. Zamora, C. Montoro, H. Zhou, A. Kirchon and D. Fairen-Jimenez, "How Reproducible are Surface Areas Calculated from the BET Equation?," *Advanced Materials,* vol. 34, no. 27, p. e2201502, Jul 2022, doi: 10.1002/adma.202201502.

[194] J. Rouquerol, P. Llewellyn, and F. Rouquerol, "Is the bet equation applicable to microporous adsorbents?," *Studies in Surface Science and Catalysis,* vol. 160, pp. 49-56, 2007/01/01/ 2007, doi: 10.1016/S0167-2991(07)80008-5.

[195] P. Tarazona, "Free-energy density functional for hard spheres," *Physical Review A,* vol. 31, no. 4, pp. 2672-2679, Apr 1985, doi: 10.1103/physreva.31.2672.

[196] S. Li, J. Zhao, P. Lu, and Y. Xie, "Maximum packing densities of basic 3D objects," *Chinese Science Bulletin,* vol. 55, no. 2, pp. 114-119, 2010, doi: 10.1007/s11434-009-0650-0.

[197] NIST. "Aluminium Oxide." https://webbook.nist.gov/cgi/cbook.cgi?ID=C1344281&Type=JANAFS&Plot=on (accessed 2024).

[198] U. Gaur and B. Wunderlich, "Heat Capacity and Other Thermodynamic Properties of Linear Macromolecules. V. Polystyrene," *Journal of Physical and Chemical Reference Data,* vol. 11, no. 2, pp. 313-325, 1982, doi: 10.1063/1.555663.

[199] H. Azzan. "Adsorption Isotherm fitting tool." https://github.com/ImperialCollegeLondon/IsothermFittingTool (accessed 2024).

[200] J. Hwang, H. Azzan, R. Pini, and C. Petit, "H_2, N_2, CO_2, and CH_4 Unary Adsorption Isotherm Measurements at Low and High Pressures on Zeolitic Imidazolate Framework ZIF-8," *Journal of Chemical & Engineering Data,* vol. 67, no. 7, pp. 1674-1686, 2022, doi: 10.1021/acs.jced.1c00900.

[201] H. Azzan, D. Danaci, C. Petit, and R. Pini, "Unary Adsorption Equilibria of Hydrogen, Nitrogen, and Carbon Dioxide on Y-Type Zeolites at Temperatures from 298 to 393 K and at Pressures up to 3 MPa," *Journal of Chemical & Engineering Data,* vol. 68, no. 12, pp. 3512-3524, Dec 14 2023, doi: 10.1021/acs.jced.3c00504.

[202] J. Toth, *Adsorption*. CRC Press, 2002.

[203] L. Greenspan, "Humidity fixed points of binary saturated aqueous solutions," *Journal of Research of the National Bureau of Standards Section A: Physics and Chemistry,* vol. 81A, no. 1, 1977, doi: 10.6028/jres.081A.011.

[204] X. Xiang, T. Guo, Y. Yin, Z. Gao, Y. Wang, R. Wang, M. An, Q. Guo, and X. Hu, "High Adsorption Capacity Fe@13X Zeolite for Direct Air CO_2 Capture," *Industrial & Engineering Chemistry Research* vol. 62, no. 12, pp. 5420-5429, 2023, doi: 10.1021/acs.iecr.2c04458.

[205] M. J. Bos, S. Pietersen, and D. W. F. Brilman, "Production of high purity CO_2 from air using solid amine sorbents," *Chemical Engineering Science: X,* vol. 2, 2019, doi: 10.1016/j.cesx.2019.100020.

[206] F. Zerobin and T. Pröll, "Concentrated Carbon Dioxide (CO_2) from Diluted Sources through Continuous Temperature Swing Adsorption (TSA)," *Industrial & Engineering Chemistry Research* vol. 59, no. 19, pp. 9207-9214, 2020, doi: 10.1021/acs.iecr.9b06177.

[207] S.-m. Kim and G. Leonard, "Process modelling of Direct Air Capture (DAC) of CO_2 using solid amine sorbents," *Computer Aided Chemical Engineering,* vol. 51, pp. 265-270, 2022/01/01/ 2022, doi: 10.1016/B978-0-323-95879-0.50045-X.

[208] Y. Ji, W. Liu, J. Y. Yong, X. J. Zhang, and L. Jiang, "Solar-assisted temperature vacuum swing adsorption for direct air capture: Effect of relative humidity," *Applied Energy,* vol. 348, 2023, doi: 10.1016/j.apenergy.2023.121493.

[209] H. M. Schellevis, T. N. van Schagen, and D. W. F. Brilman, "Process optimization of a fixed bed reactor system for direct air capture," *International Journal of Greenhouse Gas Control,* vol. 110, 2021, doi: 10.1016/j.ijggc.2021.103431.

[210] Q. Yu and D. W. F. Brilman, "Design Strategy for CO_2 Adsorption from Ambient Air Using a Supported Amine Based Sorbent in a Fixed Bed Reactor," *Energy Procedia,* vol. 114, pp. 6102-6114, 2017, doi: 10.1016/j.egypro.2017.03.1747.

[211] Q. Yu and W. Brilman, "A Radial Flow Contactor for Ambient Air CO_2 Capture," *Applied Sciences,* vol. 10, no. 3, 2020, doi: 10.3390/app10031080.

[212] M. Schellevis, T. Jacobs, and W. Brilman, "CO_2 Capture From Air in a Radial Flow Contactor: Batch or Continuous Operation?," *Frontiers in Chemical Engineering,* vol. 2, 2020, doi: 10.3389/fceng.2020.596555.

[213] C. Drechsler and D. W. Agar, "Simulation and optimization of a novel moving belt adsorber concept for the direct air capture of carbon dioxide," *Computers & Chemical Engineering,* vol. 126, pp. 520-534, 2019, doi: 10.1016/j.compchemeng.2019.04.023.

[214] A. Shaik, A. Benneker, and S. McCoy, "Achieving net negative CO_2 emissions with sorbent direct air capture under different energy inputs and climate variations," *Social Science Research Network Electronic Journal,* 2022, doi: 10.2139/ssrn.4285081.

[215] J. Klomp, A. Srinivas, and W. Brilman, "Design And Demonstration Of A 10 Kg CO_2/day DAC Pilot Facility Using Sorbent Circulation," *Social Science Research Network Electronic Journal,* 2022, doi: 10.2139/ssrn.4290510.

[216] H. M. Schellevis and D. W. F. Brilman, "Experimental study of CO_2 capture from air via steam-assisted temperature-vacuum swing adsorption with a compact kg-scale pilot unit," *Reaction Chemistry & Engineering,* vol. 9, no. 4, pp. 910-924, 2024, doi: 10.1039/d3re00460k.

[217] M. J. Bos, T. Kreuger, S. R. A. Kersten, and D. W. F. Brilman, "Study on transport phenomena and intrinsic kinetics for CO_2 adsorption in solid amine sorbent," *Chemical Engineering Journal,* vol. 377, 2019, doi: 10.1016/j.cej.2018.11.072.

[218] R. T. Driessen, S. R. A. Kersten, and D. W. F. Brilman, "A Thiele Modulus Approach for Nonequilibrium Adsorption Processes and Its Application to CO_2 Capture," *Industrial & Engineering Chemistry Research* vol. 59, no. 15, pp. 6874-6885, 2020, doi: 10.1021/acs.iecr.9b05503.

[219] Q. Shu, M. Haug, M. Tedesco, P. Kuntke, and H. V. M. Hamelers, "Direct Air Capture Using Electrochemically Regenerated Anion Exchange Resins," *Environmental Science & Technology,* vol. 56, no. 16, pp. 11559-11566, 2022, doi: 10.1021/acs.est.2c01944.

[220] DuPont. "DuPont™AmberLite™ HPR4800 OH Ion Exchange Resin." https://www.dupont.com/content/dam/dupont/amer/us/en/water-solutions/public/documents/en/IER-AmberLite-HPR4800-OH-PDS-45-D01234-en.pdf (accessed 2023).

[221] J. Elfving, C. Bajamundi, J. Kauppinen, and T. Sainio, "Modelling of equilibrium working capacity of PSA, TSA and TVSA processes for CO_2 adsorption under direct air capture conditions," *Journal of CO_2 Utilization,* vol. 22, pp. 270-277, 2017, doi: 10.1016/j.jcou.2017.10.010.

[222] J. Elfving, J. Kauppinen, M. Jegoroff, V. Ruuskanen, L. Järvinen, and T. Sainio, "Experimental comparison of regeneration methods for CO_2 concentration from air using amine-based adsorbent," *Chemical Engineering Journal,* vol. 404, 2021, doi: 10.1016/j.cej.2020.126337.

[223] J. Elfving, C. Bajamundi, and J. Kauppinen, "Characterization and Performance of Direct Air Capture Sorbent," *Energy Procedia,* vol. 114, pp. 6087-6101, 2017, doi: 10.1016/j.egypro.2017.03.1746.

[224] H. Chen, H. Dong, Z. Shi, and A. K. SenGupta, "Direct air capture (DAC) and sequestration of CO_2: Dramatic effect of coordinated Cu(II) onto a chelating weak base ion exchanger," *Science Advances,* vol. 9, no. 10, 2023, doi: 10.1126/sciadv.adg1956.

[225] Purolite. "Purolite A110." https://www.purolite.com/product-pdf/A110.pdf (accessed 2023).

[226] Lanxess. "Product Information Lewatit VP OC 1065." https://lanxess.com/en/Products-and-Brands/Products/l/LEWATIT--VP-OC-1065 (accessed 2024).

[227] G. Socrates, *Infrared and Raman Characteristic Group Frequencies: Tables and Charts, 3rd Edition*. 2004.

[228] Q. Yu, J. P. Delgado, R. Veneman, and D. W. Brilman, "Stability of a Benzyl Amine Based CO_2 Capture Adsorbent in View of Regeneration Strategies," *Industrial & Engineering Chemistry Research* vol. 56, no. 12, pp. 3259-3269, 2017, doi: 10.1021/acs.iecr.6b04645.

[229] G. T. Rochelle, "Thermal degradation of amines for CO_2 capture," *Current Opinion in Chemical Engineering,* vol. 1, no. 2, pp. 183-190, 2012, doi: 10.1016/j.coche.2012.02.004.

[230] E. Sonnleitner, G. Schöny, and H. Hofbauer, "Assessment of zeolite 13X and Lewatit® VP OC 1065 for application in a continuous temperature swing adsorption process for biogas upgrading," *Biomass Conversion and Biorefinery,* vol. 8, no. 2, pp. 379-395, 2017, doi: 10.1007/s13399-017-0293-3.

[231] R. Veneman, N. Frigka, W. Zhao, Z. Li, S. Kersten, and W. Brilman, "Adsorption of H_2O and CO_2 on supported amine sorbents," *International Journal of Greenhouse Gas Control,* vol. 41, pp. 268-275, 2015, doi: 10.1016/j.ijggc.2015.07.014.

[232] S. Sutanto, J. W. Dijkstra, J. A. Z. Pieterse, J. Boon, P. Hauwert, and D. W. F. Brilman, "CO_2 removal from biogas with supported amine sorbents: First technical evaluation based on experimental data," *Separation and Purification Technology,* vol. 184, pp. 12-25, 2017, doi: 10.1016/j.seppur.2017.04.030.

[233] R. Serna-Guerrero, Y. Belmabkhout, and A. Sayari, "Modeling CO_2 adsorption on amine-functionalized mesoporous silica: 1. A semi-empirical equilibrium model," *Chemical Engineering Journal,* vol. 161, no. 1-2, pp. 173-181, 2010, doi: 10.1016/j.cej.2010.04.024.

[234] R. Serna-Guerrero, E. Da'na, and A. Sayari, "New Insights into the Interactions of CO_2 with Amine-Functionalized Silica," *Industrial & Engineering Chemistry Research* vol. 47, no. 23, pp. 9406-9412, 2008, doi: 10.1021/ie801186g.

[235] K. N. Pai, J. D. Baboolal, D. A. Sharp, and A. Rajendran, "Evaluation of diamine-appended metal-organic frameworks for post-combustion CO_2 capture by vacuum swing adsorption," *Separation and Purification Technology,* vol. 211, pp. 540-550, 2019, doi: 10.1016/j.seppur.2018.10.015.

[236] M. Hefti, L. Joss, Z. Bjelobrk, and M. Mazzotti, "On the potential of phase-change adsorbents for CO_2 capture by temperature swing adsorption," *Faraday Discussions,* vol. 192, pp. 153-179, 2016, doi: 10.1039/c6fd00040a.

[237] R. Hughes, G. Kotamreddy, A. Ostace, D. Bhattacharyya, R. L. Siegelman, S. T. Parker, S. A. Didas, J. R. Long, B. Omell, and M. Matuszewski, "Isotherm, Kinetic, Process Modeling, and Techno-Economic Analysis of a Diamine-Appended Metal–Organic Framework for CO_2

Capture Using Fixed Bed Contactors," *Energy & Fuels,* vol. 35, no. 7, pp. 6040-6055, 2021, doi: 10.1021/acs.energyfuels.0c04359.

[238] C. Kim, H. S. Cho, S. Chang, S. J. Cho, and M. Choi, "An ethylenediamine-grafted Y zeolite: a highly regenerable carbon dioxide adsorbent via temperature swing adsorption without urea formation," *Energy & Environmental Science,* vol. 9, no. 5, pp. 1803-1811, 2016, doi: 10.1039/c6ee00601a.

[239] S. Shimizu and N. Matubayasi, "Temperature Dependence of Sorption," *Langmuir,* vol. 37, no. 37, pp. 11008-11017, 2021, doi: 10.1021/acs.langmuir.1c01576.

[240] NIST. "Saturation Properties for Water — Temperature Increments." https://webbook.nist.gov/cgi/fluid.cgi?TLow=273.15&THigh=373.15&TInc=1&Digits=5&ID=C7732185&Action=Load&Type=SatP&TUnit=K&PUnit=MPa&DUnit=mol%2Fl&HUnit=kJ%2Fmol&WUnit=m%2Fs&VisUnit=uPa*s&STUnit=N%2Fm&RefState=DEF (accessed 2023).

[241] Z. Zhang, Q. Ding, J. Cui, X. Cui, and H. Xing, "High and selective capture of low-concentration CO_2 with an anion-functionalized ultramicroporous metal-organic framework," *Science China Materials,* vol. 64, no. 3, pp. 691-697, 2020, doi: 10.1007/s40843-020-1471-0.

[242] Z. Zhang, Q. Ding, S. B. Peh, D. Zhao, J. Cui, X. Cui, and H. Xing, "Mechano-assisted synthesis of an ultramicroporous metal-organic framework for trace CO_2 capture," *Chemical Communications,* vol. 56, no. 56, pp. 7726-7729, Jul 14 2020, doi: 10.1039/d0cc03196h.

[243] D. O'Nolan, L. Chatterton, T. Bellamy, J. T. Ennis, and M. Soukri, "Enhanced CO_2 sorption properties in a polarizable $[WO_2F_4]^{2-}$-pillared physisorbent under direct air capture conditions," *Chemical Communications,* vol. 59, no. 77, pp. 11540-11543, Sep 26 2023, doi: 10.1039/d3cc02749j.

[244] D. Song, F. Jiang, D. Yuan, Q. Chen, and M. Hong, "Optimizing Sieving Effect for CO_2 Capture from Humid Air Using an Adaptive Ultramicroporous Framework," *Small,* vol. 19, no. 44, p. e2302677, Nov 2023, doi: 10.1002/smll.202302677.

[245] X. Zhang, H. Zhao, Q. Yang, M. Yao, Y.-n. Wu, and Y. Gu, "Direct air capture of CO_2 in designed metal-organic frameworks at lab and pilot scale," *Carbon Capture Science & Technology,* vol. 9, 2023, doi: 10.1016/j.ccst.2023.100145.

[246] S. Bose, D. Sengupta, T. M. Rayder, X. Wang, K. O. Kirlikovali, A. K. Sekizkardes, T. Islamoglu, and O. K. Farha, "Challenges and Opportunities: Metal–Organic Frameworks for Direct Air Capture," *Advanced Functional Materials,* 2023, doi: 10.1002/adfm.202307478.

[247] S. Ullah, K. Tan, D. Sensharma, N. Kumar, S. Mukherjee, A. A. Bezrukov, J. Li, M. J. Zaworotko, and T. Thonhauser, "CO_2 Capture by Hybrid Ultramicroporous TIFSIX-3-Ni under Humid Conditions Using Non-Equilibrium Cycling," *Angewandte Chemie International Edition,* vol. 61, no. 35, p. e202206613, Aug 26 2022, doi: 10.1002/anie.202206613.

[248] M. M. Sadiq, M. Batten, A. W. THORNTON, M. R. Hill, K. KONSTAS, J. I. MARDEL, C. C. NG, X. MULET, and X. Wang, "Adsorption and desorption apparatus," Australia Patent Appl. AU2019391604A1, 2020. [Online]. Available: https://patents.google.com/patent/AU2019391604A1/en

[249] M. M. Sadiq, M. P. Batten, X. Mulet, C. Freeman, K. Konstas, J. I. Mardel, J. Tanner, D. Ng, X. Wang, S. Howard, M. R. Hill, and A. W. Thornton, "A Pilot-Scale Demonstration of Mobile Direct Air Capture Using Metal-Organic Frameworks," *Advanced Sustainable Systems,* vol. 4, no. 12, 2020, doi: 10.1002/adsu.202000101.

[250] "Products." MOF Technologies. https://web.archive.org/web/20170906040758/http://www.moftechnologies.com/products (accessed 2024).

[251] D. Chakraborty, A. Yurdusen, G. Mouchaham, F. Nouar, and C. Serre, "Large-Scale Production of Metal–Organic Frameworks," *Advanced Functional Materials,* 2023, doi: 10.1002/adfm.202309089.

[252] J. Warfsmann, B. Tokay, and N. R. Champness, "Thin film synthesis of hybrid ultramicroporous materials (HUMs)- a comparative approach," *Micropor Mesopor Mat,* vol. 311, 2021, doi: 10.1016/j.micromeso.2020.110686.

[253] P. Halasyamani, M. J. Willis, C. L. Stern, and K. R. Poeppelmeier, "Crystal growth in aqueous hydrofluoric acid and (HF)x · pyridine solutions: syntheses and crystal structures of $[Ni(H_2O)_6]^{2+}[MF_6]^{2-}$ (M = Ti, Zr, Hf) and $Ni_3(py)_{12}F_6 \cdot 7H_2O$," *Inorganica Chimica Acta,* vol. 240, no. 1-2, pp. 109-115, 1995, doi: 10.1016/0020-1693(95)04650-x.

[254] D. Yancy-Caballero, K. T. Leperi, B. J. Bucior, R. K. Richardson, T. Islamoglu, O. K. Farha, F. You, and R. Q. Snurr, "Process-level modelling and optimization to evaluate metal–organic frameworks for post-combustion capture of CO_2," *Molecular Systems Design & Engineering,* vol. 5, no. 7, pp. 1205-1218, 2020, doi: 10.1039/d0me00060d.

[255] P. F. Rosen, M. S. Dickson, J. J. Calvin, N. L. Ross, T. Friscic, A. Navrotsky, and B. F. Woodfield, "Thermodynamic Evidence of Structural Transformations in CO_2-Loaded Metal-Organic Framework $Zn(MeIm)_2$ from Heat Capacity Measurements," *Journal of the American Chemical Society,* vol. 142, no. 10, pp. 4833-4841, Mar 11 2020, doi: 10.1021/jacs.9b13883.

[256] "Cambridge Crystallographic Data Centre." https://www.ccdc.cam.ac.uk/ (accessed 2024).

[257] V. V. Korochentsev and N. M. Laptash, "Intermetallic charge transfer in $MTiF_6 \cdot 6H_2O$ (M = Mn, Fe, Co, and Ni): A study by X-ray photoelectron spectroscopy," *Solid State Sciences,* vol. 148, 2024, doi: 10.1016/j.solidstatesciences.2023.107433.

[258] M. L. Barsoum, J. Hofmann, H. Xie, Z. Chen, S. M. Vornholt, R. Dos Reis, N. Burns, S. Kycia, K. W. Chapman, V. P. Dravid, and O. K. Farha, "Probing Structural Transformations and Degradation Mechanisms by Direct Observation in SIFSIX-3-Ni for Direct Air Capture," *Journal of the American Chemical Society* Jan 25 2024, doi: 10.1021/jacs.3c11503.

[259] K. C. Ng, M. Burhan, M. W. Shahzad, and A. B. Ismail, "A Universal Isotherm Model to Capture Adsorption Uptake and Energy Distribution of Porous Heterogeneous Surface," *Scientific Reports,* vol. 7, no. 1, p. 10634, Sep 6 2017, doi: 10.1038/s41598-017-11156-6.

[260] K. W. Chapman, G. J. Halder, and P. J. Chupas, "Pressure-induced amorphization and porosity modification in a metal-organic framework," *Journal of the American Chemical Society,* vol. 131, no. 48, pp. 17546-7, Dec 9 2009, doi: 10.1021/ja908415z.

[261] R. P. P. L. Ribeiro, C. L. Antunes, A. U. Garate, A. F. Portela, M. G. Plaza, J. P. B. Mota, and I. A. A. C. Esteves, "Binderless shaped metal-organic framework particles: Impact on carbon dioxide adsorption," *Micropor Mesopor Mat,* vol. 275, pp. 111-121, 2019, doi: 10.1016/j.micromeso.2018.08.002.

[262] J. Garrido, A. Linares-Solano, J. M. Martin-Martinez, M. Molina-Sabio, F. Rodriguez-Reinoso, and R. Torregrosa, "Use of nitrogen vs. carbon dioxide in the characterization of activated carbons," *Langmuir,* vol. 3, no. 1, pp. 76-81, 2002, doi: 10.1021/la00073a013.

[263] P. Zhao, H. Fang, S. Mukhopadhyay, A. Li, S. Rudic, I. J. McPherson, C. C. Tang, D. Fairen-Jimenez, S. C. E. Tsang, and S. A. T. Redfern, "Structural dynamics of a metal-organic framework induced by CO_2 migration in its non-uniform porous structure," *Nature Communications,* vol. 10, no. 1, p. 999, Mar 1 2019, doi: 10.1038/s41467-019-08939-y.

[264] B. R. Pimentel, M. L. Jue, E.-K. Zhou, R. J. Verploegh, J. Leisen, D. S. Sholl, and R. P. Lively, "Sorption and Transport of Vapors in ZIF-11: Adsorption, Diffusion, and Linker Flexibility," *The Journal of Physical Chemistry C,* vol. 123, no. 20, pp. 12862-12870, 2019, doi: 10.1021/acs.jpcc.9b02192.

[265] C. L. Hobday, T. D. Bennett, D. Fairen-Jimenez, A. J. Graham, C. A. Morrison, D. R. Allan, T. Duren, and S. A. Moggach, "Tuning the Swing Effect by Chemical Functionalization of Zeolitic Imidazolate Frameworks," *Journal of the American Chemical Society,* vol. 140, no. 1, pp. 382-387, Jan 10 2018, doi: 10.1021/jacs.7b10897.

[266] A. F. Moslein and J. C. Tan, "Vibrational Modes and Terahertz Phenomena of the Large-Cage Zeolitic Imidazolate Framework-71," *The Journal of Physical Chemistry Letters,* vol. 13, no. 12, pp. 2838-2844, Mar 31 2022, doi: 10.1021/acs.jpclett.2c00081.

[267] D. Danaci, M. Bui, N. Mac Dowell, and C. Petit, "Exploring the limits of adsorption-based CO_2 capture using MOFs with PVSA – from molecular design to process economics," *Molecular Systems Design & Engineering,* vol. 5, no. 1, pp. 212-231, 2020, doi: 10.1039/c9me00102f.

[268] S. M. W. Wilson, "High purity CO_2 from direct air capture using a single TVSA cycle with Na-X zeolites," *Separation and Purification Technology,* vol. 294, 2022, doi: 10.1016/j.seppur.2022.121186.

[269] S. C. Lee, C. C. Hsieh, C. H. Chen, and Y. S. Chen, "CO_2 Adsorption by Y-Type Zeolite Impregnated with Amines in Indoor Air," (in English), *Aerosol and Air Quality Research* vol. 13, no. 1, pp. 360-366, Feb 2013, doi: 10.4209/aaqr.2012.05.0134.

[270] K. S. Kencana, K. C. Kemp, and S. B. Hong, "L-lysine-assisted synthesis of gismondine and chabazite nanozeolites for direct air capture of CO_2," *Separation and Purification Technology,* vol. 329, 2024, doi: 10.1016/j.seppur.2023.125154.

[271] Q. Ke, T. Sun, X. Wei, Y. Guo, and S. Wang, "Enhanced Trace Carbon Dioxide Capture on Heteroatom-Substituted RHO Zeolites under Humid Conditions," *ChemSusChem,* vol. 10, no. 21, pp. 4207-4214, Nov 9 2017, doi: 10.1002/cssc.201701162.

[272] S. Sircar; and W. C. Kratz, "Removal of water and carbon dioxide from air," Patent Appl. US4249915A, 1979. [Online]. Available: https://patents.google.com/patent/US4249915A/en

[273] R. Kumar, "Removal of water and carbon dioxide from atmospheric air," United States Patent Appl. US4711645A, 1986. [Online]. Available: https://patents.google.com/patent/US4711645A/en

[274] Y. Wang and M. D. LeVan, "Adsorption Equilibrium of Carbon Dioxide and Water Vapor on Zeolites 5A and 13X and Silica Gel: Pure Components," *Journal of Chemical & Engineering Data,* vol. 54, no. 10, pp. 2839-2844, 2009, doi: 10.1021/je800900a.

[275] Y. Wang and M. D. LeVan, "Adsorption Equilibrium of Binary Mixtures of Carbon Dioxide and Water Vapor on Zeolites 5A and 13X," *Journal of Chemical & Engineering Data,* vol. 55, no. 9, pp. 3189-3195, 2010, doi: 10.1021/je100053g.

[276] "ZEODAC." https://www.zeodac.com/ (accessed 2024).

[277] I. Halasz, S. Kim, and B. Marcus, "Uncommon Adsorption Isotherm of Methanol on a Hydrophobic Y-zeolite," *The Journal of Physical Chemistry B,* vol. 105, no. 44, pp. 10788-10796, 2001, doi: 10.1021/jp0103530.

[278] "Zeolite Y." Zeolyst International. https://www.zeolyst.com/our-products/standard-zeolite-powders/zeolite-y.html (accessed 2024).

[279] I. Halasz and M. Agarwal, "Hydrophobic nano-layer on surface prevents H_2O adsorption in moderately aluminum deficient Y zeolite crystals," *Micropor Mesopor Mat,* vol. 310, 2021, doi: 10.1016/j.micromeso.2020.110621.

[280] S. Navalon, M. Alvaro, and H. Garcia, "Highly dealuminated Y zeolite as efficient adsorbent for the hydrophobic fraction from wastewater treatment plants effluents," *Journal of Hazardous Materials,* vol. 166, no. 1, pp. 553-60, Jul 15 2009, doi: 10.1016/j.jhazmat.2008.11.057.

[281] J. Liu and S. A. Carr, "Removal of Estrogenic Compounds from Aqueous Solutions Using Zeolites," *Water Environment Research,* vol. 85, no. 11, pp. 2157-2163, 2013, doi: 10.2175/106143013x13736496909356.

[282] B. Wadi, A. Golmakani, V. Manovic, and S. A. Nabavi, "Evaluation of Moderately Grafted Primary, Diamine, and Triamine Sorbents for CO_2 Adsorption from Ambient Air: Balancing Kinetics and Capacity under Humid Conditions," *Industrial & Engineering Chemistry Research* vol. 60, no. 36, pp. 13309-13317, 2021, doi: 10.1021/acs.iecr.1c02416.

[283] J.-T. Anyanwu, Y. Wang, and R. T. Yang, "Amine-Grafted Silica Gels for CO_2 Capture Including Direct Air Capture," *Industrial & Engineering Chemistry Research* vol. 59, no. 15, pp. 7072-7079, 2019, doi: 10.1021/acs.iecr.9b05228.

[284] F. Shakerian, K.-H. Kim, J. E. Szulejko, and J.-W. Park, "A comparative review between amines and ammonia as sorptive media for post-combustion CO_2 capture," *Applied Energy,* vol. 148, pp. 10-22, 2015, doi: 10.1016/j.apenergy.2015.03.026.

[285] K. H. M. Al-Hamed and I. Dincer, "A comparative review of potential ammonia-based carbon capture systems," *Journal of Environmental Management,* vol. 287, p. 112357, Jun 1 2021, doi: 10.1016/j.jenvman.2021.112357.

[286] V. Darde, K. Thomsen, W. J. M. van Well, and E. H. Stenby, "Chilled ammonia process for CO_2 capture," *International Journal of Greenhouse Gas Control,* vol. 4, no. 2, pp. 131-136, 2010, doi: 10.1016/j.ijggc.2009.10.005.

[287] R. K. Brow and C. G. Pantano, "Thermochemical Nitridation of Microporous Silica Films in Ammonia," *Journal of the American Ceramic Society,* vol. 70, no. 1, pp. 9-14, 2005, doi: 10.1111/j.1151-2916.1987.tb04845.x.

[288] A. V. Naumkin, A. Kraut-Vass, S. W. Gaarenstroom, C. J. Powell, and A. Y. Lee. "NIST X-ray Photoelectron Spectroscopy Database." https://srdata.nist.gov/xps/ (accessed 2024).

[289] Sigma-Aldrich. "(3-Aminopropyl)trimethoxysilane." https://www.sigmaaldrich.com/GB/en/sds/aldrich/281778 (accessed 2024).

[290] Sigma-Aldrich. "[3-(2-Aminoethylamino)propyl]trimethoxysilane." https://www.sigmaaldrich.com/GB/en/sds/aldrich/440302 (accessed 2024).

[291] G. Cruciani, "Zeolites upon heating: Factors governing their thermal stability and structural changes," *Journal of Physics and Chemistry of Solids,* vol. 67, no. 9-10, pp. 1973-1994, 2006, doi: 10.1016/j.jpcs.2006.05.057.

[292] D. M. Ruthven, J. Kärger, S. Brandani, and E. Mangano, "Sorption kinetics: measurement of surface resistance," *Adsorption,* vol. 27, no. 5, pp. 787-799, 2020, doi: 10.1007/s10450-020-00257-w.

[293] D. M. Ruthven and M. F. M. Post, "Chapter 12 Diffusion in zeolite molecular sieves," in *Introduction to Zeolite Science and Practice*, (Studies in Surface Science and Catalysis, 2001, pp. 525-577.

[294] D. M. Ruthven, *Principles of Adsorption and Adsorption Processes*. John Wiley & Sons, 1984.

[295] S. Folger, "Chapter 15 Diffusion and Reaction," in *Essentials of Chemical Reaction Engineering*: Pearson, 2020.

[296] J. Kärger, M. Avramovska, D. Freude, J. Haase, S. Hwang, and R. Valiullin, "Pulsed field gradient NMR diffusion measurement in nanoporous materials," *Adsorption,* vol. 27, no. 3, pp. 453-484, 2021, doi: 10.1007/s10450-020-00290-9.

[297] Y. Wu, C. D'Agostino, D. J. Holland, and L. F. Gladden, "In situ study of reaction kinetics using compressed sensing NMR," *Chemical Communications,* vol. 50, no. 91, pp. 14137-40, Nov 25 2014, doi: 10.1039/c4cc06051b.

[298] A. H. Berge, S. M. Pugh, M. I. M. Short, C. Kaur, Z. Lu, J. H. Lee, C. J. Pickard, A. Sayari, and A. C. Forse, "Revealing carbon capture chemistry with 17-oxygen NMR spectroscopy," *Nature Communications,* vol. 13, no. 1, p. 7763, Dec 15 2022, doi: 10.1038/s41467-022-35254-w.

[299] J.-Y. Wang, E. Mangano, S. Brandani, and D. M. Ruthven, "A review of common practices in gravimetric and volumetric adsorption kinetic experiments," *Adsorption,* vol. 27, no. 3, pp. 295-318, 2020, doi: 10.1007/s10450-020-00276-7.

[300] S. Brandani and E. Mangano, "The zero length column technique to measure adsorption equilibrium and kinetics: lessons learnt from 30 years of experience," *Adsorption,* vol. 27, no. 3, pp. 319-351, 2020, doi: 10.1007/s10450-020-00273-w.

[301] J. Karger, T. Binder, C. Chmelik, F. Hibbe, H. Krautscheid, R. Krishna, and J. Weitkamp, "Microimaging of transient guest profiles to monitor mass transfer in nanoporous materials," *Nature Materials,* vol. 13, no. 4, pp. 333-43, Apr 2014, doi: 10.1038/nmat3917.

[302] R. Pini, L. Joss, and S. A. Hosseinzadeh Hejazi, "Quantitative imaging of gas adsorption equilibrium and dynamics by X-ray computed tomography," *Adsorption,* vol. 27, no. 5, pp. 801-818, 2020, doi: 10.1007/s10450-020-00268-7.

[303] N. S. Wilkins, A. Rajendran, and S. Farooq, "Dynamic column breakthrough experiments for measurement of adsorption equilibrium and kinetics," *Adsorption,* vol. 27, no. 3, pp. 397-422, 2020, doi: 10.1007/s10450-020-00269-6.

[304] E. Glueckauf, "Theory of chromatography. Part 10.—Formulæ for diffusion into spheres and their application to chromatography," *Transactions of the Faraday Society,* vol. 51, no. 0, pp. 1540-1551, 1955, doi: 10.1039/tf9555101540.

[305] S. Sircar and J. R. Hufton, "Why Does the Linear Driving Force Model for Adsorption Kinetics Work?," *Adsorption,* vol. 6, no. 2, pp. 137-147, 2000, doi: 10.1023/a:1008965317983.

[306] W. Si, S. Ye, D. Zhang, B. Yang, Y. Hou, Z. Li, X. Zhang, J. Zhu, and L. Lei, "Kinetics and mechanism of low-concentration CO_2 adsorption on solid amine in a humid confined space," *The Canadian Journal of Chemical Engineering,* vol. 97, no. 3, pp. 697-701, 2018, doi: 10.1002/cjce.23257.

[307] T. Wang, X. Wang, C. Hou, and J. Liu, "Quaternary functionalized mesoporous adsorbents for ultra-high kinetics of CO_2 capture from air," *Scientific Reports,* vol. 10, no. 1, p. 21429, Dec 8 2020, doi: 10.1038/s41598-020-77477-1.

[308] W. Wang, F. Liu, Q. zhang, G. Yu, and S. Deng, "Efficient removal of CO_2 from indoor air using a polyethyleneimine-impregnated resin and its low-temperature regeneration," *Chemical Engineering Journal,* vol. 399, 2020, doi: 10.1016/j.cej.2020.125734.

[309] L. Qi, Y. Han, G. Bai, Q. Liu, Z. Fei, X. Chen, Z. Zhang, J. Tang, M. Cui, and X. Qiao, "Role of brush-like additives in CO_2 adsorbents for the enhancement of amine efficiency," *Journal of Environmental Chemical Engineering,* vol. 9, no. 6, 2021, doi: 10.1016/j.jece.2021.106709.

[310] C. Hou, D. R. Kumar, Y. Jin, Y. Wu, J. J. Lee, C. W. Jones, and T. Wang, "Porosity and hydrophilicity modulated quaternary ammonium-based sorbents for CO_2 capture," *Chemical Engineering Journal,* vol. 413, 2021, doi: 10.1016/j.cej.2020.127532.

[311] T. Wang, J. Liu, H. Huang, M. Fang, and Z. Luo, "Preparation and kinetics of a heterogeneous sorbent for CO_2 capture from the atmosphere," *Chemical Engineering Journal,* vol. 284, pp. 679-686, 2016, doi: 10.1016/j.cej.2015.09.009.

[312] A. Vallace, Y. Ren, C. W. Jones, and R. P. Lively, "Kinetic model describing self-limiting CO_2 diffusion in supported amine adsorbents," *Chemical Engineering Journal,* vol. 472, 2023, doi: 10.1016/j.cej.2023.144838.

[313] S. G. Subraveti, K. N. Pai, A. K. Rajagopalan, N. S. Wilkins, A. Rajendran, A. Jayaraman, and G. Alptekin, "Cycle design and optimization of pressure swing adsorption cycles for pre-combustion CO2 capture," *Applied Energy,* vol. 254, 2019, doi: 10.1016/j.apenergy.2019.113624.

[314] E. Alpay and D. M. Scott, "The linear driving force model for fast-cycle adsorption and desorption in a spherical particle," *Chemical Engineering Science,* vol. 47, no. 2, pp. 499-502, 1992, doi: 10.1016/0009-2509(92)80041-a.

[315] D. M. Scott, "The linear driving force model for cyclic adsorption and desorption: the effect of shape," *Chemical Engineering Science,* vol. 49, no. 6, pp. 914-916, 1994, doi: 10.1016/0009-2509(94)80028-6.

[316] M. I. Hossain, A. D. Ebner, and J. A. Ritter, "New linear driving force correlation spanning long and short cycle time pressure swing adsorption processes," *Adsorption,* vol. 22, no. 7, pp. 939-950, 2016, doi: 10.1007/s10450-016-9801-1.

[317] E. Hussein, "Numerical and experimental evaluation of advanced metal-organic framework materials for adsorption heat pumps," PhD, Mechanical Engineering, University of Birmingham, 2018. [Online]. Available: https://etheses.bham.ac.uk/id/eprint/8626/1/Hussein18PhD.pdf

[318] H. Marcia and H. Allan, "Thermal Conductivity of Gases," in *CRC Handbook of Chemistry and Physics*, ed: CRC-Press, Boca Raton, FL, 2011.

Appendices

Appendix 1. Literature review

The following tables summarise the physicochemical properties (Tables A1.1-A1.6) and sorption properties (Tables A1.7-A1.12) of reviewed DAC adsorbents. When data was not available in the reviewed article, best effort was made to find this data in other non-DAC publications / sources.

Some things to note:

- "-" indicates that data was not found
- If there is only one entry in a cell, it implies that it applies to all functionalisation types and/or loadings
- Units for functionalisation loading were converted to $mmol_N\ g_{ads}^{-1}$ whenever possible (and indicated with a footnote when not possible)
- For thermal stability, "or >" indicates that this was the highest temperature used in the conducted experiments but no explicit degradation temperature was provided
- For Table A1.1, the data entries for unfunctionalised SBA-15 were not repeated in the subsequent cells
- For CO_2 uptake, the measurement technique is indicated along with the CO_2 concentration and temperature conditions if these were not at 400 ppm and 25 °C, respectively
- For gas isotherms, the measurement technique is indicated, along with the measurement temperatures for O_2 and H_2O. For CO_2 and N_2, Y indicates that at least three isotherm temperatures were measured
- Temperature and relative humidity conditions are indicated for H_2O stability studies where available
- Temperature and oxygen concentrations are indicated for O_2 stability studies where available
- For O_2 stability, > 50% CO_2 indicates more than 50% of the CO_2 uptake capacity was maintained, and < 50% CO_2 indicates less than 50% of the CO_2 uptake capacity was maintained. For O_2 stability, low O_2 uptake refers to the results of the O_2 isotherm measurement.
- Measurement techniques are indicated for kinetic and cyclic studies

A1.1 Tables of physicochemical properties

Table A1.1: Summary of physicochemical properties of silica adsorbents investigated for DAC.

	Name (form)	Functionalised	Functionalisation Loading ($mmol_N\ g_{ads}^{-1}$)	ρ_{bed} ($g\ cm^{-3}$)	$\rho_{particle}$ ($g\ cm^{-3}$)	$\rho_{skeletal}$ ($g\ cm^{-3}$)	S_{BET} ($m^2\ g^{-1}$)	V_{tot} ($cm^3\ g^{-1}$)	V_{micro} ($cm^3\ g^{-1}$)	C_p ($J\ g^{-1}\ °C^{-1}$)	κ ($W\ m^{-1}\ °C^{-1}$)	Thermal Stability (°C)	Ref
1	SBA-15 (powder)	DMAPS (g)	0, 1.9, 2.5	0.08 [1], -, -	0.67 [1], -, -	2.08 [1], -, -	961, 386, 289	1.19, 0.55, 0.45	-	0.69 [2], -, - (25 °C)	0.04 [1], -, -	1200 [3], -, - (air)	[4]
2	SBA-15 (powder)	n/a APTES (g) AE-APS (g) AE-AE-APS (g)	0 2.6 2.8 3.5, 4.7	-	-	-	490 267 288 274, 115	1.2 0.63 0.74 0.66, 0.26	-	-	-	-	[5]
3	SBA-15 (powder)	DT (g)	0, 1.7, 4.5, 5.1, 5.7, 6	-	-	-	642, 458, 235, 166, 81, 16	1.03, 0.82, 0.44 0.30, 0.15, 0.03	-	-	-	-	[6]
4	SBA-15 (powder)	PEI-600-B (i)	0, 33%[a], 50%[a], 67%[a]	-	-	-	526, 166, 17, 8	0.96, 0.36, 0.03, 0.01	0.027, 0, 0, 0	-	-	200[b] (N_2)	[7]
5	SBA-15 (powder)	n/a ED-3 ED-6 PD-3 PD-6	0 2.5, 3.6, 4.6, 6.3, 8.2 3.5, 5.1, 6.9, 8.5 2.9, 3.5, 4.7, 5.9 3.3, 4.5, 6.0, 7.9	-	-	-	700 309, 252, 152, 58, 4 279, 169, 76, 14 274, 212, 116, 26 275, 204, 98, 20	0.96 0.55, 0.43, 0.26, 0.10, 0 0.48, 0.29, 0.13, 0.03 0.56, 0.38, 0.21, 0.05 0.45, 0.34, 0.18, 0.04	-	-	-	- 200 200 200 200 (N_2)	[8]
6	SBA-15 (powder)	n/a PEI-800 (i) TEPA (i)	0 25%[a], 50%[a], 75%[a] 25%[a], 50%[a], 75%[a]	-	-	-	643 206, 12, 2 250, 174, 1	1.14 0.47, 0.05, 0.003 0.60, 0.35, 0.002	-	-	-	- 200 120 (N_2)	[9]
7	SBA-15 (powder)	n/a PPI-HCl-B (i) PPI-CH_3SO_3H-B (i) PPI-HBr-B (i) PPI-$HClO_4$-B (i)	0 4.3 4.8 4.5, 5.5, 6.9, 7.4 5.4, 7.4	-	-	-	840 225 175 229, 129, 73, 29 154, 58	0.94 0.35 0.28 0.36, 0.22, 0.13, 0.06 0.25, 0.08	-	-	-	250[b] (N_2/air)	[10]

	Name (form)	Functionalised	Functionalisation Loading ($mmol_N\ g_{ads}^{-1}$)	ρ_{bed} (g cm^{-3})	$\rho_{particle}$ (g cm^{-3})	$\rho_{skeletal}$ (g cm^{-3})	S_{BET} ($m^2\ g^{-1}$)	V_{tot} ($cm^3\ g^{-1}$)	V_{micro} ($cm^3\ g^{-1}$)	C_p (J g^{-1} °C^{-1})	κ (W m^{-1} °C^{-1})	Thermal Stability (°C)	Ref
8	SBA-15 (powder)	n/a	0	-	-	-	890	1.01	-	-	-	250[b] (N_2/air)	[11]
		PPI-700-L (i)	1.5, 2.8, 4.4, 5.9, 7.5				524, 344, 315, 181, 63	0.72, 0.60, 0.52, 0.31, 0.12					
		PPI-1000-L (i)	1.5, 2.9, 4.4, 5.9, 7.6				610, 378, 308, 178, 45	0.87, 0.56, 0.48, 0.30, 0.10					
		PPI-6700-L (i)	2.0, 3.7, 5.3, 7.1, 8.7				563, 335, 217, 108, 20	0.77, 0.54, 0.36, 0.19, 0.04					
		PPI-36000-L (i)	1.7, 3.6, 5.0, 6.6, 8.0				522, 416, 288, 164, 61	0.75, 0.64, 0.46, 0.28, 0.11					
9	SBA-15[c] (powder)	n/a	0	-	-	-	890	1.01	-	-	-	250[b] [11] (N_2/air)	[12]
		PPI-700-L[c] (i)	7.5				63	0.12					
		PPI-6700-L[c] (i)	8.7				21	0.04					
		PPI-36000-L[c] (i)	8.0				61	0.11					
10	SBA-15 (powder)	n/a	0	-	-	-	684	0.95	-	-	-	250[b] [11] (N_2/air)	[12]
		PPI-700-L[d] (i)	6.8				18	0.03					
		PPI-6700-L[d] (i)	6.5				51	0.08					
		PPI-36000-L[d] (i)	6.1				45	0.07					
		PPI-700/36000-L[d] (i)	2.2, 3.9, 4.3, 6.0				365, 197, 202, 67	0.56, 0.30, 0.31, 0.01					
		PPI-700/36000-L[d] (i)	1.9, 3.1				317, 181	0.48, 0.28					
		PPI-6700/36000-L[d] (i)	1.9, 3.7, 3.8, 6.5				317, 185, 117, 32	0.49, 0.29, 0.18, 0.05					
		PPI-700/6700-L[d] (i)	2.4, 4.2, 5.7, 6.6, 7.6				306, 179, 100, 58, 50	0.48, 0.28, 0.15, 0.09, 0.09					
11	SBA-15 (powder)	n/a	0	-	-	-	700	0.96	-	-	-	150[b] (air)	[13]
		PGA (Xn = 15) (i)	2.4, 3.0, 4.2				288, 229, 87	0.50, 0.41. 0.16					
		PGA (Xn = 25) (i)	2.7, 4.1, 5.8, 8.0				292, 213, 39, 40	0.49, 0.39, 0.10, 0.09					
		PGA (Xn = 50) (i)	2.7, 3.6, 4.7, 5.4				283, 358, 241, 77	0.45, 0.36, 0.26, 0.07					
12	SBA-15 (powder)	PEI-800-B (i)	0, 4.4, 7.2, 8.1, 9.9, 10.8	-	-	-	700, 281, 164, 56, 14, 2	0.96, 0.47, 0.29, 0.17,- 0.05, 0.01	-	-	-	200[b] [9] (N_2)	[13]
13	SBA-15 (powder)	n/a	0	-	-	-	816	0.76	-	-	-	- 120 (He)	[14]
		PEI-1800-B (i)	5.3, 6.7, 8.8, 9.6, 11.2				256, 197, 68, 10, 4	0.38, 0.31, 0.15, 0.06, 0.02					
		PPG (i)	5.7, 7.7, 10.6, 11.4, 14.3				253, 205, 81, 40, 16	0.48, 0.37, 0.20, 0.12, 0.07				100 (He)	
14	SBA-15-il SBA-15-cal (powder)	APS (g)	0, 2.2 0, 1.4	-	-	-	884, 240 982, 326	1.09, 0.38 1.12, 0.47	-	-	-	350[b] (air)	[15]
15	SBA-15 (powder)	TEPA (i)	0, 67%[e]				443, -	1.4, -				130[b] [16] (N_2)	[17]

	Name (form)	Functionalised	Functionalisation Loading ($mmol_N\ g_{ads}^{-1}$)	ρ_{bed} (g cm^{-3})	$\rho_{particle}$ (g cm^{-3})	$\rho_{skeletal}$ (g cm^{-3})	S_{BET} ($m^2\ g^{-1}$)	V_{tot} ($cm^3\ g^{-1}$)	V_{micro} ($cm^3\ g^{-1}$)	C_p (J g^{-1} °C^{-1})	κ (W m^{-1} °C^{-1})	Thermal Stability (°C)	Ref
16	SBA-15 (powder)	n/a	0	-	-	-	829	1.04	-	-	-	110 or >[b]	[18]
		APS (g)	0.5, 1.0, 1.1, 1.4, 2.1				452, 423, 356, 352, 302	0.71, 0.68, 0.58, 0.49, 0.34				110 or >[b]	
		AE-APS-L (g)	0.9, 1.7, 2.2, 2.5, 3.7				423, 385, 317, 306, 280	0.64, 0.59, 0.52, 0.51, 0.42				110 or >[b]	
		AP-APS-L (g)	0.9, 1.6, 2.6, 3.4				427, 379, 292, 239	0.66, 0.58, 0.47, 0.40				110 or >[b]	
		AE-ESPE-B (g)	0.6, 1.0, 2.1, 2.5				473, 423, 377, 288	0.71, 0.70, 0.62, 0.50				110 or >[b]	
		AP-ESPP-B (g)	0.8, 1.3, 1.8, 2.3				414, 315, 283, 189	0.66, 0.54, 0.50, 0.34				(He)	
17	SBA-15 (powder)	n/a	0	-	-	-	880	1.00	-	-	-		[19]
		TETA (i)	3.3, 5.9, 8.3, 11.2				396, 312, 248, 124	0.68, 0.61, 0.48, 0.23				70[b]	
		TPTA (i)	2.7, 4.6, 6.8, 8.9				409, 367, 197, 106	0.75, 0.69, 0.36, 0.20				70[b]	
		EI-den (i)	2.5, 5.0, 7.0, 7.6 8.5, 11.0				333, 292, 217, 186, 98, 83	0.62, 0.56, 0.40, 0.35, 0.18, 0.16				70[b]	
		PI-den (i)	2.4, 4.3, 5.5, 6.6, 7.6, 9.2				282, 284, 245, 158, 63, 65	0.54, 0.55, 0.46, 0.30, 0.11, 0.13				70[b] (N_2)	
18	SG (powder)	DT (g)	0, 5.1	0.35 [20], -	0.7-1.0 [21], -	2.06[f] [21], -	309, 73	1.12, 0.31	-	0.85-1.10[g] [22], -	0.1-0.2[h] [23], -	-, 150 (air)	[24]
19	SG (powder)	n/a	0	see 19	see 19	see 19	294	1.04	-	see 19	see 19	-	[25]
		TEPA (i)	2.0, 5.0, 5.8, 11.3				247 172, 147, 33	0.76, 0.59, 0.54, 0.16					
		PEI (i)	7.8, 10.0				30, 8	0.09, 0.04					
		APTES (g)	1.1, 2.4, 3.0				196, 119, 63	0.66, 0.35, 0.23					
20	SG (monolith)	PEI-10000	10.0	-	-	-	33	0.242	-	-	-	240	[26]
		PEI-25000	12.1				17	0.141					
		PEI-750000	8.6				75	0.603					
21	SG	PD (i)	0, -	0.14, 0.50	-	-	594, 293	1.64, 0.63	-	-	-	-, 200	[27]
	SG/PEG		0, -	0.18, 0.52			756, 171	2.66, 1.23				-, 200	
	SG/CB (xerogel powder)		0, -	0.19, 0.71			798, 174	3.21, 0.64				-, 200	
22	MCM-41 (powder)	PEI-800 (i)	0, 0.2[i], 0.3[i], 0.5[i], 0.6[i], 0.6[i]	-	-	-	350, 232, 126, 58, 2, -	0.99, 0.60, 0.36, 0.18, 0.01, -		-	-	-	[28]
23	FS (powder)	n/a	0	0.05 [29]	-	2.2[k] [29]	179	0.45	-	0.79-0.85 [29] (10-50 °C)	0.02-0.06 [29] (50-200 °C)	2000 [30]	[31]
		APS	1.7, 3.3, 3.5, 65 %[j], 4.7	-			87, 56, 35, 0.3, 2	0.74, 0.58, 0.50, 0.01, 0.03		-		300 (N_2)	
		APS-CTAB5	3.5, 65 %[j], 4.7	-			21, 22, 3	0.33, 028, 0.04		-		300 (N_2)	

	Name (form)	Functionalised	Functionalisation Loading ($mmol_N\ g_{ads}^{-1}$)	ρ_{bed} ($g\ cm^{-3}$)	$\rho_{particle}$ ($g\ cm^{-3}$)	$\rho_{skeletal}$ ($g\ cm^{-3}$)	S_{BET} ($m^2\ g^{-1}$)	V_{tot} ($cm^3\ g^{-1}$)	V_{micro} ($cm^3\ g^{-1}$)	C_p ($J\ g^{-1}\ °C^{-1}$)	κ ($W\ m^{-1}\ °C^{-1}$)	Thermal Stability (°C)	Ref
24	MFS (powder)	PEI-1200 + EB (i)	6.7	0.8	-	-	43	1.7		-	-	-	[32]
25	SiO_2 (C-803) (powder)	PEI-800-B (i)	0, 0.9[l]	0.07 [33], -	0.8 [34], -	-	282, 84[m]	1.25, 0.40[m]	-	-	-	200[b] (N_2/air)	[35]
26	SiO_2 (C-803) (CA fibre composite)	PEI-800-B (i)	0, 0.9[l]	-	-	-	49, 11[m]	0.44, 0.10[m]	-	-	-	260, 200 (N_2/air)	[35]
27	MCF_a[n] (powder, pellet)	PEI-1200-B (i)	0, 0.6	0.10 [36], -	-	2.11, 1.25	594, 3	3.21[p], 0.020[p]	-	-	-	-	[37]
	MCF_b[o] (powder, pellet)		0, 0.5	0.10 [36], -		2.15, 1.26	453, 4	2.49[p], 0.021[p]					
28	HBS (powder)	DT (g)	0, 7.9	-	-	-	612, 28	1.59, 0.19		-	-	150[b] (He/air)	[38]
29	HMS (powder)	n/a	0	-	-	-	448	4.52	-	-	-	200[b] [35] (N_2/air)	[39]
		PEI-800-S_H_LV (i)	0.4[l], 0.9[l], 1.7[l], 2.0[l], 3.3[l], 4.1[l], 4.7[l]				-	-					
		PEI-800-R_L_HV (i)	0.3[l], 0.8[l], 1.0[l], 1.4[l], 2.0[l], 3.1[l]				-	-					
30	SAG (powder)	n/a	0	0.07-0.08[r] [40]	0.12-0.15 [41]	1.8-2.0 [42]	186	0.53	-	0.70-1.15 [40]	0.01-0.02 [43]	-	[44]
		K_2CO_3 (i)	0.7[q], 0.9[q], 1.2[q], 1.3[q], 1.5[q]	-	-	-	60, 48, 10, 1, 1	0.21, 0.01, 0.08, 0.002, 0.001		-	-		
31	MMSN	TEPA (i)	0, 48 %[s]	-	-	-	981, -	1.90, -	0.78, -	-	0.54[t] [45], -	100[b] (O_2)	[46]
	+CTAC10		0, 48 %[s]				933, -	1.65, -	0.72, -		-		
	+CTAC20		0, 48 %[s]				608, -	1.15, -	0.45, -		-		
	+CTAC30 (powder)		0, 48 %[s]				431, 19	0.72, 0.12	0.28, -		-		
32	EtSNT (powder)	PEI-600 (i)	0, 11.2	-	-	-	855, 185	2.11, 0.93				200[b] (air)	[47]
33	AHSA (monolith)	APTES (g)	7.6	0.12	-	2.12	146	1.52	-	-	-	280	[48]
34	SiNP-SIP (powder)	PEI-2000-b (g)	-	-	-	-	-	-	-	-	-	120 or > (N_2)	[49]
35	AHTSA (monolith)	APTES (g)	5.3, 7.9, 8.5, 8.8	0.13, 0.12, 0.11, 0.11	-	2.21, 2.21, 2.22, 2.22	374, 170, 138, 66	7.18, 7.68, 8.48, 8.81	-	-	-	230 or > (N_2)	[50]

[a] theoretical PEI wt%
[b] not relevant for 0 functionalisation loading

[c] material aged for 1.5 years
[d] material aged for 2 years
[e] theoretical TEPA wt%
[f] data for type a++ silica gel
[g] data is for pellets
[h] data for dried silica gel, form unclear
[i] $mmol_{PEI}\ g^{-1}$
[j] theoretical APS wt%
[k] given as specific gravity
[l] $mmol_{PEI}\ g^{-1}_{SiO2}$
[m] $m^2\ g^{-1}_{SiO2}$
[n] synthesis method A
[o] synthesis method B
[p] data given as mesopore volume
[q] $mmol_{K2CO3}\ g^{-1}$
[r] data given for granules
[s] TEPA wt%
[t] data for 20 nm silica nanoparticles

Table A1.2: Summary of physicochemical properties of metal oxide adsorbents investigated for DAC.

	Name (form)	Functionalised	Functionalisation Loading ($mmol_N\ g_{ads}^{-1}$)	ρ_{bed} ($g\ cm^{-3}$)	$\rho_{particle}$ ($g\ cm^{-3}$)	$\rho_{skeletal}$ ($g\ cm^{-3}$)	S_{BET} ($m^2\ g^{-1}$)	V_{tot} ($cm^3\ g^{-1}$)	V_{micro} ($cm^3\ g^{-1}$)	C_p ($J\ g^{-1}\ °C^{-1}$)	κ ($W\ m^{-1}\ °C^{-1}$)	Thermal Stability (°C)	Ref
1	$Mg_{0.55}Al$–O-a[a] (powder)	PEI-600-B (i)	0, 33%[b], 50%[b], 67%[b]	-, -, -, 0.54 [51]	-	-	185, 110, 31, 20	1.15, 0.64, 0.26, 0.02	0.01, 0.01, 0.01, 0.002	-, -, -, 1.93 [51]	-	300[c] (N_2)	[7]
2	$Mg_{0.55}Al$-O-a[a]	APS (g)	0, 2.3	-	-	-	538, -	1.42, -	0, -	-	-	-	[52]
	Mg_2Al–O-a[a] (powder)		0, 3.7				252, -	0.85, -	0, -				
3	Mg_2Al-O-urea[d]	AE-AE-APS (g)	0, 0.5	-	-	-	15, 9	0.05, 0.02	0.001, 0.002	-	-	-	[52]
	$Mg_{0.55}Al$-O-w[e]		0, 1.8				78, 11	0.18, 0.06	0.001, 0				
	Mg_2Al-O-w[e]		0, 2.2				71, 20	0.41, 0.15	0, 0.003				
	Mg_3Al-O-w[e]		0, 1.2				53, 20	0.40, 0.24	0.01, 0.003				
	$Mg_{0.55}Al$-O-a[a]		0, 6.4				538, 162	1.42, 0.55	0, 0				
	Mg_2Al-O-a[a]		0, 4.3				252, 53	0.85, 0.25	0, 0				
	Mg_3Al-O-a[a]		0, 2.1				158, 37	0.84, 0.23	0.02, 0				
	$Mg_{0.55}Al$-O-F[f]		0, 4.8				341, -	0.97, -	0, -				
	Mg_2Al-O-F[f] (powder)		0, 4.7				218, 70	0.76, 0.51	0, 0				
4	$Mg0_{.55}Al$-O	TEPA (i)	0, 33%[g], 50%[g], 67%[g], 83%[g]	-	-	-	442, 144, 37, 10, -	2.15, 0.78, 0.45, 0.14, -	-	-	-	120 or > (N_2)	[17]
	Mg_1Al-O		0, 33%[g]				422, -	1.78, -					
	Mg_2Al-O		0, 33%[g]				302, -	1.32, -					
	Mg_3Al-O		0, 33%[g]				299, -	1.30, -					
	$Mg_{0.55}Al$-CO_3		0, 33%[g], 50%[g], 67%[g]				-	-					
	MgO (powder)		0, 33%[g]				21, -	0.19, -					
5	γ-Al_2O_3 (powder)	n/a	0	0.80 [53]	1.99 [54]	3.97 [55]	225	0.39	-	0.81-0.98 [56] (25-120 °C)	35 [57]	1050 [58]	[59]
		Na_2CO_3 + $Ni(NO_3)_2$ (i)	15%[h] + 10%[i]	-	-	-	121	0.31		-	-	450 or > (air)	
6	γ-Al_2O_3 (powder)	NaO (i)	6%[j]	-	-	-	-	-	-	-	-	320 or > (air)	[60]
		NaO + Ru (i)	10%[j] + 0.5 %[k]									320 or > (air)	
7	γ-Al_2O_3 (powder)	NaO + Ru (i)	10%[j] + 1%[k]	-	-	-	-	-	-	-	-	300 or > (N_2/H_2)	[61]
		CaO + Ru (i)	10%[k] + 1%[l]									300 or > (N_2/H_2)	
8	γ-Al_2O_3 (powder)	TEPA (i)	0, 50%[g]	see 5, -	see 5, -	see 5, -	170, -	0.79, -	-	see 5, -	see 5, -	120 or >	[17]

	Name (form)	Functionalised	Functionalisation Loading ($mmol_N\ g_{ads}^{-1}$)	ρ_{bed} ($g\ cm^{-3}$)	$\rho_{particle}$ ($g\ cm^{-3}$)	$\rho_{skeletal}$ ($g\ cm^{-3}$)	S_{BET} ($m^2\ g^{-1}$)	V_{tot} ($cm^3\ g^{-1}$)	V_{micro} ($cm^3\ g^{-1}$)	C_p ($J\ g^{-1}\ °C^{-1}$)	κ ($W\ m^{-1}\ °C^{-1}$)	Thermal Stability (°C)	Ref
9	γ-Al_2O_3 (powder)	K_2CO_3 (i)	0, 1.6[m]	see 5, -	see 5, -	see 5, -	240, -	-	-	see 5, -	see 5, -	350 or > (H_2)	[62]
10	γ-Al_2O_3-O[n] γ-Al_2O_3-D[o] (powder)	APTES (g)	0, 0.9[p], 2.0[p], 3.2[p], 5.4[p] 0, 0.7[p], 1.5[p], 2.9[p], 4.1[p]	-	-	-	226[q], 234[q], 188[q], 216[q], 112[q] 322[q], 295[q], 263[q], 297[q], 224[q]	0.97[r], 0.92[r], 0.78[r], 0.77[r], 0.48[r] 0.85[r], 0.79[r], 0.67[r], 0.69[r], 0.46[r]	-	-	-	110 or > (He)	[63]
11	ZrO_2 (aerogel powder)	K_2CO_3 (i)	0, 0.7 [m], 1.2[m], 1.7[m], 2.1[lm]	0.16[s] [64], -, -, -, -	-	-	119, 86, 63, 46, 43	0.58, 0.19, 0.14, 0.13, 0.11	-	-	0.02-0.18[t] [43]	300 or > (Ar)	[65]

[a] exfoliated LDH
[b] PEI theoretical wt%
[c] not relevant for 0 functionalisation loading
[d] bulk LDH
[e] stacked LDH
[f] ultrafine LDH
[g] TEPA theoretical wt%
[h] theoretical wt% of γ-alumina
[i] theoretical wt% of Na- γ-alumina
[j] Na_2O theoretical wt%
[k] Na_2O and Ru theoretical wt%
[l] CaO and Ru theoretical wt%
[m] $mmol_{K2CO3}\ g^{-1}$
[n] ordered alumina
[o] disordered alumina
[p] $mmol\ g^{-1}_{alumina}$
[q] $m^2\ g^{-1}_{alumina}$
[r] $cm^3\ g^{-1}_{alumina}$
[s] data for monolithic material
[t] for unfunctionalized ZrO_2

Table A1.3: Summary of physicochemical properties of MOF adsorbents investigated for DAC.

	Name (form)	Functionalised	Functionalisation Loading ($mmol_N\ g_{ads}^{-1}$)	ρ_{bed} ($g\ cm^{-3}$)	$\rho_{particle}$ ($g\ cm^{-3}$)	$\rho_{skeletal}$ ($g\ cm^{-3}$)	S_{BET} ($m^2\ g^{-1}$)	V_{tot} ($cm^3\ g^{-1}$)	V_{micro} ($cm^3\ g^{-1}$)	C_p ($J\ g^{-1}\ °C^{-1}$)	κ ($W\ m^{-1}\ °C^{-1}$)	Thermal Stability (°C)	Ref
1	NbOFFIVE-1-Ni (powder)	n/a	0	0.4 [66]	1.96	-	278	0.095	-	-	-	300 (N_2)	[67]
2	NbOFFIVE-1-Ni/PA (beads)	n/a	0	0.48	-	-	219	0.194	-	-	-	340 (N_2)	[66]
3	TIFSIX-3-Ni (powder)	n/a	0	-	-	-	209 [68]	-	-	-	-	280 (N_2) or 220 (air) [69]	[70]
4	TIFSIX-2-Cu-i (powder)	n/a	0	-	1.27 [71]	-	590	-	-	-	-	250 [71]	[72]
5	SIFSIX-18-Ni-β (powder)	n/a	0	-	1.31	-	549	-	-	-	-	300 (N_2)	[73]
6	SIFSIX-3-Ni (powder)	HPMCP (c)	0, 5%[a]	-	1.61 [71], -	-	220, -	0.15 [74], -	-	1.07 [74], -	-	200 (N_2)	[75]
7	SIFSIX-3-Cu (powder) (MF monolith)	n/a	0	-	1.73 [76] -	-	300 270	0.104 [77] -	-	-	-	120 160 (N_2)	[78]
8	TIFSIX-3-Co (powder)	n/a	0	-	1.62	-	260	0.11	-	-	-	245 (N_2)	[79]
9	GeFSIX-3-Ni (powder)	n/a	0	-	1.77	-	221	0.093 [80]	-	-	-	340 (N_2)	[81]
10	GeFSIX-3-Co (powder)	n/a	0	-	1.73		257[b]	0.097 [80]				255 [80] (N_2)	[81]
11	MOF-74-Ni (powder) (monolith, 20% binder)	n/a	0	0.44 [82] -	1.19 [76] -	1.88 [82] -	1180 737	0.51 0.32	0.51 0.32	1.07 [74] -	0.09-0.16 [82] (30-150 °C) -	450 250 (N_2)	[83]
12	UTSA-16(Co) (powder) (monolith, 15% binder)	n/a	0	-	1.13 [84] -	-	727 568	0.29 0.29	0.29 0.23	1.07 [74] -	-	380 (N_2) 310 (N_2)	[83]

	Name (form)	Functionalised	Functionalisation Loading ($mmol_N\ g_{ads}^{-1}$)	ρ_{bed} ($g\ cm^{-3}$)	$\rho_{particle}$ ($g\ cm^{-3}$)	$\rho_{skeletal}$ ($g\ cm^{-3}$)	S_{BET} ($m^2\ g^{-1}$)	V_{tot} ($cm^3\ g^{-1}$)	V_{micro} ($cm^3\ g^{-1}$)	C_p ($J\ g^{-1}\ °C^{-1}$)	κ ($W\ m^{-1}\ °C^{-1}$)	Thermal Stability (°C)	Ref
13	Co_2(dobdc) – MS, irregular crystals	n/a	0	-	-	-	625	-	-	0.71-0.88 [85] (25-125 °C)	-	250-300	[86]
	Co_2(dobdc) – ST, irregular crystals	n/a	0		-		786			-		250-300	
	Co_2(dobdc) – MS, hexagonal crystals (powder)	pyrazine (g)	0, 1.8		1.17, 1.17		825, 1220			-		250-300, 400 (N_2)	
14	MIL-101(Cr) (powder)	n/a	0	0.28 [87]	0.43 [88]	1.9 [88]	2400	1.17	-	0.52 [89] (25 °C)	0.05-0.10 [90]	300 [91] (N_2)	[92]
		TEPA (i)	4.0	-	-	-	520	0.32		-	(30-200 °C)	-	
		PEI-800-B(i)	5.5	-	-	-	480	0.27		-	- -	-	
15	MIL-101(Cr) (monolith, 20% binder)	n/a TEPA (i) PEI-800-B (i)	0 0.8, 3.5 3.2, 5.3	-	-	-	2200 1400, 470 1230, 460	1.12 0.76, 0.25 0.68, 0.26	-	-	-	-	[92]
16	MIL-101(Cr) (monolith, 25% binder)	n/a	0	0.56	-	-	-	1.16	-	-	-	200 or > (air)	[87]
17	MIL-101(Cr) (powder)	TAEA (g) TAEA (i) PEI-800-B (i)	2.6 5.7 0, 0.2, 0.4, 0.8, 1.0, 1.1, 1.3, 1.8	-	-	-	- - 3340, 2480, 2140, 1055, 727, 560, -, 31	- - 2.2, 2.1, 2.0, 1.5, 1.4, 1.2, -, 0.7	- - -	-	-	- 110 (He) -	[93]
18	MIL-101(Cr) (film coating on cordierite monolith)	PEI-800 (i)	-	0.5	-	-	-	-	-	0.89	0.32		[94]
19	MIL-101(Cr)-SO_3H (powder)	TAEA (g)	0, 1.2	-	0.43 [95], -	-	1362 [96], -	1.69 [96], -	-	-	-	320 [96], -	[97]
20	$Zn(ZnOH)_4(bibta)_3$ (powder)	n/a	0	-	-	-	2522	-	-	-	-	400 (N_2)	[98]
21	$Zn_2Ni_3(OH)_4(bibta)_3$ (powder)	n/a	0	-	-	-	2285	-	-	-	-	400 (N_2)	[99]
22	$ZnCo_4(OH)_4(bibta)_3$ (powder)	n/a	0	-	-	-	1930	-	-	-	-	320 (N_2)	[99]
23	$Zn_5(OH)_4(bbta)_3$_a[c] $Zn_5(OH)_4(bbta)_3$_b[d] (powder)	n/a	0	-	-	-	1024 1122	-	-	-	-	300 (N_2)	[100]

	Name (form)	Functionalised	Functionalisation Loading ($mmol_N\ g_{ads}^{-1}$)	ρ_{bed} ($g\ cm^{-3}$)	$\rho_{particle}$ ($g\ cm^{-3}$)	$\rho_{skeletal}$ ($g\ cm^{-3}$)	S_{BET} ($m^2\ g^{-1}$)	V_{tot} ($cm^3\ g^{-1}$)	V_{micro} ($cm^3\ g^{-1}$)	C_p ($J\ g^{-1}\ °C^{-1}$)	κ ($W\ m^{-1}\ °C^{-1}$)	Thermal Stability (°C)	Ref
24	$Zn_5(OH)_4(btdd)_3$_a[c] $Zn_5(OH)_4(btdd)_3$_b[d] (powder)	n/a	0	-	-	-	2613 2882	-	-	-	-	400 (N_2)	[100]
25	$Zn_{2.35}Ni_{2.65}(OH)_4(btdd)_3$_a[c] $Zn_{2.35}Ni_{2.65}(OH)_4(btdd)_3$_b[d] (powder)	n/a	0	-	-	-	3204 2491	-	-	-	-	330 (N_2) -	[100]
26	Mg_2(dobpdc) (powder)	n/a pn (g) mpn (g)	0 151 %[e] 135 %[e]	-	0.58 [101] - 1.12	-	3934 - -	-	-	-	-	400 [101] (N_2)	[102]
27	Mg_2(dobpdc) (powder)	n/a mmen (i) spermine (i)	0 - -	-	see 26 - -	-	see 26 - -	-	-	-	-	see 26 - -	[103]
28	Mg_2(dobpdc) (fiber)	n/a mmen (i) spermine (i)	0 - -	-	-	-	960 96 96	3.4 - -	-	-	-	-	[103]
29	Mg_2(dobpdc) (powder)	mmen (g)	-	-	0.86	-	-	-	-	-	-	-	[104]
30	Mg_2(dobpdc) (film coating on cordierite monolith)	mmen (g)	-	0.5	-	-	-	-	-	0.89	0.32	-	[94]
31	Mg_2(dobpdc) (powder) (film coating on cordierite monolith)	mmen (g)	7.3	-	0.86[f] [101]	-	894 -	0.85[f] [101] -	-	-	-	-	[93]
32	Mg_2(dobpdc) (powder)	spermine (g)	0, 94%[g]	-	see 26, 1.04	-	3980, -	1.25 [101], -	-	-	-	see 26, 250 (N_2)	[105]
33	Mg_2(dobpdc) (powder)	nmen (g) een (g) ipen (g)	-	-	-	-	812-1208	0.46 0.33 0.47	-	-	-	-	[106]
34	Mg_2(dobpdc) (powder)	2-ampd (g)	-	-	1.24	-	618	-	-	1.69[h] (40-140 °C)	-	190 (N_2)	[107]

	Name (form)	Functionalised	Functionalisation Loading ($mmol_N\ g_{ads}^{-1}$)	ρ_{bed} ($g\ cm^{-3}$)	$\rho_{particle}$ ($g\ cm^{-3}$)	$\rho_{skeletal}$ ($g\ cm^{-3}$)	S_{BET} ($m^2\ g^{-1}$)	V_{tot} ($cm^3\ g^{-1}$)	V_{micro} ($cm^3\ g^{-1}$)	C_p ($J\ g^{-1}\ °C^{-1}$)	κ ($W\ m^{-1}\ °C^{-1}$)	Thermal Stability (°C)	Ref
35	Mg_2(dobpdc) (powder) (SBS membrane) -60 wt% MOF -70 wt% MOF -80 wt% MOF (SBS spray coating) -on Ti mesh -on HEPA fileter -on AC granules	epn (g)	-	-	-	-	-	-	-	-	-	160	[108]
36	Mg-MOF-74 (powder)	hydrazine (g)	0, 12.0	-	0.92, 1.18	-	1495 [109], 1012	0.67, 0.30	-	0.74-1.02 [110] (0-200 °C), 2.01	-	400 [111] (N_2), 250 (N_2)	[112]

[a] HPMCP theoretical wt %
[b] Langmuir surface area
[c] TBAOH synthesis
[d] $NaHCO_3$ synthesis
[e] % diamine loading
[f] data for sample with 7.4 mmol/g loading
[g] % functionalisation loading per 2 Mg^{2+}
[h] average heat capacity for given temperature range

Table A1.4: Summary of physicochemical properties of carbon adsorbents investigated for DAC.

	Name (form)	Functionalised	Functionalisation Loading ($mmol_N\ g_{ads}^{-1}$)	ρ_{bed} ($g\ cm^{-3}$)	$\rho_{particle}$ ($g\ cm^{-3}$)	$\rho_{skeletal}$ ($g\ cm^{-3}$)	S_{BET} ($m^2\ g^{-1}$)	V_{tot} ($cm^3\ g^{-1}$)	V_{micro} ($cm^3\ g^{-1}$)	C_p ($J\ g^{-1}\ °C^{-1}$)	κ ($W\ m^{-1}\ °C^{-1}$)	Thermal Stability (°C)	Ref
1	sawdust biochar (powder)	n/a	0	-	-	-	-	-	-	-	-	500	[113]
2	AC (monolith)	K_2CO_3 (i)	0, 0.4[a]	0.57 [114], -	-	-	729, -	0.41, -	0.29, -	0.71 [114], - (24 °C)	18 [114], -	-, 210 or > (N_2)	[115]
3	AC (monolith)	K_2CO_3 (i) Na_2CO_3 (i)	0.4[a], 0.4[a] 0.5[b]	0.41, 0.40 0.41	-	-	-	-	-	-	-	210 or > (N_2)	[116]
4	CB (PBX-51) (powder)	K_2CO_3 + MF + BCA (i)	0, 17%[c] + 17%[c] + 33%[c]	0.02-0.38 [117], -	-	1.7-1.9[d] [117], -	1441, 315	-	-	-	-	35 or > (N_2)	[118]

[a] $mmol_{K2CO3}\ g^{-1}$
[b] $mmol_{Na2CO3}\ g^{-1}$
[c] theoretical wt % of each component
[d] given as specific gravity

Table A1.5: Summary of physicochemical properties of zeolite adsorbents investigated for DAC.

	Name (form)	Functionalised	Functionalisation Loading ($mmol_N\ g_{ads}^{-1}$)	ρ_{bed} ($g\ cm^{-3}$)	$\rho_{particle}$ ($g\ cm^{-3}$)	$\rho_{skeletal}$ ($g\ cm^{-3}$)	S_{BET} ($m^2\ g^{-1}$)	V_{tot} ($cm^3\ g^{-1}$)	V_{micro} ($cm^3\ g^{-1}$)	C_p ($J\ g^{-1}\ °C^{-1}$)	κ ($W\ m^{-1}\ °C^{-1}$)	Thermal Stability (°C)	Ref
1	H-ZSM-5 (powder)	TEPA (i)	0, 4.8	0.55 [119], -	1.78 [119], -	2.29 [120], -	275, 22	0.22, 0.17	0.18, 0.16	0.8 [121], - (60-140 °C)	0.3 [122], -	750 (air) [123], -	[124]
2	SAPO-34 (powder)	TEPA (i)	0, 4.1	0.72 [125], -	1.5-1.8 [126], -	2.26 [127], -	449, 35	0.24, 0.15	0.19, 0.12	0.95[a] [128], -	0.25[a] [128], -	-	[124]
3	NH_4Y (powder)	TEPA (i)	0, 5.3	-	-	-	335, 18	0.21, 0.15	0.11, 0.10	-	-	-	[124]
4	NH_4Y (powder)	ED (g)	0, 5.6	-	-	-	628, 270	-	0.28, 0.12	-	-	-, 180 (He)	[129]
5	13X (powder)	n/a	0	0.69 [87]	1.43 [130]	2.30 [131]	770	0.31	0.31	0.84 [132]	0.08-0.13 [132] (30 – 70 °C)	800 or > [133] (N_2)	[134]
6	13X (monolith)												[134]
	-20% binder	n/a	0	-	-	-	498	0.24	0.22	-	-	-	
	-15% binder						517	0.27	0.25				
	-10% binder						571	0.27	0.26				
7	13X (monolith, 25% binder)	n/a	0	1.1	-	-	-	0.46	-	-	-	-	[87]
8	G5CO2M[b]	n/a	0	see 5	1.03	see 5	-	-	-	see 5	see 5	350 or > (He)	[137]
	APG-III[c]			-	1.07	-				-	-		
	Ca-X			0.68 [135]	1.04	-				0.92 [135]	-		
	Na-LSX			0.632 [136]	1.08	-				0.92 [136]	-		
	Z10-01[d]			see 5	1.04	see 5				see 5	see 5		
	Z10-02ND[e]			-	0.98	-				-	-		
	Na-X-HP[f] (pellet)			see 5	1.07	-				see 5	see 5		
9	5A (powder)	n/a	0	0.65 [138]	1.48 [130]	2.04 [139]	705	0.29	0.29	0.92 [140]	0.10[g] [141] (10 °C)	800 or > [133] (N_2)	[134]
10	5A (monolith)												[134]
	-20% binder	n/a	0	-	-	-	395	0.19	0.18	-	-	-	
	-15% binder						504	0.24	0.23				
	-10% binder						543	0.26	0.25				
11	NaCaA-85 (powder)	n/a	0	-	-	-	-	-	-	-	-	727 (air)	[142]

12	BaMFI SrMFI CaMFI (powder)	n/a	0	-	-	-	-	-	-	-	-	600 or > 600 or > 600 or > (vacuum)	[143]

[a] data for SAPO materials in general
[b] commercial 13X from CECA Arkema Group
[c] commercial 13X from Honeywell UOP marketed for air prepurification
[d] commercial 13X from Zeochem
[e] commercial 13X from Zeochem marketed for air prepurification
[f] commercial 13X from Hengye
[g] data is for granulates

Table A1.6: Summary of physicochemical properties of polymer adsorbents investigated for DAC.

	Name (form)	Functionalised	Functionalisation Loading ($mmol_N\ g_{ads}^{-1}$)	ρ_{bed} ($g\ cm^{-3}$)	$\rho_{particle}$ ($g\ cm^{-3}$)	$\rho_{skeletal}$ ($g\ cm^{-3}$)	S_{BET} ($m^2\ g^{-1}$)	V_{tot} ($cm^3\ g^{-1}$)	V_{micro} ($cm^3\ g^{-1}$)	C_p ($J\ g^{-1}\ °C^{-1}$)	κ ($W\ m^{-1}\ °C^{-1}$)	Thermal Stability (°C)	Ref
1	Lewatit VP OC 1065 (beads)	BA (g)	6.1	0.63-0.71[a]	0.88	-	50	0.27	-	1.58	0.43 [144]	150 (N_2) [145] or 110 (air) [146]	[147]
2	Purolite A109 (beads)	1° amine (g)	4.3	0.66-0.69[a] [148]	-	1.05[b] [148]	46[c]	0.03	-	-	-	120 (N_2)	[149]
3	Purolite A500 (beads) (dense fibres) (porous fibres)	QA (g)	-	0.67-0.70[a] [150] - -	-	1.08[b] [150] - -	-	-	-	-	-	100 [150] - -	[151]
4	IER from *Snowpure LLC* (film)	-	-	-	-	-	-	-	-	-	-	-	[151]
5	XAD-4 XAD-16 XAD-1180N (beads)	$2[N(CH_3)_4]^+ \cdot CO_3^{2-}$ (g)	0, 0.9 0, 1.0 0, 1.0	0.68[a] [152], - 0.72[a] [153], - 0.66[a] [154], -	-	1.08 [155], - 1.08 [155], - 1.02 [154], -	808, 975 864, 967 662, 636	1.04, 1.24 0.92, 0.71 1.11, 0.62	-	-	-	249 [155], - 249 [155], - 150 [155], -	[156]
6	D201 (beads)	QA (g) → K_3PO_4 (ie)	3.9	0.66-0.73[a] [157]	-	1.09[b] [157]	9[d] [149]	0.02[d] [149]	-	-	-	-	[158]
7	Resin from *Knowledge & Benefit Sphere Tech. Co., Ltd.* (beads)	PEI-600 (i)	0, 20%[e]	-	-	-	565, 20	0.72, 0.39	-	-	-	-	[159]
8	MR10 (beads)	PEI-600 (i)	0, 10.4	-	-	-	590, 16	1.30, 0.30	-	-	-	-	[160]
9	Resin from *Oy Hydrocell Ltd.* (beads)	1° amine (g)	4.7	0.45	0.72	-	32 [161]	-	-	1.58	-	100 or > (N_2)	[162]
10	QCPS-1/PES QCPS-2/PES QCPS-3/PES (film)	QA (g) → Na_2CO_3 (ie)	2.0 2.2 2.1	-	-	-	0.02[f] 16[f] 10[f]	- 0.35[f] 0.23[f]	-	-	-	-	[163]
11	NFC (powder)	APDES (g)	3.4	0.055	0.061[g] [164, 165]	1.58	12	-	-	2.07	0.04	-	[166]
12	NFC (powder)	APDES (g)	3.1	-	-	-	18	-	-	-	-	-	[167]

	Name (form)	Functionalised	Functionalisation Loading ($mmol_N\ g_{ads}^{-1}$)	ρ_{bed} ($g\ cm^{-3}$)	$\rho_{particle}$ ($g\ cm^{-3}$)	$\rho_{skeletal}$ ($g\ cm^{-3}$)	S_{BET} ($m^2\ g^{-1}$)	V_{tot} ($cm^3\ g^{-1}$)	V_{micro} ($cm^3\ g^{-1}$)	C_p ($J\ g^{-1}\ °C^{-1}$)	κ ($W\ m^{-1}\ °C^{-1}$)	Thermal Stability (°C)	Ref
13	BC (powder)	CHPTAC (g) → Na_2CO_3 (ie)	0, 0.4, 0.4, 0.6	-	-	-	-	-	-	-	-	-	[168]
14	PAN (hollow fibre)	TEPA (g)	0, 15%[h], 39%[h], 58%[h]	-	-	1.18[i] [169], -	19, 18, 15, 12	0.13, 0.11, 0.09, 0.06	-	-	-	300, 150, 150, 150	[170]
15	PAN/PMMA (hollow fibre)	TEPA (g)	0, 75%[h]	-	-	-	11, 45	0.04, 0.01	-	1.31[j] [171], -	0.07[j] [171], -	300, 150	[170]
16	PEI "snow" (powder)	n/a	0	0.5-0.6[k]	-	-	-	-	-	-	-	300 or > (N_2)	[172]

[a] for wet sample
[b] given as specific gravity
[c] after 4 h of drying (S_{BET} reduced to 26 $m^2\ g^{-1}$ after 50 h of drying)
[d] for non-ion-exchanged sample
[e] PEI theoretical wt %
[f] value for QCPS powder
[g] for NFC functionalised with N-(2-aminoethyl)-3-aminopropylmethyldimethoxysilane (AEAPDMS)
[h] TEPA % grafting
[i] for PAN in powder form
[j] for a PAN / 5% PMMA solid fibre
[k] tap density

A1.2 Tables of sorption properties

Table A1.7: Summary of sorption properties of silica adsorbents investigated for DAC.

	Name (form)	Functionalised	Functionalisation Loading ($mmol_N\ g_{ads}^{-1}$)	CO_2 uptake at 400 ppm, 25 °C ($mmol\ g^{-1}$)	ΔH_0 ($kJ\ mol^{-1}$)	Isotherms				H_2O uptake ($mmol\ g^{-1}$) (at %RH, °C)	Stability		Kinetic data	Cyclic studies	Ref
						CO_2	N_2	O_2 (° C)	H_2O (° C)		H_2O (%RH, °C)	O_2			
1	SBA-15 (powder)	DMAPS (g)	0, 1.9, 2.5	-, 0.01, 0.01 (G, 10 000 ppm, 30 °C)	29 [173], -, - (at 0.4 $mmol\ g^{-1}$)	Y [173], N, N (V)	N	N	Y (G, 30)	11.4, 3.9, 1.5 (49 %, 30)	Y [174] (90 %, 35), Y+, Y+ (49 %, 30)	-	Y, N, N (TGA)	N	[4]
2	SBA-15 (powder)	n/a APTES (g) AE-APS (g) AE-AE-APS (g)	0 2.6 2.8 3.5, 4.7	- 0.3 0.3 0.2, 0.3 (V)	-	N	N	N	N	-	- Y+ Y+ Y+ (24 %, 25)	-[a]	N Y Y Y (TGA)	N	[5]
3	SBA-15 (powder)	DT (g)	0, 1.7, 4.5, 5.1, 5.7, 6	-, 0.3, 0.4, 0.6, 0.6, 0.5 (G, 45 °C)	-	N	N	N	N	-	-	-	N, Y, Y Y, Y, Y (TGA)	N	[6]
4	SBA-15 (powder)	PEI-600-B (i)	0, 33%[b], 50%[b], 67%[b]	0.01 (V, 10 000 ppm), 1.1, 1.5, 1.9 (V)	-	N	N	N	N	-	-	-	N	N	[7]
5	SBA-15 (powder)	n/a ED-3 ED-6 PD-3 PD-6	0 2.5, 3.6, 4.6, 6.3, 8.2 3.5, 5.1, 6.9, 8.5 2.9, 3.5, 4.7, 5.9 3.3, 4.5, 6.0, 7.9	- 0.1, 0.3, 0.6, 0.8, 0.9 0.2, 0.4, 0.5, 0.4 0.1, 0.2, 0.4, 0.6 0.2, 0.2, 0.3, 0.3 (G, 35 °C)	-	N	N	N	Y N, N, N, N, Y N N N (G, 35)	47 -, -, -, -, 28 - - - (94 %, 35)	- -, -, - -, Y+ - - - (30%, 25)	- -, -, -, < 50% CO_2, - - -, -, -, < 50 % CO_2 - (after 21 % O_2, 110 °C)	N Y[c] Y Y Y (TGA)	N N, N, N, Y, N N, N, N, Y N, N, N, Y N, N, N, Y (TGA)	[8]
6	SBA-15 (powder)	n/a PEI-800 (i) TEPA (i)	0 25%[a], 50%[a], 75%[a] 25%[a], 50%[a], 75%[a]	0.1 0.7, 1.3, 1.9 0.9, 2.3, 3.4 (G)	-	N	N	N	N	-	- Y+[d] [175] Y+[d] [175] (52%, 45)	-	Y (TGA)	N Y Y (TGA)	[9]

	Name (form)	Functionalised	Functionalisation Loading ($mmol_N\ g_{ads}^{-1}$)	CO_2 uptake at 400 ppm, 25 °C ($mmol\ g^{-1}$)	ΔH_0 ($kJ\ mol^{-1}$)	Isotherms				H_2O uptake ($mmol\ g^{-1}$) (at %RH, °C)	Stability		Kinetic data	Cyclic studies	Ref
						CO_2	N_2	O_2 (° C)	H_2O (° C)		H_2O (%RH, °C)	O_2			
7	SBA-15 (powder)	n/a	0	-	-	N	N	N	N	-	-	-	N	N	[10]
		PPI-HCl-B (i)	4.3	0.1								> 50 % CO_2	N	N	
		PPI-CH_3SO_3H-B (i)	4.8	0.1								> 50 % CO_2	N	N	
		PPI-HBr-B (i)	4.5, 5.5, 6.9, 7.4	0.2, 0.2, -, 0.8								> 50 % CO_2	N, N, Y, Y	N, N, N, Y	
		PPI-$HClO_4$-B (i)	5.4, 7.4	0.2, - (G, 35 °C)								< 50 % CO_2 (after air, 110 °C)	N (TGA)	N (TGA)	
8	SBA-15 (powder)	n/a	0	-	-	N	N	N	N	-	-	-	N	N	[11]
		PPI-700-L (i)	1.5, 2.8, 4.4, 5.9, 7.5	0.04, 0.1, 0.2, 0.7, 1.2	-	N, N, N, N, Y		N				> 50 % CO_2	N, N, N, N, Y	N	
		PPI-1000-L (i)	1.5, 2.9, 4.4, 5.9, 7.6	0.1, 0.1, 0.3, 0.7, 1.3	-, -, -, -, 105	N, N, N, N, Y		N, N, N, N, Y				> 50 % CO_2	N, N, N, N, Y	N, N, N, N, Y	
		PPI-6700-L (i)	2.0, 3.7, 5.3, 7.1, 8.7	0.1, 0.2, 0.5, 0.9, 1.2	-	N, N, N, N, Y		N				> 50 % CO_2	N, N, N, N, Y	N	
		PPI-36000-L (i)	1.7, 3.6, 5.0, 6.6, 8.0	0.04, 0.1, 0.4, 0.8, 1.1 (G, 35 °C)	-	N (V)		N (V, 35)				> 50 % CO_2 (after 21 % O_2, 110 °C)	N, N, N, N, Y (TGA)	N (TGA)	
9	SBA-15[e] (powder)	n/a	0	-	-	N	N	N	N	-	-	-	N	N	[12]
		PPI-700-L[e] (i)	7.5	-								> 50 % CO_2			
		PPI-6700-L[e] (i)	8.7	1.0								> 50 % CO_2			
		PPI-36000-L[e] (i)	8.0	0.9 (G, 35 °C)								> 50 % CO_2 (after air, RT)			
10	SBA-15 (powder)	n/a	0	-	-	N	N	N	N	-	-	-	N	N	[12]
		PPI-700-L[f] (i)	6.8	0.9								> 50 % CO_2	N	Y	
		PPI-6700-L[f] (i)	6.5	0.7								> 50 % CO_2	N	Y	
		PPI-36000-L[f] (i)	6.1	0.8								> 50 % CO_2	N	Y	
		PPI-700/36000-L[f] (50:50 ratio) (i)	2.2, 3.9, 4.3, 6.0	0.2, 0.2, 0.3, 0.7								-, -, -, > 50 % CO_2	Y	N, N, N, Y	
		PPI-700/36000-L_75[f] (75:25 ratio) (i)	1.9, 3.1	-								-	Y	N	
		PPI-6700/36000-L[f] (50:50 ratio) (i)	1.9, 3.7, 3.8, 6.5	0.02, 0.3, 0.2, 0.8								-, -, -, > 50 % CO_2	Y	N, N, N, Y	
		PPI-700/6700-L[f] (50:50 ratio) (i)	2.4, 4.2, 5.7, 6.6, 7.6	0.03, 0.3, 0.6, 0.7, 1.0 (G, 35 °C)								-, -, -, > 50 % CO_2, - (after 21 % O_2, 110 °C)	Y (TGA)	N, N, N, Y, Y (TGA)	

	Name (form)	Functionalised	Functionalisation Loading ($mmol_N\ g_{ads}^{-1}$)	CO_2 uptake at 400 ppm, 25 °C ($mmol\ g^{-1}$)	ΔH_0 ($kJ\ mol^{-1}$)	Isotherms				H_2O uptake ($mmol\ g^{-1}$) (at %RH, °C)	Stability		Kinetic data	Cyclic studies	Ref
						CO_2	N_2	O_2 (° C)	H_2O (° C)		H_2O (%RH, °C)	O_2			
11	SBA-15 (powder)	n/a	0	-	-	N	N	N	Y	42.8	-	-	N	N	[13]
		PGA (Xn = 15) (i)	2.4, 3.0, 4.2	0.1, 0.3, 0.7		N			N	-		-	N	N, N, Y	
		PGA (Xn = 25) (i)	2.7, 4.1, 5.8, 8.0	0.1, 0.2, 0.6, 0.6		N			N	-		-	N	N, N, Y, N	
		PGA (Xn = 50) (i)	2.7, 3.6, 4.7, 5.4	0.2, 0.6, 0.6, 0.6 (G, 35 °C)		N, Y, N, N (V)			N, Y, N, N (G, 35)	-, 20.7 , -, - (90 %, 35)		> 50% CO_2[d] (after 21 % O_2, 110 °C)	N, Y, N, N (TGA)	N, N, N, Y (TGA)	
12	SBA-15 (powder)	PEI-800-B (i)	0, 4.4, 7.2, 8.1, 9.9, 10.8	-, 0.2 , 0.8, 1.0, 1.2, 1.4 (G, 35 °C)	-	N, N, Y, N, N, N (V)	N	N	N, N, Y, N, N, N (G, 35)	-, -, 23.1, -, -, - (95 %, 35)	-, Y+[d] [175] (52%, 45)	-	N, N, Y, N, N, N (TGA)	N	[13]
13	SBA-15 (powder)	n/a	0	-	-	N	N	N	N	-	-	-	N	N	[14]
		PEI-1800-B (i)	5.3, 6.7, 8.8, 9.6, 11.2	0.1, 0.4, 0.9, 0.9, 1.1	-, -, 99, -, -								Y, N, Y, N, Y	N, N, Y, N, N	
		PPG (i)	5.7, 7.7, 10.6, 11.4, 14.3	0.1, 0.3, 0.5, 0.6, 0.6 (G, 30 °C)	-, -, -, -, 70								N, Y, Y, N, Y (TGA)	N, N, N, N, Y (TGA)[d]	
14	SBA-15-il	APS (g)	0, 2.2	-, 0.5 (V)	-, 90 (at 0.3 $mmol\ g^{-1}$)	N, Y	N	N	N	-	-, Y+	-	N, Y (PB)	N, Y (TGA)[g]	[15]
	SBA-15-cal (powder)		0, 1.4	-, 0.2 (V)	-, 77 (at 0.1 $mmol\ g^{-1}$)	N, Y					-, Y+ (60 %, 25)		N, Y (PB)	N	
15	SBA-15 (powder)	TEPA (i)	0, 67%[h]	-, 1.8 (G)	-	N	N	N	N	-	-, Y+[d] [175]	-	N	N, Y (TGA)	[17]
16	SBA-15 (powder)	n./a	0	-	-	N	N	N	N	-	-	-	N	N	[18]
		APS (g)	0.5, 1.0, 1.1, 1.4, 2.1	0.02, 0.03, 0.1, 0.1, 0.2								>50 % CO_2	Y[i]	Y[i]	
		AE-APS-L (g)	0.9, 1.7, 2.2, 2.5, 3.7	0.02, 0.1, 0.1, 0.1, 0.4								>50 % CO_2	Y[i]	Y[i]	
		AP-APS-L (g)	0.9, 1.6, 2.6, 3.4	0.03, 0.1 0.1, 0.6								>50 % CO_2	Y[i]	Y[i]	
		AE-ESPE-B (g)	0.6, 1.0, 2.1, 2.5	0.02, 0.04, 0.2, 0.3								>50 % CO_2	Y[i]	Y[i]	
		AP-ESPP-B (g)	0.8, 1.3, 1.8, 2.3	0.1, 0.1, 0.2, 0.4								>50 % CO_2 (after 21 % O_2, 110 °C)	Y[i] (TGA)	Y[i] (TGA)	

	Name (form)	Functionalised	Functionalisation Loading ($mmol_N\ g_{ads}^{-1}$)	CO_2 uptake at 400 ppm, 25 °C ($mmol\ g^{-1}$)	ΔH_0 ($kJ\ mol^{-1}$)	Isotherms				H_2O uptake ($mmol\ g^{-1}$) (at %RH, °C)	Stability		Kinetic data	Cyclic studies	Ref
						CO_2	N_2	O_2 (° C)	H_2O (° C)		H_2O (%RH, °C)	O_2			
17	SBA-15 (powder)	n/a	0	0.02	-	N	N	N	N	-	-	-	N	N	[19]
		TETA (i)	3.3, 5.9, 8.3, 11.2	0.1, 0.4, 1.2, 2.1							Y+[d] [176] (75)	< 50 % CO_2		N, N, N, Y	
		TPTA (i)	2.7, 4.6, 6.8, 8.9	0.1, 0.4, 1.2, 1.9							-	> 50 % CO_2		N, N, N, Y	
		EI-den (i)	2.5, 5.0, 7.0, 7.6, 8.5, 11.0	0.02, 0.1, 0.3, 0.3, 0.4, 0.9							-	< 50 % CO_2		N, N, N, N, N, Y	
		PI-den (i)	2.4, 4.3, 5.5, 6.6, 7.6, 9.2	0.03, 0.1, 0.3, 0.5, 0.6, 1.3 (G, 35 °C)							-	> 50 % CO_2 (after 21 % O_2, 110 °C)		N, N, N, N, N, Y (TGA)	
18	SG (powder)	DT (g)	0, 5.1	-, 0.8 (D, 415 ppm)	23[j] [177], -	Y [178], Y (V)	Y[j,k], N [177]	Y [179], N (V[l], 0, 100)	Y, N (G, 30) [180] (V[m], 0, 25, 50, 75) [178]	18.9, - (77 %, 25)	Y, Y+ (60 %, 25)	-	N, Y (PB, TGA)	N, Y (TGA)[n]	[24]
19	SG (powder)	-	0	-	see 18	see 18	see 18	see 18	see 18	see 18	see 18	-	N	N	[26]
		TEPA (i)	2.0, 5.0, 5.8, 11.3	0.2, 1.1, 1.4, 2.1	-	-	-	-	-	-	-, -, Y+,		Y (PB)	N, N, Y, N	
		PEI (i)	7.8, 10.0	1.2, 1.4	-	-	-	-	-	-	-		N	N	
		APTES (g)	1.1, 2.4, 3.0	0.2, 0.8, 1.0	-	-	-	-	-	-	-		N	N	
											-			(TGA)	
											(50%, 25)				
20	SG (monolith)	PEI-10000	10.0	1.3	-	N	N	N	N	-	Y+	-	Y (PB)	Y (PB)	[25]
		PEI-25000	12.1	0.9							(90%, RT)			N	
		PEI-750000	8.6	0.5										N	
				(D, 5000 ppm, RT)											
21	SG	PD (i)	0, -	0.2, 0.3	-	N	N	N	N		-	-	Y (TGA)	Y (TGA)[o]	[27]
	SG/PEG		0, -	0.2, 0.5											
	SG/CB (xerogel powder)		0, -	0.2, 0.2 (G, air, RT)											
22	MCM-41 (powder)	PEI-800 (i)	0, 0.2[p], 0.3[p], 0.5[p], 0.6[p], 0.6[p]	-, 1.00 1.7, 2.2, 2.0, 2.0 (G)	-	N	N	N	N	-	-, -, -, Y+, -, - (64%, 25)	-	N, N, N Y, N, N (PB)	N, N, N Y, N, N (TGA)	[28]
23	FS (powder)	-	0	-	-	N	N	N	N	-	-	-	N	N	[31]
		APS	1.7, 3.3, 3.5, 65%[q], 4.7	0.7, 1.0, 1.2, 0.1, 0.1							Y+		Y (PB)	N	
		APS-CTAB5	3.5, 65%[q], 4.7	1.6, 1.5, 2.0 (D, 10 000 ppm, 60 °C)							Y+ (50%, 60)		N	N, Y, N (PB)	

	Name (form)	Functionalised	Functionalisation Loading ($mmol_N\ g_{ads}^{-1}$)	CO_2 uptake at 400 ppm, 25 °C ($mmol\ g^{-1}$)	ΔH_0 ($kJ\ mol^{-1}$)	Isotherms				H_2O uptake ($mmol\ g^{-1}$) (at %RH, °C)	Stability		Kinetic data	Cyclic studies	Ref
						CO_2	N_2	O_2 (° C)	H_2O (° C)		H_2O (%RH, °C)	O_2			
24	MFS (powder)	PEI-1200 + EB (i)	6.7	2.1 (D, 25 000 ppm, 40 °C)	63 [181]	N	N	N	Y (D, 40, 55, 70)	1.9 (51 %, 40)	Y+/-[r] (12%, 70)[s]	> 50% CO_2[d] [182] (after 20 % O_2, 120 °C)	Y (PB)[d]	Y [182] (TGA)[d]	[32]
25	SiO_2 (C-803) (powder)	PEI-800-B (i)	0, 0.9[t]	-	-	N	N	N	Y (G, 35)	12.5, - (85 %, 35)	-	-[a]	N, Y (TGA)	N	[35]
26	SiO_2 (C-803) (fibre)	PEI-800-B (i)	0, 0.9[t]	-, 0.6 (G, 395 ppm, 35 °C)	-	N	N	N	Y (G, 35)	6.7, 30.4 (85 %, 35)	-, Y+ (85 %, 35)	-[a]	N, Y (TGA, PB)	N, Y (TGA, PB)	[35]
27	MCF_a[u] (powder, pellet)	PEI-1200-B (i)	0, 0.6	-, 1.3	-	N	N	N	N	-	-, Y+/-[r]	-	N, Y	N	[37]
	MCF_b[v] (powder, pellet)		0, 0.5	-, 1.9 (D, 420 ppm, 46 °C)							-, Y+/-[r] (60%, 33)[w]		N, Y (PB)		
28	HBS (powder)	DT (g)	0, 7.9	-, 1.0	-	N, Y (V)	N	N	N	-	-, Y+ [24] (60 %, 25)	-	N, Y (PB)	N, Y (TGA)[n]	[38]
29	HMS (powder)	-	0	-	-	N	N	N	N	-	-	-	N	N	[39]
		PEI-800-S_H_LV (i)	0.4[t], 0.9[t], 1.7[t], 2.0[t], 3.3[t], 4.1[t], 4.7[t]	0.6, 1.2, 1.9, 2.1, 2.3, 2.3, 2.1		N, N, N, N, Y, N, N					Y+		N, Y, N, Y, Y[x], Y, N	N, N, N, N, N, Y, N, N	
		PEI-800-R_L_HV (i)	0.3[t], 0.8[t], 1.0[t], 1.4[t], 2.0[t], 3.1[t]	0.3, 0.9, 1.2, 1.3, 1.6, 2.0 (G, 30 °C)		N (V)					Y+ (19 %, 30)		N, N, N, N, N, Y (TGA)	N (PB)	
30	SAG (powder)	K_2CO_3 (i)	0	0.2,	-	N	N	N	N	-	-,	-	N,	N,	[44]
			0.7[y], 0.9[y], 1.2[y], 1.3[y], 1.5[y]	0.4, 0.7, 1.3, 0.8, 0.5 (D, 10 000 ppm, 20 °C, 85% RH)							Y[z], (85%, 20)		N, N, Y, N, N (PB)	N, N, Y, N, N (PB)	
31	MMSN	TEPA (i)	0, 48 %[aa]	-, 2.5 (G)	-	N, Y	N	N	N	-	-	-	N, Y	N, Y	[46]
	+CTAC10		0, 48 %[aa]	-, 2.8 (G)		N, Y					-		N, Y	N, Y	
	+CTAC20		0, 48 %[aa]	-, 3.3 (G)		N, Y					-		N, Y	N, Y	
	+CTAC30 (powder)		0, 48 %[aa]	-, 3.5 (G)		N, Y (V)					-, Y+ (25)		N, Y (TGA)	N, Y (TGA)[o]	

	Name (form)	Functionalised	Functionalisation Loading ($mmol_N\ g_{ads}^{-1}$)	CO_2 uptake at 400 ppm, 25 °C ($mmol\ g^{-1}$)	ΔH_0 ($kJ\ mol^{-1}$)	Isotherms				H_2O uptake ($mmol\ g^{-1}$) (at %RH, °C)	Stability		Kinetic data	Cyclic studies	Ref
						CO_2	N_2	O_2 (° C)	H_2O (° C)		H_2O (%RH, °C)	O_2			
32	EtSNT (powder)	PEI-600 (i)	0, 11.2	0.1 (V, 100 000 ppm, 30 °C), 1.05 (D, 30 °C)	-	N	N	N	N	-	-	-	N Y (PB)	N Y (PB)	[47]
33	AHSA (monolith)	APTES	7.6	3.0 (D, 10 000 ppm, 50 °C)	-	N	N	N	N	-	Y+	-	Y (PB)	Y (PB)	[48]
34	SiNP-SIP (powder)	PEI-2000-b (g)	-	1.1 (G)	-	N	N	N	N	-	Y+ (79%, 25)	-	Y (PB, TGA)	Y (TGA)[d]	[49]
35	AHTSA (monolith)	APTES	5.3, 7.9, 8.5, 8.8	-, -, 1.6, - (D, 30 °C)	-	N	N	N	N	-	-	-	Y (PB)	N, N, Y, N (PB)	[50]

[a] Some experiments done with ambient air but effect of O_2 was not investigated
[b] theoretical PEI wt %
[c] PB studies also done for 8.2 mmol g^{-1} loading sample
[d] studied at flue gas conditions
[e] material aged for 1.5 years
[f] material aged for 2 years
[g] studied at 30% CO_2 conditions
[h] theoretical TEPA wt %
[i] functionalisation loadings not specified
[j] data is for beads
[k] measurement method not stated
[l] adsorbent form not known
[m] data is for granules
[n] studied at 70% CO_2 conditions
[o] studied at 100 % CO_2 conditions
[p] $mmol_{PEI}\ g^{-1}$
[q] APS theoretical wt%
[r] changes depending on CO_2 concentration and temperature
[s] above 70% RH the CO_2 uptake increases compared to dry conditions, below 70% RH, it decreases
[t] $mmol_{PEI}\ g^{-1}{}_{SiO2}$
[u] synthesis method A
[v] synthesis method B
[w] at 60% RH the CO_2 uptake decreases compared to dry conditions, below 60% RH, it increases
[x] PB studies also done for this loading sample
[y] $mmol_{K2CO3}\ g^{-1}$
[z] H_2O needed for CO_2 adsorption mechanism
[aa] TEPA wt%

Table A1.8: Summary of sorption properties of metal oxide adsorbents investigated for DAC.

	Name (form)	Functionalised	Functionalisation Loading ($mmol_N\ g_{ads}^{-1}$)	CO_2 uptake at 400 ppm, 25 °C ($mmol\ g^{-1}$)	ΔH_0 ($kJ\ mol^{-1}$)	Isotherms				H_2O uptake ($mmol\ g^{-1}$) (at %RH, °C)	Stability		Kinetic data	Cyclic studies	Ref
						CO_2	N_2	O_2 (° C)	H_2O (° C)		H_2O (% RH, °C)	O_2			
1	$Mg_{0.55}Al$–O-a[a] (powder)	PEI-600-B (i)	0, 33%[b], 50%[b], 67%[b]	0.1, 1.1, 1.7, 2.3 (V)	-, -, -, 75	N, N, N, Y (V)	N	N	N	-	-, Y+ Y+, Y+ (95%, 25)	-	N, N, N Y (PB)	N, N, N, Y (PB)	[7]
2	$Mg_{0.55}Al$-O-a[a] Mg_2Al–O-a[a] (powder)	APS (g)	0, 2.3 0, 3.7	-, 0.4 -, 0.8	-	N	N	N	N	-	-	-	N, Y N, Y (PB)	N	[52]
3	Mg_2Al-O-urea[c] $Mg_{0.55}Al$-O-w[d] Mg_2Al-O-w[d] Mg_3Al-O-w[d] $Mg_{0.55}Al$-O-a[a] Mg_2Al-O-a[a] Mg_3Al-O-a[a] $Mg_{0.55}Al$-O-F[e] Mg_2Al-O-F[e] (powder)	AE-AE-APS (g)	0, 0.5 0, 1.8 0, 2.2 0, 1.2 0, 6.4 0, 4.3 0, 2.1 0, 4.8 0, 4.7	-, 0.04 -, 0.1 -, 0.3 -, 0.2 0.3, 1.0 0.1, 0.4 -, 0.2 0.1, 0.6 0.2, 0.4	- - - - -, 30 (69 at 1 $mmol\ g^{-1}$) - - - - -	N N N N N, Y N N N N	N	N	N	-	-	-	N, Y N N N N, Y N, Y N, Y N, Y N, Y N (TGA)	N N N N N, Y N N N N	[52]
4	$Mg0_{.55}Al$-O Mg_1Al-O Mg_2Al-O Mg_3Al-O $Mg_{0.55}Al$-CO_3 MgO (powder)	TEPA (i)	0, 33%[f], 50%[f], 67%[f], 83%[f] 0, 33%[f] 0, 33%[f] 0, 33%[f] 0, 33%[f], 50%[f], 67%[f] 0, 33%[f]	0.5, 1.4, 2.4, 3.0, 0.9 -, 1.4 -, 1.3 -, 1.2 -, 0.8, 1.4, 2.1 -, 0.6 (G)	-	N	N	N	N	-	-, -, - Y+, - - - - - - (90 %, 25)	-	Y N N N N, Y, Y, Y N (TGA)	N, N, N, Y, N N N N N N, Y (TGA)	[17]
5	γ-Al_2O_3 (powder)	n/a Na_2CO_3 + $Ni(NO_3)_2$ (i)	0 15%[g] + 10%[h]	- 0.1 (D, 450 °C)	34[i] [183] -	Y [184] N (G)	N	N	Y [183] N (G, 25)	9.4 - (93%, 25)	-	- > 50% CO_2 (after 20% O_2, 450 °C)	Y [185] Y (PB)	N Y (PB)	[59]
6	γ-Al_2O_3 (powder)	NaO (i) NaO + Ru (i)	6%[j] 10%[j] + 0.5 %[k]	0.1 0.2 (G, 350 ppm, 320 °C)	-	N	N	N	N	-	- Y (ss)	- Y (21% O_2, 320 °C)	Y (TGA) Y (PB, TGA)	N Y (PB)	[60]

	Name (form)	Functionalised	Functionalisation Loading ($mmol_N\ g_{ads}^{-1}$)	CO_2 uptake at 400 ppm, 25 °C ($mmol\ g^{-1}$)	ΔH_0 ($kJ\ mol^{-1}$)	Isotherms				H_2O uptake ($mmol\ g^{-1}$) (at %RH, °C)	Stability		Kinetic data	Cyclic studies	Ref
						CO_2	N_2	O_2 (° C)	H_2O (° C)		H_2O (% RH, °C)	O_2			
7	γ-Al_2O_3 (powder)	NaO + Ru (i) CaO + Ru (i)	10%[j] + 1%[k] 10%[k] + 1%[l]	0.6 (D) 0.5 (D)	-	N	N	N	N	-	Y+[k] (90 %, 25)	Y (air, 25 °C)	Y (PB) N	Y (PB)	[61]
8	γ-Al_2O_3 (powder)	TEPA (i)	0, 50%[f]	-, 2.3 (G)	-	N	N	N	N	-	-	-	Y (PB), N	N, Y (TGA)	[17]
9	γ-Al_2O_3 (powder)	K_2CO_3 (i)	0, 1.6[m]	-, 0.9 (D, air, 20-30% RH)	-	N	N	N	N	-	-, Y[k] (30 %, 25)	Y (air, 25 °C)	Y (PB)	Y (PB)	[62]
10	γ-Al_2O_3-O γ-Al_2O_3-D (powder)	APTES (g)	0, 0.9[n], 2.0[n], 3.2[n], 5.4[n] 0, 0.7[n], 1.5[n], 2.9[n], 4.1[n]	0.1[n], 0.2[n], 0.3[n], 0.5[n], 0.8[n] 0.2[n], 0.2[n], 0.2[n], 0.3[n], 0.6[n] (G, 30 °C)	52 (30 at 0.1 $mmol\ g^{-1}$), 69, 79, 83, 98 79 (34 at 0.1 $mmol\ g^{-1}$), 69, 76, 73, 77	N	N	N	N	-	-	-	N	N	[63]
11	ZrO_2 (aerogel powder)	K_2CO_3 (i)	0, 0.7[l], 1.2[l], 1.7[l], 2.1[l]	0.01, 0.1, 0.5, 1.1, 0.1 (D, 25% RH)	-	N	N	N	N	-	-, Y[o], Y[o], Y[o], Y[o] (25 %, 25)	-[p]	N, Y, Y Y, Y (PB)	N, N, N Y, N (PB)	[65]

[a] exfoliated LDH
[b] PEI theoretical wt%
[c] bulk LDH
[d] stacked LDH
[e] ultrafine LDH
[f] TEPA theoretical wt%
[g] theoretical wt% of γ-alumina
[h] theoretical wt% of Na- γ-alumina
[i] CO_2 loading not specified
[j] Na_2O theoretical wt%
[k] Na_2O and Ru theoretical wt%
[l] CaO and Ru theoretical wt%
[m] $mmol_{K2CO3}\ g^{-1}$
[n] $mmol\ g^{-1}_{alumina}$
[o] H_2O needed for CO_2 adsorption mechanism
[p] experiments done with ambient air but effect of O_2 was not investigated

Table A1.9: Summary of sorption properties of MOF adsorbents investigated for DAC.

	Name (form)	Functionalised	Functionalisation Loading ($mmol_N\ g_{ads}^{-1}$)	CO_2 uptake at 400 ppm, 25 °C ($mmol\ g^{-1}$)	ΔH_0 ($kJ\ mol^{-1}$)	Isotherms				H_2O uptake ($mmol\ g^{-1}$) (at %RH, °C)	Stability		Kinetic data	Cyclic studies	Ref
						CO_2	N_2	O_2 (° C)	H_2O (° C)		H_2O (%RH, °C)	O_2			
1	NbOFFIVE-1-Ni (powder)	n/a	0	1.3 (V)	49 (at 1.0 $mmol\ g^{-1}$)	Y (V)	N	N	Y (V, 25)	10.1 (95%, 25)	Y- (75%, 25)	-	Y (PB, TGA [66])	Y (PB)	[67]
2	NbOFFIVE-1-Ni/PA (beads)	n/a	0	1.4 (V)	52	Y (V)	N	N	Y (G, 25)	7.5 (95%, 25)	Y- (74%, 25)	-	Y (PB, TGA, FB)	Y (FB)	[66]
3	TIFSIX-3-Ni (powder)	n/a	0	1.2 [68] (V)	50	Y (V)	N	N	Y [73] (G, 25)	7.5 [73] (95%, 25)	Y- (75%, 40)	Y [69] (air, 220 °C)	Y [73] (PB)	N	[70]
4	TIFSIX-2-Cu-i (powder)	n/a	0	0.3 (G, 10 000 ppm)	36	Y[a] (V)	N	N	N	-	Y [71] (75%, 40)	-	Y (PB)	N	[72]
5	SIFSIX-18-Ni-β (powder)	n/a	0	0.4 (V, 500 ppm)	52	Y (V)	N	Y (V, -196, 25)	Y (G, 25, 27, 30, 35, 40)	1.6 (95%, 25)	Y- (74%, 25)	low O_2 uptake	Y (PB, TGA)	Y (TGA)	[73]
6	SIFSIX-3-Ni (powder)	HPMCP (c)	0, 5%[b]	0.3 [67] (V), 1.5 (D, 10 000 ppm)	45 [73], -	Y [186], N (V)	N	N	Y (G, 35)	8.8 [73], 2.2[c] (95%, 35)	Y- (74%, 25)	-	Y (PB)	N, Y (PB)	[75]
7	SIFSIX-3-Cu (powder)	n/a	0	1.2 [77] (V)	55 [77] (at 1.5 $mmol\ g^{-1}$)	Y [77] (G)	N	Y [77] (G, 25)	N	4.9 [187] (49%, 30)	N [187] (74%, 40)	low O_2 uptake [77]	Y [77]	Y [77]	[78]
	(MF monolith)			1.5 (G, 5000 ppm, 20 °C)	-	N		N		-	-	> 50% CO_2 (air, 20 °C)	Y (PB)	Y (PB)	
8	TIFSIX-3-Co (powder)	n/a	0	1.1 (V)	55[d] [68]	Y[a] (V)	N	N	N	-	N [68] (74%, 40)	-	Y (PB)	N	[79]
9	GeFSIX-3-Ni (powder)	n/a	0	1.1 (V)	55	Y[a] (V)	N	N	N	-	-	-	Y (PB)	N	[81]
10	GeFSIX-3-Co (powder)	n/a	0	0.3 (V)	39	Y[a] (V)	N	N	N	-	-	-	Y (PB)	N	[81]

	Name (form)	Functionalised	Functionalisation Loading ($mmol_N\ g_{ads}^{-1}$)	CO_2 uptake at 400 ppm, 25 °C ($mmol\ g^{-1}$)	ΔH_0 ($kJ\ mol^{-1}$)	Isotherms				H_2O uptake ($mmol\ g^{-1}$) (at %RH, °C)	Stability		Kinetic data	Cyclic studies	Ref
						CO_2	N_2	O_2 (° C)	H_2O (° C)		H_2O (%RH, °C)	O_2			
11	MOF-74-Ni (powder)	n/a	0	1.3	38 [74]	Y [74]	Y [74] (V)	N	Y (G, 25) [188] (V, 55, 70) [189]	30.7 [188] (91 %, 25)	N [190] (steam)	-	Y[e] [188] (TGA)	Y[f] (TGA)	[83]
	(monolith, 20% binder)			1.0 (G, 3000 ppm)	35	Y (V)	N		N	-	-		N		
12	UTSA-16(Co) (powder)	n/a	0	1.0	41 [74]	Y [74]	Y[g] [191] (V)	N	Y [191] (G, 55, 69)[g]	11 [191] (25%, 55)	Y-[e] [191] (23%, 40)	-	Y(PB)	Y[f] (TGA)	[83]
	(monolith, 15% binder)			0.6 (G, 3000 ppm)	31	Y (V)	N		N	-	-				
13	Co_2(dobdc) – MS, irregular crystals	n/a	0	0.1	-	Y[a] (V)	N	N	Y (25)[h]	18.7	Y- [194] (70%, 25)	-	Y[f] [195] (TGA)	Y[f] [195] (TGA)	[86]
	Co_2(dobdc) – ST, irregular crystals	n/a	0	0.2	34 [192]		Y [193] (V)			17.3	-		N	N	
	Co_2(dobdc) – MS, hexagonal crystals (powder)	pyrazine (g)	0, 1.8	0.64, 1.36 (V)	-, 48		N			18.6, 15.4 (92%, 25)	-, Y- (75%, 25)		Y (TGA^i), Y (TGA^i, PB)	N, Y[i] (PB)	
14	MIL-101(Cr) (powder)	n/a	0	0.1	39 [196] (at 0.1 $mmol\ g^{-1}$)	Y [196] (V)	Y [197] (V)[j]	N	Y [198] (V, 25)	56 [198] (92%, 25)	Y- [187] (49%, 25)	-	Y (TGA)	Y (TGA)	[92]
		TEPA (i)	4.0	1.4	-	N	N		-	-	-				
		PEI-800-B (i)	5.5	2.0 (G, 3000 ppm)	-	N	N		-	-	Y+[e] [199] (75)				
15	MIL-101(Cr) (monolith, 20 % binder)	n/a TEPA (i) PEI-800-B (i)	0 0.8, 3.5 3.2, 5.3	0.04 0.3, 1.6 0.6, 1.4	-	N	N	N	N	-	-	-	Y (TGA)	Y (TGA)	[92]
16	MIL-101(Cr) (monolith, 25 % binder)	n/a	0	0.2 (V, 8000 ppm, 20 °C)	-	N	N	N	N	-	-	Y (air, 200 °C)	Y (PB)	N	[87]

	Name (form)	Functionalised	Functionalisation Loading ($mmol_N\ g_{ads}^{-1}$)	CO_2 uptake at 400 ppm, 25 °C ($mmol\ g^{-1}$)	ΔH_0 ($kJ\ mol^{-1}$)	Isotherms				H_2O uptake ($mmol\ g^{-1}$) (at %RH, °C)	Stability		Kinetic data	Cyclic studies	Ref
						CO_2	N_2	O_2 (° C)	H_2O (° C)		H_2O (%RH, °C)	O_2			
17	MIL-101(Cr) (powder)	n/a TAEA (g) TAEA (i) PEI-800-B (i)	0 2.6 5.7 0.2, 0.4, 0.8, 1.0, 1.1, 1.3, 1.8	0.04 (G) 0.4 (V) 2.8 (G) 0.1, 0.1, 0.3, 1.2, 1.1, 1.2, 1.4 (G)	see 14 - - -, -, -, -, 70, -, -	see 14 N N N, N, N, N, Y, N, N (V)	see 14 N N N	N	see 14 N N N	see 14	see 14 - - Y (32 %, 25)	-	see 14 N N N, N, N, Y, N, Y, Y (TGA)	see 14 Y Y N, N, N, N, Y, N, N (TGA)	[93]
18	MIL-101(Cr) (monolith)	PEI-800 (i)	-	1.0 (V)	55[d]	Y (V)	N	N	N	-	Y (ss)	Y[k] (air, 75 °C)	Y (PB)	Y (S)	[94]
19	MIL-101(Cr)-SO_3H (powder)	TAEA (g)	0, 1.2	-, 1.1 (G, 20 °C)	32 [200], 87	N, Y (V)	N	N	Y [201], N (V, 25)	3.8, - (58%, 25)	Y [201], - (boiling water)	-	N	N, Y (TGA)	[97]
20	$Zn(ZnOH)_4(bibta)_3$ (powder)	n/a	0	2.2 (V, 27)	72 (at 2.2 $mmol\ g^{-1}$)[l]	Y (V)	N	Y (V, 27)	Y (V, 23)	12.4 (95%, 23)	N (100%, 25)	low O_2 uptake	Y (PB)	Y (TGA)	[98]
21	$Zn_2Ni_3(OH)_4(bibta)_3$ (powder)	n/a	0	2.7 (V, 27)	84 (at 2.5 $mmol\ g^{1}$)[m]	Y(V)	N	Y (V, 27)	Y (V, 23)	20.6 (92%, 23)	Y- (13%, 25)	> 50 % CO_2 (air, 25 °C)	Y (PB)	Y[i] (TGA)	[99]
22	$ZnCo_4(OH)_4(bibta)_3$ (powder)	n/a	0	1.7 (V, 27)	76[n]	Y (V)	N	N	N	-	-	-	N	N	[99]
23	$Zn_5(OH)_4(bbta)_3$_a[o] $Zn_5(OH)_4(bbta)_3$_b[p] (powder)	n/a	0	0.8 0.5 (V, 27)	-	N	N	N	N	-	-	-	Y (TGA)	Y[i] (TGA)	[100]
24	$Zn_5(OH)_4(btdd)_3$_a[o] $Zn_5(OH)_4(btdd)_3$_b[p] (powder)	n/a	0	0.5 - (V, 27)	62 -	Y (V) N	N	N	N	-	-	-	Y (TGA)	Y[i] (TGA)	[100]
25	$Zn_{2.35}Ni_{2.65}(OH)_4(btdd)_3$_a[o] $Zn_{2.35}Ni_{2.65}(OH)_4(btdd)_3$_b[p] (powder)	n/a	0	1.5 1.0 (V, 27)	73 (at 1.4 $mmol\ g^{-1}$) -	Y (V) N	N	N	N	-	-	-	Y (TGA) N	Y[i] (TGA) N	[100]
26	$Mg_2(dobpdc)$ (powder)	n/a pn (g) mpn (g)	0 151 %[q] 135 %[q]	- 0.4 0.1 (V, 40 °C)	44 [101] 68 72	Y [101] Y Y (V)	N	N	N	-	N [202] (86%, 23) - -	N (air, RT) [101] - -	Y[i] [203] N N (TGA)	N	[102]

	Name (form)	Functionalised	Functionalisation Loading ($mmol_N\ g_{ads}^{-1}$)	CO_2 uptake at 400 ppm, 25 °C ($mmol\ g^{-1}$)	ΔH_0 ($kJ\ mol^{-1}$)	Isotherms				H_2O uptake ($mmol\ g^{-1}$) (at %RH, °C)	Stability		Kinetic data	Cyclic studies	Ref
						CO_2	N_2	O_2 (° C)	H_2O (° C)		H_2O (%RH, °C)	O_2			
27	Mg_2(dobpdc) (powder) mmen (i) spermine (i)	n/a	0 - -	-	see 26 - -	see 26 N N	N	N	N	-	see 26 Y+[e] Y+[e] (100%, 35)	see 26 - -	N Y (PB) N	N	[103]
28	Mg_2(dobpdc) (PE fibre) mmen (i) spermine (i)	n/a	0 - -	- 0.7 2.0 (D, 35 °C)	- 61 101	N Y (V) Y (V)	N	N	N	-	- Y+[e] Y+[e] (100%, 35)	-	N Y Y (PB)	N Y Y (PB)	[103]
29	Mg_2(dobpdc) (powder)	mmen (g)	-	3.1 (V)	-	Y (V)	N	N	N	-	-	-	Y (PB, TGA)	N	[104]
30	Mg_2(dobpdc) (film coating on cordierite monolith)	mmen (g)	-	2.9 (V)	70[d]	Y (V)	N	N	N	-	Y (ss)	Y[k] (air, 75 °)	Y (PB)	Y (S)	[94]
31	Mg_2(dobpdc) (powder)	mmen (g)	7.3	3.0[r] [101] (V)	17 [101] (71 at 0.3 $mmol\ g^{-1}$)[t]	Y[r] [204] (V)	N	Y[t] [101] (V, 25)	Y (V, 25)	2.2 (62%, 25)	Y-[e] (70%, 25)	Y [101] (air, RT)	Y [101] (TGA)	Y [101]	[93]
	(film coating on cordierite monolith)			-[s]	-	N		N	N	-			N	Y[e] (TGA)	
32	Mg_2(dobpdc) (powder)	spermine (g)	0, 94%[u]	-, 1.7 (G, 30 °C)	see 26, 99	see 26, Y (V)	N	N, Y (V, 40)	N, Y (V, 30, 40, 50, 60)	-, 19.0 (78%, 30)	see 26, Y+ (ss)	see 26, > 50% CO_2[f] (after air, 100 °C)	see 26, Y (PB)	N Y (TGA)	[105]
33	Mg_2(dobpdc) (powder) nmen (g) een (g) ipen (g)	-	2.5 3.1 2.5 (G, 10 500 ppm, 40 °C)	72[n] 74[n] 76[n]	Y (V)	N	N	N	-	Y+[e] (51%, 40)	> 50 % CO_2[e] (5 % O_2, 50 °C)	Y (TGA) Y (TGA, PB[e]) Y (TGA)	N Y[e] N (TGA)	[106]
34	Mg_2(dobpdc) (powder)	2-ampd (g)	-	0.2 (V, 40 °C)	84	Y (V)	N	Y (V, 40)	Y (V, 30, 40, 50, 60)	15.7 (70%, 30)	Y+ (35%, 40)	> 50 % CO_2[f] (after 21% O_2, 100 °C)	Y (TGA, PB[g])	Y (TGA)	[107]

	Name (form)	Functionalised	Functionalisation Loading ($mmol_N\ g_{ads}^{-1}$)	CO_2 uptake at 400 ppm, 25 °C ($mmol\ g^{-1}$)	ΔH_0 ($kJ\ mol^{-1}$)	Isotherms				H_2O uptake ($mmol\ g^{-1}$) (at %RH, °C)	Stability		Kinetic data	Cyclic studies	Ref
						CO_2	N_2	O_2 (° C)	H_2O (° C)		H_2O (%RH, °C)	O_2			
35	Mg_2(dobpdc) (powder)	epn (g)	-	2.2	-	N	N	N	N	-	N	-	Y (TGA)	Y (VAS, TGA)	[108]
	(SBS membrane)														
	-60 wt% MOF			0.9	-	N		N	Y (V, 25)	7.6	-	-	Y (TGA)	N	
	-70 wt% MOF			1.1	-	N		N	N	-	Y-	-	Y (TGA)	N	
	-80 wt% MOF (SBS spray coating)			1.8 (V, 1000 ppm, 30 °C)	68	Y (V)		Y (V, 30)	Y (V, 25)	11.3 -	Y-	low O_2 uptake	Y (TGA)	Y (VAS, TGA)	
	-on Ti mesh			0.9	-	N		N	N	-	Y-	-	N	Y (VAS)	
	-on HEPA fileter			0.9	-	N		N	N	-	Y-	-	N	Y (VAS)	
	-on AC granules			0.8 (V, 1000 ppm, RT, 60% RH)	-	N		N	N	(89%, 25)	Y- (60%, 25)	-	N	Y (VAS)	
36	Mg-MOF-74 (powder)	hydrazine (g)	0, 12.0	0.1, 3.9	47, 90	Y [110], Y (V)	Y [110], N (V)	Y [205], N (S, 40)	Y [206], N (G, 25)	36.0, - (79%, 25)	N [207] (75%-40), Y- (82%, 40)		Y (PB)[e] [208], Y (TGA, PB)	Y[f] [208], Y[e] (TGA)	[112]

[a] one of the three temperatures is -78 °C
[b] HPMCP theoretical wt %
[c] value approximated from statement that coated adsorbent adsorbs 4x less water
[d] CO_2 loading not specified
[e] studied at flue gas conditions
[f] studied at 100% CO_2 conditions
[g] data is for pellet
[h] measurement method not stated
[i] studied at 5% CO_2 conditions
[j] data for granules with binder
[k] risk of amine degradation above this temperature
[l] ΔH_0 was 43, but authors thought this may have been an error, due to steep low-pressure CO2 uptake causing equilibration and/or pressure measurement issues during the isotherm measurements
[m] ΔH_0 was 3, but authors thought this may have been an error, due to steep low-pressure CO2 uptake causing equilibration and/or pressure measurement issues during the isotherm measurements
[n] for near 0 $mmol\ g^{-1}$ loading
[o] TBAOH synthesis
[p] $NaHCO_3$ synthesis
[q] % diamine loading
[r] for adsorbent with 7.40 mmol/g loading
[s] uptake should be 70% that of powder uptake
[t] for adsorbent with 7.80 mmol/g loading
[u] % spermine loading per 2 Mg^{2+}

Table A1.10: Summary of sorption properties of carbon adsorbents investigated for DAC.

	Name (form)	Functionalised	Functionalisation Loading ($mmol_N\ g_{ads}^{-1}$)	CO_2 uptake at 400 ppm, 25 °C ($mmol\ g^{-1}$)	ΔH_0 ($kJ\ mol^{-1}$)	Isotherms				H_2O uptake ($mmol\ g^{-1}$) (at %RH, °C)	Stability		Kinetic data	Cyclic studies	Ref
						CO_2	N_2	O_2 (° C)	H_2O (° C)		H_2O (%RH, °C)	O_2			
1	sawdust biochar (powder)	n/a	0	3.2 (G, 500 ppm)	-	N	N	N	N	-	Y-[a] [209] (100 %, 50)	-	N	N	[113]
2	AC (monolith)	K_2CO_3 (i)	0, 0.4[b]	-, 0.2 (D, 20 °C, 21% RH)	27[c] [114], -	Y [114], N (V)	Y [114], N (V)	N	Y [114], Y (G, 40)	6.7, 8.9 (60%, 40)	Y-[a] (ss) [114] (21%, 50), Y-[d,e] (21%, 20)[f] (30%, 65)[g]	-	Y[a] [210], Y (PB)	Y[a] [210], Y (PB)	[115]
3	AC (monolith)	K_2CO_3 (i) Na_2CO_3 (i)	0.4[b] 0.5[h]	0.2 0.1 (D, 30 °C, 28 % RH)	-	N	N	N	Y (G, 20, 30, 40)	15.8 (100 %)[i] 16.6 (100 %)[i]	Y[d] (26 %, 30)	-	Y (PB)	Y (PB) Y (PB)	[116]
4	CB (PBX-51) (powder)	K_2CO_3 + MF + BCA (i)	0, 17%[j] + 17%[j] + 33%[j]	-, 2.6 (D, 10000 ppm, 35 °C, 9% RH)	-	N	N	N	N	-	Y[d] (9%, 35)	-[k]	Y (PB)	Y (PB)	[118]

[a] studied at flue gas conditions
[b] $mmol_{K2CO3}\ g^{-1}$
[c] CO_2 loading not specified
[d] H_2O needed for CO_2 adsorption mechanism
[e] moisture swing adsorbent where CO_2 desorbs with increased % RH
[f] adsorption condition
[g] desorption condition
[h] $mmol_{Na2CO3}\ g^{-1}$
[i] temperature not specified
[j] theoretical wt% of each component
[k] experiments done with ambient air but effect of O_2 was not investigated

Table A1.11: Summary of adsorption properties of zeolite adsorbents investigated for DAC.

	Name (form)	Functionalised	Functionalisation Loading ($mmol_N\ g_{ads}^{-1}$)	CO_2 uptake at 400 ppm, 25 °C ($mmol\ g^{-1}$)	ΔH_0 ($kJ\ mol^{-1}$)	Isotherms				H_2O uptake ($mmol\ g^{-1}$)	Stability		Kinetic data	Cyclic studies	Ref
						CO_2	N_2	O_2 (° C)	H_2O (° C)	(at %RH, °C)	H_2O (%RH, °C)	O_2			
1	H-ZSM-5 (powder)	TEPA (i)	0, 4.8	0.3, 0.2 (G, 5000 ppm)	38[a] [211], -	Y[b] [212], - (G)	Y[b] [212], N (G)	N	Y [213] (G, 50, 85, 120)	2.6 (88 %, 50)	-	-	Y (PB)	N	[124]
2	SAPO-34 (powder)	TEPA (i)	0, 4.1	0.6, 0.5 (G, 5000 ppm)	32 [214], -	Y [215], - (V)	Y[c] [216], N (V)	N	Y [215], N (V, 21, 33, 50, 65, 80, 95)	20.0 (84 %, 21)	Y [217] (ss), -	-	Y (PB)	N	[124]
3	NH_4Y (powder)	TEPA (i)	0, 5.3	0.9, 1.1 (G, 5000 ppm)	-	N	N	N	N	-	-	-	Y (PB)	Y (TGA)	[124]
4	NH_4Y (powder)	ED (g)	0, 5.6	-, 1.5 (V, 5000 ppm, 40 °C)	-	N	N	N	N	-	-, Y-[d] (3 %, 40)	-	N, Y[d] (TGA)	N, Y[d] (TGA)	[129]
5	13X (powder)	n/a	0	0.4 [68] (V) (or 1.4 at 3000 ppm, G)	39	Y[e] [218] (V, G)	Y[e] [218] (G)	Y[a] [219] (V, 15, 30, 45)	Y[e] [220] (V, 22) (G, 22, 30, 40, 50 75)	17.8[e] (75%, 22)	Y-[d] [220] (88% 22) (ss) [190]	-	Y (PB)	Y[d] [133] (PB)	[134]
6	13X (monolith) -20% binder -15% binder -10% binder	n/a	0	 1.2 1.2 1.2 (G, 3000 ppm)	-	N	N	N	N	-	-	-	 N N Y (PB)	N	[134]
7	13X (monolith, 25% binder)	n/a	0	0.4 (D, 8000 ppm, 20 °C)	-	N	N	N	N	-	-	-	Y (PB)	N	[87]
8	G5CO2M[f] APG-III[g] Ca-X Na-LSX Z10-01[h] Z10-02ND[i] Na-X-HP[j] (pellet)	n/a	0	0.1 – 0.5 (G, 22 °C)	see 5 32 51[a] [221] 40[a] [221] see 5 - see 5	see 5 Y (G) Y [222] (V) N see 5 N see 5	see 5 N Y (G) [223] N see 5 N see 5	Y (G, 22)	see 5 N N N see 5 N see 5	-	-	low O_2 uptake	Y[k] (G)	see 5 Y (PB) N N see 5 N see 5	[137]
9	5A (powder)	n/a	0	1.5 (G, 3000 ppm)	33[a] [221]	Y[l] [178] (V)	Y[m] [224] (G)	Y [225] (V, 0, 10, 30, 70)	Y[l] [178] (V, 25, 50, 75, 100)	13.8[l] (50%, 25)	Y-[d] [133] (25)	-	Y (PB)	Y[d] [133] (PB)	[134]

	Name (form)	Functionalised	Functionalisation Loading ($mmol_N\ g_{ads}^{-1}$)	CO_2 uptake at 400 ppm, 25 °C ($mmol\ g^{-1}$)	ΔH_0 ($kJ\ mol^{-1}$)	Isotherms				H_2O uptake ($mmol\ g^{-1}$)	Stability		Kinetic data	Cyclic studies	Ref
						CO_2	N_2	O_2 (° C)	H_2O (° C)	(at %RH, °C)	H_2O (%RH, °C)	O_2			
10	5A (monolith) -20% binder -15% binder -10% binder	n/a	0	1.0 1.1 1.3 (G, 3000 ppm)	-	N	N	N	N	-	-	-	N N Y (PB)	N	[134]
11	NaCaA-85 (powder)	n/a	0	1.8 (V)	65	N	N	Y (V, 25)	N	-	-	low O_2 uptake	Y (PB)	Y (V)	[142]
12	BaMFI SrMFI CaMFI (powder)	n/a	0	0.8 0.7 0.5 (V, 1000 ppm)	80 101 81	N	N	N	N	-	-	-	N	Y (V)	[143]

[a] form unknown
[b] data is for pellets with binder
[c] data is for a membrane sample
[d] studied at flue gas conditions
[e] data is for granules
[f] commercial 13X from CECA Arkema Group
[g] commercial 13X from Honeywell UOP marketed for air prepurification
[h] commercial 13X from Zeochem
[i] commercial 13X from Zeochem marketed for air prepurification
[j] commercial 13X from Hengye
[k] studied at 100% CO_2 conditions
[l] data is for beads
[m] data is for pellets

Table A.12: Summary of adsorption properties of polymer adsorbents investigated for DAC.

	Name (form)	Functionalised	Functionalisation Loading ($mmol_N\ g_{ads}^{-1}$)	CO_2 uptake at 400 ppm, 25 °C ($mmol\ g^{-1}$)	ΔH_0 ($kJ\ mol^{-1}$)	Isotherms				H_2O uptake ($mmol\ g^{-1}$) (at % RH, °C)	Stability		Kinetic data	Cyclic studies	Ref
						CO_2	N_2	O_2 (° C)	H_2O (° C)		H_2O (%RH, °C)	O_2			
1	Lewatit VP OC 1065 (beads)	BA (g)	6.1	1.0 (G)	70	Y (G)	Y (V)[a]	N	Y (G, 25, 50, 75, 100)	8.0 (80 %, 25)	Y+ (30%, 25) (ss)[226]	> 50% CO_2[b] [145] (after air, 80 °C)	Y (PB)	Y [149] (TGA)	[147]
2	Purolite A109 (beads)	1° amine (g)	4.3	0.2 (G, 20 000 ppm)	-	N	N	N	N	-	Y	-	Y (TGA)	Y (TGA)	[149]
3	Purolite A500 (beads) (dense fibres) (porous fibres)	QA (g)	-	- 0.5 1.0 (V, air, RT)	-	N	N	N	N	-	Y-[c]	-	Y (VAS)	Y (VAS)	[151]
4	IER from *Snowpure LLC* (film)	unknown	-	1.6 (V, air, RT)	-	N	N	N	N	-	Y-[c]	-	Y (VAS)	Y (VAS)	[151]
5	XAD-4 XAD-16 XAD-1180N (beads)	$2[N(CH_3)_4]^+ \cdot CO_3^{2-}$ (g)	0, 0.9 0, 1.0 0, 1.0	-, 0.2 -, 0.3 -, 0.2 (V, 20 °C, 21% RH)	-	N	N	N	N	6.9[d], 13.1[d] 7.2[d], 14.2[d] 7.1[d], 14.0[d]	Y-[c, e] (21%, 20)[f] (100%, 20)[g]	-	N, Y N, Y N, Y (VAS)	N N, Y N (VAS)	[156]
6	D201 (beads)	QA (g) → K_3PO_4 (ie)	3.9	0.6 (V, 3% RH)	-	N	N	N	N	-	Y-[c, e] (3 %, 25)[f] (95 %, 25)[g]	-	Y (VAS)	Y (VAS)	[158]
7	Resin from *Knowledge & Benefit Sphere Tech. Co., Ltd.* (beads)	PEI-600 (i)	0, 20%[h]	-, 1.1 (D, 4000 ppm, 20 °C)	-	N	N	N	N	-, 3.3 (45 %, 20)	Y+/-[i] (60%, 20)[j]	-[k]	Y (PB)	N	[159]
8	MR10 (beads)	PEI-600 (i)	0, 10.4	-, 2.6 (D, 1000 ppm)	-	N	N	N	N	-	Y+ (50%, 25)	> 50% CO_2 (after air, 70 °C)	Y (PB)	Y (PB)	[160]
9	Resin from *Oy Hydrocell Ltd.* (beads)	1° amine (g)	4.7	0.8 [161] (D)	62 [161]	Y	N	N	Y (D, 25, 35, 50)	3.9 (60 %, 25)	Y+ (63%, 25)	-	Y (PB)	Y (PB)	[162]

	Name (form)	Functionalised	Functionalisation Loading ($mmol_N\ g_{ads}^{-1}$)	CO_2 uptake at 400 ppm, 25 °C ($mmol\ g^{-1}$)	ΔH_0 ($kJ\ mol^{-1}$)	Isotherms				H_2O uptake ($mmol\ g^{-1}$) (at % RH, °C)	Stability		Kinetic data	Cyclic studies	Ref
						CO_2	N_2	O_2 (° C)	H_2O (° C)		H_2O (%RH, °C)	O_2			
10	QCPS-1/PES QCPS-2/PES QCPS-3/PES (film)	QA (g) → Na_2CO_3 (ie)	2.0 2.2 2.1	1.1 1.0 1.0 (V, 20 °C, 21% RH)	- 30 -	N	N	N	Y (G, 30) Y (G, 30) N	6.5 (66 %, 30) 3.0 (89 %, 30) -	Y-[c, e] (21%, 20)[f] (85%, 20)[g]	-	Y (VAS)	N Y N (VAS)	[163]
11	NFC (powder)	APDES (g)	3.4	0.9 (D, 23 °C)	60	Y (V)[l] [227]	N	N	Y [227] (G, 10, 20, 30, 70, 80)[l]	5.4 (73 %, 30)	Y+ (58 %, 20)	-	Y [228] (PB)	Y [229] (PB)	[166]
12	NFC (powder)	APDES (g)	3.1	0.7 (D, 600 ppm, 35 °C)	-	see 11	N	N	see 11	3.0 (50 %, 30)	Y+ (50 %, 30)	-	Y (DB)	N	[167]
13	BC (powder)	CHPTAC (g) → Na_2CO_3 (ie)	0, 0.4, 0.4, 0.6	-, 0.1, 0.1, 0.2 (V, 66% RH)	-	N	N	N	Y, N, N, Y (G, 25[g])	10.6, -, -, 12.2 (90 %, 25[m])	Y-[c, e] (66%, 25)[f] (95 %, 25)[g]	-	N, N, N, Y (PB)	N	[168]
14	PAN (hollow fibre)	TEPA (g)	0, 15 %[n], 39%[n], 58%[n]	-, 0.9, 1.0, 1.3 (D, 3000 ppm)	-	N	N	N	N	-	Y+ (25)	-	N	N	[170]
15	PAN/PMMA (hollow fibre)	TEPA (g)	0, 75%[n]	-, 1.5 (D, 3000 ppm)	-	N	N	N	N	-	Y+ (25)	-	Y (PB)	Y (PB)	[170]
16	PEI "snow" (powder)	n/a	0	1.1 (D, air, RT)	-	N	N	N	N	-	Y+[e] (ss)	-[k]	Y (PB)	Y (PB)	[172]

[a] one of the three temperatures is -196 °C
[b] studied at flue gas conditions
[c] moisture swing adsorbent where CO_2 desorbs with increased % RH
[d] %RH and temperature not specified
[e] H_2O needed for CO_2 adsorption mechanism
[f] adsorption condition
[g] desorption condition
[h] theoretical PEI wt %
[i] changes depending on CO_2 concentration and temperature
[j] above 60% RH, CO_2 uptake decreases
[k] some experiments done with ambient air but effect of O_2 was not investigated
[l] for sample with 4.2 $mmol_N\ g^{-1}$ loading
[m] assuming measurement done at 25 °C but not explicitly stated
[n] TEPA % grafting

A1. References

[1] Y. Liu *et al.*, "Performance of mesoporous silicas (MCM-41 and SBA-15) and carbon (CMK-3) in the removal of gas-phase naphthalene: adsorption capacity, rate and regenerability," *RSC Advances,* 10.1039/C5RA27289K vol. 6, no. 25, pp. 21193-21203, 2016, doi: 10.1039/C5RA27289K.

[2] E. Ghedini, F. Menegazzo, M. Manzoli, A. Di Michele, D. Puglia, and M. Signoretto, "Multifunctional and Environmentally Friendly TiO_2–SiO_2 Mesoporous Materials for Sustainable Green Buildings," *Molecules,* vol. 24, no. 23, p. 4226, 2019, doi: 10.3390/molecules24234226.

[3] P. Shah and V. Ramaswamy, "Thermal stability of Mesoporous SBA-15 and Sn-SBA-15 Molecular Sieves: An in situ HTXRD study," *Microporous and Mesoporous Materials,* vol. 114, no. 1, pp. 270-280, 2008/09/01/ 2008, doi: 10.1016/j.micromeso.2008.01.013.

[4] J. J. Lee, C.-H. Chen, D. Shimon, S. E. Hayes, C. Sievers, and C. W. Jones, "Effect of Humidity on the CO_2 Adsorption of Tertiary Amine Grafted SBA-15," *The Journal of Physical Chemistry C,* vol. 121, no. 42, pp. 23480-23487, 2017, doi: 10.1021/acs.jpcc.7b07930.

[5] B. Wadi, A. Golmakani, V. Manovic, and S. A. Nabavi, "Evaluation of Moderately Grafted Primary, Diamine, and Triamine Sorbents for CO_2 Adsorption from Ambient Air: Balancing Kinetics and Capacity under Humid Conditions," *Industrial & Engineering Chemistry Research,* vol. 60, no. 36, pp. 13309-13317, 2021, doi: 10.1021/acs.iecr.1c02416.

[6] E. S. Sanz-Pérez, A. Fernández, A. Arencibia, G. Calleja, and R. Sanz, "Hybrid amine-silica materials: Determination of N content by 29Si NMR and application to direct CO_2 capture from air," *Chemical Engineering Journal,* vol. 373, pp. 1286-1294, 2019, doi: 10.1016/j.cej.2019.05.117.

[7] X. Zhu *et al.*, "Efficient CO_2 capture from ambient air with amine-functionalized Mg–Al mixed metal oxides," *Journal of Materials Chemistry A,* vol. 8, no. 32, pp. 16421-16428, 2020, doi: 10.1039/d0ta05079b.

[8] D. R. Kumar, C. Rosu, A. R. Sujan, M. A. Sakwa-Novak, E. W. Ping, and C. W. Jones, "Alkyl-Aryl Amine-Rich Molecules for CO_2 Removal via Direct Air Capture," *ACS Sustainable Chemistry & Engineering,* 2020, doi: 10.1021/acssuschemeng.0c03706.

[9] Y. Miao, Z. He, X. Zhu, D. Izikowitz, and J. Li, "Operating temperatures affect direct air capture of CO_2 in polyamine-loaded mesoporous silica," *Chemical Engineering Journal,* vol. 426, 2021, doi: 10.1016/j.cej.2021.131875.

[10] M. L. Sarazen, M. A. Sakwa-Novak, E. W. Ping, and C. W. Jones, "Effect of Different Acid Initiators on Branched Poly(propylenimine) Synthesis and CO_2 Sorption Performance," *ACS Sustainable Chemistry & Engineering,* vol. 7, no. 7, pp. 7338-7345, 2019, doi: 10.1021/acssuschemeng.9b00512.

[11] S. H. Pang, R. P. Lively, and C. W. Jones, "Oxidatively-Stable Linear Poly(propylenimine)-Containing Adsorbents for CO_2 Capture from Ultradilute Streams," *ChemSusChem,* vol. 11, no. 15, pp. 2628-2637, Aug 9 2018, doi: 10.1002/cssc.201800438.

[12] C. Rosu, S. H. Pang, A. R. Sujan, M. A. Sakwa-Novak, E. W. Ping, and C. W. Jones, "Effect of Extended Aging and Oxidation on Linear Poly(propylenimine)-Mesoporous Silica Composites for CO_2 Capture from Simulated Air and Flue Gas Streams," *ACS Applied Materials & Interfaces,* vol. 12, no. 34, pp. 38085-38097, Aug 26 2020, doi: 10.1021/acsami.0c09554.

[13] A. R. Sujan *et al.*, "Poly(glycidyl amine)-Loaded SBA-15 Sorbents for CO_2 Capture from Dilute and Ultradilute Gas Mixtures," *ACS Applied Polymer Materials,* vol. 1, no. 11, pp. 3137-3147, 2019, doi: 10.1021/acsapm.9b00788.

[14] S. J. Park, J. J. Lee, C. B. Hoyt, D. R. Kumar, and C. W. Jones, "Silica supported poly(propylene guanidine) as a CO_2 sorbent in simulated flue gas and direct air capture," *Adsorption,* vol. 26, no. 1, pp. 89-101, 2019, doi: 10.1007/s10450-019-00171-w.

[15] Y. Wang and R. T. Yang, "Template Removal from SBA-15 by Ionic Liquid for Amine Grafting: Applications to CO_2 Capture and Natural Gas Desulfurization," *ACS Sustainable Chemistry & Engineering,* vol. 8, no. 22, pp. 8295-8304, 2020, doi: 10.1021/acssuschemeng.0c01941.

[16] G. Zhang, P. Zhao, L. Hao, and Y. Xu, "Amine-modified SBA-15(P): A promising adsorbent for CO_2 capture," *Journal of CO_2 Utilization,* vol. 24, pp. 22-33, 2018/03/01/ 2018, doi: 10.1016/j.jcou.2017.12.006.

[17] M. Zhao, J. Xiao, W. Gao, and Q. Wang, "Defect-rich Mg-Al MMOs supported TEPA with enhanced charge transfer for highly efficient and stable direct air capture," *Journal of Energy Chemistry,* vol. 68, pp. 401-410, 2022, doi: 10.1016/j.jechem.2021.12.031.

[18] C.-J. Yoo, S. J. Park, and C. W. Jones, "CO_2 Adsorption and Oxidative Degradation of Silica-Supported Branched and Linear Aminosilanes," *Industrial & Engineering Chemistry Research,* vol. 59, no. 15, pp. 7061-7071, 2019, doi: 10.1021/acs.iecr.9b04205.

[19] S. H. Pang, L. C. Lee, M. A. Sakwa-Novak, R. P. Lively, and C. W. Jones, "Design of Aminopolymer Structure to Enhance Performance and Stability of CO_2 Sorbents: Poly(propylenimine) vs Poly(ethylenimine)," *Journal of the American Chemical Society,* vol. 139, no. 10, pp. 3627-3630, Mar 15 2017, doi: 10.1021/jacs.7b00235.

[20] DAVISIL. "Chromatographic Silica Product Selection Guide " https://fscimage.fishersci.com/cmsassets/downloads/segment/Scientific/pdf/silica_media_selection_guide.pdf (accessed 2022).

[21] O. R. F. Cevallos, "Adsorption Characteristics of Water and Silica Gel System for Desalination Cycle " Master of Science, King Abdullah University of Science and Technology, 2012.

[22] M. A. Islam, K. Thu, and B. B. Saha, " Specific heat capacity of mesoporous silica gel for adsorption heat pump applications," in *Proceedings of International Forum for Green Asia*, 2017.

[23] A. Sharafian, K. Fayazmanesh, C. McCague, and M. Bahrami, "Thermal conductivity and contact resistance of mesoporous silica gel adsorbents bound with polyvinylpyrrolidone in contact with a metallic substrate for adsorption cooling system applications," *International Journal of Heat and Mass Transfer,* vol. 79, pp. 64-71, 2014/12/01/ 2014, doi: 10.1016/j.ijheatmasstransfer.2014.07.086.

[24] J.-T. Anyanwu, Y. Wang, and R. T. Yang, "Amine-Grafted Silica Gels for CO_2 Capture Including Direct Air Capture," *Industrial & Engineering Chemistry Research,* vol. 59, no. 15, pp. 7072-7079, 2019, doi: 10.1021/acs.iecr.9b05228.

[25] P. E. Rajan, A. Krishnamurthy, G. Morrison, and F. Rezaei, "Advanced buffer materials for indoor air CO_2 control in commercial buildings," *Indoor Air,* vol. 27, no. 6, pp. 1213-1223, Nov 2017, doi: 10.1111/ina.12386.

[26] Y. Zhao *et al.*, "Indoor CO_2 Control through Mesoporous Amine-Functionalized Silica Monoliths," *Industrial & Engineering Chemistry Research,* vol. 58, no. 42, pp. 19465-19474, 2019, doi: 10.1021/acs.iecr.9b03338.

[27] G. GÜZEL KAYA, "Polyethylene glycol/silica and carbon black/silica xerogel composites as an adsorbent for CO_2 capture," *Turkish Journal of Chemistry,* vol. 45, no. 6, 2021, doi: 10.3906/kim-2101-45.

[28] A. Sayari, Q. Liu, and P. Mishra, "Enhanced Adsorption Efficiency through Materials Design for Direct Air Capture over Supported Polyethylenimine," *ChemSusChem,* vol. 9, no. 19, pp. 2796-2803, Oct 6 2016, doi: 10.1002/cssc.201600834.

[29] E. Industries. "AEROSIL - Fumed Silica Technical Overview." https://mychem.ir/uploads/supplier/11965/017535074f20c47.pdf (accessed 2022).

[30] E. Industries. "AEROSIL® 200." https://www.freemansupply.com/MSDS/Combined/Fillers/Aerosil200.pdf (accessed 2022).

[31] S. B. Jo *et al.*, "Thermally stable amine-functionalized silica sorbents using one-pot synthesis method for CO_2 capture at low temperature," *Korean Journal of Chemical Engineering,* vol. 37, no. 12, pp. 2317-2325, 2020, doi: 10.1007/s11814-020-0655-6.

[32] W. Jung and K. S. Lee, "Isotherm and kinetics modeling of simultaneous CO_2 and H_2O adsorption on an amine-functionalized solid sorbent," *Journal of Natural Gas Science and Engineering,* vol. 84, 2020, doi: 10.1016/j.jngse.2020.103489.

[33] C. Zhang, K. Zhang, Y. Cao, and W. J. Koros, "Composite Carbon Molecular Sieve Hollow Fiber Membranes: Resisting Support Densification via Silica Particle Stabilization," *Industrial & Engineering Chemistry Research,* vol. 57, no. 47, pp. 16051-16058, 2018/11/28 2018, doi: 10.1021/acs.iecr.8b02386.

[34] J. Kalyanaraman *et al.*, "Modeling and experimental validation of carbon dioxide sorption on hollow fibers loaded with silica-supported poly(ethylenimine)," *Chemical Engineering Journal,* vol. 259, pp. 737-751, 2015/01/01/ 2015, doi: 10.1016/j.cej.2014.08.023.

[35] A. R. Sujan, S. H. Pang, G. Zhu, C. W. Jones, and R. P. Lively, "Direct CO_2 Capture from Air using Poly(ethylenimine)-Loaded Polymer/Silica Fiber Sorbents," *ACS Sustainable Chemistry & Engineering,* vol. 7, no. 5, pp. 5264-5273, 2019, doi: 10.1021/acssuschemeng.8b06203.

[36] P. Bollini, "Amine-oxide adsorbents for post-combustion CO_2 capture," PhD, Georgia Institute of Technology, 2013.

[37] R. P. Wijesiri, G. P. Knowles, H. Yeasmin, A. F. A. Hoadley, and A. L. Chaffee, "CO_2 Capture from Air Using Pelletized Polyethylenimine Impregnated MCF Silica," *Industrial & Engineering Chemistry Research,* vol. 58, no. 8, pp. 3293-3303, 2019, doi: 10.1021/acs.iecr.8b04973.

[38] J.-T. Anyanwu, Y. Wang, and R. T. Yang, "CO_2 capture (including direct air capture) and natural gas desulfurization of amine-grafted hierarchical bimodal silica," *Chemical Engineering Journal,* vol. 427, 2022, doi: 10.1016/j.cej.2021.131561.

[39] H. T. Kwon, M. A. Sakwa-Novak, S. H. Pang, A. R. Sujan, E. W. Ping, and C. W. Jones, "Aminopolymer-Impregnated Hierarchical Silica Structures: Unexpected Equivalent CO_2 Uptake under Simulated Air Capture and Flue Gas Capture Conditions," *Chemistry of Materials,* vol. 31, no. 14, pp. 5229-5237, 2019, doi: 10.1021/acs.chemmater.9b01474.

[40] S. Mahesh and S. C. Joshi, "Thermal conductivity variations with composition of gelatin-silica aerogel-sodium dodecyl sulfate with functionalized multi-walled carbon nanotube doping in their composites," *International Journal of Heat and Mass Transfer,* vol. 87, pp. 606-615, 2015/08/01/ 2015, doi: 10.1016/j.ijheatmasstransfer.2015.04.046.

[41] Z. Mazrouei-Sebdani, H. Begum, S. Schoenwald, K. V. Horoshenkov, and W. J. Malfait, "A review on silica aerogel-based materials for acoustic applications," *Journal of Non-Crystalline Solids,* vol. 562, p. 120770, 2021/06/15/ 2021, doi: 10.1016/j.jnoncrysol.2021.120770.

[42] A. Ayral, J. Phalippou, and T. Woignier, "Skeletal density of silica aerogels determined by helium pycnometry," *Journal of Materials Science,* vol. 27, no. 5, pp. 1166-1170, 1992/03/01 1992, doi: 10.1007/BF01142014.

[43] R. C. Walker, A. E. Potochniak, A. P. Hyer, and J. K. Ferri, "Zirconia aerogels for thermal management: Review of synthesis, processing, and properties information architecture," *Advances in Colloid and Interface Science,* vol. 295, p. 102464, 2021/09/01/ 2021, doi: 10.1016/j.cis.2021.102464.

[44] Y. Guo, C. Zhao, J. Sun, W. Li, and P. Lu, "Facile synthesis of silica aerogel supported K_2CO_3 sorbents with enhanced CO_2 capture capacity for ultra-dilute flue gas treatment," *Fuel,* vol. 215, pp. 735-743, 2018, doi: 10.1016/j.fuel.2017.11.113.

[45] T. Gao and B. P. Jelle, "Thermal conductivity of amorphous silica nanoparticles," *Journal of Nanoparticle Research,* vol. 21, no. 6, p. 108, 2019/05/24 2019, doi: 10.1007/s11051-019-4556-8.

[46] L. Qi *et al.*, "Role of brush-like additives in CO_2 adsorbents for the enhancement of amine efficiency," *Journal of Environmental Chemical Engineering,* vol. 9, no. 6, 2021, doi: 10.1016/j.jece.2021.106709.

[47] L. Liu, J. Chen, L. Tao, H. Li, and Q. Yang, "Aminopolymer Confined in Ethane-Silica Nanotubes for CO_2 Capture from Ambient Air," *ChemNanoMat,* vol. 6, no. 7, pp. 1096-1103, 2020, doi: 10.1002/cnma.201900742.

[48] Y. Kong, X. Shen, M. Fan, M. Yang, and S. Cui, "Dynamic capture of low-concentration CO_2 on amine hybrid silsesquioxane aerogel," *Chemical Engineering Journal,* vol. 283, pp. 1059-1068, 2016, doi: 10.1016/j.cej.2015.08.034.

[49] G. Rim, T. G. Feric, T. Moore, and A. H. A. Park, "Solvent Impregnated Polymers Loaded with Liquid-Like Nanoparticle Organic Hybrid Materials for Enhanced Kinetics of Direct Air Capture and Point Source CO_2 Capture," *Advanced Functional Materials,* vol. 31, no. 21, 2021, doi: 10.1002/adfm.202010047.

[50] Y. Kong, G. Jiang, Y. Wu, S. Cui, and X. Shen, "Amine hybrid aerogel for high-efficiency CO_2 capture: Effect of amine loading and CO_2 concentration," *Chemical Engineering Journal,* vol. 306, pp. 362-368, 2016, doi: 10.1016/j.cej.2016.07.092.

[51] B. Ge *et al.*, "Innovative process integrating high temperature heat pump and direct air capture," *Applied Energy,* vol. 355, 2024, doi: 10.1016/j.apenergy.2023.122229.

[52] X. Zhu *et al.*, "Modified layered double hydroxides for efficient and reversible carbon dioxide capture from air," *Cell Reports Physical Science,* vol. 2, no. 7, 2021, doi: 10.1016/j.xcrp.2021.100484.

[53] S. Adegbite, "Particle Characterisation and Grinding Behaviour of Gamma-Alumina Slurries Prepared in a Stirred Media Mill," *Journal of Materials Science Research,* vol. 2, no. 1, 2012, doi: 10.5539/jmsr.v2n1p135.

[54] M. R. Karim, "Synthesis of γ-Alumina Particles and Surface Characterization," *The Open Colloid Science Journal,* vol. 4, no. 1, pp. 32-36, 2011, doi: 10.2174/1876530001104010032.

[55] T. Scientific. "Aluminum oxide, gamma-phase, catalyst support, high surface area." https://www.fishersci.com/store/msds?partNumber=AA43832A1&productDescription=ALUM+OXID+GAMA-PHASE+CATLS+1KG&vendorId=VN00024248&countryCode=US&language=en

(accessed 2022).

[56] "Aluminum Oxide." National Institute of Standards and Technology. https://webbook.nist.gov/cgi/cbook.cgi?ID=C1344281&Type=JANAFS&Plot=on (accessed 2022).

[57] M. Vasheghani *et al.*, "Effect of Al_2O_3 phases on the enhancement of thermal conductivity and viscosity of nanofluids in engine oil," *Heat and Mass Transfer,* vol. 47, no. 11, pp. 1401-1405, 2011/11/01 2011, doi: 10.1007/s00231-011-0806-8.

[58] J. Musil, J. Blažek, P. Zeman, Š. Prokšová, M. Šašek, and R. Čerstvý, "Thermal stability of alumina thin films containing γ-Al_2O_3 phase prepared by reactive magnetron sputtering," *Applied Surface Science,* vol. 257, no. 3, pp. 1058-1062, 2010/11/15/ 2010, doi: 10.1016/j.apsusc.2010.07.107.

[59] F. Kosaka *et al.*, "Enhanced Activity of Integrated CO_2 Capture and Reduction to CH_4 under Pressurized Conditions toward Atmospheric CO_2 Utilization," *ACS Sustainable Chemistry & Engineering,* vol. 9, no. 9, pp. 3452-3463, 2021, doi: 10.1021/acssuschemeng.0c07162.

[60] C. Jeong-Potter and R. Farrauto, "Feasibility Study of Combining Direct Air Capture of CO_2 and Methanation at Isothermal Conditions with Dual Function Materials," *Applied Catalysis B: Environmental,* vol. 282, 2021, doi: 10.1016/j.apcatb.2020.119416.

[61] C. Jeong-Potter, M. Abdallah, C. Sanderson, M. Goldman, R. Gupta, and R. Farrauto, "Dual function materials (Ru+Na_2O/Al_2O_3) for direct air capture of CO_2 and in situ catalytic methanation: The impact of realistic ambient conditions," *Applied Catalysis B: Environmental,* vol. 307, 2022, doi: 10.1016/j.apcatb.2021.120990.

[62] J. V. Veselovskaya, P. D. Parunin, O. V. Netskina, and A. G. Okunev, "A Novel Process for Renewable Methane Production: Combining Direct Air Capture by K_2CO_3/Alumina Sorbent with CO_2 Methanation over Ru/Alumina Catalyst," *Topics in Catalysis,* vol. 61, no. 15-17, pp. 1528-1536, 2018, doi: 10.1007/s11244-018-0997-z.

[63] M. E. Potter, K. M. Cho, J. J. Lee, and C. W. Jones, "Role of Alumina Basicity in CO_2 Uptake in 3-Aminopropylsilyl-Grafted Alumina Adsorbents," *ChemSusChem,* vol. 10, no. 10, pp. 2192-2201, May 22 2017, doi: 10.1002/cssc.201700115.

[64] B. Liu *et al.*, "Monolithic zirconia aerogel from polyacetylacetonatozirconium precursor and ammonia hydroxide gel initiator: formation mechanism, mechanical strength and thermal properties," *RSC Advances,* 10.1039/C8RA08263D vol. 8, no. 72, pp. 41603-41611, 2018, doi: 10.1039/C8RA08263D.

[65] J. V. Veselovskaya, V. S. Derevschikov, A. S. Shalygin, and D. A. Yatsenko, "K_2CO_3-containing composite sorbents based on a ZrO_2 aerogel for reversible CO_2 capture from ambient air," *Microporous and Mesoporous Materials,* vol. 310, 2021, doi: 10.1016/j.micromeso.2020.110624.

[66] M. Guo *et al.*, "A Highly Efficient and Stable Composite of Polyacrylate and Metal-Organic Framework Prepared by Interface Engineering for Direct Air Capture," *ACS Applied Materials & Interfaces,* vol. 13, no. 18, pp. 21775-21785, May 12 2021, doi: 10.1021/acsami.1c03661.

[67] P. M. Bhatt *et al.*, "A Fine-Tuned Fluorinated MOF Addresses the Needs for Trace CO_2 Removal and Air Capture Using Physisorption," *Journal of the American Chemical Society,* vol. 138, no. 29, pp. 9301-7, Jul 27 2016, doi: 10.1021/jacs.6b05345.

[68] A. Kumar, "Crystal engineering of hybrid ultramicroporous materials for study of direct air capture of carbon dioxide," PhD, University of Limerick, 2018.

[69] J. Warfsmann, B. Tokay, and N. R. Champness, "Thin film synthesis of hybrid ultramicroporous materials (HUMs)- a comparative approach," *Microporous and Mesoporous Materials,* vol. 311, p. 110686, 2021/02/01/ 2021, doi: 10.1016/j.micromeso.2020.110686.

[70] A. Kumar *et al.*, "Hybrid ultramicroporous materials (HUMs) with enhanced stability and trace carbon capture performance," *Chemical Communications,* vol. 53, no. 44, pp. 5946-5949, May 30 2017, doi: 10.1039/c7cc02289a.

[71] K.-J. Chen *et al.*, "Benchmark C_2H_2/CO_2 and CO_2/C_2H_2 Separation by Two Closely Related Hybrid Ultramicroporous Materials," *Chem,* vol. 1, no. 5, pp. 753-765, 2016/11/10/ 2016, doi: 10.1016/j.chempr.2016.10.009.

[72] K. J. Chen *et al.*, "Efficient CO_2 Removal for Ultra-Pure CO Production by Two Hybrid Ultramicroporous Materials," *Angewandte Chemie,* vol. 57, no. 13, pp. 3332-3336, Mar 19 2018, doi: 10.1002/anie.201706090.

[73] S. Mukherjee *et al.*, "Trace CO_2 capture by an ultramicroporous physisorbent with low water affinity," *Sci Adv,* vol. 5, no. 11, Nov 2019, doi: 10.1126/sciadv.aax9171.

[74] D. Yancy-Caballero *et al.*, "Process-level modelling and optimization to evaluate metal–organic frameworks for post-combustion capture of CO_2," *Molecular Systems Design & Engineering,* vol. 5, no. 7, pp. 1205-1218, 2020, doi: 10.1039/D0ME00060D.

[75] D. G. Madden *et al.*, "Metal-Organic Material Polymer Coatings for Enhanced Gas Sorption Performance and Hydrolytic Stability under Humid Conditions," *ACS Applied Materials & Interfaces,* vol. 12, no. 30, pp. 33759-33764, Jul 29 2020, doi: 10.1021/acsami.0c08078.

[76] J. M. Huck *et al.*, "Evaluating different classes of porous materials for carbon capture," *Energy & Environmental Science,* 10.1039/C4EE02636E vol. 7, no. 12, pp. 4132-4146, 2014, doi: 10.1039/C4EE02636E.

[77] O. Shekhah *et al.*, "Made-to-order metal-organic frameworks for trace carbon dioxide removal and air capture," *Nature Communications,* vol. 5, no. 1, p. 4228, 2014/06/25 2014, doi: 10.1038/ncomms5228.

[78] H.-G. Zhen, H. Mao, I. U. Haq, S.-H. Li, A. Ahmad, and Z.-P. Zhao, "In-situ SIFSIX-3-Cu growth into melamine formaldehyde sponge monolith for CO_2 efficient capture," *Separation and Purification Technology,* vol. 233, 2020, doi: 10.1016/j.seppur.2019.116042.

[79] Z. Zhang, Q. Ding, J. Cui, X. Cui, and H. Xing, "High and selective capture of low-concentration CO_2 with an anion-functionalized ultramicroporous metal-organic framework," *Science China Materials,* vol. 64, no. 3, pp. 691-697, 2020, doi: 10.1007/s40843-020-1471-0.

[80] Z. Zhang, Q. Ding, X. Cui, X.-M. Jiang, and H. Xing, "Fine-Tuning and Selective-Binding within an Anion-Functionalized Ultramicroporous Metal–Organic Framework for Efficient Olefin/Paraffin Separation," *ACS Applied Materials & Interfaces,* vol. 12, no. 36, pp. 40229-40235, 2020/09/09 2020, doi: 10.1021/acsami.0c07800.

[81] Z. Zhang *et al.*, "Mechano-assisted synthesis of an ultramicroporous metal-organic framework for trace CO_2 capture," *Chemical Communications,* vol. 56, no. 56, pp. 7726-7729, Jul 14 2020, doi: 10.1039/d0cc03196h.

[82] E. Hussein, "Numerical and experimental evaluation of advanced metal-organic framework materials for adsorption heat pumps," PhD, University of Birmingham, 2018.

[83] H. Thakkar, S. Eastman, Q. Al-Naddaf, A. A. Rownaghi, and F. Rezaei, "3D-Printed Metal-Organic Framework Monoliths for Gas Adsorption Processes," *ACS Applied Materials & Interfaces,* vol. 9, no. 41, pp. 35908-35916, Oct 18 2017, doi: 10.1021/acsami.7b11626.

[84] A. Ajenifuja, "Systematic Development of Adsorption Processes for the Separation of Close-boiling Gas Mixtures," PhD, University of Manchester, 2020.

[85] S. M. Moosavi *et al.*, "A data-science approach to predict the heat capacity of nanoporous materials," *Nature Materials,* vol. 21, no. 12, pp. 1419-1425, Dec 2022, doi: 10.1038/s41563-022-01374-3.

[86] P. Hu, H. Liu, H. Wang, J. Zhou, Y. Wang, and H. Ji, "Synergic morphology engineering and pore functionality within a metal–organic framework for trace CO_2 capture," *Journal of Materials Chemistry A,* vol. 10, no. 2, pp. 881-890, 2022, doi: 10.1039/d1ta09974d.

[87] W. Y. Hong, S. P. Perera, and A. D. Burrows, "Comparison of MIL-101(Cr) metal-organic framework and 13X zeolite monoliths for CO2 capture," *Microporous and Mesoporous Materials,* vol. 308, 2020, doi: 10.1016/j.micromeso.2020.110525.

[88] H. Oh, D. Lupu, G. Blanita, and M. Hirscher, "Experimental assessment of physical upper limit for hydrogen storage capacity at 20 K in densified MIL-101 monoliths," *RSC Advances,* 10.1039/C3RA46233A vol. 4, no. 6, pp. 2648-2651, 2014, doi: 10.1039/C3RA46233A.

[89] S. Liu, F. Xu, L.-T. Liu, Y.-L. Zhou, and W.-x. Zhao, "Heat capacities and thermodynamic properties of Cr-MIL-101," *Journal of Thermal Analysis and Calorimetry,* vol. 129, no. 1, pp. 509-514, 2017/07/01 2017, doi: 10.1007/s10973-017-6168-9.

[90] E. Elsayed *et al.*, "Development of MIL-101(Cr)/GrO composites for adsorption heat pump applications," *Microporous and Mesoporous Materials,* vol. 244, pp. 180-191, 2017/05/15/ 2017, doi: 10.1016/j.micromeso.2017.02.020.

[91] Q. Liu, L. Ning, S. Zheng, M. Tao, Y. Shi, and Y. He, "Adsorption of Carbon Dioxide by MIL-101(Cr): Regeneration Conditions and Influence of Flue Gas Contaminants," *Scientific Reports,* vol. 3, no. 1, p. 2916, 2013/10/10 2013, doi: 10.1038/srep02916.

[92] S. Lawson, C. Griffin, K. Rapp, A. A. Rownaghi, and F. Rezaei, "Amine-Functionalized MIL-101 Monoliths for CO_2 Removal from Enclosed Environments," *Energy & Fuels,* vol. 33, no. 3, pp. 2399-2407, 2019, doi: 10.1021/acs.energyfuels.8b04508.

[93] L. A. Darunte, A. D. Oetomo, K. S. Walton, D. S. Sholl, and C. W. Jones, "Direct Air Capture of CO_2 Using Amine Functionalized MIL-101(Cr)," *ACS Sustainable Chemistry & Engineering,* vol. 4, no. 10, pp. 5761-5768, 2016, doi: 10.1021/acssuschemeng.6b01692.

[94] A. Sinha, L. A. Darunte, C. W. Jones, M. J. Realff, and Y. Kawajiri, "Systems Design and Economic Analysis of Direct Air Capture of CO_2 through Temperature Vacuum Swing Adsorption Using MIL-101(Cr)-PEI-800 and mmen-Mg_2(dobpdc) MOF Adsorbents," *Industrial & Engineering Chemistry Research,* vol. 56, no. 3, pp. 750-764, 2017, doi: 10.1021/acs.iecr.6b03887.

[95] P. Guo, "Water Interaction with Microporous Coordination Polymers: Energy Efficient Dehumidification, Antimatter Probing and Polymer Coating," PhD, University of Michigan, 2015.

[96] L. Ma, L. Xu, H. Jiang, and X. Yuan, "Comparative research on three types of MIL-101(Cr)-SO_3H for esterification of cyclohexene with formic acid," *RSC Advances,* 10.1039/C8RA10366F vol. 9, no. 10, pp. 5692-5700, 2019, doi: 10.1039/C8RA10366F.

[97] H. Li, K. Wang, D. Feng, Y. P. Chen, W. Verdegaal, and H. C. Zhou, "Incorporation of Alkylamine into Metal-Organic Frameworks through a Bronsted Acid-Base Reaction for CO_2 Capture," *ChemSusChem,* vol. 9, no. 19, pp. 2832-2840, Oct 6 2016, doi: 10.1002/cssc.201600768.

[98] C. E. Bien *et al.*, "Bioinspired Metal-Organic Framework for Trace CO_2 Capture," *Journal of the American Chemical Society,* vol. 140, no. 40, pp. 12662-12666, Oct 10 2018, doi: 10.1021/jacs.8b06109.

[99] C. E. Bien, Q. Liu, and C. R. Wade, "Assessing the Role of Metal Identity on CO_2 Adsorption in MOFs Containing M–OH Functional Groups," *Chemistry of Materials,* vol. 32, no. 1, pp. 489-497, 2019, doi: 10.1021/acs.chemmater.9b04228.

[100] Z. Cai, C. E. Bien, Q. Liu, and C. R. Wade, "Insights into CO_2 Adsorption in M–OH Functionalized MOFs," *Chemistry of Materials,* vol. 32, no. 10, pp. 4257-4264, 2020, doi: 10.1021/acs.chemmater.0c00746.

[101] T. M. McDonald, W. R. Lee, J. A. Mason, B. M. Wiers, C. S. Hong, and J. R. Long, "Capture of Carbon Dioxide from Air and Flue Gas in the Alkylamine-Appended Metal–Organic Framework mmen-Mg_2(dobpdc)," *Journal of the American Chemical Society,* vol. 134, no. 16, pp. 7056-7065, 2012/04/25 2012, doi: 10.1021/ja300034j.

[102] P. J. Milner *et al.*, "A Diaminopropane-Appended Metal-Organic Framework Enabling Efficient CO_2 Capture from Coal Flue Gas via a Mixed Adsorption Mechanism," *Journal of the American Chemical Society,* vol. 139, no. 38, pp. 13541-13553, Sep 27 2017, doi: 10.1021/jacs.7b07612.

[103] Y. H. Lee *et al.*, "Controlled Synthesis of Metal-Organic Frameworks in Scalable Open-Porous Contactor for Maximizing Carbon Capture Efficiency," *JACS Au,* vol. 1, no. 8, pp. 1198-1207, Aug 23 2021, doi: 10.1021/jacsau.1c00068.

[104] L. A. Darunte *et al.*, "Moving Beyond Adsorption Capacity in Design of Adsorbents for CO_2 Capture from Ultradilute Feeds: Kinetics of CO_2 Adsorption in Materials with Stepped Isotherms," *Industrial & Engineering Chemistry Research,* vol. 58, no. 1, pp. 366-377, 2018, doi: 10.1021/acs.iecr.8b05042.

[105] E. J. Kim *et al.*, "Cooperative carbon capture and steam regeneration with tetraamine-appended metal-organic frameworks," *Science,* vol. 369, no. 6502, pp. 392-396, Jul 24 2020, doi: 10.1126/science.abb3976.

[106] W. R. Lee *et al.*, "Diamine-Functionalization of a Metal-Organic Framework Adsorbent for Superb Carbon Dioxide Adsorption and Desorption Properties," *ChemSusChem,* vol. 11, no. 10, pp. 1694-1707, May 25 2018, doi: 10.1002/cssc.201800363.

[107] R. L. Siegelman *et al.*, "Water Enables Efficient CO_2 Capture from Natural Gas Flue Emissions in an Oxidation-Resistant Diamine-Appended Metal-Organic Framework," *Journal of the American Chemical Society,* vol. 141, no. 33, pp. 13171-13186, Aug 21 2019, doi: 10.1021/jacs.9b05567.

[108] Y. Seok Chae *et al.*, "Moisture-tolerant diamine-appended metal–organic framework composites for effective indoor CO_2 capture through facile spray coating," *Chemical Engineering Journal,* vol. 433, 2022, doi: 10.1016/j.cej.2021.133856.

[109] S. R. Caskey, A. G. Wong-Foy, and A. J. Matzger, "Dramatic Tuning of Carbon Dioxide Uptake via Metal Substitution in a Coordination Polymer with Cylindrical Pores," *Journal of the American Chemical Society,* vol. 130, no. 33, pp. 10870-10871, 2008/08/01 2008, doi: 10.1021/ja8036096.

[110] J. A. Mason, K. Sumida, Z. R. Herm, R. Krishna, and J. R. Long, "Evaluating metal–organic frameworks for post-combustion carbon dioxide capture via temperature swing adsorption," *Energy & Environmental Science,* 10.1039/C1EE01720A vol. 4, no. 8, pp. 3030-3040, 2011, doi: 10.1039/C1EE01720A.

[111] S. Pu *et al.*, "Performance Comparison of Metal–Organic Framework Extrudates and Commercial Zeolite for Ethylene/Ethane Separation," *Industrial & Engineering Chemistry Research,* vol. 57, no. 5, pp. 1645-1654, 2018/02/07 2018, doi: 10.1021/acs.iecr.7b04391.

[112] P. Q. Liao *et al.*, "Putting an ultrahigh concentration of amine groups into a metal-organic framework for CO_2 capture at low pressures," *Chemical Science,* vol. 7, no. 10, pp. 6528-6533, Oct 19 2016, doi: 10.1039/c6sc00836d.

[113] H. W. Kua, C. Pedapati, R. V. Lee, and S. Kawi, "Effect of indoor contamination on carbon dioxide adsorption of wood-based biochar – Lessons for direct air capture," *Journal of Cleaner Production,* vol. 210, pp. 860-871, 2019, doi: 10.1016/j.jclepro.2018.10.206.

[114] M. G. Plaza, F. Rubiera, and C. Pevida, "Evaluating the Feasibility of a TSA Process Based on Steam Stripping in Combination with Structured Carbon Adsorbents To Capture CO_2 from a Coal Power Plant," *Energy & Fuels,* vol. 31, no. 9, pp. 9760-9775, 2017/09/21 2017, doi: 10.1021/acs.energyfuels.7b01508.

[115] R. Rodriguez-Mosqueda, E. A. Bramer, T. Roestenberg, and G. Brem, "Parametrical Study on CO_2 Capture from Ambient Air Using Hydrated K_2CO_3 Supported on an Activated Carbon Honeycomb," *Industrial & Engineering Chemistry Research* vol. 57, no. 10, pp. 3628-3638, Mar 14 2018, doi: 10.1021/acs.iecr.8b00566.

[116] R. Rodríguez-Mosqueda, J. Rutgers, E. A. Bramer, and G. Brem, "Low temperature water vapor pressure swing for the regeneration of adsorbents for CO_2 enrichment in greenhouses via direct air capture," *Journal of CO_2 Utilization,* vol. 29, pp. 65-73, 2019, doi: 10.1016/j.jcou.2018.11.010.

[117] CABOT. "PBXÒ 51 Carbon Black." https://www.cabotcorp.com/-/media/files/msds/cb/bnh/en/pbx51-bnh-en.pdf?la=en&rev=b7d5dbc3cbab4ad08b6d7118188b4fc5 (accessed 2022).

[118] A. R. Cuesta and C. Song, "pH swing adsorption process for ambient carbon dioxide capture using activated carbon black adsorbents and immobilized carbonic anhydrase biocatalysts," *Applied Energy,* vol. 280, 2020, doi: 10.1016/j.apenergy.2020.116003.

[119] V. R. Choudhary and A. P. Singh, "Sorption capacity and diffusion of pure liquids in ZSM-5 type zeolites," *Zeolites,* vol. 6, no. 3, pp. 206-208, 1986/05/01/ 1986, doi: 10.1016/0144-2449(86)90049-7.

[120] S. H. Madani, I. H. Arellano, J. P. Mata, and P. Pendleton, "Particle and cluster analyses of silica powders via small angle neutron scattering," *Powder Technology,* vol. 327, pp. 96-108, 2018/03/01/ 2018, doi: 10.1016/j.powtec.2017.12.061.

[121] A. Masala *et al.*, "Conductive ZSM-5-Based Adsorbent for CO_2 Capture: Active Phase vs Monolith," *Industrial & Engineering Chemistry Research,* vol. 56, no. 30, pp. 8485-8498, 2017/08/02 2017, doi: 10.1021/acs.iecr.7b01058.

[122] Y. Jiao, X. Fan, M. Perdjon, Z. Yang, and J. Zhang, "Vapor-phase transport (VPT) modification of ZSM-5/SiC foam catalyst using TPAOH vapor to improve the methanol-to-propylene (MTP) reaction," *Applied Catalysis A: General,* vol. 545, pp. 104-112, 2017/09/05/ 2017, doi: 10.1016/j.apcata.2017.07.036.

[123] M. Pérez-Page *et al.*, "Gas adsorption properties of ZSM-5 zeolites heated to extreme temperatures," *Ceramics International,* vol. 42, no. 14, pp. 15423-15431, 2016/11/01/ 2016, doi: 10.1016/j.ceramint.2016.06.193.

[124] H. Thakkar, A. Issa, A. A. Rownaghi, and F. Rezaei, "CO_2 Capture from Air Using Amine-Functionalized Kaolin-Based Zeolites," *Chemical Engineering & Technology,* vol. 40, no. 11, pp. 1999-2007, 2017, doi: doi.org/10.1002/ceat.201700188.

[125] "ZSM-5 Catalyst." ACS Material. https://www.acsmaterial.com/zsm-5-catalyst.html (accessed 2022).

[126] X. Yuan, H. Li, M. Ye, and Z. Liu, "Kinetic modeling of methanol to olefins process over SAPO-34 catalyst based on the dual-cycle reaction mechanism," *AIChE Journal,* vol. 65, no. 2, pp. 662-674, 2019, doi: 10.1002/aic.16439.

[127] S. Mahzoon, S. Fatemi, and S. J. Hashemi, "Modeling Based Investigation of Ultrafine SAPO-34 Core-shell Adsorbent in Cyclic Adsorption Process for Purification of Natural Gas from CO_2," *International Journal of Theoretical and Applied Nanotechnology,* 2012, doi: 10.11159/ijtan.2012.014.

[128] L. Calabrese, S. De Antonellis, S. Vasta, V. Brancato, and A. Freni, "Modified Silicone-SAPO34 Composite Materials for Adsorption Thermal Energy Storage Systems," *Applied Sciences,* vol. 10, no. 23, p. 8715, 2020. [Online]. Available: 10.3390/app10238715.

[129] C. Kim, H. S. Cho, S. Chang, S. J. Cho, and M. Choi, "An ethylenediamine-grafted Y zeolite: a highly regenerable carbon dioxide adsorbent via temperature swing adsorption without urea formation," *Energy & Environmental Science,* vol. 9, no. 5, pp. 1803-1811, 2016, doi: 10.1039/c6ee00601a.

[130] Q. H. Dirar and K. F. Loughlin, "Intrinsic adsorption properties of CO_2 on 5A and 13X zeolite," *Adsorption,* vol. 19, no. 6, pp. 1149-1163, 2013/12/01 2013, doi: 10.1007/s10450-013-9543-2.

[131] H. Ahn, S.-H. Hong, Y. Zhang, and C.-H. Lee, "Experimental and Simulation Study on CO_2 Adsorption Dynamics of a Zeolite 13X Column during Blowdown and Pressurization: Implications of Scaleup on CO_2 Capture Vacuum Swing Adsorption Cycle," *Industrial & Engineering Chemistry Research,* vol. 59, no. 13, pp. 6053-6064, 2020/04/01 2020, doi: 10.1021/acs.iecr.9b05862.

[132] K. C. Chan, C. Y. H. Chao, and C. L. Wu, "Measurement of properties and performance prediction of the new MWCNT-embedded zeolite 13X/$CaCl_2$ composite adsorbents," *International Journal of Heat and Mass Transfer,* vol. 89, pp. 308-319, 2015/10/01/ 2015, doi: 10.1016/j.ijheatmasstransfer.2015.05.063.

[133] C. Y. Chuah, W. Li, Y. Yang, and T.-H. Bae, "Evaluation of porous adsorbents for CO_2 capture under humid conditions: The importance of recyclability," *Chemical Engineering Journal Advances,* vol. 3, p. 100021, 2020/11/15/ 2020, doi: 10.1016/j.ceja.2020.100021.

[134] H. Thakkar, S. Eastman, A. Hajari, A. A. Rownaghi, J. C. Knox, and F. Rezaei, "3D-Printed Zeolite Monoliths for CO_2 Removal from Enclosed Environments," *ACS Applied Materials & Interfaces,* vol. 8, no. 41, pp. 27753-27761, 2016/10/19 2016, doi: 10.1021/acsami.6b09647.

[135] H. Ahn, J.-H. Moon, S.-H. Hyun, and C.-H. Lee, "Diffusion Mechanism of Carbon Dioxide in Zeolite 4A and CaX Pellets," *Adsorption,* vol. 10, no. 2, pp. 111-128, 2004/06/01 2004, doi: 10.1023/B:ADSO.0000039867.14756.ac.

[136] C. Bestfather, "Upgrading landfill gas to natural gas quality: Bulk separation by pressure swing adsorption," M.A.Sc., University of Ottawa, 2009.

[137] S. M. W. Wilson and F. H. Tezel, "Direct Dry Air Capture of CO_2 Using VTSA with Faujasite Zeolites," *Industrial & Engineering Chemistry Research,* vol. 59, no. 18, pp. 8783-8794, 2020, doi: 10.1021/acs.iecr.9b04803.

[138] A. Chemical. "5A Molecular Sieves." https://www.antenchem.com/en/products/5a_molecular_sieve_powder.html (accessed 2022).

[139] J. C. Knox, A. D. Ebner, M. D. LeVan, R. F. Coker, and J. A. Ritter, "Limitations of Breakthrough Curve Analysis in Fixed-Bed Adsorption," *Industrial & Engineering Chemistry Research,* vol. 55, no. 16, pp. 4734-4748, 2016/04/27 2016, doi: 10.1021/acs.iecr.6b00516.

[140] M. Mofarahi and S. M. Salehi, "Pure and binary adsorption isotherms of ethylene and ethane on zeolite 5A," *Adsorption,* vol. 19, no. 1, pp. 101-110, 2013/02/01 2013, doi: 10.1007/s10450-012-9423-1.

[141] U. R. Fischer, "Thermal Conductivity and Melting Point Measurements on Paraffin Zeolite Mixtures," presented at the Seventeenth European Conference on Thermophysical Propertie, 2006.

[142] A. Oda *et al.*, "Unprecedented CO_2 adsorption behaviour by 5A-type zeolite discovered in lower pressure region and at 300 K," *Journal of Materials Chemistry A,* vol. 9, no. 12, pp. 7531-7545, 2021, doi: 10.1039/d0ta09944a.

[143] A. Itadani *et al.*, "Material Exhibiting Efficient CO_2 Adsorption at Room Temperature for Concentrations Lower Than 1000 ppm: Elucidation of the State of Barium Ion Exchanged in an MFI-Type Zeolite," *ACS Applied Materials & Interfaces,* vol. 8, no. 13, pp. 8821-33, Apr 6 2016, doi: 10.1021/acsami.6b00909.

[144] M. J. Bos, T. Kreuger, S. R. A. Kersten, and D. W. F. Brilman, "Study on transport phenomena and intrinsic kinetics for CO_2 adsorption in solid amine sorbent," *Chemical Engineering Journal,* vol. 377, p. 120374, 2019/12/01/ 2019, doi: 10.1016/j.cej.2018.11.072.

[145] Q. Yu, J. d. l. P. Delgado, R. Veneman, and D. W. F. Brilman, "Stability of a Benzyl Amine Based CO_2 Capture Adsorbent in View of Regeneration Strategies," *Industrial & Engineering Chemistry Research,* vol. 56, no. 12, pp. 3259-3269, 2017/03/29 2017, doi: 10.1021/acs.iecr.6b04645.

[146] E. Sonnleitner, G. Schöny, and H. Hofbauer, "Assessment of zeolite 13X and Lewatit® VP OC 1065 for application in a continuous temperature swing adsorption process for biogas upgrading," *Biomass Conversion and Biorefinery,* vol. 8, no. 2, pp. 379-395, 2018/06/01 2018, doi: 10.1007/s13399-017-0293-3.

[147] J. Young, E. García-Díez, S. Garcia, and M. van der Spek, "The impact of binary water–CO_2 isotherm models on the optimal performance of sorbent-based direct air capture processes," *Energy & Environmental Science,* vol. 14, no. 10, pp. 5377-5394, 2021, doi: 10.1039/D1EE01272J.

[148] Purolite. "Purolite A109." https://www.purolite.com/product/a109 (accessed 2022).

[149] M. Parvazinia, S. Garcia, and M. Maroto-Valer, "CO_2 capture by ion exchange resins as amine functionalised adsorbents," *Chemical Engineering Journal,* vol. 331, pp. 335-342, 2018, doi: 10.1016/j.cej.2017.08.087.

[150] Lenntech. "Purolite A500." https://www.lenntech.com/Data-sheets/Purolite-A500-L.pdf (accessed 2022).

[151] M. Armstrong, X. Shi, B. Shan, K. Lackner, and B. Mu, "Rapid CO_2 capture from ambient air by sorbent-containing porous electrospun fibers made with the solvothermal polymer additive removal technique," *AIChE Journal,* vol. 65, no. 1, pp. 214-220, 2018, doi: 10.1002/aic.16418.

[152] Lenntech. "AMBERLITE® XAD4 " https://www.lenntech.com/Data-sheets/Amberlite-XAD4-L.pdf (accessed 2022).

[153] R. IHAAS. "Amberlite XAD16." http://file.yizimg.com/140240/2006926132310250301258.pdf (accessed 2022).

[154] Dupont. "AmberLite™ XAD™1180N Polymeric Adsorbent." https://www.lenntech.com/Data-sheets/DuPont-Amberlite-XAD-1180N-Polymeric-Adsorbent-L.pdf (accessed 2022).

[155] Sigma-Aldrich. "AMBERLITE XAD POLYMERIC RESINS." https://www.sigmaaldrich.com/deepweb/assets/sigmaaldrich/product/documents/287/103/xad4pis.pdf (accessed 2022).

[156] T. Wang, X. Wang, C. Hou, and J. Liu, "Quaternary functionalized mesoporous adsorbents for ultra-high kinetics of CO_2 capture from air," *Scientific Reports,* vol. 10, no. 1, p. 21429, Dec 8 2020, doi: 10.1038/s41598-020-77477-1.

[157] FROTEC. "Ion Exchange Resin D201 Macroporous Adsorption Styrene Series Strong Base Anion Exchange Resin." http://www.frotecfilter.com/info/?105.html (accessed 2022).

[158] J. Song, L. Zhu, X. Shi, Y. Liu, H. Xiao, and X. Chen, "Moisture Swing Ion-Exchange Resin-PO_4 Sorbent for Reversible CO_2 Capture from Ambient Air," *Energy & Fuels,* vol. 33, no. 7, pp. 6562-6567, 2019, doi: 10.1021/acs.energyfuels.9b00863.

[159] W. Si *et al.*, "Kinetics and mechanism of low-concentration CO_2 adsorption on solid amine in a humid confined space," *The Canadian Journal of Chemical Engineering,* vol. 97, no. 3, pp. 697-701, 2019, doi: 10.1002/cjce.23257.

[160] W. Wang, F. Liu, Q. zhang, G. Yu, and S. Deng, "Efficient removal of CO_2 from indoor air using a polyethyleneimine-impregnated resin and its low-temperature regeneration," *Chemical Engineering Journal,* vol. 399, 2020, doi: 10.1016/j.cej.2020.125734.

[161] J. Elfving, C. Bajamundi, J. Kauppinen, and T. Sainio, "Modelling of equilibrium working capacity of PSA, TSA and TVSA processes for CO_2 adsorption under direct air capture conditions," *Journal of CO_2 Utilization,* vol. 22, pp. 270-277, 2017/12/01/ 2017, doi: 10.1016/j.jcou.2017.10.010.

[162] J. Elfving and T. Sainio, "Kinetic approach to modelling CO_2 adsorption from humid air using amine-functionalized resin: Equilibrium isotherms and column dynamics," *Chemical Engineering Science,* vol. 246, 2021, doi: 10.1016/j.ces.2021.116885.

[163] C. Hou *et al.*, "Porosity and hydrophilicity modulated quaternary ammonium-based sorbents for CO_2 capture," *Chemical Engineering Journal,* vol. 413, 2021, doi: 10.1016/j.cej.2020.127532.

[164] C. Gebald, J. A. Wurzbacher, P. Tingaut, T. Zimmermann, and A. Steinfeld, "Amine-based nanofibrillated cellulose as adsorbent for CO_2 capture from air," *Environ Sci Technol,* vol. 45, no. 20, pp. 9101-8, Oct 15 2011, doi: 10.1021/es202223p.

[165] B. M. Balasubramaniam, P.-T. Thierry, S. Lethier, V. Pugnet, P. Llewellyn, and A. Rajendran, "Process-performance of solid sorbents for Direct Air Capture (DAC) of CO_2 in optimized temperature-vacuum swing adsorption (TVSA) cycles," *Chemical Engineering Journal,* vol. 485, 2024, doi: 10.1016/j.cej.2024.149568.

[166] J. A. Wurzbacher, C. Gebald, S. Brunner, and A. Steinfeld, "Heat and mass transfer of temperature–vacuum swing desorption for CO_2 capture from air," *Chemical Engineering Journal,* vol. 283, pp. 1329-1338, 2016/01/01/ 2016, doi: 10.1016/j.cej.2015.08.035.

[167] Y. C. Ng, L. Yang, and Z. R. Jovanovic, "The Development and Validation of a Closed-Loop Experimental Setup for Investigating CO_2 and H_2O Coadsorption Kinetics under Conditions Relevant to Direct Air Capture," *Industrial & Engineering Chemistry Research,* vol. 57, no. 42, pp. 13987-13998, 2018, doi: 10.1021/acs.iecr.8b01508.

[168] C. Hou, Y. Wu, T. Wang, X. Wang, and X. Gao, "Preparation of Quaternized Bamboo Cellulose and Its Implication in Direct Air Capture of CO_2," *Energy & Fuels,* vol. 33, no. 3, pp. 1745-1752, 2018, doi: 10.1021/acs.energyfuels.8b02821.

[169] A. Dourani, M. Haghgoo, and M. Hamadanian, "Multi-walled carbon nanotube and carbon nanofiber/ polyacrylonitrile aerogel scaffolds for enhanced epoxy resins," *Composites Part B: Engineering,* vol. 176, p. 107299, 2019/11/01/ 2019, doi: 10.1016/j.compositesb.2019.107299.

[170] J. Zhang, X. Zheng, Y. Cao, Z. Wang, S. Kawi, and X. Tan, "Tetraethylenepentamine-grafted polyacrylonitrile-poly(methyl methacrylate) hollow fibers for low concentration CO_2 capture at ambient temperature," *Process Safety and Environmental Protection,* vol. 157, pp. 390-396, 2022, doi: 10.1016/j.psep.2021.11.027.

[171] J. Hofele, G. Link, and J. Jelonnek, "Reaction Kinetics and Process Model of the Polyacrylonitrile Fibers Stabilization Process Based on Dielectric Measurements," *Materials (Basel),* vol. 15, no. 3, Feb 6 2022, doi: 10.3390/ma15031222.

[172] X. Xu, M. B. Myers, F. G. Versteeg, B. Pejcic, C. Heath, and C. D. Wood, "Direct air capture (DAC) of CO_2 using polyethylenimine (PEI) "snow": a scalable strategy," *Chemical Communications,* vol. 56, no. 52, pp. 7151-7154, Jul 4 2020, doi: 10.1039/d0cc02572k.

[173] R. Ojeda-López, A. Domínguez-Ortiz, C. Felipe, A. Cervantes-Uribe, I. J. Pérez-Hermosillo, and J. M. Esparza-Schulz, "Isosteric Enthalpy Behavior of CO_2 Adsorption on Micro-Mesoporous Materials: Carbon Microfibers (CMFs), SBA-15, and Amine-Functionalized SBA-15," *Journal of Composites Science,* vol. 5, no. 4, p. 102, 2021, doi: 10.3390/jcs5040102.

[174] A. Centineo, H. G. T. Nguyen, L. Espinal, J. C. Horn, and S. Brandani, "An experimental and modelling study of water vapour adsorption on SBA-15," *Microporous and Mesoporous Materials,* vol. 282, pp. 53-72, 2019/07/01/ 2019, doi: 10.1016/j.micromeso.2019.03.018.

[175] E. S. Sanz-Pérez, M. Olivares-Marín, A. Arencibia, R. Sanz, G. Calleja, and M. M. Maroto-Valer, "CO_2 adsorption performance of amino-functionalized SBA-15 under post-combustion conditions," *International Journal of Greenhouse Gas Control,* vol. 17, pp. 366-375, 2013/09/01/ 2013, doi: 10.1016/j.ijggc.2013.05.011.

[176] Q. Tang, W. Jiang, and G. Hu, "Effect of amine structure on CO_2 capture performance of amine-modified SBA-15," *Chemical Research in Chinese Universities,* vol. 33, no. 4, pp. 666-671, 2017/08/01 2017, doi: 10.1007/s40242-017-6340-6.

[177] D. Li *et al.*, "Experiment and simulation for separating CO_2/N_2 by dual-reflux pressure swing adsorption process," *Chemical Engineering Journal,* vol. 297, pp. 315-324, 2016/08/01/ 2016, doi: 10.1016/j.cej.2016.03.075.

[178] Y. Wang and M. D. LeVan, "Adsorption Equilibrium of Carbon Dioxide and Water Vapor on Zeolites 5A and 13X and Silica Gel: Pure Components," *Journal of Chemical & Engineering Data,* vol. 54, no. 10, pp. 2839-2844, 2009/10/08 2009, doi: 10.1021/je800900a.

[179] E. C. Markham and A. F. Benton, "The adsorption of gas mixtures by silica," *Journal of the American Chemical Society,* vol. 53, no. 2, pp. 497-507, 1931/02/01 1931, doi: 10.1021/ja01353a013.

[180] Y. Lin and J. Horita, "An experimental study on isotope fractionation in a mesoporous silica-water system with implications for vadose-zone hydrology," *Geochimica et Cosmochimica Acta,* vol. 184, pp. 257-271, 2016/07/01/ 2016, doi: 10.1016/j.gca.2016.04.029.

[181] W. Jung, J. Park, and K. S. Lee, "Kinetic modeling of CO_2 adsorption on an amine-functionalized solid sorbent," *Chemical Engineering Science,* vol. 177, pp. 122-131, 2018/02/23/ 2018, doi: 10.1016/j.ces.2017.11.003.

[182] W. Choi *et al.*, "Epoxide-functionalization of polyethyleneimine for synthesis of stable carbon dioxide adsorbent in temperature swing adsorption," *Nature Communications,* vol. 7, no. 1, p. 12640, 2016/08/30 2016, doi: 10.1038/ncomms12640.

[183] S. U. Rege, R. T. Yang, K. Qian, and M. A. Buzanowski, "Air-prepurification by pressure swing adsorption using single/layered beds," *Chemical Engineering Science,* vol. 56, no. 8, pp. 2745-2759, 2001/04/01/ 2001, doi: 10.1016/S0009-2509(00)00531-5.

[184] M. P. Rosynek, "Isotherms and energetics of carbon dioxide adsorption on .gamma.-alumina at 100-300.deg," *The Journal of Physical Chemistry,* vol. 79, no. 13, pp. 1280-1284, 1975/06/01 1975, doi: 10.1021/j100580a011.

[185] A. G. Okunev, V. E. Sharonov, Y. I. Aristov, and V. N. Parmon, "Sorption of Carbon Dioxide from Wet Gases by K_2CO_3-in-Porous Matrix: Influence of the Matrix Nature," *Reaction Kinetics and Catalysis Letters,* vol. 71, no. 2, pp. 355-362, 2000/11/01 2000, doi: 10.1023/A:1010395630719.

[186] O. Shekhah, Y. Belmabkhout, K. Adil, P. M. Bhatt, A. J. Cairns, and M. Eddaoudi, "A facile solvent-free synthesis route for the assembly of a highly CO_2 selective and H_2S tolerant NiSIFSIX metal–organic framework," *Chemical Communications,* 10.1039/C5CC04487A vol. 51, no. 71, pp. 13595-13598, 2015, doi: 10.1039/C5CC04487A.

[187] D. G. Madden *et al.*, "Flue-gas and direct-air capture of CO_2 by porous metal-organic materials," *Philosophical Transactions of the Royal Society A: Mathematical, Physical and Engineering Sciences,* vol. 375, no. 2084, p. 20160025, 2017, doi: doi:10.1098/rsta.2016.0025.

[188] A. Das, P. D. Southon, M. Zhao, C. J. Kepert, A. T. Harris, and D. M. D'Alessandro, "Carbon dioxide adsorption by physisorption and chemisorption interactions in piperazine-grafted Ni_2(dobdc) (dobdc = 1,4-dioxido-2,5-benzenedicarboxylate)," *Dalton Transactions,* vol. 41, no. 38, pp. 11739-11744, 2012, doi: 10.1039/C2DT31112G.

[189] S. Dasgupta *et al.*, "Adsorption properties and performance of CPO-27-Ni/alginate spheres during multicycle pressure-vacuum-swing adsorption (PVSA) CO_2 capture in the presence of moisture," *Chemical Engineering Science,* vol. 137, pp. 525-531, 2015/12/01/ 2015, doi: 10.1016/j.ces.2015.06.064.

[190] J. Liu, A. I. Benin, A. M. B. Furtado, P. Jakubczak, R. R. Willis, and M. D. LeVan, "Stability Effects on CO_2 Adsorption for the DOBDC Series of Metal–Organic Frameworks," *Langmuir,* vol. 27, no. 18, pp. 11451-11456, 2011/09/20 2011, doi: 10.1021/la201774x.

[191] A. Masala *et al.*, "CO_2 Capture in Dry and Wet Conditions in UTSA-16 Metal–Organic Framework," *ACS Applied Materials & Interfaces,* vol. 9, no. 1, pp. 455-463, 2017/01/11 2017, doi: 10.1021/acsami.6b13216.

[192] W. L. Queen *et al.*, "Comprehensive study of carbon dioxide adsorption in the metal–organic frameworks M_2(dobdc) (M = Mg, Mn, Fe, Co, Ni, Cu, Zn)," *Chemical Science,* 10.1039/C4SC02064B vol. 5, no. 12, pp. 4569-4581, 2014, doi: 10.1039/C4SC02064B.

[193] M.-B. Kim, S.-J. Lee, C. Y. Lee, and Y.-S. Bae, "High SF_6 selectivities and capacities in isostructural metal-organic frameworks with proper pore sizes and highly dense unsaturated metal sites," *Microporous and Mesoporous Materials,* vol. 190, pp. 356-361, 2014/05/15/ 2014, doi: 10.1016/j.micromeso.2014.02.028.

[194] A. C. Kizzie, A. G. Wong-Foy, and A. J. Matzger, "Effect of Humidity on the Performance of Microporous Coordination Polymers as Adsorbents for CO_2 Capture," *Langmuir,* vol. 27, no. 10, pp. 6368-6373, 2011/05/17 2011, doi: 10.1021/la200547k.

[195] H.-Y. Cho, D.-A. Yang, J. Kim, S.-Y. Jeong, and W.-S. Ahn, "CO_2 adsorption and catalytic application of Co-MOF-74 synthesized by microwave heating," *Catalysis Today,* vol. 185, no. 1, pp. 35-40, 2012/05/20/ 2012, doi: 10.1016/j.cattod.2011.08.019.

[196] X. Wang, H. Li, and X.-J. Hou, "Amine-Functionalized Metal Organic Framework as a Highly Selective Adsorbent for CO_2 over CO," *The Journal of Physical Chemistry C,* vol. 116, no. 37, pp. 19814-19821, 2012/09/20 2012, doi: 10.1021/jp3052938.

[197] K. Munusamy, G. Sethia, D. V. Patil, P. B. Somayajulu Rallapalli, R. S. Somani, and H. C. Bajaj, "Sorption of carbon dioxide, methane, nitrogen and carbon monoxide on MIL-101(Cr): Volumetric measurements and dynamic adsorption studies," *Chemical Engineering Journal,* vol. 195-196, pp. 359-368, 2012/07/01/ 2012, doi: 10.1016/j.cej.2012.04.071.

[198] J. Ehrenmann, S. K. Henninger, and C. Janiak, "Water Adsorption Characteristics of MIL-101 for Heat-Transformation Applications of MOFs," *European Journal of Inorganic Chemistry,* vol. 2011, no. 4, pp. 471-474, 2011, doi: 10.1002/ejic.201001156.

[199] S. Mutyala, M. Jonnalagadda, H. Mitta, and R. Gundeboyina, "CO_2 capture and adsorption kinetic study of amine-modified MIL-101 (Cr)," *Chemical Engineering Research and Design,* vol. 143, pp. 241-248, 2019/03/01/ 2019, doi: 10.1016/j.cherd.2019.01.020.

[200] Y. Xie, Z. Fang, L. Li, H. Yang, and T.-F. Liu, "Creating Chemisorption Sites for Enhanced CO_2 Photoreduction Activity through Alkylamine Modification of MIL-101-Cr," *ACS Applied Materials & Interfaces,* vol. 11, no. 30, pp. 27017-27023, 2019/07/31 2019, doi: 10.1021/acsami.9b09436.

[201] G. Akiyama, R. Matsuda, H. Sato, A. Hori, M. Takata, and S. Kitagawa, "Effect of functional groups in MIL-101 on water sorption behavior," *Microporous and Mesoporous Materials,* vol. 157, pp. 89-93, 2012/07/15/ 2012, doi: 10.1016/j.micromeso.2012.01.015.

[202] J. G. Vitillo and S. Bordiga, "Increasing the stability of Mg_2(dobpdc) metal–organic framework in air through solvent removal," *Materials Chemistry Frontiers,* 10.1039/C6QM00220J vol. 1, no. 3, pp. 444-448, 2017, doi: 10.1039/C6QM00220J.

[203] J. D. Martell, P. J. Milner, R. L. Siegelman, and J. R. Long, "Kinetics of cooperative CO_2 adsorption in diamine-appended variants of the metal–organic framework Mg_2(dobpdc)," *Chemical Science,* 10.1039/D0SC01087A vol. 11, no. 25, pp. 6457-6471, 2020, doi: 10.1039/D0SC01087A.

[204] T. M. McDonald *et al.*, "Cooperative insertion of CO_2 in diamine-appended metal-organic frameworks," *Nature,* vol. 519, no. 7543, pp. 303-308, 2015/03/01 2015, doi: 10.1038/nature14327.

[205] W. Sun, L.-C. Lin, X. Peng, and B. Smit, "Computational screening of porous metal-organic frameworks and zeolites for the removal of SO_2 and NO_x from flue gases," *AIChE Journal,* vol. 60, no. 6, pp. 2314-2323, 2014, doi: 10.1002/aic.14467.

[206] P. M. Schoenecker, C. G. Carson, H. Jasuja, C. J. J. Flemming, and K. S. Walton, "Effect of Water Adsorption on Retention of Structure and Surface Area of Metal–Organic Frameworks," *Industrial & Engineering Chemistry Research,* vol. 51, no. 18, pp. 6513-6519, 2012/05/09 2012, doi: 10.1021/ie202325p.

[207] A. Kumar *et al.*, "Direct Air Capture of CO_2 by Physisorbent Materials," *Angewandte Chemie International Edition,* vol. 54, no. 48, pp. 14372-14377, 2015, doi: 10.1002/anie.201506952.

[208] D.-A. Yang, H.-Y. Cho, J. Kim, S.-T. Yang, and W.-S. Ahn, "CO_2 capture and conversion using Mg-MOF-74 prepared by a sonochemical method," *Energy & Environmental Science,* vol. 5, no. 4, pp. 6465-6473, 2012, doi: 10.1039/C1EE02234B.

[209] J. J. Manyà, D. García-Morcate, and B. González, "Adsorption Performance of Physically Activated Biochars for Postcombustion CO_2 Capture from Dry and Humid Flue Gas," *Applied Sciences,* vol. 10, no. 1, p. 376, 2020, doi: 10.3390/app10010376.

[210] B. Verougstraete, A. Martín-Calvo, S. Van der Perre, G. Baron, V. Finsy, and J. F. M. Denayer, "A new honeycomb carbon monolith for CO_2 capture by rapid temperature swing adsorption using steam regeneration," *Chemical Engineering Journal,* vol. 383, p. 123075, 2020/03/01/ 2020, doi: 10.1016/j.cej.2019.123075.

[211] J. A. Dunne, M. Rao, S. Sircar, R. J. Gorte, and A. L. Myers, "Calorimetric Heats of Adsorption and Adsorption Isotherms. 2. O_2, N_2, Ar, CO_2, CH4, C_2H_6, and SF_6 on NaX, H-ZSM-5, and Na-ZSM-5 Zeolites," *Langmuir,* vol. 12, no. 24, pp. 5896-5904, 1996/01/01 1996, doi: 10.1021/la960496r.

[212] M. Hefti, D. Marx, L. Joss, and M. Mazzotti, "Adsorption equilibrium of binary mixtures of carbon dioxide and nitrogen on zeolites ZSM-5 and 13X," *Microporous and Mesoporous Materials,* vol. 215, pp. 215-228, 2015/10/01/ 2015, doi: 10.1016/j.micromeso.2015.05.044.

[213] W. Ding *et al.*, "Investigation of High-Temperature and High-Pressure Gas Adsorption in Zeolite H-ZSM-5 via the Langatate Crystal Microbalance: CO2, H_2O, Methanol, and Dimethyl Ether," *The Journal of Physical Chemistry C,* vol. 119, no. 41, pp. 23478-23485, 2015/10/15 2015, doi: 10.1021/acs.jpcc.5b06591.

[214] E. Pérez-Botella *et al.*, "Unusually Low Heat of Adsorption of CO_2 on AlPO and SAPO Molecular Sieves," *Frontiers in Chemistry,* Original Research vol. 8, 2020-October-28 2020, doi: 10.3389/fchem.2020.588712.

[215] Y. Luo, H. H. Funke, J. L. Falconer, and R. D. Noble, "Adsorption of CO_2, CH_4, C_3H_8, and H_2O in SSZ-13, SAPO-34, and T-Type Zeolites," *Industrial & Engineering Chemistry Research,* vol. 55, no. 36, pp. 9749-9757, 2016/09/14 2016, doi: 10.1021/acs.iecr.6b02034.

[216] B. Liu, C. Tang, X. Li, B. Wang, and R. Zhou, "High-performance SAPO-34 membranes for CO_2 separations from simulated flue gas," *Microporous and Mesoporous Materials,* vol. 292, p. 109712, 2020/01/15/ 2020, doi: 10.1016/j.micromeso.2019.109712.

[217] J. Zhu, Y. Cui, Y. Wang, and F. Wei, "Direct synthesis of hierarchical zeolite from a natural layered material," *Chemical Communications,* 10.1039/B902661D no. 22, pp. 3282-3284, 2009, doi: 10.1039/B902661D.

[218] N. S. Wilkins and A. Rajendran, "Measurement of competitive CO_2 and N_2 adsorption on Zeolite 13X for post-combustion CO_2 capture," *Adsorption,* vol. 25, no. 2, pp. 115-133, 2019/02/01 2019, doi: 10.1007/s10450-018-00004-2.

[219] M. L. Zanota, N. Heymans, F. Gilles, B. L. Su, M. Frère, and G. De Weireld, "Adsorption Isotherms of Pure Gas and Binary Mixtures of Air Compounds on Faujasite Zeolite Adsorbents: Effect of Compensation Cation," *Journal of Chemical & Engineering Data,* vol. 55, no. 1, pp. 448-458, 2010/01/14 2010, doi: 10.1021/je900539m.

[220] N. S. Wilkins, J. A. Sawada, and A. Rajendran, "Measurement of competitive CO_2 and H_2O adsorption on zeolite 13X for post-combustion CO_2 capture," *Adsorption,* vol. 26, no. 5, pp. 765-779, 2020/07/01 2020, doi: 10.1007/s10450-020-00199-3.

[221] F. Brandani, D. Ruthven, and C. G. Coe, "Measurement of Adsorption Equilibrium by the Zero Length Column (ZLC) Technique Part 1: Single-Component Systems," *Industrial & Engineering Chemistry Research,* vol. 42, no. 7, pp. 1451-1461, 2003/04/01 2003, doi: 10.1021/ie020572n.

[222] S. Oddy, J. Poupore, and F. H. Tezel, "Separation of CO_2 and CH_4 on CaX zeolite for use in Landfill gas separation," *The Canadian Journal of Chemical Engineering,* vol. 91, no. 6, pp. 1031-1039, 2013, doi: 10.1002/cjce.21756.

[223] H. Ahn, H.-K. Yoo, Y. Shul, S. Hyun, and C.-H. Lee, "Diffusion Mechanism of N_2 and CH_4 in Pelletized Zeolite 4A, 5A and CaX," *Journal of Chemical Engineering of Japan,* vol. 35, no. 4, pp. 334-345, 2002, doi: 10.1252/jcej.35.334.

[224] Z. Liu, C. A. Grande, P. Li, J. Yu, and A. E. Rodrigues, "Adsorption and Desorption of Carbon Dioxide and Nitrogen on Zeolite 5A," *Separation Science and Technology,* vol. 46, no. 3, pp. 434-451, 2011, doi: 10.1080/01496395.2010.513360.

[225] M. Mofarahi and M. Seyyedi, "Pure and Binary Adsorption Isotherms of Nitrogen and Oxygen on Zeolite 5A," *Journal of Chemical & Engineering Data,* vol. 54, no. 3, pp. 916-921, 2009, doi: 10.1021/je8006919.

[226] M. J. Bos, S. Pietersen, and D. W. F. Brilman, "Production of high purity CO_2 from air using solid amine sorbents," *Chemical Engineering Science: X,* vol. 2, p. 100020, 2019/05/01/ 2019, doi: 10.1016/j.cesx.2019.100020.

[227] C. Gebald, J. A. Wurzbacher, A. Borgschulte, T. Zimmermann, and A. Steinfeld, "Single-Component and Binary CO_2 and H_2O Adsorption of Amine-Functionalized Cellulose," *Environmental Science & Technology,* vol. 48, no. 4, pp. 2497-2504, 2014/02/18 2014, doi: 10.1021/es404430g.

[228] V. Stampi-Bombelli, M. van der Spek, and M. Mazzotti, "Analysis of direct capture of CO_2 from ambient air via steam-assisted temperature–vacuum swing adsorption," *Adsorption,* vol. 26, no. 7, pp. 1183-1197, 2020, doi: 10.1007/s10450-020-00249-w.

[229] J. A. Wurzbacher, C. Gebald, N. Piatkowski, and A. Steinfeld, "Concurrent Separation of CO_2 and H_2O from Air by a Temperature-Vacuum Swing Adsorption/Desorption Cycle," *Environmental Science & Technology,* vol. 46, no. 16, pp. 9191-9198, 2012/08/21 2012, doi: 10.1021/es301953k.

Appendix 2. Materials and methods

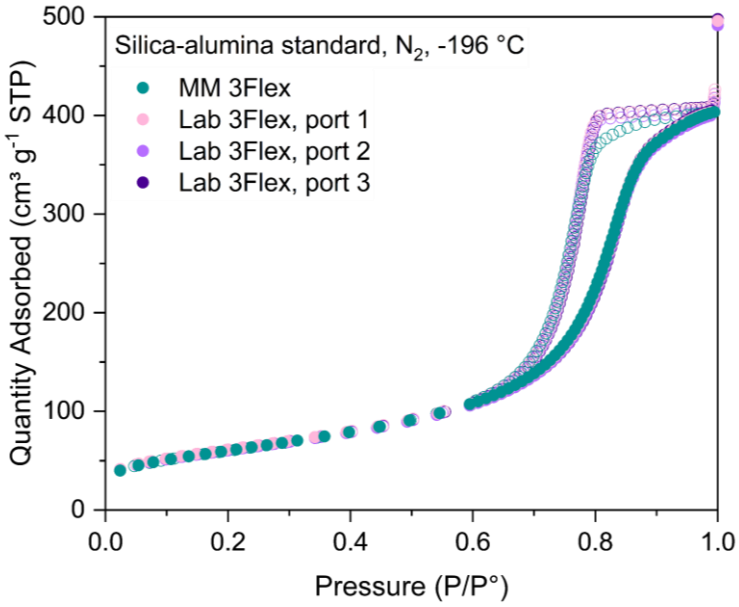


Figure A2.1. Comparison of equilibrium adsorption (filled symbols) and desorption (hollow symbols) isotherms of N_2 measured at -196 °C for a silica-alumina reference material run by both myself and Micromeritics (MM) on 3Flex porosity analysers. Samples were degassed ex-situ at 0.02 mbar for 1 h at 90 °C then at 350 °C for at least 4 h. Samples were then degassed in-situ at 350 °C and 0.00002 mbar for 4 h.

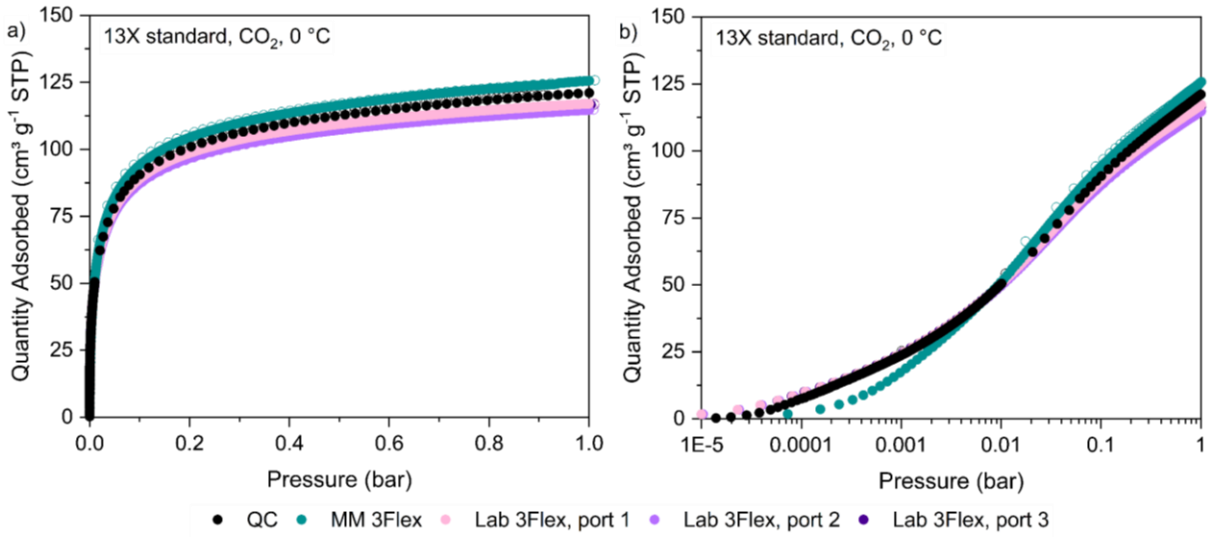


Figure A2.2. Comparison of equilibrium adsorption (filled symbols) and desorption (hollow symbols) isotherms of CO_2 for a zeolite 13X reference material measured at 0 °C by both myself and Micromeritics (MM) on 3Flex porosity analysers, and by Hassan Azzan, on a Quantachrome Autosorb iQ3 (QC) porosity analyser. Samples were degassed ex-situ at 0.02 mbar for 1 h at 90 °C then at 350 °C for at least 8 h. Samples were then degassed in-situ at 300 °C and 0.00002 mbar for 4 h. Isotherms are shown in a) linear scale and b) log scale of pressure.



Figure A2.3. 3D-printed container for measuring the bed densities of Lewatit and Purolite. The outer cube dimensions are 2.0 × 2.0 × 2.0 cm, while the cylindrical inset measures 1.6 cm in dimeter and 1.2 cm in height.

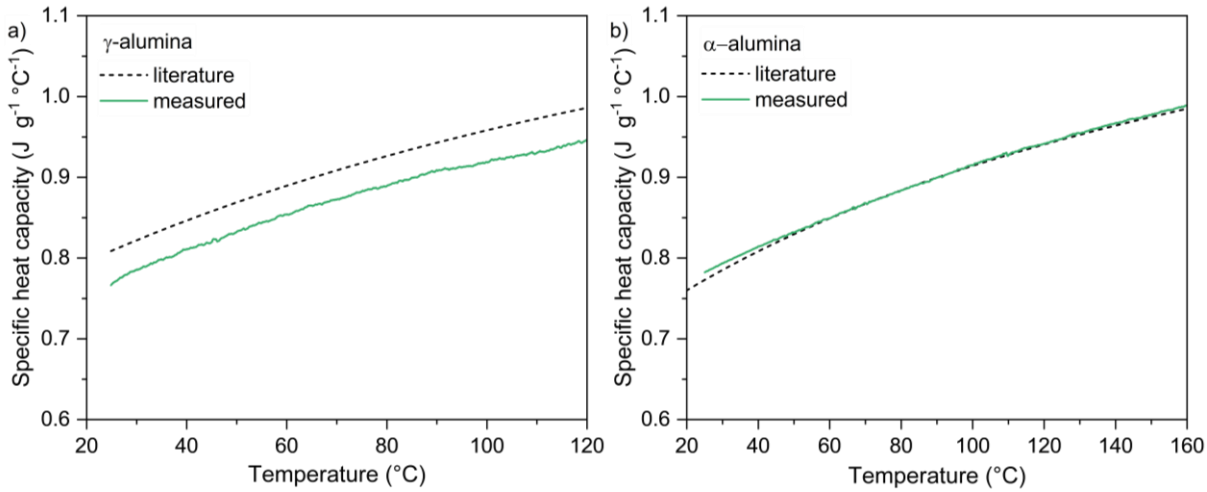


Figure A2.4. Heat capacities of measured a) γ-alumina powder and b) α-alumina disc provided by Perkin-Elmer, in comparison to literature values provided by NIST [1].



Figure A2.5. Image of the closed environment humidity setup. A 250 mL beaker filled with saturated salt solution of either sodium chloride or potassium nitrate is placed with a digital hygrometer-thermometer and an open 10 mL glass vial with TIFSIX-3-Ni sample (not shown in image) in a 1 L Kilner clip top mason jar with a rubber seal.

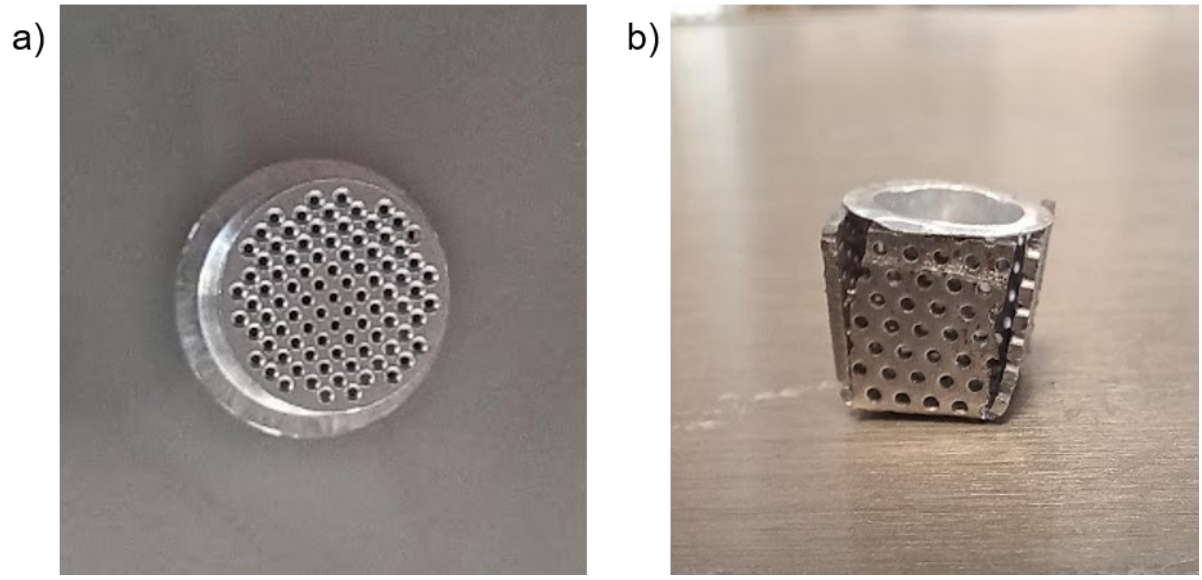


Figure A2.6. Image of a) aluminium crucible and b) its perforated stainless-steel holder for cyclic studies with TIFSIX-3-Ni using a thermogravimetric analyser.

A2. References

[1] NIST. "Aluminium Oxide." https://webbook.nist.gov/cgi/cbook.cgi?ID=C1344281&Type=JANAFS&Plot=on (accessed 2024).

Appendix 3. Lewatit and Purolite study

A3.1 Physicochemical properties

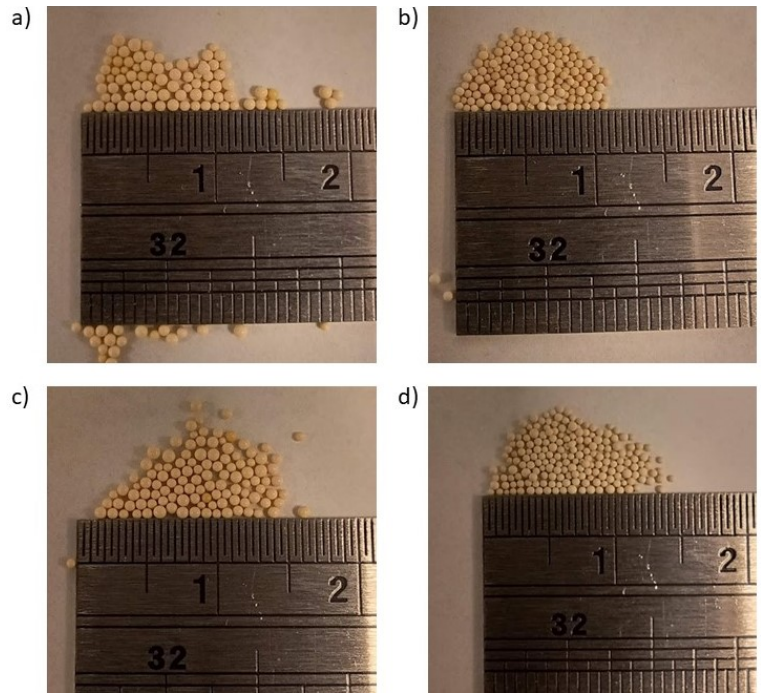


Figure A3.1. Images of fresh a) Lewatit and c) Purolite beads as well as vacuum-dried b) Lewatit and d) Purolite beads, (degassed ex-situ at 120 °C and 0.02 mbar for at least 12 h).

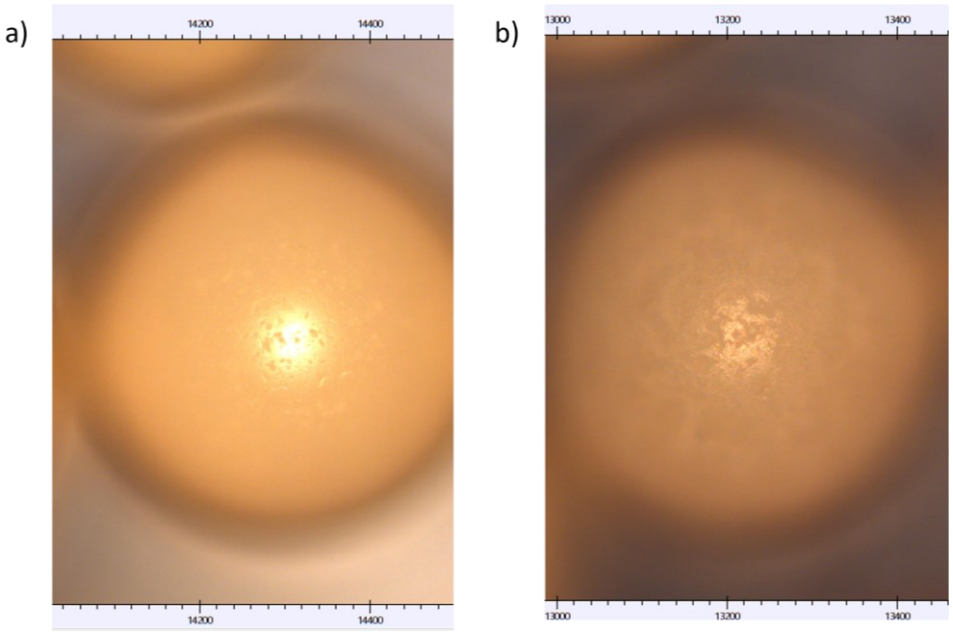


Figure A3.2. Surface of fresh a) Lewatit and b) Purolite beads under 10× magnification using a Senterra II Raman microscope, where ruler values are in microns.

Table A3.1. Literature values of textural properties for Lewatit.

Textural property	Value	Reference
$\rho_{skeletal}$ (g cm^{-3})	-	-
$\rho_{particle}$ (g cm^{-3})	0.88	[1]
ρ_{bed} (g cm^{-3})	0.63 (wet)	[2]
V_{total} (cm^3 g^{-1})	0.64	[2]
$\varepsilon_{particle}$	0.56	Calculated using [1] and [2]
S_{BET} (m^2 g^{-1})	43	[2]

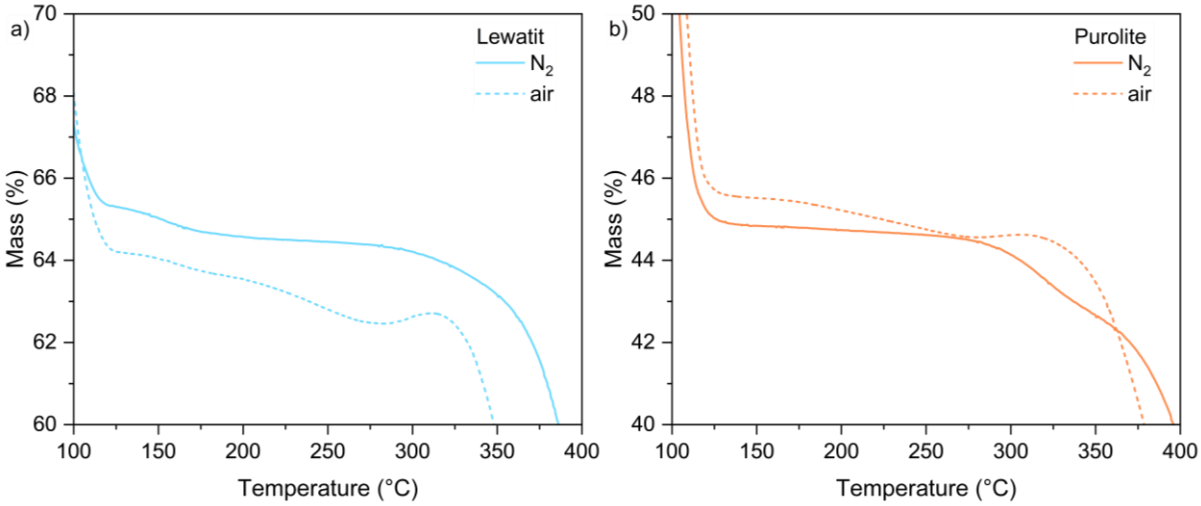


Figure A3.3. TG curves for a) Lewatit and b) Purolite under N_2 and air atmospheres between 100 °C and 400 °C.

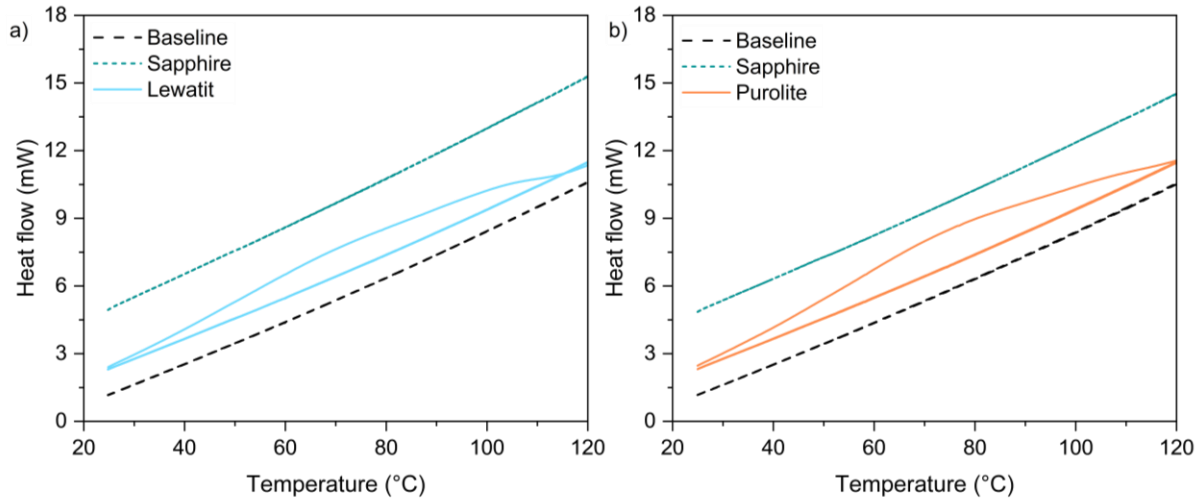


Figure A3.4. Heat flow curves of 3 baseline runs, 3 sapphire runs, and 4 sample runs for a) Lewatit and b) Purolite heat capacity measurements. For both samples, the first heat flow curve differs from the following three.

A3.2 Equilibrium sorption properties

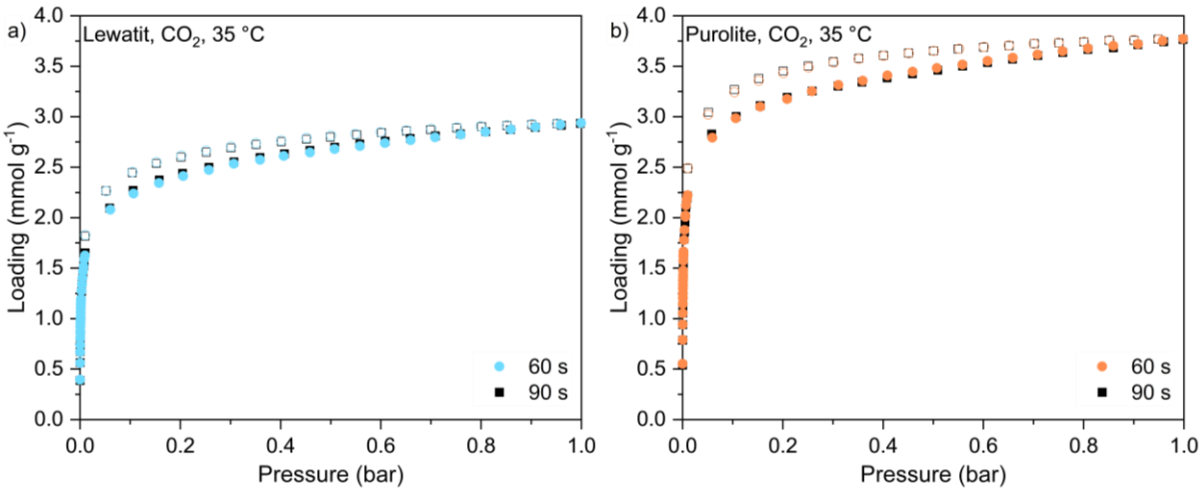


Figure A3.5. Equilibrium adsorption (filled symbols) and desorption (hollow symbols) isotherms of CO_2 at 35 °C for the same sample of a) Lewatit and b) Purolite with 60 s and 90 s equilibration intervals.

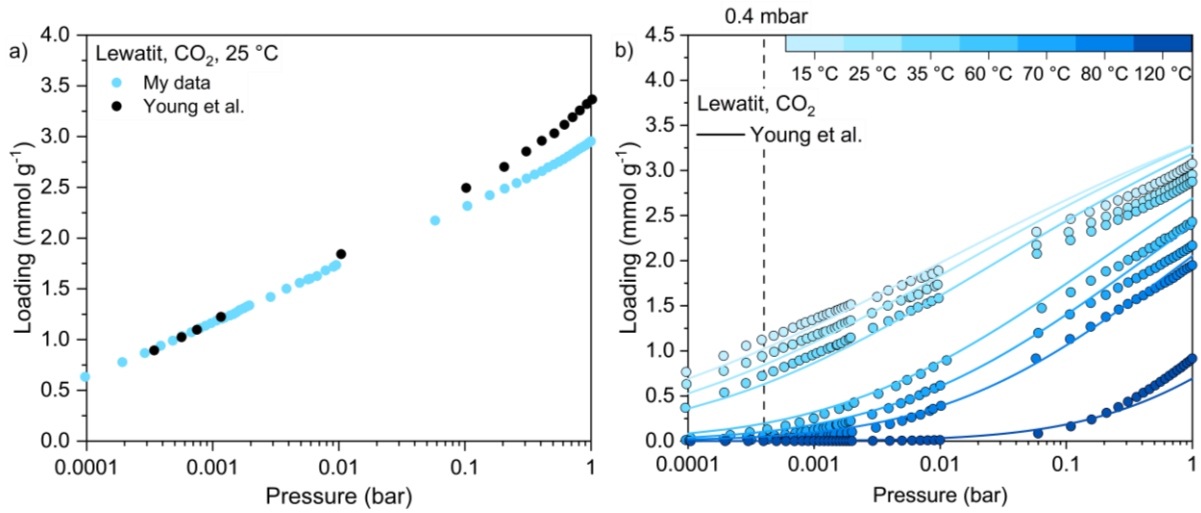


Figure A3.6. a) Comparison of our measured CO_2 equilibrium adsorption isotherm at 25 °C for Lewatit to the 25 °C CO_2 isotherm measured by Young et al. [3]. b) Overlay of our measured CO_2 equilibrium adsorption isotherm data with the td-Toth isotherm model and fitting parameters used by Young et al. [3].

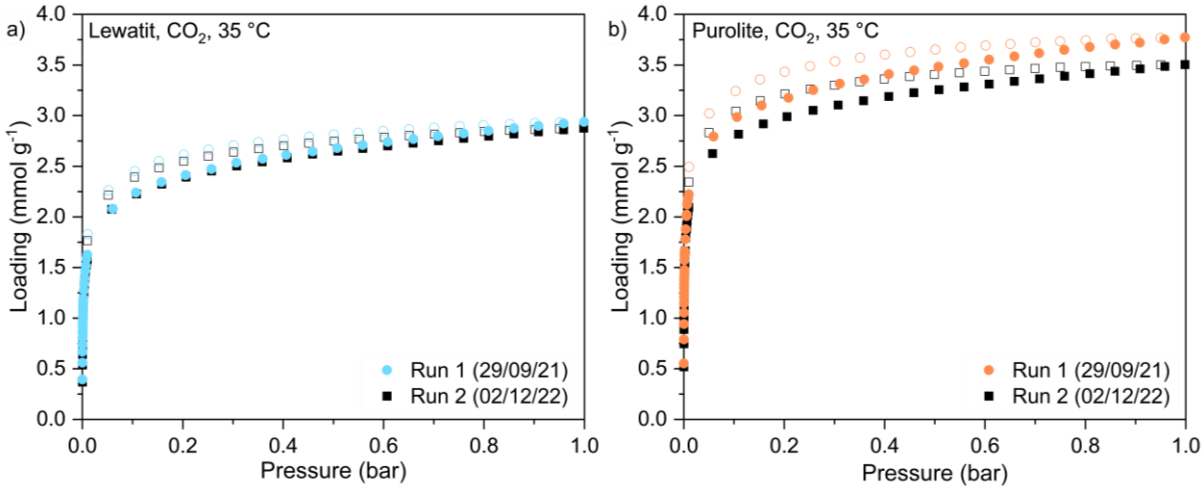


Figure A3.7. Equilibrium adsorption (filled symbols) and desorption (hollow symbols) isotherms of CO_2 at 35 °C for two samples of a) Lewatit and b) Purolite measured approximately one year apart. Each sample is from the same batch of commercial resin.

Table A3.2. Upper and lower bounds imposed on fitting parameters for the td-Toth, CP, virial, SSL, and GAB isotherm models.

Fitting equation	**Parameter**	**Units**	**Lower bound**	**Upper bound**
td-Toth	$q_{\infty,0}$	mmol g^{-1}	0	5
	b_0	bar^{-1}	1×10^{-20}	0.1
	$-\Delta U$	kJ mol^{-1}	0	130
	T_0	K	-	-
	τ_0	-	0	5
	α	-	0	5
	χ	-	0	5
CP	$q_{\infty,0}$	mmol g^{-1}	0	5
	b_0	bar^{-1}	1×10^{-20}	0.1
	$-\Delta U$	kJ mol^{-1}	0	130
	T_0	K	-	-
	τ_0	-	0	5
	α	-	0	5
	χ	-	0	5
	$q_{\infty c}$	mmol g^{-1}	0	5
	$b_{0,c}$	bar^{-1}	1×10^{-20}	0.1
	$-\Delta U_c$	kJ mol^{-1}	0	130
	E_a	kJ mol^{-1}	0	50
Virial	a_0	K	0	30 000
	a_1	K mol^{-1}	0	30 000
	a_2	K mol^{-2}	0	30 000
	a_3	K mol^{-3}	0	30 000
	b_0	-	0	30 000
	b_1	mol^{-1}	0	30 000
SSL	q_∞	mmol g^{-1}	0	10
	b_0	bar^{-1}	0	1
	$-\Delta U$	kJ mol^{-1}	0	150
GAB	q_m	mmol g^{-1}	0	10
	C	kJ mol^{-1}	0	100
	D	K^{-1}	0	0.05
	F	kJ mol^{-1}	0	100
	G	kJ mol^{-1} K^{-1}	-0.05	0

Table A3.3. Fitting parameters for the td-Toth isotherm model for CO_2 adsorption for Lewatit used by Young et al. [3].

Fitting equation	**Parameter**	**Unit**	**Lewatit**
td-Toth	q_∞	mmol g^{-1}	4.86
	b_0	bar^{-1}	2.85×10^{-16}
	$-\Delta U$	kJ mol^{-1}	117.798
	T_0	K	298.15
	τ_0	-	0.209
	α	-	0.523
	χ	-	0

F-test check:

An F-test was conducted between the fitting results of the td-Toth isotherm model, i.e. the "reduced model", and the CP isotherm model, i.e. the "full model", using the following procedure from PennState [4]:

1. Calculate the error sum of squares (SSE) of the CO_2 loading for both the reduced and full model using the following equations:

   $$SSE = \sum(experimental - fitted)^2 \quad (1)$$

2. Calculate the linear F-statistic using the following equation:

   $$F = \left(\frac{SSE(reduced) - SSE(full)}{df_{reduced} - df_{full}}\right) \div \left(\frac{SSE(full)}{df_{full}}\right) \quad (2)$$

   $$df = \#\ experimental\ data\ points - \#\ fitted\ parameters \quad (3)$$

   where *df* stands for degrees of freedom.

3. Check if the calculated F-statistic is larger than the critical value for the given degrees of freedom and a 0.95 confidence level. The critical value can be calculated using the following Excel function:

   $$F.inv\ (probability, df_1, df_2) \quad (4)$$

   where probability is the confidence level, df_1 is the numerator degrees of freedom from equation (2), i.e. $df_{reduced} - df_{full}$, and df_2 is the denominator degrees of freedom from equation (2), i.e. df_{full}. If the calculated F-statistic is larger, any better fitting by the full model is not due to an increased number of fitting parameters.

For Lewatit:

$SSE(reduced) = 5.61$

$SSE(full) = 0.20$

$\#\ experimental\ data\ points = 324$

$\#\ fitted\ parameters, reduced = 6$

$\#\ fitted\ parameters, full = 10$

$df_{reduced} = 318$

$df_{full} = 314$

$$F = \left(\frac{SSE(reduced) - SSE(full)}{df_{reduced} - df_{full}}\right) \div \left(\frac{SSE(full)}{df_{full}}\right) = \left(\frac{5.61 - 0.20}{318 - 314}\right) \div \left(\frac{0.20}{314}\right) = 2107$$

$F_{critical}(0.95, 4, 314) = 2.40$

For Lewatit, $F > F_{critical}$, and as such the better fit offered by the CP isotherm model as compared to the td-Toth isotherm model is not due to an increased number of fitting parameters.

For Purolite:

$SSE(reduced) = 5.56$

$SSE(full) = 0.63$

$\#\ experimental\ data\ points = 319$

$\#\ fitted\ parameters, reduced = 6$

$\#\ fitted\ parameters, full = 10$

$df_{reduced} = 313$

$df_{full} = 309$

$$F = \left(\frac{SSE(reduced) - SSE(full)}{df_{reduced} - df_{full}}\right) \div \left(\frac{SSE(full)}{df_{full}}\right) = \left(\frac{5.56 - 0.60}{313 - 309}\right) \div \left(\frac{0.63}{309}\right) = 605$$

$F_{critical}(0.95, 4, 309) = 2.40$

For Purolite, $F > F_{critical}$, and as such the better fit provided by the CP isotherm model compared to the td-Toth isotherm model is not due to an increased number of parameters.

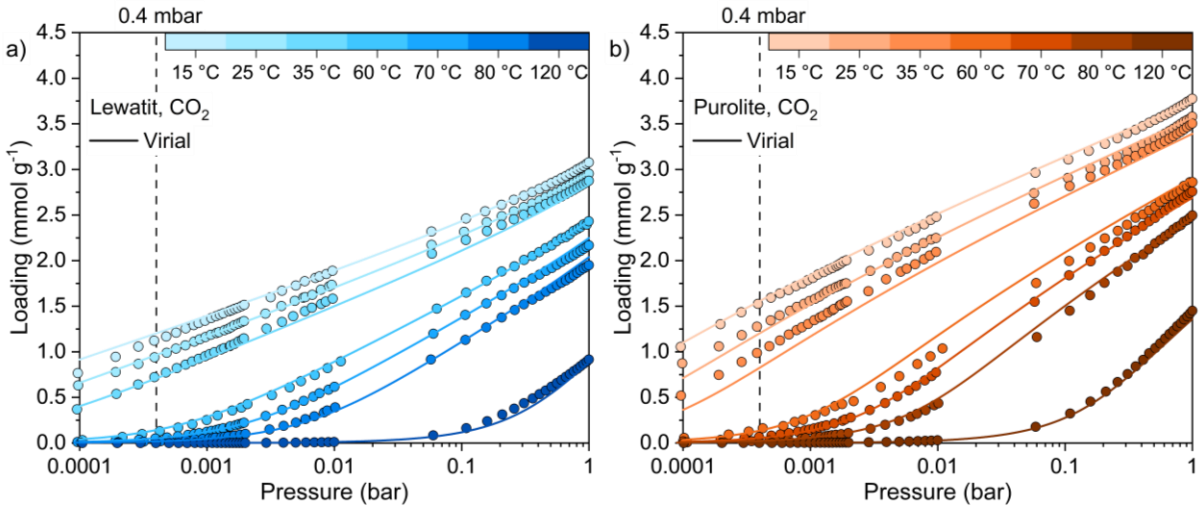


Figure A3.8. Equilibrium adsorption isotherms for CO_2 measured at 15, 25, 35, 60, 70, 80, and 120 °C up to 1 bar for a) Lewatit and b) Purolite with a log-scale of pressure. Solid lines represent the fitting results from virial equation, whose fitting parameters are found in Table A3.4.

Table A3.4. Fitting parameters with uncertainty bounds for a 95% confidence interval for the virial equation for CO_2 adsorption for Lewatit and Purolite.

Equation	**Parameter**	**Unit**	**Lewatit**	**Purolite**
Virial	a_0	K	-12910 ± 20	-10600 ± 30
	a_1	K mol^{-1}	2980 ± 20	850 ± 20
	a_2	K mol^{-2}	269 ± 7	211 ± 6
	a_3	K mol^{-3}	-57 ± 2	-18 ± 1
	b_0	-	32.68 ± 0.07	25.95 ± 0.08
	b_1	mol^{-1}	-7.78 ± 0.05	-2.29 ± 0.05

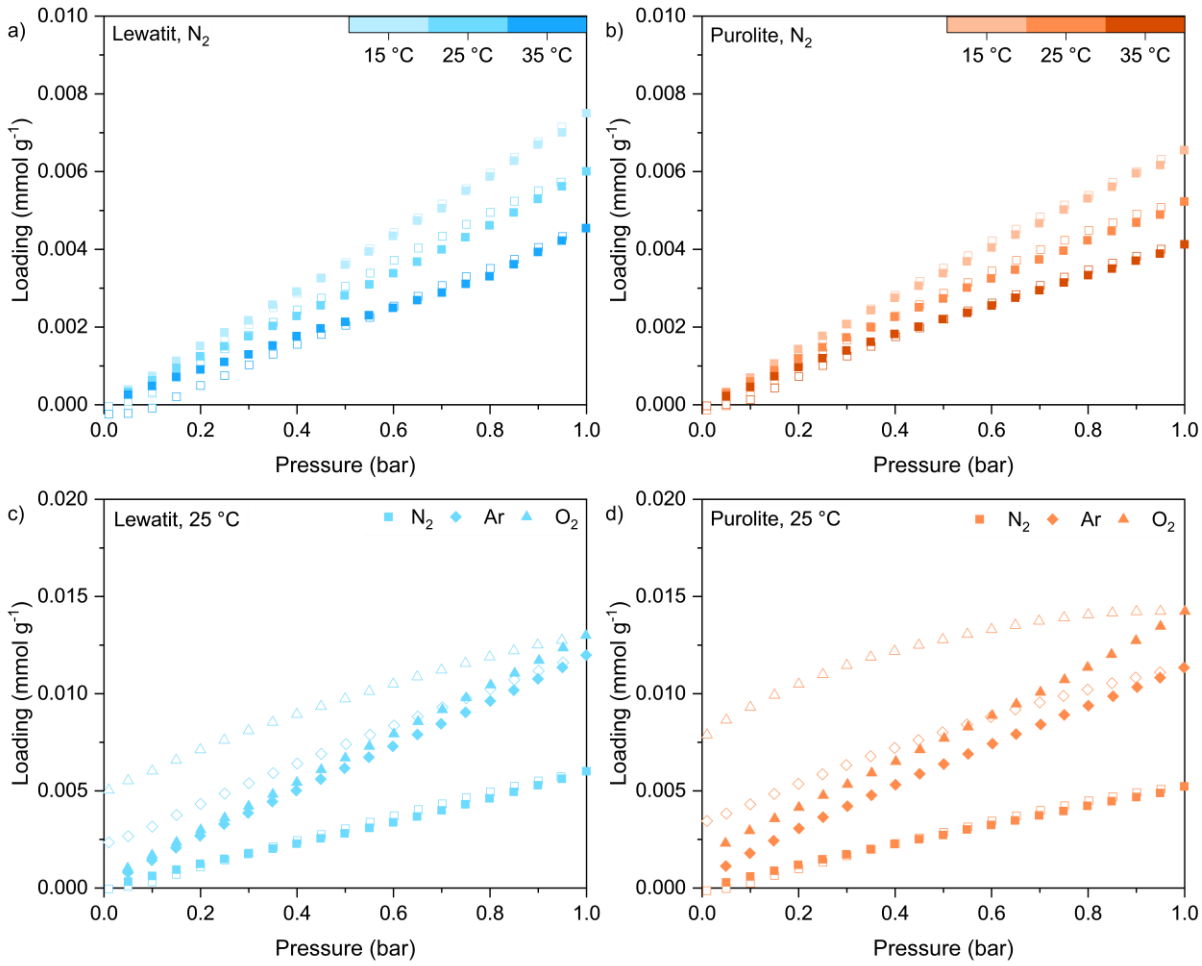


Figure A3.9. Equilibrium adsorption (filled symbols) and desorption (hollow symbols) isotherms for N_2 measured at 15 °C, 25 °C, and 35 °C up to 1 bar for a) Lewatit and b) Purolite. Equilibrium adsorption (filled symbols) and desorption (hollow symbols) isotherms for N_2, Ar, and O_2 measured at 25 °C up to 1 bar for c) Lewatit and d) Purolite.

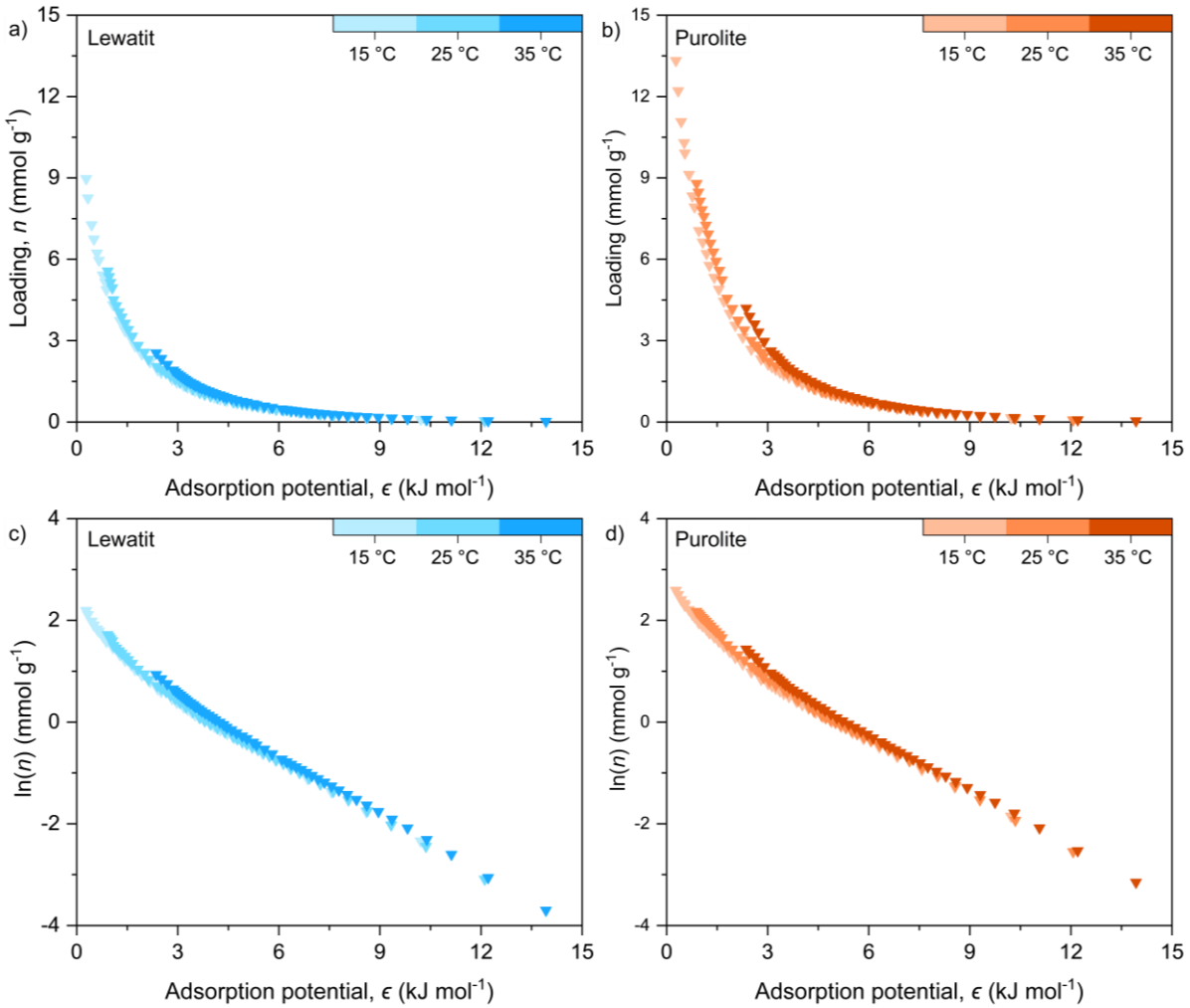


Figure A3.10. H_2O adsorption potentials for Lewatit plotted against the a) H_2O loading and c) natural log of the H_2O loading. H_2O adsorption potentials for Purolite plotted against the b) H_2O loading and d) natural log of the H_2O loading.

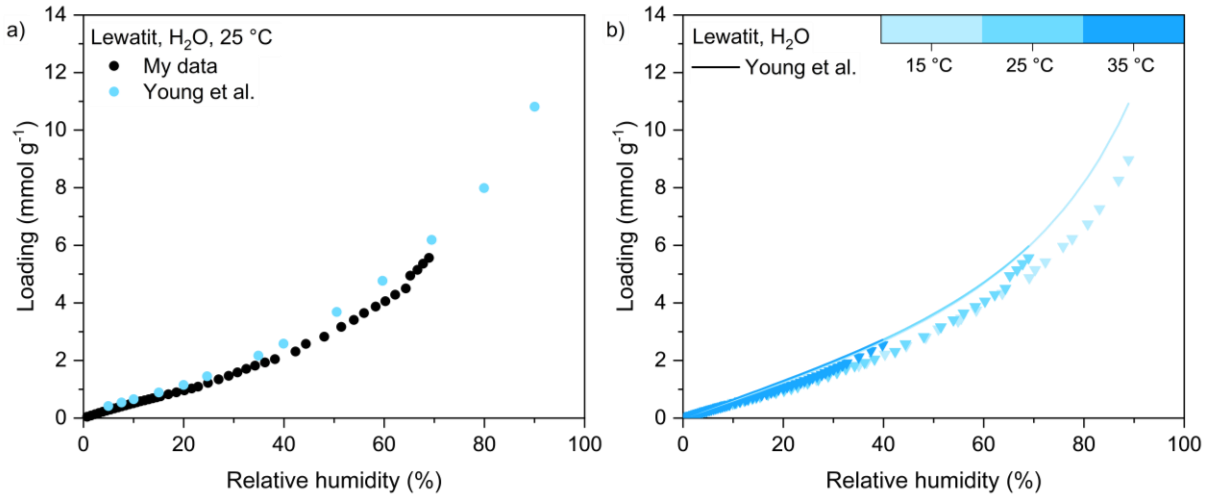
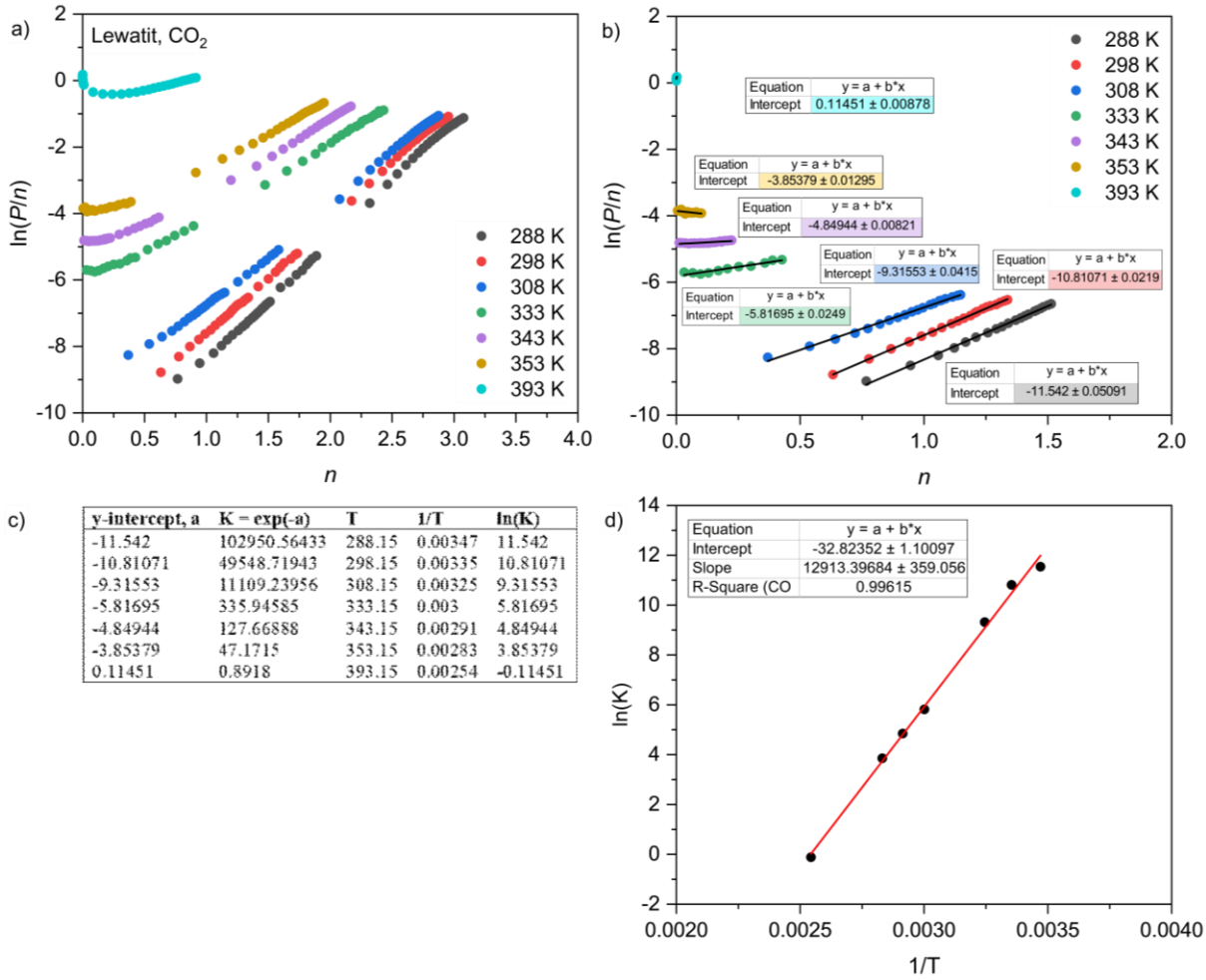


Figure A3.11. a) Comparison of our measured H_2O equilibrium adsorption isotherm at 25 °C for Lewatit to the 25 °C H_2O isotherm measured by Young et al. [3] b) Overlay of our measured H_2O equilibrium adsorption isotherm data with the GAB isotherm model and fitting parameters used by Young et al. [3].

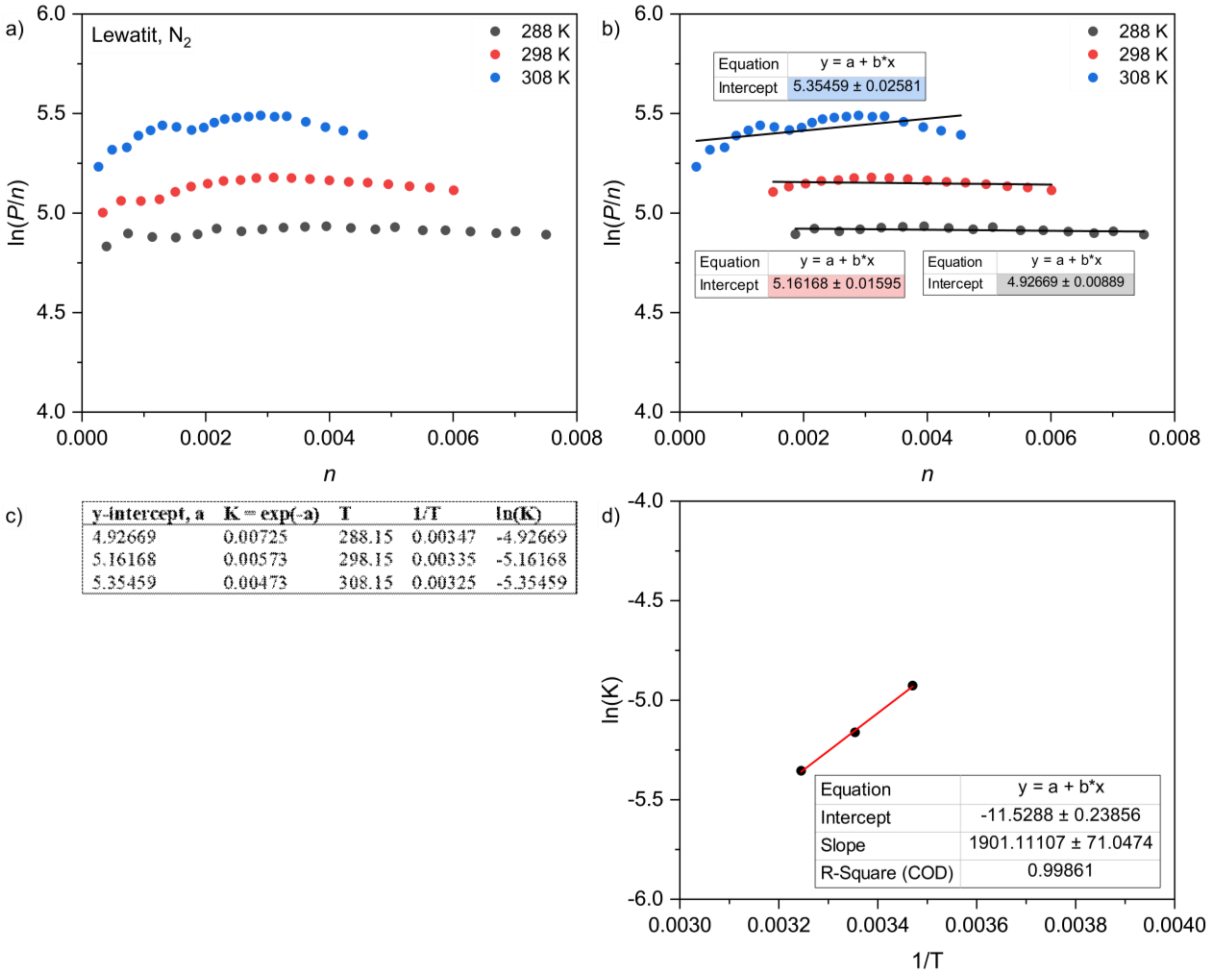
Table A3.5. Fitting parameters for the GAB isotherm model for H_2O adsorption for Lewatit used by Young et al. [3].

Fitting equation	**Parameter**	**Unit**	**Lewatit**
GAB	q_m	mmol g^{-1}	3.63
	C	kJ mol^{-1}	47.110
	D	K^{-1}	0.023744
	F	kJ mol^{-1}	57.706
	G	kJ mol^{-1} K^{-1}	-0.047814



y-intercept, a	K = exp(-a)	T	1/T	ln(K)
-11.542	102950.56433	288.15	0.00347	11.542
-10.81071	49548.71943	298.15	0.00335	10.81071
-9.31553	11109.23956	308.15	0.00325	9.31553
-5.81695	335.94585	333.15	0.003	5.81695
-4.84944	127.66888	343.15	0.00291	4.84944
-3.85379	47.1715	353.15	0.00283	3.85379
0.11451	0.8918	393.15	0.00254	-0.11451

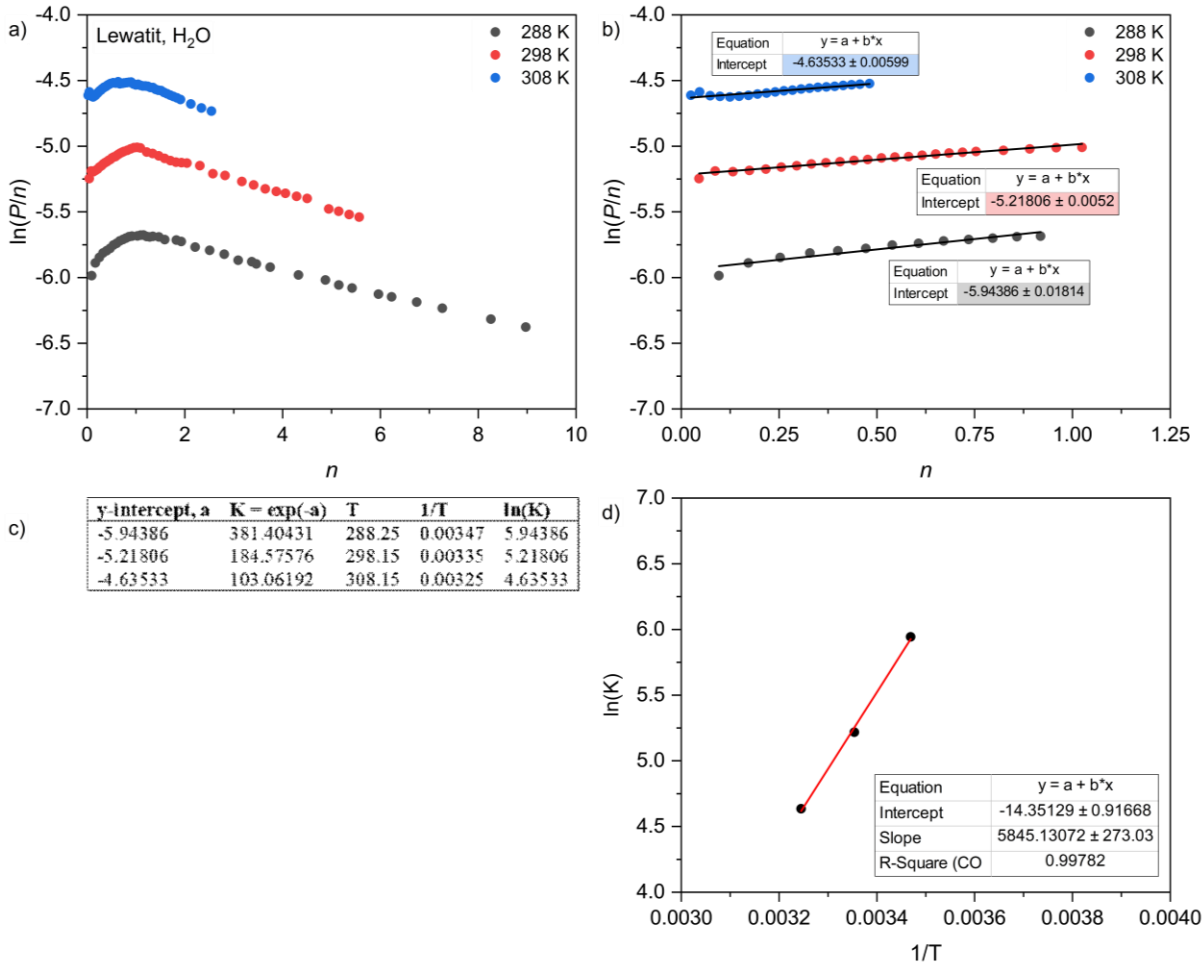
Figure A3.12. a) Virial plot of all measured CO_2 isotherm data for Lewatit, where pressure (P), loading (n), and temperature (T) values are in units of bar, mmol g^{-1}, and K, respectively. b) Virial plot showing the selected low loading data fitted to linear equations. The y-intercepts of each fitted equation are used to calculate the Henry constant K. c) Summary of fitted and calculated parameters used to determine ΔH_0. d) Plot of ln$K$ vs. $1/T$ fitted to a linear equation, whose slope is used to calculate ΔH_0.



c)

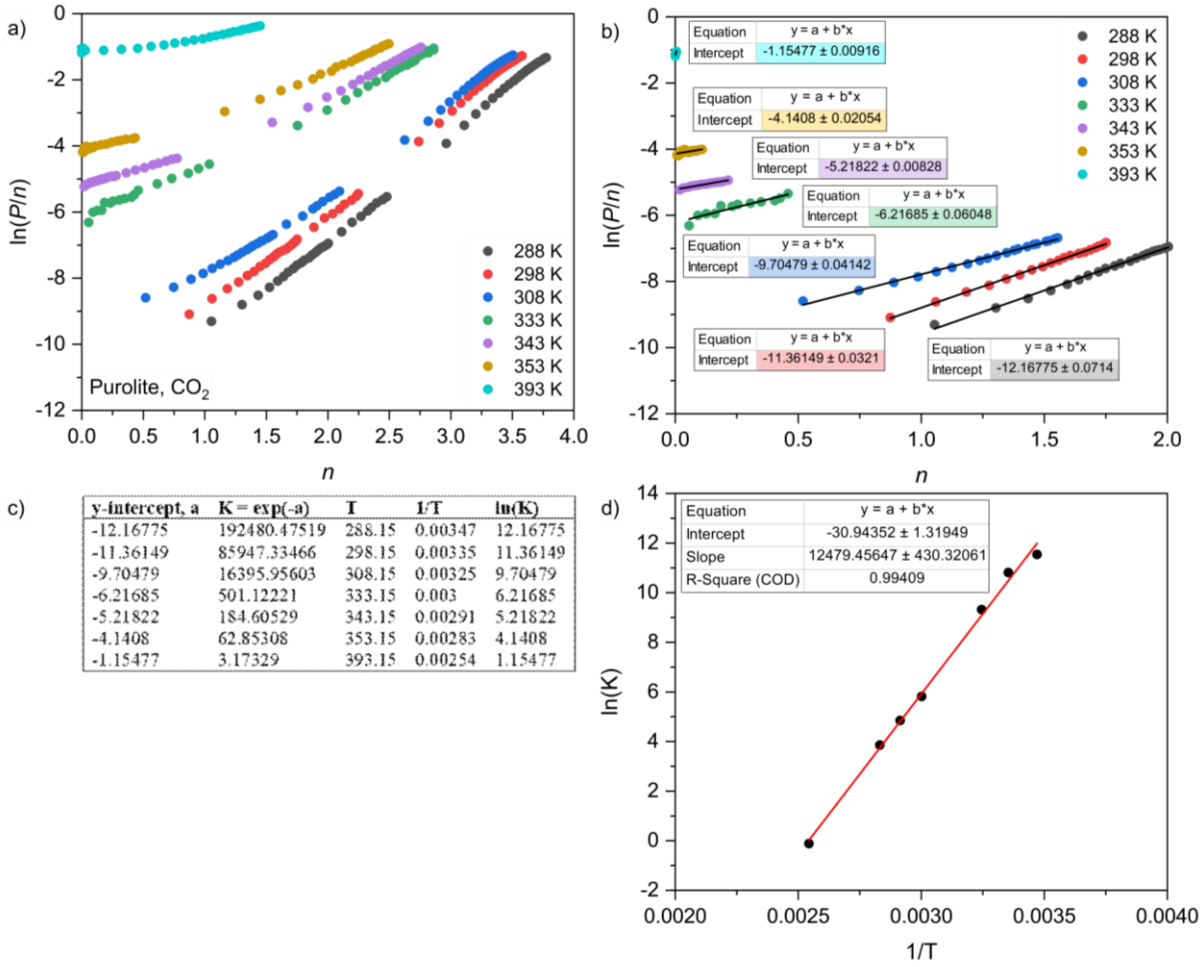
y-intercept, a	K = exp(-a)	T	1/T	ln(K)
4.92669	0.00725	288.15	0.00347	-4.92669
5.16168	0.00573	298.15	0.00335	-5.16168
5.35459	0.00473	308.15	0.00325	-5.35459

Figure A3.13. a) Virial plot of all measured N_2 isotherm data for Lewatit, where pressure (P), loading (n), and temperature (T) values are in units of bar, mmol g^{-1}, and K, respectively. b) Virial plot showing the selected low loading data fitted to linear equations. The y-intercepts of each fitted equation are used to calculate the Henry constant K. c) Summary of fitted and calculated parameters used to determine ΔH_0. d) Plot of ln$K$ vs. $1/T$ fitted to a linear equation, whose slope is used to calculate ΔH_0.



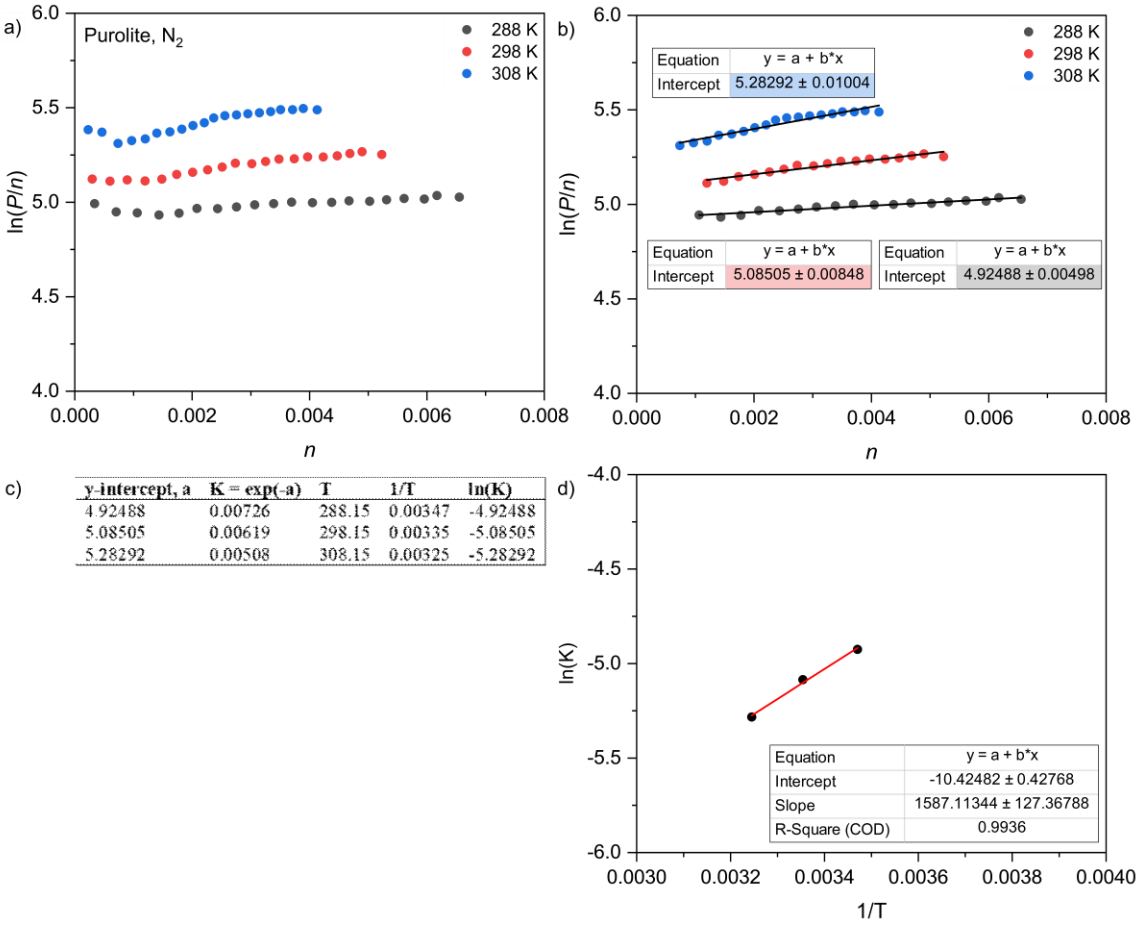
y-intercept, a	K = exp(-a)	T	1/T	ln(K)
-5.94386	381.40431	288.25	0.00347	5.94386
-5.21806	184.57576	298.15	0.00335	5.21806
-4.63533	103.06192	308.15	0.00325	4.63533

Figure A3.14. a) Virial plot of all measured H_2O isotherm data for Lewatit, where pressure (P), loading (n), and temperature (T) values are in units of bar, mmol g^{-1}, and K, respectively. b) Virial plot showing the selected low loading data fitted to linear equations. The y-intercepts of each fitted equation are used to calculate the Henry constant K. c) Summary of fitted and calculated parameters used to determine ΔH_0. d) Plot of ln$K$ vs. $1/T$ fitted to a linear equation, whose slope is used to calculate ΔH_0.



y-intercept, a	K = exp(-a)	T	1/T	ln(K)
-12.16775	192480.47519	288.15	0.00347	12.16775
-11.36149	85947.33466	298.15	0.00335	11.36149
-9.70479	16395.95603	308.15	0.00325	9.70479
-6.21685	501.12221	333.15	0.003	6.21685
-5.21822	184.60529	343.15	0.00291	5.21822
-4.1408	62.85308	353.15	0.00283	4.1408
-1.15477	3.17329	393.15	0.00254	1.15477

Figure A3.15. a) Virial plot of all measured CO_2 isotherm data for Purolite, where pressure (P), loading (n), and temperature (T) values are in units of bar, mmol g^{-1}, and K, respectively. b) Virial plot showing the selected low loading data fitted to linear equations. The y-intercepts of each fitted equation are used to calculate the Henry constant K. c) Summary of fitted and calculated parameters used to determine ΔH_0. d) Plot of ln$K$ vs. $1/T$ fitted to a linear equation, whose slope is used to calculate ΔH_0.



y-intercept, a	K = exp(a)	T	1/T	ln(K)
4.92488	0.00726	288.15	0.00347	-4.92488
5.08505	0.00619	298.15	0.00335	-5.08505
5.28292	0.00508	308.15	0.00325	-5.28292

Figure A3.16. a) Virial plot of all measured N_2 isotherm data for Purolite, where pressure (P), loading (n), and temperature (T) values are in units of bar, mmol g^{-1}, and K, respectively. b) Virial plot showing the selected low loading data fitted to linear equations. The y-intercepts of each fitted equation are used to calculate the Henry constant K. c) Summary of fitted and calculated parameters used to determine ΔH_0. d) Plot of ln$K$ vs. $1/T$ fitted to a linear equation, whose slope is used to calculate ΔH_0.

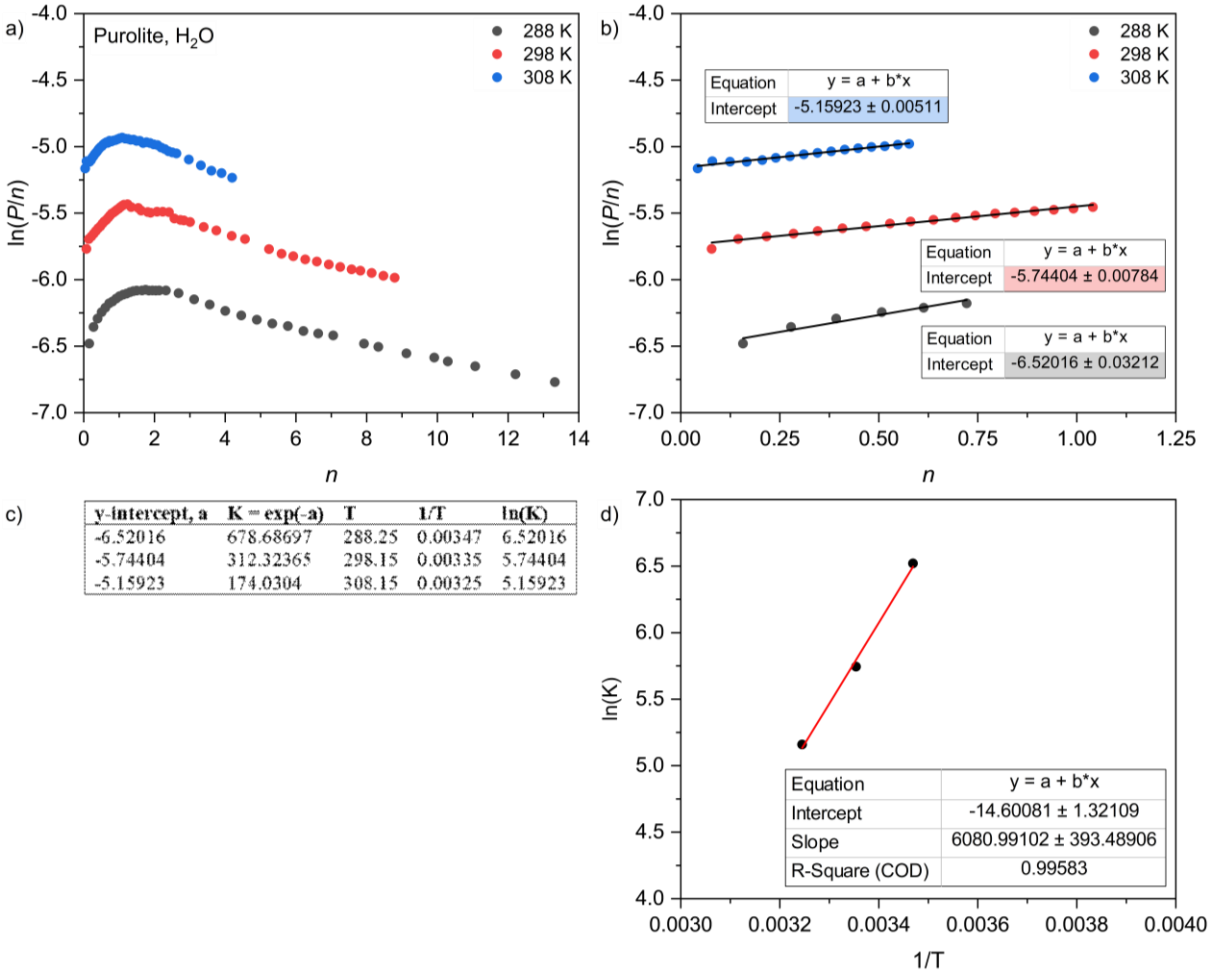


Figure A3.17. a) Virial plot of all measured H_2O isotherm data for Purolite, where pressure (P), loading (n), and temperature (T) values are in units of bar, mmol g^{-1}, and K, respectively. b) Virial plot showing the selected low loading data fitted to linear equations. The y-intercepts of each fitted equation are used to calculate the Henry constant K. c) Summary of fitted and calculated parameters used to determine ΔH_0. d) Plot of ln$K$ vs. $1/T$ fitted to a linear equation, whose slope is used to calculate ΔH_0.

Table A3.6. Smoothing spline values used in MATLAB for the interpolation of CO_2, N_2, and H_2O data to calculate the corresponding isosteric heats of adsorption for Lewatit and Purolite.

	Lewatit	**Purolite**
CO_2	0.9989	0.9997
N_2	0.9999999	0. 9999999999
H_2O	0.919	0.670

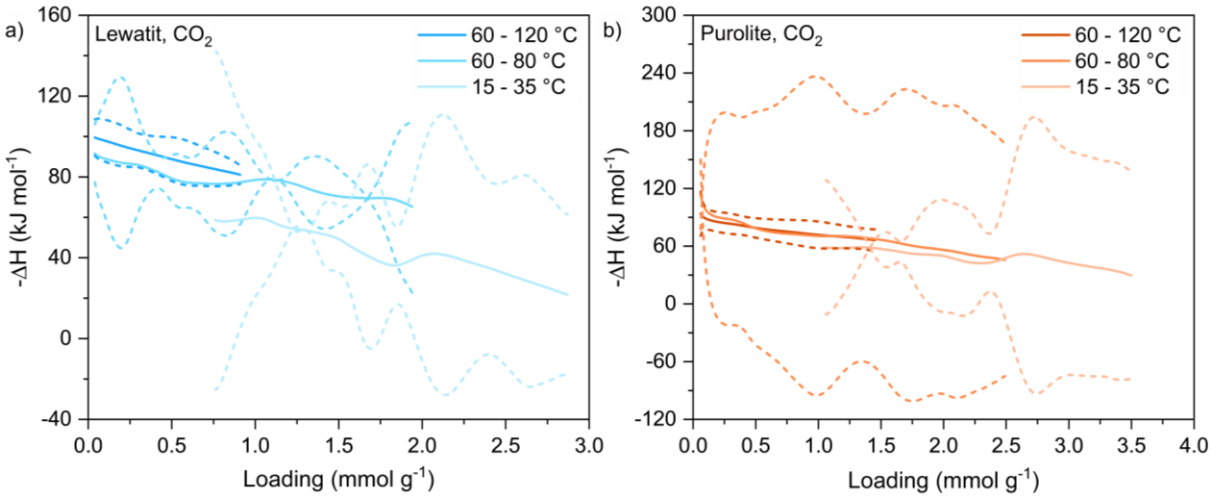


Figure A3.18. Isosteric heats of adsorption (solid lines) of a) Lewatit and b) Purolite for CO_2 calculated using isotherm data measured at 60 °C, 70 °C, 80 °C, and 120 °C, at 60 °C, 70 °C, and 80 °C, and 15 °C, 25 °C, and 35 °C. Dashed lines represent the upper and lower confidence intervals.

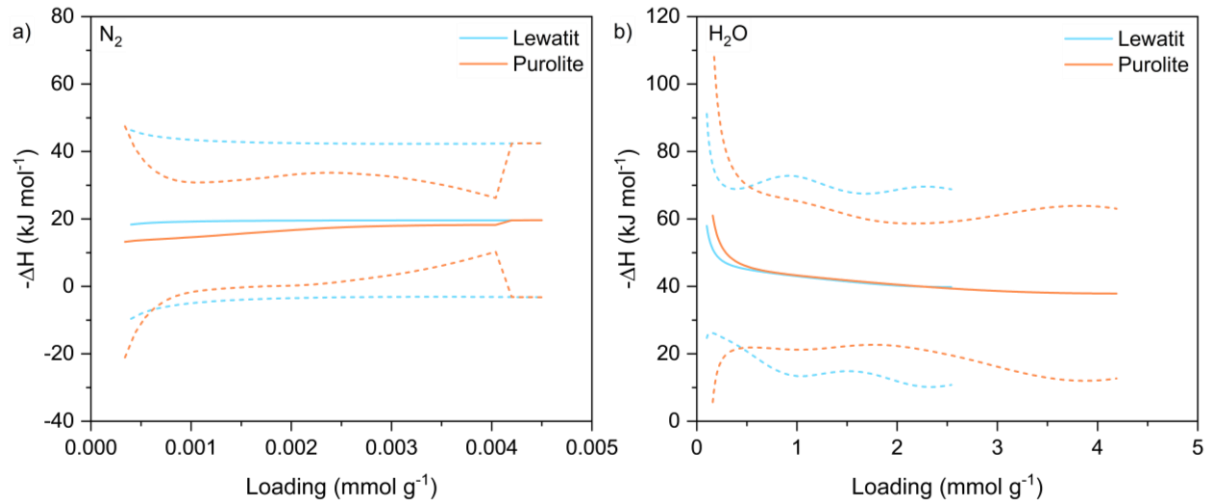


Figure A3.19. Isosteric heats of adsorption (solid lines) of Lewatit and Purolite for a) N_2 and b) H_2O with corresponding upper and lower confidence intervals (dashed lines)

A3. References

[1] R. Veneman, T. Hilbers, D. W. F. Brilman, and S. R. A. Kersten, "CO_2 capture in a continuous gas–solid trickle flow reactor," *Chemical Engineering Journal,* vol. 289, pp. 191-202, 2016, doi: 10.1016/j.cej.2015.12.066.

[2] Lanxess. "Product Information Lewatit VP OC 1065." https://lanxess.com/en/Products-and-Brands/Products/l/LEWATIT--VP-OC-1065 (accessed 202).

[3] J. Young, E. García-Díez, S. Garcia, and M. van der Spek, "The impact of binary water–CO_2 isotherm models on the optimal performance of sorbent-based direct air capture processes," *Energy & Environmental Science,* vol. 14, no. 10, pp. 5377-5394, 2021, doi: 10.1039/d1ee01272j.

[4] PennState. "6.2 The General Linear F-Test." https://online.stat.psu.edu/stat501/lesson/6/6.2 (accessed 2023).

Appendix 4. TIFISX-3-Ni study

A4.1 Physicochemical properties

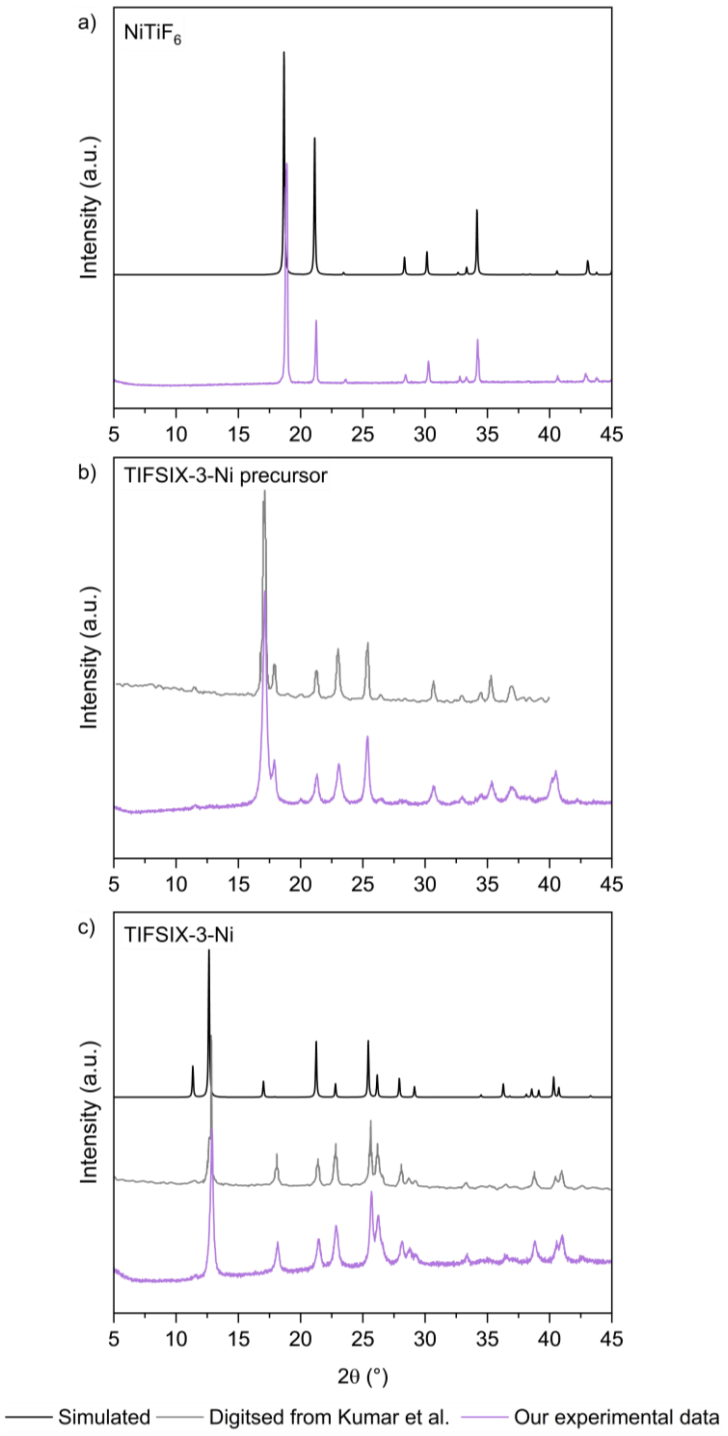


Figure A4.1. Comparison of measured XRD patterns to either simulated or digitised XRD patterns from literature for a) $NiTiF_6$, b) TIFSIX-3-Ni precursor, and c) TIFSIX-3-Ni. Simulated patterns are from the Cambridge Crystallographic Data Centre (CCDC) [1] ($NiTiF_6$: CCDC entry 404273 [2], TIFSIX-3-Ni: CCDC entry RIJGIE [3]) and digitised patterns are from Kumar et al. [3].

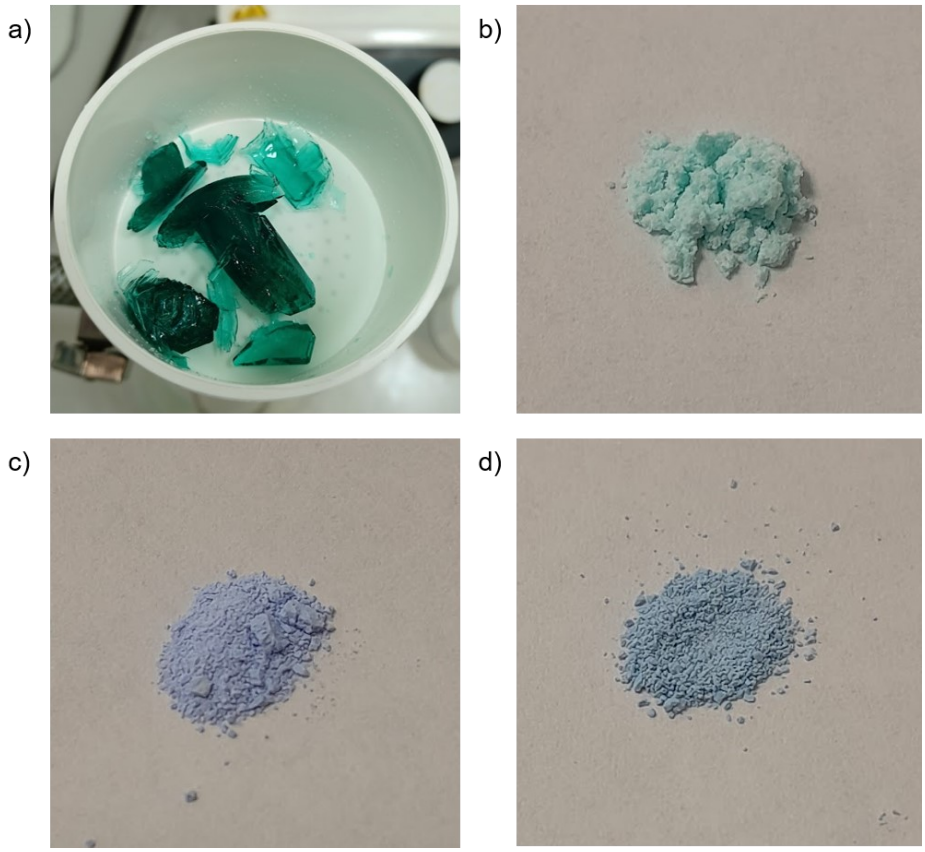


Figure A4.2. Images of a) as-synthesised $NiTiF_6$, b) ground $NiTiF_6$, c) TIFSIX-3-Ni precursor, and d) final TIFSIX-3-Ni powder.

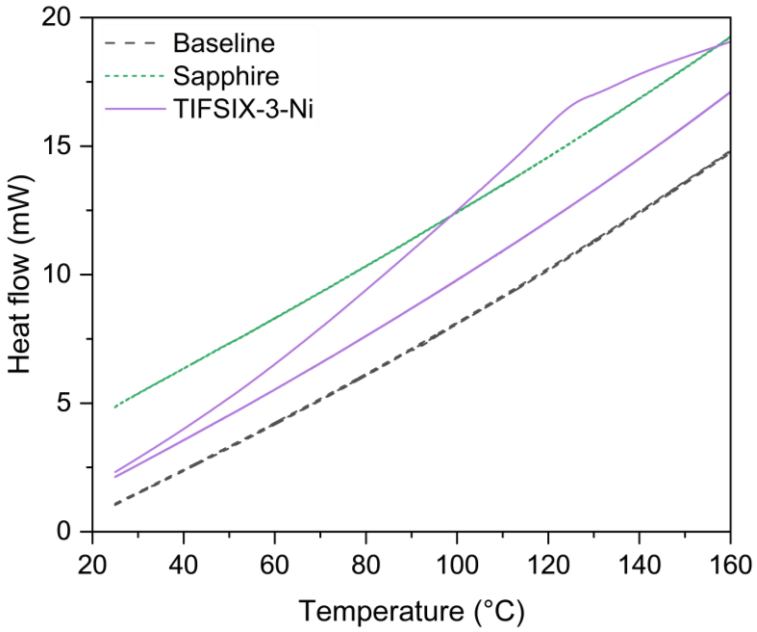


Figure A4.3. a) Heat flow curves of 3 baseline runs, 3 sapphire runs, and 4 sample runs for TIFSIX-3-Ni powder, where the first heat flow curve of the sample differs from the following three.

A4.2 Equilibrium adsorption properties

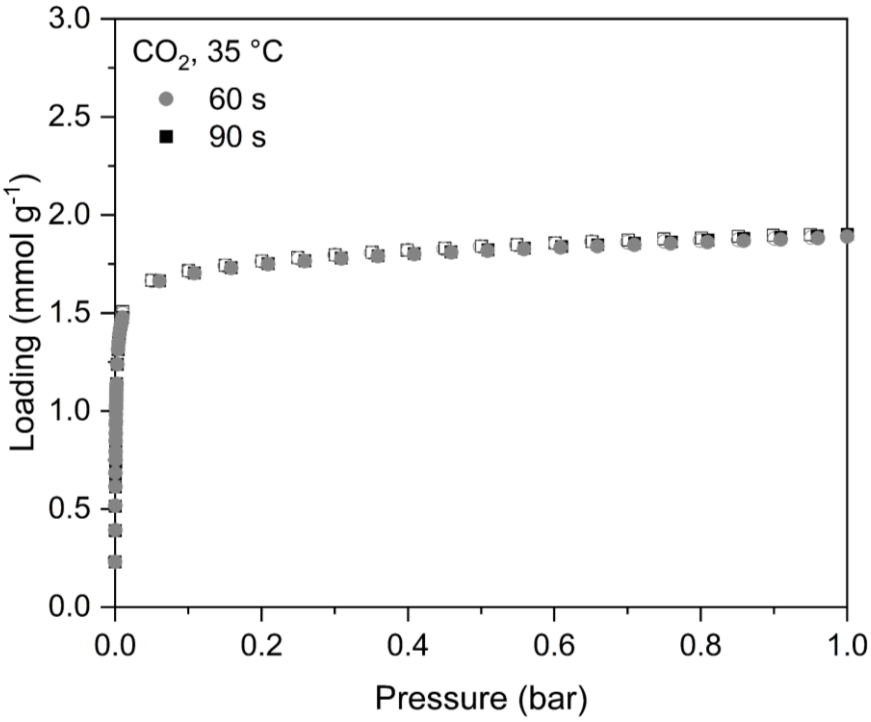


Figure A4.4. Equilibrium adsorption (filled symbols) and desorption (open symbols) isotherms of CO_2 at 35 °C for the same sample of TIFSIX-3-Ni with 60 s and 90 s equilibration intervals. Note that this is a different batch of TIFSIX-3-Ni (batch 1) from the one used to measure the CO_2 isotherms in the main study (batch 5).

TIFSIX-3-Ni theoretical loading calculations:

The following procedure was used to calculate the maximum theoretical CO_2 and H_2O loadings in TIFSIX-3-Ni:

Molecular weight of unit cell [Ni $(C_4H_4N_2)_2$ (TiF_6)]: 381 g mol^{-1} (CCDC entry RIJGIE [1, 3])

Avogadro's number: 6.022 x 10^{23} mol^{-1}

$$Mass\ of\ unit\ cell = \frac{381\ g\ mol^{-1}}{6.022\ \times\ 10^{23}} = 63.2\ \times 10^{-23} g$$

$$Number\ of\ unit\ cells\ in\ 1\ g = \frac{1}{63.2\ \times 10^{-23} g} = 0.0158\ \times 10^{23}\ g^{-1}$$

For CO_2, where one CO_2 molecule fits in a single unit cell cage:

Number of CO_2 molecules in 1 g = 0.0158 x 10^{23} g^{-1}

$$Moles\ of\ CO_2\ in\ 1\ g = \frac{0.0158\ \times 10^{23} g^{-1}}{6.022\ \times 10^{23} mol^{-1}} = 0.00263\ g\ mol^{-1} = 2.63\ g\ mmol^{-1}$$

For H_2O, where up to four H_2O molecules fit in a single unit cell cage:

$$Number\ of\ H2O\ molecules\ in\ 1\ g\ = 4 * (0.0158\ \times 10^{23}\ g^{-1}) = 0.0633\ \times 10^{23} g^{-1}$$

$$Moles\ of\ H_2O\ in\ 1\ g = \frac{0.0633\ \times 10^{23} g^{-1}}{6.022\ \times 10^{23} mol^{-1}} = 0.0105\ g\ mol^{-1} = 10.5\ g\ mmol^{-1}$$

Table A4.1. Atomic composition and molar ratio (normalised to Ni) of TIFSIX-3-Ni determined by XPS.

	C	N	O	F	Ti	Ni
Atomic composition (%)	36.7	16.6	4.7	28.8	5.4	7.8
Molar ratio (normalised to Ni)	4.7	2.1	0.6	3.7	0.7	1.0

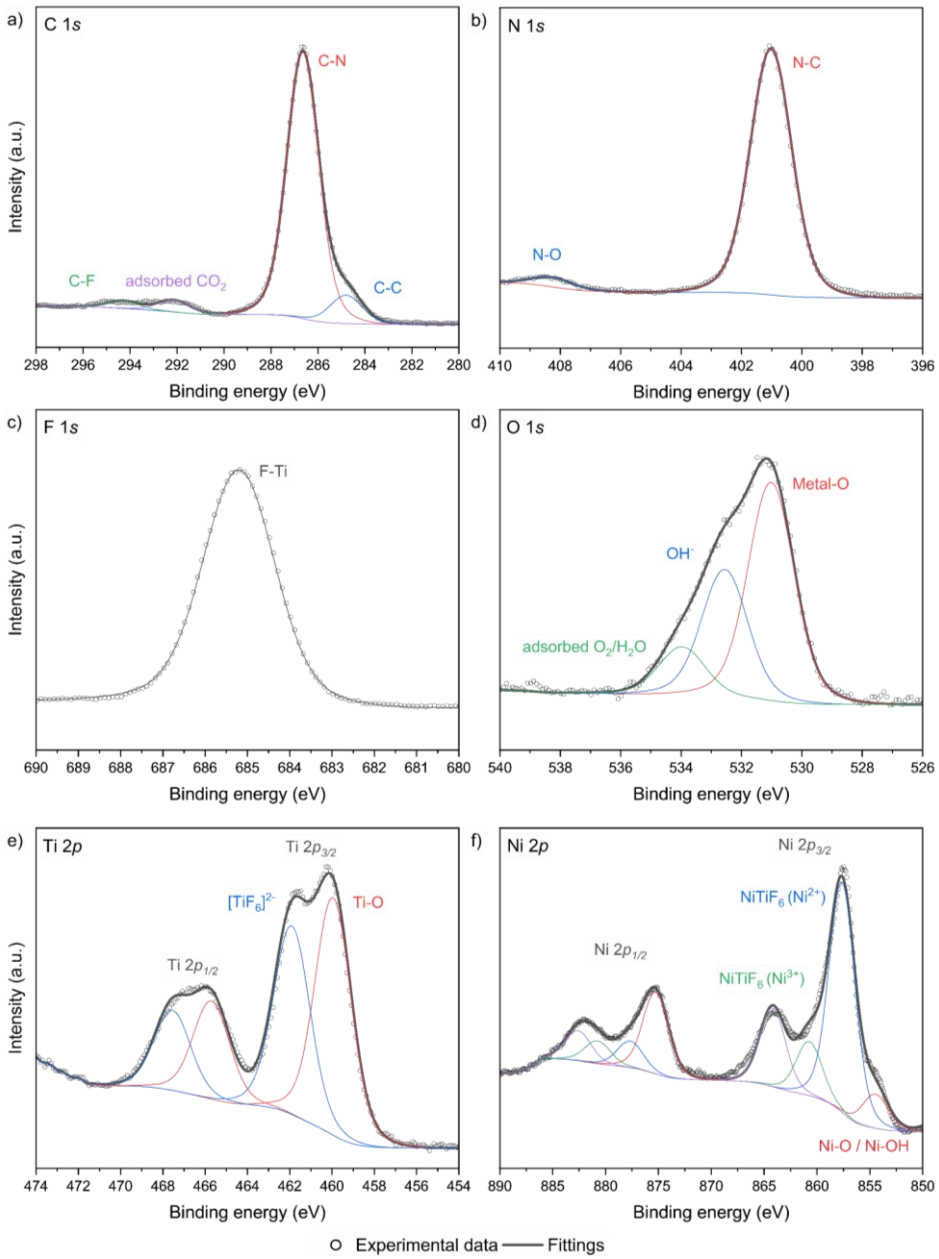


Figure A4.5. XPS data and peak fittings of the a) C 1*s*, b) N 1*s*, c) F 1*s*, d) O1*s*, e) Ti 2*p*, and f) Ni 2*p* core levels of TIFSIX-3-Ni. Peaks were assigned based on information from the NIST XPS Database [4] and the sample's structure [5].

Table A4.2. Upper and lower bounds imposed on fitting parameters for the DSL and SSL isotherm models.

Fitting equation	Parameter	Units	Lower bound	Upper bound
DSL	q_{s1}	mmol g^{-1}	0	30
	$b_{0,1}$	bar^{-1}	0	0.001
	$-\Delta U_1$	kJ mol^{-1}	0	100
	q_{s1}	mmol g^{-1}	0	30
	$b_{0,2}$	bar^{-1}	0	0.001
	$-\Delta U_2$	kJ mol^{-1}	0	100
SSL	q_s	mmol g^{-1}	0	30
	b_0	bar^{-1}	0	0.001
	$-\Delta U$	kJ mol^{-1}	0	100

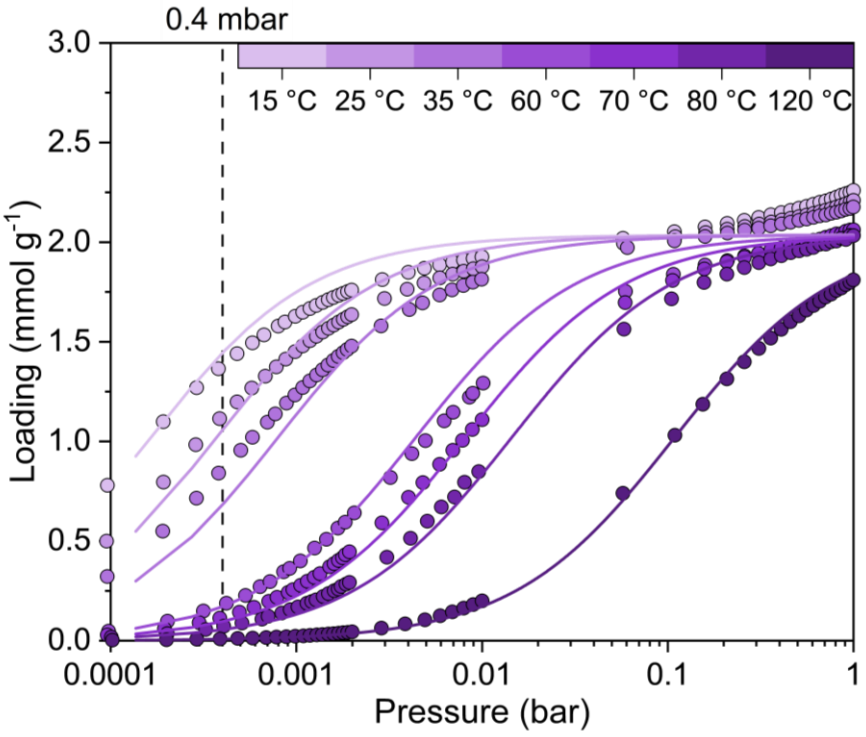


Figure A4.6. Equilibrium adsorption isotherms for CO_2, with a log-scale of pressure measured, at 15, 25, 35, 60, 70, 80, and 120 °C up to 1 bar for TIFSIX-3-Ni powder. Solid lines represent the fitting results from the SSL isotherm model, whose fitting parameters are found in Table A4.3.

Table A4.3. Fitting parameters with uncertainty bounds for a 95% confidence interval for the SSL isotherm model for CO_2 adsorption on TIFSIX-3-Ni.

Adsorbate	**Equation**	**Parameter**	**Unit**	**TIFSIX-3-Ni**
CO_2	SSL	q_s	mmol g^{-1}	2.04 ± 0.02
		b_0	$(\times 10^{-7})$ bar^{-1}	1.68 ± 0.08
		$-\Delta H$	kJ mol^{-1}	58.3 ± 0.1

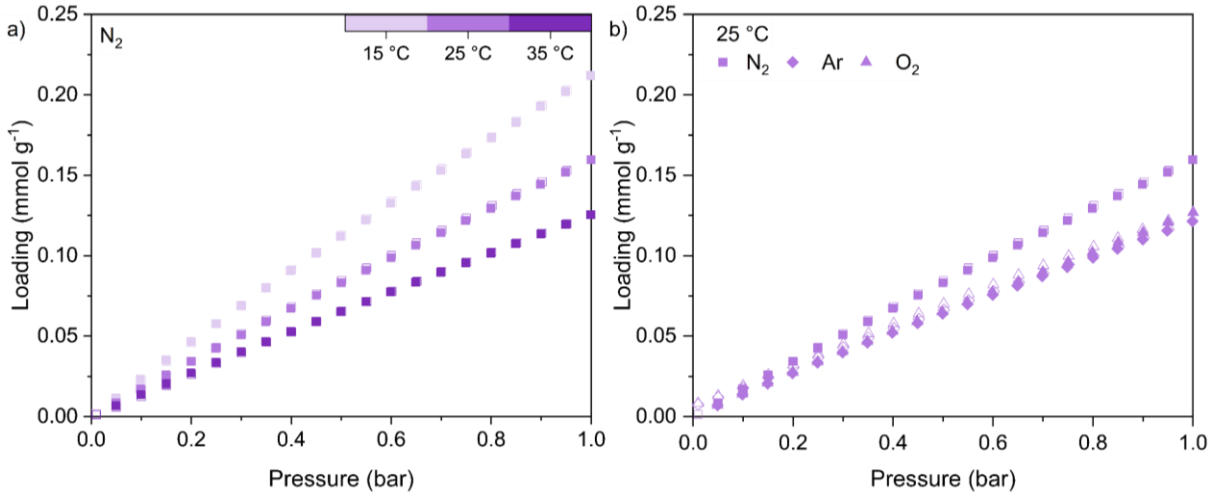


Figure A4.7. a) Equilibrium adsorption (filled symbols) and desorption (open symbols) isotherms for a) N_2 measured at 15 °C, 25 °C, and 35 °C up to 1 bar, and b) N_2, Ar, and O_2 measured at 25 °C up to 1 bar.

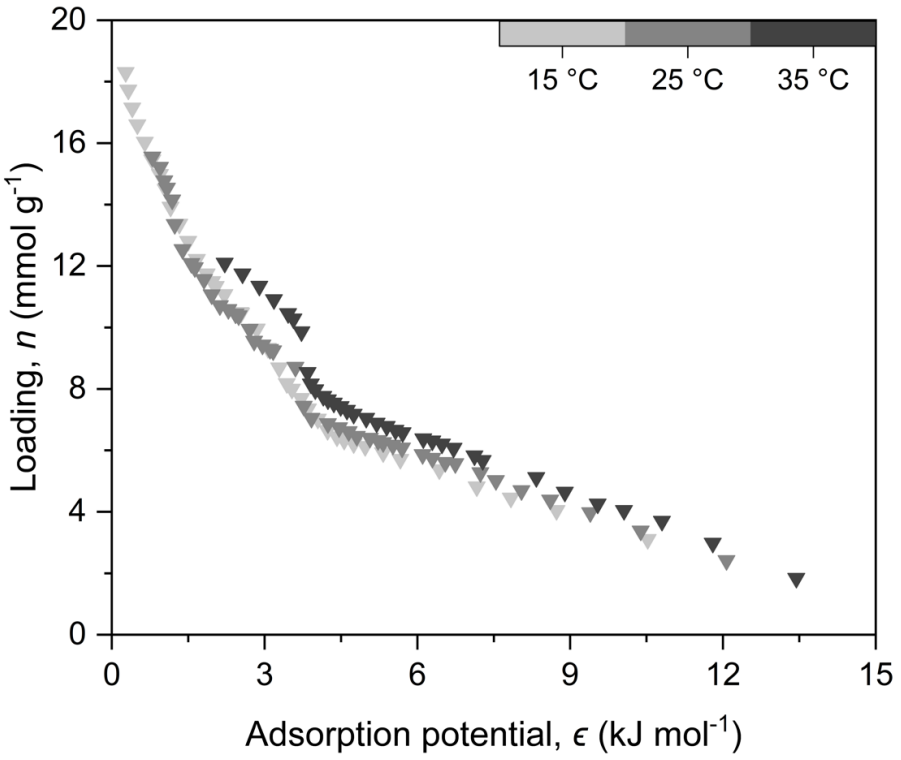


Figure A4.8. H_2O adsorption potential for TIFSIX-3-Ni plotted against the H_2O loading.

Table A4.4. Upper and lower bounds imposed on fitting parameters for the UNIV6 isotherm model. For this fitting procedure, the inverse of the adsorption equilibrium constant *K* was solved for and then converted to the final *K* value post-fitting. The bounds were also updated after every iteration with the initial and final bounds presented here. This was done as the magnitudes for the ε parameters and correspondingly the *m* parameters can vary drastically. The same initial bounds are set for all ε and *m* parameters and following the initial fitting, the upper and lower bounds are updated around the initial estimates (± 50%) and the parameter estimation is repeated by consequently updating the bounds, until the error between subsequent estimations is unchanged.

Parameter	**Units**	**Initial bounds**		**Final bounds**	
		Lower bound	Upper bound	Lower bound	Upper bound
q_s	mmol g^{-1}	0	100	18.301	119.28
α_1	-	0	1	0	1
α_2	-	0	1	0	1
α_3	-	0	1	0	1
ε_1	kJ mol^{-1}	0	0.0115129	0.21218	9688.0
ε_2	kJ mol^{-1}	0	0.0115129	0.18113	6041.1
ε_3	kJ mol^{-1}	0	0.0115129	0.19261	7257.8
ε_4	kJ mol^{-1}	0	0.0115129	0.17640	5583.3
m_1	kJ mol^{-1}	0	1	1.3451	4.0353
m_2	kJ mol^{-1}	0	1	0.29558	0.88675
m_3	kJ mol^{-1}	0	1	0.0028251	0.084754
m_4	kJ mol^{-1}	0	1	1.4323	4.2969
1/K	bar	0	0.15	16.451	4.4603×10^7

Table A4.5. Fitting parameters with uncertainty bounds for a 95% confidence interval for the UNIV6 isotherm model for H_2O adsorption for TIFSIX-3-Ni determined using experimental isotherm data only at 15 °C and 25 °C. For this fitting procedure, the inverse of the adsorption equilibrium constant *K* was solved for and will need to be converted to the final *K* value post-fitting.

Parameter	**Unit**	**TIFSIX-3-Ni**	**Initial bounds**		**Final bounds**	
			Lower bound	Upper bound	Lower bound	Upper bound
q_s	mmol g^{-1}	34.299 ± 0.4134	0	100	18.301	51.449
α_1	-	0.22737 ± 0.00745	0	1	0	1
α_2	-	0.69133 ± 0.00584	0	1	0	1
α_3	-	0.018041 ± 0.006288	0	1	0	1
ε_1	kJ mol^{-1}	51.397 ± 0.364	0	0.0115129	0.22571	11653
ε_2	kJ mol^{-1}	41.715 ± 0.051	0	0.0115129	0.20324	8520.2
ε_3	kJ mol^{-1}	43.267 ± 0.000	0	0.0115129	0.20701	9000.2
ε_4	kJ mol^{-1}	45.553 ± 0.198	0	0.0115129	0.21243	9722.8
m_1	kJ mol^{-1}	3.2648 ± 0.2670	0	1	1.6324	4.8972
m_2	kJ mol^{-1}	0.99795 ± 0.03845	0	1	0.49898	1.4969
m_3	kJ mol^{-1}	0.0014329 ± 0.0141271	0	1	0.00071643	0.0021493
m_4	kJ mol^{-1}	0.26840 ± 0.16651	0	1	0.13420	0.40260
1/K	bar	$7.4650 \times 10^5 \pm 0.1120 \times 10^5$	0	0.15	86.390	6.4498×10^9

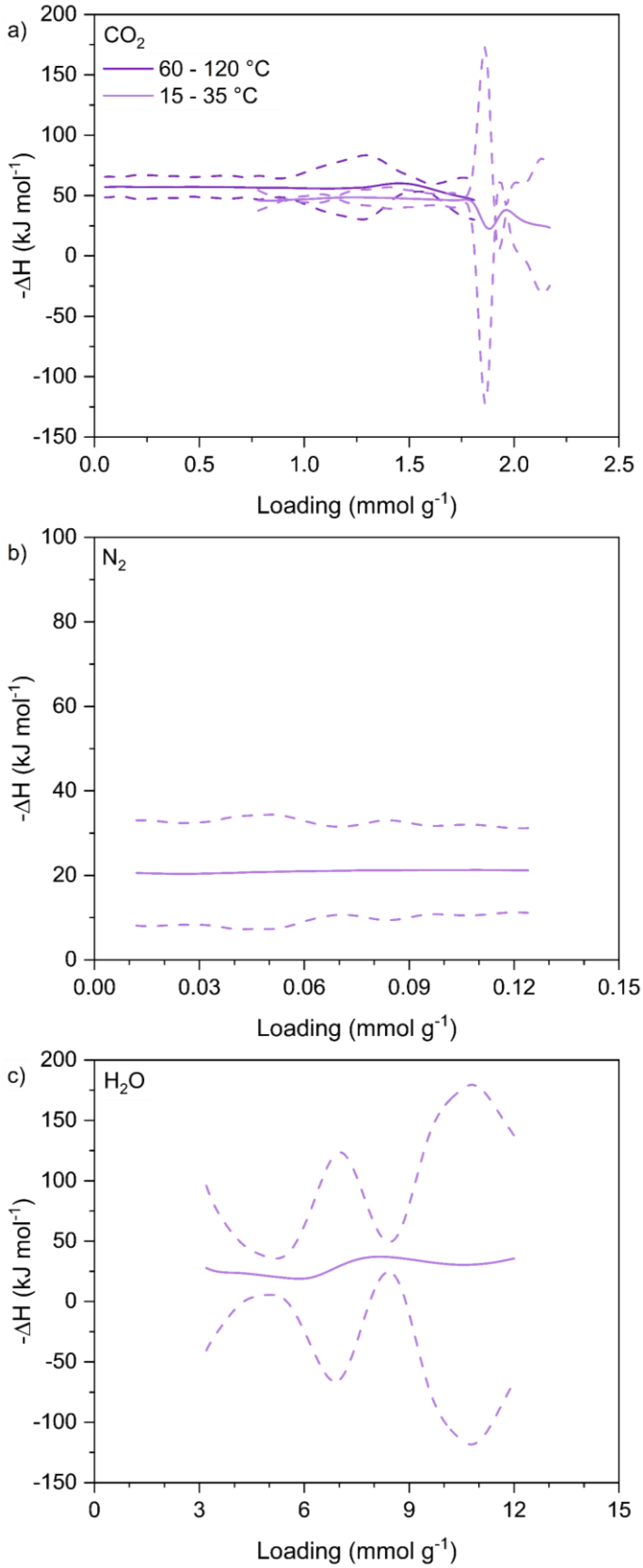


Figure A4.9. a) Isosteric heats of adsorption (solid lines) for a) CO_2 calculated using isotherm data measured at 60 °C, 70 °C, 80 °C and 120 °C, and 15 °C, 25 °C, and 35 °C, and for b) N_2 and c) H_2O, with corresponding 95% upper and lower confidence intervals (dashed lines).

Table A4.6. Smoothing spline values used in MATLAB for the interpolation of CO_2, N_2, and H_2O data to calculate the corresponding isosteric heats of adsorption for TIFSIX-3-Ni.

Adsorbate	**Smoothing values**
CO_2	0.999995
N_2	0.999999
H_2O	0.95

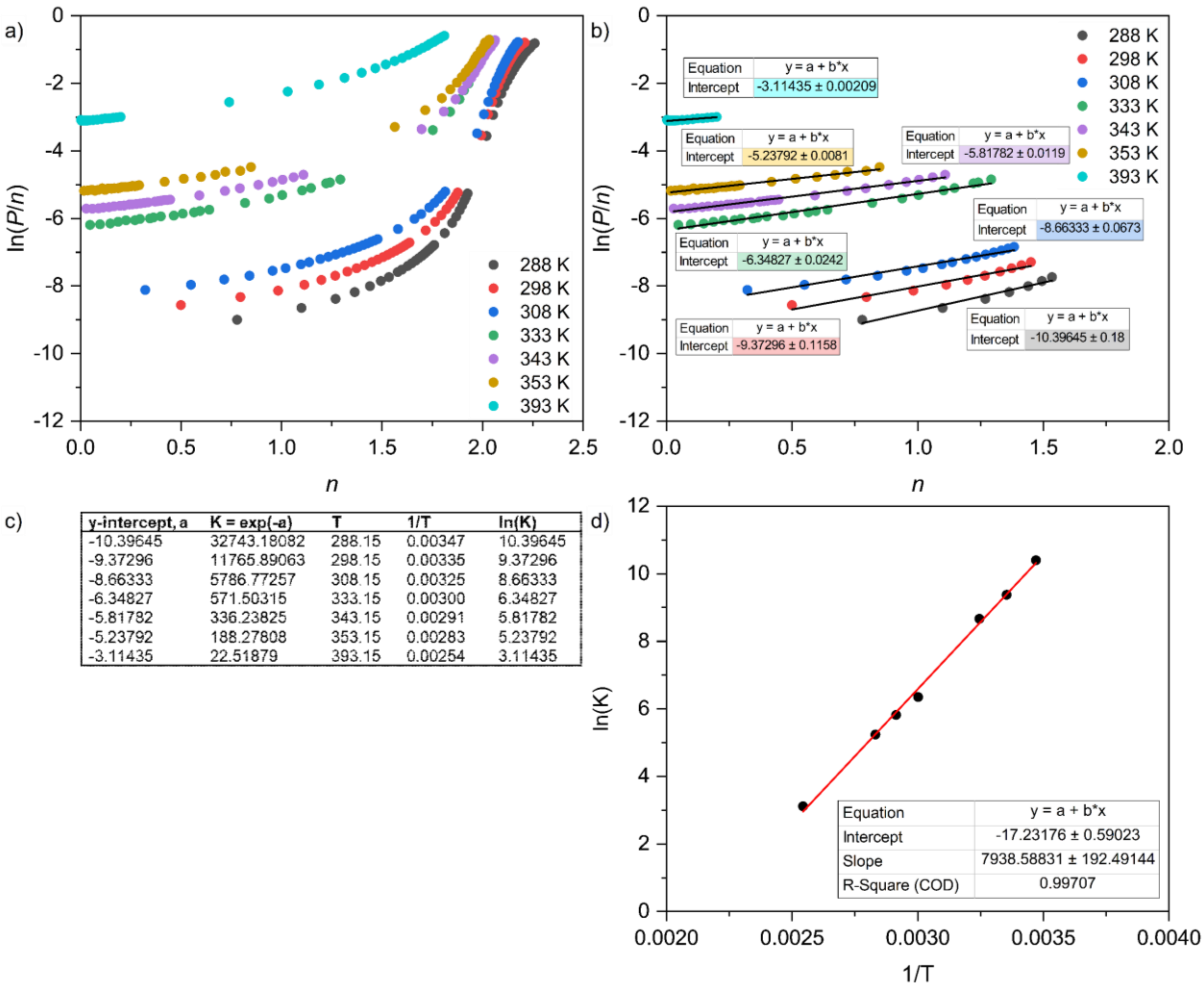
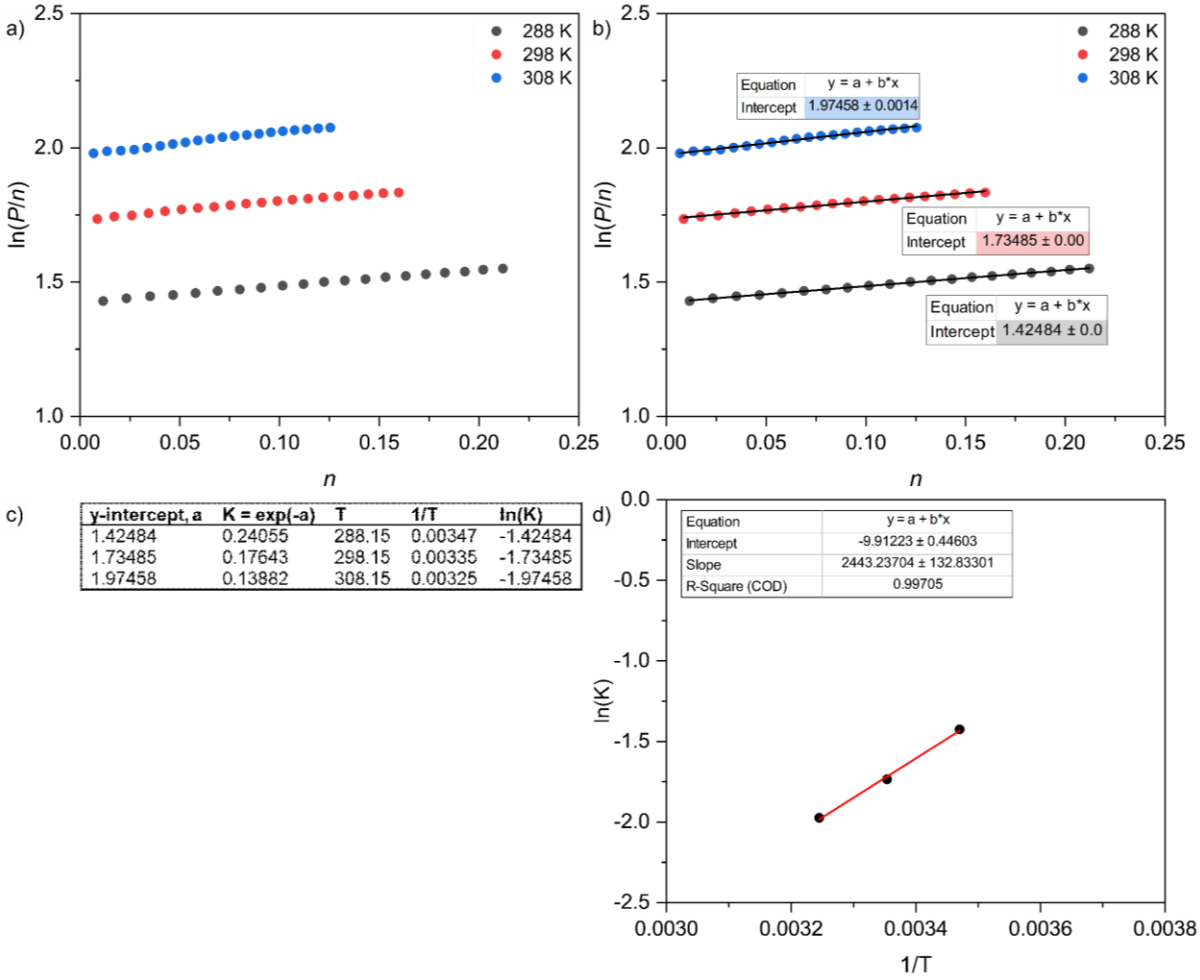
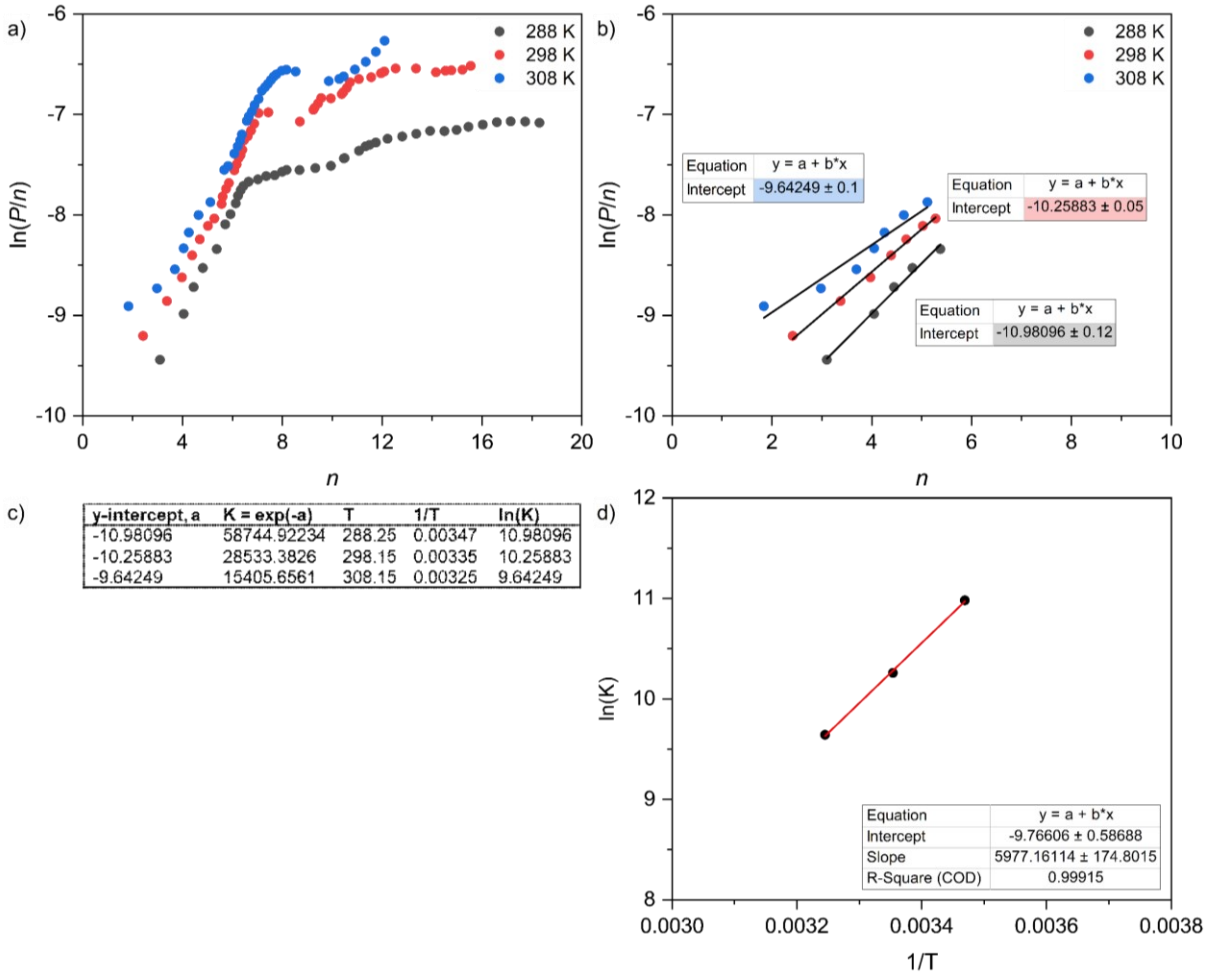


Figure A4.10. a) Virial plot of all measured CO_2 isotherm data for TIFSIX-3-Ni, where pressure (P), loading (n), and temperature (T) values are in units of bar, mmol g^{-1}, and Kelvin, respectively. b) Virial plot showing the selected low loading data fitted to linear equations. The y-intercepts of each fitted equation are used to calculate the Henry constant K. c) Summary of fitted and calculated parameters used to determine ΔH_0. d) Plot of ln$K$ vs. $1/T$ fitted to a linear equation, whose slope is used to calculate ΔH_0.



y-intercept, a	K = exp(-a)	T	1/T	ln(K)
1.42484	0.24055	288.15	0.00347	-1.42484
1.73485	0.17643	298.15	0.00335	-1.73485
1.97458	0.13882	308.15	0.00325	-1.97458

Figure A4.11. a) Virial plot of all measured N_2 isotherm data for TIFSIX-3-Ni, where pressure (P), loading (n), and temperature (T) values are in units of bar, mmol g^{-1}, and Kelvin, respectively. b) Virial plot showing the selected low loading data fitted to linear equations. The y-intercepts of each fitted equation are used to calculate the Henry constant K. c) Summary of fitted and calculated parameters used to determine ΔH_0. d) Plot of ln$K$ vs. $1/T$ fitted to a linear equation, whose slope is used to calculate ΔH_0.



y-intercept, a	K = exp(-a)	T	1/T	ln(K)
-10.98096	58744.92234	288.25	0.00347	10.98096
-10.25883	28533.3826	298.15	0.00335	10.25883
-9.64249	15405.6561	308.15	0.00325	9.64249

Figure A4.12. a) Virial plot of all measured H_2O isotherm data for TIFSIX-3-Ni, where pressure (P), loading (n), and temperature (T) values are in units of bar, mmol g^{-1}, and Kelvin, respectively. b) Virial plot showing the selected low loading data fitted to linear equations. The y-intercepts of each fitted equation are used to calculate the Henry constant K. c) Summary of fitted and calculated parameters used to determine ΔH_0. d) Plot of ln$K$ vs. $1/T$ fitted to a linear equation, whose slope is used to calculate ΔH_0.

A4.3 Manufacturing considerations

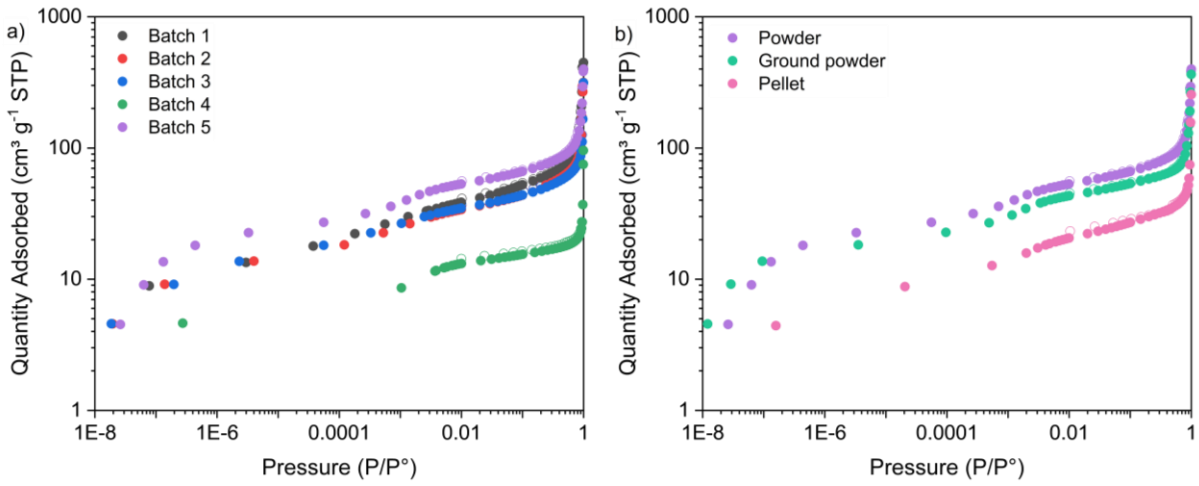


Figure A4.13. N_2 adsorption (filled symbols) and desorption (open symbols) isotherms at -196 °C with log-scale of pressure and loading for a) different batches of TIFSIX-3-Ni and b) TIFSIX-3-Ni powder, ground powder, and pellet (batch 5).

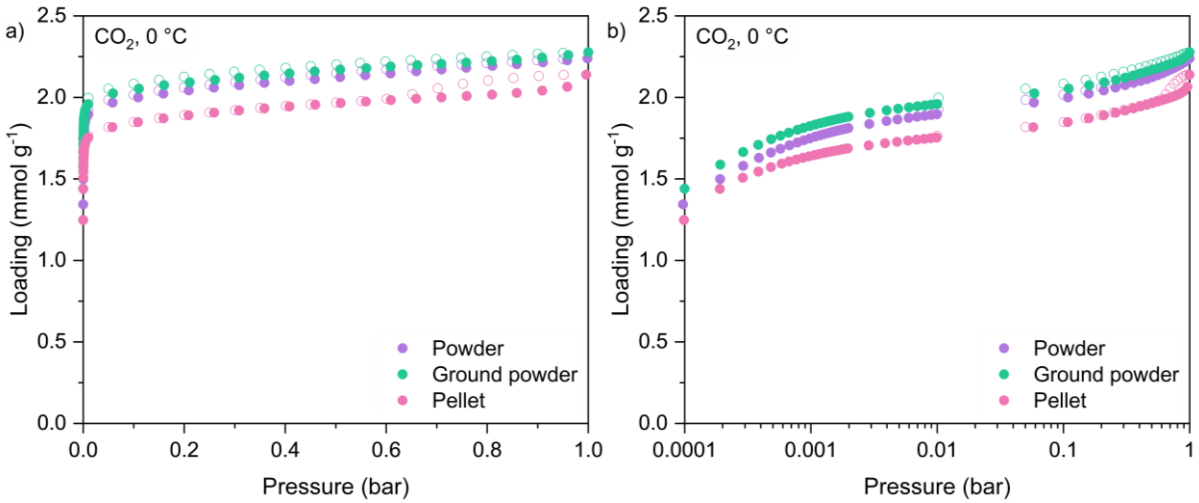


Figure A4.14. CO_2 adsorption (filled symbols) and desorption (open symbols) isotherms at 0 °C with a) linear and b) log-scale of pressure for batch 5 TIFSIX-3-Ni powder, ground powder, and pellet.

Table A4.7. Comparison of textural properties of batch 5 TIFSIX-3-Ni powder, ground powder, and pellet determined using N_2 adsorption isotherms measured at -196 °C and CO_2 adsorption isotherms measured at 0 °C.

TIFSIX-3-Ni	N_2 -196 °C			CO_2 0 °C		
	S_{BET} ($m^2\ g^{-1}$)	$V_{micropores}$ ($cm^3\ g^{-1}$)	$V_{total\ pores}$ ($cm^3\ g^{-1}$)	S_{BET} ($m^2\ g^{-1}$)	$V_{micropores}$ ($cm^3\ g^{-1}$)	$V_{total\ pores}$ ($cm^3\ g^{-1}$)
Powder	264	0.11	0.50	183	0.10	-
Ground powder	213	0.09	0.41	186	0.10	-
Pellet	106	0.06	0.24	170	0.09	-

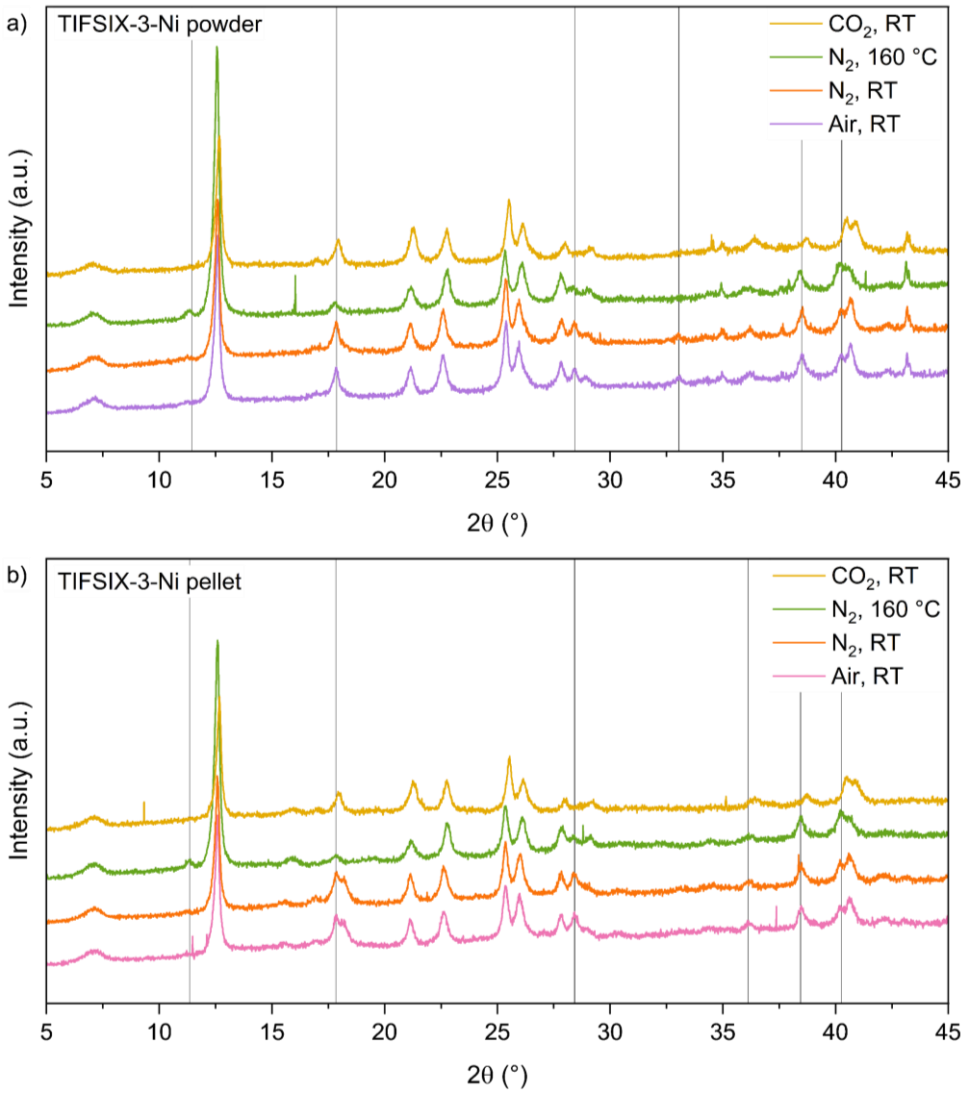


Figure A4.15. In-situ XRD patterns of batch 5 TIFSIX-3-Ni a) powder and b) pellet under different gas flows and temperatures. Vertical lines are included to help visualize the changes in the patterns.

A4.3. Adsorbent stability under process conditions

Table A4.8. Images of the colours of batch 5 TIFSIX-3-Ni powder samples after exposure to different humidity conditions and subsequent characterisations.

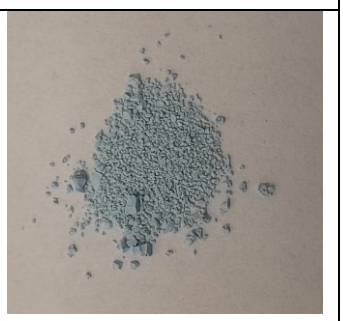
	Situation	1 Initial appearance	2 Appearance after ex-situ degas at 160 °C	3 Appearance after CO_2 25 °C isotherm measurement
A	As synthesised (batch 5)			
B	Exposure to H_2O (25 °C, 15% RH)	Similar to C1	Similar to A2	
C	Exposure to H_2O (25 °C, 48% RH)		Similar to A2	
D	Exposure to H_2O (25 °C, 77% RH)	Similar to C1	Similar to A2	

Table A4.9. Atomic composition and molar ratio (normalised to Ni) of TIFSIX-3-Ni samples (as synthesised, after H_2O exposure, and after air exposure) determined by XPS.

	TIFSIX-3-Ni sample	**C**	**N**	**O**	**F**	**Ti**	**Ni**
Atomic composition (%)	As-synthesised	36.7	16.6	4.7	28.8	5.4	7.8
	After exposure to H_2O (25 °C, 77% RH)	32.4	14.5	5.8	32.7	6.1	8.6
	After exposure to ambient air (6 months)	29.8	13	8.7	32.4	7.1	8.9
Molar ratio (normalised to Ni)	As-synthesised	4.7	2.1	0.6	3.7	0.7	1.0
	After exposure to H_2O (25 °C, 77% RH)	3.8	1.7	0.7	3.8	0.7	1.0
	After exposure to ambient air (6 months)	3.3	1.5	1.0	3.6	0.8	1.0

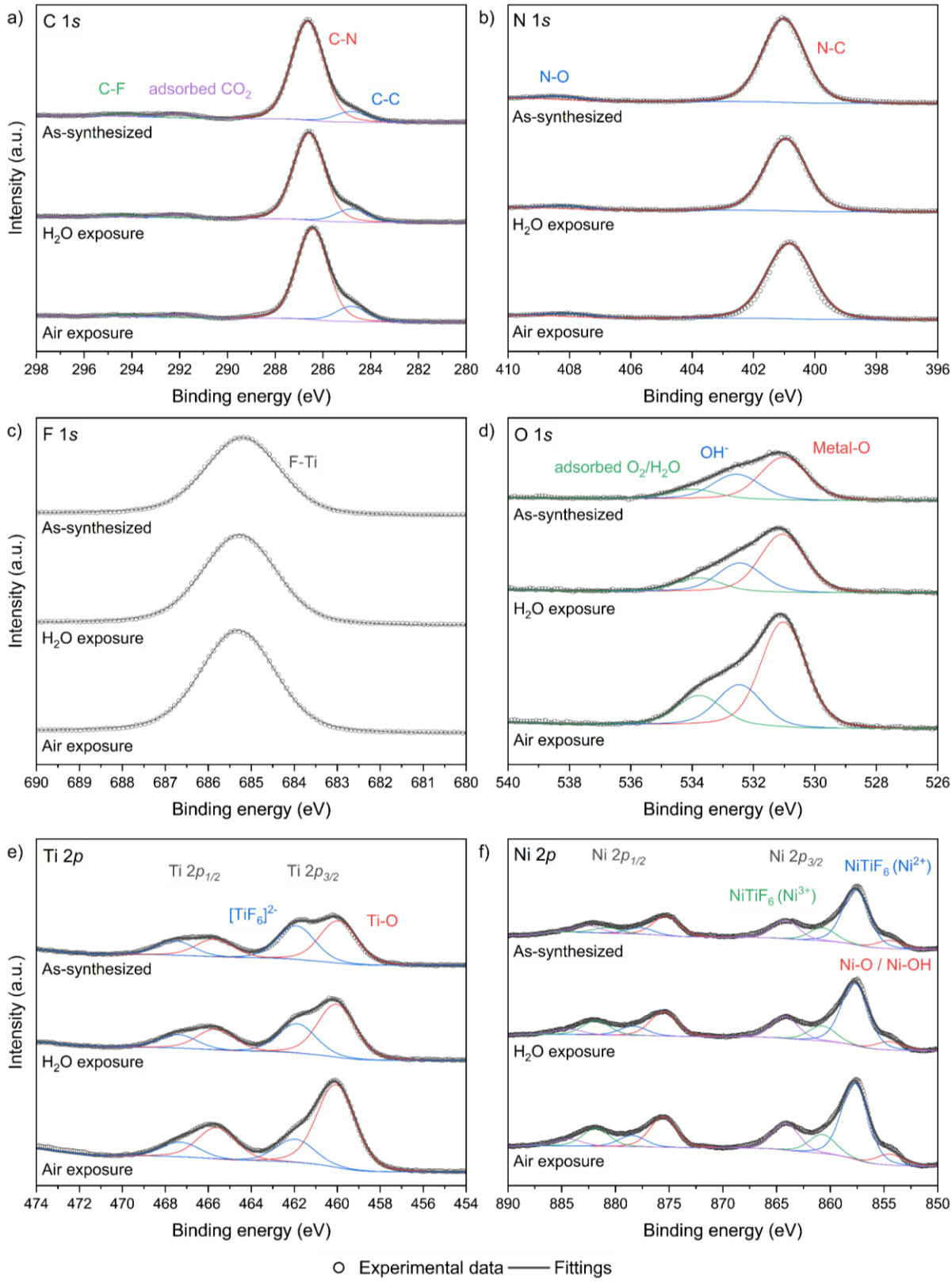


Figure A4.16. XPS data and peak fittings of the a) C 1*s*, b) N 1*s*, c) F 1*s*, d) O1*s*, e) Ti 2*p*, and f) Ni 2*p* core levels of TIFSIX-3-Ni samples (as synthesised, after H_2O exposure, and after air exposure). Peaks were assigned based on information from the NIST XPS Database [4] and the sample's structure [5].

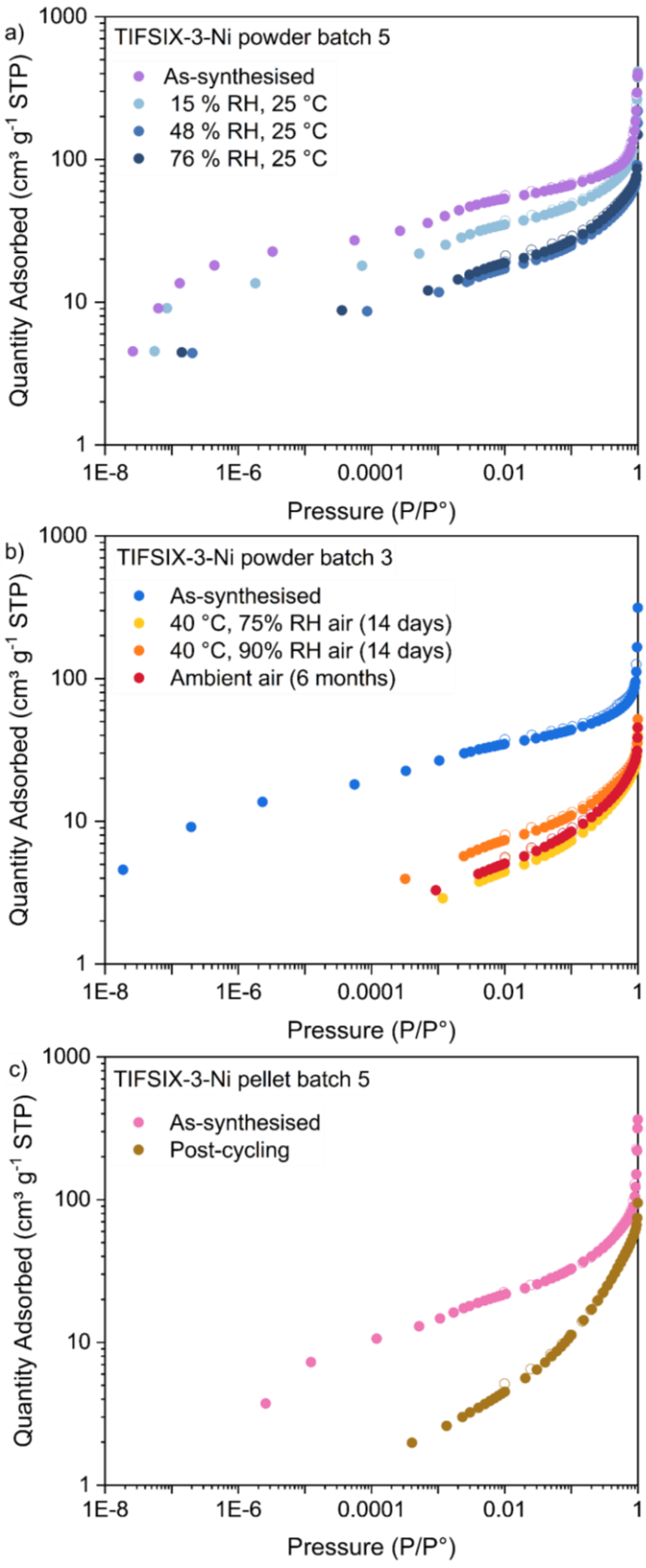
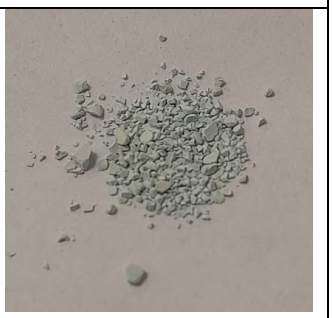
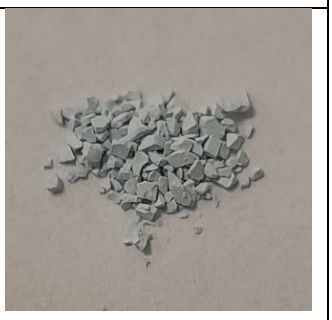


Figure A4.17. N_2 adsorption (filled symbols) and desorption (open symbols) isotherms at -196 °C with log-scale of pressure for a) batch 5 TIFSIX-3-Ni powder exposed to H_2O, b) batch 3 TIFSIX-3-Ni powder exposed to H_2O and O_2, and c) batch 5 TIFSIX-3-Ni pellet before and after cycling.

Table A4.10. Images of the colors of batch 3 TIFSIX-3-Ni powder samples after exposure to different humidity conditions in air and subsequent characterisations.

		4	5	6
	Situation	Initial appearance	Appearance after ex-situ degas at 160 °C	Appearance after CO_2 25 °C isotherm measurement
E	As-synthesised (batch 3)		Similar to Table A4.8 A2	Similar to E4
F	Exposure to air (40 °C, 75% RH, 14 days)		Similar to Table A4.8 A2	
G	Exposure to air (40 °C, 90% RH, 14 days)		Similar to Table A4.8 A2	
H	Exposure to ambient air from the laboratory for 6 months		Similar to Table A4.8 A2	

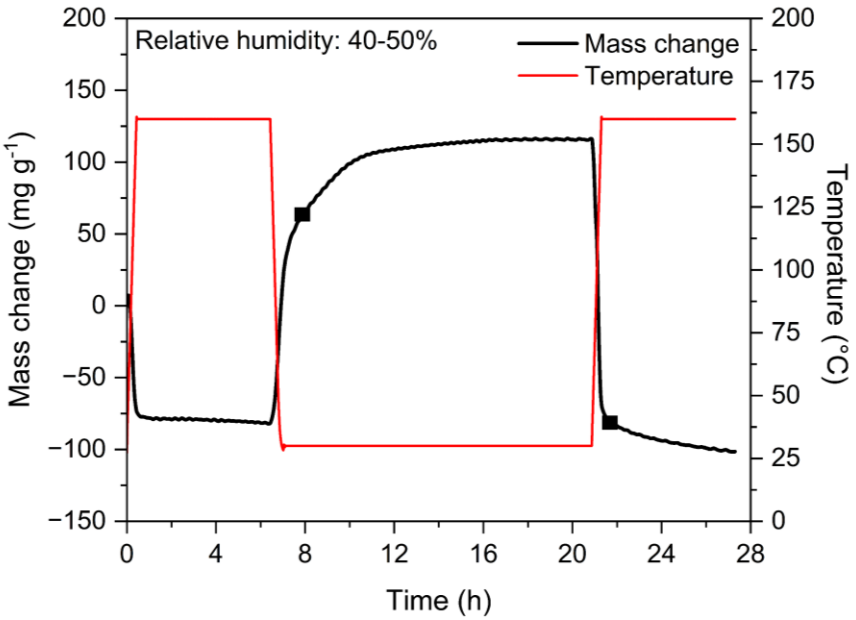


Figure A4.18. Mass change of batch 5 TIFSIX-3-Ni pellets over the course of a desorption-adsorption-desorption cycle under a flow of ambient air from the laboratory carried out using a thermogravimetric analyser. Black squares indicate the cut-off times used for adsorption and desorption segments in the cyclic experiment.

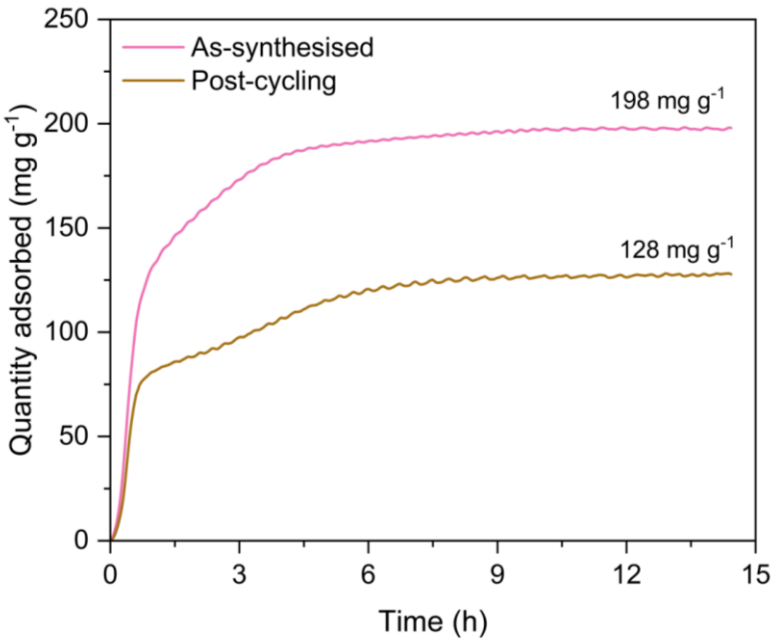


Figure A4.19. Comparison of the amount of gas adsorbed under a flow of ambient air by as-synthesised batch 5 TIFSIX-3-Ni pellets and TIFSIX-3-Ni pellets which have undergone 50 cycles of adsorption at 30 °C for 1 h and desorption at 160 °C for 15 min using a thermogravimetric analyser.

A4. References

[1] "Cambridge Crystallographic Data Centre." https://www.ccdc.cam.ac.uk/ (accessed 2024).

[2] P. Halasyamani, M. J. Willis, C. L. Stern, and K. R. Poeppelmeier, "Crystal growth in aqueous hydrofluoric acid and (HF)x · pyridine solutions: syntheses and crystal structures of $[Ni(H_2O)_6]^{2+}[MF_6]^{2-}$ (M = Ti, Zr, Hf) and $Ni_3(py)_{12}F_6 \cdot 7H_2O$," *Inorganica Chimica Acta,* vol. 240, no. 1-2, pp. 109-115, 1995, doi: 10.1016/0020-1693(95)04650-x.

[3] A. Kumar *et al.*, "Hybrid ultramicroporous materials (HUMs) with enhanced stability and trace carbon capture performance," *Chem Commun (Camb),* vol. 53, no. 44, pp. 5946-5949, May 30 2017, doi: 10.1039/c7cc02289a.

[4] A. V. Naumkin, A. Kraut-Vass, S. W. Gaarenstroom, C. J. Powell, and A. Y. Lee. "NIST X-ray Photoelectron Spectroscopy Database." https://srdata.nist.gov/xps/ (accessed 2024).

[5] V. V. Korochentsev and N. M. Laptash, "Intermetallic charge transfer in $MTiF_6 \cdot 6H_2O$ (M = Mn, Fe, Co, and Ni): A study by X-ray photoelectron spectroscopy," *Solid State Sciences,* vol. 148, 2024, doi: 10.1016/j.solidstatesciences.2023.107433.

Appendix 5. Functionalised zeolites study

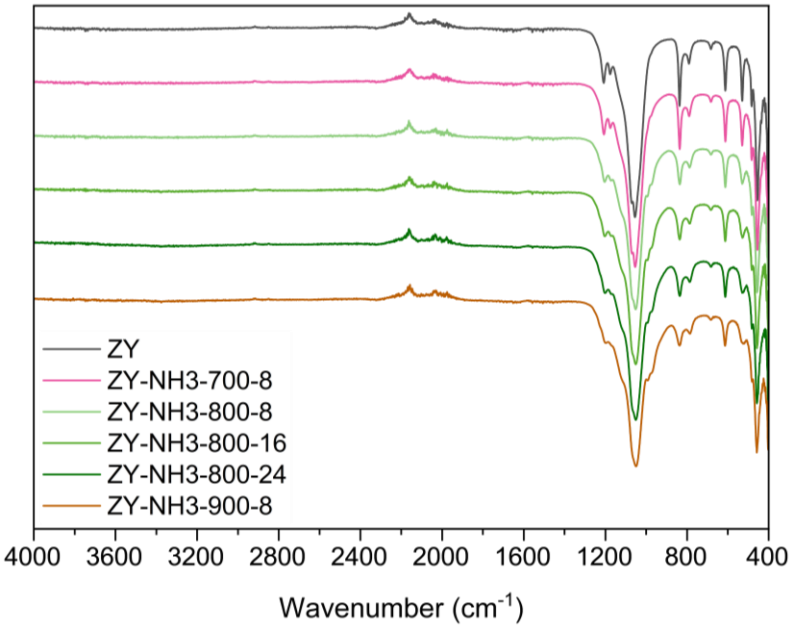


Figure A5.1. FTIR spectra for ZY samples functionalised with NH_3 from 400 to 4000 cm^{-1}.

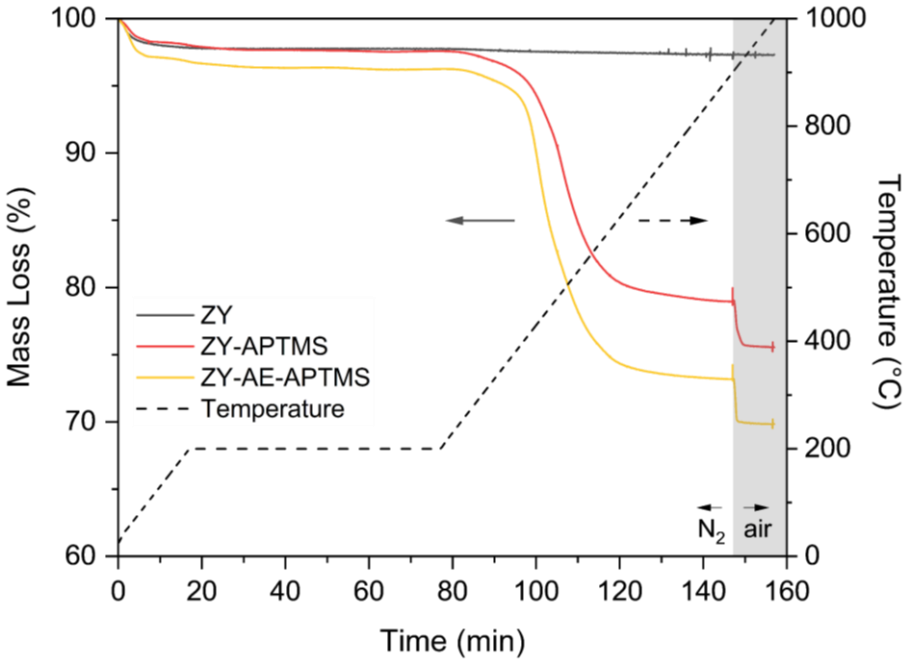


Figure A5.2. TG curves of ZY, ZY-APTMS and ZY-AE-APTMS samples.

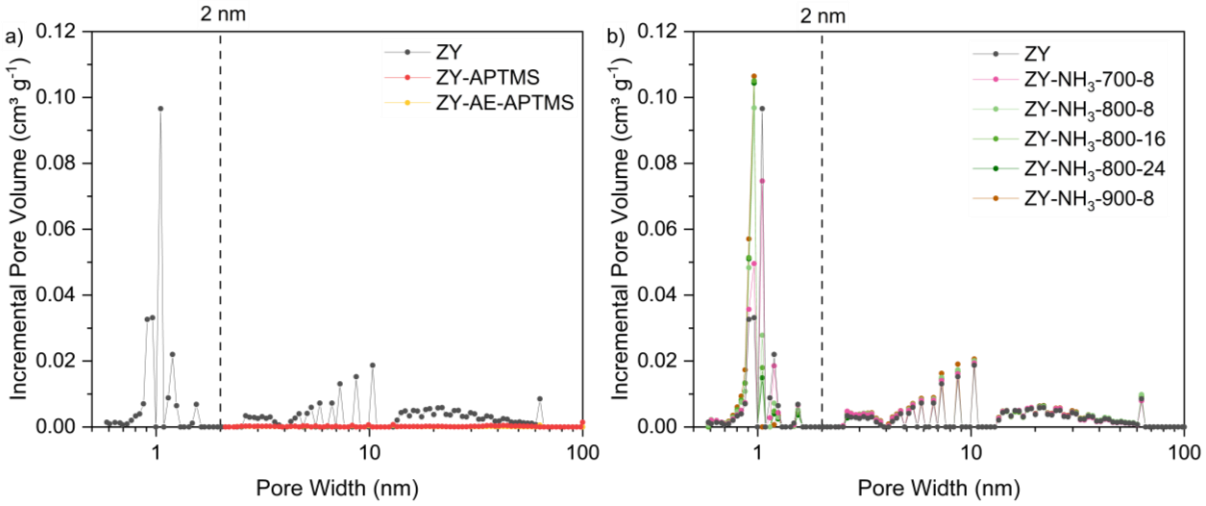


Figure A5.3. Pore size distributions for a) aminosilane-functionalised and b) ZY-NH_3 functionalised samples.

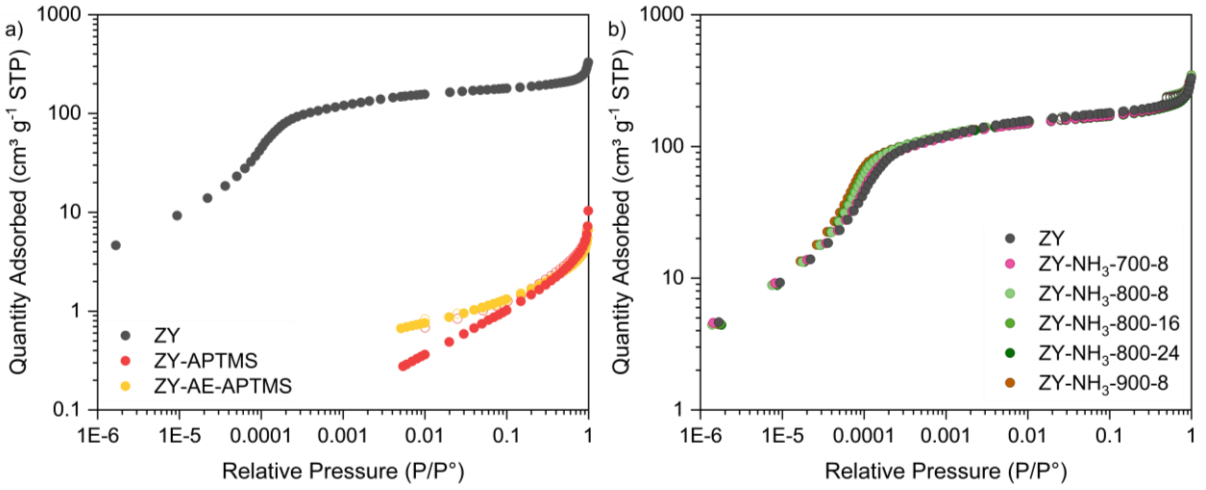


Figure A5.4. Equilibrium adsorption (filled symbols) and desorption (hollow symbols) isotherms for N_2 measured at -196 °C with a log-scale of pressure for a) aminosilane-functionalised samples and b) ZY-NH_3 functionalised samples.

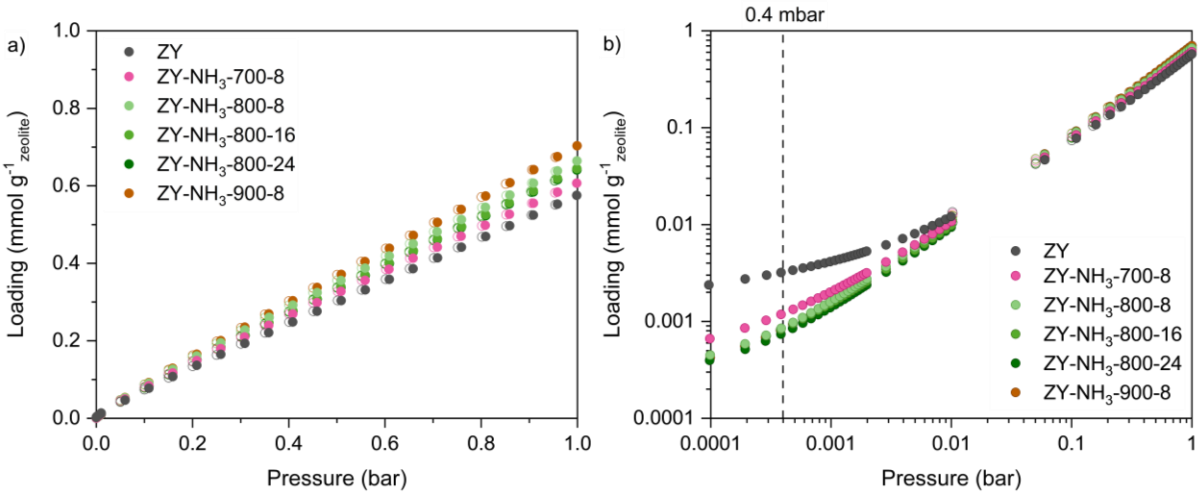


Figure A5.5. Equilibrium adsorption (filled symbols) and desorption (hollow symbols) isotherms for CO_2 measured at 25 °C up to 1 bar for ZY-NH_3 samples with a) linear and b) log-scales of pressure. CO_2 loadings are presented per gram of zeolite rather than per gram of sample.

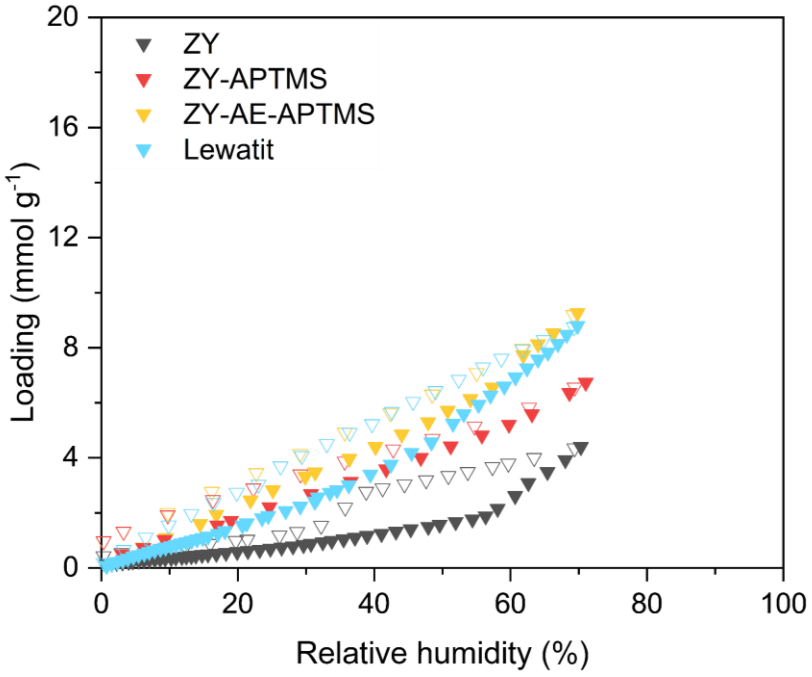


Figure A5.6. Comparison of H_2O equilibrium adsorption (filled symbols) and desorption (hollow symbols) isotherms measured at 25 °C for aminosilane-functionalised samples and Lewatit [1].

A5. References

[1] M.-Y. Low, D. Danaci, H. Azzan, R. T. Woodward, and C. Petit, "Measurement of Physicochemical Properties and CO_2, N_2, Ar, O_2, and H_2O Unary Adsorption Isotherms of Purolite A110 and Lewatit VP OC 1065 for Application in Direct Air Capture," *J Chem Eng Data,* vol. 68, no. 12, pp. 3499-3511, Dec 14 2023, doi: 10.1021/acs.jced.3c00401.

Appendix 6. CO_2 adsorption kinetics study

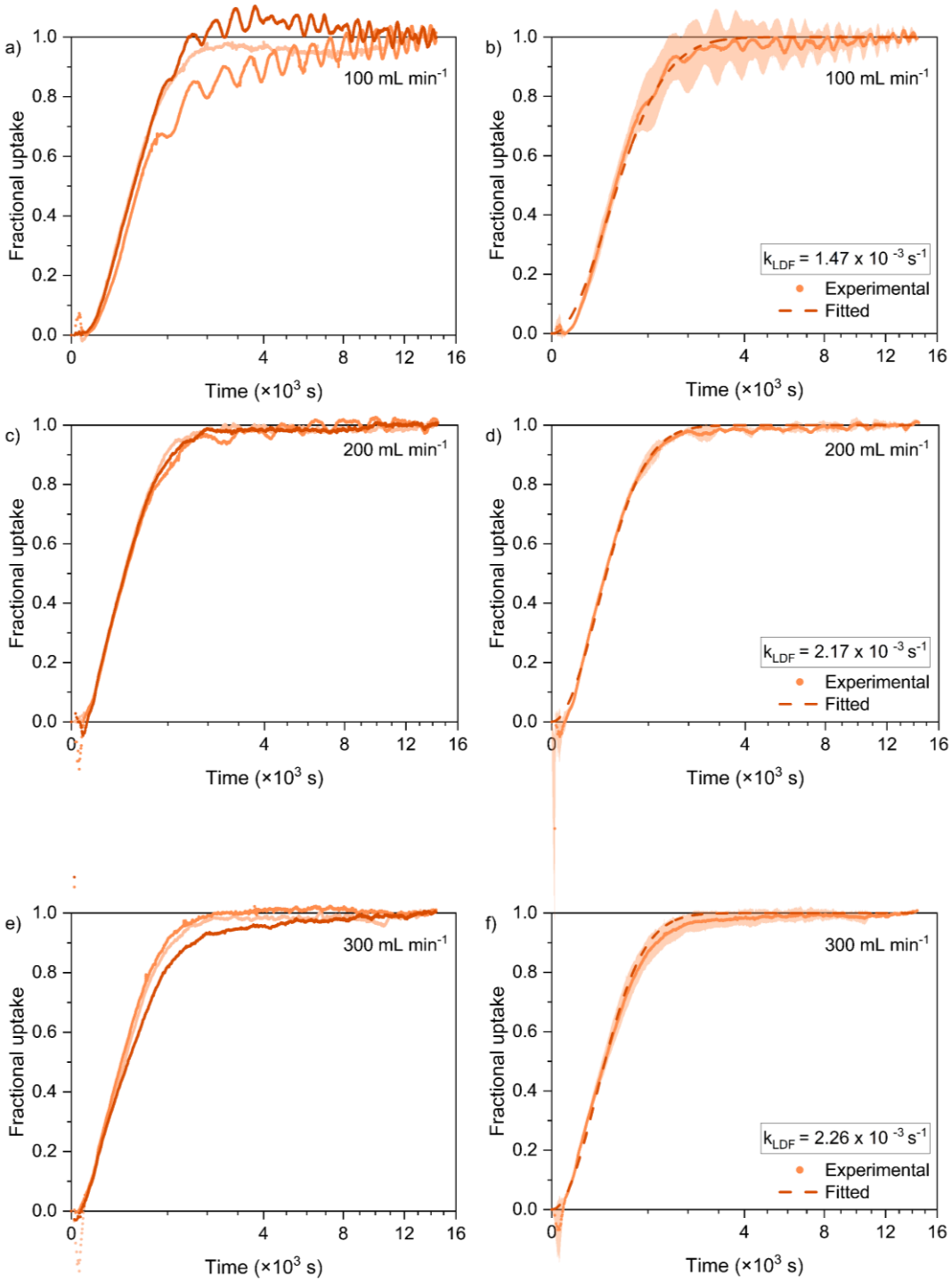


Figure A6.1. a), c), e) Experimental fractional uptake curves (filled circles) for Purolite measured three times at 60 °C using total flowrates of 100 mL min^{-1}, 200 mL min^{-1}, and 300 mL min^{-1}, respectively. b), d), f) Averaged fractional uptake curve (filled circles) with shaded areas showing the corresponding standard deviation at each time point and dashed lines showing the fitting results. Time is plotted on a square root scale for clarity.

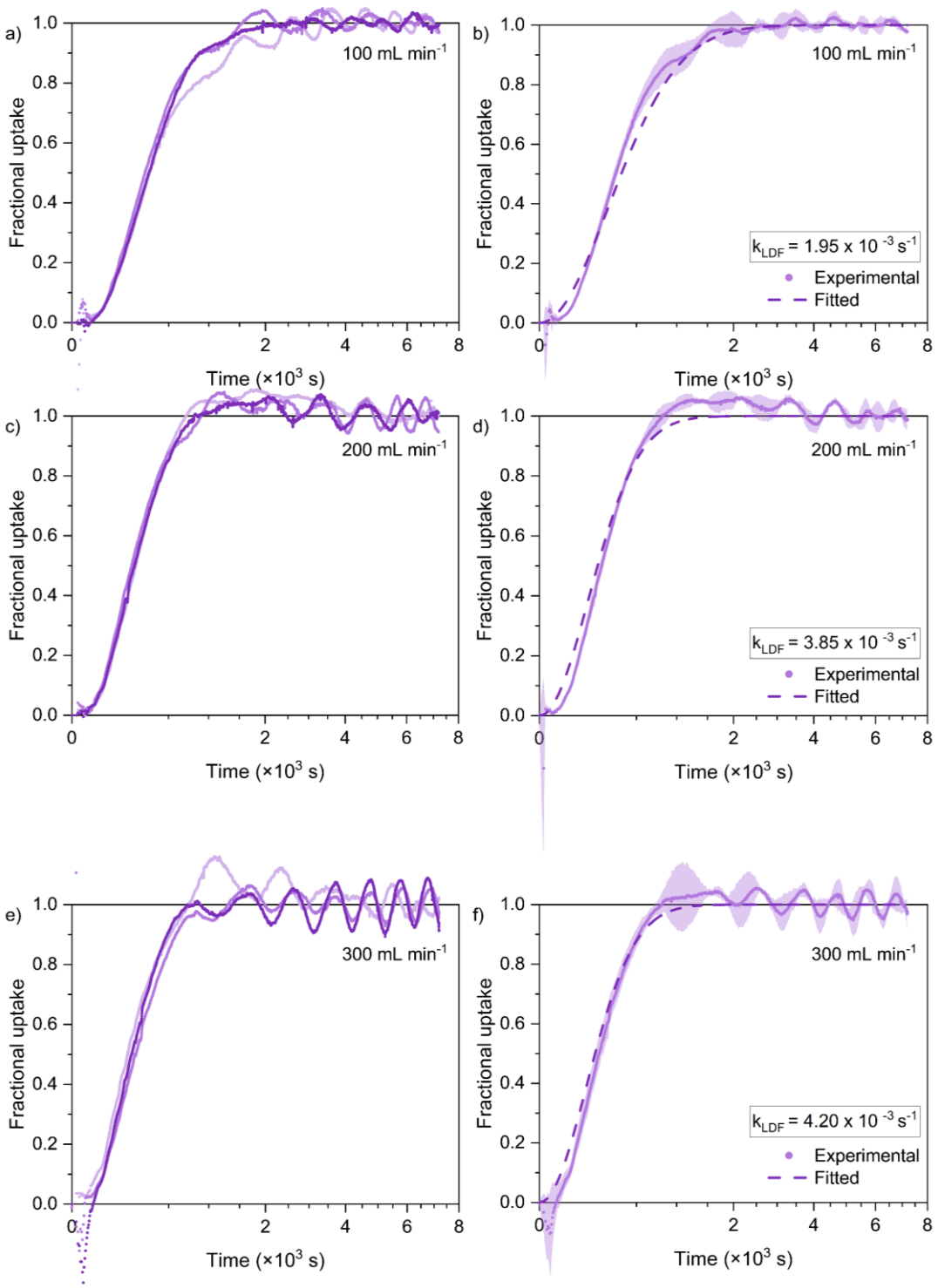


Figure A6.2. a), c), e) Experimental fractional uptake curves (filled circles) for TIFSIX-3-Ni measured three times at 60 °C using total flowrates of 100 mL min^{-1}, 200 mL min^{-1}, and 300 mL min^{-1}, respectively. b), d), f) Averaged fractional uptake curve (filled circles) with shaded areas showing the corresponding standard deviation at each time point and dashed lines showing the fitting results. Time is plotted on a square root scale for clarity.

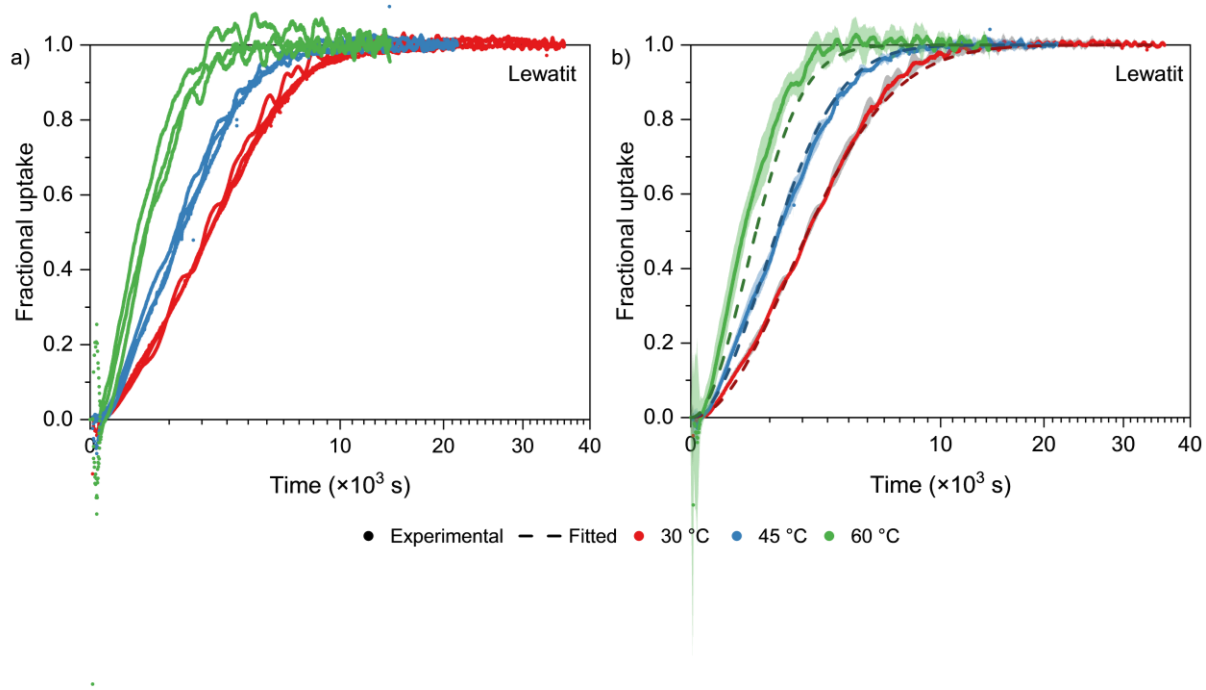


Figure A6.3. a) Experimental fractional uptake curves measured for Lewatit at 30 °C, 45 °C, and 60 °C, with three measurements performed at each temperature. b) Averaged fractional uptake curves at 30 °C, 45 °C, and 60 °C, with shaded areas showing the corresponding standard deviation at each time point and dashed lines showing the fitting results. Time is plotted on a square root scale for clarity.

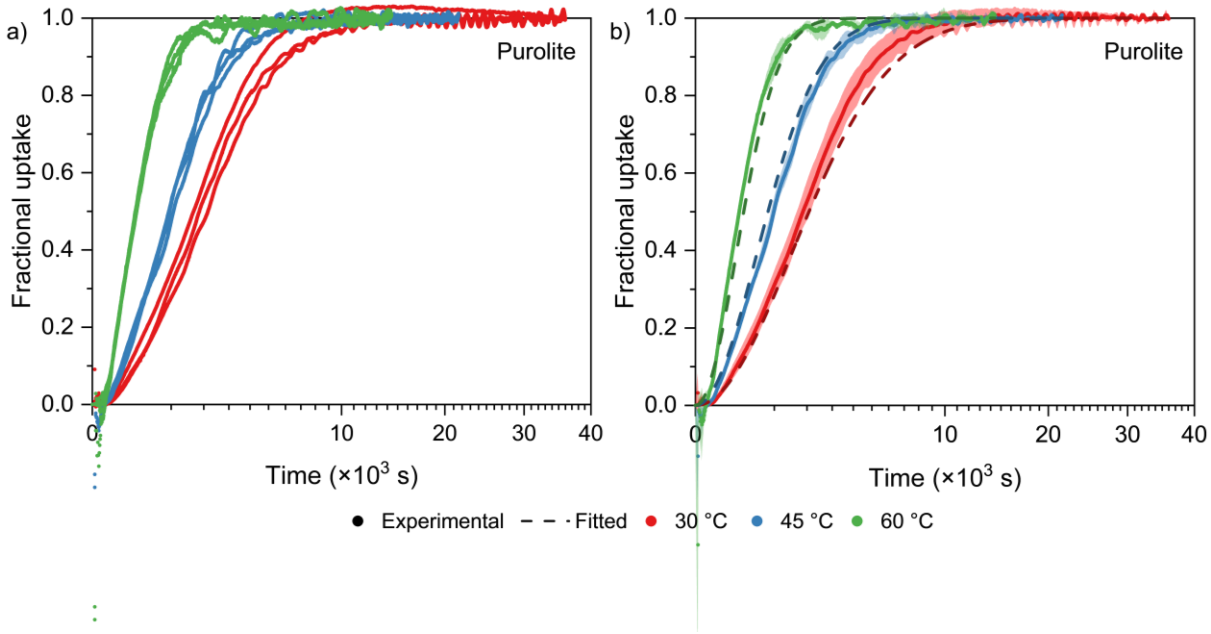


Figure A6.4. . a) Experimental fractional uptake curves measured for Purolite at 30 °C, 45 °C, and 60 °C, with three measurements performed at each temperature. b) Averaged fractional uptake curves at 30 °C, 45 °C, and 60 °C, with shaded areas showing the corresponding standard deviation at each time point and dashed lines showing the fitting results. Time is plotted on a square root scale for clarity.

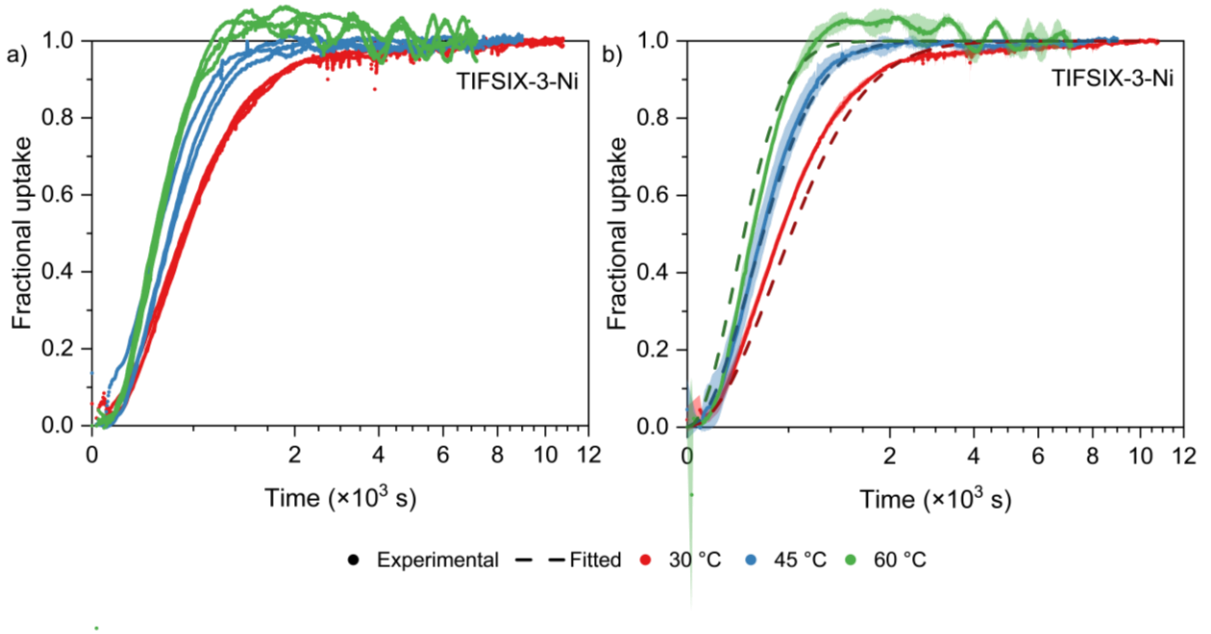


Figure A6.5. a) Experimental fractional uptake curves measured for TIFSIX-3-Ni at 30 °C, 45 °C, and 60 °C, with three measurements performed at each temperature. b) Averaged fractional uptake curves at 30 °C, 45 °C, and 60 °C, with shaded areas showing the corresponding standard deviation at each time point and dashed lines showing the fitting results. Time is plotted on a square root scale for clarity.

Check for near isothermal conditions

According to Brandani and Mangano, near isothermal conditions are achieved when the dimensionless group Γ, given by equation (A6.1), is less than 1 [1].

$$\Gamma = \frac{\Delta H^2}{R_g T_0^2} \cdot \frac{F c_0}{3 k_T V_s} \cdot R_p^2 \quad \text{(A6.1)}$$

ΔH is the heat of adsorption, R_g is the ideal gas constant, T_0 is the initial temperature, F is the volumetric gas flowrate, c_0 is the initial gas (i.e. CO_2) concentration, k_T is the carrier gas (i.e. He) thermal conductivity, V_s is the volume of the solid calculated by dividing the sample mass by the adsorbent particle density, and R_p is the adsorbent particle radius. The parameter values shown in Table A6.1 were used to calculate Γ for an experiment conducted at 30 °C, 200 mL min^{-1} total flowrate, and 400 ppm CO_2 using Lewatit, which has a particle density of 0.74 g cm^{-3} and heat of adsorption of 81 kJ mol^{-1} at the loading level corresponding to 400 ppm CO_2 [2]. I assumed a sample mass of 27 mg and particle radius of 0.5 mm.

Using these values, Γ is ~ 7.0×10^{-3}. Since the input parameters for other temperatures, flowrates, and adsorbents would be on the same order of magnitude as those shown in Table A6.1, we can assume that Γ is less than 1 for all the conducted experiments, and we are therefore operating at near isothermal conditions.

Table A6.1. Parameter values for a kinetic sorption measurement conducted at 30 °C, 200 mL min^{-1} total flowrate, and 400 ppm CO_2 using Lewatit.

Parameter	**Unit**	**Value**
ΔH	J mol^{-1}	81×10^3
R_g	J K^{-1} mol^{-1}	8.314
T_0	K	303
F	m^3 s^{-1}	3.3×10^{-6}
c_0	mol m^{-3}	1.6×10^{-2}
k_T	W m^{-1} K^{-1}	0.15 [318]
V_s	m^3	3.6×10^{-8}
R_p	m	0.50×10^{-3}

Error propagation for $k_{LDF}(T)$ calculations

Uncertainty bounds for a 95% confidence interval for $k_{LDF}(T)$ were calculated using equation (A6.2) between temperatures of 20 °C to 70 °C:

$$\sigma_k = \sqrt{\sigma_a^2 e^{\left(2a-\frac{2b}{RT}\right)} + \frac{\sigma_b^2 e^{\left(2a-\frac{2b}{RT}\right)}}{R^2T^2}} \qquad \text{(A6.2)}$$

where σ_k, σ_a, and σ_b are the 95% confidence interval half-widths for k_{LDF}, $\ln(k_0)$, and E_a, respectively, and a and b are the fitted parameter values for $\ln(k_0)$, and E_a, respectively.

TGA equilibrium loading calculations

The equilibrium loadings of the TGA measurements done at 30 °C, 45 °C, and 60 °C with a total flowrate of 200 mL min^{-1} of 400 ppm CO_2 balanced with He were calculated using the following procedure:

1. For each measurement, the mass of the dried sample (in g) is determined by subtracting the absolute value of the TGA mass reading when CO_2/He is first introduced (i.e. beginning of step 3 as described in Section 8.2.2) from the initial sample mass.
2. The mass of CO_2 adsorbed (in g) is extracted from m_{final} from equation (8.4) shown in Section 8.2.3.
3. The amount of CO_2 adsorbed is converted to units of mmol using the molar mass of CO_2 (0.04401 g $mmol^{-1}$)
4. The CO_2 loading per gram of dried sample can be determined by dividing step 4 by step 1.

Isotherm model equilibrium loadings

CO_2 loadings at 400 ppm (i.e. 0.4 mbar) and 30 °C, 45 °C, and 60 °C were calculated from the CO_2 isotherm fitting model parameters determined for each adsorbent in Chapters 5 and 6 [2, 3]. Uncertainty bounds on the loading values were determined using Monte Carlo error propagation of the uncertainty bounds of the fitted parameters. 100,000 samples were used for the Monte Carlo error propagation, and the samples were taken from a uniform distribution. The random number generator in MATLAB was reset using the "rng default" command prior to the sampling.

CO_2 isotherms for Lewatit and Purolite were fitted to the Chemi-Physisorption (CP) isotherm model given by equations (A6.3) to (A6.6), with fitted parameters and corresponding uncertainty bounds for a 95% confidence interval provided in Table A6.2.

$$n = n_{phys} + n_{chem} \cdot \eta = \left[\frac{q_\infty(T) \cdot b_p(T) \cdot P}{\left[1+\left(b_p(T) \cdot P\right)^{\tau(T)}\right]^{\frac{1}{\tau(T)}}}\right]_{phys} + \left[\frac{q_{\infty,c} \cdot b_c(T) \cdot P}{1+b_c(T) \cdot P}\right]_{chem} \cdot \exp\left(\frac{-E_a}{RT}\right) \quad \text{(A6.3)}$$

$$q_\infty(T) = q_{\infty,0} \cdot \exp\left[\chi\left(1 - \frac{T}{T_0}\right)\right] \quad \text{(A6.4)}$$

$$b(T) = b_0 \cdot \exp\left(\frac{-\Delta U}{RT}\right) \quad \text{(A6.5)}$$

$$\tau(T) = \tau_0 + \alpha\left(1 - \frac{T_0}{T}\right) \quad \text{(A6.6)}$$

P is the pressure, T is the temperature, $q_\infty(T)$ *and* $q_{\infty,c}$ are the maximum CO_2 capacities associated with physisorption and chemisorption, respectively, E_a is the activation energy, $q_{\infty,0}$ is the maximum CO_2 capacity at the reference temperature T_0, $b(T)$ is the CO_2 adsorption coefficient defined by a constant b_0 and the internal energy change during adsorption ΔU, R is the universal gas constant, $\tau(T)$ is the surface heterogeneity parameter, τ_0 is the surface heterogeneity parameter at T_0, and χ and α are factors determining the temperature dependencies of $q_\infty(T)$ and $\tau(T)$.

Table A6.2. Fitting parameters with uncertainty bounds for a 95% confidence interval for the CP isotherm model for CO_2 adsorption for Lewatit and Purolite.

Equation	Parameter	Unit	Lewatit	Purolite
CP	$q_{\infty,0}$	mmol g^{-1}	2.5649 ± 0.0112	2.9094 ± 0.0189
	$b_{0,p}$	(× 10^{-14}) bar^{-1}	1.0481 ± 0.0340	0.95981 ± 0.04947
	$-\Delta U_p$	kJ mol^{-1}	105.51 ± 0.09	105.23 ± 0.14
	T_0	K	298.15	298.15
	τ_0	-	0.34307 ± 0.00177	0.40143 ± 0.00360
	α	-	1.3867 ± 0.0384	1.9943 ± 0.0951
	χ	-	1.6364 ± 0.0535	2.5219 ± 0.0864
	$q_{\infty c}$	mmol g^{-1}	1.0509 ± 0.0259	3.5580 ± 0.0910
	$b_{0,c}$	(× 10^{-2}) bar^{-1}	1.0335 ± 0.0524	21.190 ± 1.370
	$-\Delta U_c$	kJ mol^{-1}	13.496 ± 0.137	6.9953 ± 0.1802
	E_a	kJ mol^{-1}	0.60049 ± 0.06427	3.1302 ± 0.0696

CO_2 isotherms for TIFSIX-3-Ni were fitted to the dual-site Langmuir isotherm model given by equations (A6.7) to (A6.9), with fitted parameters and corresponding uncertainty bounds for a 95% confidence interval provided in Table A6.3.

$$n = \frac{q_{s1} \cdot b_1(T) \cdot P}{1 + b_1(T) \cdot P} + \frac{q_{s2} \cdot b_2(T) \cdot P}{1 + b_2(T) \cdot P} \qquad \text{(A6.7)}$$

$$b_1(T) = b_{0,1} \cdot \exp\left(\frac{-\Delta U_1}{RT}\right) \qquad \text{(A6.8)}$$

$$b_2(T) = b_{0,2} \cdot \exp\left(\frac{-\Delta U_2}{RT}\right) \qquad \text{(A6.9)}$$

T is the temperature, P is the pressure, q_{s1} and q_{s2} are the maximum CO_2 capacities, $b_1(T)$ and $b_2(T)$ are the CO_2 adsorption coefficients defined by constant $b_{0,1}$ and $b_{0,2}$ and the internal energy change during adsorption ΔU_1 and ΔU_2, respectively, and R is the universal gas constant.

Table A6.3. Fitting parameters with uncertainty bounds for a 95% confidence interval for the DSL, isotherm model for CO_2 adsorption on TIFSIX-3-Ni.

Equation	**Parameter**	**Unit**	**TIFSIX-3-Ni**
DSL	q_{s1}	mmol g^{-1}	0.38737 ± 0.02037
	$b_{0,1}$	($\times 10^{-5}$) bar^{-1}	3.4932 ± 0.4670
	$-\Delta U_1$	kJ mol^{-1}	29.256 ± 0.360
	q_{s2}	mmol g^{-1}	1.8730 ± 0.0085
	$b_{0,2}$	($\times 10^{-7}$) bar^{-1}	1.2200 ± 0.0355
	$-\Delta U_2$	kJ mol^{-1}	59.798 ± 0.079

A6. References

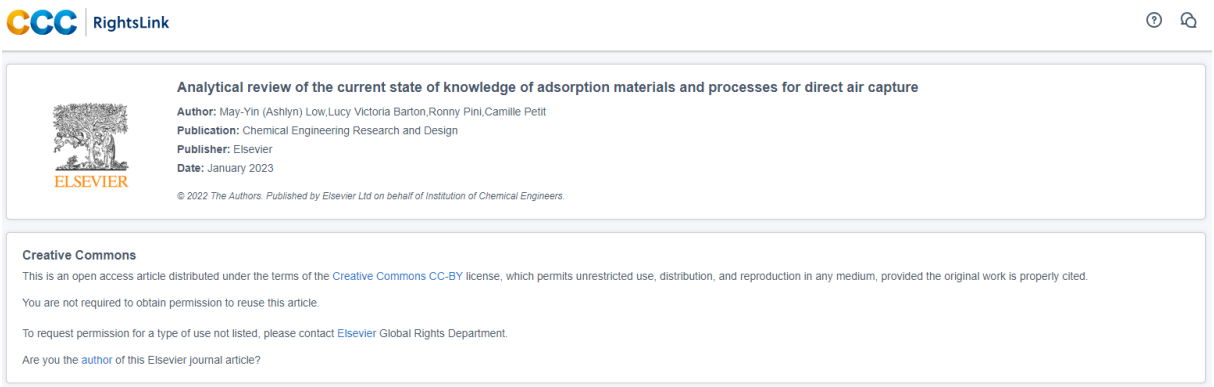
[1] S. Brandani and E. Mangano, "The zero length column technique to measure adsorption equilibrium and kinetics: lessons learnt from 30 years of experience," *Adsorption,* vol. 27, no. 3, pp. 319-351, 2020, doi: 10.1007/s10450-020-00273-w.

[2] M.-Y. Low, D. Danaci, H. Azzan, R. T. Woodward, and C. Petit, "Measurement of Physicochemical Properties and CO_2, N_2, Ar, O_2, and H_2O Unary Adsorption Isotherms of Purolite A110 and Lewatit VP OC 1065 for Application in Direct Air Capture," *J Chem Eng Data,* vol. 68, no. 12, pp. 3499-3511, Dec 14 2023, doi: 10.1021/acs.jced.3c00401.

[3] M.-Y. Low *et al.*, "Physicochemical properties, equilibrium adsorption performance, manufacturability, and stability of TIFSIX-3-Ni for direct air capture," *ChemRxiv,* 2024, doi: 10.26434/chemrxiv-2024-r5qsk.

Appendix 7. Copyrights and permissions

[1] M.-Y. Low, L. V. Barton, R. Pini, and C. Petit, "Analytical review of the current state of knowledge of adsorption materials and processes for direct air capture," *Chemical Engineering Research and Design,* vol. 189, pp. 745-767, 2023, doi: 10.1016/j.cherd.2022.11.040.



CCC RightsLink

Analytical review of the current state of knowledge of adsorption materials and processes for direct air capture

Author: May-Yin (Ashlyn) Low,Lucy Victoria Barton,Ronny Pini,Camille Petit
Publication: Chemical Engineering Research and Design
Publisher: Elsevier
Date: January 2023

© 2022 The Authors. Published by Elsevier Ltd on behalf of Institution of Chemical Engineers.

Creative Commons

This is an open access article distributed under the terms of the Creative Commons CC-BY license, which permits unrestricted use, distribution, and reproduction in any medium, provided the original work is properly cited.

You are not required to obtain permission to reuse this article.

To request permission for a type of use not listed, please contact Elsevier Global Rights Department.

Are you the author of this Elsevier journal article?

[2] M.-Y. Low, D. Danaci, H. Azzan, R. T. Woodward, and C. Petit, "Measurement of Physicochemical Properties and CO_2, N_2, Ar, O_2, and H_2O Unary Adsorption Isotherms of Purolite A110 and Lewatit VP OC 1065 for Application in Direct Air Capture," *J Chem Eng Data,* vol. 68, no. 12, pp. 3499-3511, Dec 14 2023, doi: 10.1021/acs.jced.3c00401.

Measurement of Physicochemical Properties and CO_2, N_2, Ar, O_2, and H_2O Unary Adsorption Isotherms of Purolite A110 and Lewatit VP OC 1065 for Application in Direct Air Capture

May-Yin Ashlyn Low, David Danaci, Hassan Azzan, Robert T. Woodward, and Camille Petit*

Cite this: *J. Chem. Eng. Data* 2023, 68, 12, 3499–3511
Publication Date: October 11, 2023
https://doi.org/10.1021/acs.jced.3c00401
Copyright © 2023 The Authors. Published by American Chemical Society. This publication is licensed under CC-BY 4.0.
Open Access

Article Views 3125 | Altmetric 18 | Citations 1
LEARN ABOUT THESE METRICS

Share Add to Export RIS

CC BY 4.0 DEED
Attribution 4.0 International

Canonical URL : https://creativecommons.org/licenses/by/4.0/

See the legal code

You are free to:

Share — copy and redistribute the material in any medium or format for any purpose, even commercially.

Adapt — remix, transform, and build upon the material for any purpose, even commercially.

The licensor cannot revoke these freedoms as long as you follow the license terms.

Under the following terms:

Attribution — You must give appropriate credit , provide a link to the license, and indicate if changes were made . You may do so in any reasonable manner, but not in any way that suggests the licensor endorses you or your use.

No additional restrictions — You may not apply legal terms or technological measures that legally restrict others from doing anything the license permits.

Notices:

You do not have to comply with the license for elements of the material in the public domain or where your use is permitted by an applicable exception or limitation .

No warranties are given. The license may not give you all of the permissions necessary for your intended use. For example, other rights such as publicity, privacy, or moral rights may limit how you use the material.

[3] M.-Y. Low *et al.*, "Physicochemical properties, equilibrium adsorption performance, manufacturability, and stability of TIFSIX-3-Ni for direct air capture," *ChemRxiv,* 2024, doi: 10.26434/chemrxiv-2024-r5qsk.



Physicochemical properties, equilibrium adsorption performance, manufacturability, and stability of TIFSIX-3-Ni for direct air capture

21 March 2024, Version 1

Working Paper

May-Yin (Ashlyn) Low, David Danaci, Hassan Azzan, Amanda Lim Jiayi, Gordon Wu Shun Yong, Ioanna Itskou, Camille Petit

Show author details

This content is a preprint and has not undergone peer review at the time of posting.

Version History

Mar 21, 2024 Version 1

Metrics

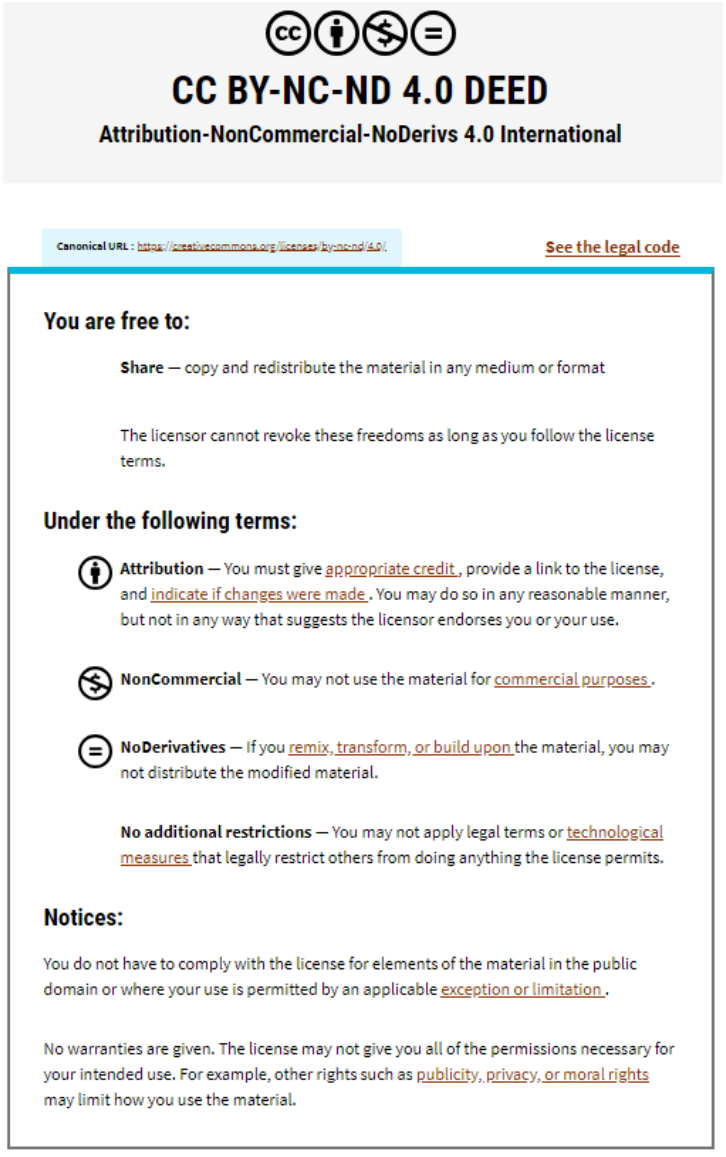
7

336 Views
221 Downloads
0 Citations

License

CC BY NC ND

The content is available under CC BY NC ND 4.0



CC BY-NC-ND 4.0 DEED

Attribution-NonCommercial-NoDerivs 4.0 International

Canonical URL : https://creativecommons.org/licenses/by-nc-nd/4.0/

See the legal code

You are free to:

Share — copy and redistribute the material in any medium or format

The licensor cannot revoke these freedoms as long as you follow the license terms.

Under the following terms:

Attribution — You must give appropriate credit , provide a link to the license, and indicate if changes were made . You may do so in any reasonable manner, but not in any way that suggests the licensor endorses you or your use.

NonCommercial — You may not use the material for commercial purposes .

NoDerivatives — If you remix, transform, or build upon the material, you may not distribute the modified material.

No additional restrictions — You may not apply legal terms or technological measures that legally restrict others from doing anything the license permits.

Notices:

You do not have to comply with the license for elements of the material in the public domain or where your use is permitted by an applicable exception or limitation .

No warranties are given. The license may not give you all of the permissions necessary for your intended use. For example, other rights such as publicity, privacy, or moral rights may limit how you use the material.